SODIUM-NaK ENGINEERING HANDBOOK

Volume V

SODIUM-NaK ENGINEERING HANDBOOK

VOLUME I SODIUM CHEMISTRY and PHYSICAL PROPERTIES

Chap. 1 Physical Properties
Chap. 2 Chemistry

VOLUME II SODIUM FLOW, HEAT TRANSFER, INTERMEDIATE HEAT EXCHANGERS, and STEAM GENERATORS

Chap. 1 Fluid Mechanics of Liquid Metals
Chap. 2 Liquid-Metal Heat Transfer
Chap. 3 Intermediate Heat Exchangers (IHX's)
Chap. 4 Steam Generators

VOLUME III SODIUM SYSTEMS, SAFETY, HANDLING, and INSTRUMENTATION

Chap. 1 Sodium and NaK Systems
Chap. 2 Safety
Chap. 3 Handling
Chap. 4 Instruments

VOLUME IV SODIUM PUMPS, VALVES, PIPING, and AUXILIARY EQUIPMENT

Chap. 1 Pumps
Chap. 2 Bearings and Seals
Chap. 3 Valves
Chap. 4 Vessels and Piping
Chap. 5 Auxiliary Equipment and System Accessories

VOLUME V SODIUM PURIFICATION, MATERIAL, HEATERS, COOLERS, and RADIATORS

Chap. 1 Purification
Chap. 2 Effects on Materials
Chap. 3 Heaters and Coolers
Chap. 4 Radiators, Condensers, and Boilers
Chap. 5 Applications

Each volume includes an index for that volume.

SODIUM-NaK ENGINEERING HANDBOOK

Volume V

Sodium Purification, Material, Heaters, Coolers, and Radiators

O. J. FOUST, Editor
Director, Engineering
Liquid Metal Engineering Center

Prepared under the auspices of the
Division of Reactor Research and Demonstration
United States Department of Energy

GORDON AND BREACH, SCIENCE PUBLISHERS, INC.
New York London Paris

Gordon and Breach Science Publishers Ltd.
42 William IV Street
London WC2N 4DE, England

Gordon & Breach
7-9 rue Emile Dubois
75014 Paris, France

Library of Congress Cataloging in Publication Data

Foust, O J
Sodium-Nak engineering handbook

"Prepared under the auspices of the Division of Rector Development and Technology, United States Atomic Energy Commission."
Includes bibliographical references and index.
CONTENTS: v. 1 Sodium chemistry and physical properties.
v. 2 Sodium flow, heat transfer, intermediate heat exchangers and steam generators.
v. 3 Sodium systems, safety, handling, and instrumentation.
1. Liquid metals—Handbooks, manuals, etc. 2. Sodium—handbooks, manuals, etc. 3. Potassium—Handbooks, manuals, etc. 4. Liquid metal cooled reactors—Handbooks, manuals, etc. I. Title.
v. 4 Sodium pumps, valves, piping and auxiliary equipment.
1. Liquid metals—Handbooks, manuals, etc. 2. Sodium—handbooks, manuals, etc. 3. Potassium—Handbooks, manuals, etc. I. Title.
v. 5 Sodium purification, material, heaters, coolers, and radiators.
1. Liquid metals—Handbooks, manuals, etc. 2. Sodium—Handbooks, manuals, etc. 3. Heat exchangers—Handbooks, manuals, etc.

TK9151.F68 621.48'33 70-129473
0 677 03060 6

Printed in the United States of America

Preface

Since publication of the *Sodium–NaK Supplement* to the *Liquid Metals Handbook* in 1955, liquid metal technology has expanded in depth, in spectra, and in the size of equipment that has been developed. Even so, further expansion is needed to satisfy the requirements of the Liquid Metals Fast Breeder Program. Reliable components, with engineering capabilities up to an order of magnitude greater than those developed to date, are required, an expansion of capability beyond the mere extrapolation of laboratory devices.

The capability increase now demanded renders the admonition contained in the Foreword to the 1955 supplement that only test will demonstrate satisfactory performance of a component constructed for an advanced technology as vital now as it was in 1955. Testing alone can demonstrate that all facets of sound engineering have been incorporated into the design and manufacture of the final product.

Through the technology described in this *Sodium–NaK Engineering Handbook,* it is hoped that designers will have a basis for freeing their imaginations from the bonds of small-scale experience and create systems and components which incorporate the lessons of the past into the industrial requirements of the future.

Robert W. Dickinson, Director
Liquid Metal Engineering Center

Editor's Preface

This handbook, comprised of five volumes, is intended for use by present and future designers in the Liquid Metals Fast Breeder Reactor (LMFBR) Program and by the engineering and scientific community performing other type investigation and experimentation requiring high-temperature sodium and NaK technology. The arrangement of subject matter progresses from a technological discussion of sodium and sodium–potassium alloy (NaK) to discussions of various categories and uses of hardware in sodium and NaK systems.

Emphasis is placed on sodium and NaK as heat-transport media; other applications of these metals are treated in the final volume. Several thousand documents were reviewed in accumulating and compiling information; those believed to be most valuable are cited as references.

Sufficient detail is included for basic understanding of sodium and NaK technology and of technical aspects of sodium and NaK components and instrument systems. Information presented is considered adequate for use in feasibility studies and conceptual design, sizing components and systems, developing preliminary component and system descriptions, identifying technological limitations and problem areas, and defining basic constraints and parameters. Preparation of a finished design, however, will require more extensive research into the reference literature.

The handbook includes the work of some 50 contributors; the efforts of each were coordinated to facilitate an end product with a common theme, each part consistent in perspective with the whole, but considerable individual license was permitted in presentation of that material. Therefore each volume and chapter reflects the style of its author and, to this extent, differs from other volumes and chapters.

In many instances, the data from various sources were in conflict and the authors had no basis for selecting those which were most valid. In such instances explanations and references are supplied in sufficient detail to permit the reader to perform independent research. Attention is invited to the existence of the Liquid Metals Information Center, located at the Liquid Metal Engineering Center, as a continuing source of current information.

O. J. Foust

Note to Reader

The reader is advised that, although the publication of this volume is in the late 1970's, the material in it was written in 1968. Although most of the information is still valid and useful, on certain topics the material is appreciably out of date. Therefore more recent publications should be consulted for the current status of some topics.

Contents

Chapter 1
Purification

R. B. HINZE

1-1 INTRODUCTION

The performance of a liquid-metal heat-transfer system can be seriously impaired by the presence of impurities in the coolant. Impurities can cause plugging, which interferes with coolant flow, and also detrimental changes in the properties of structural materials used to contain the liquid metal. Hence impurity concentration must be controlled.

Many impurities are controlled by procurement specification and by exclusion of the impurity from the liquid-metal system. For certain impurities (e.g., oxygen) this is impractical. In these cases purification-process equipment in the heat-transfer system is used to control impurity concentration.

Purification is an important part of the successful design and utilization of a sodium or NaK heat-transfer system. Purification considerations must be an integral part of the engineering effort beginning with conceptual design and continuing through piping and component manufacture and installation, plant start-up, and operation of the heat-transfer system.

In this chapter significant impurities and their sources are identified. The effects of impurities on heat-transfer systems are briefly reviewed to emphasize the necessity for sodium purification. General guidance is presented for the preparation of sodium purity requirements for particular applications.

Chemical and physical principles of the various purification methods are reviewed. The concept of saturation temperature is discussed, and the relation of saturation temperature to plugging temperature is noted. The important historical fact that almost all impurity experience has been based on plugging temperature observations, rather than on results of chemical analysis for specific impurities, is stressed. The significance of this fact and the need to be aware of the applicable impurity solubility relation in interpretation of the literature are discussed. The difference between three of the existing relations for solubility of oxygen in sodium is

emphasized.

Purification methods and equipment applicable to engineering-scale systems are described and discussed. Problems encountered with existing equipment are identified, and guidance in their solution is presented. Finally, application of these methods and equipment to sodium heat-transfer systems is outlined.

Purification principles and general information reported for sodium are also applicable to NaK unless otherwise noted.

1-2 IMPURITIES

Impurities in the sodium or NaK used in a heat-transfer system, in either a nuclear or a nonradioactive environment, can have deleterious effects on the performance and reliability of the heat-transfer system and, in some cases, on other systems (e.g., the neutron balance in a reactor). Impurities can be present as contaminants in manufactured sodium or as the result of contact with other materials (including gases) during storage, handling, and use of the liquid metal. Impurity sources are discussed in Sec. 1-2.1.

Certain impurity effects are of concern in any heat-transfer system, whether nuclear or nonnuclear. Oxygen, carbon, hydrogen and nitrogen can contribute to metallurgical changes in structural members and fuel-element cladding that affect performance, service life and reliability. Contamination with oxygen, carbon, hydrogen, and calcium can result in the formation of compounds that precipitate in sodium. These precipitates can collect, forming plugs that interfere with normal coolant flow, and can prevent the satisfactory operation of mechanical devices submerged in the liquid metal. The effect of sodium oxide precipitation on heat-transfer surfaces is discussed in Vol. II, Sec. 2-15.3. Corrosion products and certain miscellaneous impurities also may require control.

Nuclear effects must be considered when liquid metals are used to cool reactors. The possible effect of carbon and hydrogen on the neutron-moderation process in the reactor core should be evaluated. The concentration of neutron-absorbing elements and fission products in the coolant may require control.

Inert gases, such as helium and argon, dissolved or entrained in sodium might be considered impurities. Gases can collect in a system and affect coolant-flow distribution and hence the performance of heat-transfer surfaces. Gas bubbles passing through a nuclear core can cause reactor period perturbations if the reactor void coefficient is significant. Heat-transfer effects are noted in Vol. II, Sec. 2-15.2. Argon-gas transfer from the free surface of NaK in a surge tank to other places in a piping loop has been reported [1]; the transfer resulted from the differential temperature solubility of argon in NaK. Problems of this nature arising from the presence of gas in the liquid metal are considered system design problems; solutions to these problems are not discussed here.

1-2.1 *Sources*

Common sources of impurities are summarized in Table 1.1.

Possible additional sources of carbon are:

1. Cutting fluids swept in from improperly cleaned gas lines.
2. Leakage of organic lubricants in pumps.
3. Leakage of organic service coolant, if such a coolant is used.
4. Decarburization of pipe or other structural materials, e.g., ferritic steel.
5. Graphite in or adjacent to the core.

Hydrocarbons in items 1 to 3 are also sources of hydrogen. Hydrogen is released by the decomposition of zirconium

TABLE 1.1 -Impurity Sources

Source	Impurity
Impurity in manufactured sodium	Oxygen, carbon,* hydrogen, nitrogen, calcium,† neutron-absorbing elements≠
Added during shipping§ and precharge handling	Oxygen,¶ carbon,¶,** hydrogen,¶,†† nitrogen
Contamination on surface of as-installed piping or components	Oxygen,≠≠ carbon, hydrogen,≠≠ neutron-absorbing elements
Impurities in purge and cover gas	Oxygen, carbon,§§ hydrogen,†† nitrogen
Air in-leakage through seals or during fuel-handling, maintenance, and repair operations	Oxygen, carbon,§§ hydrogen,†† nitrogen
Decomposition of organic compounds that may enter the system	Carbon, hydrogen
Decomposition of water that may enter the system	Oxygen, hydrogen

*Carbon is derived from the graphite electrodes used in the fused-salt electrolytic manufacturing process.

†Calcium is present in manufactured sodium as a result of calcium chloride additions used to reduce the melting point of molten sodium chloride in the electrolytic cell. The removal of calcium to low levels (10 to 20 ppm) represents the major difference between commercial- and reactor-grade sodium. If enough oxygen is available in the sodium to react (e.g., in a charge tank) with all the calcium present, all the calcium can be oxidized to form insoluble calcium oxide. Calcium oxide can be removed by filtration prior to charging the sodium to the system. However, if the specified or inherent oxygen content is low, this technique will not remove all the calcium. Consequently it is important to specify a low calcium concentration when the oxygen content will be low, e.g., in tank car or drum shipment as opposed to sodium received in brick form.

≠Neutron-absorbing elements include both neutron poisons and elements whose neutron-activation products pose potential accessibility problems [2].

§A residual "heel" of approximately 1000 lb of sodium remains in tank cars after unloading. This residual sodium is not normally removed if the car is to be used to transport commercial-grade sodium. Consequently impurities from several shipments can accumulate in the heel. When reactor-grade sodium is to be shipped, the heel normally is removed so that sodium unloaded from the car will meet the purity requirements of reactor-grade sodium.

¶Atmospheric contaminants are more prevalent in brick sodium than in sodium cast in drums or delivered in tank cars because of relative exposure to air during handling.

**Carbon is derived from organic film on container walls.

††Hydrogen is in the form of water vapor.

≠≠Oxygen and hydrogen are in the form of liquid water.

§§Carbon is in the form of oxides of carbon.

hydride in reactors containing this compound as a moderator material. It is possible that nitrogen can enter a system by diffusion through austenitic-stainless-steel piping walls at 1100 to 1200°F [3]. It has been postulated that hydrogen formed on the water side of steam generators diffuses through tube walls and enters secondary-system sodium [4].

Improper or careless precleaning of the system can result in residual dirt, grease or oil, metal chips, weld slag, surface oxides, moisture, etc., which can be major sources of contamination, contributing to the oxygen, hydrogen, carbon, and insolubles content of the sodium. Precleaning methods are discussed in Vol. IV, Chap. 4, and in Ref. 5; even with the use of good precleaning methods, however, there will be some residual-metal surface oxides and adsorbed gases. Although occurrences are rare, foreign materials other than water and the organic compounds noted in Table 1.1 can be inadvertently introduced into sodium systems during operation or maintenance (e.g., lead shot, calcium carbonate, or other materials normally used to control liquid-metal fires outside piping systems).

Despite the use of clad fuel elements, reactor coolant systems become contaminated with fission products as a result of minor cladding defects and cracks or other failures. The use of open (vented) fuel elements, which is being considered for the liquid-metal fast breeder reactor (LMFBR), would result in an increase of orders of magnitude in fission-product concentration in the coolant.

Corrosion products are present in liquid-metal systems operating at temperatures of interest for electrical power generation [2]; i,e., above 700°F. Concentration of corrosion products in the coolant are quite small because these products are deposited at locations in the system where their chemical activity is less than at the corrosion site.

1-2.2 *Effects*

(a) *Plugging*

Mechanical difficulties are caused by excessive amounts of oxygen and other elements that have decreased solubility at low temperatures. Sodium compounds of these elements, e.g., sodium oxide and sodium hydride, precipitate as solids and deposit whenever the temperature is less than the saturation temperature for the compound. (Definitions and usage of the terms "saturation temperature" and "plugging temperature" are noted in Sec. 1-3.1.) Formation of these deposits can impede coolant flow and interfere with the operation of mechanical devices submerged in sodium. The consequences of such plugging must be carefully considered in the design of the system and in maintenance of system-coolant purity.

Experience with operating reactors and with nonnuclear test facilities containing normal sodium-piping design features demonstrated that maintenance of a saturation temperature of 300°F or less as determined by a plugging meter is adequate to prevent oxide and hydride plugging [6]. An example of such a sodium-piping feature is the location of the first block valve in a branch line close to the mainstream tee so that the temperature at the block valve exceeds saturation temperature. Another example is the provision of controlled electric heaters on an instrument-connecting pipe to maintain temperature greater than the saturation temperature.

Plugging can also be caused by oxides of elements that can reduce sodium oxide, e.g., calcium oxide and magnesium oxide [7]. Hydrocarbons in contact with sodium form residues that can contribute to plugging [8]. Other insoluble matter, notably metal chips and weld slag, can cause plugging.

Large quantities of mercury, more than 30 at.%, can cause plugging through the formation of intermetallic compounds with melting points higher than sodium

(see Vol. I, Fig. 2.25).

(b) *On Stainless and Ferritic Steels*

A brief introduction to the effects of sodium impurities on corrosion and mass transfer is given here and in Sec. 1-2.2(c) to emphasize the significance of sodium impurities on these processes. For more complete discussions, see Chap. 2 and Refs. 2 and 9.

Oxygen affects the corrosion processes and mass transfer of metallic elements [10, 11]. Decreasing the concentration of oxygen in sodium is the most effective means of controlling mass transfer of metallic elements at a given temperature.

Influence of oxygen on the behavior of carbon in sodium (on solubility of carbon in sodium and on carbon transfer in sodium systems) has been summarized [6]. Chemical reactions between carbon and oxygen reportedly play a role in carbon transfer in sodium systems [12]. The role of carbon in sodium was under study in 1969, including attempts to identify particular forms or compounds of carbon causing carburization. Consequently earlier concepts and data are being challenged and must be reevaluated for validity and applicability using recent information.

Carburization of materials is the most significant effect of carbon in sodium systems. Two types of carburization, grain boundary and volume, have been observed in 304 stainless steel exposed to sodium containing carbon [13]. Grain-boundary carburization appears to have little or no effect on mechanical properties; however, the brittle case formed by volume (bulk) carburization can produce two characteristic effects on mechanical properties, depending on the ratio of case depth to section thickness. Relatively thin carburized layers cause weakening of the section, when plastically strained, by cracking of the case; yet, under fatigue and stress-rupture testing of smooth and notched specimens, the cracks seem to have no tendency to propagate in the ductile base material [13]. The strength of members with thin carburized layers is reduced proportionally to the reduction in effective cross-sectional area resisting load. Carburized specimens with relatively high ratios of case depth to section thickness exhibit higher strength (under steady loads) and lower ductility than uncarburized material. When the case is thick, the carburized material is stronger than the uncarburized section, but failure can occur at extremely low plastic deformation. When the case depth reaches approximately 10% of section thickness, the failure mode changes from ductile to brittle [14].

The opposite effect, decarburization of material, can also occur. This is a problem with ferritic steels in particular. Decarburization is accompanied by a loss in strength.

The presence of nitrogen in sodium can cause nitriding of structural materials in the system [8] and can induce a susceptibility to cracking when materials are later exposed to relatively mild corrosive environments, e.g., moist air [15]. Nitriding results in an increase in the yield strength and flexural fatigue life and a marked decrease in the ultimate strength and ductility at temperatures up to 1000°F [16]. Calcium, and possibly carbon, acts as a carrier for nitrogen in sodium [6].

Austenitic stainless steels are insensitive to hydrogen embrittlement under ordinary conditions [17].

(c) *On Other Materials*

Oxide-film formation has a detrimental effect on the fatigue life of zirconium when stress exceeds the yield point. The surface oxide acts as a crack initiator in a fatigue situation. Because of the adherent nature of the oxide film, cracks that form in it propagate into the metal substrate and result in failure [18]. The mechanisms of corrosion of niobium and vanadium

are oxygen controlled [17]. The transfer of carbon and nitrogen from steel to refractory metals is sufficient to alter the mechanical properties of the refractory metals. Nitriding of zirconium and niobium has been reported [19]. Hydrogen can cause low-temperature embrittlement of transition and refractory metals.

(d) *Other Effects*

Certain metals, particularly potassium and mercury, are highly soluble in sodium. The thermal conductivity of sodium is sensitive to the presence of these impurities, decreasing significantly (~1%) for values of potassium or mercury much greater than 1000 ppm. Since the desirably high heat-transfer coefficient for sodium is adversely affected by decreasing the thermal conductivity, it is desirable to limit potassium and mercury to values less than 1000 ppm [20].

The electrical conductivity of a mixture of sodium and impurities such as oxides is lower than the electrical conductivity of pure sodium. This effect has been reported to be approximately 0.01% change in resistivity per parts per million change in "oxygen concentration." However, the reported change in oxygen concentration was based on chemical analysis for total alkalinity (mercury-amalgamation technique). This method included hydride and hydroxide hydrogen, which were known to be present, as well as oxygen. The result of this analysis, total alkalinity, was expressed as oxygen in sodium monoxide [21]. Hence the reported "oxygen concentration" did not reflect the concentration of oxygen actually present in the sodium.

The concentration of elements having a significant neutron-absorption probability must be limited in thermal-energy reactors for neutron-economy reasons. Sodium currently available commercially contains only a few impurities of this class (e.g., lithium and boron) which are of significance in a fast reactor.

Provision for limiting the concentration of elements with neutron-activation products posing potential accessibility problems has been a feature of sodium procurement specifications. Analysis of activity data on the Hallam Nuclear Power Facility (HNPF) sodium indicates that the sodium more than met the activation requirement; in fact, it was very free of these impurities. In reactors that have experienced some fuel damage, activity due to fission products completely controls accessibility for maintenance in pipe galleries. From experience with commercially available sodium in reactors and from qualitative consideration of (1) anticipated ruptured-fuel-cladding operating criterion, (2) possible use of open (vented) fuel elements, (3) expected fuel-cladding corrosion-product deposition in piping, and (4) ^{22}Na production, it was concluded that activity contributions from neutron-activation products of original sodium impurities do not warrant a limitation on concentration of these impurities in a sodium purity specification [6].

1-2.3 *Purity Requirements*

There is no general acceptance of any set of purity criteria applicable to sodium systems. Sodium or NaK purity requirements must be established for each system with regard to temperature levels, service life, coolant velocity, and all the cladding, structural, and special (e.g., valve trim, bearing, seal) materials that will be in contact with the liquid metal. The effect of neutron-absorbing impurities on neutron economy is a consideration for reactor core coolants. Some general guidance is presented for the use of those specifying purity requirements for individual systems.

Purity requirements from procurement specifications for four reactors and two other programs are presented in Table 1.2. Purification equipment was used at the reactors to improve purity

levels, principally of oxygen, attained by procurement specification. Similarly, sodium used in the LMFBR cladding program was conditioned in a purification loop prior to use in test rigs. Table 1.2 also gives the chemical analysis of sodium received at Experimental Breeder Reactor No. II (EBR-II), Enrico Fermi Atomic Power Plant (EFAPP), and HNPF. This sodium was purchased to the specifications summarized in the first part of the table. The final part of the table lists impurity values furnished by two vendors. One list is for reactor-grade sodium, the other for commercial grade. The striking differences in these two lists are the concentrations of calcium and silicon.

To supplement the as-received analyses given in Table 1.2, results of impurity analyses of sodium samples taken from EFAPP, Sodium Reactor Experiment (SRE), and HNPF are presented in Table 1.3.

Suggested impurity limits for use in procurement specifications are presented in Table 1.4. This table is the result of a state-of-the-art review and is presented as a reference for those preparing sodium procurement specifications. The requirements listed have been met by vendors in the United States. However, if these vendors change their sources of raw materials or their manufacturing processes, higher levels of certain impurities than now exist in their product may result. The requirements in Table 1.4 can be used as a guide for evaluating the significances of any such changes.

These requirements are considered conservative; not all need be included in each specification. For example, if sodium is to be used in a component test loop, where neutron absorption is of no importance, a neutron-absorption cross-section test need not be specified, and a higher concentration limit for lithium (i.e., 20 ppm) would be appropriate. Purity requirements should be specified to meet the particular needs of the system in which the sodium will be used.

Impurities can be arranged in two groups according to the means for controlling impurity concentration. The first group includes those impurities whose concentration is limited by procurement specification and by exclusion from the sodium system. The second group includes impurities for which purification process equipment is provided in the system. Most of the impurities listed in Table 1.4 are in the first group. Oxygen, carbon, hydrogen, and, in some instances, calcium comprise the second group. Limits on elements in the second group are included in procurement specifications to:

1. Simplify handling of the liquid metal during transport.
2. Minimize preoperational purification of new sodium at the user's site.

Air cannot be totally excluded from large sodium systems that use cover gas, require maintenance, and have periodic changes of fuel. As noted in Sec. 1-2.1, air is a source of oxygen and hydrogen. In addition, the fuel in some reactors is a source of hydrogen (e.g., fuels containing zirconium hydride). Cold traps are usually provided in large sodium systems to control oxygen concentration; they simultaneously control the concentration of hydrogen. Hence oxygen and hydrogen belong in the second group of impurities.

Carbon, which is also included in the second group, has been introduced inadvertently in some sodium systems. Carbon can also be present in sodium because of transport via sodium between sodium containment (cladding and structural) materials. Gettering equipment (hot traps) has been used for carbon removal and is sometimes installed as standby equipment.

Calcium falls into the second group of impurities if purification at the plant site is required. In the United Kingdom sodium with calcium concentration sufficiently low for use in reactors is not commercially available. It is the practice to purchase commercial

TABLE 1.2 - Impurities in New Sodium* [22-26]

Element	Specified by†						Received at			Manufacturer's data	
	EBR-II [22]	EFAPP [23]	HNPF≠	SIR§	General Electric Company [24] (space program)	Atomics International (LMFBR cladding program)	EBR-II [22] (reactor grade)	EFAPP [23] (reactor grade)	HNPF [25,26] (reactor grade)	DuPont (reactor grade)	U.S.I. Chemicals (commercial grade)
Aluminum						10				8	25
Barium						10				2	
Boron	5	5		18^{t}	1	10	<1 to 2	<1	<0.8 to 0.9	4	15
Cadmium	20			4.35^{t}	2	10	<1		<1.5	1	2
Calcium	10	10	20	50	10	20	<2 to 8	<3 to 5	<10	8	100
Carbon	50	50	30		20	30	5 to 29	11 to 37	9, 14		45
Cesium				465^{t}						5	
Chromium						10					30
Cobalt			0.5		0.5	10			<0.11 to 0.2	2	25
Copper					10					2	5
Indium	30				25		7 to 12			2	25
Iron			300		10	25			<2 to 22	2	10
Lead			10		10	10			<3 to 6.6	1	10
Lithium	20	20		193^{t}	5	10	<1	<1	<5	17	5
Mercury					35				<3 to 5	4	35
Magnesium						10				5	5
Manganese					10	10			<5 to 5	2	5
Nickel			10		10	10			<2 to 4	2	10
Nitrogen						5				3	
Oxygen					50	100					45

Phosphorus										10	
Potassium	1000		200	6750[t]	200	200	104 to 190		120	100	150
Rubidium						50					30
Silicon						10				5	150
Silver	20	20			15		<2	<2		1	
Strontium										5	
Sulfur	10	10					1 to 6	1 to 5		14	
Tin			10		2	10			<2	10	5
Chloride	30	30	30	50	10	20[¶]	2 to 22	1 to 10	2 to 8	30	12

*Impurity concentrations are given in parts per million.

†Values given are the maximum permissible concentrations.

≠In addition to the impurity limits tabulated, the following requirements were specified for HNPF sodium.

1. Minimum sodium content: 99.95% by weight.
2. Cross section: The macroscopic cross section for the absorption of 2200 m/sec thermal neutrons shall not exceed 0.0146 cm^2/g.
3. Activation: The neutron activation of the sodium shall be such that a 1-kg sample shall yield no more than 5 mr/hr measured at a distance of 1 m through a 1-cm iron shield after 20 years of irradiation, at a thermal neutron flux of 5×10^{11} and a fast neutron flux (fission spectrum) of 5×10^{12}, followed by 15 days' decay.

§Total concentration of elements marked with (t) was limited to equivalent cross section of absorption of 18 ppm boron. Values shown will increase the thermal neutron cross section by the amount equal to 18 ppm boron.

¶Maximum concentration of halogens.

TABLE 1.3 - Sodium Impurities in Reactors*

Element	EFAPP				SRE								HNPF		
	5/17/61†	5/31/61†	9/63	11/63	4/25/58≠	6/16/58≠	10/2/58≠	2/6/59≠	4/12/59≠	7/30/62	8/6/62	9/30/62	4/4/64	5/31/64	9/18/64
Aluminum					10	10	5	7	13	<5	25	<5	20	50	5
Barium					<10	<10	<10	<10	<10						
Boron	<2	<2	<5	<5	10	10	8	3	2	<5	<5	10	10	<10	<10
Cadmium					<1	<1	<1	2	<1	<1	<1	<5	<5	<5	<1
Calcium	20	7	150	50	10	<10	10	10	40	75	300	200	50	50	75
Carbon	60	77			40	50	105	150	50	←32	to	171→	←10	to	75→
Cesium															
Chromium	1	1	3	2	<5	5	<5	7	12	5	400	10	<5	5	5
Cobalt	<2	<2	<1	<1	<5	<5	<5	<5	<5	<5	<5	<5	<25	<25	<25
Copper					10	<5	5	15	20	5	30	25	50	10	15
Indium					<10		<10								
Iron	6	8	18	14	25	500	25	30	50	10	600	10	50	200	25
Lead					5	2	10	10	<10	40	10	10	15	1	5
Lithium	<1	<1	<20	<20	<5	<5	<5	5	<5	<1	<1	<1	<1	<1	<1
Mercury															
Magnesium					<10	<10	<10	<10	10	25	5	35	50	<5	5
Manganese					<5	<5	<5	5	<5	5	150	<5	<5	<1	<1
Nickel	<2	<2	1	<1	<5	<5	<5	<5	100	<5	250	<5	10	<10	5
Nitrogen															
Oxygen															
Phosphorus															
Potassium			160	100	75	400	75	300	250	375	200	300	75	50	200
Rubidium															
Silicon	10	10	18	40	100	100	100	80	300	5	25	50	200	300	75
Silver	0.5	0.5			2	5	1	1	20						
Strontium															
Sulfur	<10	<10													
Tin					25	<2	5	<2	5	<5	<5	<5	<5	<5	<10
Halogens	20	23													

*Impurity concentrations are given in parts per million.

†Data are from Ref. 23.

≠Data are from Ref. 27.

grade sodium and remove calcium at the reactor site, as discussed in Sec. 1-3.2(d). In the United States sodium usually is available with a calcium concentration sufficiently low for heat-transfer service. Hence calcium is usually considered a member of the first group of impurities. However, treatment for calcium removal may be required at the user's site if commercial-grade sodium with a high calcium concentration is purchased, or even with reactor-grade sodium if the ratio of calcium to oxygen concentrations exceeds the stoichiometric ratio (see notes, Tables 1.1 and 1.4). In this case calcium would be considered part of the second group of impurities.

For oxygen, hydrogen, and carbon (impurities in the second group) there are no firm rules available upon which to establish system-operating purity criteria. General operating experience in reactors and test facilities indicates that maintenance of sodium saturation temperature (as measured by plugging meters) at 300°F or less in sodium systems fabricated of austenitic stainless steel and operating at, or less than, 1000°F will control the concentration of oxygen and hydrogen at acceptable levels.

At higher temperatures, the state of the art is not yet adequate to permit determination of optimum levels of oxygen concentration for reactors. Results of a study [6] using empirical equations developed in the Sodium Mass Transfer program [10] indicated that an oxygen concentration corresponding to a saturation temperature of 300°F would lead to excessive fuel-cladding corrosion; i.e., degradation of cladding operating at 1300°F would require fuel replacement in less than three years. Extrapolations of the General Electric Company data [10] show a need for very low oxygen concentrations, e.g., 2 to 5 ppm [6]. However, these low levels, calculated by extrapolating existing data, have not been verified by test.

Existing technology does not permit specification of acceptable levels of carbon in sodium. In fact, the particular species of carbon that cause carburization have not been identified. Metal tabs made of cladding or structural material have been used to monitor the carburization potential of sodium by measuring change in carbon concentration in the tab resulting from exposure of the tab to high-temperature sodium. Some correlations of carbon content of metal specimens and mechanical properties are available [28]. Sinizer and Pearson [14] used a maximum surface carbon content of 0.5% in 304 stainless steel as the safe limiting criterion for operating the SRE at 1000°F in 1962. However, this specification was based on the concept that surface carbon content of a specimen would rapidly reach some maximum equilibrium value characteristic of the carburization potential of the sodium in contact with the specimen. This concept does not have general acceptance. Additional experimental work is required relating mechanical properties to carbon content of relatively thick structural sections as well as thin cladding material and relating carbon pickup by tabs in exposure of short duration to long-term carburization of sodium-system materials.

When preparing specifications of oxygen and carbon impurity levels for particular high-temperature sodium systems, we should refer to results of LMFBR materials investigations being conducted at General Electric Company, Atomics International, and Mine Safety Appliances Co. These experimental results, and any others available, should be factored into the determination of sodium purity requirements.

1-3 PURIFICATION METHODS

Various purification methods and the equipment used to effect removal of impurities in engineering test loops and large sodium and NaK systems are discussed in this section. These include

TABLE 1.4 - Procurement Specification Guide

Impurity	Impurity limit			Reason for limit, remarks					
	Maximum concentration, wppm [a]	Concentration limited by cross-section test [b]	Concentration limited by saturation temperature (maximum), °F	Operating experience [c]	Potential process changes [d]	High concentration observed [e]	Reducing agent [f]	Alkali metal [g]	Other
Aluminum	10					X	X		
Barium	10						X		
Boron		X				X	X		
Cadmium		X							
Calcium	10			X		X	X		[h]
Carbon	30				X				[i]
Cesium	5			X				X	
Chromium	10				X	X	X		
Cobalt		X							
Copper	5				X				
Hydrogen			400						[j]
Indium		X							
Iron	25			X		X			
Lead	10			X		X			

[a] Impurity concentrations are given in parts per million by weight.

[b] Composition limit is not set. Concentration is limited by requirement that the macroscopic cross section for the absorption of 2200 m/sec thermal neutrons shall not exceed 0.0146 cm^2/g. The use of this thermal neutron cross-section test in the procurement of sodium for either thermal or fast neutron reactors is discussed in Ref. 6.

[c] Similar limits have been used. There have been no apparent problems to date when sodium meeting these requirements was used in operating systems.

[d] Limits were established to provide for possible changes in sodium raw-material sources of the manufacturer or for changes in proprietary manufacturing processes which could conceivably introduce significant quantities of impurities.

[e] High concentration has been reported in commercial sodium.

[f] These are elements thermodynamically capable of reducing sodium oxide at 1200°F.

[g] Other alkali metals that may be present due to chemical similarity.

[h] Calcium concentration of 10 ppm requires 4 ppm oxygen for a stoichiometric mixture to form calcium oxide. Oxygen concentration of 4 ppm is equivalent to a saturation temperature of 320°F (see Fig. 1.1), a saturation temperature believed typical of new sodium. If the inherent oxygen concentration in a batch of sodium is less than that required to form a stoichiometric mixture with the calcium actually present, additional oxygen would be required to react with the excess calcium present to effect removal, as discussed in Sec. 1-3.2(d).

[i] Procurement specification on total carbon concentration is set to limit any purification that may be required for a particular system.

[j] Procurement specification is set to minimize plugging problems during handling.

TABLE 1.4 - Procurement Specification Guide (Continued)

Impurity	Impurity limit			Reason for limit, remarks					
	Maximum concentration, wppm [a]	Concentration limited by cross-section test [b]	Concentration limited by saturation temperature (maximum), °F	Operating experience [c]	Potential process changes [d]	High concentration observed [e]	Reducing agent [f]	Alkali metal [g]	Other
Lithium	10						X	X	[k]
Mercury	35				X				
Magnesium	10					X	X		
Manganese		X				X	X		
Nickel	10			X		X			
Nitrogen	5								[l]
Oxygen			400						[j]
Phosphorus	20			X		X	X		
Potassium	200			X		X		X	
Rubidium	50							X	
Silicon	10					X	X		
Silver		X							
Strontium	10			X			X		
Sulfur	30			X		X			
Tin	10			X					
Halogens	20								[m]

[k] A supplement to the thermal cross-section criterion is necessary. In the absence of other poisons, the 0.0146 cm^2/g criterion would permit lithium concentrations up to 135 ppm. At a neutron energy of 250 kev, ^6Li has a cross section (n,α reaction) of 3 barns. At the same energy, sodium has an absorption cross section of 0.7 mb. A lithium-absorption limit of 1% of the absorption in sodium at this energy is necessary to prevent this resonance-absorption peak of lithium from controlling neutron absorption in the sodium. This additional criterion can be met by limiting the concentration of lithium to 10 ppm.

[l] Tentative limit is recommended until additional information is available [6].

[m] Halogens are possible corrosive agents.

precipitation methods using cold traps; chemical reaction methods using hot traps (solid getters) or soluble getters; and filtration, settling, and centrifuging methods. Methods and equipment applicable only to the research laboratory are not included.

1-3.1 *Precipitation*

The precipitation method, using cold traps, is the most widely used of several liquid-sodium purification methods. Impurity removal by precipitation utilizes the difference in solubility of impurities in sodium at different temperatures. For example, when sodium is cooled, impurities such as oxygen and hydrogen precipitate as the sodium becomes saturated with the particular impurity.

First, we shall review the process

and define terminology. A solution can be defined as a homogeneous mixture of two or more substances. A saturated solution is a solution for which a state of equilibrium exists with undissolved solute. As an example, in a saturated solution of the solute oxygen in the solvent sodium, some oxygen must be present as a separate phase. In the sodium-oxygen system the second (or separate) phase is sodium oxide, present as solid particles. Because the solubility of oxygen in sodium has a positive temperature dependence, the amount of oxygen that can be held in solution increases with an increase in temperature. Solubilities of other sodium impurities, such as hydrogen, have a similar temperature dependence. For a given concentration of each of these impurities in solution, there is a finite temperature above which the solution is less than saturated (all the impurity present is in solution, and the mixture of the impurities and sodium is homogeneous). At or below this temperature, the solution is saturated (some of the impurity exists as a second phase, and the mixture is nonhomogeneous). This temperature is defined as the saturation temperature that, in the jargon of the industry, is usually referred to as "plugging temperature." In fact, plugging temperature is determined using an instrument called a plugging meter [29]. The measured plugging temperature may be at variance with the true saturation temperature because of details of design and operation of the particular plugging meter used.

Relations showing the solubility of oxygen in sodium are plotted in Fig. 1.1. A solubility curve defines the saturation temperature corresponding to a given concentration of oxygen. Several different solubility curves have been used. The solubility relation developed at Knolls Atomic Power Laboratory (KAPL) [30] has been used extensively, particularly in the 1950's.

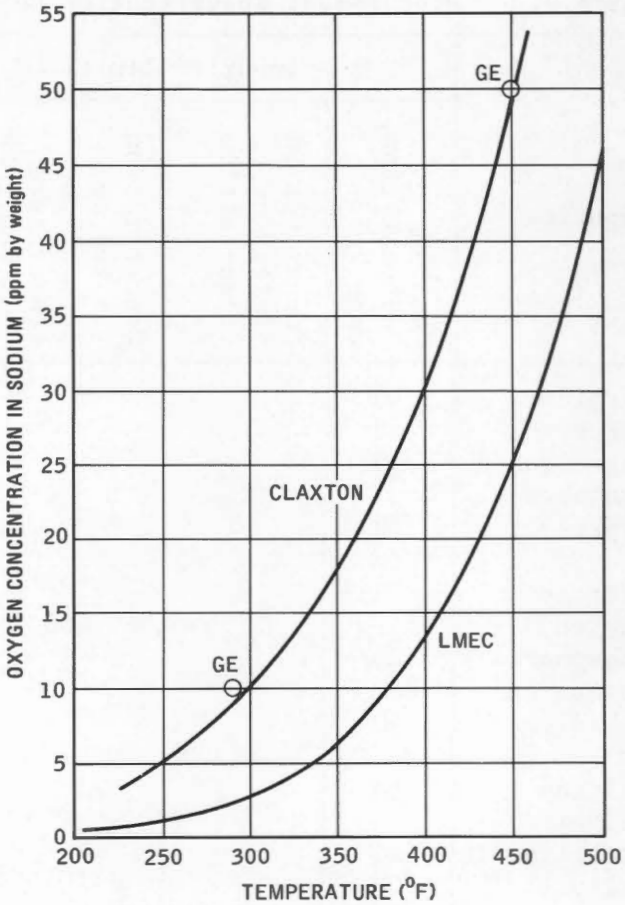

Fig. 1.1 Solubility of oxygen in sodium.

The two points marked "GE" in Fig. 1.1 are from the KAPL curve. Experimental work on the Sodium Mass Transfer Program [10] was conducted at two plugging temperatures, 290 and 450°F. The two GE points in Fig. 1.1 are the basis for the designation of 10 and 50 ppm, respectively, as the oxygen concentrations from which the oxygen factor in the mass-transfer empirical equations was developed. Based on a review and evaluation of available solubility data in 1965, Claxton [31] recommended the upper curve in Fig. 1.1. An evaluation [32] of solubility data in 1968, considering the recent data from Los Alamos Scientific Laboratory (LASL), resulted in the lower curve in Fig. 1.1, which is used at the Liquid Metals Engineering Center (LMEC).

Impurity experience, in general, has been based on plugging-temperature observations, not on impurity concentration determined by chemical analysis. Almost all corrosion, mass-transfer, and impurity-plugging experience has been directly related to plugging-temperature data (e.g., experience at the SRE and the General Electric Company mass-transfer program) [10] because of:

1. The relative ease of making plugging-temperature determinations.
2. Sodium sampling problems.
3. Lack of confidence in results of chemical analysis of impurities in sodium.

The last two reasons are losing significance as better methods are being developed in the LMFBR program. Oxygen concentrations reported in the literature were usually derived from:

1. Plugging-temperature data.
2. The assumption that oxygen was the impurity giving the plugging meter indication.
3. The use of a particular solubility curve.

Therefore, when using sodium literature, we must determine the basis for any oxygen (or other impurity) concentrations reported. If a plugging-temperature observation was the original data, the particular solubility curve used to translate plugging temperature to oxygen concentration must be known to appreciate the significance of the reported concentration.

There is another important point concerning the reporting of impurity concentrations. In the literature, reference is made to impurities both as elements (e.g., oxygen) and as the sodium compound of the element [e.g., sodium oxide (Na_2O)]. Consequently the possibility for confusion exists in the interpretation of trapping rates and trap capacity since 4 lb of sodium oxide contains approximately 1 lb of oxygen.

The purity-control device in which the precipitation method is conducted is called a cold trap. Sodium is cooled in this component, and the crystallization and collection of precipitates, such as sodium oxide and sodium hydride, take place. Precipitate collection involves one or more of the following processes and operations: crystal formation and retention on metal surfaces, filtration, and settling. The two types of cold traps, forced circulation (of sodium) and natural convection, are described in the following discussion.

Generally, the state of the art is such that the design of purification equipment is chiefly empirical. This is particularly true of cold traps. Operation of cold traps in a number of loops and reactor systems has yielded a considerable amount of information. Even so, no single design has a clearly demonstrated superiority. Existing cold-trap designs and performance, with emphasis on problems encountered, are reviewed here to show the state of the art of large-scale trapping. Design and operating problems are also summarized, and results of investigations pointing to solutions of the problems are discussed.

(a) *Forced-Circulation Cold Traps*

Engineering-scale systems (those containing more than a few hundred pounds of sodium) normally use forced-circulation cold traps. These traps can control saturation temperature in the 250 to 300°F range. This is equivalent to a concentration of 1 to 3 ppm of oxygen in sodium by weight, using the LMEC solubility curve shown in Fig. 1.1.

(1) *Existing Trap Experience.*

Beginning with the Submarine Intermediate Reactor (SIR) program, forced-circulation cold traps have been developed and evaluated, with primary emphasis on the control of oxygen concentration in sodium.

Experience with six traps of various designs at KAPL [33] demonstrated that porous-metal filters were not suitable

because they plugged rapidly, blocking flow. Data from these experiments indicated that a trap packed with steel wool removed sodium oxide and was less susceptible to plugging.

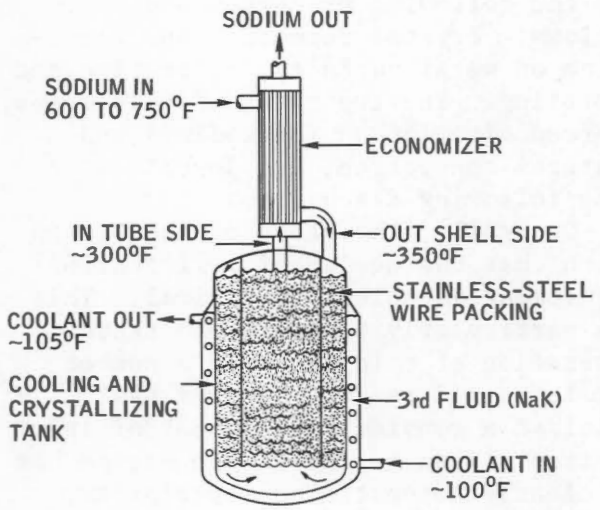

Fig. 1.2 Knolls Atomic Power Laboratory cold trap.

This led to development of the trap shown in Fig. 1.2. The crystallizer region of this cold trap is packed with knitted stainless-steel wire, 4 to 5 mils in diameter, packed to a density of 20 lb/cu ft. This packing is a continuous strand of wire, chosen to prevent slivers of wire fiber from disengaging and causing mechanical difficulties in the reactor system. This packing provides for the growth and support of sodium oxide crystals. The gross volume of the crystallizer is approximately 80 gal; this provides approximately 5 min retention in the trap at a sodium flow of 12 gpm. This optimum retention time was determined experimentally. An external cooling system using water or Dowtherm provides the cooling. NaK is used as a third fluid in the jacket to improve heat transfer from sodium to the service coolant. A regenerative heat exchanger (economizer) is provided to transfer heat from the trap inlet to effluent sodium. Analysis of SIR plugging-temperature data when a trap of this type was in service indicated that the cold-trap discharge was saturated with oxygen at the lowest cold-trap temperature, and hence the cold trap was operating at maximum efficiency [7].

This same basic design was used for the EFAPP reactor cold trap. A section of this 500-gal trap is shown in Fig. 1.3. The packing was 11-mil-diameter stainless-steel woven wire. The trap was cooled with NaK. Maximum sodium flow rate was 100 gpm, but most of the 3700 hr of operation on the first trap used was at a 50-gpm flow rate. A gas space was provided so that a frozen trap could be thawed while isolated from the coolant system. Although still operable, this trap was replaced with a fresh trap prior to nuclear operations. Examination of the removed trap indicated that it contained an estimated 50 lb of oxygen, 1 lb of carbon, and lesser amounts of hydrogen, nitrogen, and metallic impurities [34]. These impurities were concentrated in the lower (inlet) third of the wire mesh. The cylinder containing the wire mesh had collapsed, possibly because accumulated sodium oxide in the mesh had allowed a pressure drop in excess of 1 psi to be applied across the wall. Apparently performance was not impaired by deformation of this cylinder. Operation was succesful [34], but service conditions were not severe (inlet sodium appears to have been saturated with oxygen only once for a short period in 1963).

Cold traps of a design similar to the KAPL trap have performed satisfactorily in the EBR-II. The primary cold trap is a 500-gal vessel filled with 304-stainless-steel-wire mesh [35]. Sodium saturation temperature was maintained at about 320°F or lower. The initial primary trap was in use until it was removed in June 1968. One secondary cold trap, smaller than the primary trap, plugged after collecting 100 lb of sodium oxide during initial cleanup of the secondary system containing 2 1/4 Cr-1 Mo piping.

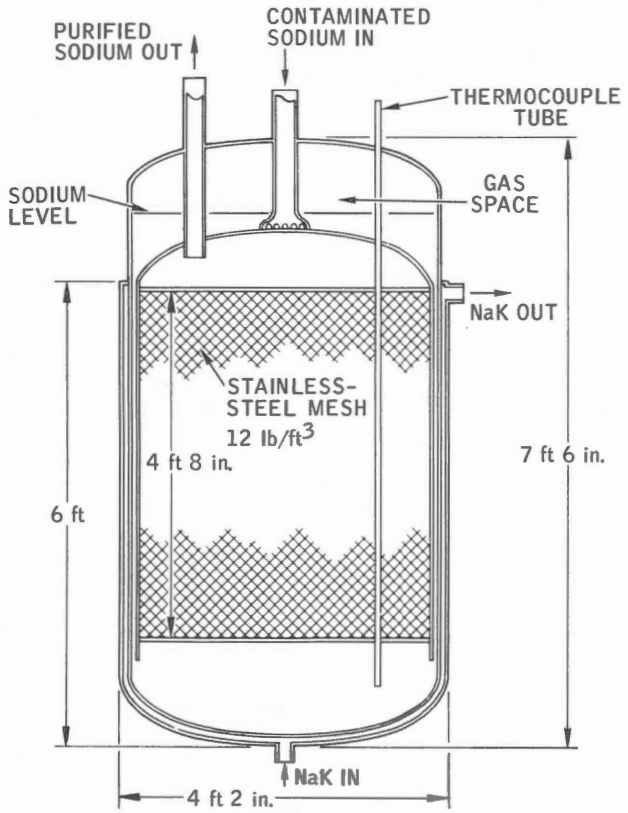

Fig. 1.3 Enrico Fermi Atomic Power Plant primary cold trap.

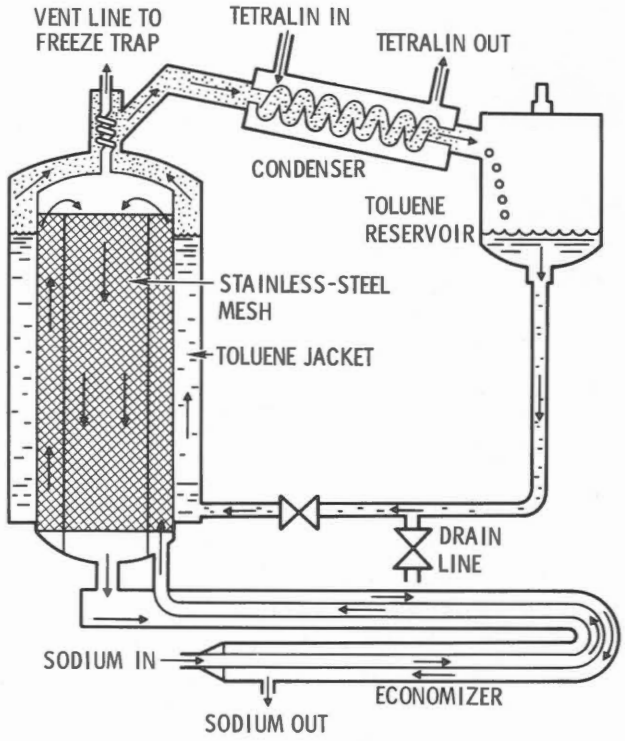

Fig. 1.4 Boiling-coolant cold trap.

A second cold trap collected an estimated 40 additional pounds of oxide [36].

Cold traps installed during construction of the SRE used boiling toluene (boiling point, 233°F) as a coolant; a diagram is shown in Fig. 1.4. The boiling-coolant trap with an economizer in the SRE main secondary (nonradioactive) system, which contained 15,000 lb of sodium, provided 18 months of satisfactory service. Operation of two of these cold-trap-economizer units in the 50,000-lb primary system was intermittent because of flow restrictions in the economizer. It was concluded that cold traps with this type of economizer are not suitable for use when saturation temperature approaches bulk sodium temperature (the condition that often exists during initial or postmaintenance cleanup) because cooling occurring in the economizer lowers incoming sodium temperature, thus causing precipitation and formation of sodium oxide plugs in the economizer tube [37].

Effectiveness of a boiling-toluene-cooled cold trap (operated without an economizer) in initial cleanup of the SRE primary system is shown graphically in Fig. 1.5; performance of this and other SRE traps is summarized in Table 1.5. Subsequent to initial cleanup, an appreciable amount of oxygen entered the reactor during core maintenance. Shortly thereafter flow through this cold trap stopped because of sodium oxide plugging. Examination showed that most of the oxide had collected in the first 2 in. of the mesh [37]. This demonstrated the general tendency of a boiling-coolant trap to precipitate oxide at the trap entrance as a result of the sharp temperature gradient existing at the inlet (jacket pressure was atmospheric) and confirmed similar findings of the prototype testing program [38]. Such localized oxide deposition limits

TABLE 1.5 - SRE Cold-Trap Performance

Trapping Rates	
Trap type	Oxygen, trapping rate, lb/hr
Boiling coolant	0.009
Forced-convection cooled	0.02

Trap Capacity		
Trap type	Oxygen, lb	Sodium oxide, lb
Boiling-coolant trap at SRE	0.67	2.6
Prototype trap [38]	1.35	5.25
Forced-convection-cooled trap	2.8	10.8

Cold-Trap Operating Parameters		
Parameter	Sodium	Organic
Boiling-coolant trap*		Toluene
Flow rate, gpm	5	0.8
Temperature, °F		
Inlet	484	193
Outlet	400	234
Minimum	358	
Forced-convection-cooled trap†		Tetralin
Flow rate, gpm	32	24
Temperature, °F		
Inlet	345	100
Outlet	305	141
Minimum	257	

*The heat-transfer rate was 62,000 Btu/hr, and the overall heat-transfer coefficient was 35 Btu/(hr)(sq ft)(°F).

†The heat-transfer rate was 190,000 Btu/hr, and the overall heat-transfer coefficient was 94 Btu/(hr)(sq ft)(°F).

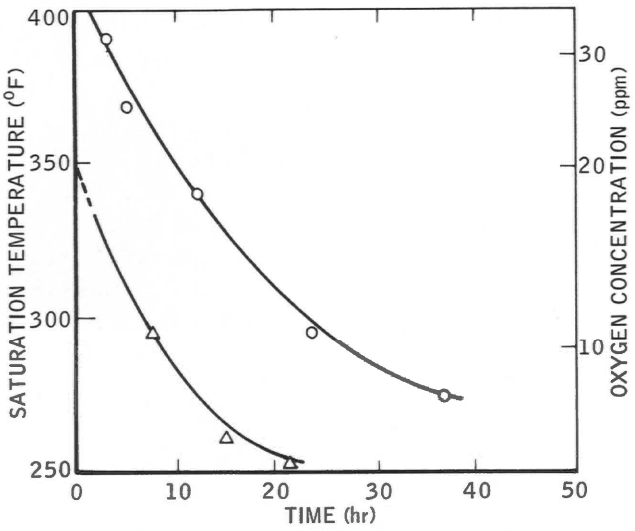

Fig. 1.5 Sodium Reactor Experiment cold-trap performance. o, boiling-coolant trap. Δ, forced-convection-cooled trap.

effective trapping volume and trap capacity.

The SRE trap [37] was changed to a forced-convection single-phase coolant design, by the method of Bruggeman [7], to improve trap capacity and heat-transfer capability. With this method of cooling, a temperature gradient is established along the heat-transfer wall, which prevents localized precipitation of oxide at the trap entrance. The sodium vessel of this trap, shown in Fig. 1.6, was 12-in. pipe; the inner tube was 6 in. in outside diameter. Knitted wire mesh made of 0.011-in.-diameter 304-stainless-steel wire had an apparent density of 24 lb/cu ft. Mesh in the central tube was separated, and bypass tubes were installed to provide additional filtering area. The upper coil of mesh was of slightly smaller diameter than the vessel to permit the oxide slurry to pass over the top of the coil to the bypass tubes and also to enter the side of the upper coil.

Although its capacity was four times that of the boiling-coolant trap, examination of the forced-convection tetralin-cooled trap showed that

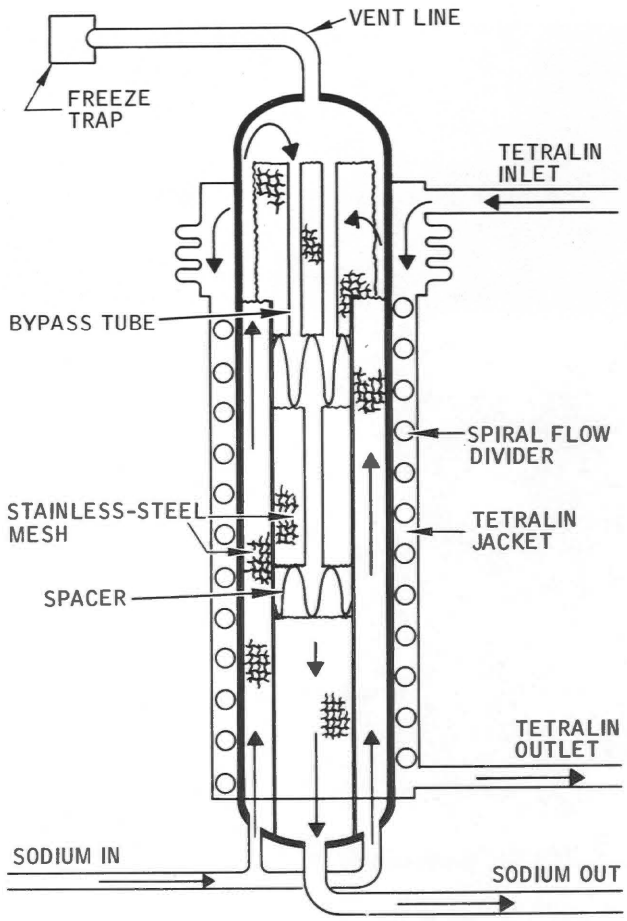

Fig. 1.6 Sodium Reactor Experiment forced-convection-cooled cold trap.

capacity again was limited by localized precipitation of sodium oxide. In this trap, however, the deposit was at the low-temperature end of the trap rather than at the trap inlet. The top portion of the mesh was filled with oxide (Fig. 1.7), and the bypass tubes were completely plugged. The quantity of sodium oxide reported in Table 1.5 was calculated from effective trapping volume determined by inspection and from apparent density of oxide deposited in the mesh. An experimental determination [37] showed the apparent density of sodium oxide in a similar deposit to be 0.02 lb/cu in.

The SRE experience was utilized in the design of cold traps for the HNPF. The cold-trap feed stream was directed over the outside of a tube coil to solve the economizer plugging problem; this elim-

Fig. 1.7 Top view of expended cold-trap insert.

inated narrow passages. For system simplification the economizer was incorporated inside the cold-trap shell, as shown in Fig. 1.8. A forced-convection coolant system (using nitrogen) was used to increase oxide capacity, and small sodium passages or spaces in all areas that might contain oxide-saturated sodium were avoided [39]. The cold-trap vessel shown in Fig. 1.8 is 20 in. in diameter and 9 ft long and is constructed of carbon steel. Sodium leaving the economizer section enters the mesh-packed section where it is further cooled by nitrogen flowing in the cooling jacket. Oxide precipitation and collection occur in this section, which is packed with stainless-steel knitted-wire mesh (24 lb/cu ft apparent density). Flow through this section is baffled to prevent channeling, thus forcing uniform cooling of the entire flow. A sodium buffer zone is used to reduce the heat-transfer rate at the bottom of the trap and thus permit a finer control of temperature. Nitrogen is recirculated through a closed cooling circuit. Nitrogen flow rate is controlled automatically to maintain a selected sodium temperature at the bottom of the trap [40]. Design requirements are given in Table 1.6.

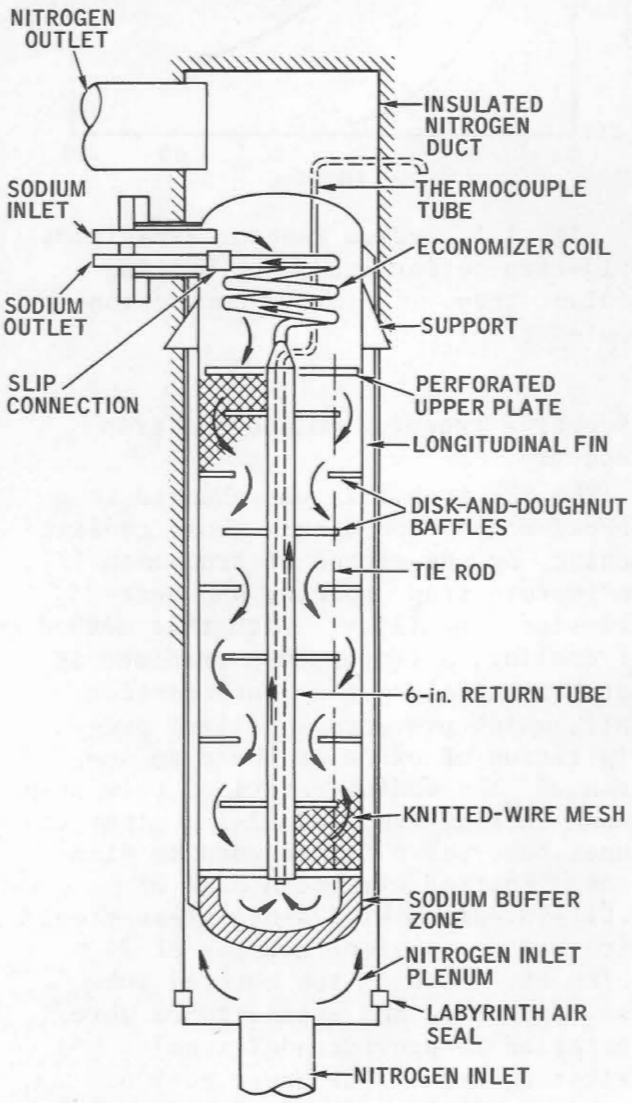

Fig. 1.8 Hallam Nuclear Power Facility cold trap.

Performance of a prototype HNPF cold trap was determined experimentally before the design was completed. The sodium side of the test trap was identical to that of the trap described previously; however, Tetralin was used as

TABLE 1.6 - HNPF Cold-Trap Data

Process requirements [40]	Normal operation	Initial cleanup
Sodium		
Flow rate, gpm	10	17
Temperature, °F		
Inlet	607	350
Minimum	250	250
Outlet (calculated)	470	294
Nitrogen		
Flow rate, cfm	1845	1845
Temperature, °F		
Inlet	130	130
Outlet (calculated)	252	216
Trapping Rate [39]		
Rate, lb sodium oxide/hr	0.26	0.72
Capacity Requirement [39]		
200 lb sodium oxide before pressure drop exceeds 20 psig		

the service coolant. Oxygen was added to sodium in the test loop as a gas. Trapping rates are given in Table 1.6. The trap capacity was greater than 100 lb of sodium oxide. No operating problems were indicated for additions of approximately 100 lb. With continuing oxide addition trap pressure drop increased. Oxide was redistributed several times by stopping oxide addition to the loop while continuing circulation through the cold trap to reduce pressure drop. An additional 100 lb was trapped by using this technique. It was concluded that a total of 200 to 250 lb of sodium oxide could be trapped with only a moderate final pressure drop across the trap (less than 7 psi) if the oxide, in excess of 100 lb, is not added continuously [39]. It should be noted that in a power-producing reactor, it likely would be impractical, either from an initial cost or plant availability standpoint, to provide the operator with capability to stop oxide addition and to recirculate clean sodium in order to increase trap capacity.

During initial system cleanup at HNPF [41], these traps operated at design conditions and expeditiously purified the approximately 400,000-lb primary system from a saturated condition at 540°F to a plugging temperature of less than 250°F. In the process the first primary cold trap was filled to capacity, which was estimated to be at least 230 lb of sodium oxide. Initially some difficulty was experienced with localized plugging in the traps when the oxide concentration of the system was high and the trap was operated with a large temperature gradient. It was found that, when the minimum internal temperature of the trap was limited to a maximum of 50°F below

TABLE 1.7 Comparison of Impurity Levels in Cold Trap with Those in Sodium Coolant

Impurity and method of analysis	In cold trap	In coolant	Concentration ratio
Carbon	144 to 1550 ppm	18 to 60 ppm	77
Gamma spectrometry:			
^{137}Cs	4.0×10^{2} μc/g	1.5×10^{-2} μc/g	2.7×10^{4}
^{125}Sb	4.3 μc/g	0.6×10^{-2} μc/g	6.8×10^{2}
Emission spectrometry:			
Fe	200 to >500 ppm	50 ppm	>10
Si	200 to >500 ppm	50 ppm	>10
Mn	50 to 500 ppm	<5 ppm	>100
Pb	5 to >500 ppm	10 ppm	>50
Cr	5 to >500 ppm	5 ppm	>100
Ni	10 to 300 ppm	5 ppm	60

the plugging temperature, no problems with plugging were experienced.

Subsequent operation at HNPF also was successful. During operations through August 1963, five traps in the primary system and three in the secondary systems were expended and required replacement [25,42]. One instance of oxide plugging at the inlet of a secondary cold trap was reported [42] during a period when the concentration of oxygen in the inlet sodium was high. During December 1963, reactor operations required frequent changes in system flow rate [43]. These changes were effected by varying primary-pump speed; this caused daily fluctuations in cold-trap flow rate between a few percent and approximately 50% flow (100% = 30 gpm). The cold-trap temperature controller (which controlled temperature by varying nitrogen flow) was unable to maintain a constant cold-trap temperature. Several cold-trap temperature increases were reflected in increases in the bulk-sodium plugging temperature; this indicated some release of oxide from the trap to the system. Control of cold-trap sodium flow rate independent of coolant-loop flow rate would have prevented this oxide release from the trap.

The HNPF cold-trap design was adapted to the SRE [44] and used successfully starting in 1960. The primary-system trap used vault nitrogen gas as its coolant. After leaving the cold trap, the nitrogen was cooled on a nitrogen-to-kerosene coil. The secondary-system trap, located outdoors, was air cooled. Both traps were equipped with 10-hp blowers. From November 1961 to August 1962, it was calculated that approximately 82 lb of sodium oxide was collected before one of these traps in the primary SRE system was removed. The oxide removal rate usually was 2 to 6 lb/day, with a maximum rate of 10 lb/day [45]. When trap feed was saturated, optimum distribution of oxide in this trap was obtained by initially maintaining minimum internal temperature (the thermocouple well was located near the bottom of the sodium return tube) at the plugging temperature and decreasing the internal-temperature-controller set point 25°F per system inventory throughout. Plugging temperature was found to follow this programmed decrease in trap minimum temperature very well [46].

Cold traps remove not only sodium oxide and sodium hydride but carbon, metallic impurities and fission products as well. For example, a trap in service at SRE from August 1962 to May 1963 was examined after it had accumulated approximately 3000 hr of operation. Samples of material from the cold trap were analyzed for a number of impurities.

Sodium from the heat-transfer system was also analyzed for these impurities. The data are presented in Table 1.7. The "concentration ratio" is the ratio of concentration of a particular impurity in the cold trap to that in the system sodium. These ratios are an indication of the effectiveness of this type of cold trap for collecting impurities other than sodium oxide [47].

Practically all the carbon in this SRE trap was present in particulate form. The size of two-thirds of the particles exceeded 5 μ. Based on measured carbon concentration, total carbon in the trap was calculated to be approximately 50 g. The trapping mechanism was not resolved; the following alternatives were considered:

1. Carbon was trapped due to saturation of sodium with carbon because of the decrease in temperature and precipitation of carbon particles.
2. Carbon particles served as nuclei for sodium oxide crystals and were trapped with the oxide.
3. Carbon particles were filtered.

A possible trapping mechanism suggested for fission products is that they become attached to carbon particles and are consequently trapped out with the carbon. However, more ^{137}Cs was collected than can be realistically associated with carbon particles, based on analysis of the activity of this isotope on carbon removed from the reactor; this suggests that another mechanism for trapping fission products was effective [47]. (This information is presented to show that cold traps can collect materials other than sodium oxide. For additional information on trapping of fission products, see Ref. 48.)

In the original design of the primary NaK coolant loops for the Dounreay Fast Reactor (DFR), air-cooled cold traps were connected in parallel with a section of main coolant pipe rather than across a pump; hence the cold traps had only a small driving head. The trap internal flow path was rather complicated (it had an internal economizer, cooling section, and basket packed with Raschig rings); however, at full cold-trap flow of 5 gpm, flow through this path was only 2 gpm (3 gpm was bypassed directly to the trap outlet). This design proved unsatisfactory because sodium oxide collected in the bypass circuits and blocked flow. Later a separate purification loop containing two cold traps, a pump, an economizer, and purity-level instrumentation was installed. Trap internal design was simplified, and knitted-wire-mesh packing was employed. Improvements were also made in traps located in the the primary coolant circuits [49, 50]. These modifications were successful. Cold-trapping capacity was increased [51], and saturation temperatures of 100°C (212°F) and lower were achieved [52]. Removal of oxygen by cold trapping was probably assisted by the gettering action of uranium exposed to the coolant [53].

(2) *Design Problems.* The foregoing descriptions of cold traps represent the the proven state of the art. The discussions on trap performance reveal the problems that must be solved by the designer. These problems can be grouped into the following design considerations:

1. Rate of impurity removal.
2. Capacity for retaining impurities.
3. Control of trap operation.

The first two items are discussed in the following paragraphs. Instrumentation, system design factors, and operating procedures affecting control of trap operation are not covered in this chapter.

Requirements on rate of impurity removal at particular saturation temperatures fix the cooling rate. Normally economizers are incorporated in purification systems for power-producing reactors to minimize heat losses. The remainder of the cooling requirement must be met by heat rejection from sodium passing through the trap. Basic

methods for calculating heat transfer are well established, applications to cold traps are discussed in Refs. 39, 40, and 54. Cooling in the trap must be distributed to minimize local build-up of oxides.

The cooled Na-Na_2O mixture must remain at low temperature long enough for sufficient crystallization to occur so that trap effluent will have a saturation temperature closely approaching the minimum temperature of sodium passing through the trap. (A trap is considered to be operating at maximum efficiency when these temperatures are equal.) Experiments at KAPL [7] showed that the trapping effectiveness was greatly increased by increasing the sodium residence time in the trap from 2.5 to 5 min but was very little affected by an increase from 5 to 10 min; the trap used in this experiment contained wire-mesh packing. A residence time of 3 to 5 min has been generally accepted by cold-trap designers for packed traps.

Maximizing the capacity of cold traps for the retention of precipitated impurities is the major design and operating problem. In an experiment at KAPL, it was determined that 35 wt.% sodium oxide could be accumulated in the crystallizer region with no change in trap pressure drop. During terminal examination of a trap operated at SRE until flow was blocked, chemical analysis of a core sample of mesh obtained where plugging occurred showed 22 wt.% sodium and 78 wt.% sodium oxide [37]. It is obvious from operating experience cited for many of the cold traps reviewed earlier that design and operating procedure for a trap should permit general distribution of oxide throughout packed sections of the trap and hence maximize oxide collection before any one portion of the flow path becomes plugged.

(3) *Increasing Trap Capacity.* Several approaches have been proposed to increase trap capacity.

Investigators in the USSR [55-57] considered a cold trap to consist of three zones (cooling, settling, and filtration) and experimentally determined precipitation and collection of sodium oxide in each zone. A schematic drawing of their test rig and generalized results is shown in Fig. 1.9. A sketch of one of their cold traps appears in Fig. 1.10. Distribution of sodium oxide in the various zones is given in Table 1.8. A preference for stainless-steel cuttings over wire for packing was reported. Packing density was 100 kg/m^3 (6 1/4 lb/cu ft). These results show that the presence of packing is not required as sites for crystallization since 65% of oxides trapped remained in the cooling and settling zones, which did not contain packing. This conclusion supports the observation made at KAPL that packing is not absolutely essential [7]. Also, the value of a settling chamber with regard to oxide-retention capacity is established by the Russian work.

TABLE 1.8 Oxide Distribution in Test Trap

Zone	Fraction of oxides trapped	Volume fraction of zone
Cooling	35	0.3 to 0.27
Settling	30	0.4 to 0.45
Filtration	35	0.3 to 0.28

Concurrently with this work in the USSR, similar consideration was given in the United States to cooling and filtration in separate zones and to adding a settling chamber. Some experimental work was done with traps without a filtration zone. A "packless trap" with only cooling and settling zones was used successfully at the Large Component Test Loop (LCTL). A similar trap, shown in Fig. 1.11, was tested in the HNPF secondary system [43]. The shell of this trap was identical to regular HNPF traps [20-in. Schedule 20 pipe); hence the length-to-diameter ratio was not necessarily optimum for

the packless configuration. The internal design differed as follows:

1. There was no packing.
2. An 18-in.-OD inner sleeve was installed to provide a low upward velocity and permit settling of entrained oxide particles.
3. The cooling zone was the 0.62-in. annulus located between the inner sleeve and outer shell.
4. The chamber at the bottom of the trap was baffled to minimize turbulence.

Considerable data and observations on performance of this HNPF packless trap were collected [43, 26, 58]. Flow through this trap decreased to zero during the first month of operation, presumably because of an oxide plug. Heating the trap to 400°F permitted reestablishment of 100% flow [43]. Based on USSR observations that one-third of the oxide was collected in the cooling section, it is suspected that the annulus might have been too small. In the HNPF secondary system, one trap served several coolant loops sequentially. Cold-trap flow and temperature upsets at the time of loop change-

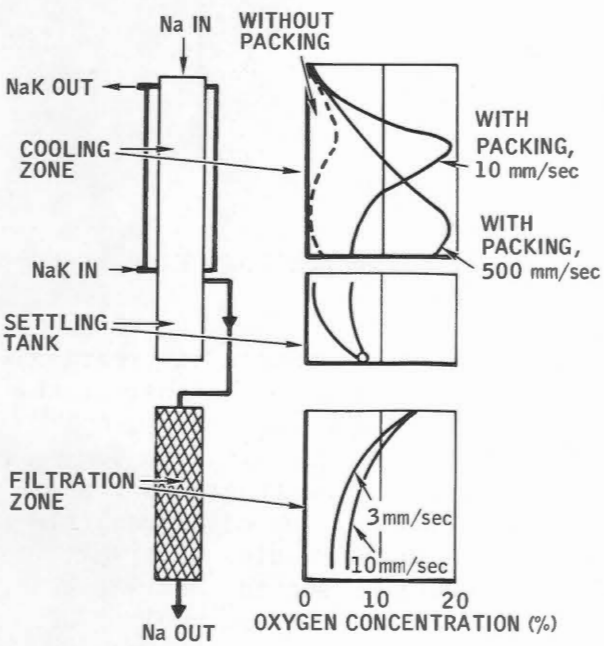

Fig. 1.9 Cold-trap test-rig schematic and generalized results.

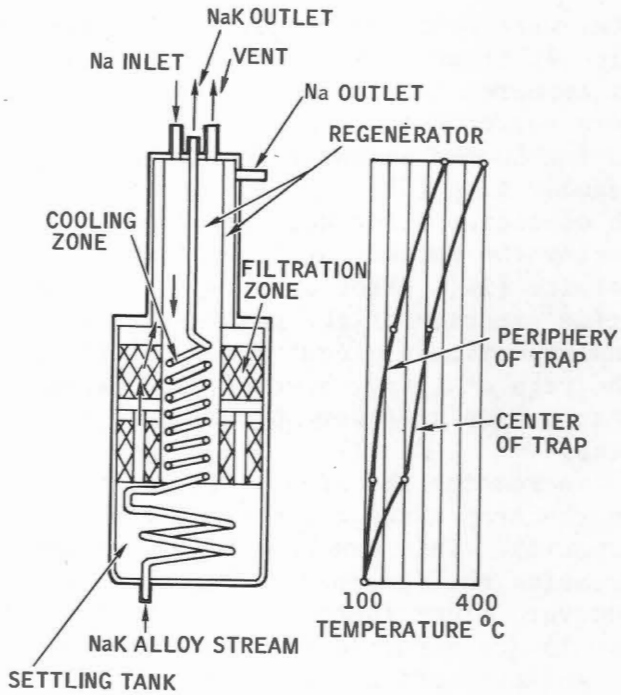

Fig. 1.10 USSR cold trap and temperature profile.

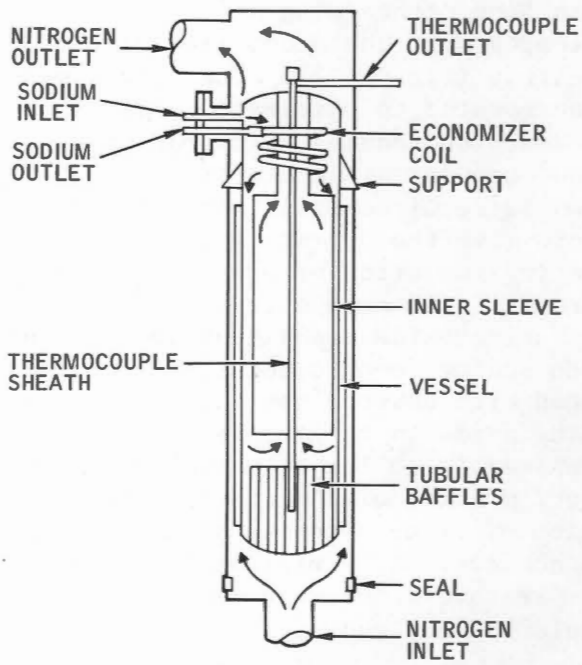

Fig. 1.11 Hallam Nuclear Power Facility experimental cold trap without packing.

over were believed to have added previously trapped oxide to the loop [45]. It appeared that the packless trap was more susceptible to release of oxide during loop-changeover upsets than the regular trap [59]. Collection of 100 lb of sodium oxide was calculated during the period when this trap was in service [26]. From data reported, the oxide capacity of the packless trap was approximately equivalent to that of the regular trap. However, the packed trap presented fewer operational problems.

Increasing the area of flow path in the trap tends to increase trap capacity. This can be achieved by increasing the diameter-to-length ratio. However, other factors (e.g., heat removal) are affected by such a change.

An interesting cold-trap control feature that has potential for increasing trap capacity has been proposed in a design study for the Fast Flux Test Facility (FFTF). The trap itself is a modification of the HNPF design. The unique feature is a bypass line, containing a flow-control valve, around the economizer section of the trap (Fig. 1.12). The bypass was incorporated to eliminate complete dependency on reduced cold-trap inlet flow when intratrap temperature regulation is required [54]. This bypass could give the operators means for preventing formation of oxide crystals upstream of the mesh section, for distributing oxide deposition in the trap when sodium feed to the trap is saturated with oxygen, and for redistributing oxide in the mesh section when the feed is no longer saturated; however, precise placement or redistribution of oxide deposits is difficult to achieve. At a minimum, additional temperature sensors in the mesh section would be required.

(4) *Basic Data.* Fundamental information on the crystallization process and filtering operation occurring in cold traps is very difficult to obtain; hence few basic data are available.

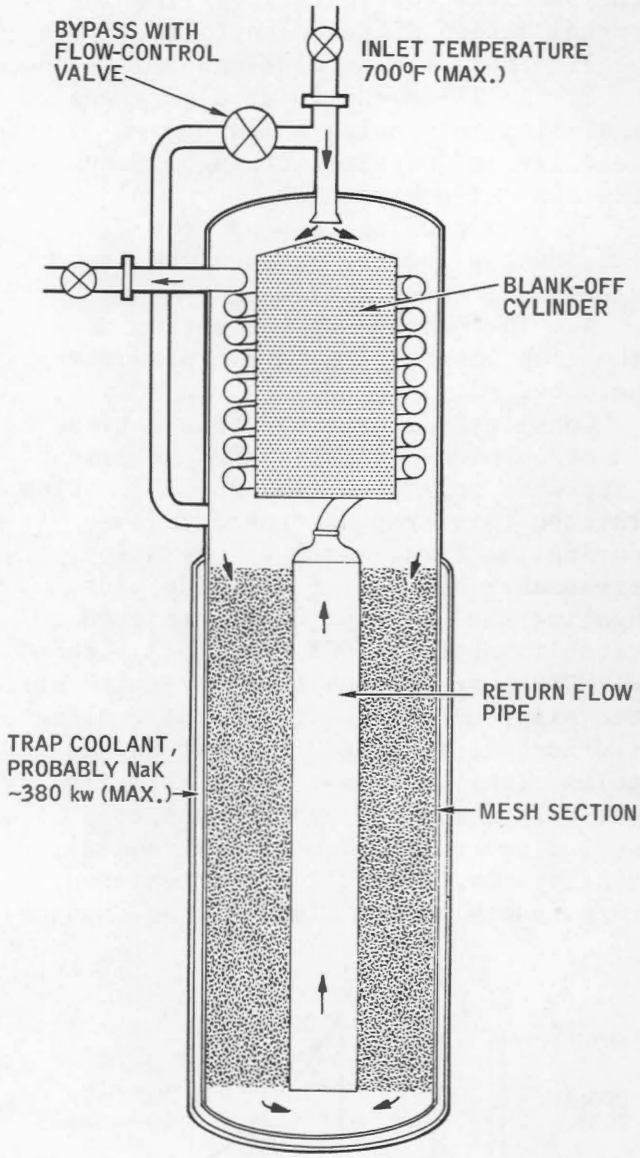

Fig. 1.12 Proposed Fast Flux Test Facility cold trap.

Several references contain information of value to a cold-trap designer on the behavior of sodium oxide.

In an early General Electric Company report [33], the theory of trapping was discussed, and cold-trap calculations and a definition of trap efficiency were presented. It was hypothesized that rapid subcooling of sodium feed to a trap yields intense nucleation, with suppression of growth of large crystals. Evidence was presented that the efficiency of a trap

can be improved by operation with filtration-zone temperature close to the desired saturation temperature.

In later work at General Electric Company [60], an investigation of sodium oxide plug formation was reported. Such plugs were found to be composed of a solid, porous structure, with metallic sodium retained in the interstices. A coefficient for oxygen diffusion through sodium was developed.

Basic cold-trap studies were included in the work [60]. The removal and retention of sodium oxide appeared to be due primarily to the mechanism of crystal growth at cooled surfaces. It appeared that packing, when used, helped support and retain the oxide. Some mechanical-filter action was also indicated. Trap capacity was found to be 16 to 20% sodium oxide by volume in this experiment. Information on hardness of the deposit was obtained. Wire mesh was demonstrated to be a more effective packing material than Raschig rings or screen.

During terminal examination of the EFAPP cold trap, samples of mesh were examined in detail. All the samples examined exhibited a similar pattern of oxide deposit on the mesh. A fairly uniform coating was observed on the wire, with a filet or web-type build-up at the intersection of the wires. As the coating thickness approached a few mils, the deposit had a fuzzy structure and a less dense appearance. This indicates the possibility of direct crystal growth on the wire. These experiments were not sufficiently sophisticated to prevent mechanical displacement of sodium oxide particles from sites where bridging might have occurred. Metallurgical examination of the stainless-steel-mesh samples from the cold trap showed no evidence of surface corrosion or intergranular attack [34].

From the data obtained in a batch crystallization experiment [61], estimates were made of sodium oxide particle size. The radius of the most probable particle size was calculated to be 0.175 in., and the approximate population-size-distribution curve was developed.

Fundamental information also appears in the Russian reports [55, 56, 57, and 62]. (Reference 62 is a survey report.)

Experimental work at LASL commenced in 1967 to determine the mechanisms of impurity precipitation in cold traps and to measure the mass-transfer coefficients involved. Initial tests were made using a simple, concentric-tube trap without any packing. Results obtained during fiscal year 1968 pointed to two important conclusions: (1) The mass-transfer coefficient is a function of velocity of sodium in the cold trap. For laminar flow the coefficient increases with increasing velocity approximately as the square root of the Reynolds number; this velocity dependence indicates that the process is diffusion-rate limited. (2) The mass-transfer coefficient is temperature dependent; the coefficient increases with increasing sodium temperature. Arrhenius graphs indicate that the activation energy for mass transfer was approximately 3 kcal/mole. This value agrees well with the activation energy for diffusion of oxygen in sodium; this is further evidence of a diffusion-controlled process [48]. This program continued in fiscal year 1969.

(5) *Conclusion.* Some existing cold-trap designs have been used successfully in large reactor coolant systems, particularly in systems where impurity concentration in the sodium has always been low (e.g., EBR-II). Where sodium oxide levels have been high because of maintenance or component replacement operations, capacity limitations of existing traps are very apparent. In these latter cases, where purification duty requirements have been severe, the time required to replace expended (plugged) traps contributed significantly to the reactor operating time lost because of postmaintenance coolant cleanup. The cost of replacement traps and replacement installation

costs also contributed to operating expense. This experience has strongly indicated the need for optimization of cold-trap design.

(b) *Natural-Convection Cold Traps*

The simplest cold trap is any surface in a system whose temperature is less than the saturation temperature of an impurity having decreased solubility at low temperature. This type of impurity will precipitate on such a cold surface. In a large system branch lines containing stagnant sodium act as cold traps if the minimum temperature of the lines is less than the saturation temperature of sodium in the system. If sufficient oxide is collected, the branch line can become completely plugged. Such a stagnant branch line has been called an "informal" or "inadvertent" cold trap.

The principle has been used to advantage to purify sodium and NaK in small systems, particularly in corrosion- and component-test loops and in charge tanks, where the rate of removal is not critical. The device utilizing this principle is called a "natural-convection" cold trap; an early, less descriptive term was "diffusion" cold trap. In its simplest form it can be a capped pipe stub mounted on a tee in a liquid-metal loop and cooled by natural convection of air. The design method for establishment of trap length utilizes heat-transfer equations developed for a finite fin with an insulated end. The application of this method is given in Ref. 63 (for valve freeze-seal design).

A similar trap mounted on the bottom of a static corrosion-test tank was constructed of two reducers, instead of a straight pipe section, to give added oxide capacity. A blower mounted adjacent to the trap was controlled automatically to maintain the desired temperature at the base of the trap. This temperature was varied in different tests to maintain specific oxygen concentrations required in the corrosion-test program (sodium peroxide had previously been added to the tank). This experience verified that solubility-temperature-dependent impurities can be returned to a tank or system by heating the cold trap.

Of the two designs (a well of straight pipe and a pot connected by smaller piping), the straight length of piping appears to furnish a faster removal rate [20]. Satisfactory operation of natural-convection cold traps appears to depend on velocity of the sodium or NaK stream at the tee where the trap is attached to the loop. At low velocities trap temperatures are steady, and impurities are removed or their concentration in the system is maintained at a constant level. In a 2 1/2-in. system with a trap mounted on the branch of a tee, a threshold velocity (or a velocity-related parameter) above which trap temperatures are unstable has been observed, and there is negligible net collection of impurities.

Although discussion of cold trapping usually is concerned with sodium oxide, the principles apply to other impurities whose solubility is temperature dependent; for example, cold trapping of sodium hydride in a natural-convection trap has been reported [64].

1-3.2 *Chemical Reaction*

One method of purification is to add a highly reactive material (getter) to the liquid-metal system to scavenge, or chemically bind, an impurity and thus effectively isolate it from further reactions in the system. These reactive materials can be in solid form in bypass or mainstream locations, or they can be added as dissolved getters in low concentrations throughout the coolant. The use of reactive materials in solid form is called "hot trapping," and the components in which the extraction operation is conducted are called "hot traps." Principal application of hot traps has been the

extraction of oxygen and carbon from sodium and NaK, although they can remove hydrogen and nitrogen as well [65]. Hot traps can maintain an oxygen concentration in sodium lower than that attainable with cold traps. Gettering material used in dissolved form in the liquid metal is termed a "soluble getter." Soluble getters, discussed in Sec. 1-3.2(c), have had limited applicability due to the plugging potential of the compound formed by chemical reaction of the getter and impurity.

(a) *Oxygen Hot Trap*

Zirconium has proved to be a useful getter for oxygen. Zirconium oxide is very stable from a thermodynamic standpoint; the equilibrium partial pressure of oxygen over zirconium oxide at 1200°F has been estimated to be 10^{-52} atm, compared with a pressure of 10^{-33} atm over sodium oxide [37]. This indicates that zirconium will reduce sodium oxide and chemically retain the oxygen gettered from sodium. Also, zirconium is quite insoluble in sodium.

A zirconium hot trap was used during early operation of the SRE core cooling (primary) system, which contained 50,000 lb of sodium. The trap was sized so that oxygen would be absorbed preferentially on the hot-trap zirconium (at 1200°F) rather than on the zirconium moderator cans (1000°F maximum temperature) in the reactor core in the ratio of ten to one. Hot traps, where the getter is the same as the material being protected, have been operated at a temperature approximately 200°F above the temperature of the material being protected so the trap can compete effectively for the impurity being extracted. Maximum trap temperature is constrained by vessel- and piping-design considerations. In the SRE, sodium entered at 1165°F, having been preheated in an economizer, and then passed through the zirconium coils and out the discharge line. Discharge temperature of 1200°F was maintained by the 30-kw furnace. Sodium flow rate was 6 gpm. Gettering material was 0.004-in.-thick zirconium sheet assembled in 14-in.-diameter by 6-in. coils made of alternate corrugated and flat sheets, as shown in Fig. 1.13. The trap contained eight of these coils, with a total area of 4300 sq ft. Fittings shown at the top of the trap were provided to permit replacement of the zirconium inserts [37]. Replacement of these inserts was not required. However, experience with other sodium components containing inserts has proved the insert-removal operation to be difficult because of the possible spread of radioactive contamination. Special handling equipment containing an inert atmosphere and gas-tight gates would be required. Because of this problem, the removable-cartridge feature was eliminated when carbon hot traps were introduced at SRE [44].

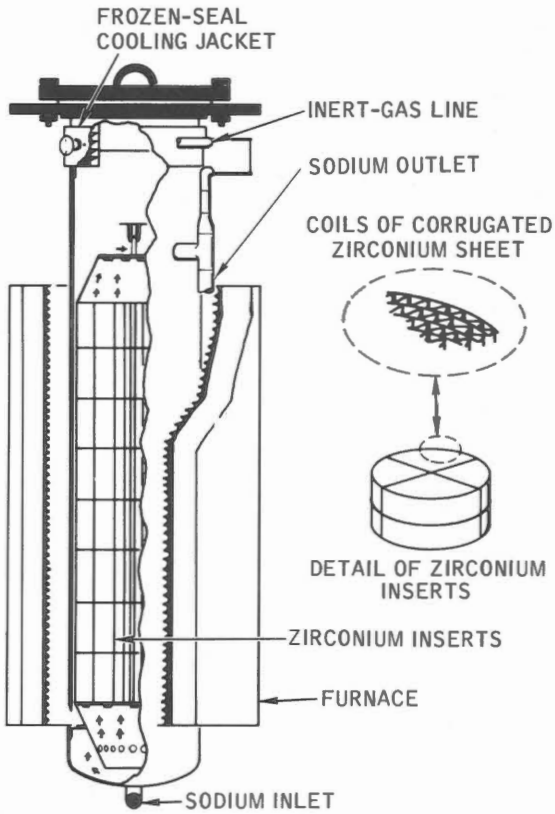

Fig. 1.13 Sodium Reactor Experiment oxygen hot trap.

Figure 1.14 shows the effect of

initial oxygen-hot-trap operation on sodium saturation temperature. The cold trap was valved out of the system at this time to avoid transferring oxygen from the cold trap to the hot trap; isolating the cold trap during oxygen hot-trap operation was standard SRE practice. At the same time the hot trap was started, system sodium temperatures were increased as a result of reactor start-up. This caused an increase in saturation temperature as residual oxide was dissolved out of informal cold traps in the piping system. At 141 hr of operation, oxide solution was essentially complete, and the saturation temperature decreased as shown. The chord of this curve between 8 and 10 ppm has a slope corresponding to an oxygen removal rate of 0.009 lb/hr. After such a start-up period, the hot trap maintains saturation temperature below the limit of detection with a plugging meter [37] (225°F).

SRE hot-trap design was based on the behavior of smooth, chemically polished zirconium exposed in sodium containing 10 ppm oxygen at 1200°F, for which the rate constant, k, relating oxidative weight gain per unit area with time, had been determined [37] to be equal to 0.0454 mg/cm^2/hr$^{1/2}$. The derivative of the equation, $w = kt^{1/2}$, with this experimentally determined constant, evaluated at 150 hr, is 0.016 lb of oxygen per hour. This predicted rate is about twice the rate determined from Fig. 1.14 after the first 150 hr of operation (0.009 lb of oxygen per hour). The difference between the rate predicted on the basis of material studies and the observed rate was attributed to the following factors [37]:

1. The original experimental work was done on chemically polished zirconium. The strip used in the SRE trap had a thin oxide film resulting from the manufacturing process. Because of this initial oxide film, the condition of the gettering strip was represented by a point somewhat out on the parabolic weight-gain vs. time curve, rather than at the origin as the calculation of predicted rate assumes. Therefore all the actual trapping rates would be less than those calculated.

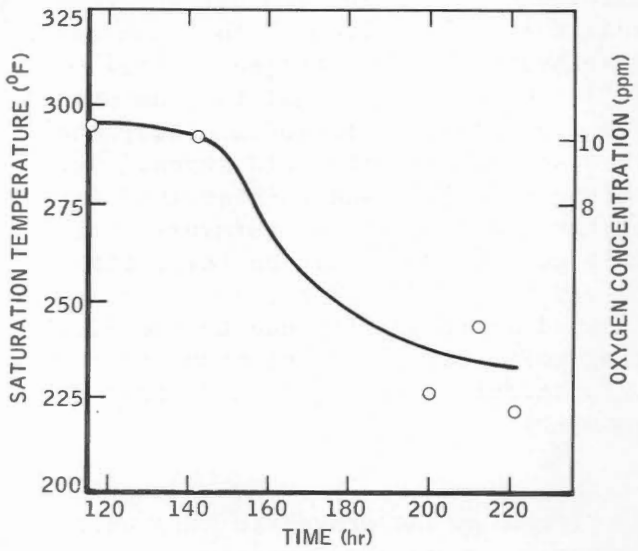

Fig. 1.14 Sodium Reactor Experiment oxygen-hot-trap performance.

2. After 150 hr of operation, the oxygen content of the sodium flowing through the trap was being depleted. The inlet concentration was 9.3 ppm, but the outlet concentration was calculated to be only 5.4 ppm. Therefore the actual rate constant, k, was less than 0.0454 mg/cm^2/hr$^{1/2}$, which had been determined in sodium containing 10 ppm oxygen. The rate constant, and hence the trapping rate, were decreasing throughout the length of the vessel.

The rate equation used at SRE was experimentally determined for relatively short exposures, compared with the expected life of a hot trap. However, the validity of the equation has been demonstrated for exposures to 4000 hr for zirconium-based alloys. The equation should be valid as long as the oxide film remains intact, since oxygen diffusion through this film controls the rate of reaction. There was no indication of cracking or spalling of the oxide film on any of the

zirconium samples exposed at Atomics International [37].

Investigators in the USSR [55] reported a permissible increase in weight of zirconium per unit surface area, from the standpoint of embrittlement and scaling, of about 4% in samples exposed to sodium cold trapped to a temperature of approximately 110°C (equivalent to 1 ppm oxygen). The permissible increase is reduced to 1.5 to 2% for samples exposed in sodium purified by a hot trap. In the former case the increase in weight is limited by embrittlement and scaling of the oxide layers, and in the latter, by embrittlement of the complete sample. The more intensive embrittlement of zirconium during its exposure to sodium containing a smaller amount of oxygen was explained by the more uniform distribution of oxygen along the cross section of the sample. With large oxygen contents a thick layer of oxide forms on the surfaces of the zirconium and hampers the diffusion of oxygen into the depth of the sample.

The effect of sodium velocity on oxidative weight gain of zirconium was recently reported [55]. No velocity effect was observed on samples exposed to sodium containing approximately 50 ppm oxygen. In sodium purified by hot trapping, however, zirconium weight gain was reduced by a factor of more than 2.3 when velocity was reduced from 0.2 to 0.02 m/sec. This was explained by the fact that diffusion of oxygen in sodium plays a significant role in the kinetics of the process when oxygen concentration in sodium is very low. This apparent rate-controlling role of the diffusion of oxygen in sodium on the oxidation of zirconium in sodium containing very little oxygen was noted in early hot-trap experiments at Atomics International when chemically polished zirconium specimens that had extracted oxygen from hot-trapped sodium did not exhibit the visible oxide layer always seen on specimens exposed to cold-trapped sodium.

Other information on the oxidation of zirconium in sodium appears in Chap. 2 and in Vol. I, Chap. 2, including references to the work of Williams [66] and Mackay [67]. Smith [68] has analyzed the literature and discussed the partition of oxygen between zirconium oxide film and zirconium metal. A zirconium getter was used to decompose Na-C compounds prior to a distillation operation in the preparation of very pure sodium for research purposes [69]. Zirconium in a hot trap will decarburize stainless steel [70]. The significance of this side reaction must be evaluated during the selection of a zirconium hot trap for service in a sodium heat-transfer system, considering temperatures, carbon activity of the various materials, and material surface areas.

In addition to zirconium, potential hot-trap materials are Ti, Zr-Ti alloys, Ta, Nb, V, U, and Pu [5]. Some gettering of oxygen from NaK at the DFR in Scotland was attributed to uranium exposed to the coolant [53]. A zirconium hot trap has been used at Los Alamos Molten Plutonium Reactor Experiment (LAMPRE) to protect tantalum in the core. A comparison of zirconium and tantalum as getter material is given in Fig. 1.15. Tantalum loses weight as the oxide formed sloughs off the base metal [71]. Niobium metal and the alloy of Ta-10% W also lose weight in sodium containing oxygen [3].

Interest at Atomics International was drawn to Zr-Ti alloy (equal atom percent) by its rapid oxidation in gas [72]. Chips (lathe turnings) of this alloy were used in early hot-trap experiments at Atomics International. The alloy does have disadvantages. This material was very brittle and hence difficult to machine or otherwise work. The alloy is pyrophoric; chips from the lathe burst into flame. Extensive settling of the lathe turnings

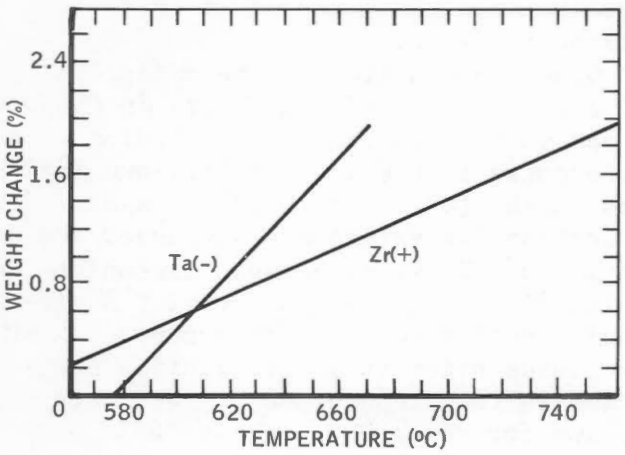

Fig. 1.15 Tantalum and zirconium weight change after 144 hr in cold-trapped sodium.

used in the hot traps was observed. The alloy hot trap performed well, but zirconium was selected for SRE, partly because of its availability.

Anodic electrolysis of oxide-coated gettering alloys in sodium was evaluated as a means of increasing their oxygen removal rate [65]. Removal rate gains were not large enough to warrant practical application. However, some of the alloys with nonadherent, porous oxide films achieved higher removal rates than had been sought by electrolysis. The best of these was Zr-13 at.% Ti, which averaged 750 $\mu g/cm^2/hr$ of oxygen removal during a 72-hr exposure at 1200°F in sodium containing about 150 ppm oxygen (cold-trap temperature, 620°F). The average removal rate of zirconium was about 20 $\mu g/cm^2/hr$ at these conditions. A 13-day test showed that this alloy would maintain its high oxygen-removal rate until completely consumed. Gettering performance of all the alloys forming nonadherent oxide films was less sensitive to temperature than gettering material that formed adherent oxide films; hence the former increased their comparative advantage at lower temperatures. It appeared that the alloys forming nonadherent films should be useful at temperatures as low as 800°F, and possibly lower. In a loop containing no cold trap, Zr-13 at.% Ti produced a minimum oxygen level of less than 1 ppm (measured with an electrochemical oxygen meter) and maintained a significantly higher removal rate than zirconium at the low-oxygen levels. It was concluded that the use of such an alloy offered the potential for significant savings in size and cost compared to conventional zirconium hot traps. The report discusses hot-trap design criteria [65].

Inconsistencies exist in the literature regarding the adherence of oxides formed on Zr-Ti alloys. McKee [65] observed that Zr-Ti, Zr-Y, and thorium-base alloys formed nonadherent oxide layers. On the contrary, Subbotin and coworkers [55] reported that the oxide layer formed on Zr-Ti alloy adheres to the base metal. When Zr-Ti (equal atom percent) alloy was exposed to cold-trapped sodium at Atomics International in 1956, alloy specimens exhibited weight gains, and the oxide formed was adherent.

Certain items are noted for the consideration of the designer in trade studies between getter materials having adherent (fixed) and nonadherent (spalling, sloughing) oxide layers. Getter material having oxides that adhere to the getter metal (e.g., zirconium) has been preferred for hot-trap applications, at least partially because of the desire to avoid the use of materials that could introduce impurities that might interfere with operation of the system and to avoid the need for additional equipment such as filters. However, thin zirconium that has gettered a lot of oxygen is very brittle and friable; a potential exists for the loss of particles of oxidized zirconium from a hot trap and entrainment of these particles in sodium discharging from the trap. The discharge plenum in the SRE hot trap, where sodium velocity was very low, was available as a settling chamber to retain any

but the finest particulate matter. Getter material that forms a non-adherent oxide presents two problems:

1. Some means must be provided to retain the loose oxide, e.g., a filter.
2. The loose oxide sloughed off the getter material may plug passages between the getter sheets or packing and restrict sodium flow and prevent full utilization of all the getter material in the trap.

(b) *Carbon Hot Trap*

Carbon has been removed from sodium by gettering through carburization of stainless steel. Feasibility of this method was indicated from studies of carburization of 304 stainless steel in sodium [13]. Carburization of stainless steel, zirconium, and other materials is discussed in Chap. 2 and in Vol. I, Sec. 2-4.2(f).

Table 1.9 lists the results of capsule tests conducted over a period of time on 0.060-in.-thick specimens to screen candidate materials for carbon removal capability [73]. Specimens were 0.060 in. thick; materials are listed in decreasing order of total carbon gain. Results available when a trap-design decision was required for SRE indicated 410 stainless steel to be the most promising material. Subsequent development work at Atomics International emphasized this material and 304 stainless steel. Candidate materials listed above 304 stainless steel in Table 1.9 are worthy of further investigation.

Equilibrium and diffusion-coefficient data were obtained for 304 and 410 stainless steels. Comparison of the data shows that the choice of material for removal and control of carbon content must be made for a particular system. The pertinent differences between these two steels are:

1. At temperatures below 1250°F, the carbon content of 304 stainless steel in equilibrium with "carbon-saturated" sodium was found to be higher than that of 410 stainless steel under the same conditions. Above 1250°F the reverse is true, as indicated in Fig. 1.16.

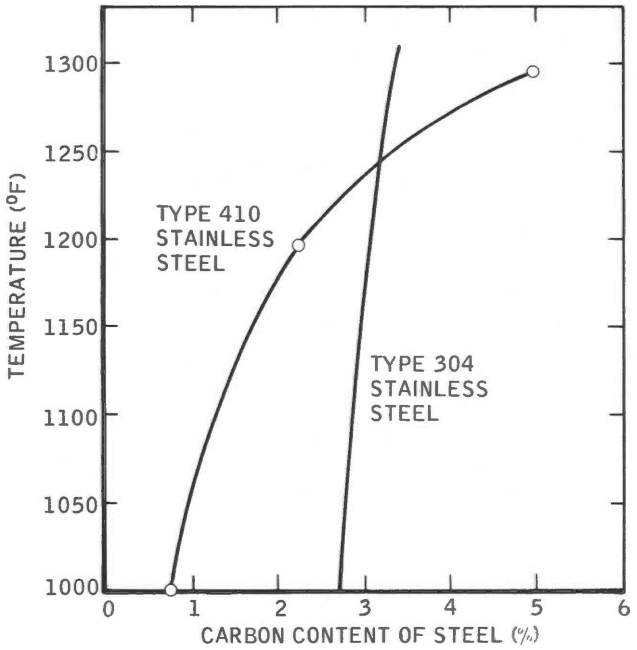

Fig. 1.16 Carbon contents of 304 and 410 stainless steels in equilibrium with carbon-saturated sodium.

2. At 1300°F the carbon content of 304 stainless steel in equilibrium with sodium containing less than approximately 55 ppm carbon (elemental carbon) was found to be higher than that of 410 stainless steel. With sodium bearing more than 55 ppm carbon, the reverse is true (Fig. 1.17).
3. The apparent diffusion coefficient of carbon in 410 stainless steel as determined in the tests is greater than that of 304 stainless steel by a factor of approximately 4 in the temperature range of 1000 to 1300°F. These comparisons show that 410 stainless steel of a given size and geometry will remove a greater amount of carbon more rapidly than 304 stainless steel provided the sodium is nearly saturated with carbon [73].

The relative rates of carburization of 304 and 410 stainless steels at 1300°F were calculated for various elemental-carbon levels in sodium (Fig. 1.18). At approximately 29 ppm carbon

TABLE 1.9 Carbon Gain of Specimens Exposed to Carbon-Saturated Sodium at 1300°F for 200 hr

Material	Initial carbon, %	Average carbon after exposure, %
9 Cr-1 Mo	0.10	1.84 to 1.84
5 Cr-0.5 Mo-Ti	0.08	1.60 to 1.66
430 S.S.	0.08	1.58 to 1.62
7 Cr-0.5 Mo	0.10	1.50 to 1.64
410 S.S.	0.10	1.50 to 1.55
5 Cr-0.5 Mo	0.10	1.39 to 1.45
2.25 Cr-1 Mo	0.12	1.27 to 1.35
5 Cr-0.5 Mo-Si	0.10	1.01 to 1.14
1.25 Cr-0.5 Mo	0.12	0.90 to 0.91
304 S.S.	0.06	0.72 to 0.78
0.5 Cr-0.5 Mo	0.12	0.55 to 0.64
Zr	Nil	0.05 to 0.06
Cr	Nil	0.04 to 0.05

concentration in the sodium, the rate of carburization of 304 stainless steel is twice that of 410 stainless steel. At approximately 40 ppm carbon concentration in sodium, their carburization rates are equal. At approximately 56 ppm carbon concentration in sodium, the rate of carburization of 304 stainless steel is one-half that of 410 stainless steel. It can be seen that 410 stainless steel will getter carbon initially at a higher rate than 304 stainless steel if the initial carbon is above 40 ppm. However, as carbon content is reduced by gettering, the relative gettering effectiveness of 304 stainless steel increases rapidly [73].

In the development of this hot-trap design information, chemical analysis for carbon in sodium was performed by using the Pepkowitz-Porter wet-oxidation method [74]; the Van Slyke reagent was used to oxidize the carbon. This method gives a value for what is currently called elemental carbon rather than a value for total carbon. There is no assurance that the kind of carbon measured by this analytical method actually carburizes stainless steel. In fact, no meaningful relation between chemical analysis of carbon in sodium and carburization of stainless steel is available [6, 75]. When this relation is resolved, that portion of the development where the concentration of carbon in sodium was used may require revision.

Anderson [73] presented nomographs relating pertinent variables in the design of carbon traps for sodium systems. The diffusion coefficients used in the preparation of the nomographs were determined on the mathematical assumption that the diffusion of carbon through stainless steel was isotropic and followed Fick's second law in its simplest form. In the mathematical analysis chemical reactions forming chromium carbide were not considered. Even if the diffusion model is not entirely correct, it appears suitable to use the diffusion equations for the same condition (i.e., temperature) from which the coefficients were derived [6].

These carbon-trap kinetic relations [73] are based on the assumption that

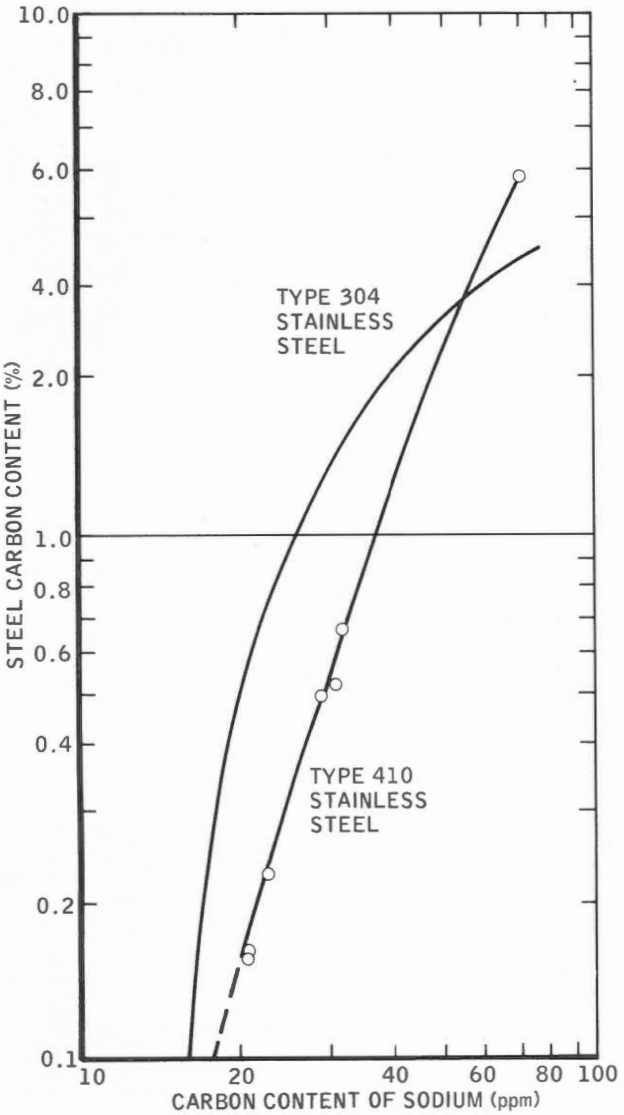

Fig. 1.17 Equilibrium carbon concentrations of sodium with 304 and 410 stainless steels at 1300°F.

diffusion of carbon in the getter material is the rate-controlling process, rather than diffusion of carbon through a sodium film. This has been shown to be valid for high carbon activity in sodium [13], the condition when trapping rate is important to the reactor operator.

Although the development presented by Anderson [73] has limitations, good use has been made of the carbon-trap design information. Traps designed on the basis of these data were used at SRE [14, 45], where demands on the

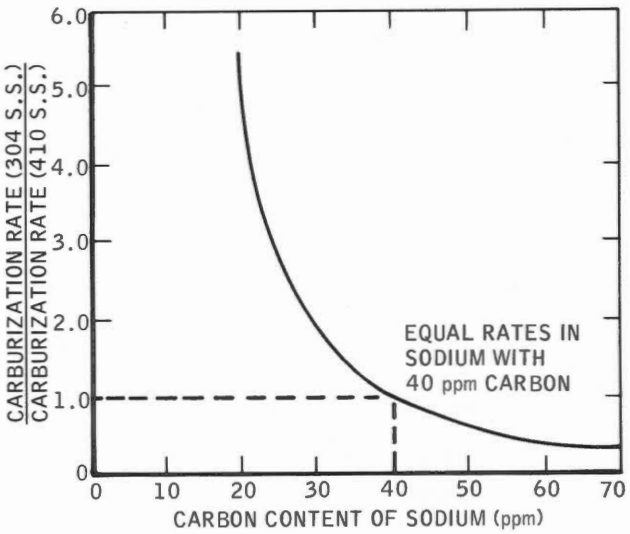

Fig. 1.18 Relative gettering rates of 304 and 410 stainless steels for removal of carbon from sodium as a function of carbon contents of the sodium (1300°F).

carbon-removal method were severe, and at HNPF [25, 26, 42, 43].

Design features of the SRE carbon hot trap are shown in Fig. 1.19. This trap was located in the same position as the oxygen hot trap discussed in Sec. 1-3.2(a) and utilized the same economizer and 30-kw furnace. A detail of the gettering coil is shown in Fig. 1.19; the coils were similar to those used in the oxygen hot trap but were mounted around the inlet tube. Both 304 and 410 stainless steels were used as the gettering material. A typical charge was 500 lb, which was theoretically capable of removing 10 to 12 lb of carbon. Sodium flow rate was 10 gpm; trap-outlet temperature was 1300°F. In this installation both inlet and outlet lines were connected to the top of the trap vessel so that they could be cut remotely (from ground level). The equipment was designed so that a vessel could be removed without personnel entry to the vault. Operational experience had demonstrated that a primary-sodium-system component of the unitized type could be removed and replaced with an entire new unit in about half the time re-

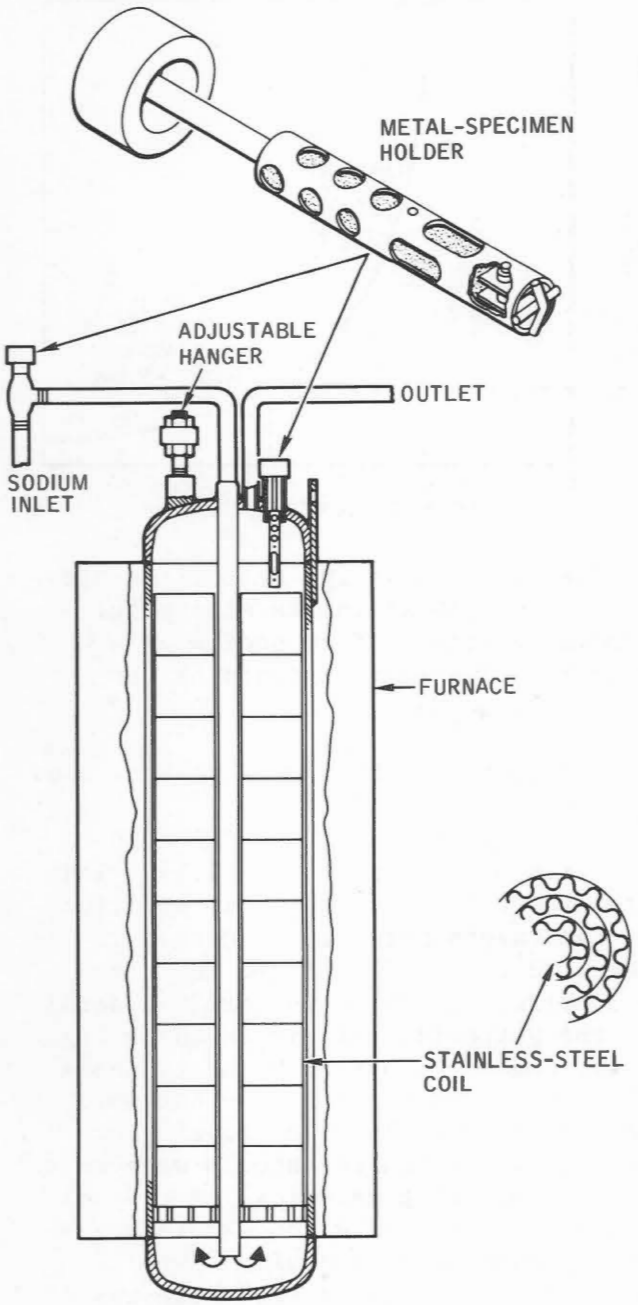

Fig. 1.19 Sodium Reactor Experiment carbon hot trap.

quired to replace an insert. Manufacturing costs for the new vessels were about the same as for the inserts in the oxygen hot traps [44].

Performance of the first three SRE carbon hot traps is shown graphically [14] in Fig. 1.20. During the first 11 months of SRE hot-trap operations, three traps (designated A1, A3, and B1) were used. Trap B1 was used for three separate runs, designated B1-1 to B1-3. The results of hot-trap inlet-tab analyses for surface carbon content of the inlet tab are plotted against time in Fig. 1.20. Specimens of 304 stainless steel were mounted in the inlet pipe and at the discharge end of the trap, as shown in Fig. 1.19.

A parameter used in considerations of carburization in Atomics International sodium systems is the surface carbon content of the structural material exposed to the sodium. This parameter characterizes the carbon activity of sodium without reference to sodium-chemical-analysis results, which have not been related to carburization of stainless steel. The surface carbon content of the metal sometimes is referred to as "carburizing potential" [14]. Surface carbon content has been related to mechanical properties of stainless steel [14, 28].

Surface carbon content of the inlet tab represented the carburizing potential of sodium in the SRE primary (reactor-coolant) system. Referring to Fig. 1.20, at the conclusion of the initial run of the hot trap (October 1961), surface carbon content of the 304-stainless-steel tabs showed 2.5% carbon instead of the as-received level of 0.06%. Later tabs indicated that the hot-trapped sodium would carburize 304 stainless steel at about 1250°F to approximately 0.4%, instead of 2.5% as in the first run. During this period system sodium temperature was limited to a maximum of 800°F to prevent carburization of components. After definition of a maximum surface carbon limit for 304 stainless steel of 0.5% by weight [14], higher temperature operations were resumed. Figure 1.20 demonstrates the removal of carbon from the SRE 50,000-lb primary sodium system.

Additional information on the performance of the hot trap used at SRE during run A3 (Fig. 1.20) was provided

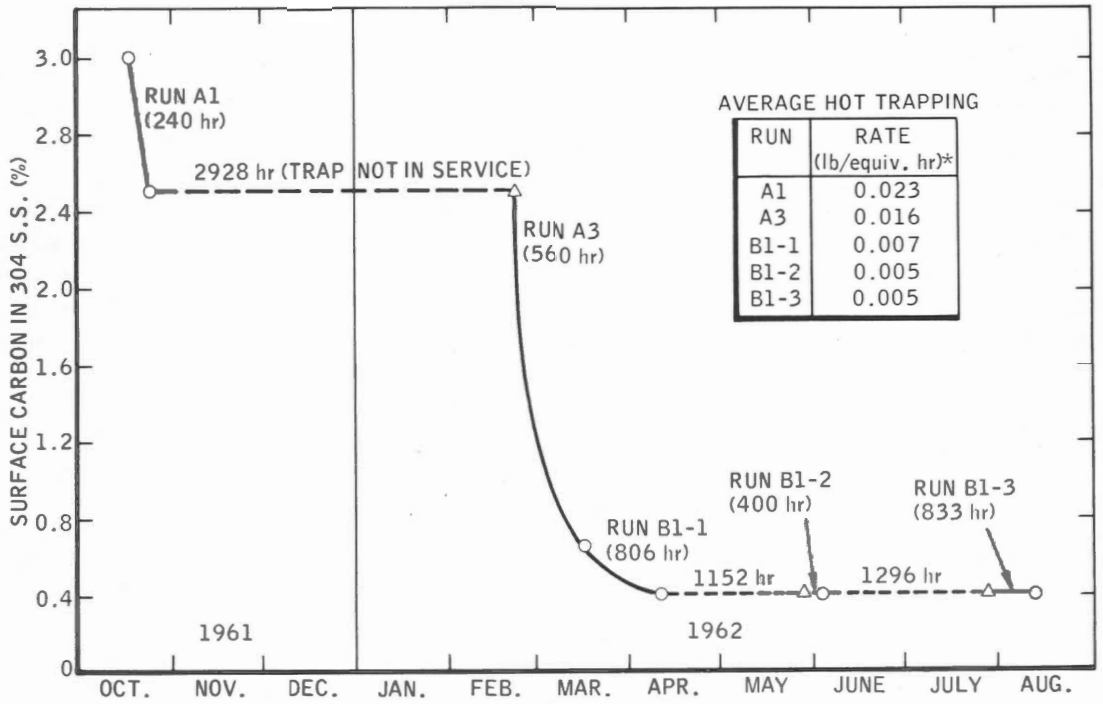

*Equivalent time at 1200°F.

Fig. 1.20 Sodium Reactor Experiment carburizing potential history. Δ, calculated. o, observed.

by postoperation examination of the component and adjacent piping [76]. Two top and two bottom getter sheet coils and a section of the inlet tube near the top of the hot trap used during run A3 were sampled. After decontamination the samples from the getter sheet coils were all found to be bright and shiny, 0.004 in. thick, and ductile. The composition of the sheet was confirmed by chemical analysis to be 410 stainless steel. Metallographic examination of the sample indicated a coarsening of the grain boundaries, but no evidence of a case was observed. The carbon content of the bottom coil averaged 0.15% carbon, as compared with 0.09% carbon for the top coil. Only a small fraction of the gettering capacity of this trap was utilized, as shown by a comparison of the 0.15% carbon content of the trap material from run A3 with the 1.50% content reported in Table 1.9. A section of the 304-stainless-steel inlet tube from a region near the top getter sheet coil was examined metallographically. A hardened case was found on the inside surface of the tube that had been exposed to the sodium as it entered the trap. Carbon analysis of thin sections of the inside surface of the tube averaged 0.25% carbon. However, a hardened case was not evident on the outside surface of the tube that was exposed to the sodium after it had passed through the getter sheet coils. Carbon analyses of thin sections of the outside surface averaged 0.10% carbon, which is below the metallographic detection limit for carbon in 304 stainless steel. Although the carbon content of the 410-stainless-steel getter sheets in the hot trap did not exceed nominal manufacturer's specification limits, the higher carbon content of the getter sheets at the bottom of the hot trap and the carburization pattern of the 304-stainless-steel inlet tube clearly indicate that the hot trap removed some carbon from the sodium.

A typical section of SRE hot-trap inlet line (1 1/2 in. in diameter, 0.150 in. wall, 304 stainless steel)

exhibited a carburized case. This section was taken between the economizer and hot trap; the line was operated at approximately 1250°F. Analysis of thin sections of the inside surface of the pipe indicated an average carbon content of 0.25%. In contrast, metallographic examination of a section from the hot-trap outlet line did not reveal any indication of carburization; except for the expected sensitization, the material appeared unaffected. This 304-stainless-steel line was installed in November 1961 and thus was exposed only to sodium that had passed through a carbon hot trap. Analysis of thin sections of the inside of this line indicated an average carbon content of 0.09%, which indicates an insignificant degree of carburization [76].

Carburizing potential of SRE primary sodium as monitored by tabs exposed to sodium was reduced by the use of hot traps. The decrease in carburizing potential was particularly significant during run A3, as shown in Fig. 1.20. Surprisingly, the getter material did not evidence much gain in carbon content. The fact that the hot-trap inlet line was carburized although the outlet line had no significant carburization supports the exposure-tab observations. Even though a number of hot traps were used, carbon introduced during the Tetralin leak [8] was not completely removed during Core II operations (1960 to 1964). May [77] summarized carbon removal at SRE.

Applications of these principles have been made to hot-carbon-trap designs for HNPF [41] and EFAPP [78]. AT HNPF, only intermittent operation of the trap was required to maintain the carbon in the sodium at low levels [79].

A temporary hot trap was operated a at the Fermi plant for 300 hr at 1200°F in 1962. At this time chemical analysis of sodium samples taken from the primary system verified the presence of carbon in the sodium. However, examination of the stainless-steel gettering material (total area, 1830 sq ft) after 300 hr of operation showed only slight carburization of the gettering material near the vessel inlet. Some loosely adherent material was deposited on the first three coils at the inlet. Analysis of samples of the deposit showed that it consisted of sodium oxide and metallic oxides and contained about 2.9% carbon [80]. It was estimated that less than 100 g of carbon was removed by this charge of gettering material. A permanent hot trap was installed, and seven carbon removal runs were made, but there was no detectable carbon pickup [81]. (The removable-sample-tab technique for monitoring carbon was not used.) The failure of these traps to remove carbon has not been resolved. The following items were presented for consideration [80]:

1. Carbon may have been absorbed by the stainless-steel components of the sodium system before the sodium entered the hot trap.
2. The preheating vessel for the hot trap might have absorbed the carbon during heating of the sodium.
3. The flow rate may have been too low for mass transport of sufficient carbon to cause significant carburization of the stainless-steel coils.

Although gettering is the best method available for removing carbon from sodium, performance of the equipment used to date has been inadequate for expeditious recovery from inadvertent carbon introductions. The rate of solution of carbon in sodium and transport to the purification equipment is a significant, perhaps the controlling, factor in the recovery problem. However, improvement in hot-trap design is needed. Suggested approaches are:

1. Increase trap temperature to improve carbon diffusion coefficients in the gettering material.
2. Increase sodium velocity to improve mass-transfer coefficients in the fluid film.
3. Perform all heating in the trap or other replaceable component to avoid

carburizing permanent piping and auxiliary components.

4. Use improved trap-monitoring methods, e.g., the carbon meter.

Prevention of carbon additions remains the most effective policy. Every effort should be made to exclude any carbon sources in all sodium systems.

(c) *Soluble Getters*

Soluble getters are materials soluble in sodium (or another liquid metal) which will react with an impurity to form a compound with limited solubility.

A survey of soluble getters for reaction with oxygen was included in a study of inhibitors to mass transfer in sodium [82]. Barium was determined to be the most effective, followed by strontium, calcium,and magnesium. From thermodynamic considerations, these elements are all capable of reducing sodium oxide at 1200°F. Formation of the oxide of the getter material is the reaction mechanism of these materials. Although soluble getters have been used in test loops, they have not been accepted for reactor use, because of potential problems with the insoluble oxides formed. These getters are by definition soluble in sodium and will be distributed around the system. The chemical reaction, which produces insoluble oxides, can occur anywhere in the system. These oxides may collect in locations where they can impede sodium flow or the operation of submerged mechanisms.

Several other references discuss soluble getters [83-85]. Soluble getters, in particular lithium, for the removal of hydrogen from NaK were considered in the SNAP-8 Corrosion Program at the Oak Ridge National Laboratory (ORNL) [1].

Carburization of austenitic stainless steel can be prevented in a sodium system containing graphite by the addition of calcium. This was demonstrated in a pumped-loop experiment [73]. Powdered graphite and graphite sticks were the carbon sources. Calcium metal chips were held in a bypass chamber. Sodium specimens removed from the metal-specimen chamber contained 555 ppm calcium by chemical analysis. Tabs of 304 stainless steel exposed in the specimen chamber at 1300°F for 620 hr would be expected to carburize to a depth of 0.016 in. in carbon-saturated sodium. None of the 304 specimens exposed during this test exhibited a carburized case; on the contrary, the specimens showed either no effects or slight decarburization. Examination of the graphite sticks located in the specimen chamber disclosed a dense white coating on the surface, which was identified by X-ray diffraction and chemical analysis as calcium carbide. The graphite suffered practically no deterioration from sodium penetration and subsequent solution or erosion. Plugging near the calcium bypass chamber was observed. These results showed that presence of calcium in sodium not only prevented carburization of 304 stainless steel, but actually the activity of carbon in solution was lower than that of carbon in the 304 specimens, as evidenced by their slight decarburization. This experiment demonstrated the potential of calcium as a soluble getter for the removal of carbon. It also pointed to the need for proper control of calcium addition and the need for a means of removal of particulate calcium carbide (and other insoluble calcium compounds that might be formed, e.g., calcium oxide) from the sodium system.

Some soluble getters can react with impurities other than the impurity forming an insoluble compound with the getter. These side reactions of soluble getters can have undesirable effects. An example is the transport of nitrogen by calcium in a sodium system, and subsequent nitriding of structural materials [see Sec. 1-2.2(b)].

(d) *Calcium Removal*

Calcium can be removed from sodium by oxidation to form calcium oxide, which can then be separated from the sodium by filtration. As noted in Sec. 1-3.2(c), calcium is thermodynamically capable of reducing sodium oxide. This method has been used to purify commercial-grade sodium in preparation for use in the Prototype Fast Reactor (PFR) at Dounreay, Scotland. Oxygen, in the form of sodium oxide, was added to the sodium, and the mixture was held at 350°C (662°F) to permit the calcium to oxidize and then filtered to remove the calcium oxide [86].

1-3.3 *Other Methods*

(a) *Filtration*

Removal of insoluble impurities from sodium is usually accomplished by filtration. The various filter media that have been used include porous sintered metals, glass, and, to a lesser extent, wire cloth [20]. Commercially available sintered-metal filters made of austenitic stainless steel have received general acceptance for use in test loops and reactor-filling service. Experience with porous sintered glass filters has been limited to low-temperature laboratory use.

The most important application of filtration is in the removal of gross amounts of oxide and other solids during initial charging to the system. A filter cake will accumulate during the life of the filter and in some instances will necessitate an increase in pressure differential to maintain a desired filtration rate. The filter pressure-drop problem can be lessened by designing for backflushing and providing for accumulation of solids below the filter. Backflushing can be accomplished by using helium or argon to blow the cake off the filter. During filtration of sodium oxides, plugging was found to occur if conditions existed which promoted oxide crystal growth within the filter bed (e.g., if the sodium was rapidly cooled and filtered or if the sodium temperature decreased during passage through the filter). Crystal growth in the filter can be prevented by retention of sodium at temperature to permit crystal formation before filtration coupled with maintenance of a uniform temperature through the filter. Crystal growth in the filter can also be prevented by heating the filter so that sodium temperature increases slightly as the sodium flows through the filter.

The efficiency of porous, sintered-metal filters for sodium oxide removal has been demonstrated to be 80 to 95% of theoretical, depending on the filtration conditions. The efficiency generally is improved after accumulation of a filter cake [20]. At the SIR Mark A prototype, brick sodium was melted in 900-lb batches and forced through a filter into a transfer tank operating under vacuum. A second filter was located in this tank. The batches of sodium were transferred by positive pressure through this second filter to the system storage tank. The filters used in both tanks were sintered stainless steel with an average pore size of 5 μ. Both filters were backflushed with helium after each transfer. As expected, heavy accumulations of sodium oxide occurred in the melt tank because of the oxidized skin on the brick sodium. This necessitated changing of filters and puddling and removing the oxide dross at approximately 6000-lb intervals. The filtration rate averaged 248 lb/hr/sq ft at an average temperature of 236°F with a 19 psi differential [7].

The difficulties resulting from the excess dross on brick sodium points up the desirability of procuring sodium in rail cars or cast in drums. Even when these forms are used, a filter is advisable. Filtration data taken on the Mark A transfer-tank filter would be applicable in these cases since the sodium filtered was relatively free of oxides. The average filtration rate from the Mark A transfer tank [7] was

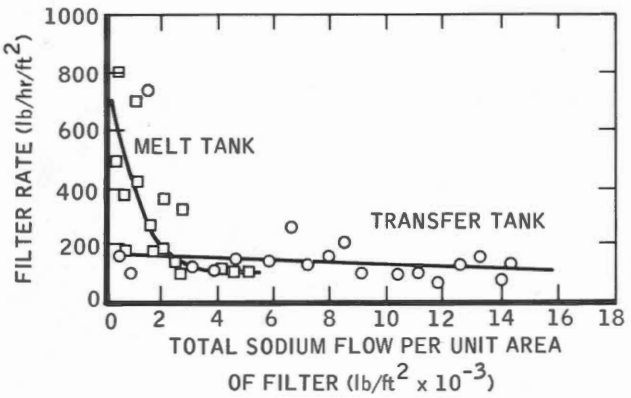

Fig. 1.21 Sodium filtration results of the SIR Mark A melt- and transfer-tank filters at an average sodium filtering temperature of 240°F. Filter medium is sintered stainless steel with 5 μ pore size. Melt-tank filter ΔP is 19 psi, and transfer-tank data are corrected to 19 psi. Both melt- and transfer-tank filters were backflushed with helium after each filtration.

177 lb/hr/sq ft at an average differential of 20.0 psi at 245°F.

Data from the SIR melt- and transfer-tank filters are plotted on Fig. 1.21. The pressure differential across the melt-tank filter was 19 psi. Transfer-tank-filter results were corrected to a 19-psi differential by use of a ratio of pressures. Chemical analysis of the sodium filtrate indicated that, of the common impurities checked (oxygen was excluded), the only element significantly reduced was calcium. Filtration decreased the concentration of calcium from 191 to less than 40 ppm. Before filtration calcium reacted with oxygen in the sodium to form the insoluble calcium oxide [7].

Filtration of sodium similar to that described here,before it is charged to a system,is practiced quite universally at reactors and sodium and NaK test installations.

During the Power Expansion Program (PEP) modifications to the SRE, a sintered stainless-steel filter was installed in the discharge line from the cold trap [87], primarily to remove particulate carbon (which had been observed in primary-fill-tank sodium) before charging the reactor, although its use was continued during reactor operations. Pore size was a nominal 20 μ. No flow was lost through the filter during its use with two cold traps. However, the radiation level of the filter gradually increased to 2 r/hr at its surface, and the filter was replaced to remove the radiation source [88].

Secondary sodium was filtered as a part of a corrective-action program at HNPF after pump binding was encountered and solid particulate material was discovered in the pumps. Sintered metallic filters having a 10-μ pore size (formerly used in the melt stations) were installed to permit bypass filtration. Sodium in each of the three secondary loops was passed through these filters approximately six times at linear velocities of about 10 ft/sec [42]. This filtration is believed to have contributed to solution of the pump-binding problem.

Sintered-metal filters are fabricated from porous sheet material. In the manufacture of the sheet material, metal or alloy powder is deposited in a flat layer of uniform thickness. Particle size range of the powder is selected to provide the final pore size desired. No binder is used. The layer of powder is heated in a furnace to a temperature just below the melting point. At this temperature, bonds develop at points of contact between adjacent particles. This material is available in a number of pore sizes (see Table 1.10). For a particular pore size, half of the fluid flows through pores smaller than the "mean pore size," as this term is defined. Manufacturing control is reported to be such that 98% of the pores are greater than one-half the mean pore size, and the largest pore is approximately twice the mean pore size. Filters fabricated of this material are available with pipe connections in a

TABLE 1.10 Properties of Porous Stainless-Steel Sheet*

Property	Grade (proprietary designation)						
	C	D	E	F	G	H	X
Mean pore opening							
In microns	165	65	35	20	10	5	15
In inches	0.0065	0.0025	0.0015	0.0008	0.0004	0.0002	0.0005
Minimum tensile strength, psi	6,000	9,000	15,000	15,000	15,000	15,000	25,000†
Approximate modulus of elasticity, 10^6 psi	1	1	1.5	2.5	2.7	3	15
Approximate voids content, %	55	50	50	50	50	45	20
Minimum flow of clean air at 1-psi differential, cfm/sq ft (1/8-in. thickness)	990	475	220	82	41	28	3.2
Minimum flow of clean water at 1-psi differential, gpm/sq ft (1/8-in. thickness)	180	120	20	8	3.5	1.5	1.2
Standard available thickness range, in.	1/8 to 1/2	1/8 to 1/2	1/16 to 1/2	1/16 to 3/8	1/16 to 1/4	1/16 to 1/4	1/16 to 1/8

*From J. B. Campbell, Porous Metal Sheet, *Mater. & Methods*, 41(4): 98-101 (1955).

†Sheets are pressed for increased strength.

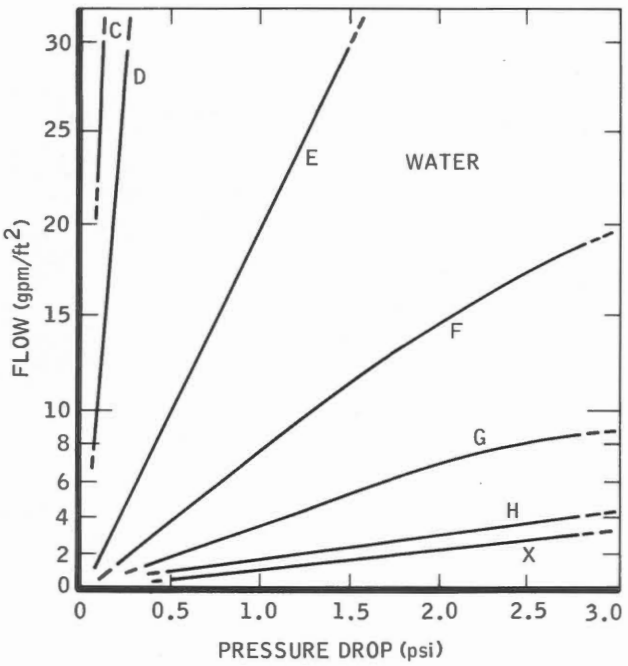

Fig. 1.22 Flow capacity of 1/8-in. porous metal sheet. (From J.B. Campbell, Porous Metal Sheet, *Mater. & Methods*, *41*(4): 98-101 (1955).

number of shapes: cylindrical, bayonet, star, and stacked disks (wafers). The last two shapes have been used successfully at Atomics International.

Flow of water through this porous metal is related to pressure drop in Fig. 1.22. The letters in this figure refer to the grade of material listed in Table 1.7. Flow capacities are double for 1/16-in. sheet, half for 1/4-in. sheet [89].

For a general relation, pressure drop for horizontal liquid flow through a sintered-metal filter can be approximated by [90]

$$\Delta P = - \frac{2.05 V_0 \mu L}{D_f^2} \qquad (1.1)$$

where

ΔP = pressure drop
V_0 = superficial velocity based on flow through filter chamber without a filter-element in place

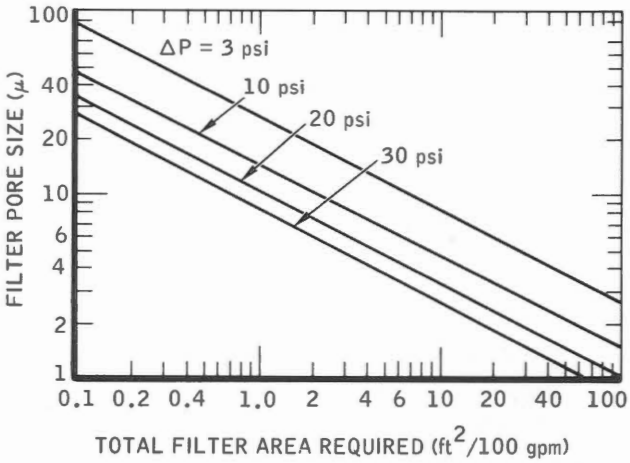

Fig. 1.23 Correlation of differential pressure, pore size, and filter area for 100 gpm horizontal flow of 750°F sodium through sintered-metal filters of uniform 1/8-in. thickness.

μ = dynamic viscosity
L = uniform filter thickness
D_f = effective pore diameter (mean pore size)

Values are in consistent units. The derivation was based on the assumptions that (1) filter structure is analogous to closely packed spheres of uniform diameter and (2) capillary energies may be ignored. The equation is presented graphically in Fig. 1.23. These operating conditions are typical for a filter installed in a bypass line. A permeability factor, K, takes account of disorders of internal geometry which cause each element of fluid to follow a tortuous path of variable cross section in passing through the porous medium. It has been used for investigating sintered-metal filters where conditions other than horizontal flow and uniform filter thickness exist. The permeability factor is related to filter pore size, D_f, by the expression

$$K = 1.23\, D_f^2 \qquad (1.2)$$

Some use of strainers (wire screens) in reactors has been noted in the literature. Both Atomic Power Development Associates, Inc. (APDA) [91] and

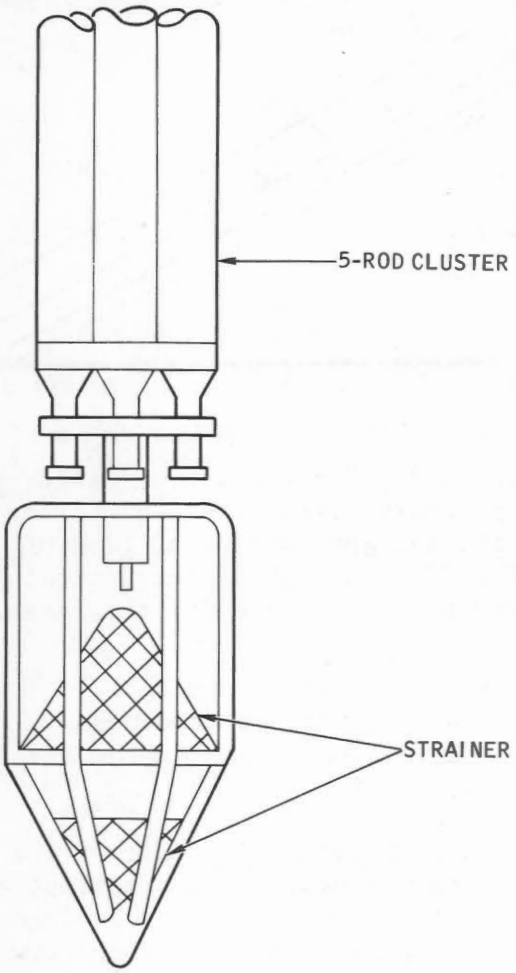

Fig. 1.24 Lower end of Sodium Reactor Experiment fuel element equipped with strainer.

Atomics International [92] have used strainers for diagnosis and examination of particulate matter in reactor sodium. At Atomics International a 20-, 60-, and 100-mesh-screen assembly was used to detect and remove carbonaceous particulates from the core. In 1960 SRE fuel elements were fitted with screens at the lower (inlet) end of the elements as shown in Fig. 1.24. The modification was made to prevent carbonaceous particles, present as a result of the Tetralin leak in the primary-coolant system [8], from entering fuel-coolant tubes. Screens were sized to prevent passage of particles larger than 0.054 in. This screen added approximately 0.75 psi to the fuel-element pressure drop

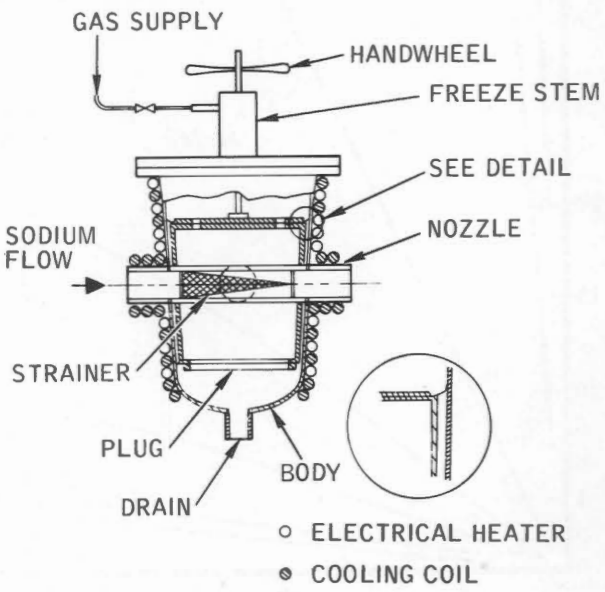

Fig. 1.25 Schematic drawing of valve-strainer device.

at a flow rate of 10 lb/sec [44].

Test results are available for an interesting combination of components - strainer and blocking valve [93]. This valve-strainer device is similar to a lift-plug valve; the strainer element is positioned in the normal flow passage of the plug, as shown in Fig. 1.25. The strainer element is stainless-steel-wire mesh with openings of 0.005 in. This device differs from a plug valve in several details: (1) an access port is built into the body at a 90° angle to the flow line to permit strainer removal, (2) the center of the plug is hollow to reduce its mass, and (3) the body has a connection for draining sodium from it before replacing strainer elements. Liberal clearances and manufacturing tolerances were a feature of this design; e.g., the annulus between plug and body was approximately 1/8 in.

This 3-in.-pipe-size combination valve and strainer device performed satisfactorily when tested in a sodium system. This device provides a means of removing an in-line strainer element from the system without draining sodium from the system and alternately serves as a plug-type blocking valve. Tests

were conducted over a temperature range of 500 to 950°F and system pressures of 0, 5, and 10 psi at sodium oxide contents of 50 to 400 ppm. The strainer element was isolated from the system by freezing the sodium around the valve plug. The time required to freeze the sodium was found to be primarily a function of system temperature, a typical value being 75 min for a system temperature of 800°F.

(b) *Settling*

Storage vessels are used for purification of sodium and NaK. Not only insoluble foreign material such as metal particles but also impurities having a temperature-dependent solubility in the liquid metal are removed in tanks.

The liquid metal is heated to above the saturation temperature of the system and then dumped into a storage tank to remove solubility-temperature-dependent materials. The metal is then allowed to cool to just above its freezing point and maintained at this temperature for several hours to precipitate the impurities. It is then recharged to the system through a filter. The process can be repeated until the impurity level has reached the required level. Purification to less than 5 ppm of oxygen has been obtained in this way. The method is suitable for initial cleanup of circuits, for removing accidental gross oxygen contamination, and for use on circuits where no installed cold trap is provided [49].

Purification of sodium used in a mass-transport-study loop was accomplished by cooling the sodium in a drain tank packed with Raschig rings to provide extended surfaces. This process was reported to be very effective [84].

Use of a horizontal cylindrical tank (4 ft in diameter by 8 ft) for removal of sodium oxide was investigated. An empirical correlation was obtained which gives oxide concentration as a function of time, initial conditions, sodium depth, and folding time of the sodium cooling. The tank was also used to remove sodium oxide from the 110,000-lb LCTL. After 25 batches had been cold trapped in the tank, oxide content of the LCTL was reduced from an initial level of approximately 115 ppm to a value of 43 ppm. It was concluded that the batch process provides an effective and economic means for removing oxides from sodium systems [61].

This method of cooling, precipitation, and settling (sedimentation) has been used successfully at ANL [94]. However, the use of a settling tank at ORNL to reduce the oxygen concentration of sodium was not successful [95]. In small-charge tanks this process is sometimes enhanced by the addition of a natural-convection cold trap to the bottom of the tank. Examples are the NaK fill tanks used in ground-test facilities for SNAP reactors. Refrigeration was provided to these cold traps to maintain minimum temperatures of 5 to 10°F [96].

In view of the purification capability of storage tanks, these tanks should be designed so that suction can be taken somewhat off the tank bottom when sodium is being transferred to an operating system such as a reactor. This feature should be incorporated into the design even if there are no plans to use the tank to remove an impurity such as sodium oxide. There is generally some foreign material, perhaps from the storage tank itself, that is best left in the tank. In addition to the operating suction line, it is normal practice to provide a separate tank drain at the very bottom of the tank.

(c) *Centrifuging*

Centrifuging has been tried on a laboratory scale at ANL to separate carbonaceous particulate material from sodium and NaK at room temperature. No significant degree of purification was obtained using 300- to 625-g centrifugal forces [97]. Only when the

forces were increased to 30,000 to 130,000 g was the content of suspended carbon reduced. Thus this method was impractical for removing particulate carbon from system sodium. A flow-through centrifuge capable of 64,000 g is being used in a development program at APDA.

(d) *Distillation*

In the early days of sodium purification, distillation (presumably under vacuum because of the low vapor pressure of sodium) was used for oxygen removal. Since the successful development of cold traps, the use of distillation for oxygen removal from sodium to be used in heat-transfer systems has not been justified in the United States. Removal of alkali metals and alkaline earths is a primary gain to be realized in a distillation procedure [20]. From the standpoint of the sodium-system operator, control of these and other metallic impurities can be achieved through proper specification at the time of procurement. However, the Russian BR-5 reactor reportedly uses a plant-scale distillation system for purification [5].

Use of distillation to prepare very pure sodium for research purposes was reported [69] in 1967. One of the reasons for using distillation was the need to achieve concentrations of metallic impurities lower than the concentrations in manufactured sodium. A zirconium getter was used prior to distillation to decompose Na-O-C compounds, thereby preventing the carrying of carbon and oxygen into the distillate. Oxygen concentrations of 0.6 to 5 ppm and a carbon concentration of 8 ppm were obtained by using this combination of methods.

Successful purification of sodium by vacuum distillation has been carried out on a small scale. Experimental results and a theoretical treatment have been reported [98]. A translation of a Russian paper reported results of vacuum distillation conducted at 10^{-5} to 10^{-6} torr. Both sodium and potassium were obtained in almost spectrographically pure form by this method [99]. A recent annotated bibliography [100] lists references on the theory and practice of high-vacuum liquid-metal distillation, covering the period from 1912 to 1963.

Distillation is relatively expensive in comparison with cold trapping. An estimate showed that 28,700 kw-hr of electricity would be required for a single distillation of 50,000 lb of sodium [101].

1-4 APPLICATION TO SYSTEMS

1-4.1 *Design Philosophy*

Purification is generally recognized to be an important part of the successful design and utilization of a sodium or NaK heat-transfer system. The importance of integrating coolant-purification considerations into the overall design effort from its beginning is, perhaps, not so widely accepted. Liquid-metal purification is not an isolated subject that can be satisfactorily handled by a specialist working outside the main stream of the design activity. Purification must be considered by the project design team concurrently with temperature, system temperature difference (ΔT), coolant velocity, materials selection, and system and component life in all trade-off studies commencing with the conceptual design.

1-4.2 *Equipment Arrangement*

Two examples of the arrangement of purification equipment, one for a "pot"-type reactor, the other for a "loop"-type system, are presented. These should not be considered optimum, but typical of arrangements which have been successfully tested in practice.

The EBR-II primary purification system, shown in Fig. 1.26, is an example of a purification system serving a pot-

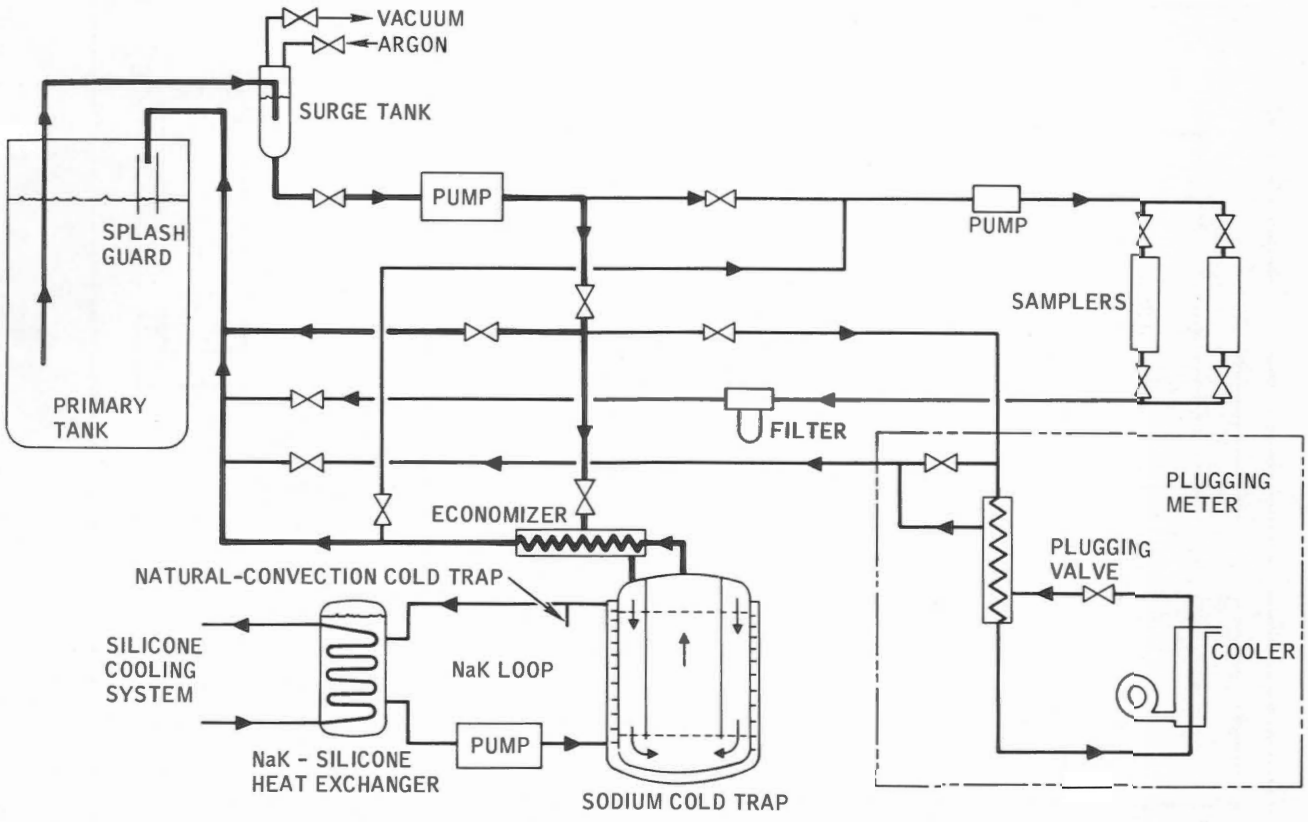

Fig. 1.26 Primary sodium purification system for Experimental Breeder Reactor No. II.

type reactor. The reactor is located in the primary tank. The primary sodium cold trap is cooled by a NaK loop, which rejects heat to the silicone coolant system. NaK is purified by a natural-convection cold trap mounted on the "hot leg" of the loop; this trap consists of a capped 2-ft length of 2-in. pipe. A regenerative heat exchanger (economizer) is installed external to the sodium cold trap. Two types of analytical devices are used to determine sodium quality. A plugging meter is mounted on the cold-trap inlet line to monitor the concentration of impurities in primary tank sodium. Two samplers are used to remove sodium samples for chemical or radiological analysis. Samples may be taken from either the cold-trap inlet or the discharge line.

Parts of the cold-trap circuit lie below the level of sodium in the primary tank. Since radioactive primary sodium is circulated in the cold-trap system, it is essential to eliminate the possibility of an accident or equipment failure that would result in the syphoning of primary tank sodium. For this reason the return line from the purification system terminates above the surface of sodium in the primary tank. To prevent syphoning through the purification-system feed line, control circuitry of the purification pump and isolation valve on the suction side of the pump are connected to leak detection and radiation monitoring equipment that will shut the system off if a sodium leak occurs or if high radiation level is sensed in the duct of the purification-vault exhaust fan. At the same time, a syphon break (which is activated by the same control circuitry) is provided as an extra safety feature

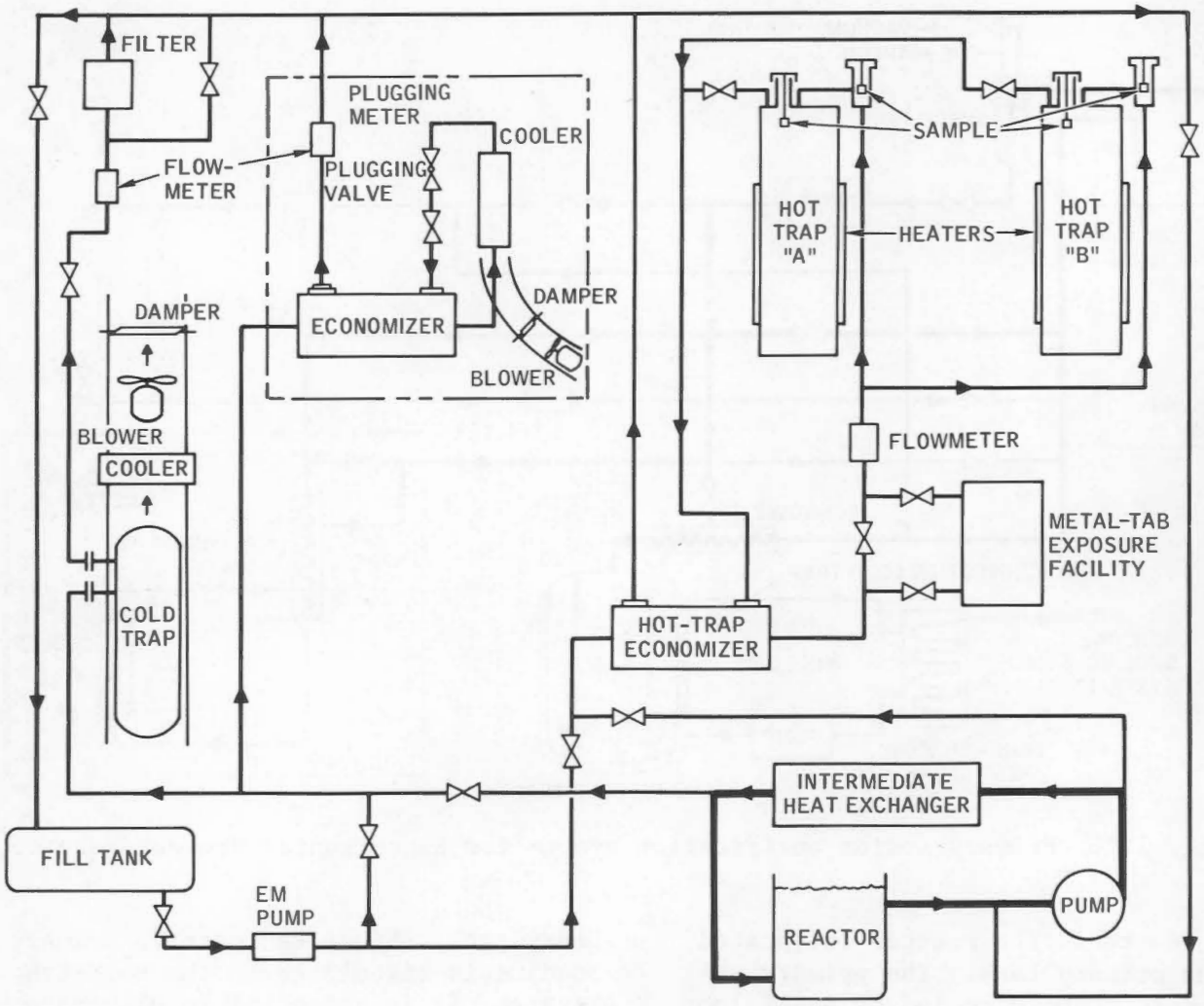

Fig. 1.27 Primary sodium purification system for Sodium Reactor Experiment.

to positively break any syphon action and empty sodium from the surge tank supply line back into the primary tank. Manual shutdown of the purification system and activation of the syphon break is also provided.

A diagram of the SRE primary (core-coolant) sodium purification system is shown in Fig. 1.27. Four improvements made during PEP modifications [87] following CORE II operations are included.

1. "Cold leg feed" (sodium at reactor-inlet temperature) was provided for the cold trap and plugging meter.

2. The former "hot leg" feed line was rerouted to serve the hot trap only.

3. A feed connection from the primary fill tank to the cold trap, hot trap, and plugging meter was provided to permit purification of sodium stored in this tank.

4. A metal-specimen exposure facility was installed in the hot-trap inlet line to permit specimen replacement without entry into the vault [102]. The first two changes were made to permit simultaneous hot trapping to remove carbon and cold trapping to remove oxygen. Vault nitrogen gas was used to cool both the cold trap and the plugging meter. At the cold trap nitrogen (at 150°F or less) was drawn past the trap; heat removed from the

cold trap was transferred to kerosene in the cooler, and the heat was rejected through the kerosene service coolant system. The vault-atmosphere cooling system easily handled the small heat load from the plugging-meter cooler.

The HNPF coolant system is similar to the SRE; i.e., it is loop type with a primary pump serving as the driving force for cold-trap flow. As noted in Sec. 1-3.1(a), changes in primary pump speed required by the HNPF reactor operating plan caused fluctuations in cold-trap flow rate. (Such reactor flow changes could be expected in an electrical-load-following plant.) The cold-trap temperature controller (which controls temperature by varying nitrogen coolant flow) was unable to compensate for these sodium-flow fluctuations. This resulted in release of sodium oxide from the trap to the system. Control of cold-trap sodium flow rate independent of coolant-loop flow rate would have prevented this oxide release from the trap. Initial operating difficulties at DFR also demonstrated the importance of controlling cold-trap sodium flow rate independently of main coolant pumps.

One way of achieving independent sodium flow control is the scheme used at EBR-II; the purification loop is served by its own pump, rather than a main coolant pump. This scheme has the additional advantage that purification-loop operation is not affected by shutdown of one of the coolant loops in a multiple-loop reactor; i.e., the purification equipment does not have to be switched from one main coolant loop to another. This switching operation can also be the cause of oxide release from a trap. Use of a separate pump for purification equipment is commended to the consideration of system designers.

1-4.3 *System Installation and Start-up*

Cleanliness of all components and assemblies must be carefully controlled during fabrication and installation to achieve a satisfactory degree of coolant purity after reactor start-up. All but the simplest of components must be cleaned on a part-by-part basis prior to assembly. It is not feasible to clean, rinse, and dry a complicated component like a cold trap or hot trap after the mesh or foil and all internal parts have been assembled and final closure welds on the vessel shell made. After components have been cleaned, they must be kept clean. Proper attention must be given to the problem of "air breathing" to prevent the accumulation of moisture in an open component subject to temperature changes during the day-night cycle. Adequate removal of condensed water vapor may not be possible, even if the presence of moisture is detected. Also, moisture can cause aqueous corrosion on internal parts of components that are no longer available for inspection. Maintenance of a dry, inert gas (e.g., argon or nitrogen under pressure) in a vessel or other component at all times between cleaning and final installation is an effective means for excluding moisture. Similarly, the piping-component system must be kept clean and dry during assembly.

After a sodium or NaK system (e.g., a reactor and associated sodium, inert gas, and vent piping) has been completely assembled, an inert-gas atmosphere must be established in the system before sodium or NaK is introduced. The best way to effect removal of residual gases from the installation activities is by evacuation of the system. Provision for evacuation before charging with the liquid metal should be a feature of all liquid-metal systems to the extent that it is economically feasible. Such provision is general in small systems, such as SNAP reactors but has not been included in the design of some large systems, e.g., SRE. If the system can be evacuated, several evacuation inert-gas-fill cycles should be per-

formed as required to effect removal of residual air, moisture, etc. Heating of the system during evacuation is an aid to the removal of gases adsorbed in the system. If the system cannot be evacuated, it must be flushed with inert gas to purge the system. Selection of purge connections should be made with due consideration for relative densities of the various gases involved.

Another item of importance to final coolant purity is the receiving of the liquid metal and preparation for charging to the heat-transfer system. If sodium is received in brick form, excessive surface contaminants can be removed by brushing the bricks with a wire brush before placing them in the melt tank. For most engineering-scale loops, sodium is received cast in drums or tank cars. NaK is received in special drums with an inert-gas cover.

After transfer from drums or cars to a receiving or "hold tank" (melt tank for bricks), sodium should be held to permit reaction of calcium and oxygen to form calcium oxide. Then the sodium should be cooled to precipitate sodium oxide and filtered with a sintered-metal filter to remove calcium oxide, sodium oxide, any other impurities whose solubility in sodium is temperature dependent, and all insoluble impurities. This filtering operation can be accomplished during transfer to the charge tank or transfer to the system if the charge tank serves as the receiving tank. Caution should be exercised in the use of sodium received with a very low oxygen content. If the oxygen concentration is less than that necessary to form a stoichiometric mixture with the calcium present, oxygen must be added to the sodium if removal of excess calcium is desired. [See Table 1.1 and Sec. 1-3.2(d).]

It may be desirable to cold trap the sodium or NaK in the charge tank before filling the system. This can be done by circulating sodium from the charge tank through a cold trap in the regular purification system of the plant, or by use of a natural-convection cold trap attached to the charge tank [see Sec. 1-3.3(b)].

Sodium or NaK flushing of a completed, purged system is the generally accepted final step in preparation of a heat-transfer system for use. The flushing operation consists of one or more high-temperature flushes (circulation of sodium throughout the system at a temperature as close to maximum operating temperature as can be obtained) followed by draining of the system at high temperature and refiltration of the sodium at low temperature [20], or other means of purification (e.g., settling in charge tank or cold trapping).

Immediately after initial filling of the system or after maintenance operations when air may have been admitted to the system, purification of system sodium should be commenced. As a new system or a system being restarted after such maintenance work is heated, oxygen adsorbed on steel surfaces or oxygen that reacted with residual sodium in the piping will cause an increase in oxygen concentration in the sodium system. Plugging temperature of the sodium should be routinely monitored.

Both plugging (saturation) temperature and system temperature must be considered for adequate knowledge of temperature-dependent-impurity content of a sodium system. For oxygen, for example, the saturation temperature alone indicates only the amount of oxygen dissolved in the sodium. If the saturation temperature equals the system temperature, the sodium is saturated with oxygen, and there may be a second phase of solid oxide in the piping system. If the observed plugging temperature was within 50°F of the system temperature, the SRE system was considered to be saturated for the purpose of planning cold-trap operations [37]. When saturation equals or is close to saturation temperature, the plugging potential of the system is

abnormally high. When cold-trap operations are planned for such a clean-up period, consideration should be given to operating with a high flow rate (compared with normal) and low trap ΔT (inlet minus coldest trap temperature), provided previously trapped oxide will not be released to the system. This will prevent plugging in the economizer, minimize oxide buildup in the cooling section of the cold trap, and may well result in faster removal of oxide from the system because of the exponential temperature dependence of oxygen solubility in sodium.

If the sodium system includes mechanical equipment having bearings with small clearances, it is highly desirable to maintain the insoluble content at a low value through filtration [20]. This can be accomplished with sintered-metal filters or, to some degree, through the filter action of a cold trap, provided the insoluble material reaches the filter. Coarse particulate matter can be retained in a relatively stagnant region, such as a core discharge plenum (located above a core), where sodium velocity is insufficient to entrain the particles.

REFERENCES

1. H.W. Savage, E.L. Compere, W.R. Huntley, B. Fleischer, R.E. MacPherson and A. Taboada, *SNAP-8 Corrosion Program Summary Report*, USAEC Report ORNL-3898, Oak Ridge National Laboratory, December 1965.

2. K. Goldmann and B. Minushkin, Sodium Technology, in *Reactor Technology. Selected Reviews*, L.E. Link (Ed.), USAEC Report TID-8541, Argonne National Laboratory, January 1966.

3. R.A. Clark, Operational Experience and Developmental Activities in LASL Sodium Systems, in *Proceedings of the Sodium Components Information Meeting, Palo Alto, Calif., Aug. 20-21, 1963*, USAEC Report SAN-8002, pp. 286-306, AEC, San Francisco Operations Office.

4. S. Berger et al., *Hallam Nuclear Power Facility Reactor Operations Analysis Program. Semiannual Progress Report No. 4, Feb. 29, 1964 - Sept. 30, 1964*, USAEC Report NAA-SR-10743, p. 106, Atomics International, May 15, 1964.

5. J.G. Yevick and A. Amorosi (Eds.), *Fast Reactor Technology: Plant Design*, The M.I.T. Press, Cambridge, Mass., 1966.

6. R.B. Hinze, *Sodium Purity Requirements (A Review and Evaluation)*, USAEC Report NAA-SR-Memo-12394, Atomics International, May 10, 1967.

7. W.H. Bruggeman, Purity Control in Sodium-Cooled Reactor Systems, *A. I. Ch. E. (Amer. Inst. Chem. Eng.) J., 2*: 153 (1956).

8. A.A. Jarrett (Ed.), *SRE Fuel Element Damage. Interim Report*, USAEC Report NAA-SR-4488, Atomics International, Nov. 30, 1959.

9. J.R. Weeks, Corrosion and Mass Transfer in Alkali Liquid Metal Systems, in *Materials Science and Technology for Advanced Applications*, Prentice-Hall, Inc., Englewood Cliffs, N.J., 1962.

10. M.C. Rowland, D.E. Plumlee and R.S. Young, *Sodium Mass Transfer. XV. Behavior of Selected Steels Exposed in Flowing Sodium Test Loops*, USAEC Report GEAP-4831, General Electric Company, March 1965.

11. P.T. Nettley, I.P. Bell, A.W. Thorley, C. Tyzack, K.Q. Bagley and D.R. Harries, Problems in the Selection and Utilization of Materials in Sodium Cooled Fast Reactors, in *Fast Breeder Reactors, Conference Proceedings, London, May 17-19, 1966*, pp. 835-849, Pergamon Press, Inc., New York, 1966.

12. V.S. Lyashenko and B.A. Nevzorov, *Mechanism of Carbon Transfer in Liquid Sodium*, USAEC Report

AEC-tr-5408, translated from IAEA Preprint No. CN-13/41 presented at the Conference on Corrosion of Reactor Materials, Salzburg, June 4-9, 1962.

13. W.J. Anderson and G.V. Sneesby, *Carburization of Austenitic Stainless Steel in Liquid Sodium*, USAEC Report NAA-SR-5282, Atomics International, Sept. 1, 1960.

14. D.I. Sinizer and E.N. Pearson, *Relationship of Carburizing Potential to Operating Temperature Limitations in SRE*, USAEC Report NAA-SR-Memo-7804, Atomics International, 1962.

15. R.L. Ashley, R.J. Beeley, F.L. Fillmore, W.J. Hallett, B.R. Hayward, Jr. and A.A. Jarrett, *SRE Fuel Element Damage. Final Report*, USAEC Report NAA-SR-4488(Suppl.), Atomics International, June 30, 1961.

16. J.J. Gill and J.C. Bokros, *Nitriding of Type 304 Stainless Steel in a Sodium-Nitrogen System*, USAEC Report NAA-SR-6162, Atomics International, May 30, 1961.

17. D.M. Donaldson, Compatibility Problems in Fast Reactors, in *Progress in Nuclear Energy*, Series IV, Vol. 5, Technology, Engineering and Safety, Pergamon Press, Inc., New York, 1963.

18. R.L. Carter, R.L. Eichelberger and S. Siegel, Recent Developments in the Technology of Sodium-Graphite Reactor Materials, in *Proceedings of the Second United Nations International Conference on the Peaceful Uses of Atomic Energy, Geneva, 1958*, Vol. 7, pp. 72-81, United Nations, New York, 1958.

19. J.R. Weeks, Mechanisms of Liquid Metal Corrosion, paper presented at the *National Association of Corrosion Engineers Conference, Kansas City, Mo., October 1963*, USAEC Report BNL-7553, Brookhaven National Laboratory, 1963.

20. C.B. Jackson (Ed.), *Liquid Metals Handbook. Sodium-NaK Supplement*, USAEC Report TID-5277, Atomic Energy Commission, Washington, D.C., and Bureau of Ships, July 1, 1955.

21. J.P. Petrek and E.C. Kovacic, Evaluation of Impurity Monitoring Devices Tested in a Dynamic System, in *Alkali Metal Coolants*, Symposium Proceedings, Vienna, 1966, International Atomic Energy Agency, Vienna, 1967 (STI/PUB/143).

22. Argonne National Laboratory, *Reactor Development Program Progress Report, July 1961*, USAEC Report ANL-6399, Aug. 15, 1961.

23. R.H. Costello et al., *APDA Reactor Components Test*, Report APDA-147, Atomic Power Development Associates, Inc., November 1962.

24. R.G. Frank, D.N. Miketta, W.H. Kearns, W.R. Young and R.B. Hand, *Potassium Corrosion Test Loop Development. Topical Report No. 2. Material and Process Specifications for Refractory Alloy and Alkali Metals*, Report R66SD-3007, General Electric Company, Dec. 13, 1965.

25. O.J. Foust et al., *Hallam Nuclear Power Facility - Reactor Operations Analysis Program. Semiannual Progress Report No. 1, Sept. 1, 1962-Feb. 28, 1963*, USAEC Report NAA-SR-8401, Atomics International, July 1, 1963.

26. O. Teszler et al., *Hallam Nuclear Power Facility Reactor Operations Analysis Program. Semiannual Progress Report No. 4, Feb. 29, 1964-Sept. 30, 1964*, USAEC Report NAA-SR-10743, Atomics International, May 15, 1965.

27. H.E. Johnson, *Corrosion and Activity Transfer in the SRE Primary Sodium System*, USAEC Report NAA-SR-5363, Atomics International, Oct.30,1961.

28. R.C. Andrews, R.H. Hiltz, L.H. Kirschler, S.J. Rodgers and F. Tepper, *Effect of High-Temperature Sodium on Austenitic and Ferritic Steels. Topical Report No. 4. Results of Mechanical Properties Tests of 316 SS Specimens in 1200°F Sodium Contaminated with Carbon,* USAEC Report MSAR 65-194, Mine Safety Appliances Research Corp., December 1965.

29. K.A. Davis, *Liquid Metal In-Line Impurity Measuring Instruments (Sodium) State-of-the-Art Study,* USAEC Report LMEC-Memo-68-3, Atomics International, Liquid Metal Engineering Center, Jan. 30, 1968.

30. I.L. Gray, R.L. Neal and B.G. Voorhees, Control of Oxygen in Sodium Heat Transfer Systems, *Chem. Eng. Prog., Symp. Ser., 53*(20): 11-18 (1957).

31. K.T. Claxton, Review of Solubility Data for the Liquid Sodium-Oxygen System, *J. Nucl. Energy, Parts A and B, 19*: 849 (1965).

32. R.L. Eichelberger, *The Solubility of Oxygen in Liquid Sodium: A Recommended Expression,* USAEC Report AI-AEC-12685, Atomics International, Nov. 1, 1968.

33. B.G. Voorhees and W.H. Bruggeman, *Interim Report on Cold Trap Investigations,* USAEC Report KAPL-612, Knolls Atomic Power Laboratory, Oct. 1, 1951.

34. J. Herb, *Examination of the Enrico Fermi Sodium Cold Trap,* USAEC Report WCAP-4321, Westinghouse Electric Corp., November 1965.

35. Argonne National Laboratory, *Reactor Development Program Progress Report,* USAEC Report ANL-6343, March 1961.

36. M. Novick, F.D. McGinnis and G.K. Whitham, EBR-I and EBR-II Operating Experience, in *Fast Reactor Technology, National Topical Meeting, Detroit, Mich., Apr. 26-28, 1965,* p. 25, American Nuclear Society.

37. R.B. Hinze, *Control of Oxygen Concentration in a Large Sodium System,* USAEC Report NAA-SR-3638, Atomics International, Dec. 1, 1959.

38. M.E. Nathan, *Performance of the SRE Prototype Cold Trap Assembly,* USAEC Report NAA-SR-Memo-1798, Atomics International, Dec. 7, 1956.

39. R. Cygan, *HNPF Cold Trap Evaluation,* USAEC Report NAA-SR-4382, Atomics International, Dec. 15, 1959.

40. W.M. Hoschouer and D.F. Casey, *Design and Thermal Analysis of Sodium Specialties Components for HNPF,* USAEC Report NAA-SR-5445, Atomics International, Feb. 15, 1961.

41. D. Bitz, G.E. Turner, L.J. Webster and L.L. Johnson, Hallam Nuclear Power Facility Preoperational Test Completion Report, Sodium Service System, in *Final Evaluation Report - Hallam Nuclear Power Facility,* USAEC Report NAA-SR-9777, Vol. 1, Atomics International, September 1964.

42. D.K. Darley et al., *Hallam Nuclear Power Facility - Reactor Operations Analysis Program Semiannual Progress Report No. 2, Mar. 1, 1963-Aug. 31, 1963,* USAEC Report NAA-SR-9265, Atomics International, Mar. 1, 1963.

43. D.K. Darley et al., *Hallam Nuclear Power Facility. Reactor Operations Analysis Program. Semiannual Progress Report No. 3, Sept. 1, 1963-Feb. 29, 1964,* USAEC Report NAA-SR-9799, Atomics International, Sept. 15, 1964.

44. G.E. Deegan et al., *Design Modifications to the SRE During FY 1960,* USAEC Report NAA-SR-5348 (Rev.), Atomics International, Feb. 15, 1961.

45. E.N. Pearson, Sodium Reactor Experiment Systems and Components Experience - Core II, in *Proceedings of the Sodium Components Information Meeting, Palo Alto, Calif., Aug. 20-21, 1963*, USAEC Report SAN-8002, pp. 78-104, AEC, San Francisco Operations Office.

46. J.O. Nicholson, Jr., Liquid Metal Engineering Center, Atomics International, personal communication, 1969.

47. A.I. Hansen, *The Effects of Long-Term Operation on SRE Sodium System Components*, USAEC Report NAA-SR-11396, Atomics International, Aug. 31, 1965.

48. Los Alamos Scientific Laboratory, *Quarterly Status Report on the Advanced Plutonium Fuels Program, Apr. 1-June 30, 1968, and Second Annual Report, FY 1968*, USAEC Report LA-3993-MS, Sept. 12, 1968.

49. J.A. Bray, Experience on the Removal of Impurities from Liquid Metal Systems by Cold Trapping, paper presented at the *European Atomic Energy Symposium on Liquid Metals*, Cadarache, France, Sept. 30-Oct. 2, 1963, Report CONF-467-5.

50. J.L. Phillips, Full Power Operation of the Dounreay Fast Reactor, in *Fast Reactor Technology, National Topical Meeting, Detroit, Mich., Apr. 26-28, 1965*, p. 7, American Nuclear Society.

51. R.R. Mathews, J.L. Phillips, K.J. Henry, R.H. Allardice, D.M. Donaldson and H.E. Tilbe, Performance and Operation of the Dounreay Fast Reactor, *Proceedings of the Third International Conference on the Peaceful Uses of Atomic Energy, Geneva, 1964*, Vol. 6, pp. 23-32, United Nations, New York, 1965.

52. J.L. Phillips, The Dounreay Fast Reactor, *Nucl. Eng., 10*: 264 (1965).

53. K.J. Henry and A.G. Edwards, A Review of the Operation of the Dounreay Fast Reactor, in *Fast Breeder Reactors*, Conference Proceedings, London, May 17-19, 1965, pp. 153-169, Pergamon Press, Inc., New York, 1966.

54. E.M. Simons et al., *Sodium Technology Support Program for Pacific Northwest Laboratories, Battelle Memorial Institute FFTF Studies, FY 1965*, USAEC Report BMI-X-10129, Battelle Memorial Institute, July 9, 1965.

55. V.I. Subbotin, P.L. Kirilov and F.A. Kozlov, *The Purification of Sodium from Oxygen and Monitoring of the Oxygen Content in Sodium*, British Report PG-Inf. Ser. 10, translated by J.K. Lomaz from USSR Report No. 701.

56. P.L. Kirilov et al., Removal of Oxides from Sodium and Tests for the Oxide Content, *Sov. J. At. Energy (Eng. Transl.), 7*: 23 (1960).

57. V.I. Subbotin and F.A. Kozlov, *Precipitation of Oxides from a Sodium Stream*, USAEC Report ORNL-TR-1611, translation of a paper presented at the International Atomic Energy Agency Symposium on Alkali Metal Coolants, Vienna, Nov. 29-Dec. 2, 1966, Oak Ridge National Laboratory.

58. G.N. Lauben, *Packless Cold Trap Evaluation*, USAEC Report NAA-SR-Memo-9920, Atomics International, June 17, 1964.

59. L.L. Johnson, Atomics International, personal communication, August 1964.

60. G. Billuris, *Experimental Investigations of the Removal of Sodium Oxide from Liquid Sodium*, USAEC Report GEAP-3328, General Electric Company, Jan. 18, 1960.

61. J.S. McDonald, *Analysis of Results of a Sodium Cold Trap Experiment*, USAEC Report NAA-SR-6801, Atomics International, July 30, 1962.

62. A.I. Leipunskii, V.I. Subbotin and M.N. Ivanovskii, *The State and Distribution, Monitoring, and Elimination of Impurities in Circulating Alkali Metal Coolants*, USAEC Report ORNL-tr-1608, translation of a paper presented at the International Atomic Energy Agency Symposium on Alkali Metal Coolants, Vienna, Nov. 29-Dec. 2, 1966, Oak Ridge National Laboratory.

63. J.S. McDonald, *Valve Stem Freeze Seal for High-Temperature Sodium*, USAEC Report NAA-SR-4869, Atomics International, July 30, 1960.

64. S.J. Rodgers and J.W. Mausteller, *Removal of NaH from Na by Cold Trapping*, USAEC file No. NP-6030, Mine Safety Appliances Co., Jan. 14, 1955.

65. J.M. McKee, *Removal of Oxygen from Sodium*, Report AD-648248, United Nuclear Corp., April 1966.

66. J.M. Williams, *The Oxidation of Refractory Metals in Liquid Sodium*, AEC-NASA Liquid Metals Information Meeting, Gatlinburg, Tenn., April 21-23, 1965, USAEC Report CONF-650411, pp. 57-60, Oak Ridge National Laboratory.

67. T.L. Mackay, *Oxidation of Zirconium and Zirconium Alloys in Liquid Sodium*, USAEC Report NAA-SR-6674, Atomics International, Feb. 15, 1962.

68. Tennyson Smith, Mechanism of the Oxidation of Zirconium in Oxygen and Liquid Sodium, *J. Electrochem. Soc.*, *112*(1): 39-46 (1965).

69. R.L. McKisson, R.L. Eichelberger and J.B. Ott, *The Construction and Operation of a Sodium Purification Apparatus*, USAEC Report NAA-SR-12444, Atomics International, July 15, 1967.

70. W.T. Lee, *Biaxial Stress-Rupture Properties of Austenitic Stainless Steels in Zirconium-Gettered Sodium*, USAEC Report NAA-SR-12353, Atomics International, Oct. 1, 1967.

71. J.E. Kemme, Components - High Purity Sodium Systems, in *Proceedings of the 1957 Fast Reactor Information Meeting*, Chicago, Nov. 20-21, 1957, USAEC Report M-7148, Atomic Energy Commission, 1957.

72. E.T. Hayes, A.H. Roberson and O.G. Paasche, *Zirconium-Titanium System; Constitution Diagram and Properties*, USAEC Report BM-RI-4826, Bureau of Mines, November 1951.

73. W.J. Anderson, *Removal of Carbon from Liquid Sodium Systems*, USAEC Report NAA-SR-6386, Atomics International, Dec. 1, 1961.

74. L.P. Pepkowitz and J.T. Porter II, *The Determination of Carbon in Sodium*, USAEC Report KAPL-1444, Knolls Atomic Power Laboratory, Nov. 28, 1955.

75. D.E. Plumlee, R.W. Lockhart, L.E. Pohl and T.A. Lauritzen, *Sodium Mass Transfer. XVIII. Extended Studies of Carbon Movement in Pumped Sodium Test Loops*, USAEC Report GEAP-4834, General Electric Company, June 1965.

76. D.A. Mannas, *Effects of Long-Term Sodium Exposure on Materials in the Sodium Reactor Experiment*, Report AI-66-53, Atomics International, June 15, 1966.

77. H.D. May, *Carbon Removal from SRE Sodium Following PEP Modifications*, USAEC Report NAA-SR-12410, Atomics International, Nov. 1, 1967.

78. Power Reactor Development Company, *Monthly Technical Report*, January 1962, USAEC Report PRDC-TR-55.

79. J.A. Leppard, Carburization Potential in Sodium Systems, in *4th Sodium Components Development Program Information Meeting, Los Angeles, Apr. 14, 1964*, USAEC Report COO-1213-20, AEC, San Francisco Operations Office.

80. J.D. Marshall, Determination of the Amount of Carbon Absorbed by the Stainless Steel Specimens in the Hot Trap at the Enrico Fermi Atomic Power Plant, The Detroit Edison Company, unpublished, Aug. 15, 1962.

81. J.F. McCarthy, *Compilation of Current Technical Experience at Enrico Fermi Atomic Power Plant*, USAEC Report Report APDA-CFE-10, Atomic Power Development Associates, Inc., July 1967.

82. J.W. Mausteller and S.J. Rodgers, *Inhibitors to the Transfer of Radioactive Stainless Steel Constituents in Sodium*, USAEC file No. NP-5740, Mine Safety Appliances Co., Aug. 24, 1955.

83. S. Siegel, R.L. Carter, F.E. Bowman and B.R. Hayward, Basic Technology of the Sodium Graphite Reactor, in *Proceedings of the International Conference on the Peaceful Uses of Atomic Energy, Geneva, 1955*, Vol. 9, pp. 321-330, United Nations, New York, 1956.

84. M. Davis and A. Draycott, Compatibility of Reactor Materials in Flowing Sodium, in *Proceedings of the Second United Nations International Conference on the Peaceful Uses of Atomic Energy, Geneva, 1958*, Vol. 7, pp. 94-110, United Nations, New York, 1958.

85. F.L. Bett and A. Draycott, The Compatibility of Beryllium with Liquid Sodium and NaK in Dynamic Systems, *Proceedings of the Second United Nations International Conference on the Peaceful Uses of Atomic Energy, Geneva, 1958*, Vol. 7, pp. 125-131, United Nations, New York, 1958.

86. J.A. Bray, United Kingdom Atomic Energy Authority, Dounreay, Scotland, personal communication, November 1968.

87. W.J. Freede and J.K. Roberts (Eds.), *Sodium Reactor Experiment. Power Expansion Program - Heat Transfer Systems Modifications*, Report NAA-SR-10379 (Rev.), Atomics International, June 1965.

88. A. Gunby, *Nonnuclear Performance of SRE-PEP Systems*, USAEC Report NAA-SR-12408, Atomics International, June 30, 1967.

89. J.B. Campbell, Porous Metal Sheet, *Mater. & Methods, 41*(4): 98-101 (1955).

90. J.S. McDonald, *Sintered-Metal Filters for Sodium Coolant Systems*, USAEC Report NAA-SR-Memo-2830, Atomics International, June 27, 1958.

91. A. Amorosi, Development Work for the Enrico Fermi Atomic Power Plant, in *Proceedings of Symposium on Sodium Reactors Technology, Lincoln, Neb., May 24-25, 1961*, USAEC Report TID-7623, pp. 122-130.

92. R.B. Hinze, *Observations of Carbon in SRE Sodium*, USAEC Report NAA-SR-Memo-4479, Atomics International, Oct. 12, 1959.

93. F.S. Nayor and J.S. McDonald, *A Combination Strainer and Blocking Valve for Liquid-Metal Systems*, USAEC Report NAA-SR-5241, Atomics International, Aug. 30, 1960.

94. F. Smith, Argonne National

Laboratory, personal communication, 1958.

95. R. MacPherson, Oak Ridge National Laboratory, personal communication, December 1967.

96. J.P. Beall and M.W. Hulin (Eds.), *The Final Report on the SNAP-2 Experimental Reactor (SER) Operation and Test Program*, USAEC Report NAA-SR-7088, Atomics International, Apr. 30, 1962.

97. Argonne National Laboratory, *Reactor Development Program Progress Report*, February 1965, USAEC Report ANL-7017, Mar. 18, 1965.

98. G.W. Horsley, *The Purification of Sodium by Vacuum Distillation*, British Report AERE-M/R-1152, May 12, 1953. (Classified)

99. C. Kunze, *The Purification of Potassium and Sodium*, British Report DEG-Inf.-Ser.-87, translated by J.C. Ruckman from *Vakuum-Tech.*, *8*: 168-170 (1959).

100. D.E. Westerheide and G. Burnet, *High-Vacuum Liquid-Metal Distillation: An Annotated Bibliography*, USAEC Report IS-799, Ames Laboratory, May 1964.

101. J.J. Droher, J.A. Hagel and R.S. Hart, *Interim Report. Removal of Contaminants from SRE Sodium and Primary Piping Walls*, Atomics International, unpublished, 1959.

102. C.L. Peckinpaugh, Preoperational Testing Experience at SRE-PEP, Paper WA/NE-19, from the *Winter Annual Meeting and Energy Systems Exposition, New York, December 1966*, American Society of Mechanical Engineers.

Chapter 2
Effects on Materials

Principal Authors: J. K. BALKWILL, J. L. LOCKETT, and R. K. WAGNER

2-1 INTRODUCTION

This chapter describes the effects produced in various structural materials by their exposure in sodium or NaK. The principal effects discussed are:

1. Changes in such mechanical properties as tensile, creep, stress rupture, fatigue, and impact.
2. Corrosion by simple solution, localized attack such as intergranular penetration or pitting, and alloying.
3. Compositional changes due to mass transfer.
4. Reaction with impurities from the liquid metal.

These effects influence the selection of all structural materials used in a liquid-metal system. Frequently, combined effects must be evaluated; e.g., compositional changes can result in a degradation of mechanical properties caused by removal of a strengthening element from the material. Because these effects are time and temperature dependent, their relative importance varies from negligible for low-temperature short-lived applications to critical for long-term service at high temperature.

Although most of the state-of-the-art information is reasonably complete, the data are insufficient to apply the statistical methods normally adopted for the development of minimum design criteria and allowable stresses, where mechanical properties are involved. For example, corrosion data are wholly valid only for the particular material and system under test. The many variables and corrosion types present in a liquid-metal system may preclude direct application of these data. Thus, for the sections operating in a liquid-metal environment, the corrosion allowables described must be supplemented by engineering judgment.

On the basis of extensive experimental work, either planned or in progress, it is apparent that the information presented is limited and represents the current state of the art.

2-2 EFFECTS OF SODIUM ON THE MECHANICAL PROPERTIES OF MATERIALS

2-2.1 *Introduction*

In recent years development work and technical literature on liquid metals have continued to increase.

The compatibility of structural, containment, and cladding materials with sodium was emphasized in the development work, and corrosion and mass-transfer effects received the major attention.

Recent extensive programs initiated by the U.S. Atomic Energy Commission (AEC) to evaluate types of steels anticipated for use in large sodium systems should determine whether current design allowables, developed after testing in conventional mediums (air and inert gas), are reliable for long-term exposure in high-temperature sodium. Horton et al. [1] prepared a comprehensive summary based on this work which describes the effects of sodium on the mechanical properties of austenitic and ferritic steels. Information from that summary is presented throughout this section. That this work was fuel-cladding oriented is indicated by the thickness of material investigated. Results should be more conservative on extrapolation to heavier sections where shallow surface effects become less important.

Sodium has little effect on mechanical properties, tensile, creep, and stress rupture. In most cases, differences observed can be attributed to corrosion or mass transfer to or from the alloy under test.

2-2.2 *Austenitic Stainless Steels*

Nearly all existing liquid-metal (sodium and NaK) systems and components are fabricated from one of the austenitic stainless steels. This wide acceptance is based on the familiar standards for material selection: elevated-temperature strength, compatibility, fabricability, and availability. These steels perform satisfactorily in liquid-metal systems operating to 1000°F. Except for unusual future requirements, their widespread use is expected to continue, as evidenced by the experimental efforts concentrated on the austenitic stainless steels.

(a) *Tensile Properties*

During an investigation of sodium effects on the tensile properties of 316 stainless steel, investigators at MSA Research Corp. (MSAR) [2,3,4] found that carbon-contaminated sodium produced the greatest effect. Exposure in low- (30 ppm) and high- (300 ppm) oxygen sodium before testing had no appreciable effect on the tensile properties. Testing was performed on 0.065-in.-thick specimens taken from sheet material of the composition shown in Table 2.1.

TABLE 2.1 - Chemical Composition of 316 Stainless Steel (Heat 880347) [4]

Element	Wt.%	Element	Wt.%
C	0.045	Si	0.48
Mn	1.94	Cr	18.00
P	0.02	Ni	12.84
S	0.01	Mo	2.33

Since all tensile testing was performed after a prolonged exposure to a variety of environments, the effect of liquid metal on the tensile properties does not reflect behavior under actual conditions of loading. For example, the effect of sodium at the higher strain rates normally employed in tensile testing was not developed. The samples were preexposed in helium, high- and low-oxygen sodium, and high-carbon (30 to 50 ppm) sodium for 4000 hr at 1200°F and the postexposure tensile testing was conducted at room temperature in either air or helium and at elevated temperature (1200°F) in helium.

The tensile properties developed for various exposure environments and test temperatures are given in Table 2.2. The tensile-strength data are shown graphically in Fig. 2.1. Data from United States Steel Corporation, Bulletin 26, were plotted on the same graph for comparison. The results indicate

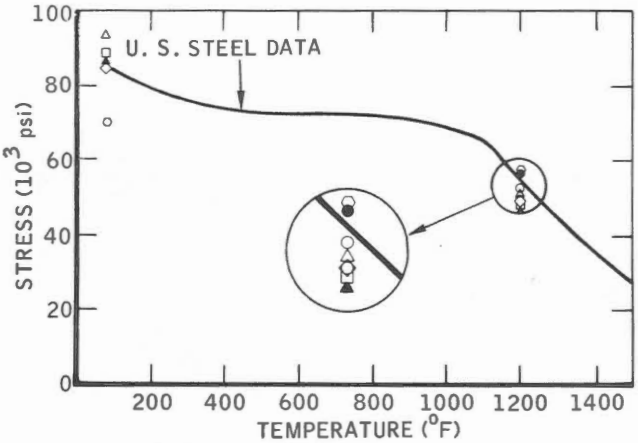

Fig. 2.1 - Tensile strength of 316 stainless steel exposed 4000 hr at 1200°F in contaminated sodium.

	Exposure environment	Test environment and temperature
○	None	Air, 1200°F
□	None	He, RT and 1200°F
△	Low-oxygen (300 ppm) Na	He, RT and 1200°F
⬡	Na-C (30 to 50 ppm)	Air, RT; He, 1200°F
▲	He	Air, RT; He, 1200°F
◇	High-oxygen (300 ppm) Na	Air, RT; He, 1200°F
●	He	Air, RT; He, 1200°F

that "as-received" material had room- and elevated-temperature tensile strength comparable to that of other heats of 316 stainless steel. Exposure to high-carbon sodium apparently strengthened the material at the high temperature but lowered the room-temperature tensile strength. Exposure in other environments did not affect the tensile strength significantly.

The data presented in Fig. 2.2. reflect a modification of the measured tensile strength to show a comparison with the 25% allowable American Society of Mechanical Engineers (ASME) Code values. Except for the room-temperature strength of material exposed in high-carbon sodium, the sodium exposures did not degrade the tensile strength below

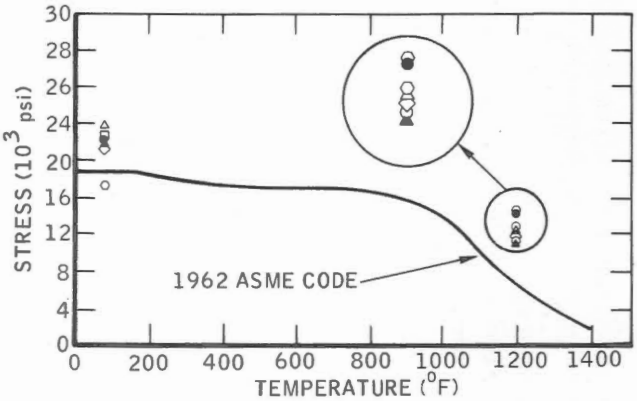

Fig. 2.2 - Tensile strength of 316 stainless steel exposed 4000 hr at 1200°F in contaminated sodium. (Points are 25% of tensile data.)

	Exposure environment	Test environment and temperature
○	None	Air, 1200°F
□	None	He, RT and 1200°F
△	Low-oxygen Na	He, RT and 1200°F
⬡	Na-C	Air, RT; He, 1200°F
▲	He	Air, RT; He, 1200°F
◇	High-oxygen Na	Air, RT; He, 1200°F
●	He	Air, RT; He, 1200°F

the current Code allowable.

The effect of the exposures on the yield strength is shown in Fig. 2.3. In Fig. 2.4 the 62 1/2% yield-strength values are compared with the allowables defined in the ASME Code. Again the sodium exposures had no detrimental effect with respect to the current design allowables.

The effect of sodium exposure is most apparent on the ductility of 316 stainless steel. As shown in Fig. 2.5, the ductility of samples exposed in high-carbon sodium was degraded virtually to zero. This behavior indicates that a high degree of carburization occurred during the exposure period. Although the material exposed in helium and sodium shows a marked reduction in elongation, its behavior was still regarded as ductile (it exhibited over 20% elongation).

Andrews et al. [5,6] later reported

TABLE 2.2 - Tensile Properties for 316 Stainless Steel After 4000-hr Exposure in Contaminated Sodium at 1200°F

Exposure environment	Test environment and temperature	Tensile strength, psi	Average tensile, psi	0.2% Offset yield strength, psi	Average yield, psi	Elongation, %	Average elongation, %	Reduction of area, %	Average reduction, %
None	Helium, RT*	89,500	89,000	49,700	49,550	65	66	59	59
None	Helium, RT	88,500		49,400		66		59	
Low-oxygen Na+	Helium, RT	93,200	92,850	44,600	43,930	47	48	46	47
Low-oxygen Na	Helium, RT	92,000		43,750		48		50	
Low-oxygen Na	Helium, RT	92,500		42,000		46		40	
Low-oxygen Na	Helium, RT	91,400		43,700		49		52	
Low-oxygen Na	Helium, RT	92,500		43,900		49		52	
Low-oxygen Na	Helium, RT	95,500		45,600		46		40	
High-oxygen Na†	Air, RT	85,200	84,917	40,000	40,600	34	40	32	32
High-oxygen Na	Air, RT	85,900		41,250		48		34	
High-oxygen Na	Air, RT	84,900		39,750		39		34	
High-oxygen Na	Air, RT	85,000		39,750		38		30	
High-oxygen Na	Air, RT	85,600		41,250		42		32	
High-oxygen Na	Air, RT	82,900		41,600		40		32	
Helium§	Air, RT	87,000	87,300	38,500	36,100	55	54	54	56
Helium§	Air, RT	87,700		29,300		53		56	
Helium§	Air, RT	87,200		40,500		53		58	
High-carbon Na	Air, RT	67,800	69,767	53,750	57,833	<1¶	1.7	<1	5.5
High-carbon Na	Air, RT	66,500		57,500		1¶		5.5	
High-carbon Na	Air, RT	78,100		57,250		2.4¶		7.4	
High-carbon Na	Air, RT	68,800		57,750		2.0¶		8.5	
High-carbon Na	Air, RT	68,400		62,250		1.2¶		9.2	
High-carbon Na**	Air, RT	69,000		58,500		2.4¶		7.0	
Helium††	Air, RT	87,100	87,000	40,250	40,783	53	54	57	51
Helium††	Air, RT	86,400		38,600		59		56	
Helium††	Air, RT	87,500		41,250		49		39	
None	Air, 1200°F	49,400	50,280	26,100	26,020	43	43	47	46
None	Air, 1200°F	50,250		25,650		41		48	
None	Air, 1200°F	51,200		26,300		47		44	

None	Helium, 1200°F	47,200		26,600		46		58	
None	Helium, 1200°F	47,500	47,770	25,900	25,930	52	47	54	55
None	Helium, 1200°F	48,600		25,300		44		53	
Low-oxygen Na	Helium, 1200°F	48,850		24,500		39		46	
Low-oxygen Na	Helium, 1200°F	46,900	48,580	24,800	25,170	52	44	52	48
Low-oxygen Na	Helium, 1200°F	50,000		26,200		41		46	
Low-oxygen Na†††	Helium, 1200°F	49,100		26,750		41		56	
Low-oxygen Na†††	Helium, 1200°F	46,400	48,470	25,200	25,870	46	44	55	54
Low-oxygen Na†††	Helium, 1200°F	49,900		25,650		46		51	
High-oxygen Na	Helium, 1200°F	46,700		24,400		27		46	
High-oxygen Na	Helium, 1200°F	47,800	47,867	24,000	24,300	31	28	42	45
High-oxygen Na	Helium, 1200°F	49,100		24,200		25		46	
High-oxygen Na†††	Helium, 1200°F	49,500		23,300		25		38	
High-oxygen Na†††	Helium, 1200°F	49,250	49,083	25,000	24,300	24	23	26	33
High-oxygen Na†††	Helium, 1200°F	48,500		24,600		21		36	
Helium*	Helium, 1200°F	48,000		23,500		23		48	
Helium*	Helium, 1200°F	54,250	55,750	27,600	26,283	24	24	47	48
Helium*	Helium, 1200°F	65,000		27,750		26		50	
High-carbon Na	Helium, 1200°F	57,300		39,700		2.1¶		2.1	
High-carbon Na	Helium, 1200°F	54,300	56,200	40,500	40,167	1.7¶	2.2	4.3	3.6
High-carbon Na	Helium, 1200°F	57,000		40,300		2.7¶		4.5	
High-carbon Na†††	Helium, 1200°F	59,000		38,000		2.3¶		1.5	
High-carbon Na†††	Helium, 1200°F	56,375	57,875	41,250	40,417	1.7¶	2.0	3.6	2.6
High-carbon Na†††	Helium, 1200°F	58,250		42,000		2.0¶		2.6	
Helium††	Helium, 1200°F	48,100		23,600		14		62	
Helium††	Helium, 1200°F	46,400	46,867	23,400	23,500	31	23	67	64
Helium††	Helium, 1200°F	46,100		23,500		25		62	

* RT is room temperature.
\+ Low-oxygen sodium contained about 10 ppm oxygen.
† High-oxygen sodium contained about 300 ppm oxygen.
§ Exposed simultaneously with high-oxygen sodium exposures.
¶ Failed at gauge mark.
** High-carbon sodium contained about 30 to 50 ppm carbon.
†† Exposed simultaneously with high-carbon sodium exposures.
††† Not washed before testing (all other specimens were washed with alcohol and water before testing).

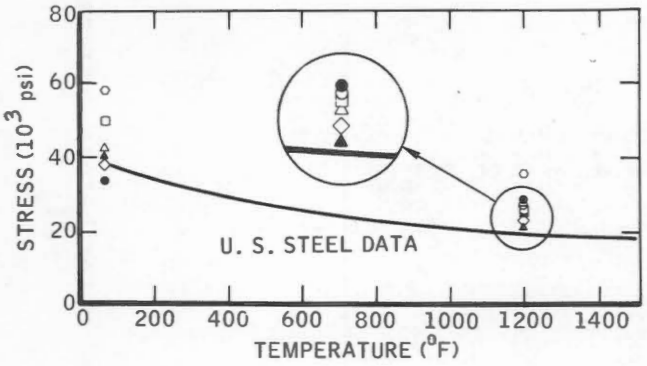

Fig. 2.3 - Yield strength of 316 stainless steel exposed 4000 hr at 1200°F in contaminated sodium.

	Exposure environment	Test environment and temperature
○	None	Air, 1200°F
□	None	He, RT and 1200°F
△	Low-oxygen Na	He, RT and 1200°F
⬡	Na-C	Air, RT; He, 1200°F
▲	He	Air, RT; He, 1200°F
◇	High-oxygen Na	Air, RT; He, 1200°F
●	He	Air, RT; He, 1200°F

similar work on the effect of sodium exposure on the tensile properties of 304 stainless steel. Specimens were exposed stress free for 4000 hr to high-oxygen (300 ppm), dynamic, 1200°F sodium and in another loop to low-oxygen (10 ppm), dynamic, 1200°F sodium contaminated with carbon from a source of continuous supply. The specimens were then tensile tested in air at room temperature and at 1200°F. Other specimens exposed to 1200°F helium for 4000 hr as a control were also tested in air at room temperature and at 1200°F. The tensile properties developed for the various exposure environments are given in Table 2.3. It was concluded that the specimens exposed to high-oxygen sodium were only slightly degraded in tensile properties, but the ductility at 1200°F dropped to 23% from the as-received values of 38%. This loss of ductility could be significant over a longer exposure time.

The samples exposed to high-carbon

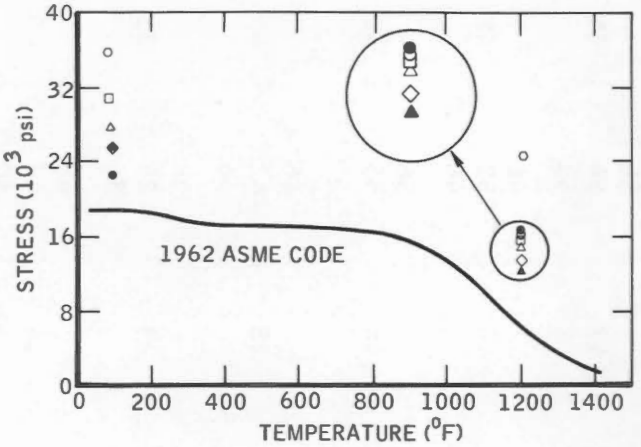

Fig. 2.4 - Yield strength of 316 stainless steel exposed 4000 hr at 1200°F in contaminated sodium. (Points are 62½% of yield data.)

	Exposure environment	Test environment and temperature
○	None	Air, 1200°F
□	None	He, RT and 1200°F
△	Low-oxygen Na	He, RT and 1200°F
⬡	Na-C	Air, RT; He, 1200°F
▲	He	Air, RT; He, 1200°F
◇	High-oxygen Na	Air, RT; He, 1200°F
●	He	Air, RT; He, 1200°F

sodium and tested at room temperature failed at the pinhole for the extensometer attachment, showing extreme brittleness; those tested at 1200°F showed tensile and yield strengths increased with almost total loss of ductility. This confirmed the results previously obtained for 316 stainless steel which showed the detrimental effects of carburization on ductility.

The tensile strength, yield strength, and elongation of these two austenitic stainless steels after 4000-hr exposures are compared in Figs. 2.6 to 2.8.

The effect of sodium on the tensile properties of various austenitic stainless steels was also investigated by Lyashenko, Zotov, and Ivanov [7] in tests similar to those at MSAR [2] where the test specimens were exposed

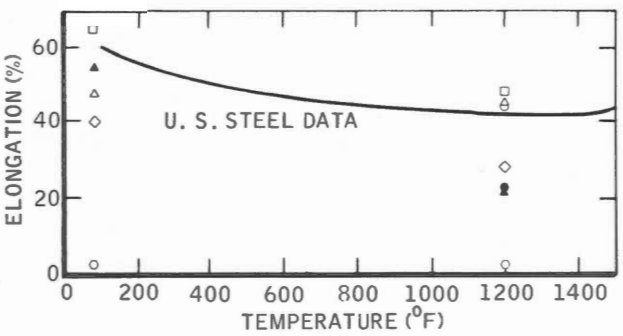

Fig. 2.5 - Elongation of 316 stainless steel exposed 4000 hr at 1200°F in contaminated sodium.

	Exposure environment	Test environment and temperature
○	None	Air, 1200°F
□	None	He, RT and 1200°F
△	Low-oxygen Na	He, RT and 1200°F
⬡	Na-C	Air, RT; He, 1200°F
▲	He	Air, RT; He, 1200°F
◇	High-oxygen Na	Air, RT; He, 1200°F
●	He	Air, RT; He, 1200°F

in sodium prior to tensile testing. Lyashenko et al. preexposed thin-wall tubular specimens (12 mm in diameter with 0.4-mm wall thickness) at 600°C (1112°F) in high- (300 ppm) and low- (70 ppm) oxygen sodium and at 700°C (1292°F) in low- (40 ppm) oxygen sodium and tested them in air at room temperature. The composition of the three grades of austenitic steels evaluated is given in Table 2.4.

The tensile properties measured after sodium exposure and the tensile values obtained on as-received material and after long-term exposure in inert gas are tabulated in Table 2.5. The tabulated values represent the average of five determinations.

The data indicate that the tensile strength and elongation of the steels evaluated were not significantly affected by exposure to low-oxygen sodium at 600°C (1112°F). However, at the increased oxygen level, the ductility of the steels was noticeably reduced, particularly for the 1Kh18N9T grade (the elongation was reduced from 35 to 4% after exposure). Interestingly, the presence of calcium (0.2 wt.%) in the high-oxygen sodium diminished the observed effects. The calcium was added to lower the corrosive effect of high-oxygen sodium by forming calcium oxide, which has a low solubility in sodium. The high-oxygen sodium becomes low-oxygen sodium after the calcium scavenges oxygen from the system. The corrosive effects of the sodium were in fact so reduced by the calcium additive that the ductility loss in high-oxygen sodium noted in Table 2.5 was prevented.

In general, the results of this investigation are similar to those of Andrews and Kirschler. [4] Table 2.3 shows a reduction of about one-third from as-received values in average elongation of specimens tested after exposure in high-oxygen sodium. Both investigations showed that high-oxygen sodium is detrimental to the ductility of austenitic steels. The tensile strength showed only minor variations, with no well-defined trends apparent.

(b) *Creep Strength*

(1) *316 Stainless Steel.* Investigators at MSAR [2-4] determined the creep strength for 316 stainless steel in 1200°F sodium at various purity levels. For comparison similar tests were also performed in air and in helium with some samples exposed to high-oxygen (300 ppm) or high-carbon (30 to 50 ppm) sodium for 4000 hr prior to testing. All specimens were taken from 0.065-in.-thick sheet material (see Table 2.1 for composition). The minimum creep rates obtained are shown in Figs. 2.9 and 2.10. These creep values were subsequently extrapolated to provide the familiar design criteria for creep stress to produce a creep rate of 1% in 100,000 hr. These design data are shown in Table 2.6, where various environmental conditions are considered.

TABLE 2.3 - Tensile-Test Data for 304 Stainless Steel After 4000-hr Exposure in Contaminated Sodium at 1200°F

Specimen No.	Exposure environment	Test environment and temperature	Tensile strength, psi	Average tensile, psi	0.2% Offset yield strength, psi	Average yield, psi	Elongation, %	Average elongation, %	Reduction of area, %	Average reduction, %
831	None	Air, RT*	92,775		43,200		53		63	
832	None	Air, RT	92,900	92,960	43,400	43,050	53	53	62	67
833	None	Air, RT	93,650		42,400		53		74	
834	None	Air, RT	92,500		43,200		52		70	
807	High-oxygen Na†	Air, RT	87,500		35,500		45		51	
808	High-oxygen Na	Air, RT	85,700	84,350	37,000	35,375	47	50	50	57
809	High-oxygen Na	Air, RT	86,900		36,500		45		52	
810	High-oxygen Na	Air, RT	77,300		32,500		62		76	
760	Helium††	Air, RT	92,500		38,500		49		64	
804	Helium††	Air, RT	94,100	92,475	37,500	37,250	49	53	65	64
805	Helium††	Air, RT	90,700		36,000		49		56	
806	Helium††	Air, RT	92,600		37,000		65		70	
674	High-carbon Na§	Air, RT			67,000¶					
675	High-carbon Na	Air, RT			71,000¶	67,300				
676	High-carbon Na	Air, RT			64,000¶					
665	Helium**	Air, RT	91,500		37,000		48		60	
666	Helium**	Air, RT	92,100	91,530	36,500	36,500	62	52	63	61
667	Helium**	Air, RT	91,000		36,000		47		61	
826	None	Air, 1200°F	47,350		23,200		37		55	
827	None	Air, 1200°F	45,700	46,730	22,100	22,900	40	38	54	55
828	None	Air, 1200°F	46,750		23,600		39		55	
829	None	Air, 1200°F	47,100		22,600		38		57	
811	High-oxygen Na†	Air, 1200°F	41,700		20,700		24		30	
812	High-oxygen Na	Air, 1200°F	41,600	41,833	21,800	21,033	24	25	38	34
813	High-oxygen Na	Air, 1200°F	42,200		20,600		27		34	
769	High-oxygen Na†††	Air, 1200°F	43,850		22,000		20		48	
770	High-oxygen Na†††	Air, 1200°F	44,150	43,933	21,800	21,767	24	23	25	40
771	High-oxygen Na†††	Air, 1200°F	43,800		21,500		23		46	

756	Helium††	Air, 1200°F	43,800		21,500		34		57	
757	Helium††	Air, 1200°F	45,900	44,650	22,200	22,100	27	35	58	58
758	Helium††	Air, 1200°F	43,200		22,200		34		56	
759	Helium††	Air, 1200°F	45,700		22,500		43		59	
671	High-carbon Na§	Air, 1200°F	63,000		34,700		5.3		14	
672	High-carbon Na	Air, 1200°F	63,100	63,030	35,000	35,630	4.6	5.1	5	9.3
673	High-carbon Na	Air, 1200°F	63,000		37,200		5.6		9	
668	High-carbon Na†††	Air, 1200°F	63,350		37,000		5.0		14	
669	High-carbon Na†††	Air, 1200°F	63,550	63,330	37,300	36,430	3.7	4.6	9	11
670	High-carbon Na†††	Air, 1200°F	63,100		35,000		5.3		10	
662	Helium**	Air, 1200°F	44,250		22,000		28		54	
663	Helium**	Air, 1200°F	44,300	44,400	21,500	21,670	32	31	55	54
664	Helium**	Air, 1200°F	44,650		21,500		33		53	

* RT is room temperature
† High-oxygen sodium contained 300 ppm oxygen.
†† Exposed simultaneously with high-oxygen exposures.
§ High-carbon sodium was exposed to a continuous carbon source.
¶ Specimen failed at pinhole made for extensometer attachment.
** Exposed simultaneously with high-carbon exposures.
††† Specimens not washed before testing (all others were washed with alcohol and water before testing).

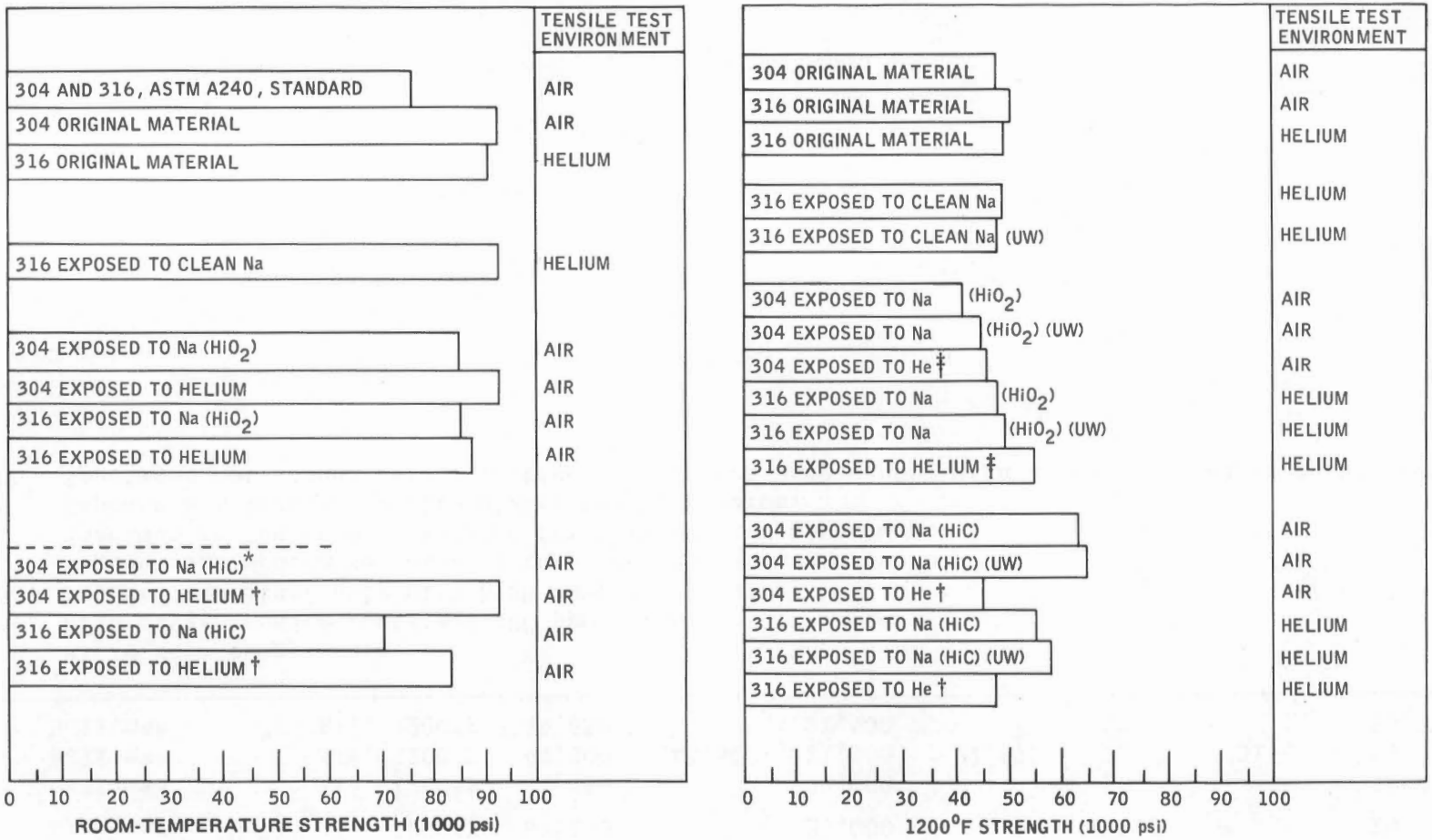

Fig. 2.6 - Tensile strength of 304 and 316 stainless steels following 4000-hr exposure in 1200°F dynamic sodium. The abbreviation (UW) means not washed prior to testing; all other samples were washed with alcohol and water before testing. Clean sodium contains <10 ppm O_2; Na (HiO_2) contains 300 ppm O_2; and Na (HiC) contains a continuous source of carbon, resulting in high carbon activity.

* Triplicate specimens failed at pinholes.
† Exposed simultaneously with high-carbon Na exposures.
‡ Exposed simultaneously with high-oxygen Na exposures.

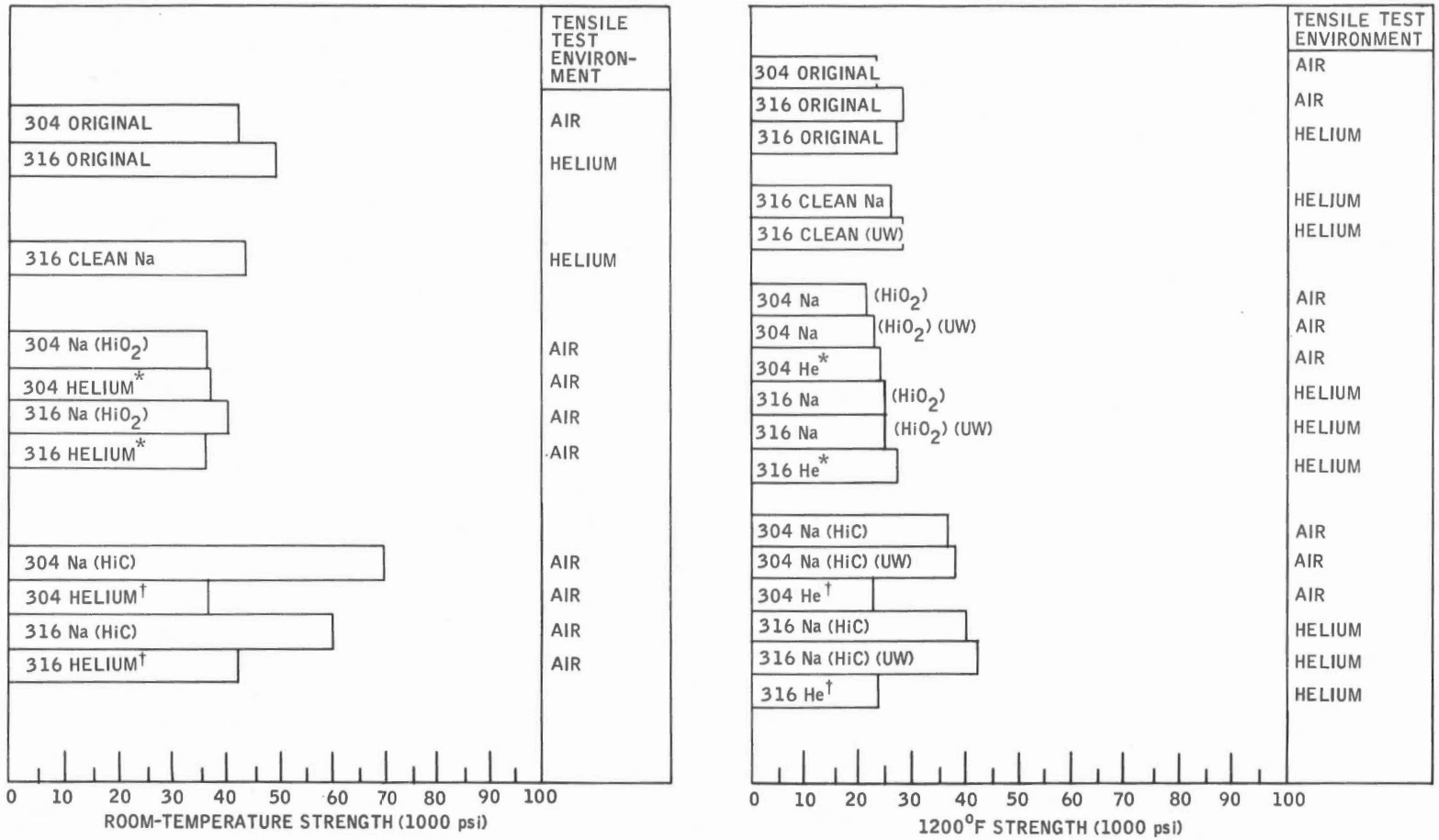

Fig. 2.7 - Yield strength of 304 and 316 stainless steels following 4000-hr exposure in 1200°F dynamic sodium. The abbreviation (UW) means not washed prior to testing; all other samples were washed with alcohol and water before testing. Clean sodium contains <10 ppm O_2; Na (HiO_2) contains 300 ppm O_2; and Na (HiC) contains a continuous source of carbon, resulting in high carbon activity.

* Exposed simultaneously with the high-oxygen Na exposures.
† Exposed simultaneously with the high-carbon Na exposures.

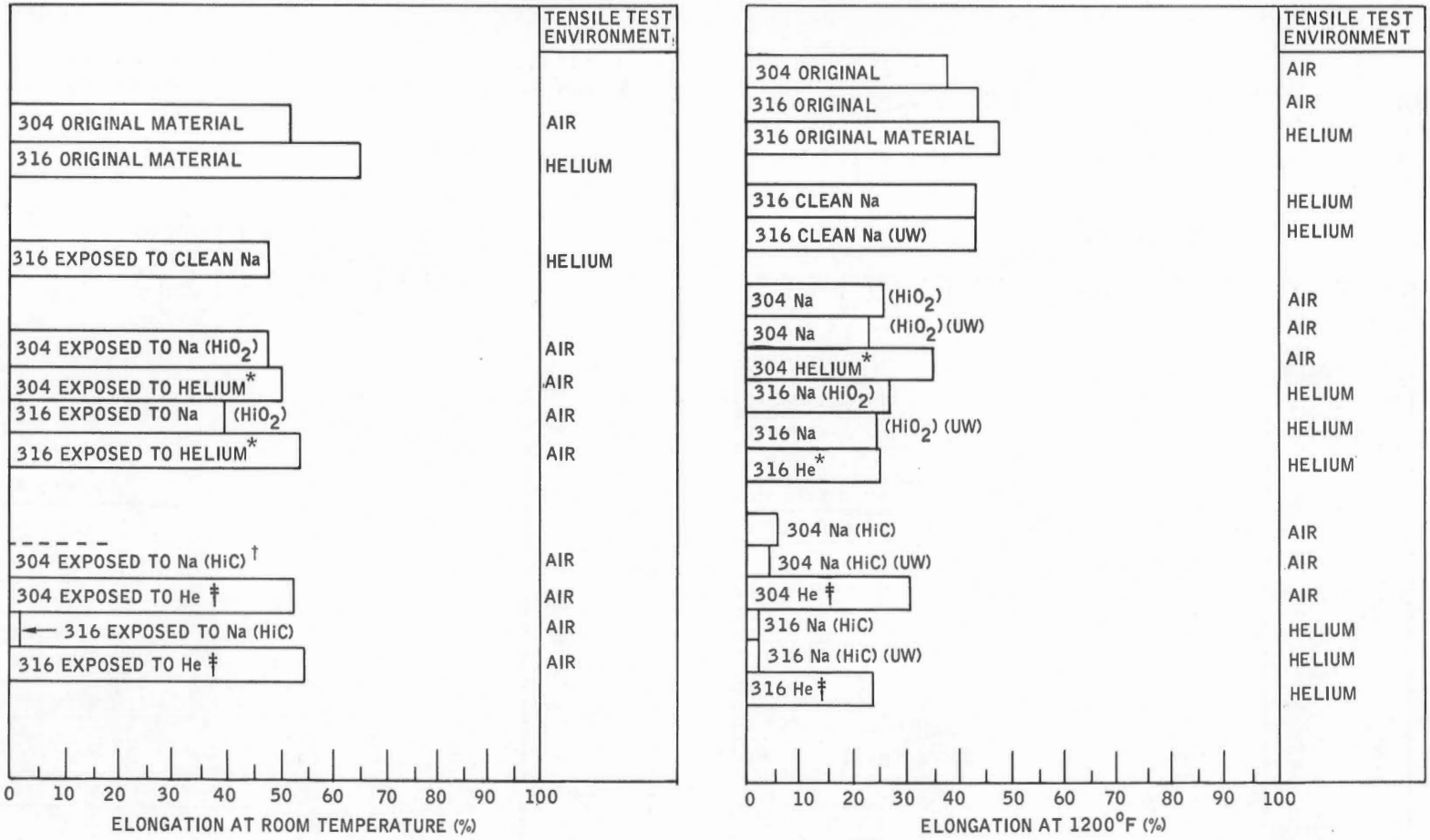

Fig. 2.8 - Elongation of 304 and 316 stainless steels following 4000-hr exposure in 1200°F dynamic sodium. The abbreviation (UW) means not washed prior to testing; all other samples were washed with alcohol and water before testing. Clean sodium contains <10 ppm O_2; Na (HiO_2) contains 300 ppm O_2; and Na (HiC) contains a continuous source of carbon, resulting in high carbon activity.

* Exposed simultaneously with the high-oxygen Na exposures.
† Triplicate specimens failed at pinholes.
‡ Exposed simultaneously with the high-carbon Na exposures.

TABLE 2.4 - Chemical Composition of Three Austenitic Steels* [7]

Grade	C	Mn	Si	Cr	Ni	Nb	W	Ti
1Kh14N20V2B	0.11	0.6	0.27	13.75	19.13	1	2.34	
1Kh14N15B	0.09	0.63	0.35	14.0	15.7	1		
1Kh18N9T	0.06	1.17	0.43	17.75	10.25			0.45

* Composition is given in weight percent.

TABLE 2.5 - Tensile Properties for Three Austenitic Steels [7]

Grade	Exposure environment*	Exposure time, hr	Tensile strength		Elongation, %
			Kg/mm^2	10^3 psi	
1Kh14N20V2B	None		55	78.2	20
at 600°C	Inert gas	2500	54	76.7	16
(1112°F)	Inert gas	5500	53	75.3	15
	Low-oxygen Na	2400	58	82.4	24
	Low-oxygen Na	5500	58	82.4	20
	High-oxygen Na	1500	61	86.6	18
	High-oxygen Na†	1500	59	83.9	24
1Kh14N15B	None		53	75.6	30
at 600°C	Inert gas	2500	58	82.4	28
	Inert gas	5500	56	79.5	23
	Low-oxygen Na	2400	57	81	31
	Low-oxygen Na	5500	57	81	24
	High-oxygen Na	1500	58	82.4	19
	High-oxygen Na†	1500	53	75.6	31
1Kh18N9T	None		65	92.4	35
	Inert gas (600°C)	3100	69	98	26
	Low-oxygen Na (600°C)	3100	69	98	27
	High-oxygen Na (600°C)	1500	68	96.7	4
	High-oxygen Na† (600°C)	1500	49	69.5	36
	Inert gas (700°C, 1292°F)	5000	66	93.7	19
	Low-oxygen Na (700°C)	2500	67	95.2	27
	Low-oxygen Na (700°C)	6500	70	99.5	26

* Low-oxygen sodium contained 40 to 70 ppm oxygen. High-oxygen sodium contained 300 ppm oxygen.

† Includes 0.2 wt.% calcium.

A comparison of the creep strength developed in these tests with the American Society for Testing Materials (ASTM) average values for 316 stainless steel is shown in Fig. 2.11. The creep strengths developed during these tests are greater than the ASTM average; the carburized material exhibited the highest creep strength. Because these design data were developed from a limited number of tests - usually three - they should be used cautiously.

(2) *Austenitic-Stainless-Steel Tubing*. The creep strength and rupture life for 304- and 316-stainless steel

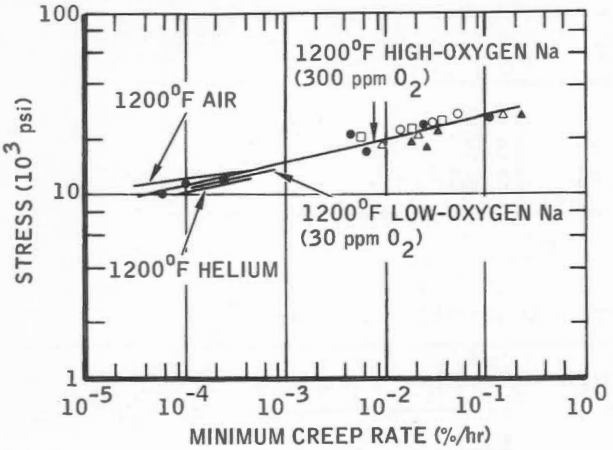

Fig. 2.9 - Minimum creep rate of 316 stainless steel in air, helium, and high- and low-oxygen sodium tested at 1200°F after 4000-hr exposure at 1200°F.

	Exposure environment	Test environment
○	High-oxygen Na	High-oxygen Na
△	High-oxygen Na	Air
□	High-oxygen Na	Helium
●	As received	High-oxygen Na
▲	Helium	Air

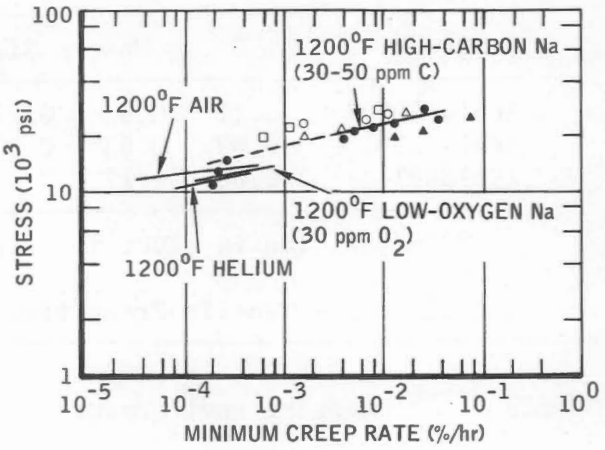

Fig. 2.10 - Minimum creep rate of 316 stainless steel in air, helium, and high-carbon and low-oxygen sodium tested at 1200°F after 4000-hr exposure at 1200°F.

	Exposure environment	Test environment
○	Na-C	Na-C
△	Na-C	Air
□	Na-C	Helium
●	As received	Na-C
▲	Helium	Air

tubing (0.010-in. wall thickness) in high-purity, static sodium were studied at Atomics International. [8,9] In the earlier investigations the short-term rupture strength and rupture life for both steels were found to be significantly lower in an environment of zirconium-gettered sodium than in an atmosphere of helium. Biaxial stress-rupture data from these experiments for 316 stainless steel are shown in Fig. 2.12 and for 304 stainless steel in Fig. 2.13. The creep rate of 316 stainless steel at 1350°F is shown in Fig. 2.14; the creep rate is higher in sodium than in helium. The unexpected loss of creep-rupture strength in the sodium environment was traced to decarburization of the tubing. Zirconium foil, which was placed in the sodium in the static-test retorts to getter oxygen, acted as a sink for carbon transported from the stainless-steel tubing through the sodium bath. In tests on 304 stainless steel, the carbon content was found to be reduced by 30 to 50% in less than 1000 hr at 1300°F; 316 stainless steel lost 30% of its original carbon in less than 1000 hr at 1350°F. Chemical analysis of the zirconium foil showed that its carbon increased from 0.01% before exposure to 0.33% after exposure. The average oxygen concentration in the sodium was below 10 ppm during the tests as determined by sampling during each run and at the end of each run.

In continued work [9] with the same equipment but without the zirconium foil, sodium samples withdrawn from the retort during and after each test showed that the original low oxygen content (∿ 10 ppm) was maintained during the test without difficulty. Figs. 2.15 and 2.16 show that the biaxial stress-

TABLE 2.6 - Creep Data for 316 Stainless Steel in Various Environments [4]

Exposure environment (4000 hr, 1200°F)	Test environment (1200°F)	Stress to produce creep rate of 1% in 100,000 hr, psi
None	Helium	8,200
None	Air	10,500
None	Low-oxygen Na	8,500
None	High-oxygen Na	8,500
None	High-carbon Na	10,000
High-oxygen Na	High-oxygen Na	8,500
High-oxygen Na	Air	8,500
High-oxygen Na	Helium	10,400
Helium	Air	8,600
High-carbon Na	Air	11,800
High-carbon Na	Helium	13,200
High-carbon Na	High-carbon Na	17,000

rupture properties of thin-walled tubing of both austenitic stainless steels in an environment of high-purity sodium were unchanged from results obtained in high-purity helium.

The test pattern of work completed and in progress in this program [9] is shown in Table 2.7. Figs. 2.17 and 2.18 present the biaxial stress-rupture properties of annealed and cold-worked austenitic-stainless-steel thin-walled tubing in high-purity sodium at 1000, 1200, and 1400°F, as determined from the latest data. [10] Conclusions drawn from these data include:

1. No significant degradation of mechanical properties of 304 and 316 stainless steel was found in a high-purity environment (∿ 10 ppm oxygen) for testing times up to 3000 hr at temperatures up to 1400°F. The same lack of environmental effect was found for both 10 to 15% cold-worked tubing and annealed tubing. No significant embrittlement effect due to 1400°F sodium was found. Microstructural characteristics of the ruptured tubing from 1400°F sodium and helium environments were comparable.

2. The long-term stress-rupture curves of cold-worked tubing have a steeper slope than those of annealed material. Although the cold-worked material has higher short-term rupture strength, the two curves converge and cross, the annealed material having superior long-term rupture strength when tested at temperatures where recovery processes are operative. The crossover point at a given temperature for 316 stainless steel occurred at a much longer time than for 304 stainless steel, probably because of the stabilizing effect of the molybdenum in the former.

3. At 1200 and 1400°F, 10 to 15% cold-worked 316 stainless steel had significantly higher long-term rupture strength than cold-worked 304 stainless steel and comparable ductility (diametral strain).

Shively [11] reported the results of stress-rupture tests of internally heated and pressurized thin-wall tubes of 304 stainless steel immersed in high-purity, flowing, 1200°F sodium. The tubing material was identical with that previously tested by Lee. [8,9] Shively first ran four control tests in which the tubes were stress-rupture tested in flowing sodium internally pressurized with NaK but not internally

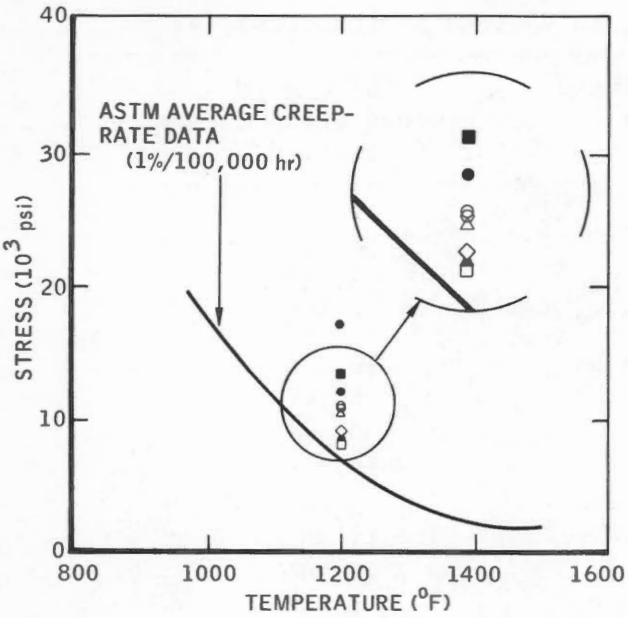

Fig. 2.11 - Creep rate of 316 stainless steel (1% in 100,000 hr) tested at 1200°F after 4000-hr exposure at 1200°F (extrapolated).

	Exposure environment	Test environment
○	None	Air
□	None	Helium
▲	None	Na-C
▲	None	Low-oxygen Na
▲	None	High-oxygen Na
▲	High-oxygen Na	Air
▲	High-oxygen Na	High-oxygen Na
⬡	High-oxygen Na	Helium
◇	Helium	Air
●	Na-C	Air
■	Na-C	Helium
⬢	Na-C	Na-C

heated. The actual rupture time at 1210 to 1245°F ranged from 0.9 to 1.1 times that predicted from Lee's[9] stress-rupture data in static sodium with helium pressurization. This demonstrated that the internal NaK environment and the external dynamic sodium did not substantially alter the biaxial stress-rupture life of the material. It was further noted that the salient features of the microstructures of both static and dynamic specimens were identical, indicating that failure modes were the same in both tests. Ten more stress-rupture tests with internal heating are reported; in two tests the heating was continuous, and in eight tests the heater was cycled on and off at 2- or 12-min intervals. Test conditions are reported in Table 2.8. The strain profiles of tube tests with internal heating were found to follow the temperature profile along the wall of the tube as shown in Fig. 2.19. The failures occurred in the peak strain positions, which are also peak temperature positions. For the constant-internal-heat tests, the stress-rupture behavior of 304-stainless-steel thin-wall tubes was directly predicted from the data obtained by Lee [9] in static sodium for the stress and temperature corresponding to the peak midwall position of the tubes. The average strain rate also agreed with that predicted from static tests. Steady internal heating therefore did not alter the biaxial stress-rupture life of the material from that observed in static tests.

However, the results of tests of internally heated and pressurized specimens operated in a cyclic mode showed a pronounced influence of cycling on the stress-rupture life and on the rate of deformation. The strain at the peak temperature was 50% greater for the cyclic than for the steady-heat tests (Fig. 2.19), and the strain profile was much sharper, indicating more localized deformation. The appearance of the microstructure and cracking was different for the thermally cycled specimens; extensive void formations found in previous tests were absent in the cyclic specimens except in the rupture area, and multiple cracks were found.

These differences indicate that thermal cycling altered the creep-deformation mechanisms. It was found that conventional secondary-creep equations do not rationalize the increased strain or reduction in life; observed cyclic life and that predicted from Lee's

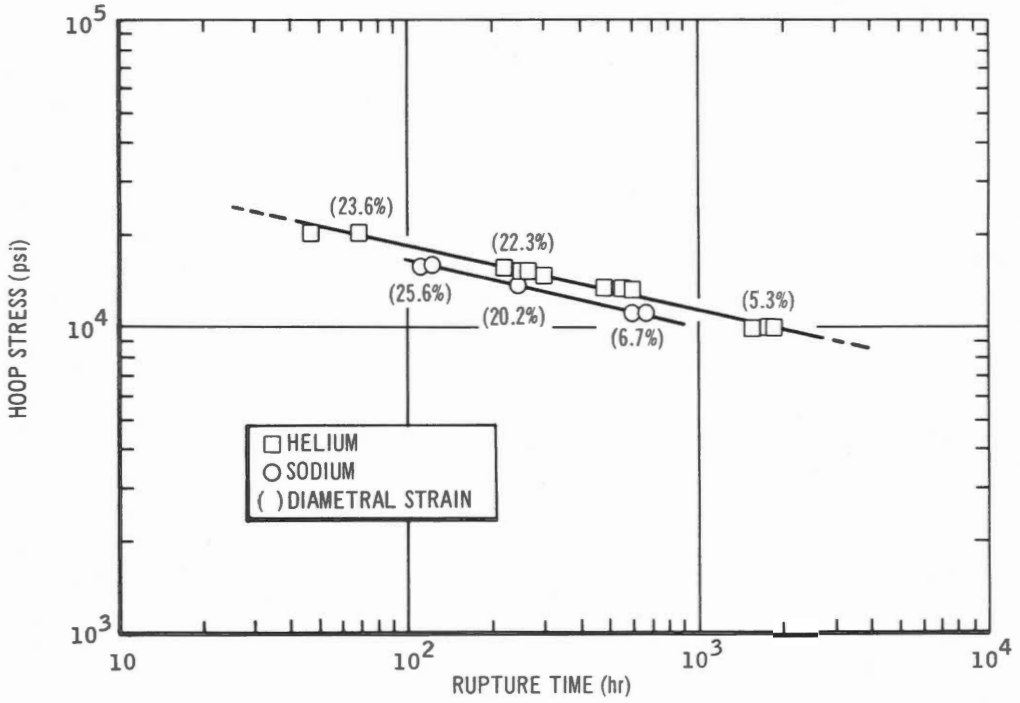

Fig. 2.12 - Biaxial stress-rupture data for annealed 316 stainless steel, Heat 90016, in 1350°F sodium and helium. The biaxial stress ratio was 1:2; the pressurizing gas was helium; and the environment was zirconium-gettered sodium.

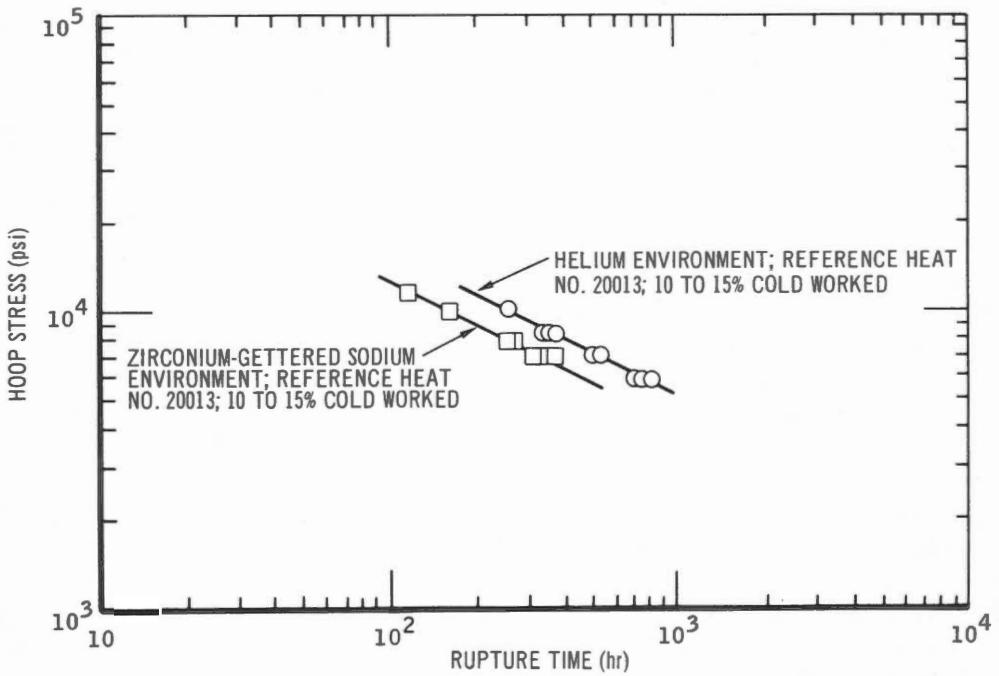

Fig. 2.13 - Biaxial stress-rupture data for 304 stainless steel at 1400°F in sodium and in helium.

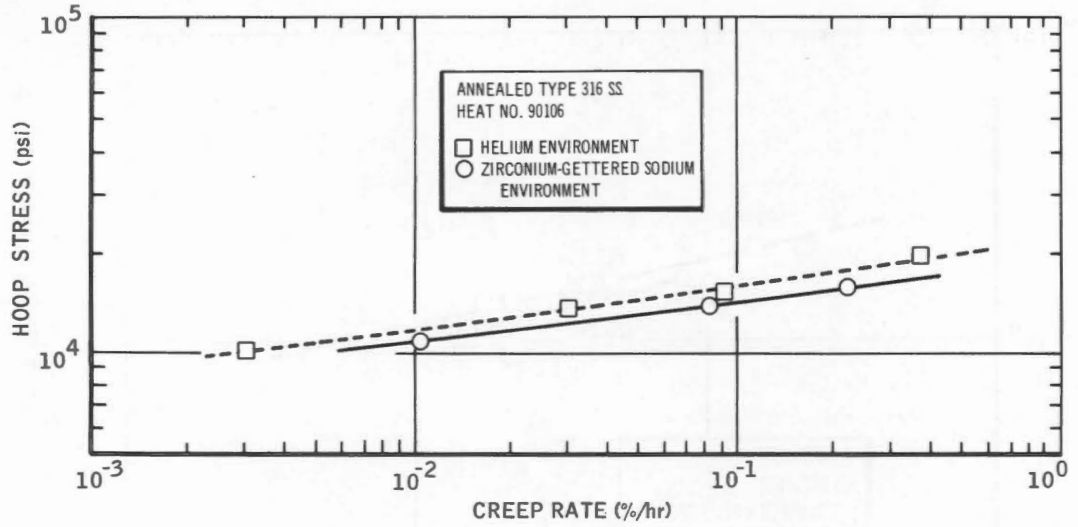

Fig. 2.14 - Creep rate of 316 stainless steel at 1350°F in helium and zirconium-gettered sodium.

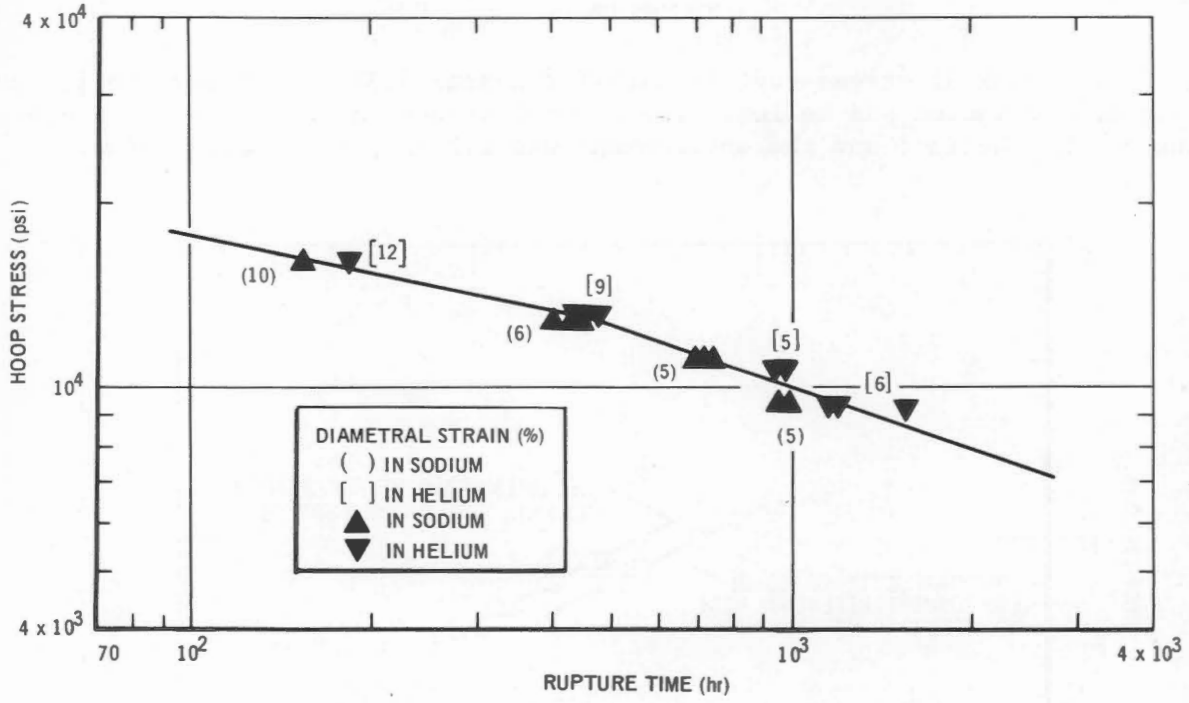

Fig. 2.15 - Stress-rupture properties of 10 to 15% cold-worked 316 stainless steel in 1400°F sodium and helium.

static tests [9] are compared in Fig. 2.20. A preliminary conclusion was that primary-creep mechanisms were operative in addition to secondary creep, and the resulting superposition produced a ratchetting effect and increased strain.

Studies on the stress-rupture behavior of 304 stainless steel in copper-contaminated sodium were performed

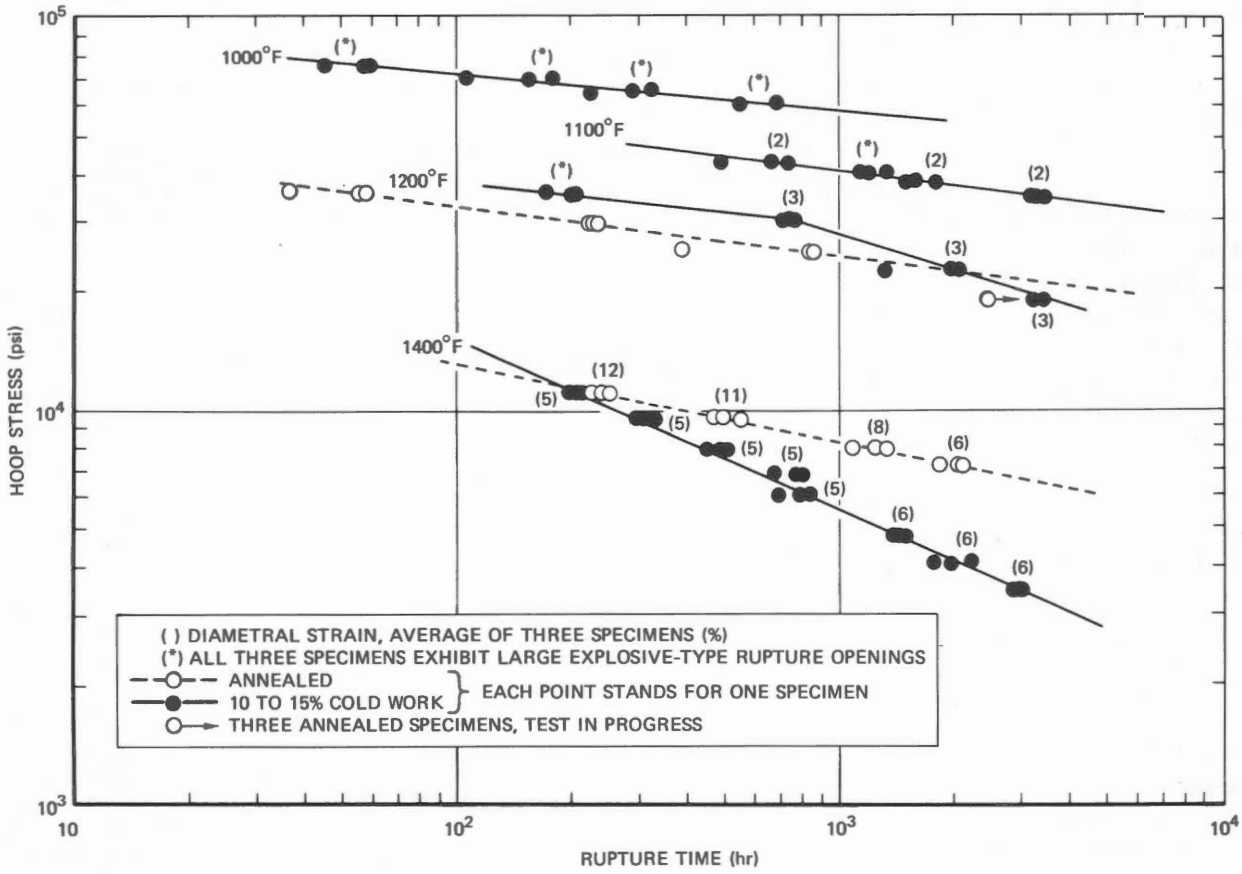

Fig. 2.16 - Biaxial stress-rupture properties of 304 stainless steel in high-purity sodium.

by Atomics International. [10] Biaxial stress-rupture specimens, both copper-plated (0.0002 in. and 0.0006 in.) and unplated 304 stainless-steel tubing, were exposed to static sodium saturated with copper for up to 2000 hr at 950, 1100, and 1300°F. Charpy impact specimens and pure copper corrosion tabs were also exposed in the retorts.

Results of the stress-rupture tests are plotted in Fig. 2.21. Both copper-plated and unplated specimens gave essentially the same values. In addition, the 1100°F test results agree with previous tests at 1100°F carried out on the same heat of tubing in high-purity sodium; similar previous tests in high-purity sodium at 1200°F and 1400°F are shown in Fig. 2.21 as dashed lines. It was concluded from these studies that the presence of copper in sodium was not detrimental to the stress-rupture properties of the 304-stainless-steel tubing under these test conditions.

Strain measurements taken on the diameter of the specimens after the test showed [10] that the strain rate was the same for both copper-plated and unplated specimens in copper-saturated sodium at 950 and 1100°F (Fig. 2.22). Preliminary results from the 1300°F test also indicated that copper contamination did not affect strain rate.

Charpy impact tests on specimens exposed to copper-saturated sodium at 950 and 1100°F showed [10] a reduction in impact strength attributable wholly to thermal-aging effects. Metallographic examination did not show any copper penetration into the stainless

TABLE 2.7 - Biaxial Stress-Rupture Test Matrix of 304 and 316 Stainless Steel [9]

Test	304 Stainless steel*						316 Stainless steel*					
	Temperature, °F						Temperature, °F					
	900	1000	1100	1200	1300	1400	900	1000	1100	1200	1300	1400
Reference condition†												
Scoping tests (100 to 1000 hr)		O	O	O	O			O	O			O
Design tests (100 to 5000 hr)	⊗	⊗		⊗	O		×					
Design tests (to 10,000 hr)		⊗		⊗				⊗	⊗			
Variable tests												
Annealed (100 to 5000 hr)		⊗		⊗	O		×	⊗	⊗			O
Annealed (to 10,000 hr)		⊗		⊗				⊗	⊗			
Thermal aging (100 to 1000 hr)				⊗								
Helium‡ (500 to 5000 hr)				⊗	O			⊗				O
Preexposed (100 to 5000 hr)				×								

* Symbols are: O, test completed; ⊗, test in progress; ×, test planned. Each test contains 12 specimens.

† External environment is high-purity sodium, and internal environment is high-purity helium.

‡ Both external and internal environments are helium.

steel. Preliminary results from the specimens exposed at 1300°F also indicated no effect of copper contamination on impact strength.

(c) *Stress Relaxation (EI-853 Steel)*

The influence of sodium on the relaxation of stresses in a high-chromium steel, EI-853, was investigated by Nikitin. [12] In this experiment split rings with suitable reference marks were partially submerged in sodium (100 ppm oxygen) at 600°C (1112°F). Initial stress levels of 16, 14, and 9 kg/mm^2 were applied by spreading the rings and inserting wedges of dimensions appropriate to maintain the desired stress. Similarly, rings were tested in an air medium at the same temperature and initial stress levels. The chemical composition of the test material, EI-853, is shown in Table 2.9.

Residual stresses in a ring were calculated by the formula

$$\sigma_t = AE(C_2 - C_1) \qquad (2.1)$$

where σ_t = residual stress at time t
A = constant (0.000583 mm^{-1})
E = modulus of elasticity
C_1 = distance between reference marks with ring unstressed (mm)
C_2 = distance between reference marks with wedge inserted, ring stressed (mm)

In Fig. 2.23 pairs of relaxation-time curves are shown for specimens with identical initial stresses tested

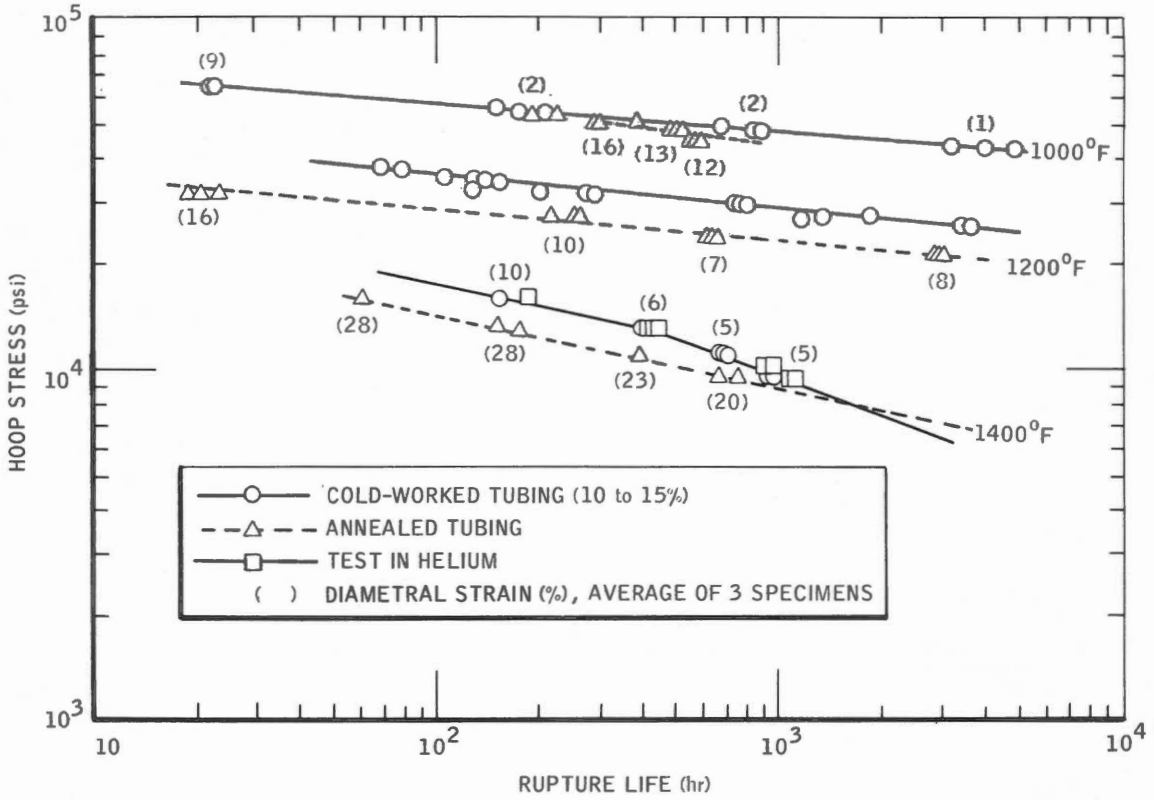

Fig. 2.17 - Biaxial stress-rupture properties of cold-worked and annealed 316 stainless steel in sodium.

in different media. The graphic data indicate that the process of stress relaxation occurs earlier in sodium than in an air atmosphere. At all initial stresses the liquid metal accelerates relaxation.

(d) *Creep-Rupture Strength*

(1) *316 Stainless Steel.* Typical curves for 316 stainless steel in 1200°F sodium have been developed, [2,3,4] based on the results obtained from numerous tests performed on uniaxially loaded sheet-type specimens exposed to a variety of test media. The chemical composition of the 0.065-in.-thick stress-rupture specimens is shown in Table 2.1.

The stress-rupture data developed do not reveal any significant variation in rupture life for material exposed in air, helium, or low- (30 ppm) and high- (300 ppm) oxygen sodium, but the rupture strength increased markedly for material exposed in high-carbon (30 to 50 ppm) sodium. Figure 2.24 shows this varied behavior. From the maximum rupture life measured (5400 hr), the curves were extrapolated to 100,000 hr. When compared with the ASTM average rupture life in 100,000 hr, the data as shown in Fig. 2.25 indicate higher strengths for the material tested in high-carbon (30 to 50 ppm) sodium and lower strengths for that tested in the other media.

The curves developed from the test data for both as-received and preexposed material are shown in Figs. 2.26 to 2.29. Preexposure decreased the time required to produce equivalent strains up to 2%, but little change in time was required to produce 5% strain or rupture in 1200°F, high-oxygen sodium. The time required to produce equivalent strain

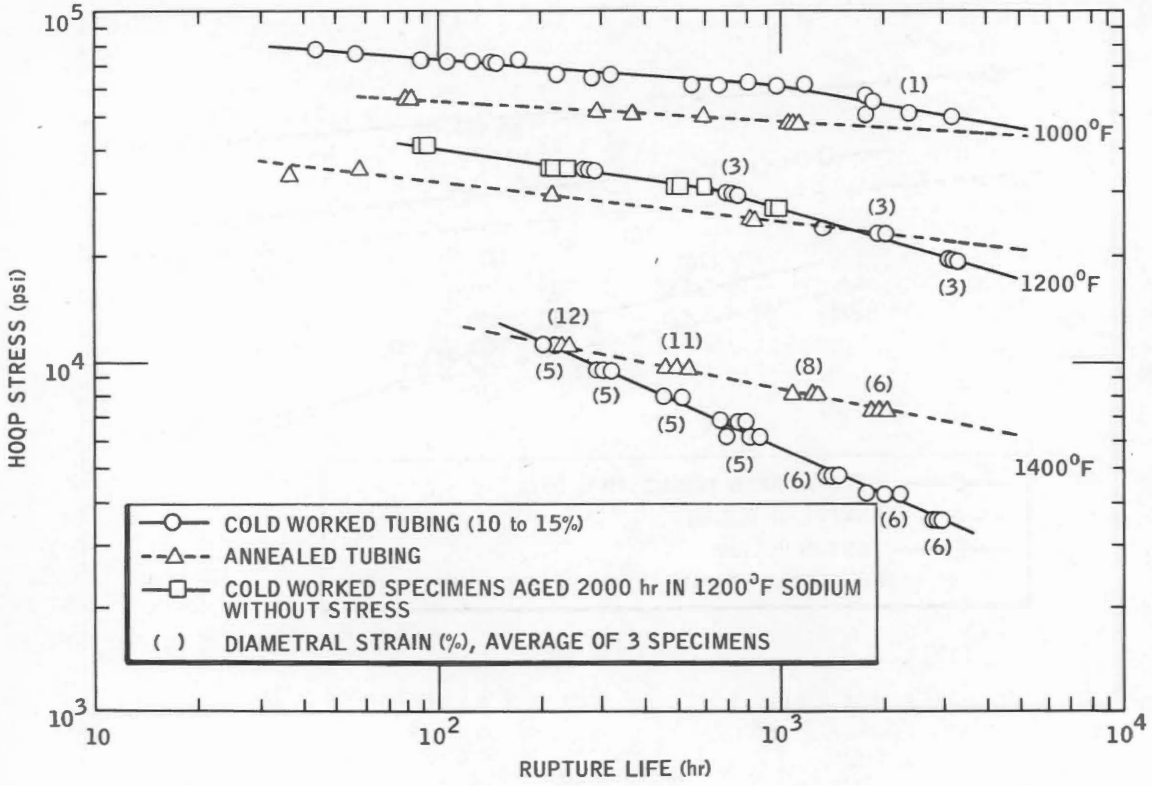

Fig. 2.18 - Biaxial stress-rupture properties of cold-worked and annealed 304 stainless steel in sodium.

is longer for material tested in high-carbon sodium than for that in high-oxygen sodium. That this apparent increase in strength is accompanied by a significant loss in ductility is indicated by the time differences between the curves for 5% strain and rupture.

The data, extrapolated to 100,000 hr, are presented in Table 2.10. Because of the limited number of tests used to derive them, these data should be applied cautiously.

(2) *304 Stainless Steel.* Andrews et al. [5,6] later reported comparable work on the effect of sodium exposure on the creep behavior of 304 stainless steel. Specimens were exposed stress free at 1200°F for 4000 hr to helium (as a control), to high-oxygen (300 ppm), dynamic sodium, and to low-oxygen (10 ppm), dynamic sodium contaminated with carbon from a continuous source and were then tested at 1200°F in air and in the high-oxygen sodium. Unexposed specimens were tested at 1200°F in air as a control and in the high-oxygen and high-carbon sodium environments at stress levels selected to provide rupture times of 100 to 4000 hr. The creep-rupture-test data are shown in Table 2.11. The creep-rupture strength of as-received material tested in high-oxygen sodium showed rupture times about one-third those in air, creep rates about twice as fast, and ductility considerably decreased. The 316 stainless steel showed no change in rupture strength when tested in high-oxygen sodium; however, the 304 stainless steel is indicated to have a longer life when the data are extrapolated past 10,000 hr.

Samples of 304 stainless steel exposed for 4000 hr to sodium had slightly higher rupture strengths

TABLE 2.8 - Biaxial Stress-Rupture with Internal Heating

Specimen No.	Heat flux, Btu/hr/sq ft	Heat flux condition	Rupture time, hr	Mechanical hoop stress, psi	Calculated thermal stress, psi	Peak strain, %	Peak strain rate,* in./in./hr	Actual life / Predicted life†
30	1×10^6	Steady	177	21,000	8,300	2.2	1.2×10^{-4}	0.9
36	1×10^6	Steady	558	16,000	8,300	2.8	4.5×10^{-5}	1.1
34	1.5×10^6	12-min cycle	5‡	21,000	12,400	3.6		
38	1×10^6	12-min cycle	198‡	16,000	8,300	1.0	1.1×10^{-4}	
32	1×10^6	12-min cycle	227	21,000	8,300	3.6	3.2×10^{-4}	0.57
40	1×10^6	12-min cycle	173	21,000	8,300	3.6	4.2×10^{-4}	0.43
42	1×10^6	2-min cycle	134	21,000	8,300	3.6	5.4×10^{-4}	0.33
44	1×10^6	2-min cycle	163	21,000	8,300	3.6	4.4×10^{-4}	0.41
46	1×10^6	12-min cycle	398	17,700	8,300	3.6	1.8×10^{-4}	0.55
48	1×10^6	12-min cycle	419	17,700	8,300	3.6	1.8×10^{-4}	0.56

* Based on the time the heat flux is on.
† Prediction is based on isothermal data obtained in static sodium.
‡ Heater failed prior to cladding.

for short times but lower strengths for longer times than the as-received samples. The effect of high-oxygen sodium on 304 stainless-steel creep behavior was decidedly detrimental. The rupture strengths of 304 stainless steel tested in 1200°F air and in high-carbon sodium were equal; but there were significant decreases in ductility, increasing at longer rupture times. Exposure of test material for 4000 hr in 1200°F, high-carbon sodium caused a drastic reduction in ductility when the specimens were later tested in air and in high-carbon sodium although the rupture strength was not changed significantly.

The creep-rupture properties of the 304 and 316 stainless-steel specimens tested at 1200°F are presented in Fig. 2.30 to 2.32. The curves represent the as-received material, and the points represent material affected by some exposure.

(3) *Chromium-Nickel Austenitic Steel (Long-Term Strength).* In stress-rupture tests performed on an austenitic stainless steel, Nikitin [13] observed a reduction in rupture life and an increased creep rate for material exposed to 700°C (1292°F) sodium. The specimen was a tube of an austenitic chromium-nickel steel (13.6% Cr, 18.9% Ni, 2.3% W, and 1.2% Nb) 11 mm in diameter, 0.5 mm in wall thickness, and 50 mm long. During the tests sodium with oxygen levels of 100 and 2500 ppm was contained inside the uniaxially loaded, tubular specimens.

Figure 2.33 shows the results of the stress-to-rupture tests. Sodium with 100 ppm oxygen had no apparent effect, but the high-oxygen sodium (2500 ppm) produced a significant reduction in rupture life. The total elongation was apparently unaffected by environment - values of 1 to 5% were measured.

Figure 2.34 shows the minimum creep rates measured during exposure to the various test media. It is again apparent that only the high-oxygen sodium, in which the differences in creep rate are more pronounced at the lower stress levels, had an appreciable effect.

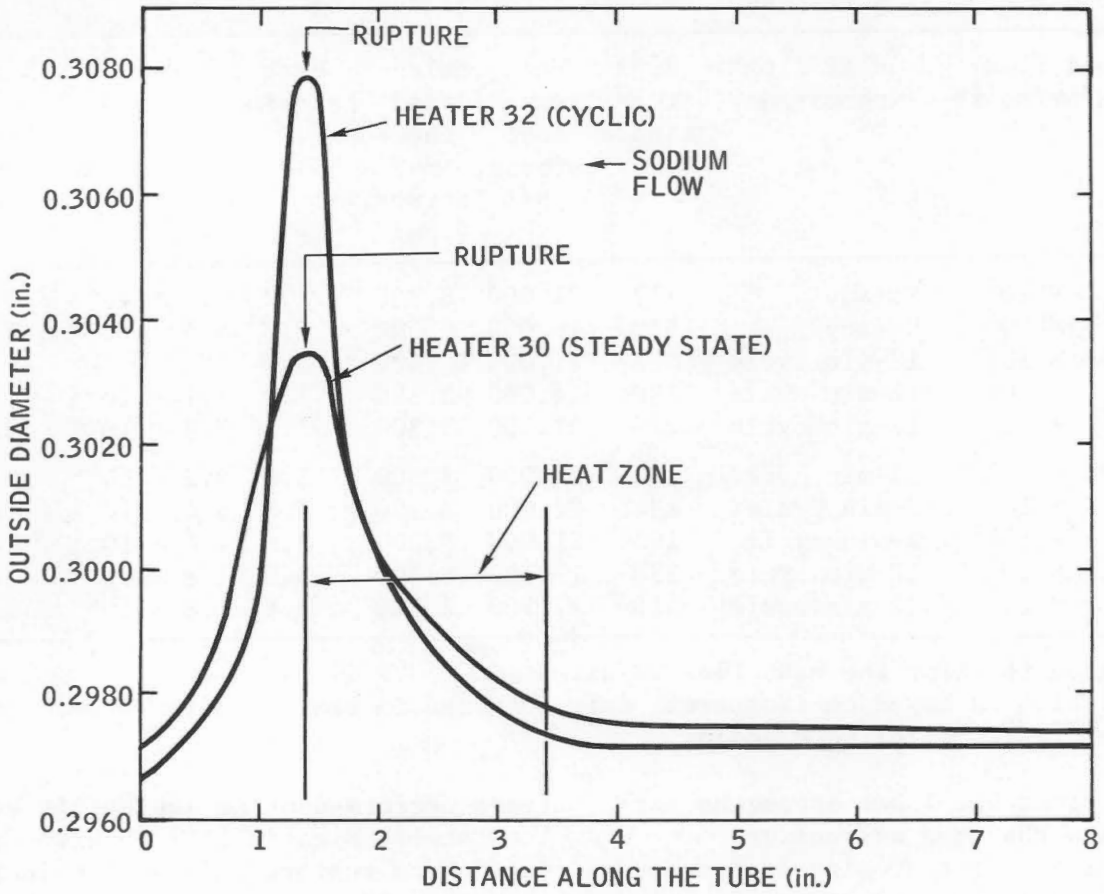

Fig. 2.19 - Longitudinal strain profiles of internally heated and pressurized tubes.

The effect of the liquid metal on the long-term properties of the samples was attributed to the corrosive and adsorptive action of the medium. In these experiments the interaction between adsorption and corrosion effects of the contaminated sodium led to more-rapid development of intercrystalline cracks and ultimate fracture of the steel. The adsorptive action of the medium and the corrosive damage to the metal in a crack combined to produce the shortened rupture life observed.

(4) *Effect of Mass Transfer on Chromium Stainless Steel.* In later tests Nikitin [14] observed that under conditions of mass transfer the 1000-hr rupture strength of a chromium stainless steel was reduced by a factor of 2. These tests were similar to the earlier ones, the principal difference involving the extended length of the tubular test specimen. Thus two temperature zones could be maintained on the test specimen to promote movement of the liquid metal (presumably sodium) within the hollow specimen by thermal convection. Typical results (Fig. 2.35) indicate that rupture life is reduced significantly under conditions conducive to mass transfer. Since the degree of mass transfer is time dependent, the greatest percentage of reductions in rupture life occurred at lower stress levels (longer exposures).

(e) *Fatigue Strength (Austenitic Stainless Steel)*

The effect of sodium on the fatigue

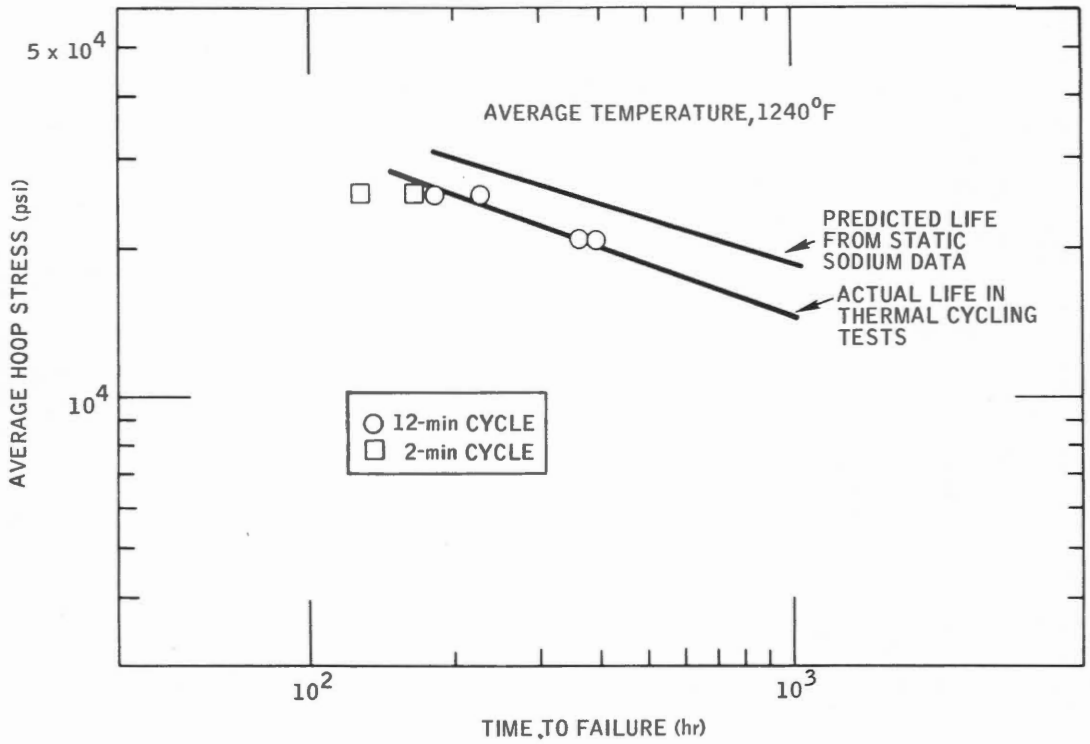

Fig. 2.20 - Predicted life vs. actual life for stress-rupture tests of 304 stainless-steel tubing in high-purity sodium with thermally cycled internal heating.

strength of 304 and 316 stainless steels was evaluated in two separate experiments. At MSAR [2 - 6] fatigue tests (or cyclic-strain tests) were performed at 180 cycles/hr using stainless-steel sheet in various environments at 1200°F. In another investigation Thiruvengadam and Preiser [15] determined the high-frequency fatigue life of 316 stainless steel in 1000 and 1500°F sodium.

(1) *High-Temperature Cyclic-Strain Testing*. In their evaluation of fatigue life of 316 stainless steel in sodium, investigators at MSAR [4] employed controlled-radius bend tests in which three levels of cyclic strain (2, 1, and 0.5%) were imposed on 0.065-in.-thick sheet specimens. The elastic strain could not be determined during these tests; therefore the described values for cyclic strain represent maximum strain values. For most combinations of strain and test environment, a minimum of three specimens was tested. In addition to testing the as-received material in a variety of environments including air, helium, low- (30 ppm) and high-oxygen (300 ppm) sodium, and high-carbon (30 to 50 ppm) sodium, the fatigue life of material preexposed for 300 hr in low- and high-oxygen sodium and high-carbon sodium was also determined. The combinations of test variables and the resulting data are given in Table 2.12.

From the data shown in Fig. 2.36, it is apparent that the fatigue life of 316 stainless steel in liquid sodium exceeds that in air but is less than that in helium. Note, however, that the superiority over the air environment is only apparent for the three strain levels investigated. For strain levels below 0.5%, the graphic data indicate that the fatigue life of 316 stainless steel in high-oxygen sodium may be less

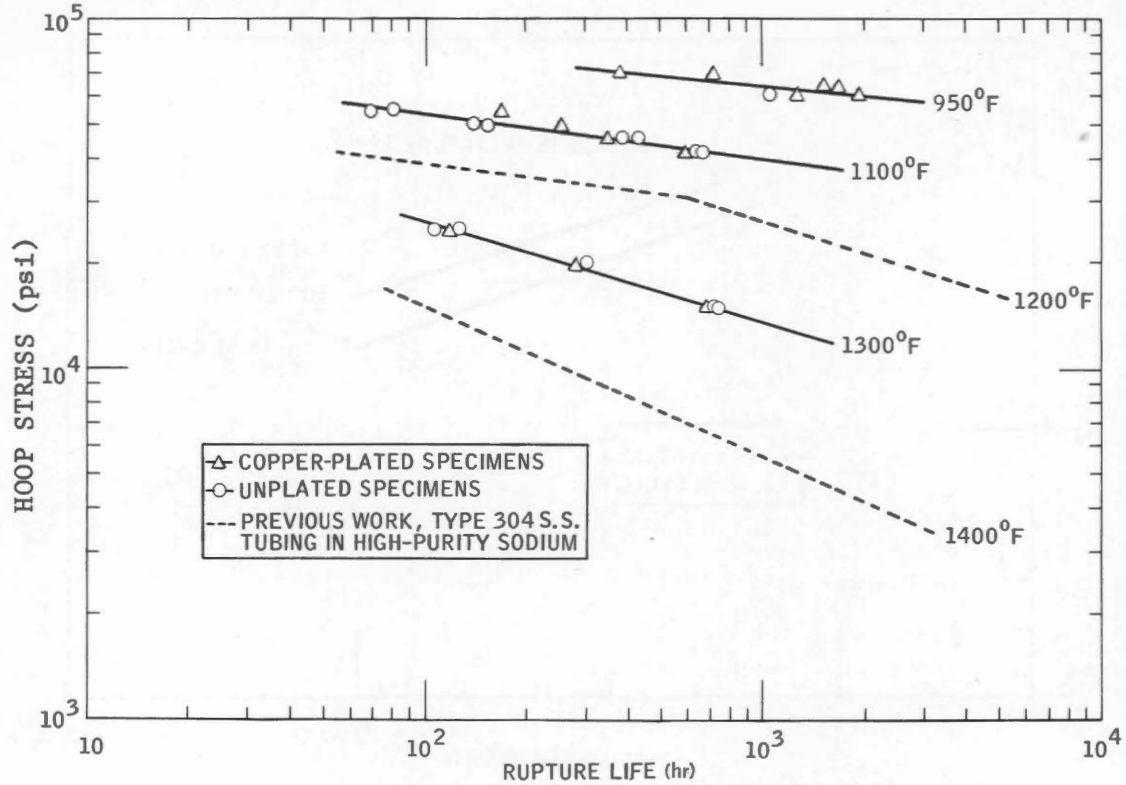

Fig. 2.21 - Biaxial stress rupture of type 304 stainless steel tubing (10 to 15% cold worked) in contaminated sodium.

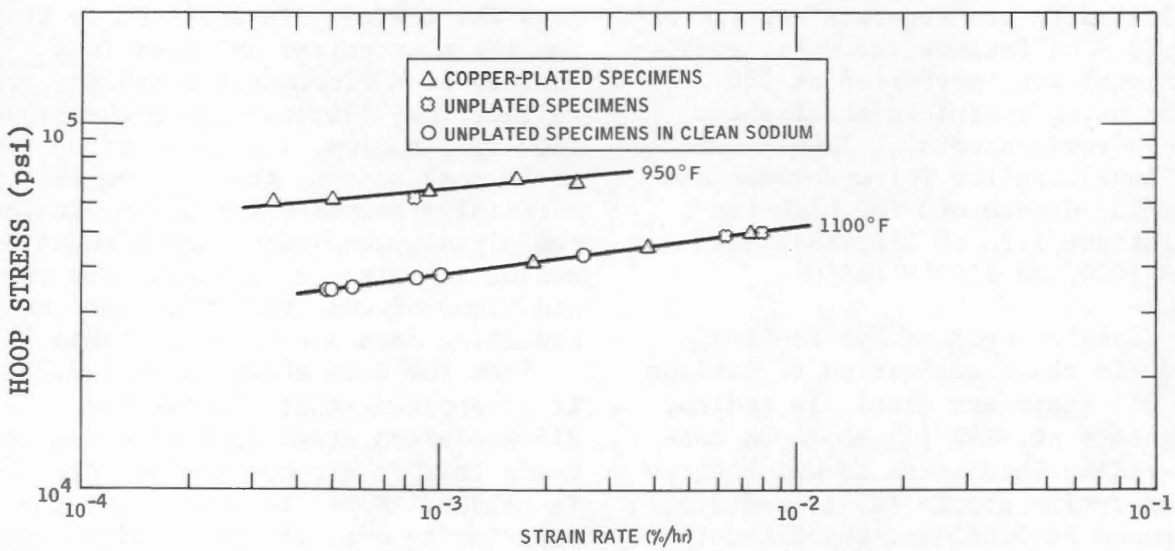

Fig. 2.22 - Strain-rate behavior of 304 stainless steel tubing (10 to 15% cold worked) in copper-contaminated sodium.

than that in air. In addition, the high-strain fatigue life in the low- and high-oxygen sodium environments was influenced by random carburization of

TABLE 2.9 - Chemical Composition of EI-853 Steel*

Element	Wt.%	Element	Wt.%
C	0.16	Cr	16.30
Mn	0.44	Mo	0.88
Si	1.78	Nb	1.78

*Data from Ref. 12.

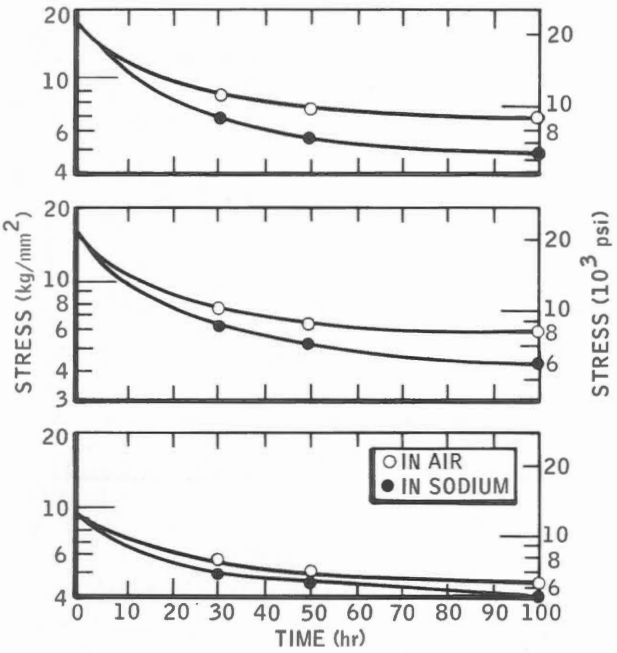

Fig. 2.23 - Stress relaxation of EI-853 steel at 600°C (1112°F).

the test specimens. Thus the high-strain fatigue values presented have been corrected for the carbon increases that occurred.

Although not measured during the experiment, plastic-strain values were subsequently calculated. In Fig. 2.37 the fatigue life for 316 stainless steel at 1200°F is shown as a function of these calculated plastic-strain values.

Data for similar cyclic-strain tests [5,6] on 304 stainless steel in high-oxygen and high-carbon sodium, air, and helium environments at 1200°F are presented in Table 2.13. Like 316 stainless steel, 304 stainless steel had greatly increased fatigue life in helium compared with air. However, the accidental absorption of carbon by the steel during the high-oxygen sodium exposure sharply reduced the cycles to failure at higher strain rates. Regardless of the carbon-absorption phenomenon, the effects of high-oxygen sodium on the fatigue life of stainless steel are concluded to be detrimental, especially at low strain levels; thus the fatigue life at low strain levels is considerably shorter in high-oxygen sodium than in air (Fig. 2.38). Samples in the high-carbon sodium environment rather than air showed a slight decrease in cycles to failure at the 2% strain

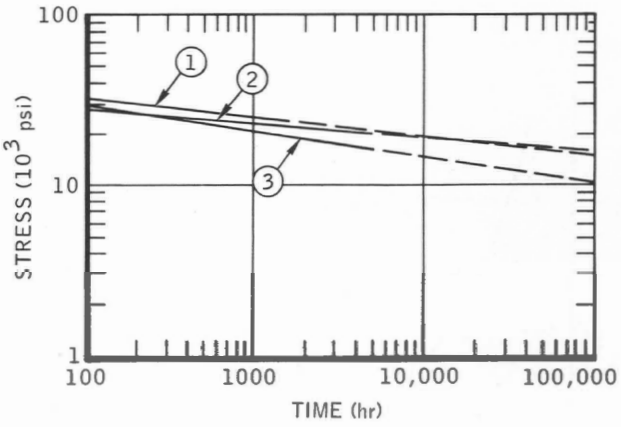

Fig. 2.24 - Creep-rupture strength of 316 stainless steel (extrapolated to 100,000 hr) tested at 1200°F after 4000 hr exposure at 1200°F.

Curve	Exposure environment	Test environment
1	Na-C (30 to 50 ppm)	Na-C (30 to 50 ppm)
2	None	Na-C (30 to 50 ppm)
3	None	Air; He; low-oxygen Na (30 ppm O_2) High-oxygen Na (300 ppm O_2)

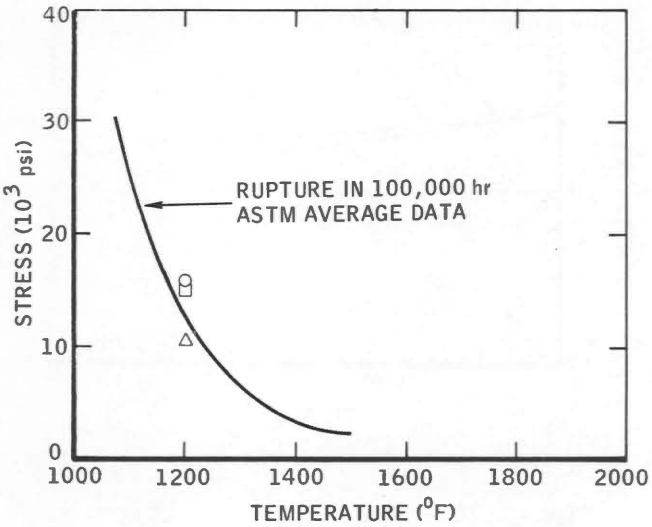

Fig. 2.25 - Creep-rupture strength of 316 stainless steel (extrapolated to 100,000 hr) tested at 1200°F after 4000-hr exposure at 1200°F.

	Exposure environment	Test environment
	None	Air
	None	Helium
	None	Low-oxygen Na
	None	High-oxygen Na
Δ	Low-oxygen Na	Air
Δ	Low-oxygen Na	Helium
Δ	Low-oxygen Na	Low-oxygen Na
Δ	High-oxygen Na	Air
Δ	High-oxygen Na	Helium
Δ	High-oxygen Na	High-oxygen Na
○	None	Na-C
□	Na-C	Na-C

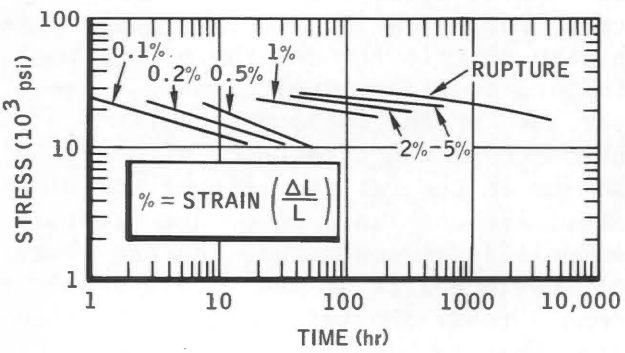

Fig. 2.26 - Creep-rupture strength of 316 stainless steel in high-oxygen sodium at 1200°F.

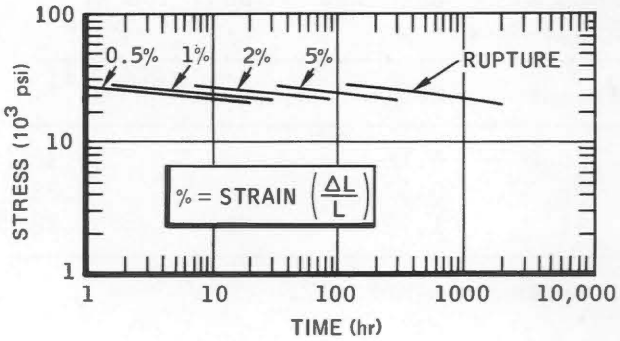

Fig. 2.27 - Creep-rupture strength of 316 stainless steel exposed for 4000 hr in high-oxygen (300 ppm O_2) sodium at 1200°F and tested in the same environment.

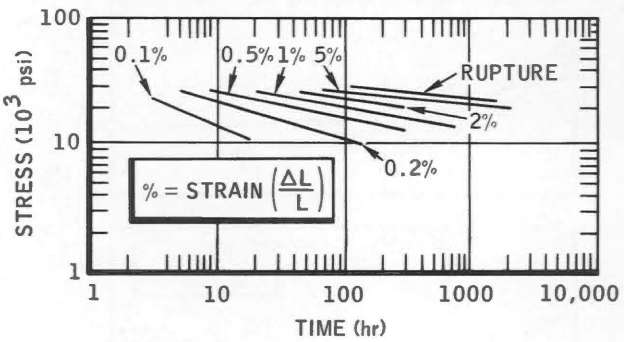

Fig. 2.28 - Creep-rupture strength of 316 stainless steel in high-carbon sodium at 1200°F.

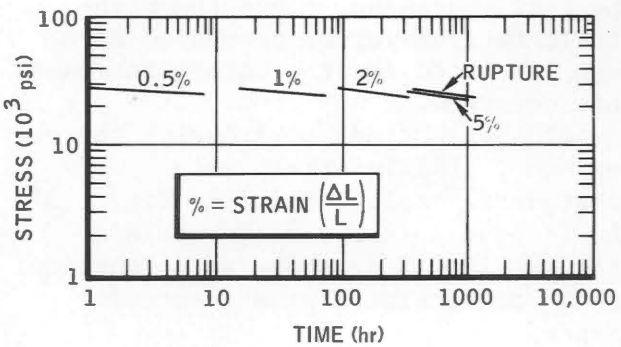

Fig. 2.29 - Creep-rupture strength of 316 stainless steel exposed for 4000 hr in high-carbon sodium at 1200°F and tested in the same environment.

TABLE 2.10 - Stress Required to Produce Strain in 316 Stainless Steel in 100,000 hr at 1200°F. [4]

Degree of strain, %	Stress required, psi: In sodium with 300 ppm oxygen	Stress required, psi: In sodium with 30 to 50 ppm carbon
0.1	820	260
0.2	950	1,300
0.5	5,000	3,700
1.0	7,000	5,500
2.0	9,000	8,500
5.0		13,500
Rupture	11,000	14,500

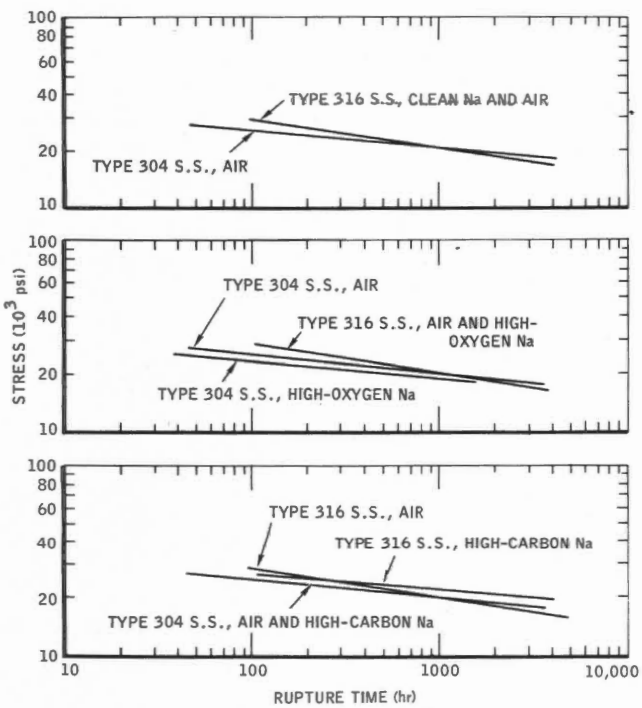

Fig. 2.30 - Rupture strength of 304 and 316 stainless steels at 1200°F.

level but a considerable increase at the low strain rate of 0.5%. The carbon environment reduced the fatigue life as compared with helium.

(2) *High-Frequency Fatigue Strength.* To measure the fatigue strength of 316 stainless steel, Thiruvengadam and Preiser [15] employed a magnetostriction device to vibrate rod-type specimens immersed in sodium (30 and 100 ppm oxygen) at 1000 and 1500°F and at a frequency of 14,000 cycles/sec. The results of these tests are shown in Figs. 2.39 and 2.40. The data indicate that, of the test variables investigated, temperature exerted the greater influence. However, since these tests were of rather short duration, any environment-induced effects may not have been created or were sufficiently slight to escape detection.

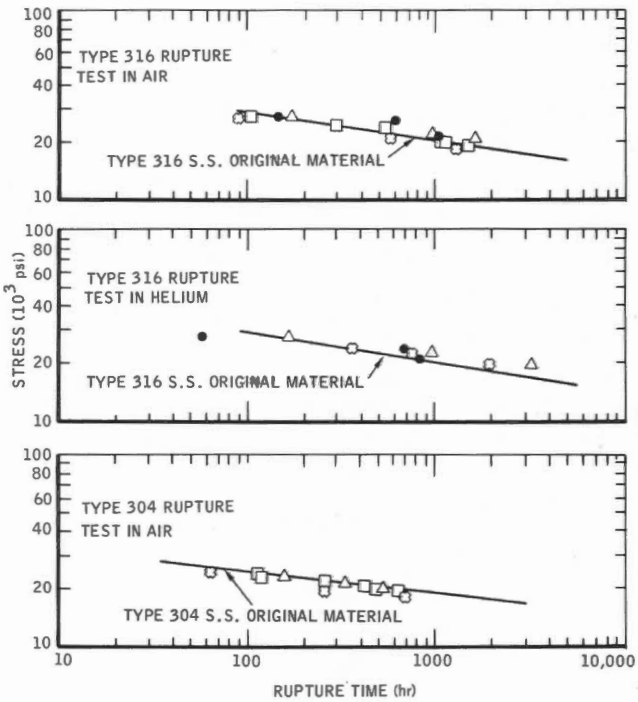

Fig. 2.31 - Rupture strength of 304 and 316 stainless steels after 4000-hr exposure at 1200°F in air and helium. ●, clean sodium exposure. ✣, high-oxygen sodium exposure. △, high-carbon sodium exposure. □, helium exposure, including specimens exposed with high-oxygen and high-carbon sodium.

(f) *Impact Strength (316 Stainless Steel)*

The impact characteristics of 316 stainless steel exposed in sodium at 1200°F were determined at MSAR [4] in

TABLE 2.11 - Creep-Rupture Test Data for 304 Stainless Steel

Exposure environment (1200°F; 4000 hr)	Test environment (1200°F)	Stress, psi	Elongation %	Reduction of area, %	Rupture time, hr	Minimum creep rate, %/hr
None	Air	25,780	68	50	75	0.250
None	Air	23,000	62	49	255	0.096
None	Air	21,000	41	51	859	0.030
None	Air	19,000	53	56	2224	0.010
None	Air	28,000	70	56	39	0.620
None	Air	24,000	54	55	118	0.180
None	Air	22,000	50	57	421	0.042
None	Air	21,000	36	46	792	0.0210
None	Air	19,500	15	36	1684	0.0062
None	Air	18,000	26	33	3079	0.0021
None	High-oxygen Na	25,000	35	26	41	0.5850
None	High-oxygen Na	23,000	33	27	71	0.2390
None	High-oxygen Na	21,000	27	23	230	0.0577
None	High-oxygen Na	20,000	34	24	518	0.0126
None	High-oxygen Na	18,000	25	18	1588	0.0070
None	High-oxygen Na	16,000			6105*	0.0005
None	High-oxygen Na	14,000			4222†	0.0001
High-oxygen Na	Air	24,000	39	47	65	0.280
High-oxygen Na	Air	21,000	35	41	254	0.088
High-oxygen Na	Air	19,000	23	60	663	0.020
Helium‡	Air	24,000	58	71	120	0.220
Helium‡	Air	22,000	52	65	251	0.100
Helium‡	Air	20,500	39	55	480	0.047
High-oxygen Na	High-oxygen Na	23,000	58	37	121	0.250
High-oxygen Na	High-oxygen Na	21,000	59	37	206	0.1085
High-oxygen Na	High-oxygen Na	19,000	45	27	448	0.0440
None	High-carbon Na	26,000			49§	
None	High-carbon Na	26,000	50	39	59	0.39
None	High-carbon Na	24,000	18	21	195	0.0206
None	High-carbon Na	22,000	22	16	390	0.0150
None	High-carbon Na	19,500	16	13	1037	0.0110
None	High-carbon Na	18,500	13	9	3661	0.0025
None	High-carbon Na	17,500	18	10	3228	0.0027
High-carbon Na	Air	24,000	8.0	17	153	0.02
High-carbon Na	Air	22,000	6.5	17	317	0.01
High-carbon Na	Air	20,000	7.0	14	538	0.0065
Helium¶	Air	24,000	72	63	117	0.23
Helium¶	Air	21,000	48	64	455	0.049
Helium¶	Air	19,500	55	60	623	0.040
High-carbon Na	High-carbon Na	22,000	12	7	776	0.0075
High-carbon Na	High-carbon Na	21,000	13	9	843	0.0067
High-carbon Na	High-carbon Na	20,000	12	9	1696	0.0043

*Footnotes are on facing page.

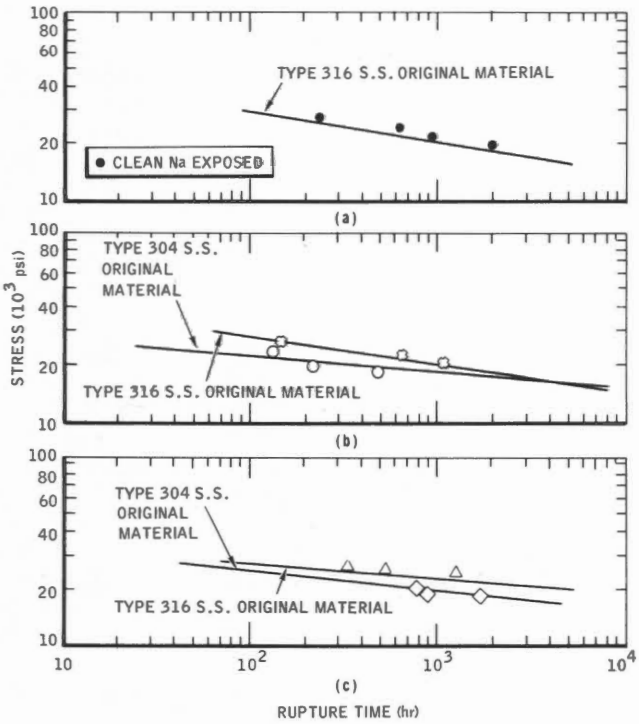

Fig. 2.32 - Rupture strength of 304 and 316 stainless steel after 4000-hr exposure at 1200°F in sodium. (a) Exposed and tested in clean sodium. (b) Exposed and tested in high-oxygen sodium. (c) Exposed and tested in high-carbon sodium.

tests performed at room temperature in a variety of environments including helium, high-oxygen (300 ppm) sodium, and high-carbon (37 ppm average) sodium. The composition of the 0.098-in.-thick stainless-steel sheet used for the impact specimens is shown in Table 2.14.

For most conditions of time and environment, triplicate tests were performed. Exposure periods prior to impact testing extended to a maximum duration of 5688 hr.

The results of the impact tests (Fig. 2.41) including the impact strength for the various exposure

(Footnotes to Table 2.11)

* Terminated before specimen rupture because of valve failure.

† Terminated before specimen rupture.

‡ Exposed simultaneously with high-oxygen exposures.

§ Failed at gauge mark; specimen data voided.

¶ Exposed simultaneously with high-carbon exposures.

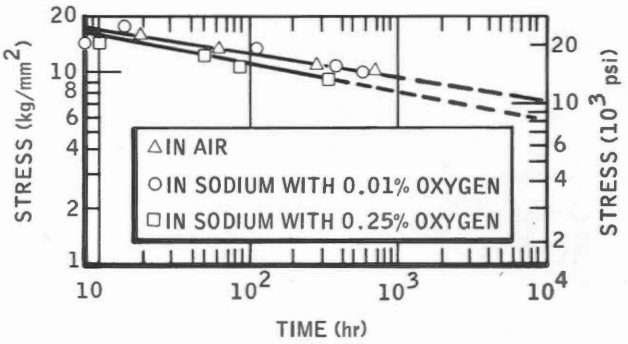

Fig. 2.33 - Stress rupture for Cr-Ni austenitic steel at 700°C (1292°F).

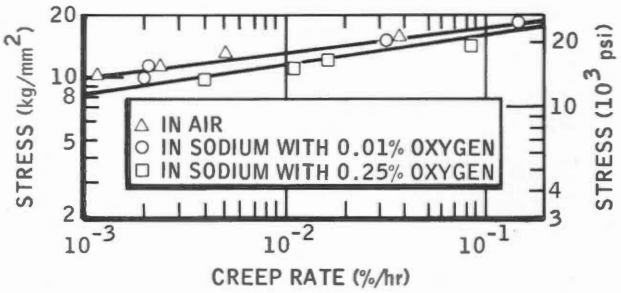

Fig. 2.34 - Minimum creep rate for Cr-Ni austenitic steel at 700°C (1292°F)

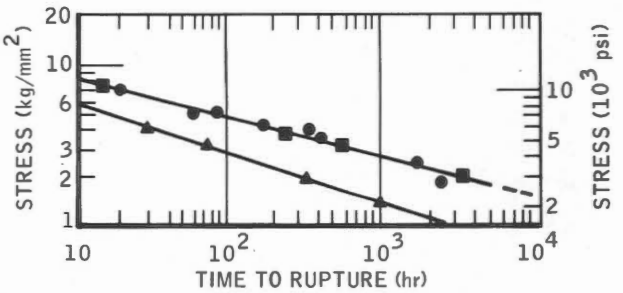

Fig. 2.35 - Stress-rupture times for chromium stainless steel in air. ■, hollow specimens filled with static liquid metal. ▲, hollow specimens filled with thermally convective liquid metal.

TABLE 2.12 - High-Temperature Cyclic-Strain (Fatigue) Test Data for 316 Stainless Steel [4]

Exposure environment	Exposure time, hr	Test environment	Cyclic strain, %	Cycles to failure	Average cycles to failure
None	0	Air	2.14	270	
None	0	Air	2.11	360	333
None	0	Air	2.14	369	
None	0	Air	1.00	1,498	
None	0	Air	1.00	1,663	1,554
None	0	Air	1.00	1,500	
None	0	Air	0.554	8,956	
None	0	Air	0.568	8,060	8,524
None	0	Air	0.565	8,556	
None	0	Helium	2.13	1,325	
None	0	Helium	2.19	848	1,098
None	0	Helium	2.14	1,122	
None	0	Helium	1.00	9,693	
None	0	Helium	0.99	9,058	8,856
None	0	Helium	1.00	7,816	
None	0	Helium	0.558	50,004	
None	0	Helium	0.571	38,804	41,940
None	0	Helium	0.573	37,011	
None	0	Low-oxygen Na	2.16	615	
None	0	Low-oxygen Na	2.18	275	464
None	0	Low-oxygen Na	2.16	492	800*
None	0	Low-oxygen Na	2.16	475	
None	0	Low-oxygen Na	0.985	2,385	
None	0	Low-oxygen Na	1.00	2,110	3,130
None	0	Low-oxygen Na	0.995	3,914	4,750*
None	0	Low-oxygen Na	1.01	4,112	
None	0	Low-oxygen Na	0.565	55,925	
None	0	Low-oxygen Na	0.556	29,400	39,460
None	0	Low-oxygen Na	0.558	33,055	
Low-oxygen Na	286	Air	2.11	296	
Low-oxygen Na	286	Air	2.12	302	308
Low-oxygen Na	286	Air	2.12	326	
Low-oxygen Na	286	Helium	2.13	1,116	
Low-oxygen Na	286	Helium	2.16	1,233	1,033
Low-oxygen Na	286	Helium	2.11	749	

* Value after correction for carbon.

TABLE 2.12 - (Continued)

Exposure environment	Exposure time, hr	Test environment	Cyclic strain, %	Cycles to failure	Average cycles to failure
Low-oxygen Na	286	Low-oxygen Na	2.18	700	
Low-oxygen Na	286	Low-oxygen Na	2.16	751	665
Low-oxygen Na	286	Low-oxygen Na	2.16	545	
None	0	High-oxygen Na	2.18	207	
None	0	High-oxygen Na	2.19	427	341
None	0	High-oxygen Na	2.18	390	750*
None	0	High-oxygen Na	1.01	4,013	
None	0	High-oxygen Na	1.01	5,280	
None	0	High-oxygen Na	1.01	3,200	4,178
None	0	High-oxygen Na	0.98	4,220	
None	0	High-oxygen Na	0.565	14,580	
None	0	High-oxygen Na	0.566	13,400	
None	0	High-oxygen Na	0.566	9,474	11,772
None	0	High-oxygen Na	0.554	9,633	
High-oxygen Na	312	Air	2.19	404	
High-oxygen Na	312	Air	2.18	225	303
High-oxygen Na	312	Air	2.18	280	
High-oxygen Na	312	Helium	2.19	597	
High-oxygen Na	312	Helium	2.18	555	
High-oxygen Na	312	Helium	2.19	374	491
High-oxygen Na	312	Helium	2.18	439	
High-oxygen Na	312	High-oxygen Na	2.18	614	
High-oxygen Na	312	High-oxygen Na	2.18	807	716
High-oxygen Na	312	High-oxygen Na	2.18	729	
None	0	High-carbon Na	2.18	399	
None	0	High-carbon Na	2.11	181	306
None	0	High-carbon Na	2.14	331	
None	0	High-carbon Na	1.01	1,323	
None	0	High-carbon Na	1.01	1,690	1,675
None	0	High-carbon Na	0.99	2,013	
None	0	High-carbon Na	0.558	12,600	
None	0	High-carbon Na	0.558	17,460	15,365
None	0	High-carbon Na	0.562	14,580	
None	0	High-carbon Na	0.567	16,820	
High-carbon Na	272	Air	2.14	245	
High-carbon Na	272	Air	2.14	144	171
High-carbon Na	272	Air	2.14	124	

* Value after correction for carbon.

TABLE 2.12 - (Continued)

Exposure environment	Exposure time, hr	Test environment	Cyclic strain, %	Cycles to failure	Average cycles to failure
High-carbon Na	272	Helium	2.18	290	
High-carbon Na	272	Helium	2.14	195	266
High-carbon Na	272	Helium	2.14	315	
High-carbon Na	272	High-carbon Na	2.12	103	
High-carbon Na	272	High-carbon Na	2.16	122	108
High-carbon Na	272	High-carbon Na	2.14	100	

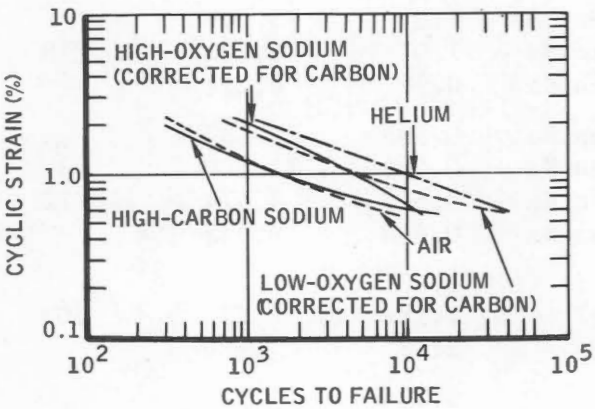

Fig. 2.36 - Fatigue behavior of 316 stainless steel in air, in helium, and in low-oxygen, high-oxygen, and high-carbon sodium environments at 1200°F.

environments against exposure time, show that the effect of preexposure was most pronounced for the first 500 hr. Regardless of the exposure environment, the extended exposures produced only a small change over that observed for the initial 500-hr period. The approximate loss in impact strength was 45% for material exposed in helium, 65% in high-oxygen sodium, and 82% in high-carbon sodium. Thus the major portion of the strength loss appears as a result of thermal effects. The increased loss of strength for material exposed in high-carbon sodium is, of course, due to the formation of a brittle carbide layer at the surfaces. Metallurgical examinations performed after the impact tests showed that the fracture characteristics of specimens exposed in high-carbon sodium indicated brittle failure. The embrittling effect observed for the carburized material was considered to represent a minimal condition since the material was in an unstressed state during exposure. It was further suggested that if applied stresses had been involved the degree of carburization could have been increased and impact strength further decreased. In view of the apparent sharp losses of impact strength over a relatively short time span, it would be prudent to adopt adequate measures to minimize short-time oxygen and carbon excursions in a sodium system.

(g) *Design Stresses for Sodium Service (316 Stainless Steel)*

Design data pertinent to the application of 316 stainless steel to sodium-cooled reactor systems with design life of 30 years were developed by Anstine. [16] Formulation of the design stresses was based on the nonoxidizing characteristics of sodium and mass transfer effects, and the extended life was factored into the analysis.

The long-term criteria (100% of the average stress to produce 1% creep in 210,000 hr and 100% of the stress to produce rupture in 210,000 hr) were applied in the development of the curve shown in Fig. 2.42. The other curves shown include a plot of design stresses taken from the 1962 ASME *Boiler and Pressure Vessel Code*, Section VIII, and

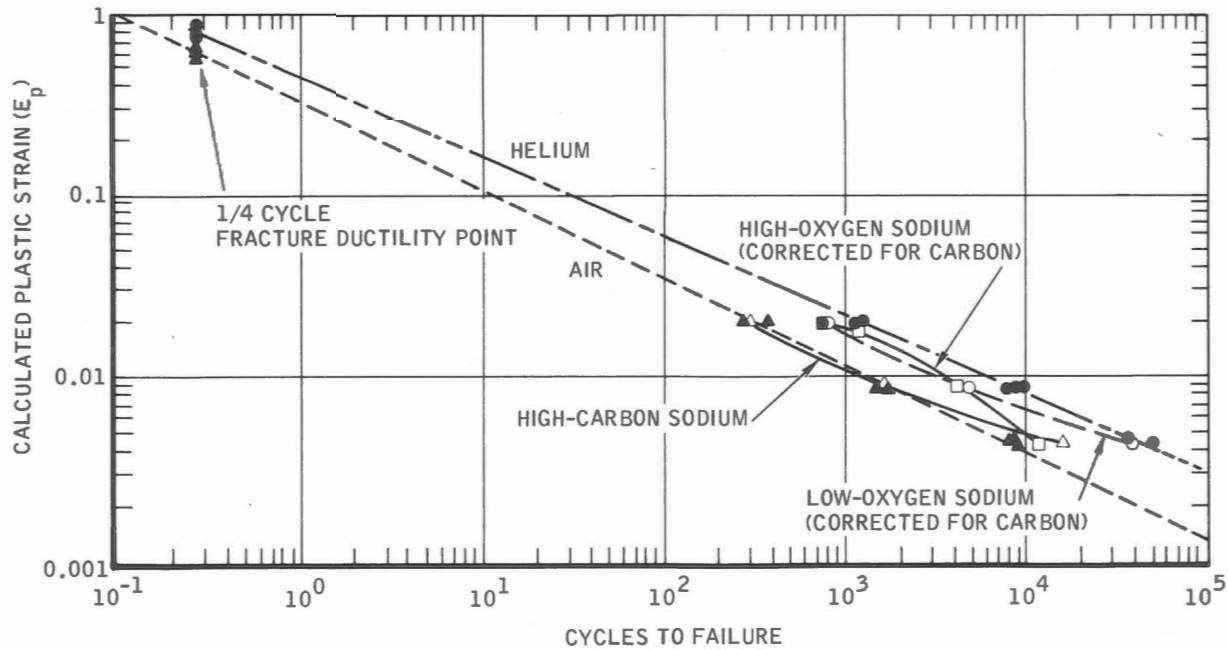

Fig. 2.37 - Plastic strain vs. cycles to failure for 316 stainless steel at 1200°F. The formula for plastic strain is

$$E_p = E_t - E_e$$

where

$$E_t = 2\left(\frac{\text{½ specimen thickness}}{\text{test mandrel radius}}\right)$$

and

$$E_e = \frac{\text{average 1200°F yield strength}}{\text{1200°F Young's modulus of elasticity}}$$

The formula for the ¼-cycle fracture ductility point is

$$E_p = \frac{\text{½ in. } [100/(100 - RA)]}{\sqrt{0.25}}$$

where RA is the percent reduction of area in 1200°F tensile tests

a plot of 70% of the design stresses from the same Code. This design curve does not include the effects of either carburization or nickel and chromium transfer observed in sodium systems. At the time of this analysis, the availability of such data was limited. However, for 316 stainless steel carburization tends to increase mechanical properties at the expense of ductility and fatigue strength. Although the developed design stresses are regarded as conservative, the carburization and mass-transfer effects should be factored into their design application.

(h) *Crack Propagation and Long-Term Behavior (Austenitic Cr-Ni Steels)*

Böhm and Schneider [17] investigated the influence of sodium on rupture life and creep behavior for two austenitic steels. The compositions of the test

TABLE 2.13 - High-Temperature Cyclic-Strain (Fatigue) Test Data for 304 Stainless Steel

Exposure environment	Exposure time, hr	Test environment	Cyclic strain, %	Cycles to failure	Average cycles to failure
None	0	Air	1.86	445	
None	0	Air	1.88	525	
None	0	Air	1.87	465	478
None	0	Air	0.86	2,400	
None	0	Air	0.84	2,684	2,652
None	0	Air	0.87	2,871	
None	0	Air	0.49	29,610	
None	0	Air	0.49	27,795	29,210
None	0	Air	0.50	30,225	
None	0	Helium	1.92	900	
None	0	Helium	1.92	1,365	1,144
None	0	Helium	1.92	1,320	
None	0	Helium	1.92	990	
None	0	Helium	0.89	18,495	
None	0	Helium	0.89	15,465	16,370
None	0	Helium	0.89	15,150	
None	0	Helium	0.50	98,325	
None	0	Helium	0.50	67,410	76,512
None	0	Helium	0.50	63,800	
None	0	High-oxygen Na	1.89	210	
None	0	High-oxygen Na	1.88	247	
None	0	High-oxygen Na	1.87	277	517
None	0	High-oxygen Na	1.90	777	1,090*
None	0	High-oxygen Na	1.89	787	
None	0	High-oxygen Na	1.89	804	
None	0	High-oxygen Na	0.88	3,075	
None	0	High-oxygen Na	0.88	1,980	2,585
None	0	High-oxygen Na	0.89	3,081	2,740*
None	0	High-oxygen Na	0.89	2,205	
None	0	High-oxygen Na	0.50	6,555	
None	0	High-oxygen Na	0.49	6,724	6,116
None	0	High-oxygen Na	0.49	5,070	
High-oxygen Na	287	Air	1.87	285	
High-oxygen Na	287	Air	1.92	300	325
High-oxygen Na	287	Air	1.90	390	560*
High-oxygen Na	287	Helium	1.82	774	
High-oxygen Na	287	Helium	1.92	480	593
High-oxygen Na	287	Helium	1.92	500	1,340*
High-oxygen Na	287	Helium	1.89	618	

* Value after correction for carbon.

TABLE 2.13 - (Continued)

Exposure environment	Exposure time, hr	Test environment	Cyclic strain, %	Cycles to failure	Average cycles to failure
High-oxygen Na	287	High-oxygen Na	1.92	369	
High-oxygen Na	287	High-oxygen Na	1.92	363	370
High-oxygen Na	287	High-oxygen Na	1.90	379	405*
None	0	High-carbon Na	1.89	330	
None	0	High-carbon Na	1.89	285	315
None	0	High-carbon Na	1.87	330	
None	0	High-carbon Na	0.89	2,140	
None	0	High-carbon Na	0.88	3,220	2,572
None	0	High-carbon Na	0.87	2,355	
None	0	High-carbon Na	0.49	70,650	
None	0	High-carbon Na	0.50	74,790	71,497
None	0	High-carbon Na	0.49	69,050	
High-carbon Na	427	Air	1.92	180	
High-carbon Na	427	Air	1.92	587	
High-carbon Na	427	Air	1.92	585	403
High-carbon Na	427	Air	1.92	258	
High-carbon Na	427	Helium	1.92	465	
High-carbon Na	427	Helium	1.89	531	473
High-carbon Na	427	Helium	1.89	422	
High-carbon Na	427	High-carbon Na	1.89	117	
High-carbon Na	427	High-carbon Na	1.91	102	130
High-carbon Na	427	High-carbon Na	1.92	170	

* Value after correction for carbon.

TABLE 2.14 - Chemical Composition of 316 Stainless Steel Impact Specimens (Heat 31083) [4]

Element	Wt.%	Element	Wt.%
C	0.053	Si	0.42
Mn	0.93	Cr	17.42
P	0.019	Ni	13.58
S	0.018	Mo	2.82

materials, X8CrNiMoVNb and Incoloy 800, are shown in Table 2.15. Incoloy 800 (30 Ni-20 Cr) was investigated to show the influence of higher nickel content. The specimens were tubes filled with sodium or air under uniaxial loading conditions at 700°C (1292°F). The oxygen content of the sodium was 50 ppm or less.

The effect of sodium on the rupture life of the alloys is evident in the data presented in Figs. 2.43 and 2.44. The rupture life of the 16 Cr-13 Ni steel appeared unaffected by the sodium environment, but the rupture life for Incoloy 800 was significantly reduced, the effect of sodium being more pronounced at the lower stress levels (longer exposure time).

The minimum creep rates determined for both alloys are shown in Fig. 2.45. The presence of sodium exerted no influence on the minimum creep rates; however, as shown in Figs. 2.46 and

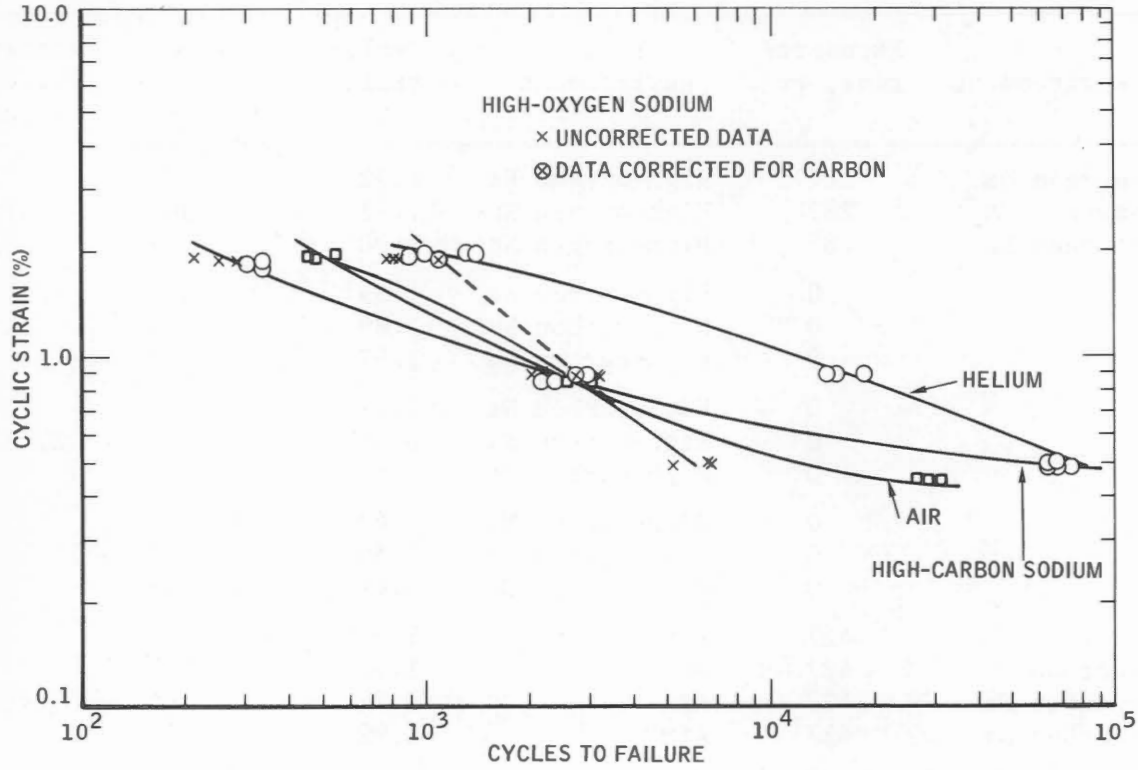

Fig. 2.38 - Cycle life of 304 stainless steel (original material) at 1200°F.

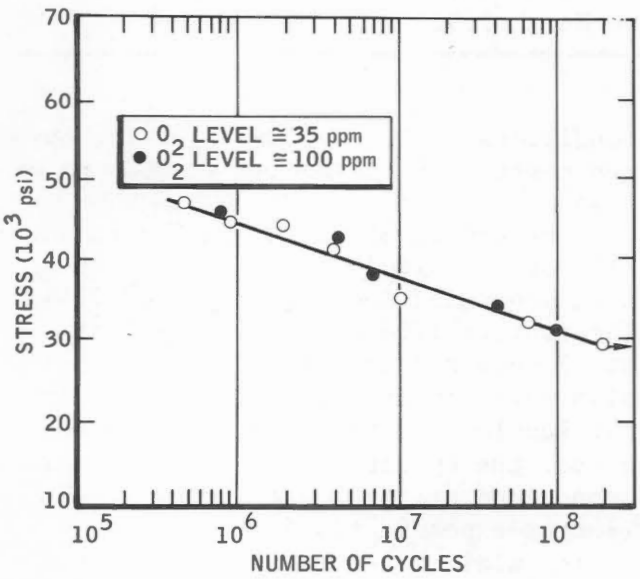

Fig. 2.39 - High-frequency (14,143 cps) fatigue of 316 stainless steel in 1000°F sodium at two oxide levels.

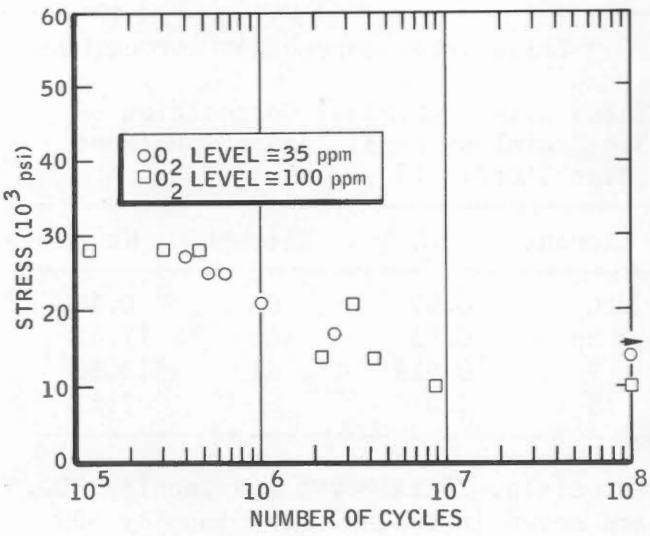

Fig. 2.40 - High-frequency (14,080 cps) fatigue of 316 stainless steel in 1500°F sodium at two oxide levels.

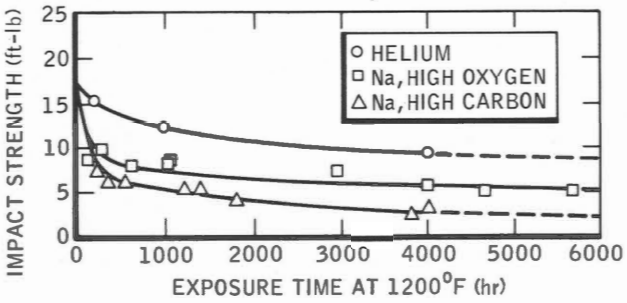

Fig. 2.41 - Impact test results for 316 stainless steel following exposure in various environments.

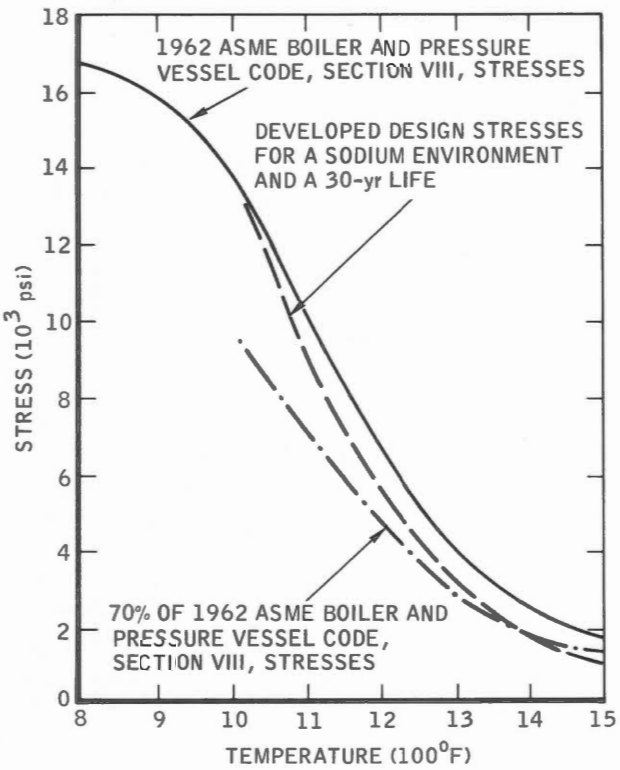

Fig. 2.42 - Developed design stresses for 316 stainless steel in a sodium environment for a 30-year life.

2.47, the total strain-to-rupture for both alloys was reduced significantly by the presence of sodium. This observed reduction can be explained by the relatively short duration of the

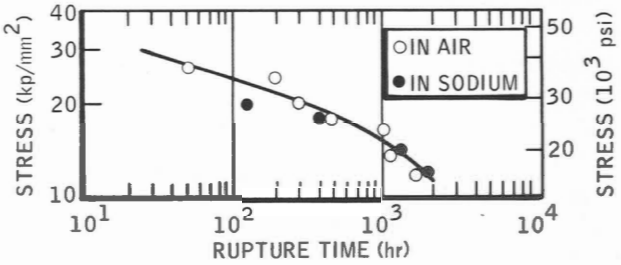

Fig. 2.43 - Stress rupture for 16/13 Cr-Ni steel at 70°C (1292°F).

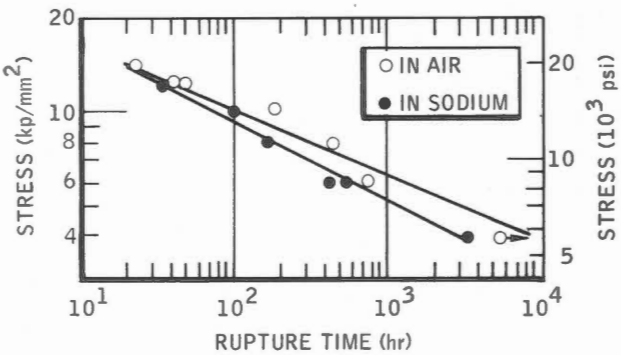

Fig. 2.44 - Stress rupture for Incoloy 800 at 700°C (1292°F).

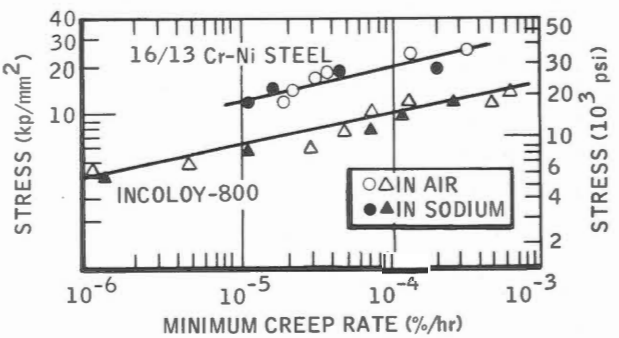

Fig. 2.45 - Minimum creep rates for 16/13 Cr-Ni steel and Incoloy 800 at 700°C (1292°F).

third-stage creep (Fig. 2.48). This figure shows a creep curve for the 16 Cr-13 Ni steel at 700°C (1292°F) under a stress of 18 kp/mm² (25,600 psi). No effect due to sodium is apparent through the second stage, but the effect on

TABLE 2.15 - Chemical Composition of Cr-Ni Steel and Incoloy 800 *†

Material	C	Si	Mn	P	S	Cr	Ni	Mo	V	Nb-Ta
X8CrNiMoVNb (16-13)	0.07	0.40	1.22	0.02	0.007	17.10	13.61	1.30	0.70	0.85
Incoloy 800 (30 Ni-20 Cr)	0.016	0.60	1.35	0.01	0.006	20.6	31.9			

* From H. Böhm and H. Schneider, Time to Failure and Creep Behavior of Austenitic Cr-Ni Steels in the Presence of Sodium, *J. Nucl. Mater.*, *24*: 188-197 (1967).
† Composition is given in weight percent.

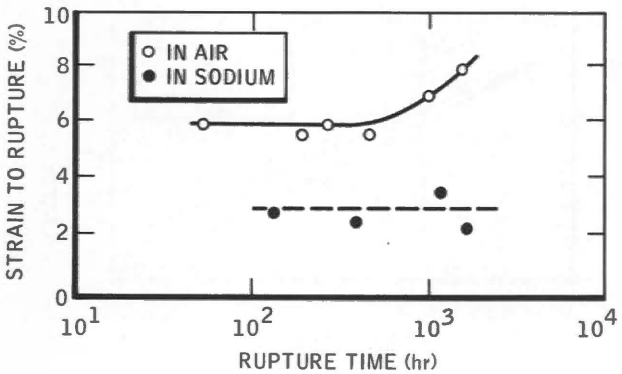

Fig. 2.46 - Strain to rupture for 16/13 Cr-Ni steel at 700°C (1292°F).

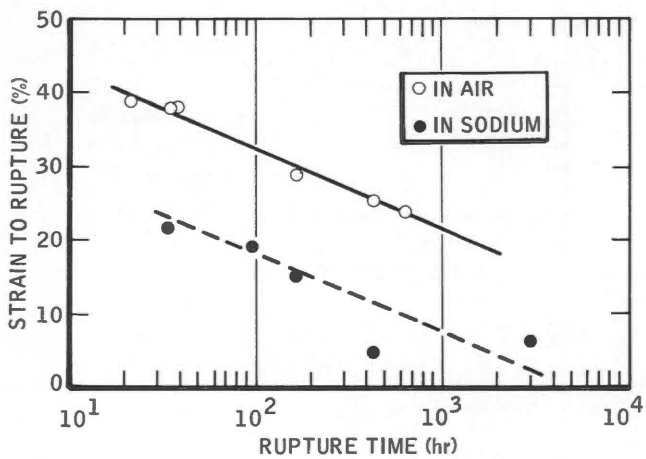

Fig. 2.47 - Strain to rupture for Incoloy 800 at 700°C (1292°F).

tertiary creep is more pronounced. Note that fracture occurred soon after initiation of third-stage creep, thus limiting the strain to rupture. Similar

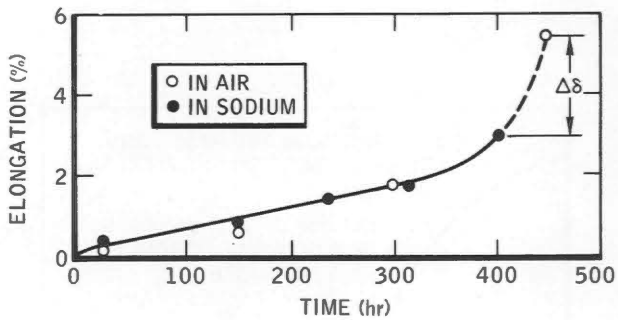

Fig. 2.48 - Creep curves for 16/13 Cr-Ni steel at 18 kp/mm^2 and 700°C (1292°F).

behavior was observed for Incoloy 800, but, in addition, sodium was found to cause an earlier initiation of third-stage creep, which led to a reduction in the time to failure.

The fractures were characterized in subsequent metallurgical examinations where intergranular cracking was found in all failed specimens. Specimens fractured in air contained cracks on both surfaces: those which failed in the sodium environment contained cracks originating only on the surface in contact with sodium.

From these data it is apparent that the rate of crack initiation or propagation (or both) is influenced by the presence of sodium. The crack propagation of the material exposed in air followed a stable rate, but failure of the specimens in sodium was apparently catastrophic, as evidenced by the abbreviated tertiary-creep stage. Calculations showed that the surface energy

in the presence of sodium had been reduced by more than 90%. Thus a reduction in surface energy would reduce the critical crack length for the applied stress, causing rapid propagation soon after crack initiation. For the 16 Cr-13 Ni steel sodium apparently had a greater influence on the crack propagation rate than on the initiation of cracking since the transition from second- to third-stage creep was the same for both the sodium and air environments.

The effect of a liquid metal on the rate of crack propagation through a solid metal was the subject of a theoretical study by Robertson. [18] Based on a dissolution-diffusion mechanism, his calculations showed that high crack velocities, of the order of tens of centimeters per second or higher, were possible. This significant acceleration of crack propagation in sodium has not been actually observed experimentally.

2-2.3 *Chromium-Alloy Steel (2 1/4 Cr-1 Mo)*

The chromium-alloy steels have received attention as candidate materials for sodium and NaK containment at temperatures to 1100°F. Compared with the austenitic stainless steels, these materials derive their potential from such attractive characteristics as their thermal properties, reasonable strength at the operating temperatures under consideration, higher resistance to stress corrosion cracking in strain, and low cost. The designers of large liquid-metal systems find the thermal behavior of these materials particularly attractive because their high thermal conductivity combined with their low thermal expansion coefficient lead to a significant reduction in thermal stresses and fatigue.

At the high operating temperatures anticipated for liquid-metal systems, the allowable design-stresses for chromium-alloy steels have not been defined. The ASME Codes provide allowable stress values for these steels operated in air at elevated temperatures, but design stresses for these materials operating in a liquid-metal environment have not been defined. To offset this lack of design information, an extensive program initiated by the U.S. AEC was carried out at the MSA Research Corp. The bulk of the information presented in this section was derived from this program, the reported results herein pertaining to 2 1/4 Cr-1 Mo steel. Although the mechanical properties generated have not achieved design-allowable status, designers of liquid-metal systems should find them to be valuable guidelines.

(a) *Tensile Properties*

The effects of prolonged sodium exposure on the tensile properties of 2 1/4 Cr-1 Mo steel were investigated at MSAR. [4,19] The actual tensile testing was not performed in sodium. Instead, following their exposure in sodium, the tensile specimens were tested in helium at 75 and 1100°F. The composition of the 0.065-in.-thick sheet specimens used is shown in Table 2.16.

The tensile data for the 36 specimens tested are tabulated in Table 2.17. The samples were preexposed in a variety of environments.

It is apparent that the tensile strength of the material exposed in either helium or sodium has been appreciably reduced. The surprising difference in tensile strength between helium and air could not be explained. Since preexposed specimens were not subsequently tested in air, it is uncertain whether the exposure treatment or the test environment exerts greater influence. However, during the exposure treatment the potential for thermal aging and decarburization would be greater than that expected during short-term tensile testing; hence the exposure treatment is probably the more influential factor. This possibility is supported, in part, by the behavior after

TABLE 2.16 - Chemical Composition of 2 1/4 Cr-1 Mo Steel Tensile Specimens [19] (Heat 51030)

C	Mn	P	S	Si	Cr	Mo
0.097	0.56	0.007	0.022	0.33	2.19	1.01

exposure in high-oxygen (300 ppm) sodium where the greatest overall strength loss occurs.

The results of carbon analysis showed that decarburization occurred during the exposure of 2 1/4 Cr-1 Mo steel to 1100°F sodium, with higher decarburization rates resulting in the presence of higher oxygen. Decarburization was considered to be particularly responsible for the apparent increase in ductility and the observed reduction in hardness (both macro and micro profile).

The effect of sodium on the yield strength follows the same pattern as that on the ultimate tensile strength. Again the reason for the appreciable variations is regarded as inexplicable, although the roles of thermal aging and decarburization are considered most influential.

The data show that the ductility of 2 1/4 Cr-1 Mo is increased as a result of exposure to sodium. In view of the corresponding decrease in strength, this behavior is not considered abnormal. The elevated-temperature ductility in helium after preexposure in helium, however, is comparably high. This leads to uncertainties regarding the role of decarburization since the decarburizing potential of helium is appreciably less than that of sodium.

The factors for safe design for current design applications, as defined in the ASME *Boiler and Pressure Vessel Code*, Section VIII, for power boilers and unfired pressure vessels, include:

1. One-fourth the minimum tensile strength at room temperature.
2. One-fourth the minimum tensile strength at operating temperature.
3. Sixty-two and one-half per cent of the minimum yield strength (0.2% offset) at operating temperature.

The tensile data developed and the design allowables are presented in Figs. 2.49 and 2.50 for comparison with these criteria. The measured tensile values, after application of the appropriate factors, appear comparable to those of the established Code.

(b) *Creep Strength*

Investigators at MSAR [4,19] determined the creep strength for 2 1/4 Cr-1 Mo steel in various environments including sodium containing 30 and 300 ppm oxygen. One heat of steel was used for these determinations; the composition is shown in Table 2.18; the composition defined in the ASTM Standard Specification (SA 182-F22) is included for comparison. The tests were performed at 1100°F, and three specimens were tested at each of the three selected stress levels.

The minimum creep rates developed are shown in Fig. 2.51. These data were extrapolated to 100,000 hr for 1% creep for design applications (Table 2.19).

These design stresses represent a small number of tests performed on one heat of material. In addition, it was suggested that some scatter, though not obvious from the data, could have influenced the creep tests.

(c) *Creep-Rupture Strength*

The creep-rupture strength for 2 1/4 Cr-1 Mo steel was determined by investigators at MSAR [4,19] in tests performed at 1100°F in various environments, including air, helium, and sodium with 30 and 300 ppm oxygen. A series of specimens were preexposed to either helium or sodium for 4000 hr prior to testing. The preexposed specimens were subsequently tested at three different stress levels in each test environment.

As shown in Fig. 2.52, the rupture strength of 2 1/4 Cr-1 Mo steel is higher in tests in air or helium than

TABLE 2.17 - Tensile Properties for 2 1/4 Cr-1 Mo Steel [4]

Exposure environment (1100°F; 4000 hr)	Test environment and temperature*	Tensile strength, psi	Average tensile strength, psi	0.2% Offset yield strength, psi	Average yield strength, psi	Elongation, %	Average elongation, %	Reduction of area, %	Average reduction of area, %
None	Air, RT	68,050		42,500		30			
None	Air, RT	68,350		43,000		31			
None	Air, RT	72,900	70,710	32,450	37,060	29	29		
None	Air, RT	73,400		34,150		29			
None	Air, RT	70,850		33,200		28			
High-oxygen Na†	Helium, RT	61,600		28,600		23		62	
High-oxygen Na	Helium, RT	69,280		25,800		33		65	
High-oxygen Na	Helium, RT	57,910	61,437	24,400	26,950	28	28	60	60
High-oxygen Na	Helium, RT	59,550		28,300		21		55	
High-oxygen Na	Helium, RT	59,760		27,300		28		65	
High-oxygen Na	Helium, RT	60,520		27,300		32		53	
Helium‡	Helium, RT	67,300		29,700		28		57	
Helium‡	Helium, RT	64,500	66,000	26,900	28,766	23	26	65	61
Helium‡	Helium, RT	66,200		29,700		28		62	
None	Air, 1100°F	49,170		25,800		28		64	
None	Air, 1100°F	56,800	55,123	28,800	27,990	32	31	57	61
None	Air, 1100°F	59,400		29,370		32		62	
None	Helium, 1100°F	39,700		25,000		26		63	
None	Helium, 1100°F	38,120	38,547	22,600	23,700	31	33	44	60
None	Helium, 1100°F	37,820		23,500		41		74	
Low-oxygen Na§	Helium, 1100°F	26,620		17,200		45		54	
Low-oxygen Na	Helium, 1100°F	25,250	26,148		17,100	46	45	55	50
Low-oxygen Na	Helium, 1100°F	26,580		16,800		47		41	
Low-oxygen Na	Helium, 1100°F	26,160		17,300		41		50	
Low-oxygen Na	Helium, 1100°F	25,800		16,150		40		65	
Low-oxygen Na	Helium, 1100°F	26,410	27,137	17,950	17,833	42	40	56	59
Low-oxygen Na	Helium, 1100°F	29,200		19,400		38		57	

(Table continues on next page.)

TABLE 2.17 - (Continued)

Exposure environment (1100°F; 4000 hr)	Test environment and temperature*	Tensile strength, psi	Average tensile strength, psi	0.2% Offset yield strength, psi	Average yield strength, psi	Elongation, %	Average elongation, %	Reduction of area, %	Average reduction of area, %
High-oxygen Na	Helium, 1100°F	23,800		18,300		46		64	
High-oxygen Na	Helium, 1100°F	20,620	21,720	14,700	16,000	38	41	63	61
High-oxygen Na	Helium, 1100°F	20,740		15,000		39		57	
High-oxygen Na¶	Helium, 1100°F	23,400		14,500		37		62	
High-oxygen Na¶	Helium, 1100°F	22,300	22,567		13,850	36	37	67	65
High-oxygen Na¶	Helium, 1100°F	22,000		13,200		37		66	
Helium‡	Helium, 1100°F	20,800		13,500		33		81	
Helium‡	Helium, 1100°F	28,200	25,733	18,000	16,767	30	37	73	77
Helium‡	Helium, 1100°F	28,200		18,800		47		76	

* RT is room temperature.
† High-oxygen sodium contained about 300 ppm oxygen.
‡ Exposed simultaneously with high-oxygen sodium exposures.
§ Low-oxygen sodium contained about 10 ppm oxygen.
¶ Not washed prior to testing (all other specimens were washed with alcohol and water before testing).

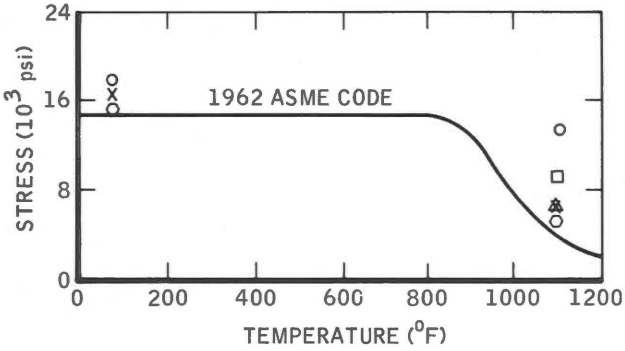

Fig. 2.49 - Tensile strength of 2 1/4 Cr-1 Mo steel exposed for 4000 hr at 1100°F. (Points are 25% of measured tensile values.)

Exposure environment	Test environment and temperature
○ None	Air, RT and 1100°F
□ None	He, 1100°F
△ Low-oxygen (30 ppm) Na	He, 1100°F
⬡ High-oxygen (300 ppm) Na	He, RT and 1100°F
× Helium	He, RT and 1100°F

in tests in sodium. The data for preexposed material are presented in Fig. 2.53. Note that the curves for material preexposed in high-oxygen sodium and tested in either helium or high-oxygen sodium exhibit slopes different from those for other environmental conditions.

In developing the 100,000-hr creep-rupture strength for 2 1/4 Cr-1 Mo steel (Fig. 2.54) investigators assumed that the experimental data would follow a linear extension to the extended life. The measured strength values are compared with Timken extrapolated data and, for further comparison, with the average ASTM 100,000-hr rupture strength at various temperatures. After exposure in the various environments, the strength values for 100,000 hr were highest in air and helium. The lowest rupture strength was obtained on material exposed and

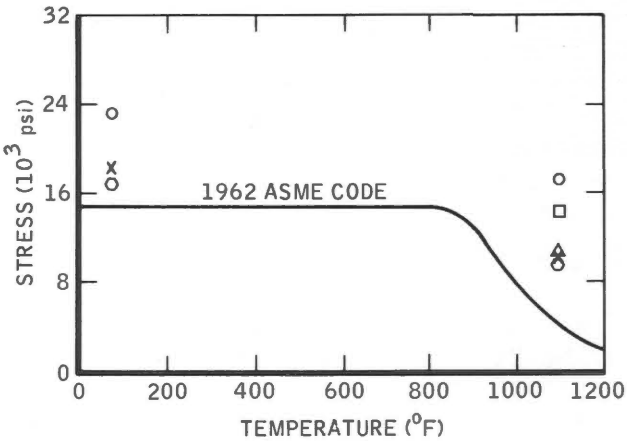

Fig. 2.50 - Yield strength of 2 1/4 Cr-1 Mo steel exposed for 3000 hr at 1100°F. (Points are 62½% of measured yield values.)

Exposure environment	Test environment and temperature
○ None	Air, RT and 1100°F
□ None	He, 1100°F
△ Low-oxygen (30 ppm) Na	He, 1100°F
⬡ High-oxygen (300 ppm) Na	He, RT and 1100°F
× Helium	He, RT and 1100°F

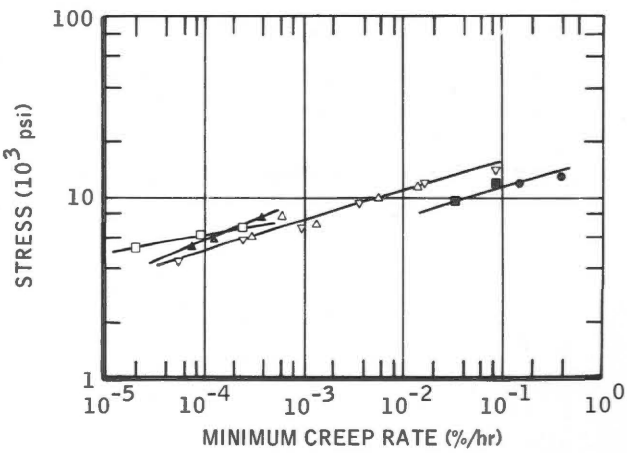

Fig. 2.51 - Minimum creep rate of 2 1/4 Cr-1 Mo steel at 1100°F. (All creep rates over 0.001%/hr were obtained from creep-rupture data.) △, low-oxygen (30 ppm) Na. ▽, high-oxygen (300 ppm) Na. ▲, air. □, helium, ●, exposed in low-oxygen Na. ■, exposed in high-oxygen Na.

TABLE 2.18 - Chemical Composition for 2 1/4 Cr-1 Mo Steel* [19]

Test material	C	Mn	P	S	Si	Cr	Mo
Heat 51030	0.097	0.56	0.007	0.022	0.33	2.19	1.01
ASTM standard specification for SA 182-F22	0.15 max.	0.30 to 0.60	0.04 max.	0.04 max.	0.50 max.	2.0 to 2.5	0.90 to 1.10

* Composition is in weight percent.

TABLE 2.19 - Creep Strength for 2 1/4 Cr-1 Mo Steel in Various Environments [4]

Test environment (1100°F)	Stress to produce 1% creep in 100,000 hr, psi
Helium	5000
Air	3400
Sodium (30 ppm oxygen)	3400
Sodium (300 ppm oxygen)	3400

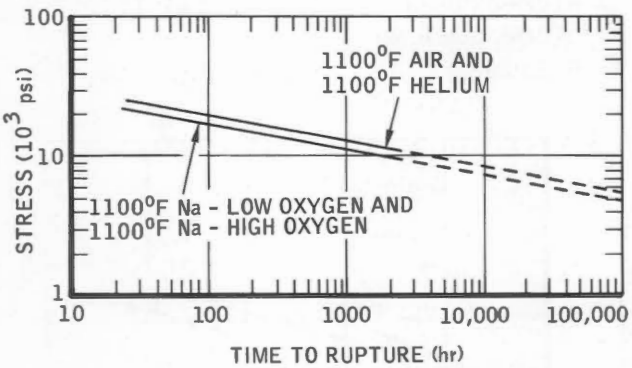

Fig. 2.52 - Creep-rupture strength of 2 1/4 Cr-1 Mo steel before 4000-hr exposure.

tested in a high-oxygen environment. This strength is lower than the "60% average" rupture curve.

Typical curves for 2 1/4 Cr-1 Mo steel are presented in Figs. 2.55 and 2.56. The supporting data were obtained from the semicontinuous elongation values measured during the tests performed in 1100°F, high-oxygen sodium. Unfortunately elongation data were not

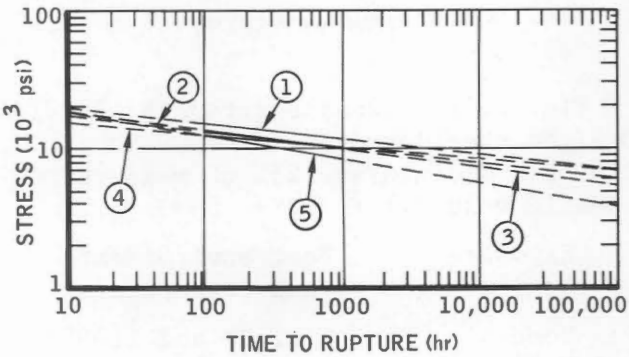

Fig. 2.53 - Creep-rupture strength of 2 1/4 Cr-1 Mo steel tested at 1100°F after 4000-hr exposure at 1100°F (extrapolated).

Curve	Exposure environment	Test environment
1	Helium	Helium
2	Low-oxygen Na	Air
3	Low-oxygen Na	Helium
4	Low-oxygen Na	Low-oxygen Na
5	High-oxygen Na	Helium; high-oxygen Na

taken during the tests conducted in the other environments; thus the data available for developing design information are limited.

From these figures it is apparent that preexposure in high-oxygen sodium had a significant effect, decreasing the time required to produce a given amount of strain. Similarly, there was a decrease in the time to rupture. This reduction in strength was attributed to thermal aging and decarburization.

Table 2.20 presents the stress required to produce varying degrees of strain in 100,000 hr. These values

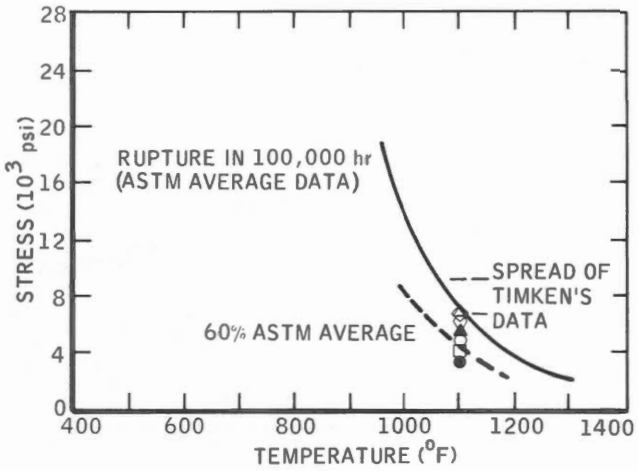

Fig. 2.54 - Creep-rupture strength of 2 1/4 Cr-1 Mo steel (extrapolated to 100,000 hr) tested at 1100°F after 4000-hr exposure at 1100°F.

	Exposure environment	Test environment
○	None	Air and helium
□	None	Low- and high-oxygen Na
△	Helium	Helium
⬡	Low-oxygen Na	Air and helium
▲	Low-oxygen Na	Low-oxygen Na
◇	High-oxygen Na	Helium
●	High-oxygen Na	High-oxygen Na

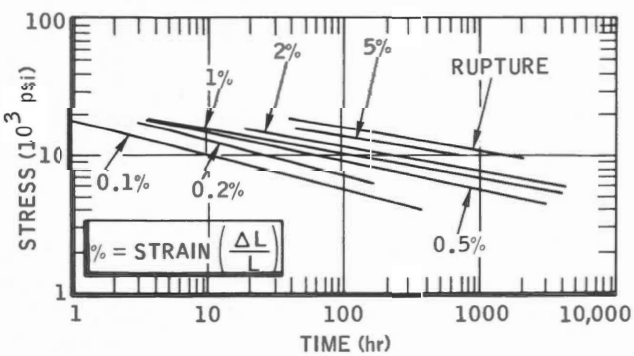

Fig. 2.55 - Creep strength of 2 1/4 Cr-1 Mo steel in high-oxygen sodium at 1100°F.

represent extrapolated data for material in an 1100°F, high-oxygen sodium environment. Care must be exercised in the application of the design information presented.

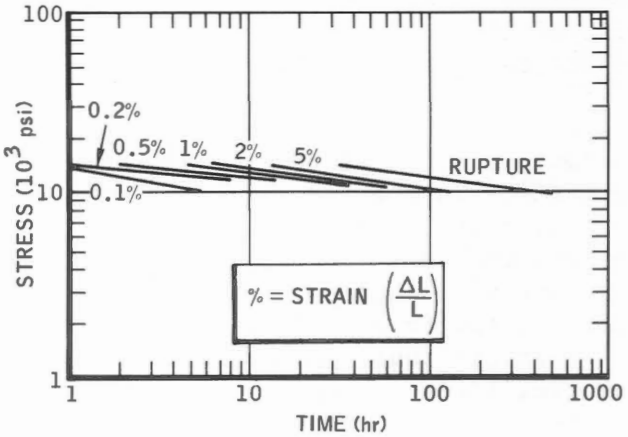

Fig. 2.56 - Creep strength of 2 1/4 Cr-1 Mo steel exposed 4000 hr at 1100°F in high-oxygen (300 ppm) sodium and tested in the same environment.

TABLE 2.20 - Stress for Varying Strain in 100,000 Hr for 2 1/4 Cr-1 Mo Steel in 1100°F High-Oxygen Sodium [4]

Degree of strain, %	Stress required, psi
0.1	910
0.2	1125
0.5	2175
1.0	2950
2.0	3300
5.0	4400
Rupture	4600

(d) *Fatigue Strength*

Fatigue tests for 2 1/4 Cr-1 Mo steel in sodium (these could more accurately be described as cyclic-strain tests) were performed at MSAR [4,19] in three different environments (air, helium, and sodium) at 1100°F. In each environment three specimens were cycled at three different levels of strain, 2.2, 1.0, and 0.56%. The flat specimens were bent over mandrels of the appropriate configuration to produce the

described strain levels at a cyclic rate of 180 cycles/hr.

The test results (Fig. 2.57) show a wide variation in behavior between the two gaseous environments (air and helium), the behavior in helium being superior. In the liquid-metal environment the cyclic-strain behavior was comparable to that in helium. It was concluded that designing on the basis of the fatigue life for this alloy in air would appear safe within the time limits investigated.

The chemical composition of the steel used in this series of tests is described in Table 2.18.

(e) *Impact Strength*

The effect of sodium exposure on the impact strength of 2 1/4 Cr-1 Mo steel was determined by investigators at MSAR. [4,19] Prior to impact testing at room temperature, the test specimens were exposed in either helium, high-carbon (30 to 50 ppm) sodium, or high-oxygen (300 ppm) sodium. The exposure temperature employed for all of the Charpy keyhole specimens (0.394 in. × 0.098 in.) was 1200°F. The experimental results are shown in Fig. 2.58. Regardless of the pretest environment, the impact strength is not reduced below that of the original material. Initially the impact strengths were found to increase for specimens exposed for short time periods. Increased exposure periods had no further effect on the material exposed in high-oxygen sodium. However, the long time exposures in helium and high-carbon sodium produced a reduction in impact strength below that for shorter exposure periods.

(f) *Design Stresses for Sodium Service*

Anstine [16] developed design information relative to the use of 2 1/4 Cr-1 Mo steel in large-scale sodium-cooled reactor systems with design life of 30 years. In the development of the stress curves shown in Fig. 2.59 he considered three principal effects,

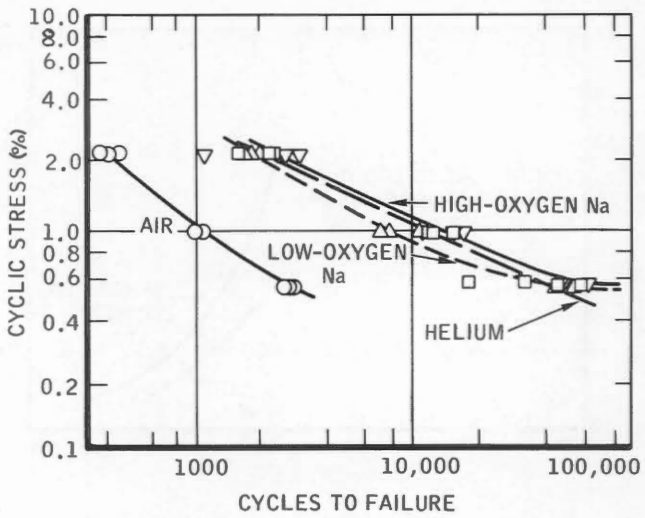

Fig. 2.57 - Fatigue tests of 2 1/4 Cr-1 Mo steel in sodium, air, and helium at 1100°F. Δ, tested in low-oxygen (30 ppm) Na. O, tested in air. □, tested in helium. ∇, tested in high-oxygen (300 ppm) Na.

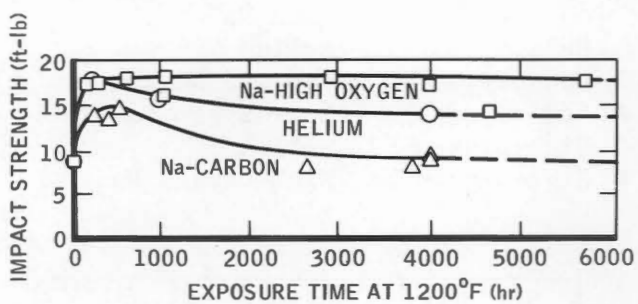

Fig. 2.58 - Charpy keyhole impact test results for 2 1/4 Cr-1 Mo steel.

the nonoxidizing nature of the sodium environment, mass transport, and the extended life. Using reduced stress values caused by the extended life and considering the environmental effects, he employed the following factors in developing the curves: (1) 100% of the average stress to produce 1% creep in 210,000 hr, and (2) 100% of the stress to produce rupture in 210,000 hr. (The standard normalization for creep data is 100,000 hr.)

The curves in Fig. 2.59 include plots

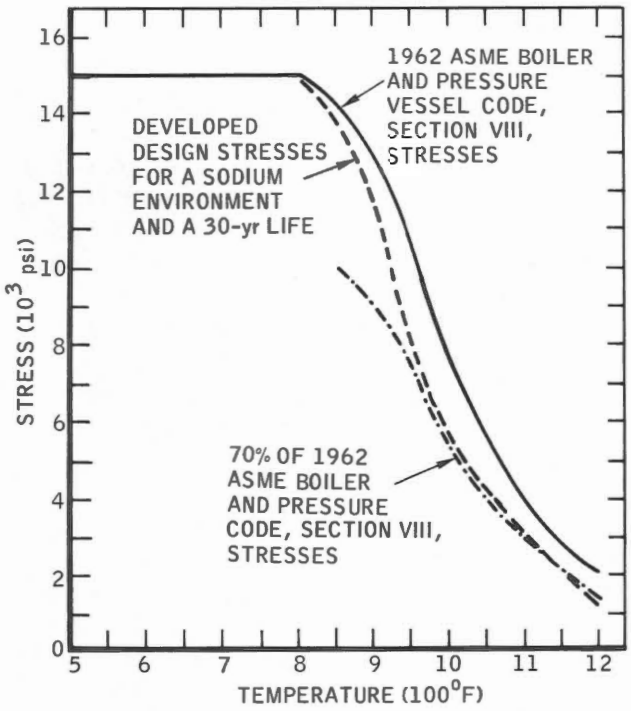

Fig. 2.59 - Developed design stresses for 2 1/4 Cr-1 Mo steel in a sodium environment for a 30-year life.

of

1. Design stresses from Section VIII of the 1962 ASME *Boiler and Pressure Vessel Code*, which was used as a basis for this analysis.
2. Seventy percent of the 1962 ASME *Boiler and Pressure Vessel Code* design stress curve.
3. Design stresses developed by using all the factors for extended life (210,000 hr) and the known environmental effects (nonoxidizing environment, mass transport, and complete decarburization).

The developed design stresses are thought to be conservative, and the validity of this observation is supported by the use of strength values for completely decarburized material. In addition, the design stresses reflect the influence of known corrosion factors.

2-2.4 *Beryllium*

Koenig [20] investigated the effect of sodium on the rupture life of beryllium using three forms of beryllium, hot-pressed, hot-pressed and extruded at 800°F, and hot-pressed and extruded at 2000°F. The data shown in Fig. 2.60 indicate that the extrusion of hot-pressed beryllium produced a degrading effect on the rupture life of the hot-pressed product. Examination of the samples used for stress-rupture testing revealed no evidence of either stress corrosion or significant intergranular penetration after exposure to static sodium at 1000°F.

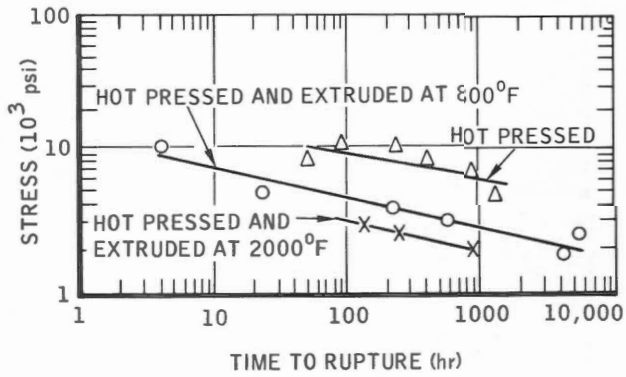

Fig. 2.60 - Rupture life of beryllium in 1000°F sodium.

2-2.5 *Nickel-Base Alloys*

The nickel-base alloys have been considered as alternates for the austenitic stainless steels for service in sodium and NaK, primarily because of the limited strength of the stainless steels above 1200°F. Hence investigations of the nickel-base alloys have been concentrated principally on behavior in liquid metals at temperatures in excess of 1100°F.

(a) *Creep Strength of Inconel*

In preliminary experiments at ORNL [21,22] the creep strength of Inconel in sodium was significantly less than in an argon atmosphere. This difference is evident in Fig. 2.61, which shows strain-time curves for Inconel sheet tested at 1500°F and 4000 psi. The behavior was attributed to the

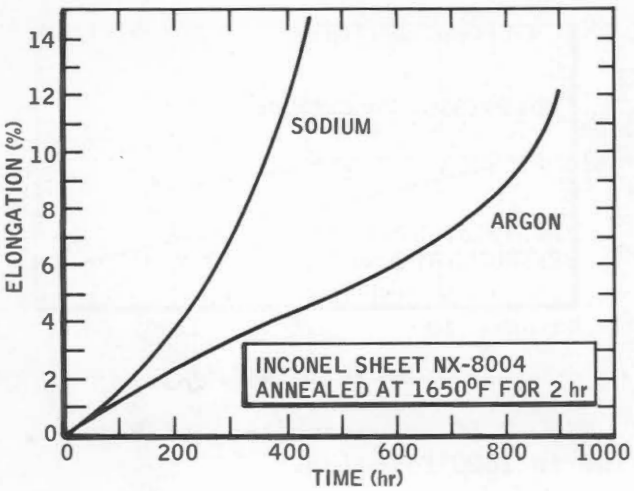

Fig. 2.61 - Comparison of Inconel sheet tested in sodium and argon at 1500°F and 4000 psi.

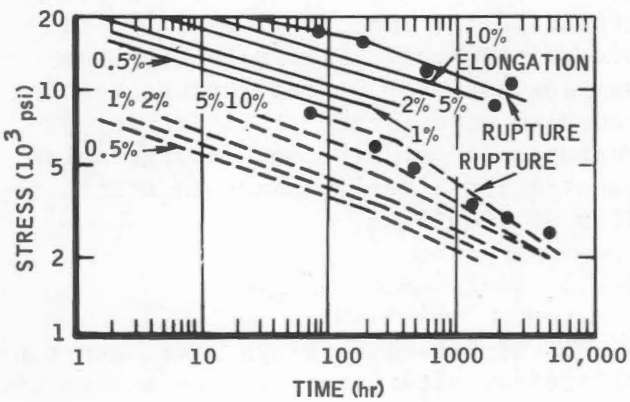

Fig. 2.62 - Stress-rupture properties of Inconel sheet tested in sodium and argon. ●, rupture in argon. —, 300°F. ----, 1500°F.

decarburization of the material exposed in sodium and the oxide contamination (undefined level) of the sodium.

However, in subsequent tests (Fig. 2.62) the variation in strength was not so pronounced. It was suggested that the close agreement of these data can be attributed to the use of high-purity sodium in combination with a system free of contamination. These data indicate that the mechanical properties are relatively unaffected by sodium.

Douglas et al. [23] evaluated the effect of grain size in Inconel sheet by creep- and stress-rupture tests performed in three environments (argon, sodium, and fused salt) at temperatures from 1300 to 1650°F. The fine-grain material was superior at all test temperatures to 1650°F. At this temperature adverse effects due to metallurgical instabilities were observed. In the fused-salt environment, however, the fine-grain Inconel was stronger than the coarse-grain material at 1300°F but weaker at 1500°F and above.

(b) *Creep and Stress Rupture of Other Nickel-Base Alloys*

The longtime strength properties of two nickel-base alloys in sodium were determined by investigators in the USSR. [24] Compositions of the two alloys, EI-437B and EI-869 (see Table 2.21), are similar to those of Nimonic 80A and Inconel X, respectively.

These tests were performed on uniaxially loaded tubular specimens 11 mm in diameter, 0.5 mm in wall thickness, and 50 mm long. The capped specimens contained sodium with an oxygen content below 0.02 wt.%. Identical specimens were tested in air for control.

Figure 2.63 shows the stress-rupture data at 750°C (1382°F) for EI-869 and 800°C (1472°F) for EI-437B. The effect of the test environment on the EI-869 alloy was negligible, but the stress-rupture life of EI-437B was significantly decreased by the presence of sodium. The influence of sodium became more pronounced with increasing time, as indicated by the slopes of the in-air and in-sodium curves shown in the figure. For the EI-437B alloy the stress to rupture in 1000 hours was reduced from 10.5 kg/mm^2 in air to 7 kg/mm^2 in sodium; extrapolation to 10,000 hr indicate a still greater divergence.

The creep rates for both alloys in sodium and in air are shown in Fig. 2.64. These data show that the creep rate for EI-869 was unaffected by

TABLE 2.21 - Composition of USSR Nickel-Base Alloys EI-437B and EI-869*

Alloy	Nominal composition, wt.%								
	C	Cr	Ti	Al	B	Cb	Fe	Ni	Other
EI-437B	0.06 max.	20.5	2.5	0.75	0.006			Balance	
EI-869	0.08 max.	15.5	1.7	1.2	0.005 max.	1.3	3 max.	Balance	0.005 Zn max.

* Data from Ref. 25.

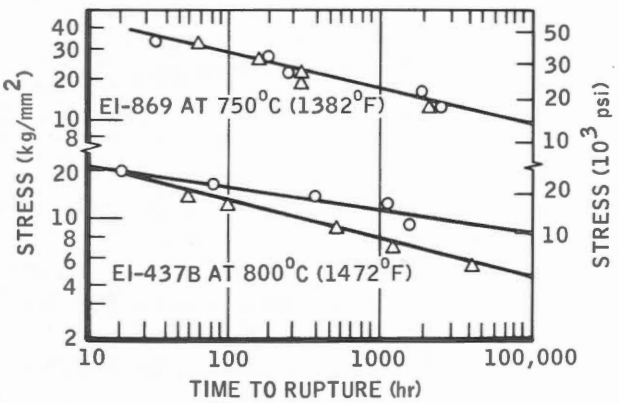

Fig. 2.63 - Variation of time to rupture with applied stress in sodium, Δ, and in air, O.

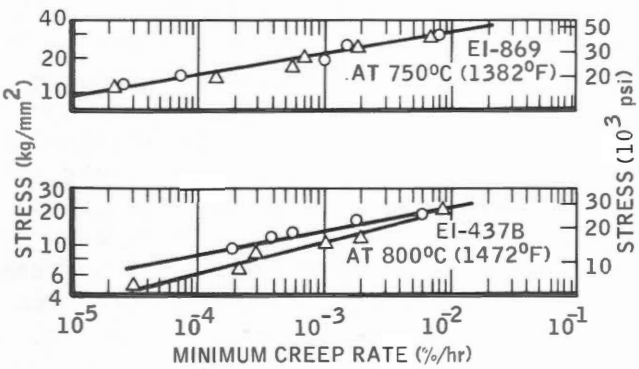

Fig. 2.64 - Variation of minimum creep rate with stress in sodium, Δ, and in air, O.

sodium and the creep rate for EI-437B increases in sodium. In addition, the average first- and third-stage creep rates were found to be similarly

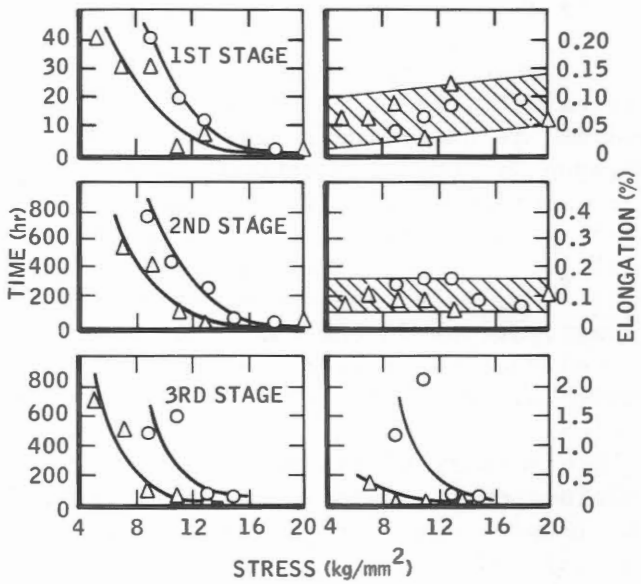

Fig. 2.65 - Variation of duration of individual stages of creep and relative elongation with stress for alloy EI-437B at 800°C (1472°F) in sodium, Δ, and in air, O.

affected. The influence of sodium on the creep process is clearly evident in Fig. 2.65, which shows the variation of time and elongation vs. stress for the three stages of creep. Obviously the duration of all three periods is reduced in a sodium environment, but only the elongation in the third stage is affected by the liquid-metal environment. These changes increase with decreasing stress except that at high stresses no significant difference is observed.

Subsequent metallographic examination of the test specimens revealed no

changes in the microstructures, including the surfaces in direct contact with the liquid metal. Thus the influence of sodium on alloy EI-437B was not corrosion induced; nor did sodium diffusion affect the mechanical behavior of the alloy, since spectrographic analysis showed no diffusion penetration of sodium. The influence of sodium on the long-term strength of EI-437B was concluded to be caused by the adsorptive effect of sodium.

(c) *Stress Rupture of Nickel-Base-Alloy Weld Metal*

The creep- and stress-rupture properties of nickel-alloy weld metal in sodium are under investigation at the Argonne National Laboratory (ANL). [26] The material initially selected for testing in sodium was Nimonic 80A (21 wt.% Cr, 1 wt.% Al, 2.5 wt.% Ti, balance Ni). This selection was based on the investigations in the USSR [24] which showed that the long-term tensile properties of this alloy were degraded by sodium.

Preliminary stress-rupture results obtained on 0.125-in.-diameter tensile specimens exposed in sodium (<20 ppm oxygen) and in vacuum tend to confirm the behavior observed by Dykova and Nikitin. [24] A Nimonic 80A specimen stressed to 46.2 kg/mm^2 ruptured prematurely after 225 hr in 650°C (1202°F) sodium, whereas a control specimen exposed in vacuum at 650°C (1202°F) had not ruptured after 575 hr.

This investigation will continue and will include the evaluation of welded Incoloy 800 in sodium.

2-2.6 *Tantalum (Creep)*

During the development studies for the Los Alamos Molten Plutonium Reactor Experiment (LAMPRE) reactors, tantalum was considered for some applications. In these reactor systems molten plutonium-alloy fuel was to be contained in tantalum capsules positioned within the small sodium-cooled core. Tantalum was considered a potential material for construction of the core where a peak sodium temperature of 1200°F was anticipated. In support of this program, investigators at Battelle Memorial Institute (BMI) [27] evaluated the performance of tantalum in flowing sodium.

Experiments to determine the creep behavior of arc-cast tantalum sheet were performed in forced-convection-flow sodium loops of 316 stainless steel, with additional accessories for application of tensile loads and for monitoring specimen extension. In the 1200°F, flowing sodium, the oxygen content was maintained at low levels (<10 ppm) by means of a zirconium-foil hot trap. Control testing to develop baseline data was performed in a helium atmosphere. Conventional sheet-type annealed test specimens identical to those used for testing in sodium were used in the inert-gas environment. The creep tests for both environments were terminated prior to the transition from second- to third-stage creep.

The creep data developed during this investigation (Table 2.22) indicate that low-oxygen sodium has no significant effect on the creep behavior of tantalum at 1200°F. Note that the minimum creep rates at the 26,000-psi stress level are not significantly different for the two test media, sodium and helium. Posttest examination of the exposed specimens did not reveal any unusual corrosion effects; this indicates that tantalum was susceptible to stress-aggravated corrosion. Since the creep tests were discontinued prior to the initiation of third-stage creep, no predictions regarding the effect of sodium on crack-initiation or crack-propagation rates can be made.

2-2.7 *Vanadium Alloys (Creep)*

A series of vanadium-base alloys was evaluated for potential fuel-cladding application in sodium-cooled fast-reactor systems. These alloys were designed for improved corrosion resistance

TABLE 2.22 - Creep Behavior of Arc-Cast Tantalum* Exposed to 1200°F Sodium [27]

Stress, psi	Length of test, hr	Time to reach indicated percentage deformation, hr				Total deformation, %	Minimum creep rate, %/hr
		0.1%	0.2%	0.5%	1.0%		
Standard In-Sodium Exposures†							
20,000‡	258	2	5			0.40	<0.0001
22,000	1100	4	240			0.43	<0.0001
26,000	1090	<1	3	12	264	1.74	0.0007
26,000	934	<1	1.8	7	18	2.00	0.0004
26,000‡	998	<1	<1	4	130	4.36§	0.0012
Special In-Sodium Exposure¶							
26,000	1200	<1	<1	<1	7	2.25	0.0003
Control Exposures in Helium							
26,000	600	<1	14	300		0.64	0.0003**
26,000	547	††	525			0.20	0.0006**
		††	††	††	<1	1.80	0.0005

*A control specimen from this group had the following analysis and hardness:

Analysis		Hardness	
Oxygen	236 ppm	Gauge section	∿195 VHN
Hydrogen	0.8 ppm	Grip section	∿170 VHN
Nitrogen	230 ppm		
Carbon	40 ppm		

† Load was applied at start of exposure.

‡ The fluid-temperature cycle in these experiments was 160°F; in other sodium tests it was 80°F.

§ Part of this relatively high total deformation was incurred during startup periods following power-failure shutdowns.

¶ Load was applied after 455 hr to reduce oxygen content of the test piece prior to initial loading.

** These creep data were obtained by reading internal extensometers attached directly to the gauge section of the specimens; all other creep data were obtained by reading externally mounted dial gauges.

†† These deformations were surpassed during initial loading.

and elevated-temperature strength in sodium at temperatures from 1150 to 1400°F. To evaluate the performance of these alloys, investigators at ANL [28,29] performed creep tests on sheet material exposed in flowing sodium at 1200°F. The mechanical tests were subsequently performed in vacuum on the preexposed test specimens.

In the initial evaluation of the creep strength of vanadium alloys in sodium, emphasis was placed on a binary composition (V-20 wt.% Ti). The sheet material employed was 0.4 to 1.5 mm thick and in the recrystallized condition after a 900°C (1652°F) anneal. For the preliminary creep tests [28] 0.5-mm-thick specimens were preexposed

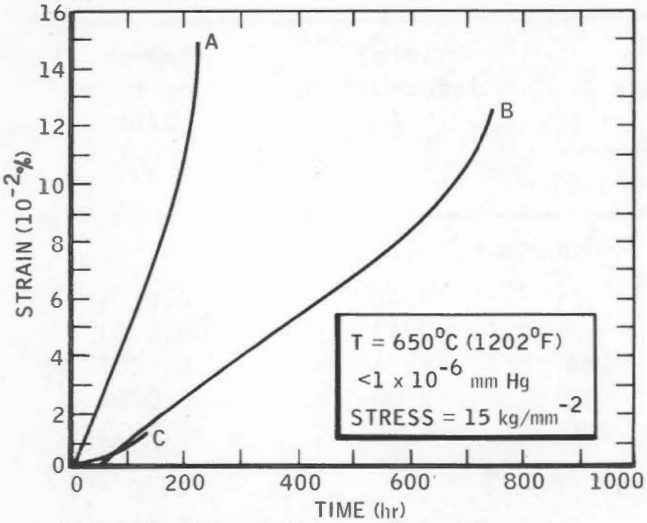

Fig. 2.66 - Effect of sodium exposure on creep strength of V-20 wt.% Ti. Curve A shows the creep of a specimen preexposed to sodium for 7 days; curve B shows the creep of a control specimen heated in vacuum at 650°C (1202°F) before loading; and curve C shows the effect of material thickness in specimens 1.5 mm thick tested in vacuum.

in 650°C (1202°F), flowing sodium (15 cm/sec). Vacuum-distillation analyses performed on two sodium samples indicated oxygen levels of 18 and 20 ppm. Some of the early test results at 650°C are shown in Fig. 2.66. The effect of the variables indicates that the seven-day exposure to sodium apparently decreases the creep resistance of the binary vanadium alloy V-20 wt.% Ti.

A series of uniaxial creep and hardness tests [29] were performed on the vanadium alloy V-20 wt.% Ti under conditions similar to those employed previously. In addition, the effects of sodium purity on preloaded sheet specimens 0.4 mm thick, exposed in 650°C (1202°F) sodium containing either 20 ppm or less than 10 ppm oxygen, were investigated. Following the exposure in sodium, uniaxial creep tests were performed in vacuum ($\sim 10^{-7}$ mm Hg) at 650°C at a stress level of 15 kg/mm^2.

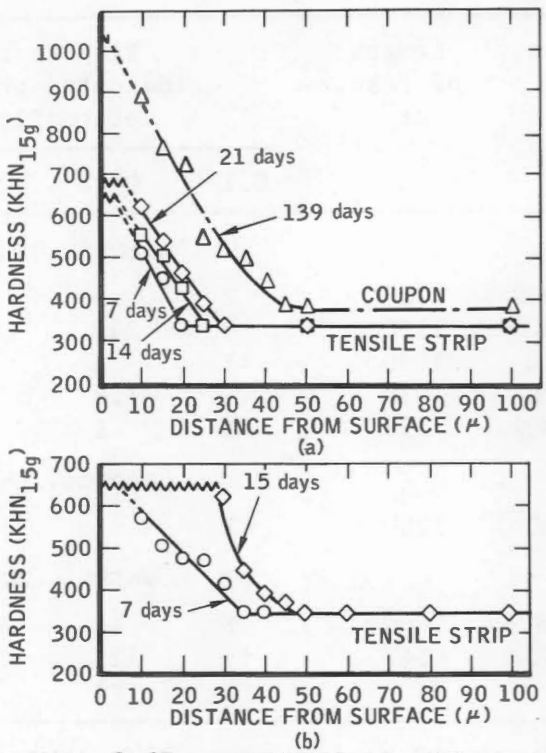

Fig. 2.67 - Hardness profiles of V-20 wt.% Ti after exposure to sodium at 650°C (1202°F). (a) Exposed in sodium with <10 ppm O_2; coupon, stainless-steel flowing loop; tensile strip, stainless-steel static autoclave; ∿∿, depth of adherent oxide layer. (b) Exposed in sodium with ∿20 ppm O_2; stainless steel flowing loop; ∿∿, depth of adherent oxide layer.

Hardness measurements on the sodium-exposed specimens showed a significant increase in surface hardness. Figure 2.67 shows the hardness profiles obtained. The hardened layer extends to a greater depth in the material exposed to the lower-purity sodium (20 ppm oxygen). A relation between the depth of the hardened layer and the duration of sodium exposure was developed from the hardness data (Fig. 2.68).

In view of the presence of the layers on the creep specimens, the creep behavior was reevaluated. Figure 2.69 indicates that the creep behavior of the vanadium alloy is influenced by the

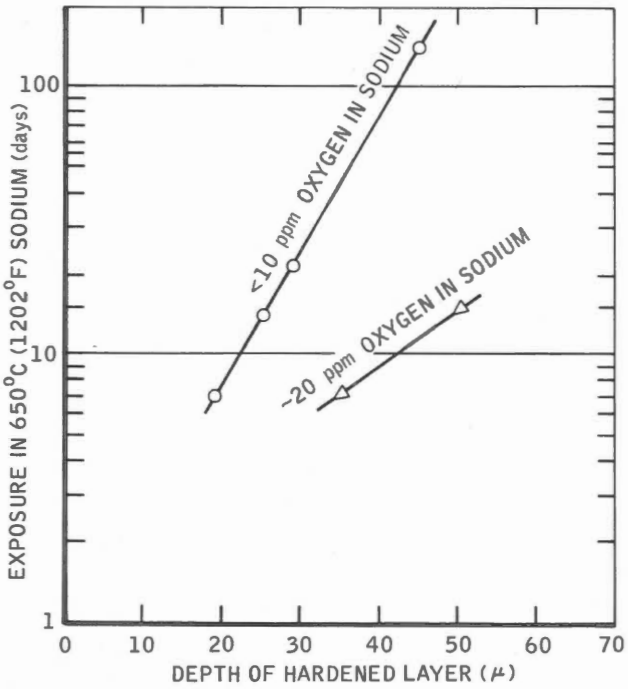

Fig. 2.68 - Depth of hardened layers vs. sodium exposure for V-20 wt.% Ti.

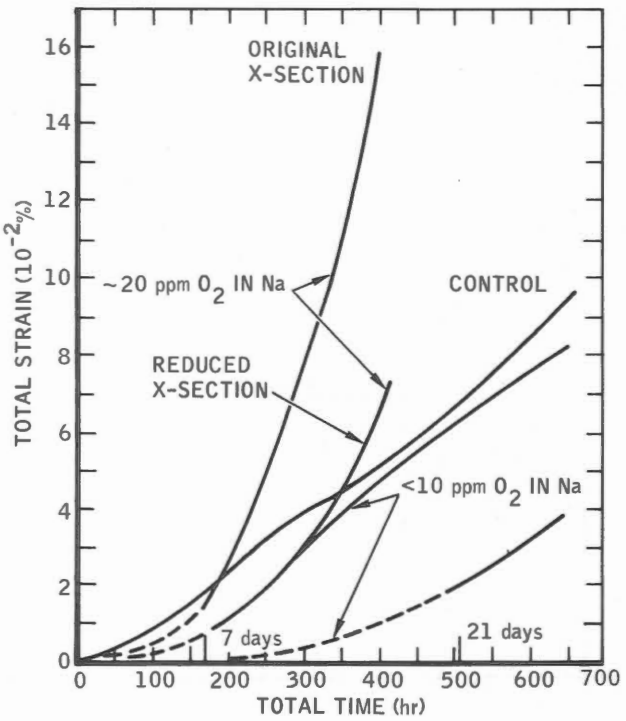

Fig. 2.69 - Creep of V-20 wt.% Ti; 0.4-mm sheet specimen annealed at 900°C (1650°F) and tested at 650°C (1202°F) and a stress of 15 kg/mm^2. ----, initial atmosphere (liquid sodium). ——, final atmosphere [vacuum (<1 × 10^{-6} mm Hg)].

presence of a surface layer. The strain-time curves indicate that the creep properties are degraded by the presence of the hardened layer. A calculated strain-time curve was incorporated into Fig. 2.69 to compensate for the 20% reduction in metal cross section due to sodium corrosion. Although the strain is lower for the reduced cross section, it is still higher than that for the vacuum-exposed control specimen. Note, however, that the strain rates for specimens exposed in the higher-purity sodium (<10 ppm oxygen) are comparable to the control strain rate. Thus the creep resistance of the vanadium alloy V-20 wt.% Ti preexposed in sodium appears to depend primarily on sodium purity and the development of a surface reaction layer.

2-2.8 *Zirconium and Zirconium Alloys*

The principal attractive feature of zirconium for application in thermal nuclear reactors is its low absorption cross section for thermal neutrons; however, its elevated-temperature strength is unacceptably low. In an effort to overcome the inadequate strength at elevated temperatures, particularly in the operating regime of sodium-cooled systems, a variety of alloys have been developed for investigation.

Baldwin and Weisinger [30] evaluated the stress-rupture behavior in sodium of a group of zirconium alloys, including Zr-1.7 wt.% Al, and Zr-4.2 wt.% Sn. These alloys were qualified for stress-rupture testing on the basis of their yield strength at 932°F; the yield strengths were comparable to the yield strength of 347 stainless steel. Bar-type specimens were dead-weight loaded in tension at 1000°F in a static sodium system. The test results for two of the

TABLE 2.23 - Rupture Strength of Two Zirconium Alloys in 1000°F Sodium [30]

Alloy	Stress, 1000 psi	Time, hr	Elongation, %	Reduction of area, %
Zr-1.7 wt.% Al	40	34	30.7	57.5
	33	81	31.7	78.4
	25	877	27.3	71.5
Zr-4.2 wt.% Sn	25	32	33.4	60
	21	90	45.1	96.7
	16	983	50.5	82.7

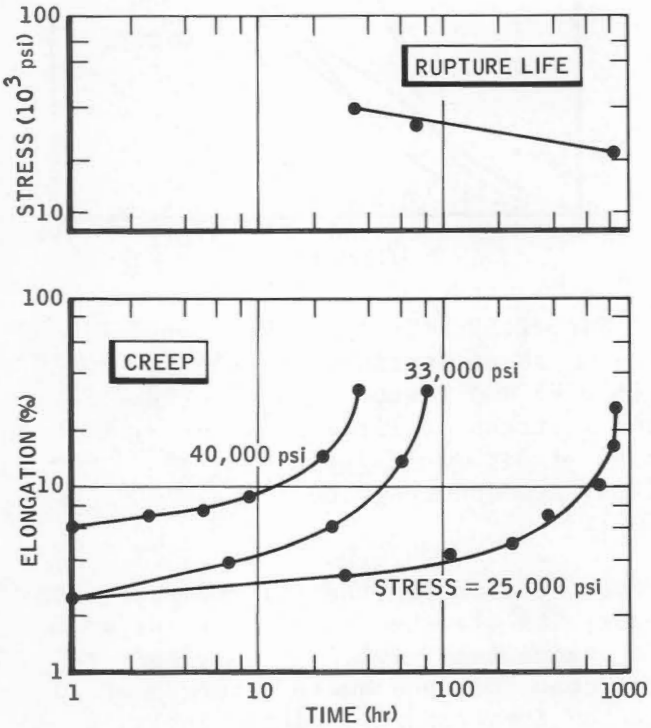

Fig. 2.70 - Creep and rupture life of Zr-Al alloy in static sodium at 1000°F.

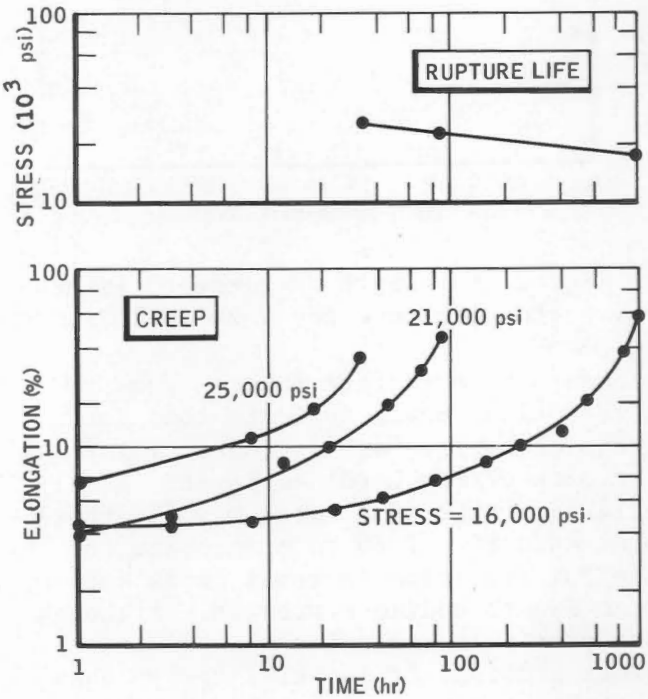

Fig. 2.71 - Creep and rupture life of Zr-Sn alloy in static sodium at 1000°F.

eight alloys evaluated are presented in Table 2.23 and in Figs. 2.70 and 2.71. In addition, the short-time tensile properties in argon at 932°F are given in Table 2.24. The weight changes experienced during the stress-rupture tests are shown in Table 2.25.

Although the alloys exhibited short-time tensile properties comparable to the tensile property of 347 stainless steel, their stress-rupture strengths were appreciably lower; however, all the alloys possessed strength in excess of that typical for crystal-bar zirconium.

2-2.9 *Plastics*

Under various conditions of time and temperature, operating liquid-metal

TABLE 2.24 - Short-Time Tensile Properties of Two Zirconium Alloys in 932°F Argon [30]

Alloy	Ultimate strength, psi	Yield strength, psi	Elongation, % in 1 in.	Reduction in area, %
Zr-1.7 wt.% Al	47,000	37,000	33	39
Zr-4.2 wt.% Sn	30,400	22,600	36	47

TABLE 2.25 - Weight Changes of Two Zirconium Alloys in 1000°F Sodium [30]

Alloy	Weight change, gm	Time in sodium, hr	Corrosion rate, mg/dm^2/month
Zr-1.7 wt.% Al	+0.0077	96	+706.0
	+0.0060	144	+368.5
	+0.0107	432	+219.2
	+0.0081	984	+ 72.8
Zr-4.2 wt.% Sn	+0.0052	∿114	+403.7
	+0.0080	∿981	+ 72.1

systems, whether dynamic or static, require suitable gaskets and seals. At lower operating temperatures plastics may be used, particularly for the containment of liquid-metal vapors in combination with cover gases. The performance and compatibility of several plastics and elastomers have been evaluated. [31]

Following exposure (75 to 250 hr) in sodium at 250 and 350°F, the plastics were examined for exposure-induced variations in weight, hardness, tensile strength, elongation, and flexibility. The materials evaluated, including their polymer chemical composition, and their original properties, are partially listed in Table 2.26. The experimental results for materials exposed in sodium are given in Table 2.27. The value for each property of interest represents an average of three specimens tested.

The final evaluation of material performance and compatibility was based on (1) weight loss of material, (2) formation of powdery deposits on the material surface, and (3) degradation of material properties. Because minimized contamination of the liquid metal was of major concern, the first two criteria were given greater consideration in the final evaluation. The materials that demonstrated the most acceptable behavior in sodium at 250°F for 9 days were

Kel-F 3700 Buna-N

and in sodium at 350°F for 7 days

Neoprene Buna-N

In view of the behavior of plastics in liquid metals, it was postulated that alkali-metal-induced deterioration can be caused by reaction (1) along the polymer chain, (2) at the chain cross linkages, (3) with various additives (fillers, curing agents, plasticizers, etc.) or combinations of these. Examples of the first reaction mechanism were exhibited by Kel-F, in which a portion of the polyhalogenated carbon chain was reduced to elemental carbon. However, the rate of attack in 250°F sodium was considered slow. Cross-linkage attack was apparently evident in the sulfur-vulcanized polymers such as Buna-N, Buna-S, butyl rubber, and natural rubber. The most likely site of attack in these materials would be the

TABLE 2.26 - Plastic and Elastomer Specimens [31]

Material	Polymer chemical	Original properties*			
		Instantaneous Shore A hardness	15-sec Shore A hardness	Tensile strength, psi	Elongation, %
Buna-N	Butadiene-acrylonitrile copolymer	68	62	3180	547
Buna-S	Butadiene-styrene copolymer	72	67	1540	390
Butyl rubber	Isobutylene-isoprene copolymer	67	57	1100	517
Natural rubber	Polyisoprene	39	39	†	†
Neoprene	Polychloroisoprene	74	72	1610	443
Silicone rubber, 371	Methyl vinyl siloxane polymer	74	74	1010	97
Silicone rubber, 751	Methyl vinyl siloxane polymer	48	48	390	153
Kel-F 5500	Chlorotrifluoroethylene-vinylidene fluoride copolymer	66	64	2120	400
Kel-F 3700	Chlorotrifluoroethylene-vinylidene fluoride copolymer	68	66	1880	300

* As measured in this investigation.
† Did not rupture at maximum grip separation.

disulphide cross-linkage. Since organic esters react with sodium, butyl rubber, which contains an ester (paraplex plasticizer), is typical of the third type of reaction mechanism. This reaction was considered to be the primary cause of the weight loss exhibited by the butyl rubber. Thus elastomers containing reactive additives (e.g., organic esters) must be used with caution for sodium service.

2-3 CORROSION

Liquid-metal corrosion depends primarily on the rate of solution of the containment material and the solubility limit of the dissolved material or alloying elements in the liquid metal. However, complications are introduced by a number of factors that affect these solubility rates. Temperature and concentration gradients and impurities strongly influence the corrosive nature of a particular system. Several types of corrosive attack between liquid and solid metals have been observed - simple solution and alloying, impurity reaction, and temperature- and concentration-dependent mass transfer.

The primary purpose of research on corrosion of materials in liquid-metal environments has been to discover a means by which rates of material loss and of material weakening can be safely predicted. This goal has been elusive because of the many variables involved and the difficulty of separating their effects in a test system. Materials subject to rapid dissolution or chemical attack (e.g., aluminum, copper, silver, gold) have long been eliminated

TABLE 2.27 - Experimental Results of Immersing Several Plastics and Elastomers in Sodium [31]

Material	Change in original properties, %					180° Bend flexibility*	Change in appearance*
	Weight	Instantaneous Shore A hardness	15-sec Shore A hardness (cold flow)	Tensile strength	Percent elongation		
Specimens Immersed in Sodium at 250°F for 219 Hr							
Buna-N	-0.70	3	6	-12	-41	Y	M
Buna-S	-0.50	8	11	-57	-69	N	M,Br
Butyl rubber	-3.15	11	16	-18	-11	Y	M,g
Natural rubber	-2.88	-13	-13			Y	D,M,P
Neoprene	-2.19	11	13	- 9	-59	Y	G
Silicone rubber,371	-0.72	3	3	-70	-67	N	M
Silicone rubber,751	-2.13	17	17	-65	-65	S	M
Kel-F 5500	-0.06	- 1	- 3			Y	D,P,Bl
Kel-F 3700	-0.22	- 1	5	- 9	0	Y	D,M,Bl
Specimens Immersed in Sodium at 350°F for 168 Hr							
Buna-N	-3.13	16	24	-59	-75	Y	M
Buna-S	-0.96	18	25	-71	-94	N	M,P,Br
Butyl rubber	-6.98	15	25	-12	-39	Y	M,P,Br
Natural rubber	-4.98	-10	-10			Y	D,M
Neoprene	-2.69	11	13	- 9	-59	Y	G
Silicone rubber,371	-6.99	7	7	-67	-57	N	B,M
Silicone rubber,751	-7.81	31	31	-58	-66	S	B

* Abbreviations are:

B	Bleached surface	G	Appearance good	P	Powdery surface deposits
Bl	Black	g	Gray	S	Surface cracks on bending 180° or less
Br	Brown	M	Mottled surface	Y	Bends 180° without cracking
D	Darkened surface	N	Cracks in two on bending 180° or less		

from consideration for structural use in sodium or NaK. Materials most commonly considered below 1200 to 1300°F are the refractory metals, steels, and high-temperature alloys. Above 1300°F the refractory metals are considered to be superior (See Secs. 2-3.5, 2-3.6, and 2-3.7.)

Progress has been made in identifying the variables, however, and models have been proposed for qualitatively predicting corrosion rates. A state of the art has not been reached where corrosion rates can be predicted quantitatively for new systems. Therefore the objectives of this section are:

1. To present the variables and explain their influence.
2. To present test data and discuss their meaning.

2-3.1 *Solution Erosion* [32]

One of the mechanisms of corrosion in sodium or NaK is solution erosion (or simple solution), which progresses in two steps (see Fig. 2.72):

1. Dissolution of solid material into the liquid-metal film.
2. Diffusion of the solute through the liquid away from the surface of the solid material.*

The dissolution step can be described as the breaking of the metallic bonds holding the surface atom to its neighbors in the solid metal and the simultaneous formation of metallic bonds between the solute and solvent atoms. Little is known about the mechanism of this exchange; however, it is recognized to be highly sensitive to surface imperfections in the solid metal, as the surface bond energies are related to crystal imperfections. Thus selective grain-boundary attack and dislocation etching are factors controlling the dissolution rate of a solid, especially in the absence of impurities in the grain boundaries.

In pure systems Step 2, diffusion, is generally the rate-controlling process. This is indicated by sensitivity of solution erosion to the flow rate of the liquid metal. The driving force for diffusion through the solvent layer

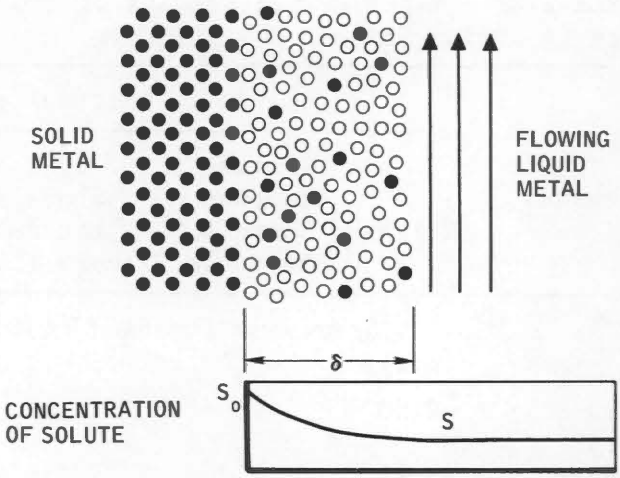

Fig. 2.72 - Dissolution of a solid metal into a liquid metal.

is therefore the diffusion gradient - the difference between the solubility at the dissolution temperature, S_0, and the solution concentration in the bulk solvent, S, divided by the thickness of the solvent layer, δ,

$$\text{Diffusion driving force} = \frac{S_0 - S}{\delta} .$$

(a) *Variables Affecting Solution Erosion* [32-37]

Velocity affects the rate of solution erosion by varying the thickness of the solvent layer, δ. Rates of both dissolution and diffusion vary with temperature. In a loop where a saturated solution is flowing from a hot leg to a cold leg, part of the solute may be deposited from solution in the cold leg, creating a renewed capacity for dissolution in the hot leg. The rate of precipitation also varies with velocity, which determines the time of exposure to the lower temperature and the turbulence level. Deposition of a compound or metal film from chemical reactions or alloying tendencies may inhibit or increase both solution erosion and chemical corrosion. In a dissimilar metal system the more soluble (or

* Diffusion of metallic elements through the solid may also be an important variable. [See Sec. 2-3.1(b).]

active) metal will migrate to and a film will be deposited on the less soluble (or noble) metal. This film may be tightly adherent and impervious to solution erosion and chemical action, or it may be nonadherent and easily removed by flow action. In either case the corrosion of the more active metal will be increased.

(b) *Leaching* [38]

The process of elemental leaching has been described as a combination of dissolution and chemical reaction mechanisms which removes alloy constituents at various rates. Observations made on 316 stainless-steel samples in 1200°F pumped sodium loops verified this process. Analysis of sample surfaces by electron microprobe showed Fe-Cr-Ni ratios that differed notably from the original compositions (Fig. 2.73). This change in surface composition produces a visible surface layer. If the layer continues to develop and the depletion of alloy constituents persists beyond a specific minimum threshold level, the layer becomes ferritic.

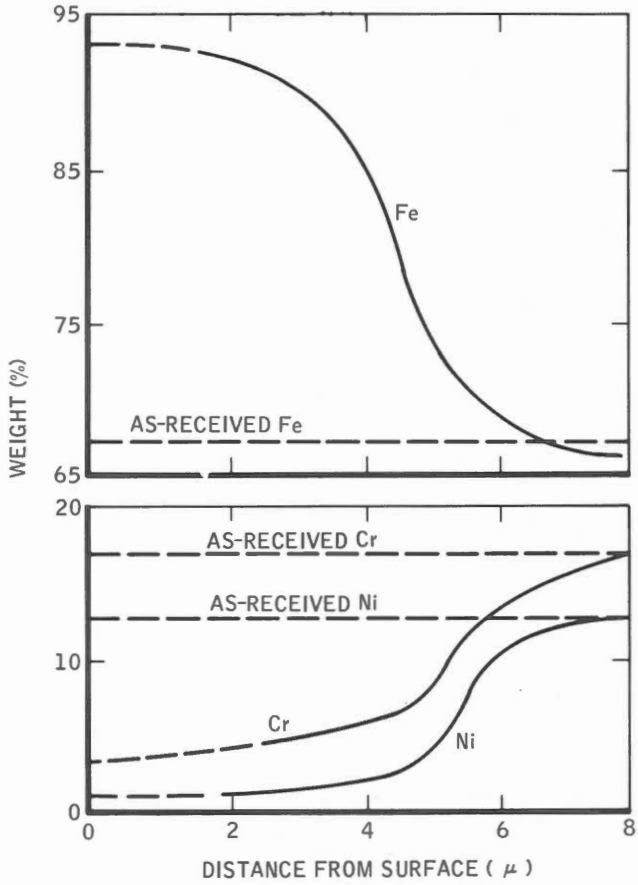

Fig. 2.73 - Typical compositional change in 316 stainless steel associated with elemental leaching in sodium. [38]

2-3.2 *Chemical Corrosion*

Chemical corrosion is the result of a chemical reaction between the solid metal and an impurity in the sodium.

(a) *Oxygen*

The chemical reaction between oxygen in sodium and most of the more insoluble metals, with the exception of nickel and possibly cobalt-base alloys, is the controlling corrosion mechanism.

(b) *Nitrogen*

Nitrogen, which is an interstitial impurity in most metals, including steels, appears to play some role in corrosion in sodium and NaK, but no plausible mechanisms have been advanced. Nitrogen is thought to be nearly insoluble in sodium; yet the nitriding of steel surfaces completely submerged in liquid sodium has been observed. [39] One possible explanation is that calcium, which is present as an impurity in sodium, acted as a carrier in the form of Ca_3N_2 for the nitrogen in these tests. In other instances entrained nitrogen gas in the NaK was the source for the nitrogen, as, e.g., in the nitriding of niobium fuel cladding at Dounreay. [33]

(c) *Hydrogen*

Hydrogen in sodium will readily react with refractory metals such as zirconium, niobium, and tantalum. It is also suspected, but not proved, that hydrogen plays an interacting role in oxygen- and carbon-promoted corrosion processes. Evidence of hydrogen-oxygen

and hydrogen-carbon interactions in sodium systems has been reported. [40,41]

Examination of corrosion products from iron-base-alloy systems has confirmed the existence of the double oxide $FeO(Na_2O)_2$, a compound suspected of being involved in some way in the mass transfer of iron. [42] The effects of oxygen on the corrosion rate of 316 stainless steel can be seen in Table 2.28 and Fig. 2.74.

Tyzack [43,44] suggested that there are three classes of metals which, when exposed to sodium at low activity, exhibit different types of behavior relative to the stability of their oxides compared to sodium oxide. The first class is exemplified by nickel, whose oxide is readily reduced by sodium and which forms no stable ternary compounds with oxygen and sodium when the latter is at unit activity. Thus, after initial removal of any residual oxide coating, nickel corrosion proceeds at a rate suggesting solution-erosion control. This rate is not sensitive to changes in oxygen concentration within the range of 0 to 30 ppm.

The second class of metals is exemplified by zirconium, whose oxide has a much greater standard free energy of formation than sodium oxide at unit or lower activity in sodium. A tightly adherent oxide film is formed through which oxygen must diffuse to reach zirconium metal. As the film thickness grows, the corrosion rate is reduced in a predictable fashion. [For a more detailed discussion, see Sec. 2-3.6(a).] If the film is nonadherent and subject to removal by flow action, the corrosion rate will be more rapid, depending on the oxygen concentration, and unpredictable, depending on the adherence and physical properties of the film.

The third class of metals includes those having oxides of comparable thermodynamic stability to sodium oxide at the temperature of interest and forming ternary metal-sodium oxides in sodium of low oxide content. These

TABLE 2.28 - Effects of Oxygen on Corrosion Rate of 316 Stainless Steel [33]

Temperature, °F	Corrosion rate, mils/year	
	At 10 to 15 ppm oxygen	At 45 to 50 ppm oxygen
1100	1/4	1
1200	1/2	2
1300	1	4

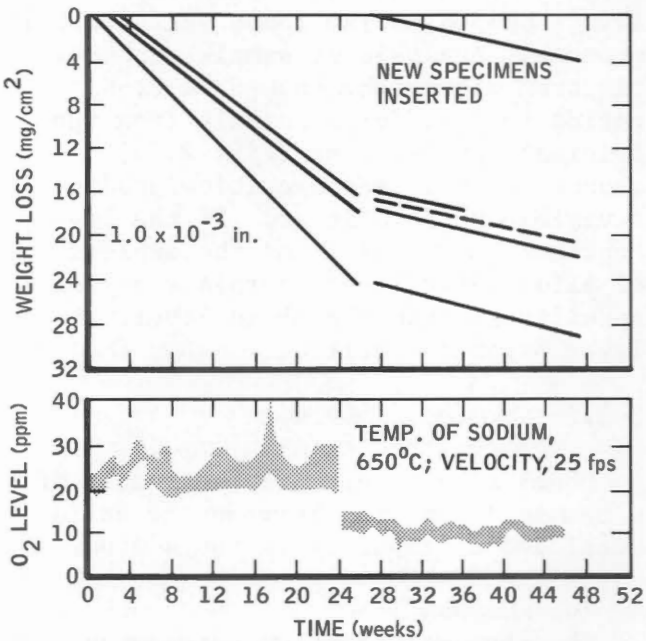

Fig. 2.74 - Effect of changing the oxygen level of liquid sodium on the rate of metal loss of 316 stainless steel specimens. [42]

metals generally show a number of oxides of varying valency, and the precise oxide formed during corrosion in sodium may depend critically on the oxidation potential of the sodium. This type of behavior is exemplified by niobium, which is highly sensitive to oxygen concentration and velocity. [For a detailed discussion of the corrosion of

niobium in sodium, see Sec. 2-3.6(c).]

2-3.3 *Intergranular Penetration*

Intergranular penetration is an attack on the grain boundaries of a metal, through a dissolution or chemical process, by impurities in the sodium or NaK or in deposited corrosion products. (For more detailed information, see the listing of the metal of interest in this section.)

2-3.4 *Summary and Design Criteria*

Solution attack and impurity reactions are treated separately in the foregoing discussion, but the presence of one impurity in sodium alters the solubility or solution kinetics for other impurities and other materials. Thus, in practice, solution attack and impurity reactions are interdependent.

Rowland, Plumlee, and Young, [45] in a 20,000-hr test, observed that the corrosion rate seemed to decrease linearly with distance from the hot zone of the test loop independent of temperature. This effect, termed "downstream effect," lends support to the theory that corrosion of metals in sodium is self-quenching. That is, in a nonisothermal loop corrosion depends on the increasing or the decreasing concentration of some corrosion product (as yet unidentified) in solution. It can easily be postulated then that the rate of corrosion in the hot leg of a nonisothermal loop may be controlled at steady state by the rate at which dissolved corrosion products are plated or precipitated out of a supersaturated solution in the cold leg or cold trap.

Because of the many variables involved and the lack of knowledge concerning their behavior, the only definite recommendations that can be made to the designer are as follows:

1. Oxygen concentration in the sodium or NaK should be maintained at the lowest possible level.
2. Proposed structural metals should be investigated for sensitivity to impurities other than oxygen, e.g., hydrogen and nitrogen, as well as for potential interaction.
3. Piping and equipment should be sized so that a certain amount of corrosion or deposition of corrosion products can be tolerated. Amounts cannot be calculated with precision, but an insight can be gained from the following sections dealing with specific metals.

Most of the metals discussed in Secs. 2-3.5 to 2-3.8 have been subjected to extensive testing in sodium. If he observes the three precautions listed, the designer will find that all these metals will exhibit tolerable corrosion rates and are suitable for long-term use in sodium at the temperatures noted.

2-3.5 *Steel*

Much has been published on the compatibility of sodium and NaK with stainless steel. The common chromium and austenitic stainless steels (304, 316, and 347) can be used in sodium and NaK flow systems up to 1000°F with virtually unlimited life if the oxygen and carbon contents of the liquids are low. The austenitic grades are preferred at high temperatures for strength considerations. Static-test data are many and varied; typical results for the austenitic grades are (1) negligible weight change at 930°F, <-0.1 mg/cm^2/month, (2) slight weight gain at 1100°F, 0.1 mg/cm^2/month, and (3) substantial weight gain at 1830°F, 40 mg/cm^2/month. Maximum service temperatures in static systems approach 1500 to 1600°F. In dynamic systems austenitic steels are good construction materials.

The presence of oxygen and carbon seriously affects service performance. High oxygen levels greatly increase the corrosion rate. These contents are controlled to low levels by hot or cold traps.

(a) *Corrosion and Deposition Rates*

A recent series of tests [45,46] of

steels in sodium showed that both austenitic and ferritic steels corrode at much the same rates after long-term exposure to flowing sodium at 1100 to 1300°F. The materials tested were 316 stainless steel, 2 1/4 Cr-1 Mo, and 5 Cr-1/2 Mo-1/2 Ti. Nickel and chromium were readily leached from a fresh surface, but after initial depletion further solution into the sodium was limited by the diffusion of these constituents through the ferritic boundary layer. After approximately 2000 hr an equilibrium was reached in which the ferritic surface was removed by the sodium at the same rate as the nickel and chromium were diffusing to the surface. [45] The corrosion and deposition rates experienced in these tests are given in Figs. 2.75 to 2.78.

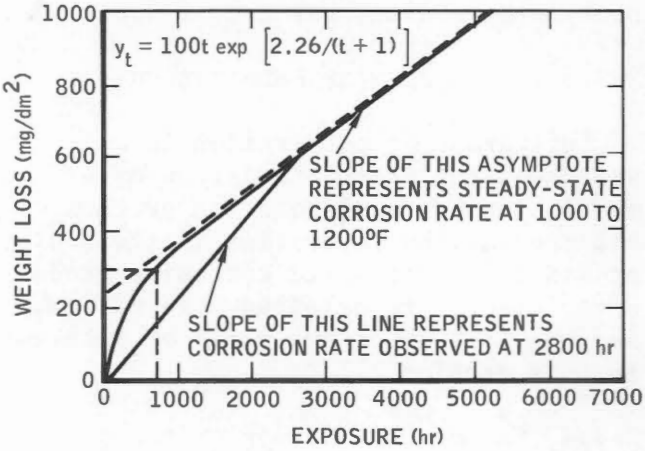

Fig. 2.75 - Hot-leg weight loss vs. time. [46]

Figure 2.79 is a general representation of corrosion rates of austenitic stainless steels in flowing sodium. The data are based on converting the weight change of thin samples to loss rates in mils per year and thus do not include intergranular penetration damage that could affect the mechanical properties more severely if present. The data show the effect of temperature on corrosion rate and indicate that at 1200°F a maximum surface recession rate of about 2 mils/year can be expected in reactor-grade sodium at 20 to 30 ft/sec. Other data not plotted [47,48] indicate that at a 5 ft/sec flow rate the corrosion rate is well below 0.1 mil/year.

For information on carbon transfer, which also may be a problem in steels, see Sec. 2-5. (For further discussion of mass transfer of steels, see Sec. 2-4.)

(b) *Intergranular Penetration*

Steels are susceptible to intergranular penetration under certain conditions. Rapid oxidation of grain boundaries has been observed where oxide concentrations were 5000 ppm or more or where oxygen-rich precipitates were deposited. Chemical activity at grain boundaries is accelerated by the presence of a stress.

Intergranular penetrations discovered in loops designed to study mass-transfer phenomena are believed to have occurred in the following way. During periods of shutdown for loop repair, the loop interior was exposed to air, which oxidized the residual sodium on the pipe walls. The loop was then preheated before introduction of sodium; this caused those regions in which intergranular penetrations were observed to be exposed to thermal stresses, as well as to Na_2O and NaOH. The products of oxidation were then washed away by the introduction of sodium to the loop. It was concluded that the total intergranular penetration (0.007 in.) occurred in short increments during loop preheat after each maintenance shutdown. [38]

(c) *Sensitization*

Intergranular penetration can be accelerated in austenitic stainless steels because of a phenomenon known as sensitization. [49] Stainless steel becomes sensitized when chromium and carbon combine to form chromium carbide, which is subsequently precipitated in the grain boundaries. The metal immediately adjacent to the grain boundaries becomes depleted in chromium and consequently

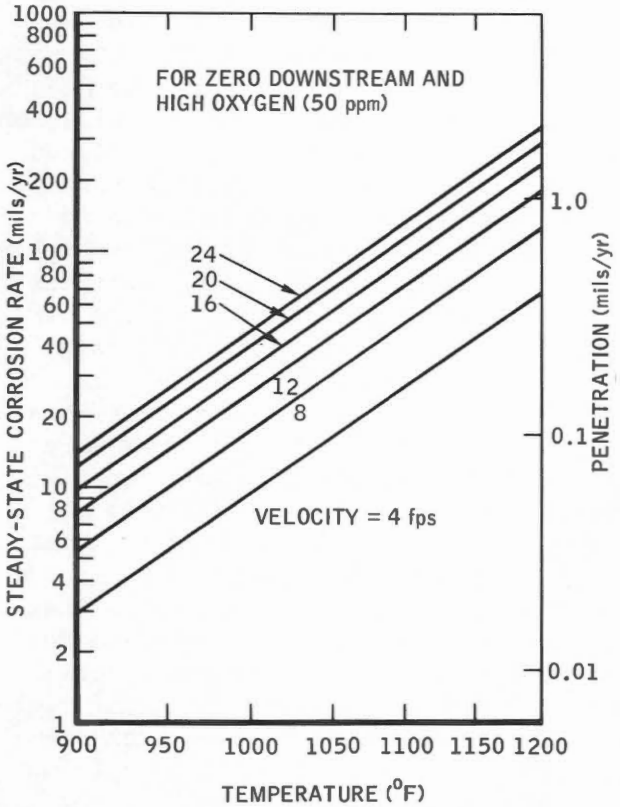

Fig. 2.76 - Hot-leg corrosion-rate-prediction curves. [46] For low oxygen (12 ppm), multiply results by 0.19; at D diameters downstream, multiply results by correction factor F.

D	F
50	0.71
130	0.42
270	0.16
350	0.09

more susceptible to oxygen attack. Sensitization is a function of the activity and distribution of carbon and chromium, as well as a temperature cycle (between 800 and 1500°F) favoring the precipitation of chromium carbides. Some evidence suggests that sensitization occurs more readily in carbon-contaminated sodium than in other media, [50] probably because of exposure to dissolved carbon. When free carbon has been exhausted, chromium will diffuse to the chromium-impoverished zones, and resistance to oxygen attack will be restored.

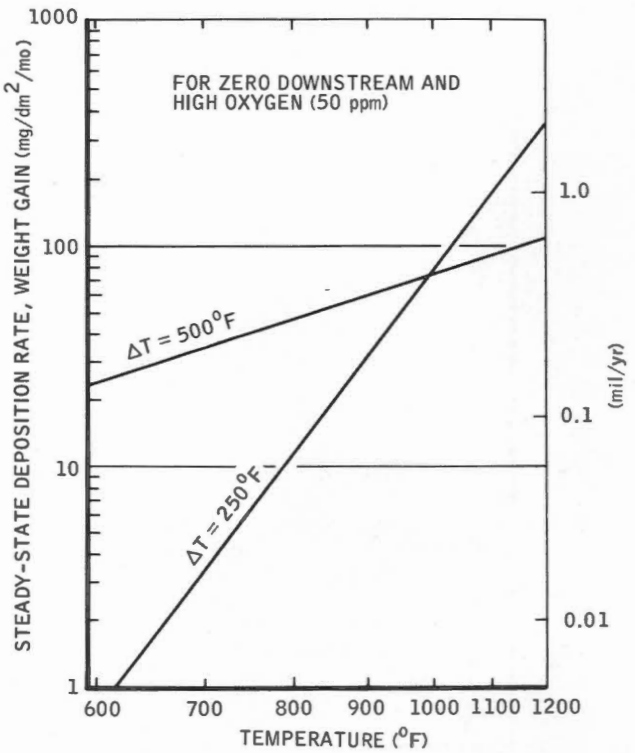

Fig. 2.77 - Cold-leg deposition-rate-prediction curves. [46] For low oxygen (12 ppm), multiply results by 0.26; at D diameters downstream, multiply results by correction factor F.

D	F
50	0.85
130	0.66

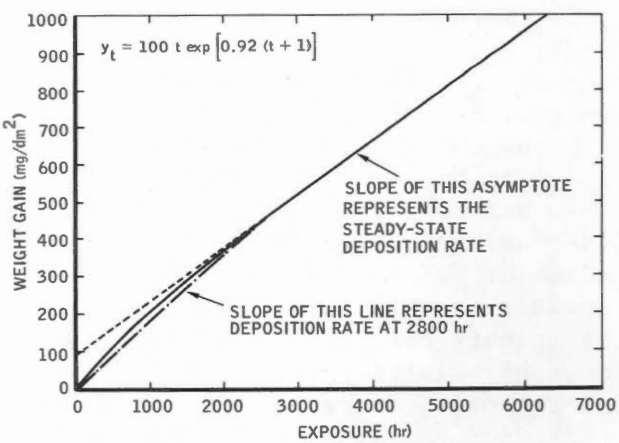

Fig. 2.78 - Cold-leg weight gain vs. time. [46]

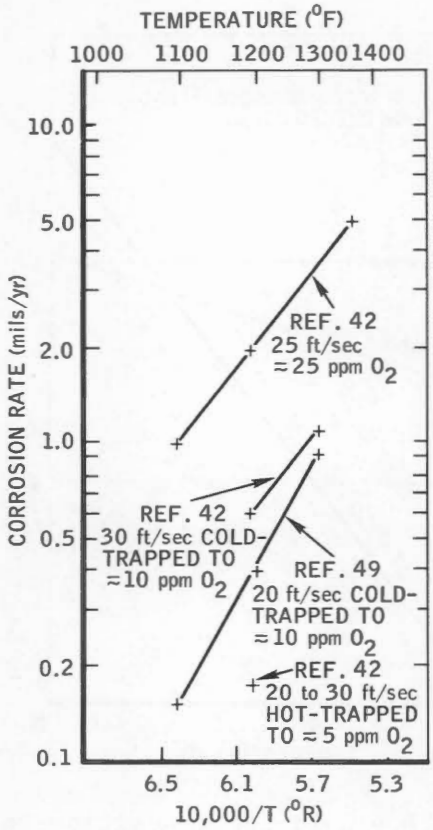

Fig. 2.79 - Corrosion rates of stainless steels in sodium.

2-3.6 *Refractory and Other Metals*

The metals Zr, Nb (Cb), Be, V, Ta, Mo, U, Th, W, and Ti are recommended over steels for use in sodium or NaK at temperatures of 1200°F and above if a very low concentration of oxygen in the sodium or NaK can be maintained.

In general, refractory metals are less susceptible to solution erosion in sodium or NaK than steels and more susceptible to oxidation. Oxidation is the primary corrosion mechanism. The rates of oxidation vary with the chemical potential energy, ionic diffusion rates, and the behavior of the resultant oxide coating. In sodium or NaK, zirconium, titanium, and thorium develop an insoluble adherent oxide coating. Therefore for these metals the rate of corrosion is eventually controlled by the diffusion of oxygen through the oxide coating. A mathematical model similar to those developed for oxidation of materials in air has been developed [see Sec. 2-3.6(a)]. Beryllium forms a stable insoluble oxide coating in sodium, but the adherency of BeO is highly uncertain, being subject to variations in sodium velocity. Oxides of the other refractory metals (except molybdenum and tungsten) are either soluble or nonadherent, and these all require that oxygen levels in the sodium or NaK be maintained at a very low concentration. Oxygen also can be interstitially absorbed by most of the refractory metals, causing severe embrittlement. A more powerful means of removing oxygen than cold trapping alone is recommended for sodium systems containing refractory metals. One of the more efficient techniques used to remove oxides from sodium is gettering. A metal that forms a stable oxide in sodium at high temperature is placed in the system with no function other than to permanently remove oxygen from solution. Zirconium is frequently used as a getter (Fig. 2.80). Oxygen reacts chemically with zirconium to form an adherent oxide layer. At the same time oxygen is taken directly into the zirconium lattice to form a dilute O-Zr alloy. [51] Many alloys of zirconium have been investigated for their effectiveness as oxygen getters. The most effective zirconium-alloy getter was found to be Zr-13 at.% Ti. It is estimated that a hot trap using Zr-13 at.% Ti alloy can provide the same overall oxygen-removal rate and total oxygen capacity as an unalloyed zirconium hot trap 10 times larger. [52]

(a) *Zirconium*

(1) *General Compatibility.* The exposure of zirconium to sodium or NaK containing 10 ppm or more of oxygen is normally characterized by weight gains that are indicative of a strong

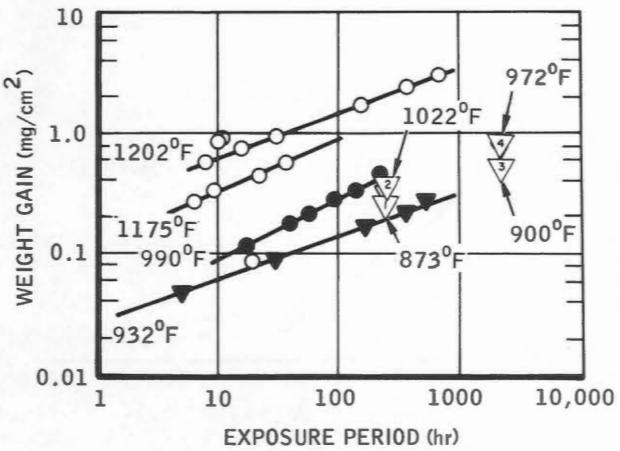

Fig. 2.80 - Oxidation of zirconium in sodium and NaK-78 as a function of time and temperature. For NaK-78: ▽[1], average of values from 0.08 to 0.62 mg/cm , flowing. ▽[2], average of values from 0.08 to 0.46 mg/cm², flowing. ▽[3], average of values from 0.46 to 0.56 mg/cm² flowing. ▽[4], average of values from 0.59 to 0.73 mg/cm², flowing. (Values are from Ref. 1.) For sodium: ●, static (Ref. 55). ○, static (Ref. 54). ▽, static (Ref. 51).

---

tendency* for surface-film formation by the reaction

$$Zr + 2Na_2O \rightarrow ZrO_2 + 4Na \qquad (2.2)$$

The oxide films are adherent and sufficiently protective to inhibit or slow down the reaction as time passes and the ZrO_2 product film builds up. The behavior can be described by the equation [53]

$$\Delta W^n = kt \qquad (2.3)$$

where

ΔW = weight gain
t = time
k = rate constant
n = reciprocal of slope of the linear log (ΔW) vs. log t line [a value of n greater than 1 (see the following test data) indicates a decreasing reaction rate with time]

Weight losses of zirconium in sodium were recorded for low-temperature and low-oxygen exposures. Under these special conditions removal of metal by dissolution was apparently not limited by a protective oxide film.

Oxidation-rate constants for zirconium alloys in sodium can differ from these for unalloyed zirconium by a factor of nearly 10. However, even the highest of these is substantially lower than rates reported in the literature for comparable exposures of zirconium to steam or to gases such as oxygen, air, or CO_2. The basic solid-state oxidation mechanism is suspected to be the same for exposure to both liquid sodium and to the oxidizing gases (O_2, H_2O, CO_2, and air). In this mechanism the rate of reaction is controlled by the diffusion of oxygen ions, O^{2-}, through the zirconium dioxide product layer into the base metal (anion diffusion). However, the large difference in oxidation rates is probably due to the additional diffusion effect occurring in the sodium exposure, in which the oxygen must undergo not only solid-state diffusion but also diffusion from the bulk stream to the zirconium dioxide surface.

(2) *Test Results.* [*51, 54, 55*] Data showing the oxidation of zirconium, weight gain per square centimeter, in sodium and NaK-78 as a function of time and temperature are presented in Fig. 2.80. Data showing the oxidation of zirconium as a function of temperature after 350 hr exposure are presented in Fig. 2.81.

Values cited [51] for n in the equation $\Delta W^n = kt$ for sodium exposure include (1) for arc-melted material, 2.80 to 2.87 at 930°F and 2.72 to 2.82 at 1110°F, (2) for arc-melted material preheated by cold-working or charging with

---

* For example, at 1000°K (1340°F) the free energy of formation of ZrO_2 by means of Eq. 2.2 is calculated to be -85,050 cal/mole; this indicates the tendency of metallic zirconium to reduce Na_2O.

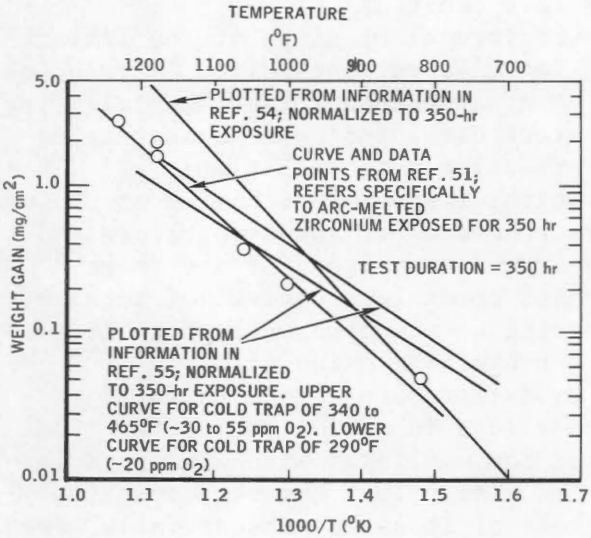

Fig. 2.81 - Oxidation of zirconium in sodium as a function of temperature.

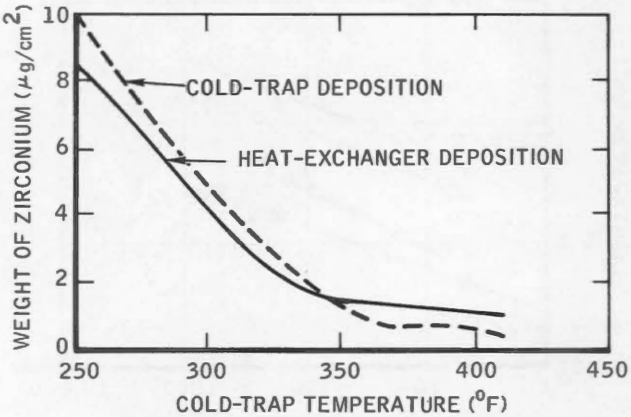

Fig. 2.82 - Dissolution effect of zirconium in cold-trapped sodium system.

approximately 50 ppm N_2, 2.35, and (3) for carbon-melted material, 2.00 to 2.05.

At 740°F, zirconium inserts in NaK-78 containing approximately 15 ppm oxygen lost about 0.2 mg/cm² during 500-hr exposures.

At 1020°F, sparse cold-trap and heat-exchanger deposits were observed in a sodium system where the oxygen level was maintained at 15 to 25 ppm by cold trapping. [51] This dissolution effect for zirconium is illustrated in Fig. 2.82.

The oxidation of zirconium and several zirconium alloys was investigated [54] in a static sodium system with oxygen concentration of approximately 10 ppm. The materials investigated are those listed in Table 2.29. Their rate constants, based on $n = 2$, are presented in Fig. 2.83.

Table 2.29 presents values of $1/n$, and Table 2.30 presents further data from tests by Davis and Draycott. [51]

(b) *Beryllium [53]*

(1) *General Compatibility.* Beryllium, like zirconium, forms a much more stable oxide than does sodium. [For example, at 1000°K (1338°F) the free energy of formation of BeO by means of Eq. 2.4 is calculated to be ΔF = 54,150 cal/mole.]

Consequently BeO will form at the surface of a beryllium sample exposed to sodium containing oxygen according to the reaction

$$Be + Na_2O \rightarrow BeO + 2Na \qquad (2.4)$$

Unlike ZrO_2 films, the BeO films are nonadherent and readily dislodged by flowing sodium; thus they are nonprotective. Control of the oxidation rate has been realized through reductions of the oxygen level in Be-Na systems by gettering with either calcium or thorium, both of which form more stable oxides than does beryllium.

Another corrosion characteristic is the migration of beryllium to other materials in a composite system. There is no evidence that this occurs to any significant degree at temperatures of 1000°F or lower, but it has been noted repeatedly at 1200°F and higher. [56-59]

Figure 2.84 presents values from 250-hr experiments. [60] A dependency on temperature and flow rate is apparent; the latter points to increased spalling of nonadherent oxide with increased NaK flow velocity.

Calcium and thorium were added to sodium in other experiments [60,61] with the following results:

1. Calcium was effective in reducing

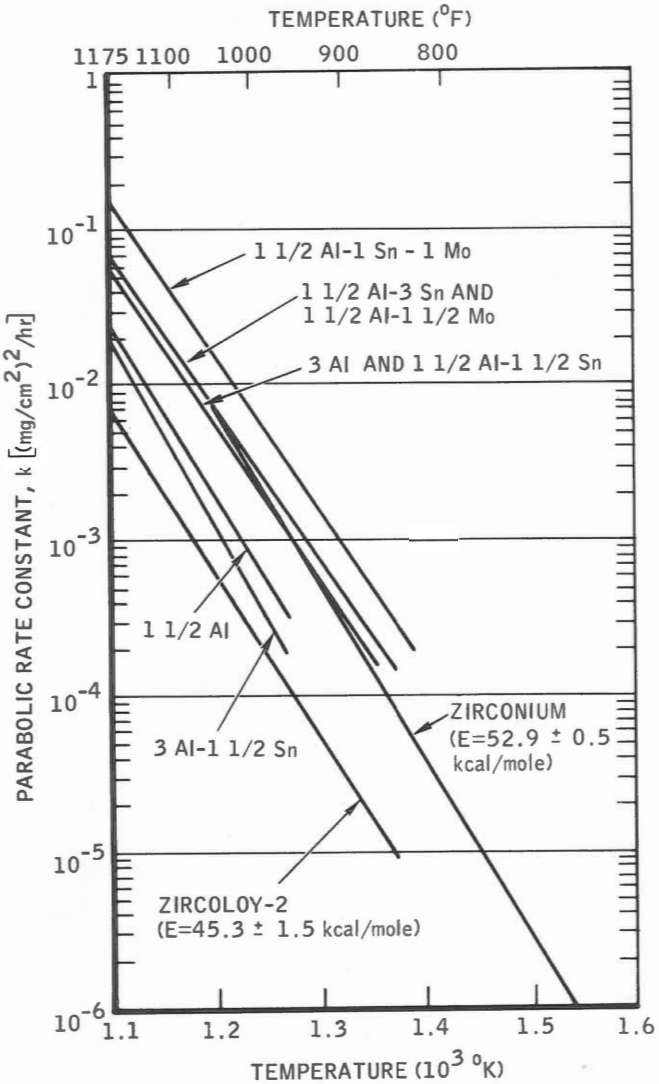

Fig. 2.83 - Oxidation-reaction-rate constants for zirconium and zirconium alloys as a function of temperature.

corrosion of beryllium by oxygen. In fact, slight weight gains were noted.

2. Thorium was less effective than calcium in reducing corrosion of beryllium by oxygen. The gettering efficiency decreased at an impractical rate. There was evidence of hot-to-cold-zone mass transfer of thorium.

3. In experiments in which a nitrogen cover gas was used, no nitriding of beryllium was noted. In other experiments [61] a Be_3N_2 film appeared.

Seven types of hot-pressed beryllium samples from different starting powders

TABLE 2.29 - Value of $1/n$ in Eq. 2.3 at Indicated Temperature [53]

Material	Temperature, °F		
	1030	1105	1175
Zirconium	0.45	0.45	0.46
Zr-1.5 Al	0.41	0.46	0.52
Zr-1.5 Al-1.5 Sn	0.50	0.50	0.50
Zr-1.5 Al-3 Sn	0.42	0.46	0.50
Zr-1.5 Al-1.5 Mo	0.41	0.45	0.49
Zr-1.5 Al-1 Sn-1 Mo	0.45	0.45	0.48
Zr-3 Al	0.41	0.48	0.46
Zr-3 Al-1.5 Sn	0.40	0.45	0.50
Zircaloy 2	0.41	0.46	0.50

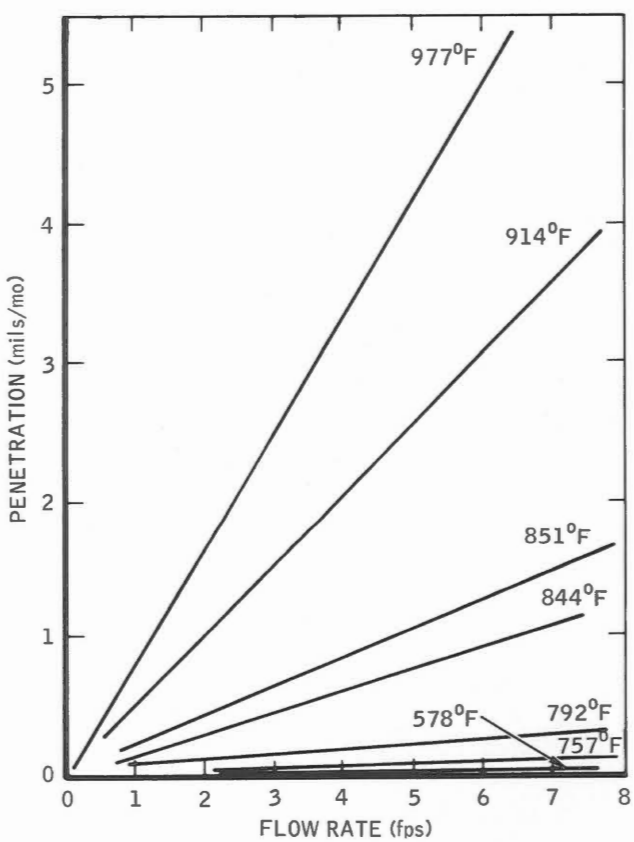

Fig. 2.84 - Beryllium corrosion rate vs. NaK velocity and temperature. [60] NaK-78 cold trapped at 248°F.

TABLE 2.30 - Zirconium Corrosion in Cold-Trapped Circuits*

Test No.†‡	Specimen	Specimen temp., °C	Velocity, ft/sec	Cold-trap temperature, °C	Weight change, g/dm²
1	Tube, pickled§	393	1.0	120	-0.012
2	Tube, pickled	393	1.6	120	-0.016
3	Tube, pickled	393	2.8	120	-0.013
4	Tube, pickled	393	4.6	120	-0.022
5	Tube, pickled	393	8.8	120	+0.006
6	Tube, pickled	467	1.05	120	+0.008
7	Tube, pickled	467	1.7	120	+0.015
8	Tube, pickled	467	2.9	120	+0.021
9	Tube, pickled	467	4.7	120	+0.013
10	Tube, pickled	467	9.0	120	+0.062
11	Tube, pickled	550	1.08	120	+0.028
12	Tube, pickled	550	1.7	120	+0.042
13	Tube, pickled	550	3.0	120	+0.046
14	Tube, pickled	550	4.8	120	+0.039
15	Tube, pickled	550	9.3	120	+0.006
16	Tube, pickled	481	2.1	180	+0.0563
17	Tube, pickled	481	3.4	180	+0.0527
18	Tube	481	3.4	180	+0.0461
19	Tube, pickled	523	2.2	180	+0.0727
20	Tube, pickled	523	3.5	180	+0.0725
21	Tube	523	3.5	180	+0.0593
22	Arc melted, pickled	550	3.5	150	+0.0463
23	Arc melted, pickled	550	2.0	150	+0.0500
24	Carbon melted, as received	600	4.8	145	+0.225
25	Carbon melted, as pickled	600	4.8	145	+0.156
26	Arc melted, as received	600	4.8	145	+0.163
27	Arc melted, as pickled	600	4.8	145	+0.162
28	Arc melted, pickled	650	4.8	160	+0.309
29	Arc melted, pickled	650	3.5	160	+0.300
30	Arc melted, pickled	650	2.0	160	+0.294
31	Arc melted, + 200 ppm N_2	650	4.8	160	+0.339
32	Arc melted, + 100 ppm N_2	650	4.8	160	+0.329
33	Arc melted	650	3.5	160	+0.344
34	Arc melted, + 50 ppm N_2	650	4.8	160	+0.352
35	Arc melted	650	2.0	160	+0.325

*From M. Davis and A. Draycott, *Compatibility of Reactor Materials in Flowing Sodium*, British Report IGR-TN/C-857, p. 31, 1958.

†Liquid metal for tests 1 to 21 was 22% NaK and for tests 22 to 35, sodium.

‡Duration of tests 1 to 5 was 500 hr; tests 6 to 15, 250 hr; tests 16 to 21, 2288 hr; tests 22 to 27, 350 hr; and tests 28 to 35, 700 hr.

§Pickling decreases the weight gains over a period of 350 hr at 600°C but apparently increases the gains over a period of 2300 hr at 480 and 523°C. No satisfactory explanation of this behavior can be given at this time.

(virgin, blend, recycling) were exposed to sodium under the following conditions:

1. Exposure time of 47 hr at 900°F, followed by 520 hr at 1000°F.
2. Flow velocity of 20 ft/sec.
3. Low oxygen level maintained by cold trapping and calcium gettering (1% addition).

The specimen weight losses were less than 1 mg/cm^2/month without evidence of erosion or flaking. Black films about 50 μ thick which appeared on the sample were identified as Be_3N_2. The source of nitrogen was presumed to be an impurity in the argon cover gas or in the calcium. [61]

In multimetallic loop systems [56-59] transfer of beryllium to nickel surfaces was noted. Spacing between beryllium and the other metals was found to be an important variable. Thermal-convection-loop exposures were conducted with sodium for 1000 and 1500 hr each with a beryllium insert positioned in the hot zone so that a few mils separated its surfaces from the surface of a nickel-base alloy. Selected corrosion results are as follows:

Loop material	Hastelloy B	Hastelloy B
Temperature, °F	1200	1300
Corrosion, mils		
Loop material in hot leg	1	1
Beryllium insert	3	3

Loop material	Inconel	Inconel*	Inconel
Temperature, °F	1200	1300	1500
Corrosion, mils			
Loop material in hot leg	1	1	1
Beryllium insert	3	6	12

* These conditions resulted in very low concentrations of beryllium on the Inconel walls, specifically about 6×10^{-3} mg/cm^2 in the hot zones and about 1×10^{-3} mg/cm^2 in the cold zones.

Compounds identified as BeNi or $Be_{21}Ni_5$ were observed:

1. At beryllium-nickel-base alloy surfaces in contact in the 1300°F range. A reaction zone nearly 20 mils thick occurred during a 1000-hr exposure. Chromium plate was evaluated as a barrier, but Be_2Cr formation rendered its use impractical.
2. As a layer to about 3 mils thick on the surface of the inserts in the loops described.

The distance between the beryllium and the third material was found to exert strong control over the transfer of beryllium. The following tabulations are relevant data from static experiments.

Conditions	Distance between sodium-immersed Hastelloy B and Beryllium, mils	Equivalent concentration of beryllium in Hastelloy B surface, 10^{-3} mg/cm^2
1200°F 1000 hr	0	8800
	5	6.3
	20	1.06
	50	0.63
	100	0.74

Conditions	Distance between NaK-44-immersed 304 stainless steel and beryllium, mils	Equivalent concentration of beryllium in 304 stainless steel surface, 10^{-3} mg/cm^2
1470°F 500 hr	2	4950
	5	2300
	10	800
	15	310
	25	170
	50	140

(c) *Niobium (Columbium)*

(1) *General Compatibility.* [44] The behavior of sodium-exposed niobium and niobium-base alloys was found to be highly sensitive to variations in oxygen concentration. The thermodynamic stability of niobium oxides is comparable to that of sodium oxide at the temperature of interest. Niobium forms ternary metal-sodium oxides in sodium of low oxygen content. Corrosion is characterized by weight losses, and the corrosion rate depends linearly on the oxygen content of the sodium - the higher the oxygen level, the higher the corrosion rate at any temperature. Corrosion of niobium is also velocity dependent up to the highest test velocity, 35 ft/sec — the higher the velocity, the higher the corrosion rate. Below 750°F the observed corrosion rates are small and tolerable, even in sodium with up to 40 ppm oxygen. Above this temperature stringent control of oxygen in sodium must be maintained if niobium service components are to have a useful life in a reactor. The use of hot trapping or liquid (magnesium) or solid (zirconium and titanium) deoxidizing agents is recommended.

(2) *Test Results.* Niobium was originally selected for the canning material for the Dounreay fast-reactor fuel on the basis of its high-temperature creep strength and compatibility with uranium and with sodium. Preliminary tests to determine niobium compatibility with sodium were performed in low-oxygen static sodium; no adverse reaction was experienced. Later, in pumped nonisothermal loop tests, extremely rapid loss of metal occurred. [44] Some of these results at 400 to 600°C under dynamic conditions (25 ft/sec) at various levels of oxygen in the sodium are summarized in Fig. 2.85 and are discussed here.

In experiments conducted with oxygen controlled by cold trapping, the major part of the corrosion product probably was removed from the surface on which it formed by the erosive action of the

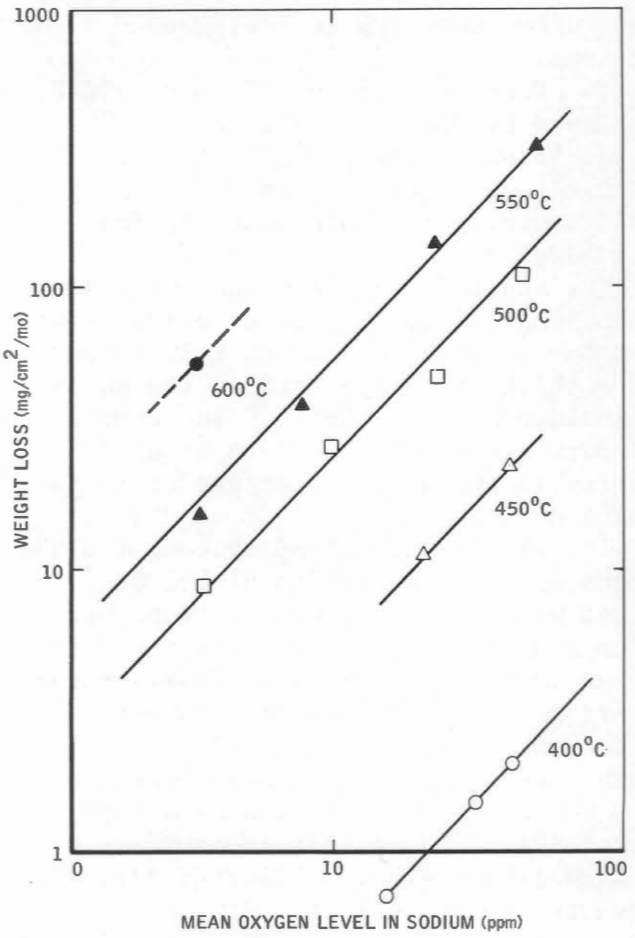

Fig. 2.85 - Corrosion of niobium in sodium under dynamic conditions.

flowing sodium. In high-temperature tests the corrosion product remaining on the surface of specimens exposed in sodium containing 10 ppm oxygen was black and powdery in appearance. In tests conducted in sodium containing approximately 3 ppm oxygen the remaining product was a lustrous brittle skin that tended to peel off in thin sheets metallic in appearance. Analysis of X-ray powder photographs of the corrosion products showed the presence of niobium with a diffuse pattern, a probable indication of oxygen in solution, plus the presence of a phase with sodium chloride structure but with a lattice spacing greater than NbO. Four other unidentified phases were

also found. Other researchers made a compound by reacting Nb_2O_5 with sodium which they identified by chemical analysis as $Na_2Nb_2O_5$. This compound has a sodium chloride structure of a similar spacing to the one obtained as a corrosion product. In other tests Nb_2O_5 in porous steel dispensers was immersed in dynamic sodium of low oxygen content (∿ 3 ppm) at 600°C. After various periods of exposure the product was subjected to X-ray analysis. A phase with the rock-salt structure and an X-ray pattern identical to $Na_2Nb_2O_5$ was found [44] along with two other phases, one of which is likely to have been Na_3NbO_4.

The thermodynamic data summarized in Fig. 2.86 suggest that Nb_2O_5 cannot be formed from niobium in sodium containing less than 100 ppm oxygen; thus it can be ruled out for practical purposes (Nb_2O_5 has been observed in static corrosion tests in sodium containing 3000 ppm oxygen). Below 30 or 40 ppm oxygen at temperatures of interest, NbO_2 cannot be formed, but NbO can be formed in sodium containing 10 ppm oxygen at temperatures up to 850°C and at 5 ppm oxygen at temperatures up to 550°C. Above this temperature a solid solution of oxygen in niobium is possible. At 600°C the reaction

$$3Na_2O + Nb_2O_5 \rightarrow 2Na_3NbO_4 \qquad (2.5)$$

requires 64,000 cal if Na_3NbO_4 is to be stable in relation to NbO. Similarly, the reaction

$$Na_2O + 2NbO_2 \rightarrow Na_2Nb_2O_5 \qquad (2.6)$$

requires 12,500 cal to make $Na_2Nb_2O_5$ stable relative to NbO. Thus the corrosion products obtained may depend critically on the reaction temperature and the oxygen content of the sodium. [44]

Static experiments involving niobium inserts in 316-stainless-steel containers indicated that carbon and nitrogen are transferred from the steel to the refractory metal in sufficient

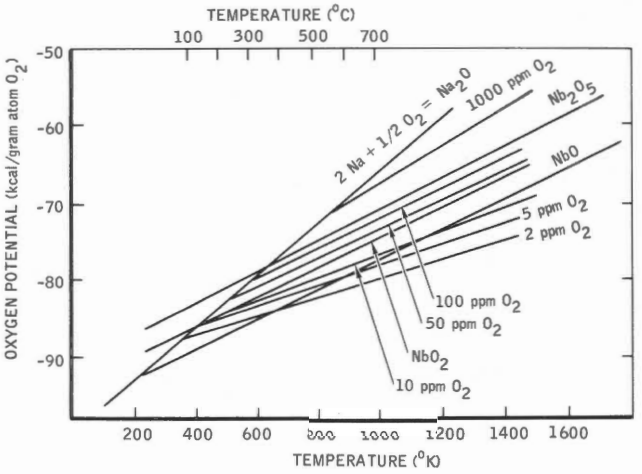

Fig. 2.86 - Thermodynamics of the Nb-Na-O system.

quantity to alter the mechanical properties of the metal. The carbon was confined to the surface, but the nitrogen penetrated the entire distance across the 40-mil-thick inserts. Surface layers were identified by X-ray analysis [62] as Nb and Nb_2N.

Transfer of niobium to the stainless steel also occurred. At 1700°F 40-mil-thick stainless-steel inserts picked up about 0.5% niobium as a surface layer.

Data on the effects of boiling sodium (Table 2.31) on alloys of niobium and tantalum were obtained by Romano, Fleitman and Klamut [63] from pumped loops gettered at 650°C with zirconium foil. Table 2.32 contains compositions of alloys used in these tests. Analysis of the purified sodium by a mercury-amalgamation procedure indicated the oxygen concentration to be less than 10 ppm.

The results of other tests are given in Tables 2.33 to 2.35.

(d) *Vanadium*

(1) *General Compatibility.* Evaluation of the corrosion behavior of sodium-exposed vanadium and vanadium alloys has been in close alliance with the corresponding evaluation of niobium and niobium alloys. As a result it has been common to draw comparisons between

TABLE 2.31 - Corrosion Results on High-Strength Refractory-Metal Alloys Tested in Sodium at 1315°C*

Alloy designation	Monometallic capsule (test time, 6271 hr)	Insert in D-43 capsule (test time, 3000 hr)
D-43	No corrosion	No corrosion
FS-85	0.05-mm grain-boundary attack in weld, both liquid and vapor regions	0.05-mm grain-boundary attack, liquid region
FS-60		No corrosion
T-111	No corrosion	0.025 mm grain-boundary attack, vapor region
TZM	0.01-mm grain-boundary attack in weld, vapor region	No corrosion
X-34	No corrosion	

* Mercury-amalgamation procedure indicated the oxygen concentration to be less than 10 ppm.

TABLE 2.32 - Nominal Composition of Alloys Tested in Program

Alloy designation	Alloying element, wt.%						
	Nb	Ta	W	Zr	Ti	Hf	C
D-43	Bal.		10	1			0.1
FS-60		Bal.	10				
FS-85	Bal.	27	10	1			
T-111		Bal.	8			2	
TZM		Bal.		0.08	0.5		
X-34	Bal.		5	3			0.1

the performance of the two types of materials. As might be expected from thermodynamic considerations, the corrosion behavior of unalloyed vanadium has been found to be similar to that of unalloyed niobium. However, vanadium alloys demonstrated corrosion resistance superior to that of niobium alloys [67].

(2) *Test Results.* Table 2.36 presents pumping-loop corrosion data for vanadium; the corresponding data for niobium appear in Table 2.34. [51] Each presents evidence of high corrosion rates in cold-trapped circuits and reduced corrosion rates through the use of strong oxygen getters.

Table 2.37 and 2.38 present pumping-loop data for vanadium alloys; Table 2.35 is the niobium-alloy counterpart. Fig. 2.87 shows the effects of changes in velocity on the corrosion of unalloyed vanadium. [51]

In tests to determine the corrosion resistance of vanadium-base alloys to sodium in an austenitic-stainless-steel system, V-20 Ti, V-15 Ti-7 1/2 Cr, and V-5 Cr had satisfactory behavior in flowing sodium at 650°C containing

TABLE 2.33 - Data for Exposures Involving Niobium or Nb-1 Zr in Pump Loops Fabricated of Another Material

Ref.	Fluid	Materials arrangement	Maximum temp., °F	Time	Regulation of oxygen level in liquid metal	Corrosion findings
51	NaK-78 and -70	Nb inserts in high-velocity austenitic-stainless-steel systems	698 to 932	500 hr	Oxygen level regulated only by cold trapping at 284°F	Inserts suffered high weight losses (see Table 2.34 for selected values); sensitivity to flow velocity points to a nonadherent, nonprotective oxide corrosion product
64	Sodium	Nb and Nb-alloy inserts in low-velocity (2 fps) austenitic stainless-steel systems	1202	21 days	Oxygen level maintained at 1 to 5 ppm Na_2O by gettering with uranium	Corrosion was generally light (see selected values in Table 2.35)
65	NaK-78	Nb-1 Zr inserts in high-velocity (∿7 fps) 316-stainless-steel systems	1250	3000 hr	<30 ppm of oxygen	Carbide layers built up on Nb-1 Zr to a maximum thickness of 0.1 mil in 1000 hr; surface carbon increased by about 300 ppm in 1000 hr and then remained constant; nitrogen increased periodically by about 300 ppm; oxygen did not change; Nb-1 Zr showed no change in microstructure, hardness, or ductility
66	NaK-78	Nb-1 Zr hot zone with remainder of high-velocity (to 11 1/2 fps) loop fabricated of 316 stainless steel; inserts of both materials throughout systems	1257	2000 hr	Oxygen concentration controlled to 20 ppm by cold trapping	Small quantities of carbon and nitrogen transferred to the Nb-1 Zr; layers to 0.1 in. thick showed NbC-Nb_2N composition; no significant insert weight changes

TABLE 2.34 - Behavior of Niobium in Sodium or NaK Circulating in Austenitic Stainless-Steel Pumping Loops [51,53]

	Temperature, °F	Flow velocity, ft/sec	Weight change,* mg/cm^2/month
Cold trap at 284°F; NaK-78; 500 hr	698	1.3	- 0.9
		11.3	- 0.9
	761	1.3	- 15.7
		11.4	- 52.1
	852	11.3	- 77.7
		11.4	- 52.1
	932	11.3	-175
		11.8	Completely corroded
Cold trap at 257°F; NaK-30; 350 hr	1112	16.2	-333
		29.5	-716
Pretest cold trapping; 10% of flow through Mg dispenser at 752°F; NaK-78; 250 hr	932	1.3	- 0.3
		11.5	- 1.4
Pretest cold trapping; hot trap with Ti at 1202°F; Na; ∿ 300 hr	1022	30	- 1.1
	1112	5.5	- 7.0
Pretest cold trapping; hot trap with Zr at 1112°F; Na; ∿ 200 hr	1112	30	-0.6 to 63.4

* The uniform removal of 1 mil/year from the exposed surface is approximately equivalent to a weight loss of 2 mg/cm^2/month.

TABLE 2.35 - Behavior of Niobium-Base Materials in 1202°F Sodium Circulating in Stainless-Steel Pumping Loops* [53,64]

Alloy composition, wt.%	Weight change,† mg/cm^2/month
Unalloyed Nb	- 0.33
Cb-1.84 Cr	± 0.00
Cb-3.21 Cr	± 0.00
Cb-4.33 Zr	+ 0.01
Cb-20 Ti-4.28 Cr	+ 0.33
Cb-5 Mo	- 0.04
Cb-1 V	+ 0.30
Cb-3 V	- 0.09
Cb-5 V	- 0.10

* Samples were exposed for 21 days to sodium containing 1 to 5 ppm Na_2O regulated by uranium gettering.

† The uniform removal of 1 mil/year from the exposed surface is approximately equivalent to a weight loss of 2 mg/cm^2/month.

TABLE 2.36 - Behavior of Vanadium in Sodium or NaK-78 Circulating in Austenitic Stainless-Steel Pumping Loops*

	Temperature, °F	Flow velocity, ft/sec	Weight change,† mg/cm^2/month
Cold trap at 284°F; NaK-78; 500 hr	632	1.8	- 8.3
		15.9	- 5.2
	742	0.8	- 27.8
		7.8	- 94.2
	762	1.88	- 54.6
		16.5	-219
	860	0.9	- 77
		7.5	-231
Cold trap at 248°F; NaK-30; Nak-30; 350 hr	1112	5.5	- 91.2
Pretest cold trapping; NaK-78, (0.01% Mg added); 350 hr	1112	5.5	- 0.72
Pretest cold trapping; hot trap with Ti at 1292°F; Na; 136 hr	1112	25	- 0.19
Pretest cold trapping; hot trap with Zr at 1112°F; Na; 127 hr	1112	25	- 3.0

* Data from Ref. 51

† The uniform removal of 1 mil/year from the exposed surface is approximately equivalent to a loss of 2 mg/cm^2/month.

TABLE 2.37 - Effect of Rolled-Sheet Alloy Composition on Corrosion in 650°C Static, Refreshed Sodium Containing ∿ 45 ppm Oxygen* [67]

Alloy	External loss, μ/side	ΔW, mg/cm^2	Depth of hardened layer, μ	Total metal penetration, μ
V-5 Ti-15 Cr	9	- 9.2	60 to 70	69 to 79
V-15 Ti-5 Cr	24	-14.7	40 to 45	64 to 69
V-15 Ti-7½Cr	21	-15.6	34 to 38	55 to 59
V-20 Ti-5 Cr	23	-19.5	32 to 35	55 to 58
V-30 Ti-5 Cr	14	-13.1	20 to 22	34 to 36
V-30 Ti-10 Cr	18	-14.1	15 to 18	33 to 36
V-20 Ti-2 Mo	17	- 8.5	40 to 45†	57 to 62
V-20 Ti-2 Ta	34	-11.2	35 to 40†	69 to 74
V-20 Ti-2 Nb	34	-14.7	40 to 50†	74 to 84
V-20 Ti (Reference)‡	42	-16.3	30 to 35	72 to 77

* Samples were tested for 7 days with about 50% cold work.
† Longitudinal surface cracks in hardened layer 10 to 20 μ deep.
‡ V-20 Ti was rolled and annealed at 900°C.

TABLE 2.38 - Behavior of Vanadium-Base Materials in 1202°F Sodium Circulating in Stainless-Steel Pumping Loops* [53,64]

Alloy composition	Weight change, mg/cm^2/month
Unalloyed V	-0.23
V-10 Ti-1 Nb	+0.16
V-10 Ti-3 Nb	+0.26, +0.30†
V-10 Ti-3 Ta	+0.20, +0.37
V-5 Ti-20 Nb	+0.07, +0.27

* Samples were exposed for 21 days to sodium containing 1 to 5 ppm Na_2O regulated by uranium gettering.
† Double listings indicate two exposures, each specimen in a different metallurgical condition - cold rolled, stress relieved, recrystallized, etc.

oxygen at concentration levels achievable by cold trapping, i.e., in the range of 10 to 15 ppm. [67] All these alloys showed weight gains in 650°C sodium containing 10 to 12 ppm oxygen, even in flowing (6.1 m/sec) sodium. When oxygen was increased to concentrations greater than about 15 ppm, a spalling film appeared and weight losses occurred. Sensitivity to velocity did not develop until the nonadherent film appeared. Some results from these tests are shown in Tables 2.37 and 2.39 to 2.41.

Analysis of the sodium for oxygen was accomplished by attaching a vacuum-distillation apparatus to the top of the experimental system. A nickel crucible was vacuum annealed in place and then used to sample the sodium. Distillation of the sodium was completed at 325 to 350°C and the residue titrated as Na_2O.

TABLE 2.39 - Corrosion Behavior of Vanadium Binary Alloys Exposed 7 Days in Static, Refreshed Sodium at 650°C [67]

Alloy composition	O_2 concentration in Na, ppm	Weight loss, mg/cm^2	External loss, μ/side
V-20 Ti*	15	9.7	
V-20 Ti*	42 to 50	28.4	34
V-10 Al†	42 to 50	51.2	93
V-10 Cu†	42 to 50	104	180
V-5 Cr‡	15	9.1	
V-10 Cr†	42 to 50	9.3	100
V-10 Cr‡	15	61.4	
V-20 Cr†	42 to 50	27.5	32
V-10 Fe†	42 to 50	88.5	129
V-20 Fe†	42 to 50	91.8	64
V-10 Ni†	42 to 50	93.8	146
V-20 Ni†	42 to 50	115	189
V-2 Si†	42 to 50	82.5	133

* Rolled and annealed at 900°C.
† Levitation melted, chill cast, and machined.
‡ As rolled.

TABLE 2.40 - Effect of Titanium Concentration on Corrosion Behavior in Static, Refreshed Sodium at 650°C Containing 45 to 50 ppm Oxygen [67]

Alloy*	External loss, μ/side	ΔW, mg/cm^2	Depth of hardened layer,† μ	Total metal penetration, μ
V-10 Ti	77	-51.7	68 to 72	145 to 149
V-30 Ti	39	-20.0	12 to 15	51 to 54
V-50 Ti	27	-12.4	12 to 15	39 to 42
V-70 Ti	17	- 7.6	7 to 10	24 to 27‡
V-90 Ti	13	- 5.3	50 to 55	63 to 68‡

* Samples were exposed for 7 days and tested as levitation melted, chill cast, and machined.
† Including adherent oxide.
‡ Does not include stringer penetration.

(e) *Tantalum* [53]

(1) *General Compatibility.* As might be expected from consideration of thermodynamic constants and solubility information, the corrosion behavior of tantalum in contact with sodium is sensitive to the temperature level and the oxygen content of the sodium.

(2) *Test Results.* Results of exposing tantalum inserts containing about 200 ppm oxygen to sodium circulating in a polythermal pumping loop of 316 stainless steel [68] are illustrated in Fig. 2.88. Cold trapping and

TABLE 2.41 - Effect of Treatment on Corrosion of V-Ti Alloys (Rolled Sheet) Exposed for 7 Days to Static, Refreshed Sodium at 650°C Containing 45 to 50 ppm Oxygen [67].

Alloy	External loss, μ/side	Internal penetration, μ	Total metal penetration, μ
V-20 Ti Control (annealed, 900°C, 1 hr in vacuum)	42	43 to 46	85 to 88
V-30 Ti Cold worked*	52	23 to 27	75 to 79
V-30 Ti Annealed†	33	15 to 17	48 to 50
V-40 Ti Cold worked*	28	13 to 16	41 to 44
V-40 Ti Annealed†	14	13 to 16	27 to 30
V-50 Ti Cold worked*	25	12 to 18	37 to 43

* As cold rolled.
† Annealed same as V-20 Ti.

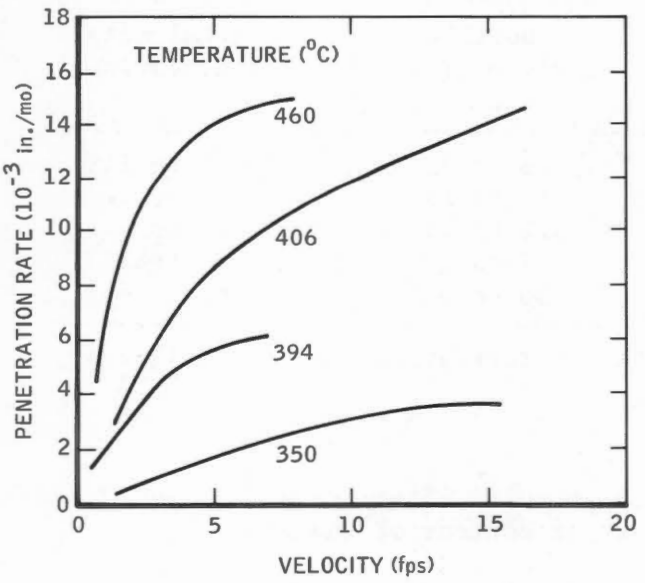

Fig. 2.87 - Variation of penetration rate of vanadium with sodium velocity (cold-trap temperature, 140°C). (From M. Davis and A. Draycott, *Compatibility of Reactor Materials in Flowing Sodium*, British Report IGR-TN/C-857, 1958.)

gettering by zirconium foil were used to maintain the oxygen levels indicated. Other observed compatibility characteristics included the following:

1. There was no evidence of cold-zone mass-transfer deposits of significant magnitude.
2. Intergranular penetration was not a significant mode of attack, although it occurred in specimens fabricated of arc-cast tubing exposed to sodium containing 80 ppm of oxygen.
3. Oxygen migrated from tantalum containing approximately 200 ppm oxygen to high-purity sodium. Final oxygen levels in the tantalum were usually less than 50 ppm. This behavior could not have been predicted from available thermodynamic information* except for very pure sodium, e.g., containing oxygen in the 1-ppm range.

* Tantalum forms a more stable oxide than sodium according to free-energy data; e.g., at 1000°K (1338°F) for the reaction $2Ta + 5Na_2O \rightarrow Ta_2O_5 + 10Na$, the free-energy change is $\Delta F^0 = -56{,}050$ cal/mole. This suggests that tantalum will readily reduce Na_2O.

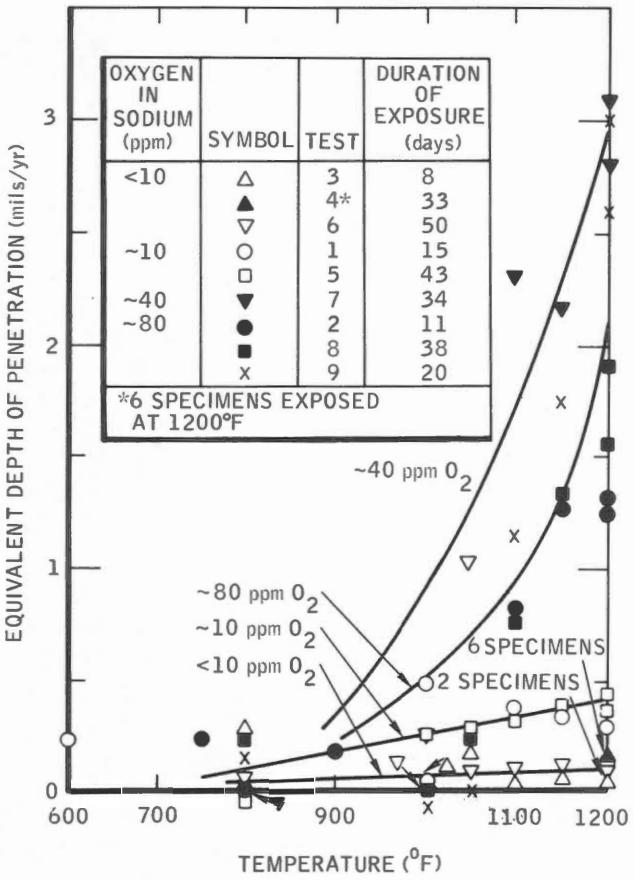

Fig. 2.88 - Effects of temperature and oxygen content of sodium on its attack on tantalum. [68]

4. Exposure to low-oxygen sodium did not have a deleterious effect on the creep characteristics of tantalum at 1200°F.

The results shown in Fig. 2.88 are similar to those obtained in another T-Na investigation, [69] where weight losses for tantalum (1) began at about 1075°F and increased to an equivalent of about 8 mils/year at 1220°F when the tantalum was exposed to cold-trapped sodium, and (2) began at about 970°F and increased to an equivalent of about 0.5 mils/year at 1220°F when the tantalum was exposed to hot-trapped sodium.

There is little information on the performance of tantalum and tantalum alloys in sodium at temperatures above 1200°F. One exception is the indication of good corrosion resistance exhibited by a tantalum insert exposed to 2200°F sodium in a Nb-1 Zr refluxing-capsule experiment operated for 5000 hr. The oxygen in the sodium is probably permanently removed by the zirconium, and, since tantalum solubility is very low, very little corrosion would be expected. Another exception involves a series of Ta-10 W refluxing capsules exposed to sodium boiling at 2310°F for 168 hr. [70] Insert specimens with longitudinal test welds were utilized. The material exhibited generally poor corrosion behavior characterized by severe intergranular penetration of the weld zones in one capsule with sodium contaminated with air during the loading operation. A second capsule with high-purity sodium showed less severe intergranular attack and only in the weld area in the vapor region.

(f) *Molybdenum* [53]

Information relative to the corrosion behavior of molybdenum in sodium or NaK indicates that molybdenum is exceptionally inert to sodium. Good corrosion resistance is indicated by the fact that inserts of molybdenum in a thermal-convection loop exhibited no attack, pitting, or intergranular corrosion after exposure to 1400°F NaK-78 for periods up to 3000 hr. In addition, there was no evidence of corrosion of a molybdenum insert exposed to 2200°F sodium in a Nb-1 Zr refluxing-capsule experiment operated for 5000 hr. [70]

Analysis of the possible reactions of molybdenum and sodium oxide led to the conclusion that sodium molybdate is the probable reaction product.* At 1340°F calculated free energies of formation (ΔF^0) are†

*From thermodynamic considerations (free-energy data), metallic molybdenum does not appear to be oxidized by Na_2O to the simple oxides, MoO_2, MoO_3, etc.

†The free-energy data presented in Ref. 71 have been revised, and the values given here are the new values.

$$4Na_2O + Mo \rightarrow Na_2MoO_4 + 6Na \quad (2.7a)$$
$$\Delta F^0 = -2 \text{ kcal/gram mole}$$

$$2Na_2O + MoO_2 \rightarrow Na_2MoO_4 + 2Na \quad (2.7b)$$
$$\Delta F^0 = -36 \text{ kcal/gram mole}$$

$$2Na + 2MoO_2 \rightarrow Na_2MoO_4 + Mo \quad (2.7c)$$
$$\Delta F^0 = -69 \text{ kcal/gram mole}$$

$$Na_2O + MoO_3 \rightarrow Na_2MoO_4 \quad (2.7d)$$
$$\Delta F^0 = -80 \text{ kcal/gram mole}$$

$$2Na + 4/3\ MoO_3 \rightarrow Na_2MoO_4 + 1/3\ Mo \quad (2.7e)$$
$$\Delta F^0 = -106 \text{ kcal/gram mole}$$

These findings were in conjunction with an investigation [71] of characteristics of molybdenum rubbing surfaces, both dry and in contact with liquid sodium. The data obtained indicated that the liquid-sodium case was characterized by the presence of a Na_2MoO_4 film, which reduced friction, and that the film was continuously replenished by reaction with oxygen in the sodium.

(g) *Tungsten* [53]

Tungsten, like molybdenum, is generally regarded to be resistant to attack by sodium although there is even less evidence on which to judge. Chemically tungsten is similar to molybdenum, and the thermodynamics are favorable for the formation of Na_2WO_4 as the product of the reaction between tungsten and sodium oxide*. For example, at 1340°F the free-energy values† are

$$4Na_2O + W \rightarrow Na_2WO_4 + 6Na \quad (2.8a)$$
$$\Delta F^0 = -31 \text{ kcal/gram mole}$$

$$Na_2O + WO_3 \rightarrow Na_2WO_4 \quad (2.8b)$$
$$\Delta F^0 = -87 \text{ kcal/gram mole}$$

$$2Na + 4/3\ WO_3 \rightarrow Na_2WO_4 + 1/3\ W \quad (2.8c)$$
$$\Delta F^0 = -106 \text{ kcal/gram mole}$$

*Tungsten does not appear to be oxidized by Na_2O to the simple oxides, WO_2, WO_3, etc.

†The free-energy data presented in Ref. 71 have been revised, and the values given here are the new values.

The sodium tungstate film (Na_2WO_4) had frictional characteristics comparable to those of the corresponding molybdate film (Na_2MoO_4) previously mentioned. [61]

(h) *Uranium and Thorium and Their Alloys* [53]

(1) *General Compatibility.* When exposed to sodium containing oxygen, both uranium and thorium react with the Na_2O impurity to form stable oxides at exposed surfaces.‡ The uranium oxide is not adherent and consequently not protective; however, the thorium oxide appears to be fairly adherent.

(2) *Test Results.* The available exposure data [72] for uranium show somewhat erratic values but high specimen weight losses; this indicates that sloughing off of the oxide layers is the rule rather than the exception. Illustrative data for dynamic-corrosion situations are presented in Table 2.42. In samples from the tilting-furnace experiments, there was evidence that constituents of the 347-stainless-steel containers were deposited on the uranium samples. It is not clear whether this accounted in part for the weight gains recorded for the 1200 and 1250°F peak-temperature exposures. [58]

In similar experiments with pre-

‡For example, at 1000°K (1340°F), from the thermodynamics of the reactions

$$U + 2Na_2O \rightarrow UO_2 + 4Na$$
$$\Delta F^0 = -87{,}100 \text{ cal/mole}$$

$$3U + 8Na_2O \rightarrow U_3O_8 + 16Na$$
$$\Delta F^0 = -167{,}500 \text{ cal/mole}$$

$$Th + 2Na_2O \rightarrow ThO_2 + 4Na$$
$$\Delta F^0 = -115{,}650 \text{ cal/mole}$$

both uranium and thorium would be expected to reduce Na_2O.

TABLE 2.42 - Selected Corrosion Data for Uranium Exposed to Sodium or NaK in Dynamic Systems*

	Temperature, °F	Flow velocity, ft/sec	Weight change,† mg/cm²/month
In pumping loops cold trapped at 356°F; NaK-78; 500 hr [51]	940	1.02	-65
	940	1.67	-90
	1075	1.67	-139
	1075	3.21	-222
In pumping loops; Na (mostly 10 to 80 ppm O_2 but as high as 610 ppm); 781 hr accumulated in 8-hr increments	752 to 932	8	-616
In tilting-furnace capsules; Na (200 to 250 ppm O_2); 100 hr [73]	1250 (high) 1050 (low)		+34
	1200 (high) 980 (low)		+47
	1000 (high) 752 (low)		-21
	1000 (high) 752 (low)		-9

* Data from Refs. 51 and 73.

† A weight loss of 47 mg/cm²/month is approximately equivalent to uniform dissolution of 1 mil/month.

irradiated uranium samples, the progress of corrosion was followed by monitoring of the buildup of radioactivity throughout the containment system. Generally, no differences were observed between the corrosion behavior of irradiated and unirradiated samples.

Static-exposure data for thorium and uranium samples are given in Table 2.43. There is some indication that thorium is more resistant than uranium to the oxygen impurity in sodium. The likelihood of a difference in protectiveness of the oxide films is discussed by Pearlman [72] in relation to the adherence of oxide films to base metals:

"The adherence ... is governed by, among other factors, the ratio V_{ox}/V_m:

$$E = \frac{V_{ox}}{V_m} = \frac{\text{volume per metal atom in oxide}}{\text{volume per atom in metal}}$$

Maximum adherence would be expected in systems where $E = 1$. For both UO_2 and ThO_2 the ratio is given by

$$E = \frac{\text{molecular weight oxide}}{\text{atomic weight metal}} \times \frac{\text{density metal}}{\text{density oxide}}$$

For ThO_2 E is about 1.3; for UO_2, about 2. Based on this criterion, the oxide of thorium should be more adherent than that of uranium and should, in fact,

TABLE 2.43 - Selected Corrosion Data for Thorium and Uranium and Their Alloys in Sodium and NaK in Static Systems [72]

Material	Temperature, °F	Time, hr	Oxygen level in liquid metal	Weight change, mg/cm²/month	
				In sodium	In NaK
Thorium	1382	720	200 to 250 ppm	+2	2
Th-3 U	1382	720		+1	2
Th-4 U	1382	720		-40, +3	-12
Thorium	1132	144		+4.5	
Uranium	392	144	Reduced by gettering with		-0.08
Uranium	1132	144	uranium		+3.1
Uranium	761	160			+7
Uranium	745	160			+1.4
Uranium	932	166	Reduced by gettering with beryllium or calcium	-0.1	
U-10 Pu	662	160	Reduced by double filtering		-216
U-10 Pu	761	160			-288
U-60 Al	844	124	Reduced by gettering with	-30	
U-60 Al	932	170	beryllium or calcium	+8	
U-60 Al	1220	164		-720	
U-69 Al	932	167		-220	

TABLE 2.44 - Uranium Corrosion in Cold-Trapped Circuits*†

Test No.	Temperature of specimen, °C	Velocity, ft/sec	Weight change, g/dm²/month	Penetration change, 0.001 in./month
1	511	1.02	- 6.53	1.33
2	511	1.67	- 9.04	1.84
3	581	1.67	-13.95	2.85
4	581	3.21	-22.2	4.33

*From M. Davis and A. Draycott, *Compatibility of Reactor Materials in Flowing Sodium*, British Report IGR-TN/C-857, p. 27, 1958.

†Test conditions were form of material, quadrant of 1.5-in. disk (pickled); duration of test, 500 hr; cold-trap temperature, 180°C; liquid metal, 22% NaK.

compare favorably with such well-known protective oxides as Al_2O_3 (E = 1.3 to 1.5)."

See Table 2.44 for additional data on corrosion behavior of uranium in cold-trapped circuits.

(i) *Titanium* [51]

The titanium data are presented in Table 2.45.

2-3.7 *Nickel- and Cobalt-Base Alloys* [53]

(a) *General Compatibility*

Nickel- and cobalt-base alloys have been examined for sodium and NaK service with emphasis at temperatures above

TABLE 2.45 - Titanium Corrosion in Sodium Cold Trapped at 120°C*†

Test No.	Duration of test, hr	Temperature, °C	Weight change, g/dm²/month
1	440	400	+ 0.0012
2	6.7	500	-12.0
	16.7		-15.0
	33		-16.4
	83		-11.7
	167		- 9.1
3	6.7	650	-47.0
	16.7		-42.8
	33		-40.0
	83		-54.4
	167		-40.8

*From M. Davis and A. Draycott, *Compatibility of Reactor Materials in Flowing Sodium*, British Report IGR-TN/C-857, p. 36, 1958.

†Sodium velocity was 5.5 ft/sec.

1200°F, the approximate temperature at which the usefulness of austenitic stainless steels may be limited by mechanical strength.

It is generally accepted that the solubility process dominates the mass-transfer behavior of nickel-base alloys in flowing nonisothermal systems and that the rate-controlling step in the process is the rate of diffusion of reaction products through the boundary layer at the hot zones. These characteristics can be deduced on the basis of the particularly distinct pattern of mass-transfer dependency on temperature, temperature differential, and flow velocity. The effect of velocity is especially well illustrated by a comparison of thermal-convection-loop data (which indicate sparse mass transfer) with pump-loop data (which indicate fairly copious deposits) under similar conditions of temperature and time.

Cobalt-base alloys appear to be more resistant to corrosion than nickel alloys. Cobalt, however, has some undesirable nuclear characteristics.

(b) *Test Results*

Corrosion-loop data for nickel- and cobalt-base alloys are included in Tables 2.46 and 2.47 (pump loops) and 2.48 (thermal-convection loops). Below 1300°F nickel-base alloys suffer very little corrosion in sodium environments. Above this temperature, however, corrosion and mass transfer in pump-loop experiments are much greater than for stainless steel experiencing the same thermal conditions. The corrosion is characterized by the selective leaching of nickel and, to a lesser degree, chromium. A typical composition of material deposited by mass transfer of Inconel is 90 Ni-8 Cr-0.5 Fe.

A preliminary examination of the behavior of certain nickel-rich alloys of the Nimonic type (Table 2.49) showed that with increasing nickel content the rates of metal loss increased to values that were probably unacceptable for a fuel-cladding application. The short-term results from two-month exposures at 650°C in sodium containing ∿25 ppm oxygen and flowing at a velocity of 30 to 40 ft/sec past the specimens are summarized in Tables 2.50 and 2.51. Since Nimonic 80A has good high-temperature strength and is readily available in tube form, additional tests were carried out to establish whether the extent of corrosion could be reduced by lowering the oxygen content or the velocity of the sodium. Over the velocity range 5 to 40 ft/sec, the material was relatively insensitive to oxygen level in the range investigated (i.e., <10 ppm and ∿25 ppm), but, in contrast to austenitic steels, there was a marked dependence on velocity in this range. The corrosion rate observed at 650°C at a linear velocity of 17.5 ft/sec was in line with that observed in stainless steels in sodium containing 25 ppm oxygen at high velocities. [42] (Fig. 2.89).

2-3.8 *Miscellaneous Materials* [53]

(a) *Braze Alloys*

Braze alloys containing copper,

TABLE 2.46 - Data for Pump-Loop Experiments Involving Selected Nickel-Base Alloys*

Loop material	Corrosion findings
T_{max} = 1500°F; ΔT = 300°F; t = 1000 hr	
Inconel	Hot-zone attack to 2 mils; heavy cold-zone deposits to 18 mils
Incoloy	Almost identical to Inconel
Hastelloy B†	Heavy hot-zone surface pitting to 1 1/2 mils; slightly more cold-zone deposits than for Inconel
Hastelloy W	Hot-zone intergranular attack to 1 1/2 mils; about 17% greater cold-zone deposits than for Hastelloy B
T_{max} = 1700°F; ΔT = 650°F; t = 305 hr	
Hastelloy X (as heater leg with pump cell of Inconel and remaining sections of 316 stainless steel)	Hot-zone attack characterized by large subsurface voids, to 3 1/2 mils (Hastelloy X); intergranular attack to ∿1 mil at entrance to cooler (316 stainless steel); deposits up to 32 mils in cooler; no observation regarding interactions among construction materials

* Data from Refs. 58 and 74.

† At 1300°F peak temperature Hastelloy-B system (ΔT = 300°F, t = 1000 hr) showed very sparse mass-transfer deposits. The depth of intergranular attack, however, was about the same as in the 1500°F system.

TABLE 2.47 - Data for Pump-Loop Experiments Involving Haynes Alloy No. 25 and NaK-56 [75]

T_{max}, °F	ΔT, °F	Time, hr	Hot-leg flow, ft/sec	Pretest oxygen level, ppm	Corrosion findings	
					Attack in hot zone, mils	Mass-transfer deposit, mils
1800	400	275	14.7	< 50	2.5 to 3.5	6.0
1800	400	500	14.7	< 50	3.0 to 5.0	10.0
1650	400	497	14.4	<100	1.0 to 1.5	8.0
1650	400	1000	14.4	<100	2.5 to 4.0	5.0

silver, and precious metals are generally not useful for sodium-environment service since the individual metals are readily attacked. The most useful brazes are nickel with alloying ingredients such as silicon and boron. Table 2.52 summarizes the results of static-corrosion tests [77] of several nickel-base alloys in sodium at 1500°F for 100 hr. Several materials that appeared promising on the basis of these static tests (together with others thought to hold promise) were investigated more extensively in seesaw-furnace

TABLE 2.48 - Data for Thermal-Convection-Loop Experiments Involving Nickel- and Cobalt-Base Alloys*

Fluid	Material	T_{max}, °F	Time, hr	Corrosion findings
NaK-78† (<20 ppm O_2)	Inconel X	1400	To 4500	1000 hr: No apparent attack 2000 hr: Very slight general corrosion 3000 hr: Very slight pitting
	Hastelloy C			1000 hr: 1-mil pitting 2000 hr: 1.7-mils decarburization
	Hastelloy N			1500 hr: Slight evidence of intergranular attack 2500 hr: General corrosion to 1/2 mil 4500 hr: 2 1/2-mils decarburization
	Haynes Alloy No. 25			1000 hr: 0.2-mil pitting 2000 hr: Very slight evidence of general corrosion 3000 hr: 1.1-mils decarburization
Sodium	Hastelloy B	1600	1008	Slight amount of mass transfer: 1- to 2-mils intergranular attack
Sodium	Hastelloy X	1500	1000	No hot-zone attack or evidence of metallic deposits in cold zones
Sodium	Hastelloy W	1500	1000	No hot-zone attack but scattered nickel deposits in the cold zones
Sodium	Ni-Mo experimental alloys Ni-11 Mo-2 Al Ni-17 Mo-2 W Ni-15 Mo-3 Nb-0.5 Al-3 W Ni-16 Mo-5 Cr-1.5 Ti-1 Mn Ni-20 Mo-1 Nb-2 Ti-0.8 Mn	1500	1000	Average hot-zone attack about 1 mil, appearing as subsurface voids and pits rather than intergranular attack; sparse deposits in cold zone

* Data from Refs 59 and 76.

† Experiments listed for NaK exposure were conducted in 304 stainless steel and Inconel; evaluations were made on insert specimens.

TABLE 2.49 - Nickel-Alloy Compositions [42]

Nickel alloys	Composition, wt.%	Condition*
	Solid-Solution Strengthened	
Inconel 600	77 Ni, 6 Fe, 16 Cr, 0.02 C	HT; 2 hr at 940°C in vacuum
Nilo 50	50 Ni, 50 Fe, 0.03 C	HT; 1 hr at 900°C in vacuum
Nilo K	53 Fe, 29 Ni, 16 Co, 0.03 C	HT; 1 hr at 950°C in vacuum
	Precipitation Hardening	
Nimonic 80A	75 Ni, 20 Cr, 2.3 Ti, 1.4 Al, 0.06 C	AN; 10 min at 1100°C Water quenched Oxide pickled AC; 8 hr at 1050°C + 16 hr at 700°C
PE.11	35 Fe, 38 Ni, 18 Cr, 5.2 Mo, 2.2 Ti, 0.9 Al, 0.07 C	AC; 20 min at 1020°C + 16 hr at 700°C
PE.16	34 Fe, 43 Ni, 16.5 Cr, 1.2 Al, 1.2 Ti, 0.06 C	AC; 30 min at 1020°C + 2 hr at 800°C + 16 hr at 700°C Cold worked

* Abbreviations are: HT, heat treated; AN, annealed; and AC, age conditioned.

TABLE 2.50 - Data for Materials Exposed to Dynamic Sodium (30 to 40 Ft/Sec) Containing 25 to 30 ppm Oxygen at 650°C for 8 Weeks [42]

Material	Extrapolated loss in metal section, 0.001 in./year
Inconel 600 (soft)	6.1
Nimonic 80A	4.9
Nickel	3.9
PE.11 (soft)	2.9
PE.16 (soft)	2.8
Nilo 50 (soft)	2.5
18/8/1 Ti	2.4
PE.16 (opt. props.)	2.3
316 S.S.	1.8
PE.11 (opt. props.)	1.8
Nilo K (soft)	0.95

experiments in which sodium was circulated for 100 hr at a hot-zone temperature of 1500°F and a cold-zone temperature of 1100°F. Since the seesaw tests provided a more rigorous means of evaluating corrosion data, no brazing alloy that had poor corrosion resistance to sodium in the static test was seesaw tested. The results of these seesaw-furnace experiments (Table 2.53) indicate several promising brazing alloys for short-time sodium service.

TABLE 2.51 - Corrosion of PE.16 at 650°C

O_2 level of Na, ppm	Velocity of sodium	
	15+ ft/sec*	30 to 40 ft/sec
∿10		1.5×10^{-3} in./year (1-month test) 1.6×10^{-3} in./year (repeat 2-month test)
∿25	1.8×10^{-3} in./year (6-month test)	2.3×10^{-3} in./year (2-month test)

*This is a down-rated velocity value caused by failure of a loop component. It was the minimum value finally measured. During the experiment the velocity was considered to be higher than 20 ft/sec.

TABLE 2.52 - Summary of Results of 100-hr Static-Corrosion Tests at 1500°F for Nickel-Base Brazing Alloys [77]

Materials with Good Corrosion Resistance	
General Electric No. 81	Ni-10 Si-8 Mn
Coast Metals No. 52	Ni-16 Si-6 Mn
Ni-10 P-10 Cr	Ni-13 Si
Nicrobraz	Ni-10 P-13 Cr
Ni-25 Ge	Ni-6 Si-30 Mn
Ni-25 Mo-25 Ge	Ni-9 P-11 W
Ni-25 Ge-10 Cr	Ni-10 Si-13 Cr-19 Fe-3 Mo
Ni-9 Si-18 Cr	Ni-5 P-6 Si
Ni-3 P-9 Si	Ni-8 P-3 Si
Materials with Poor Corrosion Resistance (>5 mils Attack or Other Deterioration)	
Ni-60 Mn	Ni-9 P-15 Fe-5 Cr
Ni-55 Mn-10 Cr	Ni-11 P-9 Si
Ni-32 Sn	Ni-10 P-4 Mo
Ni-57 Mn-3 Cr	Ni-12 P
Ni-23 P	Ni-11 P-8 Mn
Ni-12 P	Ni-10 P-4 Mo
Ni-11 P-8 Mn	Ni-10 P-11 Fe

At Atomics International [78] several nickel-base brazing alloys were tested in a liquid-sodium thermal-convection loop for periods up to 10,000 hr at 1200 and 700°F. On the basis of gross weight changes and photomicrographic examinations of the exposed brazing-alloy specimens, the investigators concluded that Ni-Cr-Si-B (Coast Metals No. 53, or CM53) and Ni-Si-B (CM52) were the most resistant to sodium attack. Ni-Cr-Si (CM60) was judged to be suitable only for short-term use (less than 1500 hr) or low-temperature (below 700°F) applications. Also, CM59 and Nicrobraz 135 were shown to have good resistance to sodium attack up to 5000 hr at 1200°F. However, CM1700N and

TABLE 2.53 - Brazing Alloys on Inconel T-Joints Seesaw Tested in Sodium for 100 hr at a Hot-Zone Temperature of 1500°F and a Cold-Zone Temperature of 1000°F [77]

Brazing-alloy composition (in order of decreasing corrosion resistance)	Weight change (for braze and base material)		Metallographic notes
	Gram	%	
Coast Metals No. 52	-0.0011	-0.073	No attack along surface of braze fillet
Coast Metals No. 53	-0.0009	-0.071	Erratic 1-mil attack along surface of braze fillet
Low-melting Nicrobraz	-0.0007	-0.051	Subsurface voids to a maximum depth of 1.5 mils along surface of braze fillet
Coast Metals No. 50	-0.0012	-0.077	Very erratic 1.5-mil attack along fillet
Ni-13 Ge-11 Cr-6 Si	-0.0023	-0.139	Nonuniform attack along surface of braze fillet to a depth of 2.5 mils
Coast Metals NP	-0.0069	-0.622	Uniform 2.5-mil attack along surface of braze fillet
Nicrobraz	0.0	0.0	Very erratic stringer attack to a maximum depth of 4 mils along surface of braze fillet
Ni-25 Ge-10 Cr	-0.0019	-0.113	Intermittent surface attack to a maximum depth of 4 mils along braze fillet

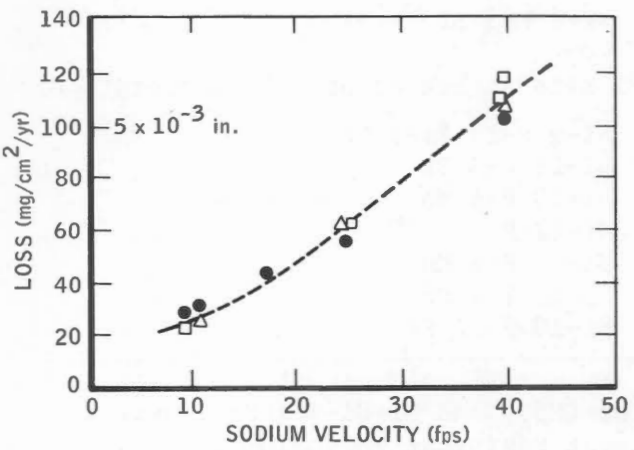

Fig. 2.89 - Effect of velocity on the rate of metal loss from Nimonic 80A at 650°C. [42] At oxygen levels of 25 to 30 ppm: Δ, soft material. □, aged material. At oxygen levels <10 ppm: ○, soft material. ●, aged material.

CM1700CN underwent deleterious attack at 700°F after the 5000-hr exposure. Of the last two, CM1700N appeared to be superior.

(b) *Graphite*

Graphite has been employed as the moderating medium in liquid-metal-cooled thermal reactors such as the Sodium Reactor Experiment (SRE) and the Hallam Nuclear Power Facility (HNPF). Unfortunately its corrosion resistance to sodium is poor, and any graphite used in a sodium system must be kept from direct contact with the sodium. [79,80]

Numerous investigations have been conducted in an attempt to explain the action of liquid sodium on graphite at elevated temperatures. Carniglia [81] reviewed many of the earlier works. The effects observed included swelling or dilation, cracking or spalling, and

corrosion and mass transfer at temperatures above 1200°F. High-density carbon-impregnated graphites, as well as the normal commercial grades, have not been immune to these deleterious effects, and they exhibit the same poor corrosion resistance. Liquid sodium readily wets graphite, ultimately soaking into the pores and becoming rather uniformly distributed throughout the capillary space available. Coultas and Cygan [82] studied this capillarity, or "sponge" effect, by immersing a graphite rod in a reservoir of sodium within an evacuated chamber. Their data indicated that roughly 60% of the connected voids were filled by liquid at 842°F and 100% at 1022°F. Carbon impregnation of the graphite did little to alleviate the situation. In similar experiments Greening and Davis [83] observed that 68% of the connected voids were filled at 1202°F, and Collins [84] found 90% impregnation at 1355°F.

This uptake of sodium is accompanied by an anisotropic dilation or swelling of the graphite. Greening and Davis [83] measured this dilation as a function of temperature from 302 to 1202°F. Interestingly, the addition of 1% potassium greatly aggravated the situation. Gill [85] conducted a series of static-capsule experiments on the dilating effect of graphite using graphite samples ranging in density from 1.6 to 1.89. His results indicate linear dilations of the order of 1% decreasing somewhat with increasing density in times up to 100 hr at 950°F. The greater degree of expansion perpendicular to the axis of extrusion stems from the anisotropy of the graphite. Dilation does not vary markedly with exposure time (500 to 2000 hr) or temperature (950 to 1200°F). Gill further observed that in some cases decrepitation and disintegration (loss of strength) occurred in the graphite owing to the dilation.

Some investigators attribute the dilation and disintegration of graphite to the formation of interlamellar compounds between the graphite and sodium. [79, 80] It is well known that potassium, rubidium, and cesium form interlamellar compounds with graphite, although early experimental and theoretical work indicated that sodium could not participate in reactions of this type. [86] Later work at Harwell [87] provided evidence for the existence of at least one interlamellar compound of sodium, $C_{64}Na$.

The structure of this material, determined by X-ray diffraction, is shown in Fig. 2.90. In this interesting compound the sodium-metal atoms are located between the plane sheets of carbon atoms which comprise the graphite structure. The sodium has penetrated into every eighth interplanar gap and exists in a ratio of 64 carbon atoms to one sodium atom. At the sodium-carbon gap position, the interplanar spacing has increased from 3.35 Å to about 4.6 Å in the compound. It is postulated [79] that the sodium atom is too large to be comfortably accommodated in the graphite structure and tends to distort the graphite. Hence this distortion and the resulting stresses cause the material to disintegrate.

Radiation can also contribute appreciably to the dilation and swelling of graphite in liquid sodium and appears to have contributed to the severe distortion following moderator-sheath failures in the Hallam reactor. [88] Atomics International found that graphite absorbed sodium up to 20% in volume upon exposure to reactor neutron fluxes.

(c) *Cermets and Ceramic Materials* [53]

The resistance of cermet and ceramic materials to sodium and NaK has been investigated to some extent, inasmuch as these materials are potentially useful for speciality applications such as bearing surfaces in practical flow systems. In cermets emphasis has been placed on evaluation of the commercially available cemented-carbide materials, and many have been found to be stable

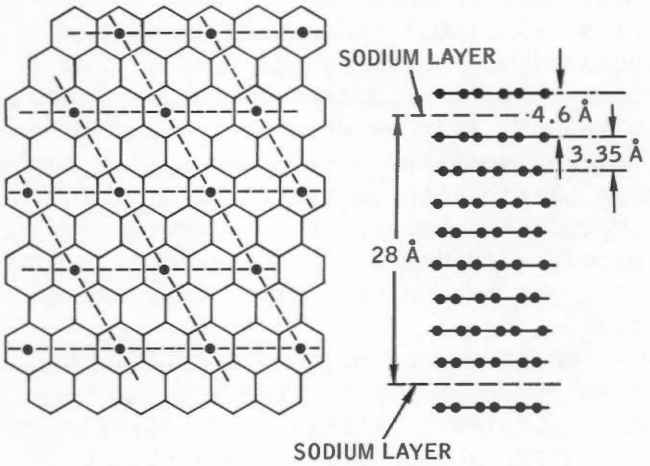

Fig. 2.90 - Top and side views of the sodium-graphite compound $Na_{64}C$ as deduced from X-ray diffraction measurements. [53, 87]

in high-temperature exposures, as demonstrated by the information in Table 2.54. However, as indicated in Table 2.55, subtle changes in surface quality can occur even for materials that resist gross attack very well. In applications where surface integrity is essential, these microscopic surface changes may limit reliability and long life.

Ceramics exposed to sodium or NaK resist attack, usually in accordance with their stability predicted on the basis of the thermodynamic data, their purity, and their freedom from porosity. For the most part, the exposure data presented in Table 2.56 substantiate these generalizations. Exceptions of some interest include Sm_2O_3 in particular and Si_3N_4 which appear to possess resistance to attack although they are quite porous.

A set of pertinent data for lower-temperature exposures is presented in Table 2.57.

2-4 MASS TRANSFER OF METALLIC CONSTITUENTS

2-4.1 *Categories and Mechanisms*

In liquid-metal systems mass-transfer phenomena are considered part of the broad field of corrosion. In general, mass transfer involves the movement of one or more components (i.e., elements or compounds) within or between phases. This section is concerned with the movement of metallic elements from cladding, structural, or special (bearing, valve trim, etc.) material through the liquid metal to a different location in the heat-transfer system.

Mass transfer has been categorized into two types, temperature gradient and concentration gradient (or dissimilar metal). [92] In both the driving force for transfer of a metallic constituent of construction materials is a difference in chemical activity (effective concentration) of the constituent at different locations in the heat-transfer system.

For temperature-gradient mass transfer, the driving force is the difference in solubility of the dissolved element at the high and low temperatures existing in the system. Figure 2.91 indicates the movements of metallic atoms in temperature-gradient mass transfer. If there is selective removal of one element from an alloy, these atoms must diffuse to the surface and then go into solution. The atoms must then diffuse through the laminar film into the bulk-liquid stream and are finally carried to the cold portion of the system where supersaturation occurs. A collection of such atoms can accumulate and form a nucleus that grows to a stable size and then drops from the liquid. On the other hand, the atom can supersaturate close to the wall, diffuse through the laminar film, and then nucleate on the metallic wall and form a dendritic crystal, or it can diffuse into the wall. [92]

The other type of mass transfer is dissimilar-metal or concentration-gradient mass transfer. A schematic view of the manner in which dissimilar-metal mass transfer takes place is seen in Fig. 2.92. Atoms of metal A go into

TABLE 2.54 - Corrosion Resistance of Cermets to Sodium and NaK*[89, 90]

Exposure to 1500°F static Na or to Na in tilting-furnace equipment where T_{high} = 1500°F and T_{low} = 1100°F (each involves a 100-hr exposure)	Exposure to NaK-50 for 168 hr in tilting-furnace equipment where T_{high} = 1600°F and T_{low} = 1200°F
Cermets Showing No Observable Attack and Very Slight Weight Losses	
WC-6 Co (Carboloy 44A)†	WC-4 Co (K-8)
WC-9 Co (Carboloy 779)†	WC-12 Co (K-94)
WC-13 Co (Carboloy 55a)†	WC-12 Ni
WC-20 TaC-6 Co (Carboloy 907)†	TiC-20 Co (K-138)
TiC-10 NbC-10 Ni (K-150A)‡	TiC-20 Ni (K-151)
TiC-10 NbC-20 Ni (K-151A)‡	TiC-20 Fe
TiC-6 NbC-30 Ni (K-152B)‡	TiC-15 CbC-5 Co (K-139A)
TiC-6 NbC-5 Mo-25 Ni (K-162B)‡	TiC-15 NbC-20 Co (K-138A)
Cr_2C_3-20 WC-15 Ni (Carboloy 608)†	TiC-10 NbC-10 Ni (K-150A)
	TiC-10 NbC-20 Ni (K-151A)
	TiC-6 NbC-30 Ni (K-152B)
	TiC-6 NbC-40 Ni (K-153B)
	TiC-6 NbC-5 Mo-25 Ni (K-162B)
	Cr_3C_2-20 WC-15 Ni (Carboloy 608)
	Mo_2C-4 Ni
Cermets Showing Significant Degrees of Attack	
SiC-Si	Mo_2C-12 Co
	$MoSi_2$-12 Co
	$MoSi_2$-12 Ni

*Data from Refs. 89 and 90.

†Static test.

‡Tilting-furnace test. In this test a sample of test material is confined to one end of a sealed tube partially loaded with liquid metal. The tube is rocked in such a way that the fluid flows back and forth over the sample, which is maintained at a temperature higher than that at the opposite end. Thus as the fluid moves it undergoes a temperature cycle.

solution and move to the surface of metal B either by diffusion (in a stagnant system) or by movement of the liquid. When they reach the surface of metal B, they come out of solution, alloy with metal B, and diffuse inward. The driving force for dissimilar-metal transfer is the decrease in the free energy that is achieved through the alloying of the two metals. The greater the difference in the chemical potentials of A and B in the two solid phases, the greater will be the driving force for the occurrence of mass transfer. The rate of mass transfer depends on the temperature since an increase in temperature, of course, increases the diffusion rate in both the liquid and the solid phases. A high solubility of metal A in B, B in A, or both, also facilitates mass transfer. [92]

Contacting two or more solid metals having different chemical activities of a metallic constituent with sodium (or another liquid metal) produces the effects associated with dissimilar-metal mass transfer. For example, nickel was

TABLE 2.55 - Surface-Roughness Data for Selected Materials Exposed to NaK-50 for 158 hr in 1600°F Peak-Temperature Tilting-Furnace Experiments [53,90]

Material	Average surface roughness (measured by profilometer)			
	Before exposure		After exposure	
	μin.	rms	μin.	rms
WC	1 1/2	1	2 1/2	3
TiC	1	1/2	3 1/2	1
WC-12 Co (K-94)	3	4	6	6
WC-12 Ni	5	5	12	12
TiC-15 NbC-5 Co (K-139A)	5	5	6	7
TiC-15 NbC-5 Co (K-138A)	6	5	7	6
TiC-6 NbC-5 Mo-25 Ni (K-162B)	7	7	6	6
TiC-6 NbC-30 Ni (K-152B)	4		9	
TiC-6 NbC-40 Ni (K-153B)	5	4	20	10

observed to migrate through sodium at 1000°C to form a reaction layer on a molybdenum surface. [93] Dissimilar-metal mass transfer is usually discussed in the context of an isothermal system.

Systems with temperature differences (ΔT's) are of interest to the designer and operator of heat-transfer systems. Consequently they are concerned with overall mass-transfer effects, whether caused by thermal-gradient or dissimilar-metal mass transfer since both types can occur in engineering systems operating with a temperature gradient.

The processes involved in release of a metallic constituent to the liquid metal are common to both types of mass transfer. They consist of diffusion of the metallic constituent through the parent metal to the surface in contact with the liquid metal, solution attack of the parent metal, and chemical reactions resulting from interaction of nonmetallic impurities with both the liquid and the structural metals. These processes are all temperature dependent; their rates increase with increasing temperature. In the discussions that follow, sodium is used as an example, but the same principles apply to NaK.

Diffusion of a particular alloy constituent through the parent metal is of significance when its concentration at the surface of the metal in contact with the sodium is depleted through release of the constituent to the sodium. Diffusion of the atoms involved (in the mass-transfer process) to the surface of the metal often becomes the rate-controlling step in the overall mass-transfer process. Since diffusion of alloy constituents within metals is a subject unto itself, and one that is not unique to liquid-metal technology, it is not covered in this handbook.

Most solid metals are soluble to some extent in liquid sodium. Solution attack of the parent metal can be considered to occur in two steps. The first, or "dissolution," step can be pictured as the breaking of metallic bonds that hold the surface atom to its neighbors in the solid parent metal and the simultaneous formation of metallic bonds between the solute and solvent (sodium) atoms. Very little is known about the mechanism of this exchange; however, it is believed to be highly sensitive to surface imperfections in the solid metal as the surface bond energies are related to crystal

TABLE 2.56 - Corrosion Resistance of Ceramics to Sodium and NaK*

Exposure to 1500°F static Na for 100 hr	Exposure to NaK-50 for 168 hr in tilting furnace equipment where T_{high} = 1600°F and T_{low} = 1200°F†	
No Observable Attack and Very Slight Weight Losses		
Cr_3C (98.7)	CbC (<1)	
TiC (97.4)	TiC (<1)	
ZrC (100)	WC (<3)	
Al_2O_3 (single crystal) (100)	BeO (<1)	
BeO (96)		
MgO (single crystal) (100)		
Mg_2AlO_4 (single crystal) (100)		
Sm_2O_3 (79)		
∿49.5 Sm_2O_3-27 Gd_2O_3-balance: other rare-earth oxides (90)		
ZrB_2		
Relatively Little Attack		
B_4C (80 to 90)	TiN (<3)	
SiC	TiB_2 (2)	
ThO_2 (75 to 80)		
Si_3N_4 (67.7)		
$MoSi_2$		
Significant Degrees of Attack		
ZrO_2 (Ca stabilized)	B_4C (0.5)	
BN (60 to 98)	B_4C-20 Mo_2C (8)	ZrB_2 (0.4)
TiN	SiC-Si (0.3)	ZrB_2 (0.7)
	ZrC (<1)	CaF_2 (1)
	Ta_2O_5 (2)	$MoSi_2$ (<1)
	ThO_2 (<2)	MoS_2 (19)
	UO_2 (2)	CeS (19)

* Data from Refs. 89 and 90.

† In the left column the numbers in parentheses refer to percent of theoretical density; in the right column the numbers in parentheses refer to apparent porosity in percent.

imperfections. Selective grain-boundary attack and dislocation etching are therefore indicative of dissolution rate control by the first step, especially in the absence of impurities in the grain boundaries. [32]

The second step in solution attack of the parent metal is the diffusion of the solute species through the laminar sodium film immediately adjacent to the surface of the parent metal (Fig. 2.93). The driving force for diffusion through the laminar film is the difference between the equilibrium solubility at the dissolution temperature, S_0, and the solute concentration in bulk sodium, S. The diffusion rate, J (in units of mass/time/area), is

$$J = \frac{D(S_0 - S)}{\delta} \qquad (2.9)$$

from Fick's law, where D is the diffusion coefficient of the solute species

TABLE 2.57 - Resistance of Selected Ceramics and Cermets to Attack by Aged and Filtered Sodium [53,91]

Mole compositions (except as indicated)	Corrosion rate, mg/cm^2/month		Absorption, %	Density, g/cm^3
	932°F	1382°F		
Ceramics				
Artificial periclase crystal	-0.4	-0.25		
BeO	0.14			
Stabilized ZrO	2.7			
1BeO:1Al_2O_3	0.0003		0.18	
1MgO:4ZrO_2	-0.091	-14.6	0.01	
1MgO:8BeO:1Al_2O_3	-0.44	- 1.6	0.03	
76BeO:4Al_2O_3:20ZrO_2 (+2 wt.% CaO)	-0.64	0.54	0.01	
3MgO:90BeO:1ZrO_2	-0.68	- 0.96	0.03	
Hot-pressed synthetic mica	Disintegrated			2.74
TiN	Spalled			2.39
$CaZrO_3$	28.7			4.28
CdO	Missing			5.33
ZnO	Missing			2.33
Be_2C (swelled due to hydration after test)	4.5			
$MoSi_2$	Missing			6.10
Cermets				
K-138 (Co-bonded TiC)	-0.275			
K-138A (Co-bonded CbC)	-0.225			
K-L7 (Co-bonded WC)	-0.15	- 0.1		
K-152 (Ni-bonded TiC)	-0.15	- 1.77		
K-152B (Ni-bonded CbC)	-0.05	- 1.6		
100% TiC	-0.025	- 0.22		

in the liquid-metal solvent (sodium); D is generally of similar magnitude for most liquid alloys. Thickness of the laminar film, δ, is flow and viscosity dependent.

Of the two steps, diffusion through the laminar film is generally indicated to be the rate-controlling step in pure systems by the sensitivity of the overall solution rate to liquid-metal velocity. In experimental results from ORNL, [94,95] the mass transfer of nickel from Inconel in sodium was linearly dependent on sodium flow rate (Fig. 2.94).

Chemical reactions of coolant impurities, chiefly oxygen, are often involved in the release of alloy constituents to the liquid metal. It is well established that the amount of mass transfer is strongly dependent on the level of oxygen impurity in the sodium, and this is illustrated by the removal rates of individual constituents from 347 stainless steel in a flowing, isothermal (925°F) sodium loop: [96]

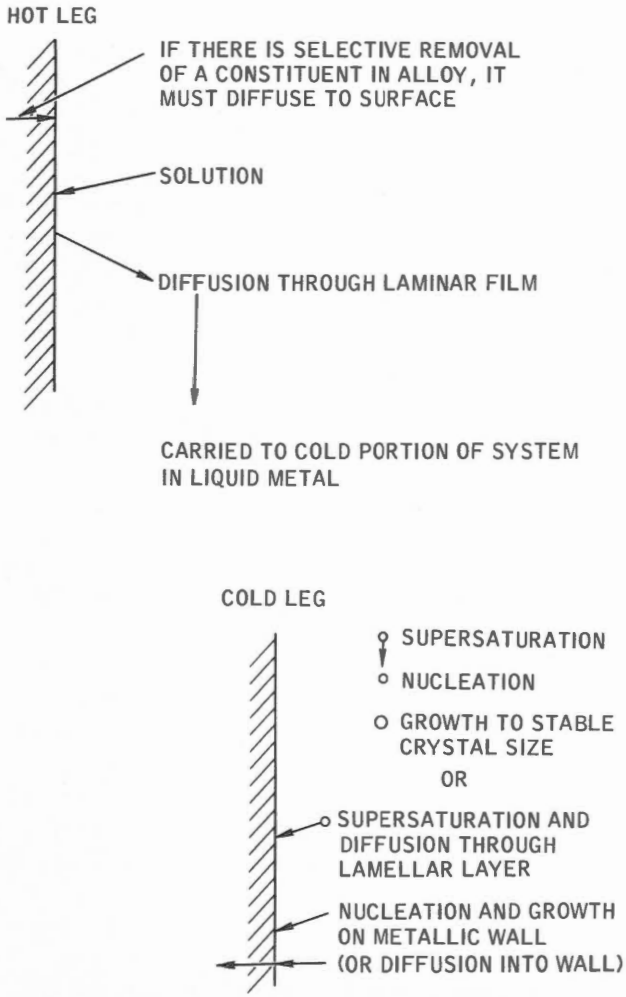

Fig. 2.91 - Schematic diagram of the manner in which temperature-gradient mass transfer occurs.

Element	Rate of leaching by Na(100 ppm O_2) / Rate of leaching by Na(30 ppm O_2)
Iron	17
Cobalt	54
Tantalum	5
Manganese	4

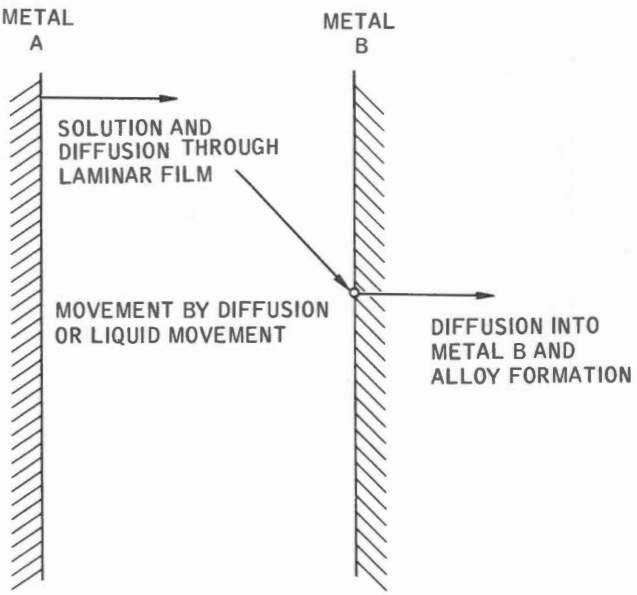

Fig. 2.92 - Schematic diagram of the manner in which dissimilar-metal (concentration-gradient) mass transfer occurs.

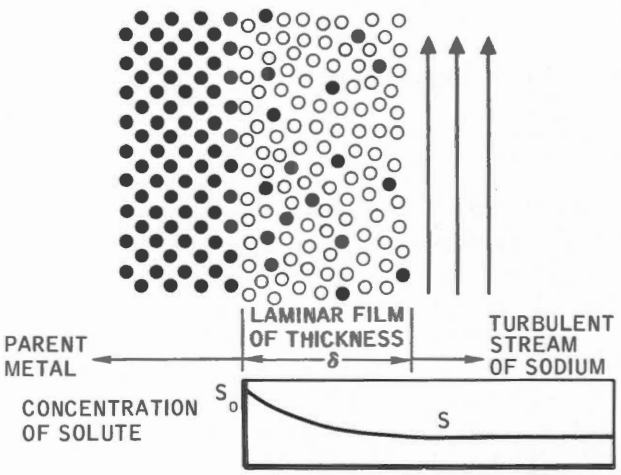

Fig. 2.93 - Schematic diagram of dissolution of a solid metal into sodium.

Another example of the significance of oxygen concentration is the factor of 3 decrease in corrosion rates of ferritic and stainless steels with a decrease in oxygen concentration from 25 to 10 ppm. [97] The exact role of oxygen has not been determined, but it may accelerate dissolution and/or participate directly in a corrosion

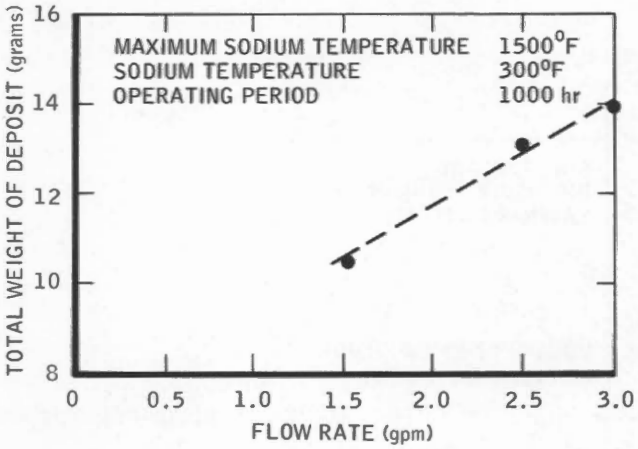

Fig. 2.94 - Effect of flow rate on mass transfer of nickel by dynamic sodium in Inconel loops.

reaction involving compounds of the form, $Na_xM_yO_z$, where M is an alloy constituent. It is generally accepted that mass transfer of iron is dominated by reaction rather than dissolution; the reaction occurring when the sodium contains sufficient oxygen is believed to be

$$Fe(sol) + 3Na_2O \text{ (in Na)} \rightarrow 2Na(liq) + (Na_2O_2)_2 \cdot FeO \text{ (in Na)} \qquad (2.10)$$

In cold zones the reverse reaction occurs, releasing iron, which crystallizes out of solution. This particular Na-Fe complex compound was isolated and identified in residues obtained from heavily contaminated sodium (1 to 2% oxygen) that had been held in iron capsules. From the appearance of the compound, it was estimated to have precipitated from solution during cooling of the capsules. [98] The existence of this compound was confirmed by mass balance and chemical analysis. [42,90]

2-4.2 *Empirical Equations*

A significant recent contribution in the field of mass transfer is the work done at General Electric Company [45, 99] using statistical analyses of weight changes of samples exposed in flowing-sodium test loops to develop empirical equations relating weight changes to the significant variables. Three materials, selected as representative candidates for reactor applications, were studied. Chosen to represent the austenitic stainless steels, 316 stainless steel, which has higher strength characteristics at elevated temperature than lower grades, was used as hot-leg material in four of the loops and simulates the material in a reactor primary or secondary coolant circuit. Two Cr/Mo steels, 2 1/4% chromium-1% molybdenum steel (2 1/4 Cr) and 5% chromium-1/2% molybdenum-1/2% titanium steel (5 Cr), were chosen because of their relatively low cost and extensive use in fossil-fueled power plants. These ferritic steels were used in hot- and cold-leg combinations to simulate use in secondary sodium systems and in steam generators. Combinations of the austenitic 316 stainless steel and the ferritic materials were used also to simulate secondary reactor sodium systems.

A statistical plan including the following test variables was devised to determine mass transfer by measuring weight-change data during five runs on each of five loops:

1. Maximum hot-leg temperatures of 1100 and 1200°F.
2. Two temperature differentials from the hottest to the coldest sodium in the loop, ΔT = 250 and 500°F.
3. Two sodium-purity levels, 10 and 50 ppm oxygen.

Sodium purity was determined with a plugging indicator. An "oxygen" flow break at 450°F was taken to represent an oxygen concentration of 50 ppm, and a break at 290°F, 10 ppm.

Weight-change data from samples exposed during a total of 25 test runs in the five loops were analyzed. The following empirical equations were developed to relate the weight-change data to the test variables. The complete statistical analysis of the weight-change data

was reported. [46,100] For the removal (weight loss) of material from the hot leg,

$$R = V^{0.884} O_x^{1.156} \exp\left[12.845 - \frac{23,827}{T + 460} - 0.00676\left(\frac{L}{D_i}\right) + \frac{2.26}{t + 1}\right] \quad (2.11)$$

For deposition of mass-transfer products (weight gain) in the cold-leg, or low-temperature region,

$$R = O_x^{0.94} \exp\left[\left(22.61 - 0.038\ \Delta T\right) - \left(\frac{31,980 - 55.24\ \Delta T}{T + 460}\right) - 0.0032\left(\frac{L}{D_i}\right) + \frac{0.92}{t + 1}\right] \quad (2.12)$$

where

R = steady-state rate of removal or deposition of metal ($mg/cm^2/month$)
ΔT = maximum sample-holder temperature minus minimum sample-holder temperature, representing heat-transfer system ΔT(°F)
O_x = oxide level in the sodium (ppm oxygen)
V = sodium velocity (ft/sec)
T = corrosion- or deposition-site temperature (°F)
L/D_i = downstream factor (site location in number of hydraulic diameters downstream from beginning of isothermal section)
t = exposure time (months)

In later related work at General Electric Company [101,102] in support of the Liquid-Metal Fast-Breeder Reactor (LMFBR) and Fast Flux Test Facility (FFTF) development problems, the ranges of test parameters covered in the previous project were extended to simulate the expected range of temperatures, velocities, sodium purity, and corrosion potentials for a 1000-MW reactor system. The effects of sodium velocity (from 0.7 to 24 ft/sec), sample position, and flow rate are being studied on 316- and 304-stainless-steel test materials at top temperatures of 1300°F. Oxide purity is controlled by cold trap to <300°F plugging temperatures.

The first result of analysis of preliminary data was the separation of the downstream factor L/D (of Eqs. 2.11 and 2.12) into two components, $(L/D)_1$, distance downstream in an isothermal region, and $(L/D)_2$, distance downstream in an isovelo (constant-velocity) region. [101] A series of samples with very little change in downstream factor showed corrosion rates dropping by a factor of 2 along the section. The series was not at the beginning of an isothermal region but at the beginning of an isovelo region after a change in velocity. Some sort of entrance effect causing the change in corrosion rate was postulated to exist; this effect could not be detected in the work that led to Eqs. 2.11 and 2.12 because there was only one sample along an isovelo region.

The second result of analysis of the preliminary data was the establishment of significantly different velocity-term and time-term coefficients. [102] Raw data from two runs with the parameters noted in Table 2.58 were transformed to fit the previous model for the corrosion-rate equation. Combined analyses of corrosion data for 1000-, 2000-, and 3000-hr time points, together with oxygen and temperature variables previously determined, yielded the following empirical equation for hot-leg corrosion:

$$\ln CR = 14.14 + 0.435 \ln(V) - 0.000958\left(\frac{L}{D}\right)_1 - 0.122\ hr\left(\frac{L}{D}\right)_2 + 1.445\ [1/(t + 1)] + 1.156 \ln O_x - [23,827/(T + 460)] \quad (2.13)$$

TABLE 2.58 - Run Parameters*

Velocity, ft/sec		Downstream factor (L/D)		Flow, gpm	Samples		
Hot leg	Cold leg	Hot leg	Cold leg		Tube	Ring	Pressurized
0.7 to 14.3	0.7 to 8.1	450	980	3.0	189	63	4
1.3 to 26.3	1.3 to 14.9	450	980	5.7	189	63	12

* Common parameters were T_{max} = 1300°F, T_{min} = 800°F, test duration = 3000 hr, Na_2O impurity = <10 ppm (260 to 280°F plugging), test materials = 304 and 316 stainless steel.

where

CR = rate of weight loss to time t (mg/dm^2/month)
V = sodium velocity (ft/sec)
$(L/D)_1$ = downstream factor = number of hydraulic diameters downstream in an isothermal region
$(L/D)_2$ = downstream factor = number of hydraulic diameters downstream in an isovelo region
t = months' exposure
T = sample temperature (°F)
O_x = oxygen impurity (ppm)

The difference (almost 2 to 1 ratio) between the velocity coefficients of Eqs. 2.11 and 2.13 is related to the range of velocity data for the two sets of experiments. It is suggested [102] that a plot of corrosion rate vs. velocity is an S-type curve and that the corrosion rate is relatively insensitive to velocity up to about 1 or 2 ft/sec, where the velocity effect becomes more pronounced and the corrosion rate becomes more sensitive to velocity. At a velocity of 15 to 20 ft/sec, it is believed that the corrosion rate again becomes relatively insensitive to velocity. The velocity range of the work that yielded Eq. 2.11 was limited to one part of this S-curve, but the velocity range for the later work included sensitive and nonsensitive parts of the S-curve. Therefore, the velocity coefficient of Eq. 2.13 is the result of averaging two different types of velocity variation. Work to clarify this point is continuing.

The difference between time coefficients of Eqs. 2.11 and 2.13 is expected to be resolved when data for more different exposure times are available. The steady-state corrosion rates for both sets of data are the same, the time coefficient determining the time at which steady state is reached.

An important result of these tests was the finding that corrosion rates are the same for all three steels tested. This steady-state equivalence arises from the selective nature of the transport process. In low-oxygen experiments chromium and nickel surface concentrations are decreased and the iron concentration is increased. It is postulated that this selective depletion of chromium and nickel can change the surface composition of all three materials so that they eventually present a similar iron-rich surface to the sodium stream. After an initial transient condition, steady-state corrosion is controlled by corrosion of the ferritic surface layer remaining. In the higher-oxygen systems, the selective direction is reversed. Iron is preferentially removed from the surface, and the alloys all tend to behave like Cr-Ni-rich alloys. [45,99]

Results from other investigations [97] also showed that the steady-state corrosion rates for the stainless steels (16-12-2, similar to 316, and 18-8-Ti, similar to 321) and the ferritic steels

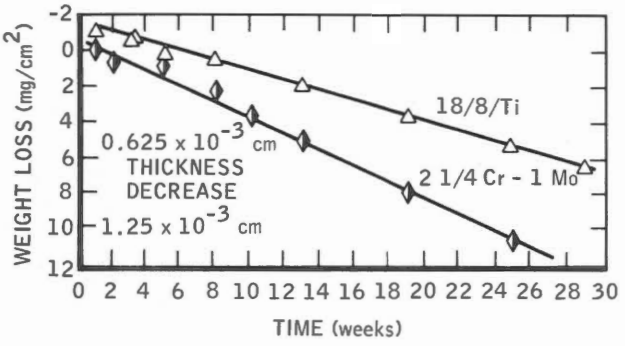

Fig. 2.95 - Behavior of 18/8/Ti stainless steel and $2\frac{1}{4}$ Cr-1 Mo ferritic steel in flowing sodium at 600°C, ~25 ppm oxygen, and 5.5 m/sec sodium velocity.

(2 1/4 Cr-1 Mo, 2 1/4 Cr-1 Mo-0.4 Nb-0.4 Ti, and 9 Cr-1 Mo-V) are very similar when the steels are tested under identical conditions (Figs. 2.95 and 2.96). A hypothesis similar to that given for the depletion of chromium and nickel was postulated. It was further reported that the metallurgical condition (i.e., whether annealed or 20% cold worked) of their test samples did not affect the corrosion rate. [97]

The empirical mass-transfer equations (Eqs. 2.11 and 2.12) can be used to predict average corrosion rates under a given set of conditions, as shown in the example. However, the variation of Young's data points [101,102] around the average was significant and must be considered in the application of these equations. For the hot-leg data the measured residual variance of 0.95 is equivalent to stating that an estimated 95% of the samples will have measured corrosion rates within a factor of 5.3 of the average. Average corrosion rates calculated from Eq. 2.11 are shown in Table 2.59, along with approximate maximum corrosion rates falling within the 95% confidence levels.

For convenience in evaluating results of the calculation, the total weight loss was converted to a decrease in wall thickness by using an assumption of uniform surface recession. This assumption

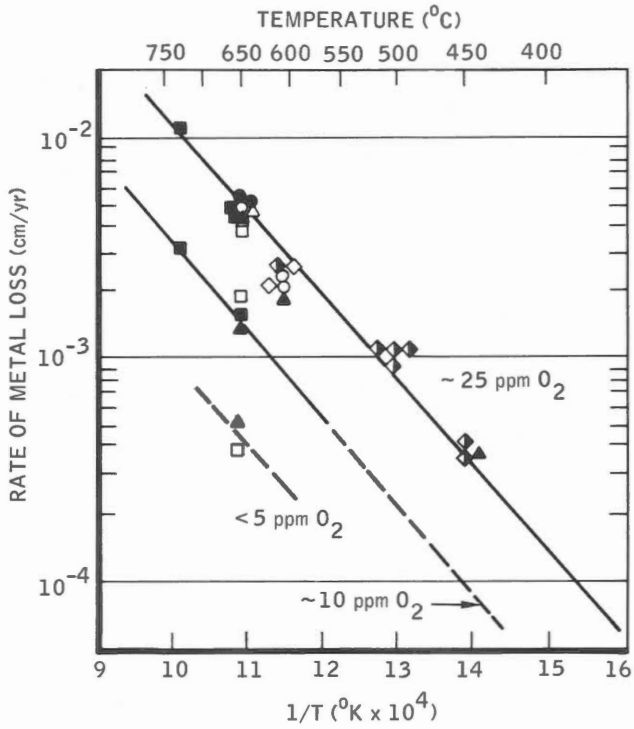

Fig. 2.96 - Effect of temperature and oxygen concentration on the rate of metal loss from various materials after exposure to flowing sodium. □, 316 stainless steel, annealed. ■, 316 stainless steel, annealed 20% reduction of area; ●, 316 L stainless steel, annealed. ▲, 18/8/Ti stainless steel, annealed. △, Nimonic PE.16. ◑, $2\frac{1}{4}$ Cr-1 Mo ferritic steel, annealed, normalized, and tempered, + 30% reduction of area. ○, $2\frac{1}{4}$ Cr-1 Mo-Nb Ti ferritic steel, annealed, normalized, and tempered. ◇, 9 Cr-1 Mo-V ferritic steel.

is acceptable here because the corrosion mechanisms uniformly affected the entire surface of the isothermal-weight-change specimens.

Material deposition rates in low-temperature locations were found to be the same for the three steels tested. Average deposition results calculated by using Eq. 2.12 are given in Table 2.60 along with approximate maximum deposition rates falling within the 95% confidence levels.

TABLE 2.59 - Rate of Hot-Leg Metal Loss* [45]

Sample temperature, °F	Oxygen content of the sodium			
	10 to 15 ppm		45 to 50 ppm	
	Average	Maximum	Average	Maximum
1000	0.05†	0.25	0.25	1.25
1100	0.15	0.75	0.75	3.75
1200	0.39	1.95	1.9	9.5
1300	0.95	4.95	4.7	23.5

* Velocity of sodium was 20 ft/sec, corrected to 0 downstream.
† Mils per year.

TABLE 2.60 - Rate of Cold-Leg Deposition* [45]

Sample temperature, °F	Oxygen content of the sodium			
	10 to 15 ppm		45 to 50 ppm	
	Average	Maximum	Average	Maximum
900	0.006†	0.023	0.029	0.11
1000	0.022	0.087	0.11	0.43
1100	0.056	0.22	0.27	1.1
1200	0.14	0.55	0.68	2.7

* Velocity of sodium was 7 ft/sec, corrected to 0 downstream.
† Mils per year.

Cold-leg deposition results showed more variance and were more difficult to interpret than hot-leg results. Such problems might be expected in sodium systems where the measured cold-leg weight gains were partially caused by semiadherent or loose deposition products. Removal of test samples from the loops, together with the sodium removal and handling required, might easily have resulted in loss of some of these deposits prior to weighing operations. [45]

The assumption that deposits had uniform depth and density does not appear to be well justified considering the type of deposits observed - loose, semiadherent, porous, etc. This assumption was used to convert weight gains calculated by using Eq. 3.12 to thickness of deposit.

From examination of Young's test loops, [101,102] it was noted that preferential deposition occurred in cold legs whenever there was a change in the direction of a sodium flow path or a cross-sectional change in the piping. Surface roughness, sharp bends, flow restrictions, and abrupt section changes are potential sites for abnormally large deposits and should be avoided in the design of piping and sodium components.

The designer should be aware of the reasons why calculations of the weight of mass-transfer deposits based on Eq. 2.12 do not give conservative results. Variance of the results has been noted. Also, loss of deposition products during sample handling prior to weighing operations would have given lower than true values of weight gain. The calculation might also give low results because of specimen location in the test loops. The first specimen holder was located just downstream from the first cooler (see Fig. 1, Ref. 45). In high-temperature runs this cooler reduced sodium temperature from 1200 to 1100°F. From results of the deposition calculation, it is apparent that deposition decreases by a factor of 2 for the 100°F temperature difference between 1200 and 1100°F. Hence it must be assumed that significant deposition occurred in the first cooler, depleting the concentration of mass-transfer products in the sodium stream prior to the first specimen holder. Therefore, results of calculations based on these test-loop results do not represent the maximum deposition that would occur at the entrance to the intermediate heat exchanger; results of these calculations underestimate the true situation.

2-4.3 *Effects of Variables*

(a) *Time*

After an initial period the corrosion rates of all the ferritic and stainless steels tested by Nettley and his co-workers [97] (these metals are listed in the previous section) were constant when sodium velocity, temperature, and oxygen concentration in the sodium were maintained at fixed levels. Figure 2.95 illustrates the behavior of 18-8-1 stainless steel and 2 1/4 Cr-1 Mo ferritic steel in tests of six months' duration.

Similar findings were made at General Electric. [45] After an initial period both hot-leg corrosion and cold-leg deposition rates became linear with time. This linearity was tested to ∿20,000 hr. The response of hot-leg corrosion rate is plotted in Fig. 2.97 and the response of cold-leg deposition rate, in Fig. 2.98. Areas under each of the rate-response curves were integrated graphically and the integral curves plotted.

The transition from a nonlinear to a linear corrosion rate arises from the influence of a linear rate-controlling step in the transport process. Seven potential rate-controlling steps were considered for linearity: the four transport phases, (1) the steel alloy, (2) an oxide film, (3) a stagnant sodium boundary layer, and (4) the turbulent sodium stream, and the three interfaces, (1) alloy-oxide interface, (2) oxide-stagnant-sodium-boundary-layer interface, and (3) stagnant-sodium-layer-turbulent-sodium-stream interface. The linear rate law rules out metallic diffusion in the alloy as the steady-state controlling step. If we assume no accumulation at a specific point along the flow path in the turbulent sodium stream and perfect mixing at the stagnant-layer-turbulent-sodium interface, rate control must be imposed at or in one of the following steps:

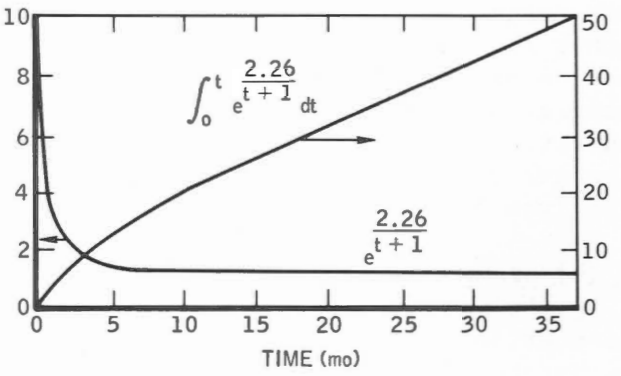

Fig. 2.97 - Hot-leg corrosion response.

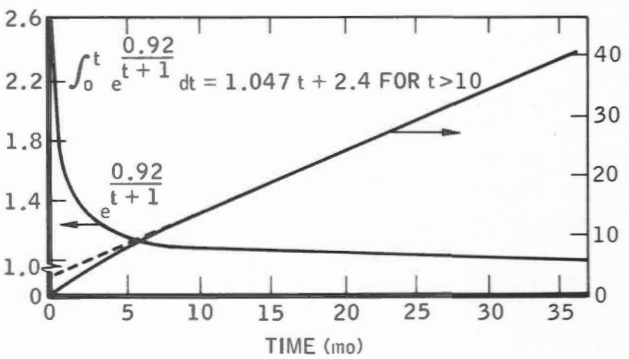

Fig. 2.98 - Cold-leg deposition response.

1. The alloy-oxide interface.
2. The oxide film.
3. The oxide-stagnant-sodium-boundary-layer interface.
4. The stagnant boundary layer.

Solution-rate control at either interface will eventually drive the total transport process linear, as will saturation in either intermediate phase. [45]

The effect of time was determined by these investigators for periods up to about 20,000 hr. [45] It is possible that for longer exposures mass-transfer rates of these materials will be controlled by diffusion of chromium and nickel through the parent material;[97] the response of cumulative effects of

mass transfer will then become parabolic rather than linear. In this event extrapolation of the linear portion of the integral curves in Figs. 2.97 and 2.98 tends to overestimate the amount of mass transfer and therefore is conservative from a design standpoint.

(b) *Temperature*

Of the variables affecting mass transfer, only time and sodium velocity are independent of temperature. Diffusion, solution, and chemical reaction rates all increase with increasing temperature, as do the solubilities of the alloy constituents being transferred. If other conditions are fixed, steady-state mass-transfer rates are very dependent on temperature. The dependence follows the Arrhenius relation as shown in Fig. 2.96, which shows that the corrosion rate, R, of stainless and ferritic steels is related to the absolute temperature, T (°K), in the temperature range 450 to 725°C, by the equation

$$R = 2.3 \times 10^{-6} \exp - \frac{17{,}500}{RT} \text{ cm/sec} \qquad (2.14)$$

In these tests the oxygen concentration was maintained at 20 to 30 ppm.

As a general guide, little mass transfer would be expected in an austenitic stainless steel in a sodium system with oxygen concentration at 10 to 20 ppm if the temperature is less than 1000°F. However, a temperature increase of 100°F produces approximately a threefold increase in corrosion rate. [45]

(c) ΔT

In Sec. 2-4.1 the driving force for temperature-gradient mass transfer was said to be the difference in solubility of the dissolved metal at the high and low temperatures in the system. Consequently an increase in the temperature difference in the system (ΔT) results in an increase in mass-transfer rate for this type of mass transfer. An example of such mass transfer is the movement of nickel in an Inconel loop;

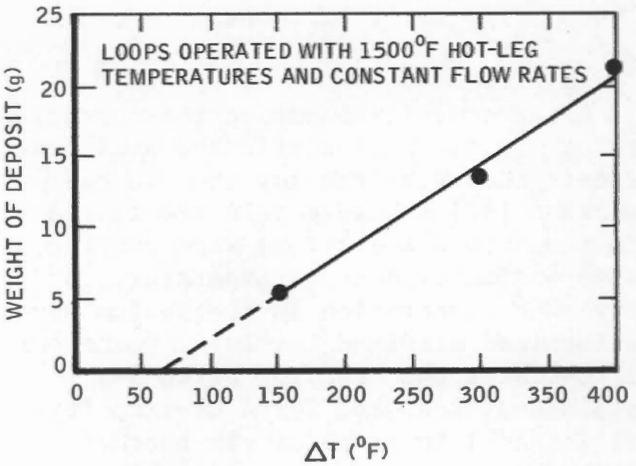

Fig. 2.99 - Effect of ΔT on mass transfer in sodium, Inconel pump loops.

Fig. 2.99 shows that the rate was linear with ΔT.

On the contrary, tests at General Electric showed that ΔT within the 250 to 500°F range of values had very little effect on the mass-transfer rates. Consequently there is no ΔT term in the hot-leg removal equation (Eq. 2.11). A ΔT term does appear in the cold-leg prediction equation (Eq. 2.12) as a temperature-coefficient adjustment term. [45]

(d) *Impurities*

The amount of oxygen dissolved in sodium has long been recognized as a very significant factor in mass-transfer processes. Other impurities in sodium (excluding oxygen getters) may play roles in the processes, but their effects are not well identified.

Other experimental results [97] confirmed that steady-state corrosion rates of stainless and ferritic steels are markedly dependent on the oxygen content of the sodium. As shown in Fig. 2.96, in tests at 650°C a change of oxygen content from 25 to 10 ppm reduces the corrosion rate by a factor of about 3; a change from 25 ppm to less than 5 ppm reduces the rate by an order of magnitude. Figure 2.74 shows that at 650°C reducing the oxygen concentration from 25 to 10 ppm reduces the mass-transfer

rate by a factor of approximately 2.

In the tests at General Electric [45] corrosion rates varied in a direct ratio with the oxide content of the sodium as determined by the plugging indicator. An oxygen change from 12 ppm (305°F oxygen flow break) to 50 ppm (450°F oxygen flow break) produced approximately a fourfold corrosion increase.

(e) *Velocity*

Measured mass-transfer rates were approximately linear with sodium velocity in the tests at General Electric. [45] Actually, the exponent of velocity in Eq. 2.11, 0.884, is between 1 (which represents a linear relation) and the 0.8 predicted from the analogy with heat transfer (which assumes a fluid-diffusion-controlled process).

The weight-change data obtained from slotted sample holders used in the test loops show that corrosion depends on velocity of sodium past the test specimens. Both one- and three-slot holders were used, and they were so constructed that the velocity of the sodium through the single-slot holder was three times the velocity through each of the multiple slots. In the hot leg the measured corrosion rates were approximately proportional to velocity. The samples in the single-slot holders showed about three times as much corrosion as identical samples in the three-slot holders. The cold-leg sample holders contained only triple-slot holders, and the in-pipe samples were located in the minimum deposition region; thus no cold-leg velocity-effect data were obtained (note absence of the velocity term in Eq. 2.12). Loop-examination data appear to indicate the existence of cold-leg velocity or impingement effects.

The effects attributed to sodium velocity are not entirely clear. It may be that mass flow of sodium is the controlling variable rather than velocity. Because of the fixed geometry in the test loops, the mass flow and velocity are proportional and vary in an identical amount in the standard "hockey-stick" sample holders. Therefore it is impossible to separate the effects of velocity vs. mass flow in these tests. Some samples of a different geometrical configuration were exposed in the loop piping. Here the mass flow does not vary in the same ratio as velocity; thus the effects of these two variables can be separated. For these samples the mass flow parameter was consistently better than the velocity term in relating hot-leg in-pipe samples to standard slot samples. Because the number of checks was limited by the very low corrosion rates of the in-pipe samples and because of the paucity of data pertinent to this point, no definite conclusions can be made at this time. Further testing is needed to determine the relative importance of these two variables. [45]

Recent information reported by the Reactor Materials Laboratory at Culcheth indicates that the rate of mass transfer of ferritic and austenitic materials is proportional to velocity only up to some limiting Reynolds number. [42] From the data now available (see Fig. 2.100) for austenitic stainless steel at 1200°F in sodium containing 25 ppm oxygen, it appears that a point of inflection occurs somewhere between 10 and 15 ft/sec above which velocity has very little effect on the rate of metal loss. The data also show the expected approximately linear increase in mass-transfer rate up to about 10 ft/sec.

At the lower oxygen levels, 10 ppm and <5 ppm O_2, velocity changes have been investigated up to 40 ft/sec. Here again very little change in corrosion rate is recorded in the range 15 to 40 ft/sec for 316 stainless steel. It is noteworthy that the substantially velocity-independent rate established is a function of oxygen content of the liquid metal.

At the higher velocities some mechanism other than diffusion through the laminar sodium film appears to be rate controlling. The investigators hypothesize that it is a combination of the

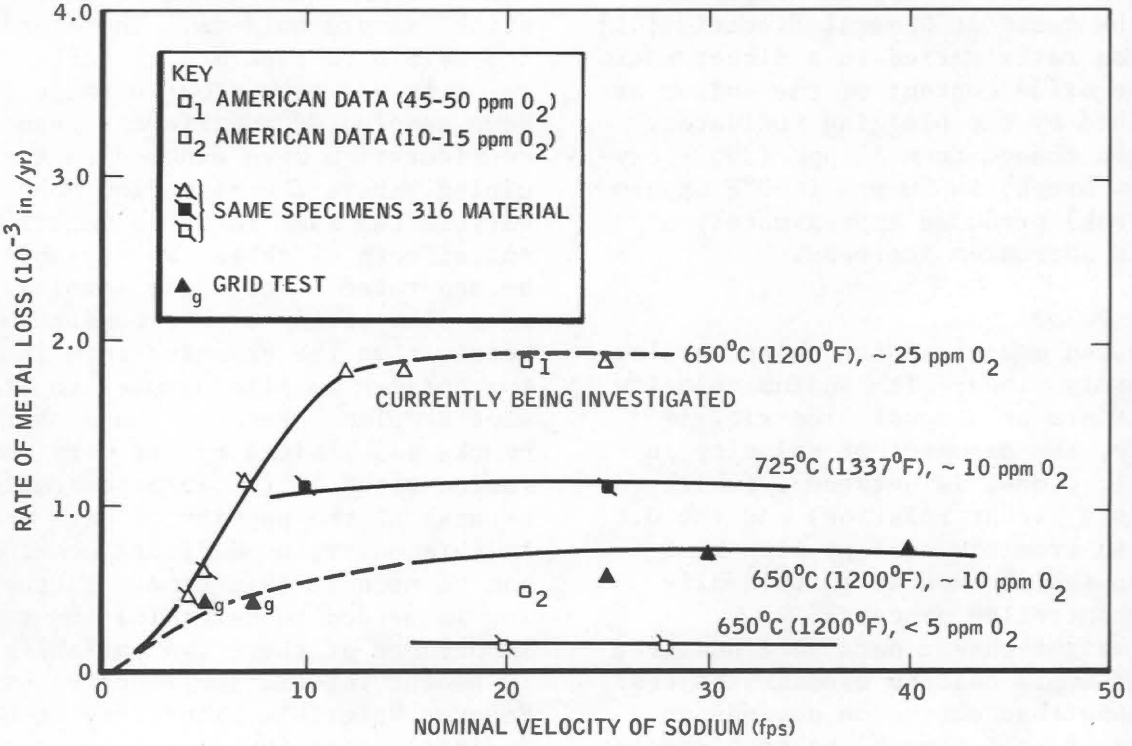

Fig. 2.100 - Effect of velocity on the rate of metal loss from various stainless steels (flow area constant).

processes limiting iron removal from the sodium in the cold leg, as discussed in Sec. 2-4.1.

Later work at General Electric, [101, 102] discussed in Sec. 2-4.2, tends to support the existence of an S-type curve to describe the corrosion rate-velocity relation, with corrosion rate becoming relatively insensitive to velocity at high velocities. Work at General Electric and at Culcheth is continuing in an effort to better define the velocity effect.

In contrast to that of austenitic stainless steel, the weight loss of the high-nickel Nimonic 80A depends on sodium velocity throughout the range investigated, i.e., up to 40 ft/sec; this implies sodium-film-diffusion control (see Fig. 2.89). [42]

(f) *Alloy-Constituent Concentration in Sodium*

An effect of mass-transfer rate dependent on location along an isothermal section of the sodium flow path has been noted. [42,45] At General Electric this was designated the "downstream effect," [45] and the effect was observed in all loop testing. The first test sample exposed at a given set of conditions always evidenced maximum corrosion or deposition. Samples located downstream at the same temperature showed progressively lower mass-transfer rates, whether weight loss (removal) or weight gain (deposition). Consequently a factor to account for this effect was included in Eqs. 2.11 and 2.12.

The effect is considered to be caused by the concentration of the particular alloy constituent in the bulk sodium stream at a given location in the piping system. The value of equilibrium solubility, S_0, in Eq. 2.9 is fixed by temperature. When the concentration of the constituent (solute) in the sodium stream, S, is low (the relative condition existing at the beginning of a

high-temperature, isothermal section of a system), the driving force (S_0 - S) for dissolution of the constituent is large. As the solute enters the sodium stream, S increases. As S approaches S_0 the driving force (S_0 - S) decreases, approaching zero. The decrease in the driving force with distance along an isothermal section in the hot leg of a heat-transfer system is taken to be the cause of the downstream effect. Decrease in oxygen content of the sodium as S increases with distance along the hot-leg isothermal section may also contribute to the downstream effect. A similar argument can be applied to the cold leg.

The existence of a downstream effect has been interpreted as indirect evidence that solute concentration around the loop stays relatively close to the saturation concentration at the highest temperature in the loop. In this case the cold-leg deposition rate would be the controlling step in metallic mass transfer. [103]

2-4.4 *Compositional Changes*

The extent of compositional changes in an austenitic stainless steel and in ferritic structural steels during an extensive sodium mass-transfer program was determined by Rowland et al., [45] who observed that:

1. In low-oxygen sodium (12 ppm), chromium, nickel, and manganese were removed from samples positioned in the hot leg.
2. In sodium at 1100°F containing higher oxygen concentrations (50 ppm), iron was selectively removed.
3. Regardless of oxygen concentration, the metallic constituents removed were deposited in the form of layers on the surfaces of cold-leg samples and also in the form of semi-adherent material.

These effects were developed for material samples exposed in dynamic sodium systems operated at 1100 and 1200°F. Oxygen levels of 12 and 50 ppm were maintained throughout the 23,000-hr exposure period. The structural materials evaluated included an austenitic stainless steel, 316, and two ferritic steels, 2 1/4 wt.% Cr-1 wt.% Mo and 5 wt.% Cr-1/2 wt.% Mo-1/2 wt.% Ti.

Regardless of material composition (austenitic or ferritic steel), the behavior patterns after exposure in low-oxygen sodium were similar in that the exposed surfaces had been depleted in chromium, nickel, and manganese and enriched in iron. The typical effect of temperature and exposure time on this behavior is reflected in the data presented in Fig. 2.101. It can be seen that the extent of chromium depletion from 316 stainless steel depends on time as well as temperature, although the latter apparently exerts the greater influence.

Corresponding to the depletion in the hot leg, samples positioned in the cold leg contained surfaces enriched in chromium, nickel, and manganese. Evidence typical of this buildup in the cold leg is shown in Fig. 2.102, where chromium is again used in the example. Note that in this case the cold-leg samples were a ferritic steel.

The effect of increased oxygen (from 12 ppm to 50 ppm) produced a different mass-transfer pattern (see Fig. 2.103). Material positioned in the 1100°F hot leg exhibited a preferential depletion of iron accompanied by an apparent increase in the chromium, nickel, and manganese levels. This behavior was independent of material composition, iron depletion being noted for the austenitic as well as for the ferritic steels exposed. However, a reversal in behavior was observed when the hot-leg temperature was increased to 1200°F with the oxygen level in the sodium maintained at 50 ppm. Instead of an iron depletion, the material evidenced a depletion in chromium similar to that obtained from the exposure in low-oxygen sodium.

It was postulated that the varied

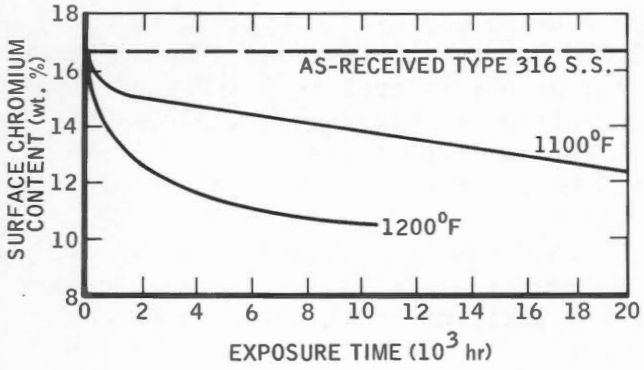

Fig. 2.101 - Surface chromium content vs. exposure time for hot-leg samples.

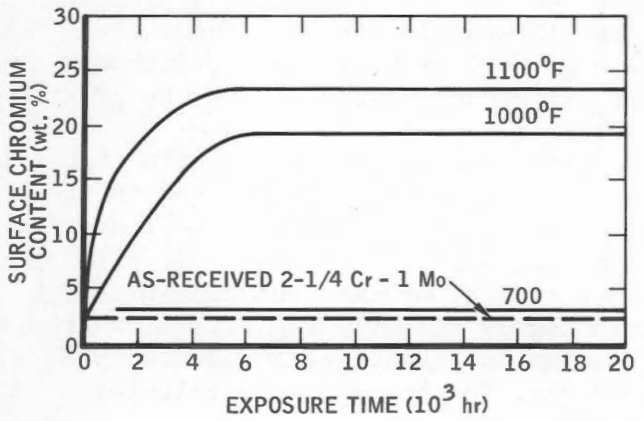

Fig. 2.102 - Surface chromium content vs. exposure time for cold-leg samples.

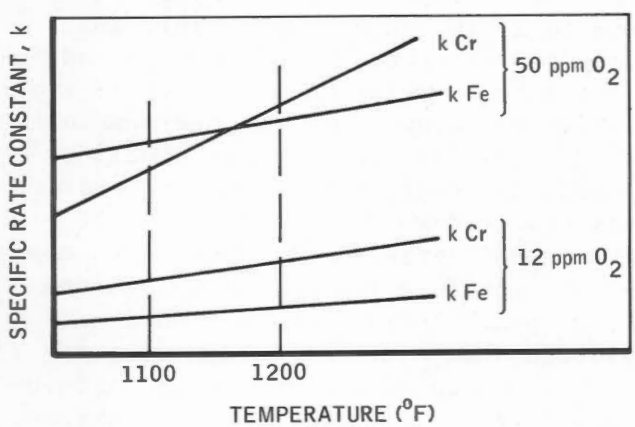

Fig. 2.103 - Elemental rate constant vs. temperature.

behavior caused by the temperature increase from 100°F to 1200°F is related to the initial nonlinear stage of corrosion. [104] During this nonlinear transient stage, elements corroding at greater than stoichiometric proportions show surface concentration decreases; conversely, those corroding in less than stoichiometric proportions show increased concentrations. The behavior of each alloy element depends on its specific rate constant, which could vary owing to the interaction of temperature and oxygen, as shown in Fig. 2.103. Thus the compositional variations in the high- and low-oxygen sodium established in the initial stage of corrosion would result.

A typical example of compositional changes for hot-leg material, determined by electron-microprobe techniques, is shown in Fig. 2.104. These graphical data show the concentration gradients developed in 316 stainless steel exposed in 1200°F, low-oxygen sodium for 5700 hr. The composition of unexposed material is included for reference.

Similar observations regarding the surface composition of 316 stainless steel exposed in sodium were developed by Nettley et al. [97] The surfaces of material exposed for three months at 650°C (1202°F) in sodium containing 25 ppm oxygen and six months at the same temperature in sodium containing 5 ppm oxygen were analyzed for iron, chromium, and nickel. Electron-microprobe examinations showed that the surfaces were depleted in chromium and nickel and correspondingly enriched in iron. The measurements at the surfaces indicated that the concentration gradient extended to a depth of 10 to 14 μ below the surface. Subsequent X-ray diffraction measurements of the surface layers indicated a ferritic structure, which was confirmed by additional measurements (magnetic permeability) indicating ferromagnetic character. This behavior pattern for 316 stainless steel is in close agreement with that developed by Rowland et al. [45]

Additional work is required to

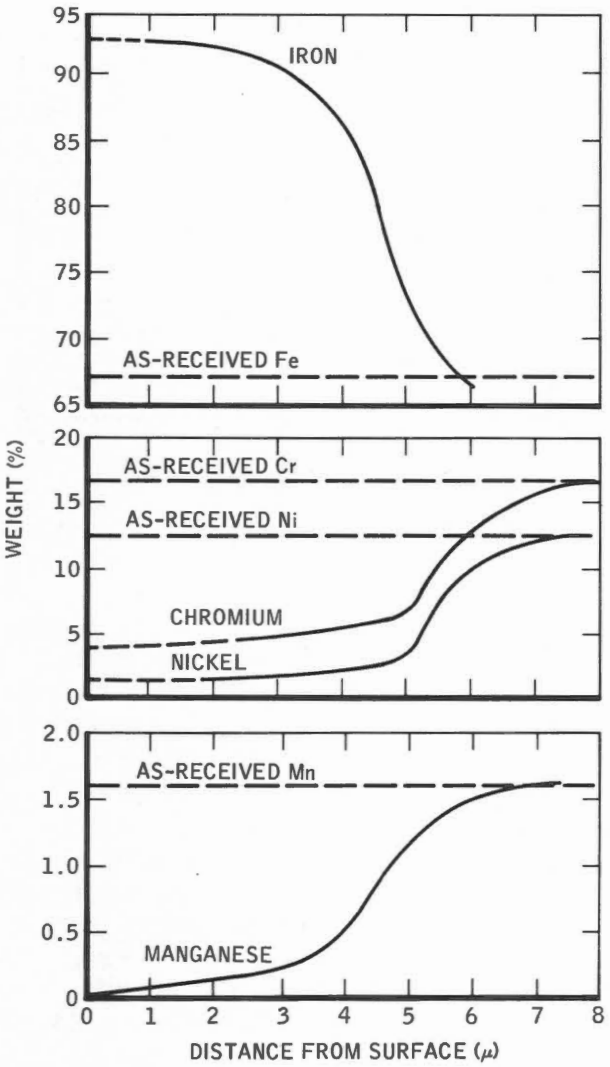

Fig. 2.104 - Compositional changes in 316 stainless steel measured by microprobe analysis after 5704-hr exposure at 1200°F. T_{max} = 1200°F. ΔT = 500°F. Oxygen = 12 ppm.

provide the designer with firm rules for predicting the growth of the ferritic layers in low-oxygen sodium with time. However, it seems likely that the rate of growth will ultimately be determined by parameters that control the diffusion of chromium and nickel through iron, after an initial allowance has been made for the corrosion of the ferritic layer by sodium.

2-5 CARBON TRANSFER

In sodium heat-transfer systems, carbon is present in the sodium as dissolved, particulate, or chemically combined carbon. It also occurs in varying forms and amounts in the containment materials that contact sodium. In most systems the initial thermodynamic activity of the carbon in the sodium is different from that in the contacting materials, and, because of the difference in activities, carbon exchange toward an equilibrium condition takes place. [33]

When metals or alloys with different carbon activities are in contact with sodium in the same system or when a single metal or alloy is in contact with sodium at different temperatures, carbon migrates via the sodium from regions with the higher carbon activity to those with lower activity. The carbon transfer tends toward an equilibrium activity at all surfaces in contact with the sodium. The resulting carbon concentrations may be very different from the original carbon levels.

2-5.1 *Decarburization of Cr-Mo Steels*

The low-alloy Cr-Mo steels are attractive for use in sodium-heated steam generators because of their low cost and relative freedom from susceptibility to water-side stress-corrosion cracking. There is adequate operating experience to recommend the 2 1/4 Cr-1 Mo steel for use up to 1000°F, but the steel decarburizes at a significant rate above this temperature. This decarburization has two undesirable effects. First, it causes the Cr-Mo steel to lose short-time tensile strength and reduces its stress-rupture life. Second, the carbon transferred to the sodium will carburize austenitic stainless steels in the system, with a resultant loss in ductility of the stainless steel.

The rate of decarburization depends on the temperature and on the carbon

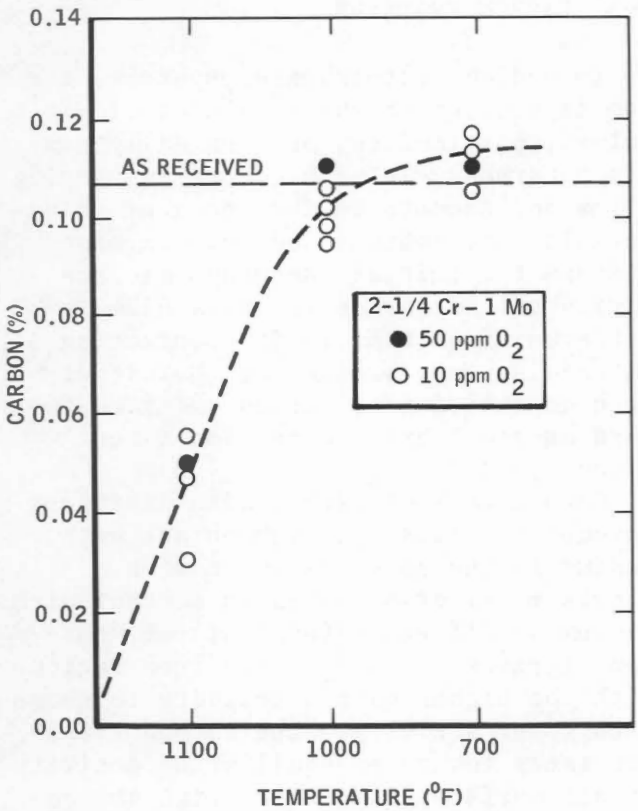

Fig. 2.105 - Decarburization of $2\frac{1}{4}$ Cr-1 Mo steel samples, 1/16 in. thick, exposed for 700 hr.

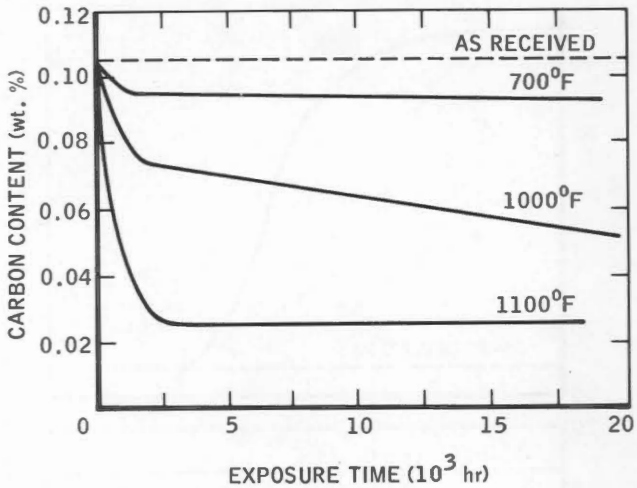

Fig. 2.106 - Decarburization of $2\frac{1}{4}$ Cr-1 Mo steel specimens 1/16 in. thick.

activity in the steel. Fig. 2.105 shows the carbon content of 2 1/4 Cr-1 Mo steel specimens 1/16 in. thick as received and after 700 hr exposure to flowing sodium at three temperatures. [105] The 1100°F specimens have lost more than half their original carbon. Figure 2.106 shows the carbon content of similar specimens exposed to flowing sodium for more than 19,000 hr. [106] Decarburization of the 1100°F specimens is essentially complete after 2500 hr. Definite, though slow, decarburization is taking place at the lower temperatures.

The loop piping in which the data of Fig. 2.106 were obtained was examined for carbon content at the end of the 20,000-hr run. A 2 1/4 Cr-1 Mo steel section operated at 1100°F was almost completely decarburized, although the material was twice as thick as the samples and was being decarburized from one side only. (Actually, the piping appeared to decarburize to the same lower limit of 0.025 wt.% C as the 1100°F samples of Fig. 2.106.)

Materials examination of a single-tube sodium-heated model steam generator showed [107] the same temperature-dependent decarburization of 1/2-in. tube and 1 1/4-in. pipe made of Croloy 2 1/4 that had been exposed to flowing sodium for 8000 hr at 630 to 1000°F. The 1000°F sample showed (metallographically) almost complete decarburization to a depth of 5 mils and partial decarburization to a depth of 25 to 30 mils. About 5 mils was machined from the sodium-exposed surfaces and analyzed for carbon by conventional combustion techniques. All the samples operated at 775 to 920°F lost carbon from this surface layer; only the lowest-temperature section (630°F) showed no significant change in carbon content.

No effect of oxygen content on decarburization rate was observed where the oxygen in the sodium was kept below 50 ppm (see Fig. 2.105). However, in the MSAR program to study the effects of high-temperature sodium on the

physical properties of austenitic and ferritic steels, sodium containing 300 ppm oxygen was found to decarburize 2 1/4 Cr-1 Mo steel faster than sodium with only 30 ppm oxygen. [19,4] Specimens cut from an 80-mil sheet were exposed to flowing sodium for times up to 5000 hr in tensile, fatigue, and stress-rupture tests. Figure 2.107 shows the carbon content of stressed specimens. More-rapid decarburization at the start is indicated in the high-oxide sodium although after 5000 hr exposure the percent of original carbon remaining is roughly comparable in both environments. The decarburization appeared to be partially responsible for the following observed effects:

1. Reduction of stress-rupture life below that of air and helium environments;
2. Further reduction of stress-rupture life of specimens exposed unstressed in sodium for 4000 hr before testing;
3. Increase in ductility, reduction in macrohardness and in microhardness.

The most critical effects were the decrease of rupture and creep strengths; the extrapolated 100,000-hr rupture strengths in both sodium environments were below the 60% ASTM average values, and the creep strengths were less than ASTM average values. The fatigue life was not adversely affected by either of the sodium environments.

Decarburization of Cr-Mo steels by sodium was prevented by adding a carbon stabilizer to the alloy's chemistry. Titanium, vanadium, niobium, and chromium have all been used successfully for this purpose. The strong carbide formers tie up the carbon as carbide more strongly than does the iron in the low-alloy steel, reducing the carbon activity in the stabilized steel to the point where no driving force remains to put the carbon in solution in the sodium.

Early work at Knolls Atomic Power Laboratory (KAPL) [108] showed that simply increasing the chromium content

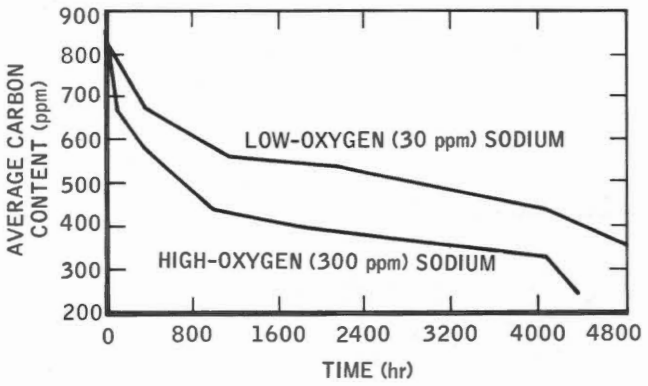

Fig. 2.107 - Decarburization of $2\frac{1}{4}$ Cr-1 Mo steel in 1100°F sodium.

of the Cr-Mo steel did not prevent decarburization at high temperatures. Steels with chromium contents of 1 to 12% showed no decarburization after one month in static and dynamic sodium at 930°F with oxygen contents ranging from 0.01 to 0.5%. But, when the steel with 12% chromium was tested for three months in static 1300°F sodium containing 0.01% oxygen, the decarburization was severe, averaging 0.04 mil/hour. Later work at ORNL with Croloy 9M (9% Cr, 1% Mo) showed very large losses of carbon in dynamic sodium at 1300 and 1450°F; carbon contents as low as 0.002% were recorded [109] after 2000 hr exposure.

Use of carbide stabilizers other than chromium has produced Cr-Mo steels resistant to decarburization at temperatures as high as 1200°F. The General Electric mass-transfer studies included 5 Cr-1/2 Mo-1/2 Ti stabilized steels in two loops, and no decarburization was noted in any of the test runs (up to 2800 hr at 1200°F). [45] A 2 1/4 Cr-1 Mo steel stabilized with niobium (10XC) was reportedly [110] free of carbon transport up to 1100°F.

In an investigation of the suitability of modified 2 1/4 Cr-1 Mo steels for sodium service, eleven modifications of the basic alloy were examined. [111] The modified alloys showed a substantial increase in decarburization resistance when tested for up to 3000 hr in dynamic sodium at 1200°F. The degree of

TABLE 2.61 - Decarburization Resistance of Modified Cr-Mo Alloys in 1200°F Sodium

Alloy	Composition, wt.%						Carbon		Exposure time, hr
	Cr	Mo	Nb	Ti	Ni	V	Before exposure	After exposure	
4S2	2.29	1.07		0.32			0.145	0.09	3000
4S1	2.30	1.07	0.40	0.47				0.18	3000
4S5	2.42	1.04	0.12	0.35			0.145	0.125	3000
7S1	5.05	1.03	0.46	0.38			0.155	0.18	2000
5S1	2.23	2.01	0.44	0.40			0.17	0.18	2000
5S2	2.33	1.03	0.42	0.40	1.3		0.16	0.16	2000
4S3	2.32	1.09	0.37				0.14	0.065	3000
4S7	2.18	0.94	0.73	0.01			0.16	0.145	2000
4S4	2.34	1.08				0.6	0.135	0.09	3000
4S8	2.23	0.99	0.10			0.6	0.14	0.105	2000
4S9	2.27	0.97	0.25			0.6	0.14	0.135	1500
2.25 Cr-1 Mo							0.11	0.045	3000
304 S.S.							0.065	0.08	2000

TABLE 2.62 - Mechanical Properties of Modified Cr-Mo Alloys

Alloy	Room temperature				1100°F		
	Yield, 10^3 psi	Tensile, 10^3 psi	Impact, ft-lb	Elongation, %	Yield, 10^3 psi	Tensile, 10^3 psi	Elongation, %
4S2	129	140	2	17			
4S1	93	106	2.75	16	64	67	15
4S5	97	119	2	19	80	86	18
7S1	82	92	4.5	19			
5S1	80	96	3.6	20			
5S2	83	97	6.5	19			
4S3	108	118	> 60	18	69	73	20
4S7	90	102	5	19			
4S4	94	111	101	24	64	70	19
4S8	91	107	>120	23	61	66	24
4S9	86	104	>120	24	54	59	23

increased resistance varied with the amounts of modifiers (Nb, Ti, V, Cr) added to the alloy (Table 2.61).

The short-time tensile properties shown in Table 2.62 at room and elevated temperatures appeared to be acceptable for high-temperature sodium applications for all the alloy modifications after the optimum heat-treating cycle had been established for each alloy. However, the room-temperature impact strengths of the titanium-bearing alloys were unacceptably low; the ductile-brittle transition temperatures were above room temperature. These seven alloys were therefore eliminated from

further testing in the development program, even though six of the seven were approximately neutral to carbon transfer in the 1200°F sodium tests. The four remaining alloys, modified with vanadium and/or niobium additions, had tensile properties comparable with the titanium-modified alloys and also had satisfactory impact strengths. The 4SE alloy, modified with niobium only, was eliminated from the program because its resistance to decarburization was inferior to that of the three vanadium-bearing alloys, which were subjected to further evaluation. The yield and ultimate tensile strengths from room temperature to 1300°F, the creep strength at 1100 and 1200°F, and the stress-rupture strength at 1000, 1100, and 1200°F were shown to be equal to or superior to those of annealed 304 stainless steel.

The decarburization behavior of these three V-Nb modified alloys is compared with that of the unmodified Cr-Mo steel in Fig. 2.108 for exposure in dynamic 1200°F sodium in a stainless loop. The equilibrium carbon concentration of the modified alloys is shown to be progressively raised with increasing additions of strong carbide-formers. The increase in decarburization resistance is attributed to the formation of niobium and vanadium carbides that resist resolution and effectively lower the carbon activity in the steel.

The effect of exposure in dynamic 1200°F sodium in a stainless loop on the ultimate tensile strengths of these three modifications is shown in Table 2.63. The progressive loss of strength with loss of carbon is much less for the V-Nb modified alloys than for the unmodified Cr-Mo standard.

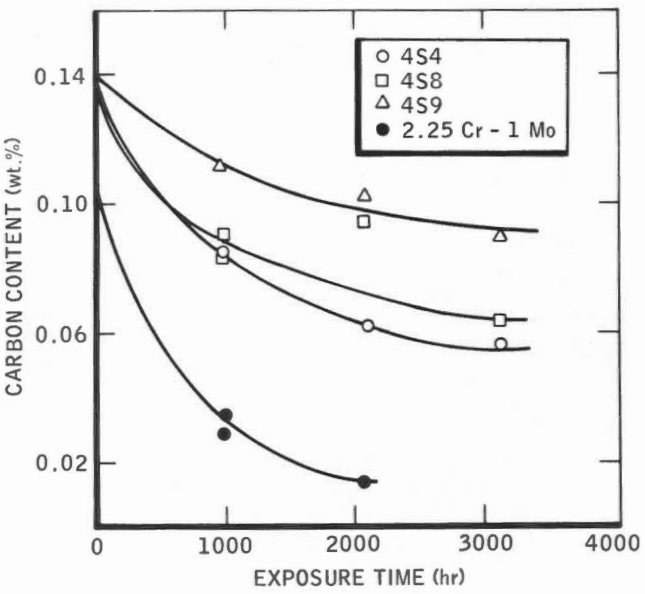

Fig. 2.108 - Decarburization of modified Cr-Mo steels in 1200°F dynamic sodium.

2-5.2 *Decarburization of Austenitic Stainless Steels*

In studying the creep-rupture properties of 304- and 316-stainless-steel tubing (10-mil wall) in high-purity static sodium, Lee [8] reported that the tubing was decarburized during the test. Zirconium foil had been placed in the sodium in the static-test retorts to getter oxygen from the sodium. The foil also acted as a sink for carbon transported from the stainless-steel tubing through the sodium bath. The carbon content of 304 stainless-steel specimens tested in 1400°F sodium was reduced from 0.06% to 0.03% (50% loss) and that of the 1300°F specimens was reduced from 0.06% to 0.04% (33% loss), both in less than 1000 hr. Chemical analysis of the zirconium foil showed an increase of carbon content from 0.01% before exposure to 0.33%. The average oxygen concentration in the sodium was below 10 ppm during the tests. The 316-stainless-steel specimens tested in 1350°F sodium showed a reduction in carbon content from 0.06% to 0.043% in less than 1000 hr.

The decarburization of the austenitic stainless steels reduced their creep-rupture strength by up to 25% as compared with tests in a helium environment.

TABLE 2.63 - Effects of 1200°F Dynamic Sodium Exposure on the Room-Temperature Tensile Strengths of Ferritic Alloys

Alloy	Exposure time, hr	Initial carbon, wt.%	Final carbon, wt.%	Room-temperature tensile strength,* psi	
				Before exposure	After exposure
2.25 Cr-1 Mo	1000	0.11	0.03		64,000
2.25 Cr-1 Mo	1000	0.11	0.036		64,600
2.25 Cr-1 Mo	2131	0.11	0.014		65,200
4S4	1000	0.14	0.085	108,000	79,700
4S4	1000	0.14	0.084	108,000	82,600
4S4	2131	0.14	0.061	108,000	73,500
4S4	3130	0.14	0.055	108,000	68,400
4S8	1000	0.14	0.09	100,800	87,500
4S8	1000	0.14	0.083	100,800	72,900
4S8	2131	0.14	0.093	100,800	81,000
4S9	1000	0.14	0.11	96,800	90,500
4S9	2131	0.14	0.099	96,800	79,000
4S9	3130	0.14	0.087	96,800	80,100

* Data from single specimen.

The effect on creep behavior is discussed in Sec. 2-2.2(b)(2). Decarburization also contributed strongly to the formation of sigma phase that was found randomly distributed across the 304-stainless steel samples tested at 1400°F. Carbon is a stabilizer of austenite and retards sigma formation. In general, sigma phase is not expected to occur in annealed 304 stainless steel even after long exposure to elevated temperatures, but it has been found in 304L stainless steel creep-tested at 1100 and 1500°F. Decarburization in Lee's tests in effect converted the 304 to 304L stainless steel, and sigma formation resulted.

2-5.3 *Carburization of Austenitic Stainless Steels*

The carbon level in austenitic stainless steel at equilibrium with carbon-saturated sodium was found [112] to be greater than the solubility of carbon in the alloy and greater than the dissolved carbon in equilibrium with the carbide phase. The surface carbon content of 304 stainless steel in equilibrium with carbon-saturated sodium is shown as a function of temperature in Fig. 2.109. The solubility of carbon in sodium containing appreciable amounts of oxygen is shown [113] as a function of temperature in Fig. 2.110. Later work using conventional combustion-analysis techniques and sodium with low oxygen content gave carbon solubilities an order of magnitude lower; radiochemical-tracer techniques gave very low solubility numbers, several orders of magnitude below the data of Fig. 2.110. However, the data of Fig. 2.110 are considered representative of the Na-C-O system, showing that the solubility of carbon in oxygen-contaminated sodium is much greater than in oxygen-free sodium at the same temperature. Data from several papers on carbon solubility in sodium are presented and discussed in Vol. I, Sec. 2-4.1(k).

Anderson and Sneesby [112] varied the carbon content of sodium while holding the temperature constant at 1200°F; the results are shown in Fig.

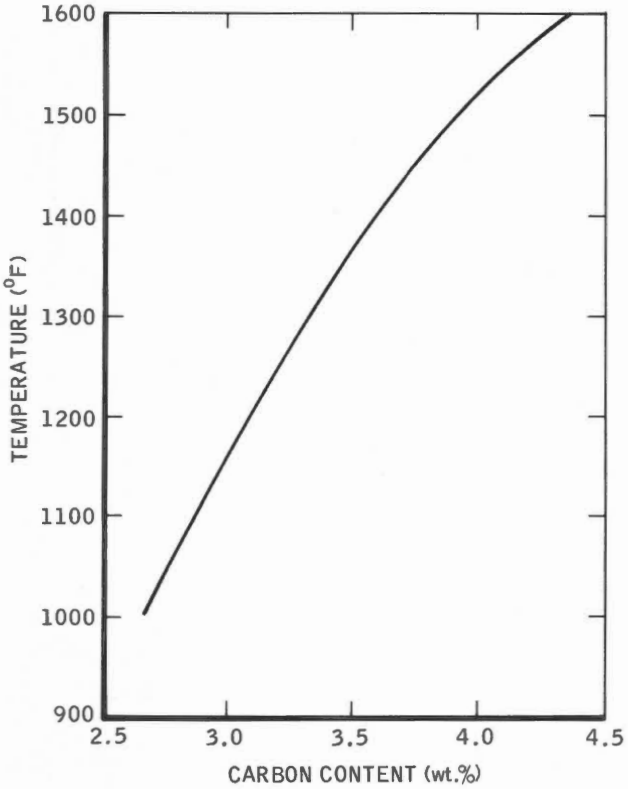

Fig. 2.109 - Equilibrium surface-carbon content of 304 stainless steel carburized in carbon-saturated sodium vs. temperature of exposure.

2.111. Even at very low values of carbon in sodium, surface carbon in the stainless steel rises sharply with a small increase in carbon in the sodium. If surface carburization of stainless components is to be kept to a minimum, carbon in the sodium must also be kept to a very low level, both at the time of purchase and during operation. The carbon content of normal austenitic stainless steels (0.04 to 0.08 wt.% C) would apparently be in equilibrium with 1200°F sodium containing 15 to 18 ppm C; raising carbon in the sodium to only 30 ppm would raise the equilibrium surface carbon content of austenitic stainless to over 1%.

In further calculations [112] of the diffusion rates of carbon in austenitic stainless steel from these results (Fig. 2.112), a straight line was drawn

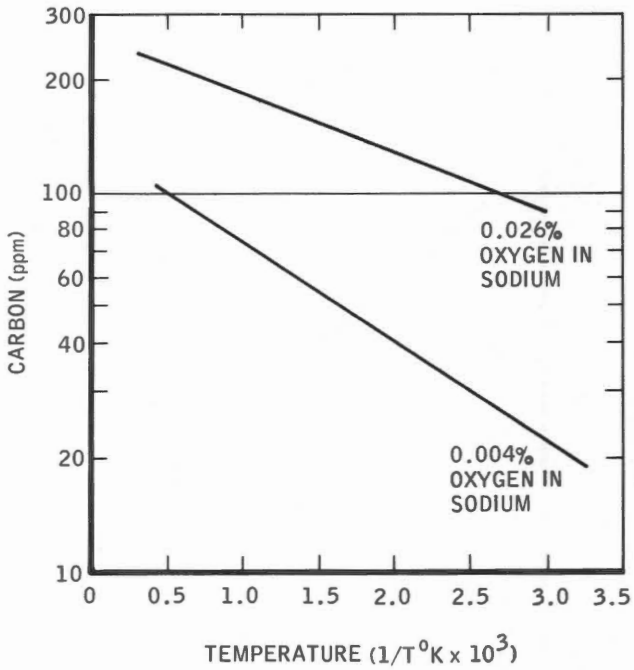

Fig. 2.110 - Solubility of carbon in sodium as a function of temperature for two oxygen levels.

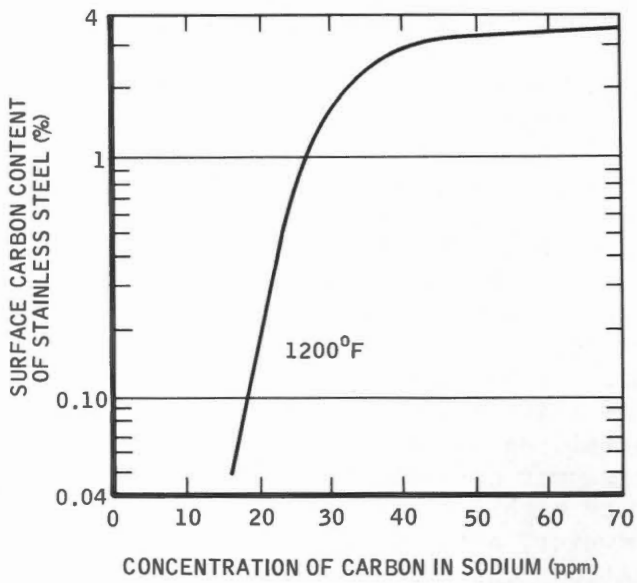

Fig. 2.111 - Equilibrium surface carbon in 304 stainless steel at varying concentrations of carbon in 1200°F sodium.

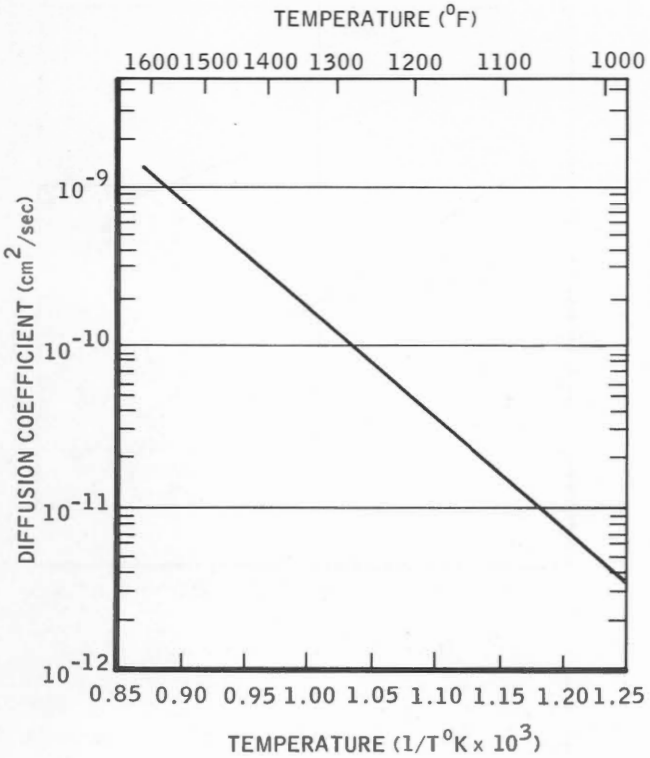

Fig. 2.112 - Diffusion coefficient of carbon in 304 stainless steel.

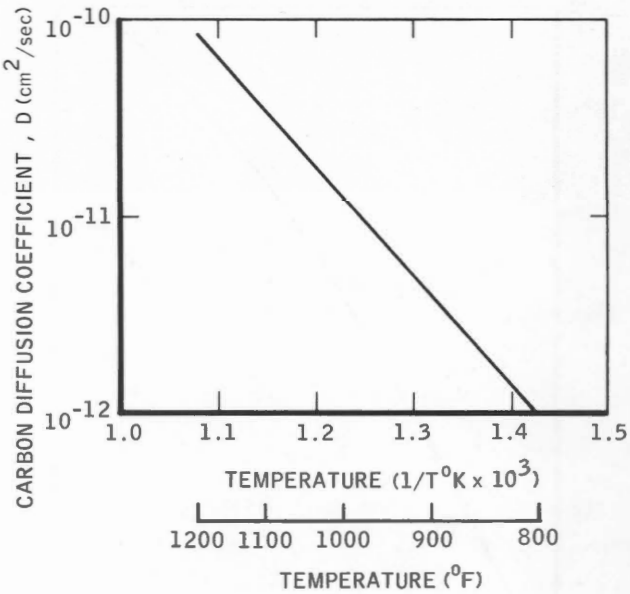

Fig. 2.113 - Diffusion coefficient of carbon in 316 stainless steel.

through the average values obtained by chemical analysis for carbon in specimens exposed at 1000 and 1200°F. Measurements of carbon-diffusion coefficients for 304 and 316 stainless steels, also determined empirically at 1200°F, [114] were in excellent agreement, 4.0×10^{-11} cm²/sec for 304 and 1.8×10^{-11} cm²/sec for 316 stainless steel. Later work [3] showed the coefficients to be even closer, that is, 3.2×10^{-11} cm²/sec for 304 and 2.9×10^{-11} cm²/sec for 316 stainless steel, again at 1200°F. This indicates a slower carburization rate for the more highly alloyed 316 stainless steel. However, a third series of carburization runs [106] carried out at 850 to 1050°F on only 316 stainless steel reported carbon-diffusion coefficients higher than either of the two previous studies (Fig. 2.113). This work demonstrated that 316 stainless steel will carburize at temperatures as low as 850°F in carbon-contaminated sodium.

Campbell and Tyzack [115] noted that the diffusion coefficient for carbon in stainless steel, derived empirically by Anderson and others as 3 to 4×10^{-11} cm²/sec at 1200°F, was much lower than the values of 11×10^{-10} cm²/sec determined by extrapolation of experimental results for diffusion of carbon in iron at higher temperatures. Their proposed model of the kinetics of carburization of stainless steel included the effects of carbide precipitation on the diffusion coefficient.

Their model assumed that at the specimen surface the equilibrium activity of carbon is set by the carbon activity of the sodium and that a carbon-activity gradient extends from the surface into the matrix of the steel, the growth of the carburized zone being controlled by the diffusion of carbon down the activity gradient. Within this carburized zone chromium-rich carbide was assumed to precipitate to bring the local level of dissolved chromium into equilibrium with the local carbon activity as required by the composition

of the carbide and the law of mass action. Using their model and Anderson's data, [112] Campbell and Tyzack calculated a diffusion coefficient of about 4×10^{-10} cm^2/sec at 1200°F. It was thought that the remaining difference between the calculated coefficient and that obtained by extrapolation of high-temperature data could be due to the effects of dissolved chromium in reducing the carbon-diffusion rate.

Andrews et al. [3] described the differences in carburizing behavior of 304- and 316-stainless-steel tabs in carbon-saturated sodium at 1200°F. Carbon penetration in both is first evidenced by an increase in grain-boundary carbide followed by general precipitation of fine carbides within the grains. The thickness of the case increases slowly with time, but the transition area between the case and the unaffected base metal maintains a reasonably constant thickness. For 60-mil-thick 316-stainless-steel tabs, the carbon level increased from an initial value of 480 to ∿8000 ppm after 5300 hr at 1200°F. Comparable exposure of 304-stainless-steel tabs resulted in carbon contents in excess of 10,000 ppm. The carbon-saturation level for thin tabs of 316 stainless steel was 3.5%, for 304, 3.8%. With long exposure and high carbon, there was some transformation of the 316-stainless-steel matrix to ferrite, but even at very high carbon contents the amount of ferrite was small. In 304 stainless steel, however, when carbon exceeded 1000 ppm, sufficient ferrite was formed to cause the tabs to be attracted by a simple magnet. At this carbon level ferrite was restricted to the surface, but at the highest carbon levels the ferrite was nearly the predominant phase.

Tensile specimens of 316 stainless steel were exposed [3] unstressed for 4000 hr to a high-carbon sodium environment at 1200°F. The specimens were then tensile tested in air at room temperature and in helium at 1200°F, along with control specimens exposed to helium at 1200°F for 4000 hr, to compare the effects of the environments on tensile strength. The results are shown in the bar charts in Fig. 2.114. The more-important conclusions are that unstressed exposure for 4000 hr in high-carbon sodium:

1. Reduced room-temperature tensile strength about 22% and increased 1200°F tensile strength about 20%;
2. Increased room-temperature yield strength 17% and increased 1200°F yield strength about 51%;
3. Reduced room-temperature elongation 98% and reduced 1200°F elongation 96%.

The exposure of 316 stainless steel to high-carbon sodium is not particularly detrimental to the tensile or yield strengths, but practically all the ductility is lost.

2-6 NITROGEN TRANSPORT BEHAVIOR

Although nitrogen is considered practically insoluble in sodium, nitriding of ferrous alloys, beryllium, and refractory-metal specimens completely submerged in sodium with nitrogen cover gas has been reported. Suggested mechanisms for transport of nitrogen from cover gas to metal include diffusion of dissolved nitrogen, entrainment, and transfer as calcium nitride (Ca_3N_2) formed with the calcium present as an impurity in the sodium.

Brush and Rodd [39] exposed 347-stainless-steel and beryllium specimens to 900°F sodium for one week in static capsules pressurized with enough nitrogen to give a pressure of 100 psig at test temperature. This was followed by a second one-month exposure of six materials in 1100°F, filtered sodium in a diffusion-cold-trapped static container pressurized with nitrogen to 10 psi, with nitrogen bubbled continuously through the sodium and bled to atmosphere. Test results given in Table 2.64 show that under these conditions 347 stainless steel nitrides at 900°F. The beryllium samples, which were

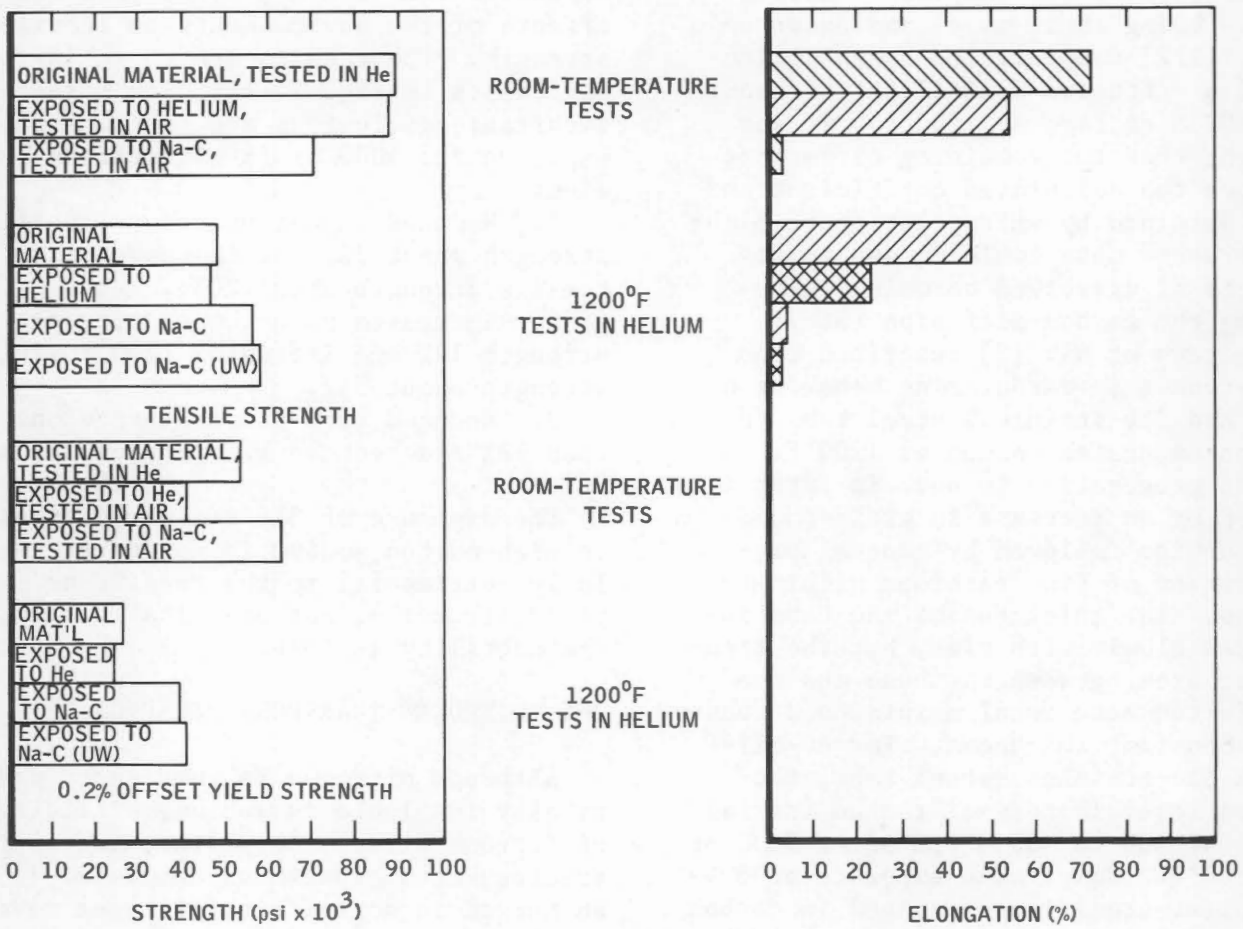

Fig. 2.114 - Tensile tests of 316 stainless steel after 4000-hr exposure in 1200°F high-carbon sodium. The abbreviation (UW) means not washed after exposure (all other samples were washed).

covered with a brittle film that flaked off during posttest cleaning procedures, suffered the severest nitriding. The lack of nitriding in the 2 1/4 Cr-1 Mo alloy and the fairly extensive nitriding in 410 stainless steel (12% Cr) were taken to be indicative of the role of chromium as a nitride former in promoting the nitriding reaction. The nitriding rate for beryllium, 347 stainless steel, and 18-4-1 tool steel was strongly dependent on temperature (more than doubling for a 100°F rise in temperature, so that the rate at 1100°F was more than 10 times the rate at 800°F).

The hardness of the nitrided layers was much lower than the hardness of a commercially nitrided steel, which is about 900 Knoop. This lower hardness was attributed to the relative thinness of the layer, to incomplete nitriding, and to the annealing effect of the longtime high-temperature exposure that may have allowed the nitrogen to diffuse from the surface layer into the bulk of the metal.

Wheeler [116] reported a continuation of this work in which specimens of 304 and 347 stainless steel, beryllium, and 18-4-1 tool steel were exposed to flowing nitrogen-covered sodium at 600 to 1100°F and 1/2 to 7 ft/sec. No nitrogen case was found on stainless- or tool-steel samples exposed to flowing sodium except on portions of the sample

TABLE 2.64 - Nitriding of Various Materials in Sodium Under a Nitrogen Cover Gas

Test	Material	Surface area, dm^2	Weight change (average of 3 specimens), mg	Thickness of nitride layer, mils	Knoop hardness		X-ray diffraction data
					Nitride layer	Base material	
Static-capsule tests	Be	0.072	+ 0.4*	None†			Film identified as Be_3N_2
900°F, 7 days; O_2 = 0.003 wt.%; Ca = 10 ppm	347 S.S.	0.074	+ 1.0	0.25	285	178	None taken‡
Static-container tests	347 S.S.	0.196	+ 9.0	0.4	243	182	None taken‡
1100°F, 30 days;	304 S.S.	0.163	+ 9.0	1.0	350	156	Layer identified as γCrN
O_2 = 0.003 wt.%;	410 S.S.	0.163	+18.0	2.25	263	154	Layer identified as γCrN
Ca = 10 ppm	2 1/4 Cr-1 Mo	0.163	0.0	None	155§	131	
	18-4-1 tool steel	0.102	+ 2.0	1.5	310	243	None taken‡
	6-6-2 tool steel	0.163	+ 7.0	1.5	277	212	None taken‡

*After descaling; film weight (per specimen) was 1.6 mg.

†No visible nitride effect on descaled surface, except remaining nitride film caught in narrow irregularities owing to incomplete descaling.

‡Structure similarity between this film and X-ray identified films, plus the increase in hardness, are taken as evidence that this film carries a nitride.

§Too small an increase to be significant in the absence of a visible film.

surface protected from the flow. It was assumed that the nitride case that adhered in static tests corroded away in dynamic tests and that all the metal loss observed was caused by removal of the nitride case as fast as it was formed. The mutually competing reactions of nitrogen pickup and corrosion loss made weight-change data unreliable, and the specimens were measured to determine metal losses. These data were extrapolated to predict a loss of 4 mils of thickness per surface in four years for 18-4-1 tool steel and 347 stainless steel in flowing 900°F sodium.

The effect of these sodium-produced nitride cases on mechanical properties of stainless steel was observed [116] by nitriding completely machined test specimens in static sodium to various case depths before testing at room temperature and at 850 and 1000°F. Results of the tensile tests are given in Fig. 2.115 as a function of the case depth. At temperatures up to at least 850°F, the strength, ductility, and strain-fatigue resistance of nitrided specimens were markedly below those of unnitrided specimens. The brittleness of the case produced surface cracks in the specimens at relatively low strains and the specimen behaved as a notched specimen. The severity of cracking increased with case thickness and decreased with temperature; cracking was practically absent at 1000°F. It was estimated that a 347-stainless-steel part nitrided to a depth of 5% of its thickness would have tensile strength reduced by 5%, ductility reduced by 50%, and cycles-to-failure in fatigue reduced by 95% (all at 850°F).

The results observed in these studies were confirmed in later work with 304 stainless steel. [117] Tubing specimens of 304 stainless steel were exposed to 1000°F sodium (10 ppm oxygen) flowing at 0.1 to 0.2 ft/sec and to the nitrogen cover gas. Specimens were examined metallographically at 660, 1140, and 1400 hr, with the results shown in Table 2.65.

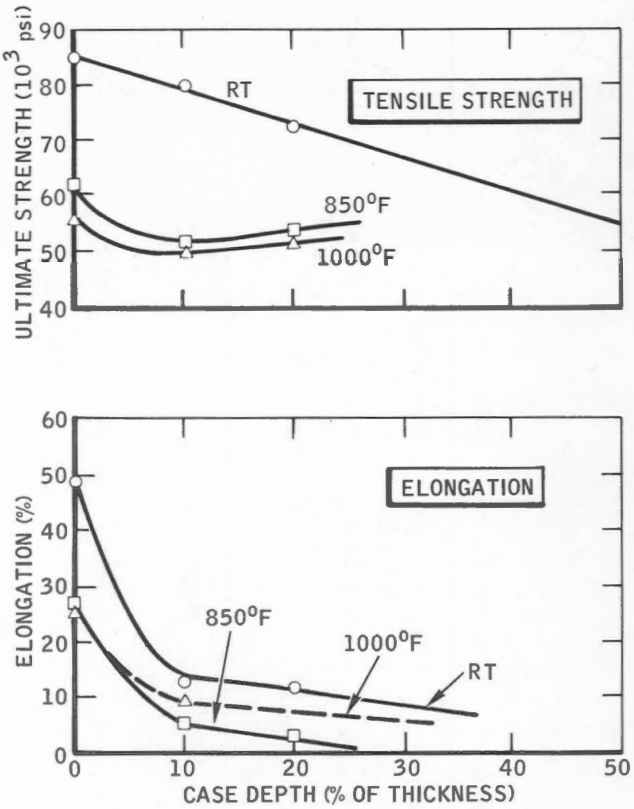

Fig. 2.115 - Effect of nitride case on mechanical properties of 347 stainless steel. Abbreviation RT is room temperature.

A very thin case formed after 1400 hr exposure on the specimens completely submerged 18 in. below the Na-N interface. The flow rate was apparently too low to remove the nitride case as it formed, as reported in Ref. 116; the results more closely compare with the static-exposure tests of Ref. 39. Mechanical test specimens 32 mils thick were nitrided with ammonia by standard commercial techniques to give a light case (1 to 2 mils) and a heavy case (4 to 6 mils), tensile tested at room temperature and at 500 and 1000°F, and stress-rupture tested at 1000°F to determine the effects of nitriding on 304 stainless steel. Results of the tensile tests are given in Table 2.66, and results of the stress-rupture tests are shown in Fig. 2.116. An increase in yield strength and a marked decrease in

TABLE 2.65 - Nitride-Case Thickness for 304 Stainless Steel Exposed to a 1000°F Na-N System

Exposure time, hr	Specimen position			
	Sodium side		Nitrogen side	
	Slightly below Na-N interface, mil	3 in. below Na-N interface, mil	Slightly above Na-N interface, mil	3 in. above Na-N interface, mil
660	0.9	0.1	None	None
1140	1.5	0.1	0.1	0.1
1400	2.0	0.3		0.4

TABLE 2.66 - Tensile Data for Nitrided 304 Stainless Steel

Temperature	As received	1- to 2-mil case	4- to 6-mil case
	Yield strength, psi		
Room	35,300	34,000	39,500
500°F	22,500	28,400	29,800
1000°F	18,800	26,900	29,800
	Ultimate strength, psi		
Room	93,100	74,000	60,000
500°F	67,900	53,500	41,600
1000°F	61,900	48,100	41,700
	Elongation, %		
Room	65.2	35.6	17.5
500°F	34.9	19.6	10.5
1000°F	32.8	18.3	6.5

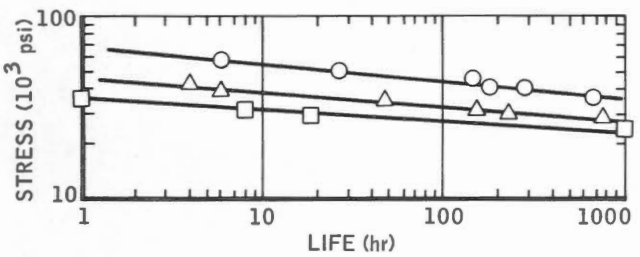

Fig. 2.116 - Stress-rupture data at 1000°F for nitrided 304 stainless steel. O, as received. Δ, 1- to 2-mil case. □, 4- to 6-mil case.

ultimate strength, ductility, and stress-rupture life were found in the nitrided specimens. At 1000°F and 40,000 psi, the stress-rupture life of an as-received specimen was 50 times that of the specimen with the light nitride case.

Experiments at Dounreay showed that niobium and vanadium will nitride when immersed in NaK under nitrogen cover gas if the temperature is high enough. [118] Nitriding of vanadium appeared to begin at about 400°C (750°F); samples picked up 600 ppm in six days. Niobium did not nitride at this temperature but did show signs of nitriding when

TABLE 2.67 - Effect of Mass Transfer of Carbon and Nitrogen on Room-Temperature Tensile Properties of Niobium* Tested in Sodium in 316-Stainless-Steel† Containers

Temperature, °F	Time, hr	Surface-area ratio of stainless steel to niobium	Change in concentration in niobium, ppm		Room-temperature tensile properties			
					Ultimate tensile strength, psi		Elongation in 2.5 in., %	
			Carbon	Nitrogen	Before test	After test	Before test	After test
1700	1000	0.1	+100	-20				
1700	500	6.5	+240	+ 660	22,800	48,200	17.5	5
1700	500	6.5	+420	+1920	22,800	46,200	17.5	11
1800	500	20	+790	+.860	22,800	50,400	17.5	6

*All specimens used in these tests were annealed for 2 hr at 1600°C in vacuum before exposure; specimens were 0.040 in. thick.

†18% Cr-13% Ni-2.5% Mo-1.8% Mn-0.06% C-0.03% N.

TABLE 2.68 - Carbon and Nitrogen Concentration of Niobium Specimen* Before and After Exposure in Sodium-316-Stainless-Steel System for 1000 hr at 1700°F

Specimen condition	Concentration, ppm	
	Carbon	Nitrogen
Before test	90	80
After test	510	2000
After surface layers machined off	150	590

*Specimens were 0.040 in. thick.

immersed for five days at 550°C (1020°F).

In refractory-metal-stainless-steel-sodium systems, the transfer of interstitial nitrogen from stainless steel to the surface of the refractory metal, which forms more stable nitrides, has been observed. [62] The system Nb-316 stainless steel-Na was investigated in detail at 1500 to 1800°F. The results shown in Table 2.67 indicate that time, temperature, and surface-area ratio (316 stainless steel to niobium) all affect nitrogen transfer. When the surface area was 1:10, no significant increase in nitrogen in the niobium was found; when the ratio was 6.5:1, nitriding of the niobium occurred, causing an increase in ultimate tensile strength and a decrease in ductility of the niobium. Metallographic and X-ray examination revealed two surface layers on the niobium, NbC and Nb_2N. Further studies showed that carbon was confined to the carbide surface layer but that nitrogen had diffused into the base metal, as shown in Table 2.68. Tensile tests on specimens with the surface layers of carbide and nitride removed gave results comparable with the as-exposed samples, indicating that nitrogen contamination in the bulk of the sample was responsible for the observed changes in tensile properties.

Other refractory-metal systems in which similar effects have been noted are Nb-1 Zr-K-Haynes 25 (or Hastelloy X) and Nb-1 Zr-Cs-Haynes 25.

Roberts, [119] testing nitrided tool steels in a sodium-lubricated friction-wear apparatus, reported high wear rates at 750 and 950°F. The initial surface hardness before the test was 700 to 800 VPN, but hardness measurements after the 100-hr runs showed a pronounced loss of hardness to about 200 VPN. It was concluded that the loss of the nitrided case was the result of a chemical reaction with the sodium.

REFERENCES

1. K.E. Horton, R.C. Andrews, R.C. Werner, and D.F. Atkins, The Effects of Sodium on the Metallurgical and Mechanical Properties of Candidate LMFBR Alloys, in *Alkali Metal Coolants,* Symposium Proceedings, Vienna, 1966, pp. 247-260, International Atomic Energy Agency, Vienna, 1967 (STI/PUB/143).

2. R.C. Andrews and K.R. Barker, *Effect of High Temperature Sodium on Austenitic and Ferritic Steels. Physical Properties of Materials. Topical Report No. 2. Results of Physical Property Tests of 316 SS Specimens in 1200°F Sodium with Low Oxygen,* USAEC Report MSAR-64-18, Mine Safety Appliances Research Corp., March 1964.

3. R.C. Andrews, R.H. Hiltz, L.H. Kirschler, S.J. Rodgers, and F. Tepper, *Effect of High-Temperature Sodium on Austenitic and Ferritic Steels. Topical Report No. 4. Results of Mechanical Properties Tests of 316 SS Specimens in 1200°F Sodium Contaminated with*

Carbon, USAEC Report MSAR-65-194, Mine Safety Appliances Research Corp., December 1965.

4. R.C. Andrews and L.H. Kirschler, *Effect of High-Temperature Sodium on Austenitic and Ferritic Steels. Topical Report No. 7. Design Properties of One Heat of 2 1/4 Cr-1 Mo Steel and 316 Stainless Steel in High-Temperature Air, Helium and Sodium Environments*, USAEC Report MSAR-66-174, Mine Safety Appliances Research Corp., Sept. 14, 1966.

5. R.C. Andrews, R.H. Hiltz, L.H. Kirschler, S.J. Rodgers, and F. Tepper, *Effect of High-Temperature Sodium on Austenitic and Ferritic Steels, Mechanical Properties of Materials. Topical Report No. 8. Results of Mechanical Properties Tests of 304 SS Specimens Conducted in: 1. 1200°F Sodium Contaminated with Oxygen (∿300 ppm); 2. 1200°F Sodium Contaminated with Carbon*, USAEC Report MSAR-67-103, Mine Safety Appliances Research Corp., July 1967.

6. R.C. Andrews, R.H. Hiltz, L.H. Kirschler, and R.J. Udavcak, *A Limited Comparison of the Relative Merits of 304 Versus 316 Stainless Steel for Liquid-Metal Service*, USAEC Report MSAR-67-216, Mine Safety Appliances Research Corp., December 1967.

7. V.S. Lyashenko, V.V. Zotov, and V.A. Ivanov, *Resistance to Corrosion of Austenitic and Ferrito-Pearlitic Steels in a Stream of Liquid Sodium at Temperatures of 600 and 700°C*, translated from IAEA Preprint No. CN-13/50 presented at the Conference on Corrosion of Reactor Materials, Salzburg, June 4-9, 1962, USAEC Report AEC-tr-5409.

8. W.T. Lee, *Biaxial Stress-Rupture Properties of Austenitic Stainless Steels in Zirconium-Gettered Sodium*, USAEC Report NAA-SR-12353, Atomics International, Oct. 1, 1967.

9. W.T. Lee, *Biaxial Stress-Rupture Properties of Austenitic Stainless Steels in Static Sodium*, USAEC Report AI-AEC-12694, Atomics International, June 30, 1968.

10. Atomics International, *Annual Technical Progress Report, AEC Unclassified Programs, FY 1968*, USAEC Report AI-AEC-12721, Atomics International, Feb. 15, 1969.

11. J.H. Shively, *Thermal-Gradient Effects on Stress-Rupture Behavior of Thin-Walled Tubing*, USAEC Report AI-AEC-12695, Atomics International, June 25, 1968.

12. V.I. Nikitin, Influence of Liquid Sodium on Relaxation of Stresses in Steel, *Zhidkie Metal. Sb. Statei* 1963.

13. V.I. Nikitin, Long-Time Strength of Steel in Liquid Sodium Containing Oxygen, *Fiz. Metal. Metalloved.*, *14*(4): 613-617 (1962).

14. V.I. Nikitin, Stress Rupture Test of Material in Liquid Metal Under Conditions of Mass Transfer, *Zavod. Lab.*, *30*(2): 213-215 (1964).

15. A. Thiruvengadam and H.S. Preiser, *Cavitation Damage in Liquid Metals*. Final Report. Report NASA-CR-72035, Hydronautics, Inc., Nov. 29, 1965.

16. R.C. Anstine, *The Combined Effects of Sodium Environment and Extended Life on Type 316 Stainless Steel and Croloy 2 1/4 Alloy Steel Design Stresses. Sodium-Heated Steam Generator Development*, USAEC Report BW-67-3, Babcock and Wilcox Co., September 1964.

17. H. Böhm and H. Schneider, Time to Failure and Creep Behavior of Austenitic Cr-Ni Steels in the Presence of Sodium, *J. Nucl. Mater.*, *24*: 188-197 (1967).

18. W.M. Robertson, Propagation of a

Crack Filled with Liquid Metal, *Trans. Met. Soc. AIME*, *236*: 1478-1482 (1966).

19. R.C. Andrews and K.R. Barker, *Effect of High-Temperature Sodium on Austenitic and Ferritic Steels. Physical Properties of Materials. Topical Report No. 3. Results of Physical Property Tests of 2 1/4 Cr-1 Mo Steel Specimens in Sodium with High and Low Oxygen, Air and Helium Environments at 1100°F*, USAEC Report MSAR-64-81, Mine Safety Appliances Research Corp., July 1964.

20. R.F. Koenig, Corrosion of Beryllium in Liquid Metals, in *The Metal Beryllium*, D.W. White, Jr., and J.S. Burke (Eds.), The American Society for Metals, Cleveland, Ohio, 1955.

21. W.D. Manly et al., *Aircraft Reactor Experiment - Metallurgical Aspects*, USAEC Report ORNL-2349, Oak Ridge National Laboratory, Jan. 9, 1958.

22. R.B. Oliver, D.A. Douglas, and J.H. DeVan, Effect of Environment on Creep Properties of High-Temperature Alloys, in *Papers Presented at ANP Materials Meeting, Nov. 16-18, 1954, Dayton, Ohio*, USAEC Report ORNL-2685, pp.17-34, Oak Ridge National Laboratory, Sept. 9, 1960.

23. D.A. Douglas et al., *Mechanical Properties Studies*, Aircraft Nuclear Propulsion Program Progress Report, Dec. 31, 1957.

24. C.P. Dykova and V.I. Nikitin, Influence of Liquid Sodium on the Long-Time Strength of Structural Materials, *Zhidkie Metal. Sb. Statei.* (1963).

25. H.J. Wagner and J. Prock, Jr., Where Soviet Super Alloys Stand, *Metal Prog.*, *91*(3): 75-78 (1967).

26. Argonne National Laboratory, *Reactor Development Program Progress Report, February, 1967*, USAEC Report ANL-7308, pp. 34-35, Mar. 28, 1967.

27. G.E. Raines, C.V. Weaver, and J.H. Stang, *Corrosion and Creep Behavior of Tantalum in Flowing Sodium*, USAEC Report BMI-1284, Battelle Memorial Institute, Aug. 21, 1958.

28. Argonne National Laboratory, *Reactor Development Program Progress Report, January 1966*, USAEC Report ANL-7152, p. 34, Feb. 24, 1966.

29. Argonne National Laboratory, *Reactor Development Program Progress Report*, November 1966, USAEC Report ANL-7279, pp. 32-35, Dec. 21, 1966.

30. E.E. Baldwin and F.W. Weisinger, *The Stress-Rupture Strength of Zirconium-Base Alloys Sodium at 1000°F (538°C)*, USAEC Report KAPL-M-FWW-1, Knolls Atomic Power Laboratory, Oct. 14, 1954.

31. L. Rosenblum and H. Putre, *Compatibility of Several Plastics and Elastomers with Sodium, Potassium, and Rubidium*, Report NASA-TN-D-1284, National Aeronautics and Space Administration, April 1962.

32. J.R. Weeks, Corrosion and Mass Transfer in Alkali Liquid Metal Systems, in *Materials Science and Technology for Advanced Applications*, p. 709, Prentice-Hall, Inc., Englewood Cliffs, N.J., 1962.

33. K. Goldmann and B. Minushkin, Sodium Technology, in *Reactor Technology. Selected Reviews*, L. E. Link (Ed.), USAEC Report TID-8541, Argonne National Laboratory, January 1966.

34. Charles F. Bonilla, Mechanisms in Liquid-Phase Corrosion. A. Diffusion Controlled, in *Proceedings of the NASA-AEC Liquid-Metals Corrosion Meeting, Volume I, Cleveland, Ohio, Oct. 2-3, 1963*, USAEC Report NASA SP-41, pp. 35-43, National Aeronautics and Space Administration, 1964.

35. Leo F. Epstein, Mechanisms in Liquid-Phase Corrosion. B. Solution Controlled, in *Proceedings of the NASA-AEC Liquid-Metals Corrosion Meeting. Volume I. Cleveland, Ohio, Oct. 2-3, 1963*, USAEC Report NASA SP-41, pp. 45-47, National Aeronautics and Space Administration, 1964.

36. J.R. Weeks, Heterometallic Phenomena, in *Proceedings of the NASA-AEC Liquid-Metals Corrosion Meeting. Volume I, Cleveland, Ohio, Oct. 2-3, 1963*, USAEC Report NASA SP-41, pp. 73-74, National Aeronautics and Space Administration, 1964.

37. D.H. Gurinsky, J.R. Weeks, C.J. Klamut, L. Rosenblum, and J.H. DeVan, Corrosion in Liquid-Metal Systems, *Proceedings of the Third International Conference on the Peaceful Uses of Atomic Energy, Geneva, 1964*, Vol. 9, pp. 550-560, United Nations, New York, 1964.

38. F.A. Comprelli, F.J. Hetzler, and T.A. Lauritzen, Clad Compatibility with Mixed-Oxide Fuel and Sodium, in *Proceedings of the Conference on Safety, Fuels, and Core Design in Large Fast-Power Reactors, Argonne, Ill., Oct. 11-14, 1965*, USAEC Report ANL-7120, pp. 355-373, Argonne National Laboratory.

39. E.G. Brush and C.R. Rodd, *Preliminary Experiments on the Nitriding of Reactor Materials in Sodium*, Report KAPL-M-EGB-21, Knolls Atomic Power Laboratory, Sept. 22, 1955.

40. D.M. Donaldson, Chemical Experience with the Dounreay Fast Reactor, paper presented at the Colloquium of the European Society of Atomic Energy on Liquid Metals, Aix-en-Provence, Cadarache, France, Sept. 30 - Oct. 2, 1963.

41. W.C. Hays, W.J. Anderson, P.E. Elkins, and D.L. Johnson, Materials for Sodium Graphite Reactors, in *Nuclear Metallurgy*, Vol. IX, pp. 275-277, IMD Special Report Series, No. 12, American Institute of Mining, Metallurgical, and Petroleum Engineers, New York, 1963.

42. A.W. Thorley and C. Tyzack, *The Corrosion Behavior of Iron and Nickel-Based Alloys in High-Temperature Sodium*, USAEC file No. NP-16413, United Kingdom Atomic Energy Agency, Oct. 17, 1966.

43. C. Tyzack, The Behavior of Materials in Liquid Sodium, in *Advanced Materials Inter-Disciplinary Symposium*, Third-Fourth Sessions of London, 1964, pp. 239-264.

44. C. Tyzack, Application of Sodium Chemistry in Fast Reactors, in *The Alkali Metals*, Symposium Proceedings, Nottingham, England, July 19-22, 1966, Special Publication No. 22, The Chemical Society, London, 1967.

45. M.C. Rowland, D.E. Plumlee, and R.S. Young, *Sodium Mass Transfer. XV. Behavior of Selected Steels Exposed in Flowing Sodium Test Loops*, USAEC Report GEAP-4831, General Electric Company, March 1965.

46. J.L. Jaech, E.L. Dunn, and K.B. Stewart, *Sodium Mass Transfer. XIV. Statistical Analysis of 1961 to 1964 Sample Weight-Change Data*, USAEC Report GEAP-4830, General Electric Company, October 1965.

47. L. Champeix, J. Sannier, R. Darras, W. Graff, and P. Juste, *Compatibility of Various Austenitic Steels with Molten Sodium*, translated from a paper presented at the Colloquium of the European Society of Atomic Energy on Liquid Metals, Aix-en-Provence, Cadarache, France, Sept. 30 - Oct. 2, 1963, USAEC Report AEC-tr-6328, Oak Ridge National Laboratory.

48. G. Ilincev, Corrosion Resistance of Stainless Chrome-Nickel Steels in Sodium as a Function of Its Oxygen Content, *At. Energ. (USSR)*, *14*(4): 375-382 (1963).

49. R.S. Young and R.W. Lockhart, General Electric Mass-Transfer Program, in *Proceedings of Sodium Components Development Program Information Meeting, Chicago, Ill., June 16-17, 1965*, USAEC Report CONF-650620, pp. 18-35, Chicago Operations Office (AEC).

50. Argonne National Laboratory, *Reactor Development Program Progress Report, January 1966*, USAEC Report ANL-7152, pp. 48-49, Feb. 24, 1966.

51. M. Davis and A. Draycott, *Compatibility of Reactor Materials in Flowing Sodium*, British Report IGR-TN/C-857, 1958.

52. J.M. McKee, *Removal of Oxygen from Sodium*, Report AFAPL-TR-66-27, United Nuclear Corp., April 1966.

53. J.H. Stang, E.M. Simons, J.A. DeMastry, and J.M. Genco, *Compatibility of Liquid and Vapor Alkali Metals with Construction Materials*, Report DMIC-227, Battelle Memorial Institute, Apr. 15, 1966.

54. T.L. Mackay, Oxidation of Zirconium and Zirconium Alloys in Liquid Sodium, *J. Electrochem. Soc.*, *110*(9): 960-964 (1963).

55. R.L. Eichelberger, Recent Information on Moderator Sheath Conversion in Liquid Sodium, in *Proceedings of the French-American Conference on Graphite Reactors, Upton, N.Y., Nov. 12-15, 1957*, USAEC Report BNL-489, pp. 168-173, Brookhaven National Laboratory.

56. Oak Ridge National Laboratory, *Metallurgy Division Semiannual Progress Report for Period Ending Apr. 10, 1956*, USAEC Report ORNL-2080, Nov. 2, 1956.

57. Oak Ridge National Laboratory, *Metallurgy Division Semiannual Progress Report for Period Ending Oct. 10, 1956*, USAEC Report ORNL-2217, Dec. 19, 1956.

58. Oak Ridge National Laboratory, *Metallurgy Division Annual Progress Report for Period Ending Oct. 10, 1957*, USAEC Report ORNL-2422, Dec. 13, 1957.

59. Oak Ridge National Laboratory, *Aircraft Nuclear Propulsion Project Quarterly Progress Report for Period Ending Mar. 31, 1957*, USAEC Report ORNL-2274 (Pts. 1-5), July 11, 1957.

60. F.L. Bett and A. Draycott, The Compatibility of Beryllium with Liquid Sodium and NaK in Dynamic Systems, in *Proceedings of the Second United Nations International Conference on the Peaceful Uses of Atomic Energy, Geneva, 1958*, Vol. 7, pp. 125-131, United Nations, New York, 1958.

61. W.W. Kendall, *Corrosion of Beryllium in Flowing Sodium*, USAEC Report GEAP-3333, General Electric Company, Jan. 15, 1960.

62. J.R. DiStefano and E.E. Hoffman, *Corrosion Mechanisms in Refractory Metal-Alkali Metal Systems*, USAEC Report ORNL-3424, Oak Ridge National Laboratory, Sept. 16, 1963.

63. A. Romano, A. Fleitman, and C. Klamut, *The Behavior of Refractory Metals and Alloys in Boiling Sodium and Other Boiling Alkali Metals*, USAEC Report BNL-10723, Brookhaven National Laboratory, 1966.

64. Argonne National Laboratory, *Annual Report for 1962, Metallurgy Division*, USAEC Report ANL-6677.

65. C.J. Lymperes, J.D. Chapman, and G.F. Schenck, *Interactions in a Type 316 Stainless Steel-NaK-Cb-1 Zr Alloy System*, USAEC Report TIM-896, Pratt and Whitney Aircraft, June 23, 1965.

66. S. Peterson (Comp. and Ed.), *Metals and Ceramics Division Annual Progress Report for Period Ending June 30, 1965*,

USAEC Report ORNL-3870, Oak Ridge National Laboratory, November 1965.

67. S. Greenberg, W.E. Ruther, and H.A. Levin, Corrosion of Vanadium - Base Alloys in Sodium at 550°C to 750°C, in *Alkali Metal Coolants*, Symposium Proceedings, Vienna, pp. 63-84, International Atomic Energy Agency, Vienna, 1967 (STI/PUB/143).

68. G.E. Raines, C.V. Weaver, and J.H. Stang, *Corrosion and Creep Behavior of Tantalum in Flowing Sodium*, USAEC Report BMI-1284, Battelle Memorial Institute, Aug. 21, 1958.

69. H.I. Bowers and W.E. Ferguson, *Structural Materials in LASL Liquid - Sodium Systems*, USAEC Report LADC-5783, Los Alamos Scientific Laboratory, November 1963.

70. D.H. Gurinsky, Sodium Corrosion Studies, in *Nuclear Engineering Department Annual Report, Dec. 31, 1964*, USAEC Report BNL-900, p. 139, Brookhaven National Laboratory.

71. J.W. Kissel, W.A. Glaeser, and C.M. Allen, Frictional Behavior of Sodium - Lubricated Materials in a Controlled High-Temperature Environment, *Wear*, 5: 446-457 (1962).

72. H. Pearlman, Corrosion of Uranium, Thorium, and Uranium Alloys in Sodium and Organics, in *Fuel Elements Conference, Paris, Nov. 18-23, 1957*, USAEC Report TID-7546, Book 2, pp. 565-587, Commissariat à l' Energie Atomique and Atomic Energy Commission.

73. E.E. Hoffman, *Compatibility of Dynamic Uranium - Sodium, Type 347 Stainless Steel System*, ORNL Corrosion Report No. 167, Oak Ridge National Laboratory, Sept. 16, 1957.

74. R.C. Shaw, *Hastelloy X-Type 316 Stainless Steel Forced - Convection Sodium Corrosion Loop Test, HXLM-3*, USAEC Report TIM-573, Pratt and Whitney Aircraft, Sept. 23, 1958.

75. R.C. Ellington, *Haynes Alloy No. 25 Forced - Convection NaK Corrosion Loop Tests NHHA-1A1, -2A2, -3B1 and -5B2*, USAEC Report TIM-654, Pratt and Whitney Aircraft, Apr. 26, 1961.

76. M.A. Perlow, *SNAP 2 Primary Coolant Development*, USAEC Report NAA-SR-6439, Atomics International, July 15, 1961.

77. E.E. Hoffman, P. Patriarca, C.F. Leitten, Jr., and G.M. Slaughter, *An Evaluation of the Corrosion and Oxidation Resistance of High-Temperature Brazing Alloys*, USAEC Report ORNL-1934, Oak Ridge National Laboratory, Nov. 7, 1956.

78. S.K. Lee, *An Investigation of Nickel - Base Brazing Alloys and Brazed Joints for Service in Liquid Sodium*, USAEC Report NAA-SR-11326, Atomics International, Dec. 15, 1965.

79. L.F. Epstein, Nonmetallic Solids. A. Ceramics (Thermodynamics). B. Graphite, *Proceedings of the NASA-AEC Liquid-Metals Corrosion Meeting. Volume I. Cleveland, Ohio, Oct. 2-3, 1963*, USAEC Report NASA-SP-41, pp. 75-81, National Aeronautics and Space Administration, 1964.

80. Nuclear Development Corp. of America, *Resistance of Barrier Materials to Sodium Jet Impingement*, USAEC Report NDA-084-4, Feb. 26, 1958.

81. S.C. Carniglia, Interactions of Graphite with Liquid Sodium, in *Proceedings of the French-American Conference on Graphite Reactors, Upton, N.Y., Nov. 12-15, 1957*, USAEC Report BNL-489, pp. 159-167, Brookhaven National Laboratory.

82. T.A. Coultas and R. Cygan, *Compatibility of Sodium, Graphite, and*

Stainless Steel, USAEC Report NAA-SR-258, North American Aviation, Inc., July 8, 1953.

83. W.J. Greening and W.A. Davis, *The Compatibility of Sodium and Graphite*, Report NAA-SR-M-1852, Atomics International, Mar. 1, 1957. (Internal distribution only).

84. J.F. Collins, NEPA Division of Fairchild Engine and Aircraft Company, Unpublished Memorandum on Stability of Ceramic Materials in Liquid Sodium at Temperatures up to 2000°F, Jan. 13, 1951.

85. J.J. Gill, *Sodium-Graphite Interaction and Graphite Protective Coatings*, USAEC Report NAA-SR-6094, Atomics International, May 1, 1961.

86. R.C. Asher and S.A. Wilson, Lamellar Compound of Sodium with Graphite, *Nature*, *181*: 409-410 (1958).

87. R.C. Asher, A Lamellar Compound of Sodium and Graphite, *J. Inorg. Nucl. Chem.*, *10*: 238-249 (1959).

88. R.H. Davidson, Moderator Element Failures in the Hallam Nuclear Power Facility, *Trans. Amer. Nucl. Soc.*, *8* (Suppl.): 35 (1965).

89. W.H. Cook, *Corrosion Resistance of Various Ceramics and Cermets to Liquid Metals*, USAEC Report ORNL-2391, Oak Ridge National Laboratory, June 15, 1960.

90. S.J. Basham, J.H. Stang, and E.M. Simons, Corrosion Screening of Component Materials for NaK Heat-Exchange Systems, *Chem. Eng. Progr., Symp. Ser.*, *55*(23): 53-60 (1959).

91. L.R. McCreight, Ceramics for Nuclear Power Applications, *Ind. Eng. Chem.*, *46*: 185 (1954).

92. W.D. Manly, *Fundamentals of Liquid-Metal Corrosion*, USAEC Report ORNL-2055, Oak Ridge National Laboratory, July 25, 1956.

93. E.E. Hoffman, Liquid Metal Corrosion, in *Corrosion Fundamentals Symposium*, A.S. Brasunas and E.E. Stansbury (Eds.), p. 78, University of Tennessee Press, Knoxville, Tenn., 1957.

94. J.H. DeVan, *Reactor Core Mater.*, p. 131 *1*(2): 28 (May 1968).

95. J.H. DeVan, Corrosion of Iron- and Nickel-Base Alloys in High-Temperature in Sodium and NaK, in *Alkali Metal Coolants*, Symposium Proceedings, Vienna, pp. 643-661, International Atomic Energy Agency, Vienna, 1967 (STI/PUB/143).

96. J.W. Mausteller and E.F. Batutis, *Effect of Oxygen on the Mass Transport of Stainless-Steel Components in Sodium*, USAEC file No. NP-5583, Mine Safety Appliances Co., Mar. 16, 1955.

97. P.T. Nettley, I.P. Bell, A.W. Thorley, C. Tyzack, K.Q. Bagley, and D.R. Harries, Problems in the Selection and Utilization of Materials in Sodium Cooled Fast Reactors, in *Fast Breeder Reactors*, Conference Proceedings, London, May 17-19, 1966, pp. 825-849, Pergamon Press, Inc., New York, 1967..

98. G.W. Horsley, *J. Iron Steel Inst.*, *182*: 43 (1956).

99. E.L. Zebroski, R.S. Young, F.A. Comprelli, and D. Dutina, Effects of Mass Transfer, and of Changes in Properties, on Austenitic Steels in Flowing Sodium, in *Alkali Metal Coolants*, Symposium Proceedings, Vienna, 1966, pp. 195-211, International Atomic Energy Agency, Vienna, 1967 (STI/PUB/143).

100. E.L. Dunn, *Sodium Mass Transfer. VI. Statistical Correlation of 1961-1962 Corrosion Data*, USAEC Report GEAP-4183, General Electric Company, July 1963.

101. R.S. Young, *Sodium Components Development Program, Mass Transfer Investigations in Liquid-Metal Systems. Quarterly Progress Report No. 1, March-May 1967*, USAEC Report GEAP-5508, General Electric Company, June 1967.

102. General Electric Company, *Sodium Components Development Program Mass Transfer Investigations in Liquid-Metal Systems. Quarterly Progress Report No. 2, June-August 1967*, USAEC Report GEAP-5546, September 1967.

103. J.R. Weeks, C.J. Klamut, and D.H. Gurinsky, Corrosion by the Alkali Metals, in *Alkali Metal Coolants*, Symposium Proceedings, Vienna, 1966, pp. 3-23, International Atomic Energy Agency, Vienna, 1967 (STI/PUB/143).

104. E.G. Brush, *Sodium Mass Transfer. XVI. The Selective Corrosion Component of Steel Exposed to Flowing Sodium*, USAEC Report GEAP-4832, General Electric Company, March 1965.

105. R.W. Lockhart and G. Billuris, Materials Selection Considerations for FCR and SEFOR, *Nuclear Metallurgy*, Vol. IX, p. 207, IMD Special Report Series, No. 12, American Institute of Mining, Metallurgical, and Petroleum Engineers, New York, 1963.

106. D.E. Plumlee, R.W. Lockhart, L.E. Pohl, and T.A. Lauritzen, *Sodium Mass Transfer. XVIII. Extended Studies of Carbon Movement in Pumped Sodium Test Loops*, USAEC Report GEAP-4834, General Electric Company, June 1965.

107. D.W. Koch and P.J. Kovach, *Materials Examination of a Model Sodium-Heated Steam Generator*. Final Report. Research Report No. 5136, USAEC Report BAW-1280-37, Babcock and Wilcox Co., June 30, 1966.

108. E.G. Brush and R.F. Koenig, *Evaluation of Ferritic Substitutes for the Austenitic Stainless Steels. I. Resistance to Attack by Sodium*, USAEC Report KAPL-1103, Knolls Atomic Power Laboratory, Apr. 22, 1954.

109. H.W. Savage, E.L. Compere, W.R. Huntley, B. Fleischer, R.E. MacPherson, and A. Taboada, *SNAP 8 Corrosion Program Summary Report*, USAEC Report ORNL-3898, Oak Ridge National Laboratory, December 1965.

110. J. Motz, Investigation of Several Ferritic Steels for High-Temperature Service and Their Applicability in Sodium Systems up to Temperatures of About 600°C, *Z. Metallk.*, *55*: 489 (1964).

111. W.J. Anderson, G.S. Sheffield, and A.J. Birkle, *Development of Ferritic Steels for High-Temperature Sodium Service. Part III*, USAEC Report NAA-SR-7544, Atomics International, Nov. 30, 1963.

112. W.J. Anderson and G.V. Sneesby, *Carburization of Austenitic Stainless Steel in Liquid Sodium*, USAEC Report NAA-SR-5282, Atomics International, Sept. 1, 1960.

113. J.G. Gratton, *Solubility of Carbon in Sodium at Elevated Temperatures*, USAEC Report KAPL-1807, Knolls Atomic Power Laboratory, June 30, 1957.

114. Mine Safety Appliances Research Corp., *Effect of High-Temperature Sodium on Austenitic and Ferritic Stainless Steels. Physical Properties of Materials. Progress Report No. 44*, USAEC Report MSAR-64-51, May 15, 1964.

115. C.S. Campbell and C. Tyzack, A Preliminary Model for the Carburization of Stainless Steel at High Temperature in Sodium Containing Carbon at Unit Activity, in *Alkali Metal Coolants*, Symposium Proceedings, Vienna, 1966, pp. 159-170, International Atomic Energy Agency, Vienna, 1967 (STI/PUB/143).

116. G.C. Wheeler, *The Effect of Nitro-*

gen - Covered Sodium on S2G Structural Materials, USAEC Report AECU-3656, Knolls Atomic Power Laboratory, Mar. 21, 1957.

117. J.J. Gill and J.C. Bokros, *Nitriding of Type 304 Stainless Steel in a Sodium-Nitrogen System*, USAEC Report NAA-SR-6162, Atomics International, May 30, 1961.

118. V.M. Sinclair, R.A.H. Pool, and A.E. Ross, Impurities in a Liquid-Metal Coolant and Their Effect on the Fuel-Element Canning Materials Niobium and Vanadium, *Nuclear Reactor Chemistry, Second Conference, Gatlinburg, Tenn., Oct. 10-12, 1961*, USAEC Report TID-7622, pp. 35-36, Oak Ridge National Laboratory.

119. W.H. Roberts, Friction and Wear Behavior of Possible Bearing Materials in High-Purity Liquid Sodium at Temperatures Up to 500°C, in *Non-Conventional Lubricants and Bearing Materials Such as Used in Nuclear Engineering. Proceedings of the First Annual Meeting of the Lubrication and Wear Group, Manchester, England, April 12, 1962*, p. 22, The Institute of Mechanical Engineers, London, 1962.

Chapter 3
Heaters and Coolers

Principal Author: E. N. PEARSON

Contributing Authors: J. SUSNIR, R. S. BAKER, and E. LARSEN

3-1 INTRODUCTION

This chapter is concerned with the uses, design, and operating experience of sodium-NaK heaters and coolers. The sodium-NaK cooler, a type of liquid-metal heat exchanger, is sometimes referred to as a radiator. (This is not to be confused with the radiators for space applications discussed in Chap. 4.) Therefore in this chapter [specifically in Sec. 3-2.9(a)] the words cooler, heat exchanger, and radiator will be used interchangeably.

Heaters used to preheat or to maintain sodium temperature in piping, pumps, and heat exchangers are discussed in Vol. IV, Chap. 5, and are therefore not presented here.

Sodium-NaK coolers can be categorized as follows:

1. Liquid metal to air. In a liquid-metal system, this cooler functions as a heat sink either in an experimental loop or in a reactor plant, in place of or in conjunction with the production of steam and electricity. Reactor plants are sometimes designed and operated with a liquid-metal cooler serving as an emergency safety or backup device. The Aircraft Reactor Experiment (ARE) used a liquid-metal cooler to preheat engine air.
2. Liquid metal to nonmetallic fluids.

Fossil-fueled and electrical sodium-NaK heaters are discussed.

3-2 LIQUID-METAL-TO-AIR COOLERS

3-2.1 *General Information*

Gas-cooled liquid-metal heat exchangers have been used almost exclusively with air as the cooling medium. The liquid metal flows inside the tubes, and air flows across the exterior tube surfaces.

Air-cooled heat exchangers (nonmetallic fluid-to-air) are being used increasingly by the chemical and power-plant industries. Many of the techniques developed can be used in liquid-metal-to-air coolers after the effects of the higher temperature of liquid metals have been thoroughly evaluated.

3-2.2 *Heat Transfer and Pressure Drop*

The design of an air-cooled liquid-metal heat exchanger is concerned with:

1. Heat transfer.
   a. Tube-side film coefficient.
   b. Tube-wall conduction.
   c. Air-side or fin-side heat transfer.
2. Fluid flow.
   a. Tube-side flow distribution and pressure drop.
   b. Air-side or fin-side flow distribution and pressure drop.

Kern [1] presents a complete chapter on the design of units with extended surfaces. In general, the calculational techniques and typical applications are for hot fluids at temperatures no greater than 400°F. At the 1964 American Society of Mechanical Engineers [2] (ASME) Symposium on Air-Cooled Heat Exchangers eleven papers dealing with technical and economic aspects of air-cooled heat exchangers were presented. Emphasis was on relatively low-temperature (400°F or less) coolers. Several other recent papers [3-6] present information on cooler optimization and elliptical-tube construction. [4]

This section is limited to discussion of units with transverse or perpendicular fins on the exterior of the tube. This type is most commonly required and used for air-cooled liquid-metal coolers. Space radiators (Chap. 4) have an entirely different construction principle, in which forced convection plays no part. Their radiating fins are longitudinal, whereas the coolers (radiators) discussed here have fins that are transverse or perpendicular to the tube.

The heat-transfer design of an air-cooled heat exchanger begins with the relation

$$q = UA\,(\Delta t)_{lm} \tag{3.1}$$

where

$$U = \frac{1}{(1/h_i) + (x/k) + (1/h_o)} \tag{3.2}$$

where A = heat-transfer area
U = overall heat-transfer coefficient
$(\Delta t)_{lm}$ = logarithmic-mean temperature difference
q = rate of heat transfer
h_i = heat-transfer coefficient on inside surface
h_o = heat-transfer coefficient on outside surface
k = thermal conductivity of wall material
x = thickness of wall

Equation 3.2 is true for plane surfaces and can be applied to curved surfaces if the wall thickness is small compared to the radius of curvature.

The increased exterior surface area of the fin tubes must be considered; this can be done by defining the overall heat-transfer coefficient (neglecting radiation):

$$U = \frac{1}{(1/h) + (A/A_i)[(1/h_i) + (x/k)]} \tag{3.3}$$

where A is the total outer surface of finned tube, A_i is the inner surface of tube, and h is the apparent surface coefficient of finned surface. Assuming $h_f = h_o$, the apparent heat-transfer coefficient for the finned surface, h, can be expressed as

$$h = h_f\left[1 - (1 - \eta_f)\frac{A_f}{A}\right] \tag{3.4}$$

where η_f = fin efficiency (values for various fin configurations are found in Refs. 1 and 7.)
A = total outside surface area (base plus fin)
A_f = surface area of fins
h_f = heat-transfer coefficient of fins
h_o = heat-transfer coefficient on outer surface of tubes

Equations 3.3 and 3.4 should be qualified in three areas: (1) The heat-transfer coefficient U is based on the outer surface area, (2) radiant heat transfer is not considered, and (3) contact resistance between the fins and the tubes is not considered here (see Ref. 8).

The assumption in the Eq. 3.3 derivation is that the exterior h is uniform everywhere. This is generally not rigorously correct. [6] When a radiation heat-transfer coefficient h_r is added, the variation in h becomes more significant. Not only is the h_r between fins much less than h_r from the tube surface but, depending on the number of tube passes across the air stream, the values of h_r for the lower and upper tube rows (assuming the liquid metal is flowing essentially horizontally in a multipass arrangement) could be significantly different.

An effective h_r can be derived based on area weighting of the tube and fins. This is added to the convective film coefficient h_f. Chambers and Somers [9] present a theoretical analysis of radiant heat transfer from annular fins.

It has been only recently that radiation from fins has received much attention. [10] In 1963 Cobble [11] found the temperature of a fin transferring heat by forced convection and radiation. Therefore much remains to be done in this area before meaningful design information is developed.

After the correct expression for the overall heat-transfer coefficient is formulated, the individual film coefficients must be evaluated on the basis of reliable empirical correlations.

The tube-side liquid-metal heat-transfer coefficient can be obtained from correlations in Vol. II, Chap. 2. The Lubarsky-Kaufman equation [12] (see Vol. II, Chap. 3) is a frequently used correlation for the tube-side liquid-metal heat-transfer coefficient:

$$\mathrm{Nu} = 0.625\ \mathrm{Pe}^{0.4} \qquad (3.5)$$

Other correlations by Dwyer [13] (see Vol. II, Chap. 2) and Skupinski [14] are also used. The Lubarsky-Kaufman equation appears to give conservative estimates of Nu, and Dwyer's correlation tends to give the highest values of the correlations now used. Skupinski's equation,

$$\mathrm{Nu} = 4.82 + 0.0185\ \mathrm{Pe}^{6.827} \qquad (3.6)$$

tends to give an average value of Nu, based on results obtained from a number of experiments.

The convection coefficient on the fin side is a function [4] of

$$h_f = g(A_O/A, S/l, V_{\mathrm{air}}) \qquad (3.7)$$

where A_O/A is the ratio of outer surface area of bare tube to total outer surface area of fin tube and S/l is the ratio of fin pitch to fin height.

One correlation [5] used is

$$\mathrm{Nu} = 0.28\ \mathrm{Re}^{0.6}\ \mathrm{Pr}^{0.33} \qquad (3.8)$$

where d is the Nu and Re is the tube outer diameter. This equation is for air outside finned tubes in a staggered close-pitched arrangement. Lohrisch [5] further simplified Eq. 3.8 to obtain the film coefficient in terms of pressure drop and number of tube banks. For air [5] between 60 and 300°F,

$$h = 9.55\ (\Delta p/n)^{0.343}\ (1/d^{0.4}) \qquad (3.9)$$

where Δp is pressure drop in inches of water, n is number of tube rows, and d is root diameter of tube in feet.

Figure 3.1 illustrates specific heat duty for elliptical and circular tubes. Average design air velocity (face velocity) for air-cooled heat exchangers was stated [5] to be 675 ft/min (approximately 11 ft/sec). An increase in air velocity increases the heat-transfer coefficient but also the

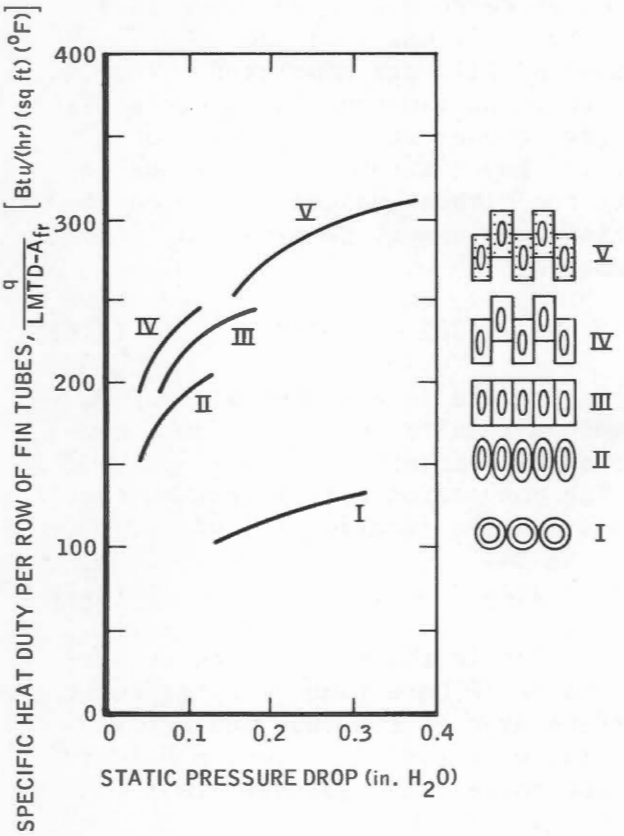

Fig. 3.1 Specific performance of some fin-tube heat-exchanger rows. [From F.J. Schulenberg, Finned Elliptical Tubes and Their Application in Air Cooled Heat Exchangers, *Trans. ASME (Amer. Soc. Mech. Eng.), Ser. B: J. Eng. Ind.*, 179-190, May 1966.]

pressure drop and power requirements of the fan. Various techniques and methods of optimization are presented in Refs. 3 to 6. Here again, note the differences between standard commercial air coolers and the higher temperature liquid-metal coolers.

Airflow distribution is of concern, particularly if a significant amount of air is bypassing or leaking around the tube bundle; this causes ineffective airflow and heat-transfer performance.

The vibration characteristics of the tube bundle and cooler structure must be evaluated. Vibration caused by airflow can be prevented by proper design techniques based on analysis and test. Cohan and Deane, [15] Chester, [16] and Cantes and Johnson [17] presented valuable boiler-flow and vibration studies. Heat-exchanger noise and vibration were also investigated. [18]

Liquid-metal pressure drop can be handled by the standard incompressible flow techniques presented in Vol. II, Chap. 1. Since the cooler will have a number of parallel tubes between inlet and outlet headers, parallel-flow networks are involved. Thus nonuniform flow distribution between tubes must be considered.

Both liquid-metal-flow and airflow distribution can lead to thermal-stress problems [see Sec. 3-2.9(a)].

A final point to be considered is freezing of the liquid metal in local areas. This may be caused by low liquid-metal flow combined with low inlet temperature or by low ambient temperature. Freezing of the liquid metal is only an inconvenience; however, remelting or liquefying the solid sodium requires rigid safety considerations because of volumetric expansion. Remelting must begin at a free surface, a requirement that is not always practical.

The air temperature for which the unit is designed must be realistic. Kassat [19] presented data for a specific location showing a probability curve of ambient temperature. An air temperature covering 95% of all operating hours was considered sufficient. In addition, day-to-evening cyclic temperature variations must be considered in the design.

3-2.3 *Fin Tubes*

In air-cooled heat exchangers, the high heat-transfer coefficients of liquid metals suggest the use of extended surfaces (fins) in contact with the cooling air to which heat is transferred.

The many types of fin tubes used in air-cooled heat exchangers can be broadly classified under four headings: [20]

1. Integral fins.
2. Embedded fins.
3. Soldered or brazed fins.
4. Interference-fit fins:
   a. Edge tension-wound helical fins.
   b. Footed tension-wound helical fins.
   c. Helically extruded fins.
   d. Expanded-plate fins.

Tubes with aluminum fins have been developed; these have the fin strip either wound tightly around the tube or rolled into a groove cut into the outer tube surface. Another type of tube can be manufactured by winding on an L-shaped aluminum strip with the foot of the fin embracing the tube and producing a contact surface about 3 mm wide. The fins of the so-called bimetal tube are rolled out of an aluminum tube that is at the same time mechanically bonded to an inner steel tube.[19]

Such materials as copper and aluminum are not recommended for use in high-temperature liquid-metal systems. Copper cannot be used in direct contact with oxidizing atmospheres at metal temperatures above 400°F because of the formation of nonadherent oxide films that impede heat transfer and ultimately destroy the fins. Aluminum does not suffer this disadvantage and might be considered for use at metal temperatures as high as 1000°F except for its almost complete lack of mechanical strength and its high thermal-expansion coefficient relative to the basic metals to which it is customarily attached. [21]

In spite of their low conductivity, [of the order of 10 Btu/(hr)(sq ft)(°F/ft)], the austenitic steels, Monel, and Inconel are customarily used when the fin-metal temperatures are beyond the limits of suitability of copper and aluminum. However, the recent development of clad copper fins may make it possible to operate at fin-metal temperatures as high as 1900°F with all the advantages of copper's high conductivity and the corrosion resistance and high mechanical strength of the cladding material.[21]

3-2.4 *Structural Design*

Since liquid sodium may be hazardous in contact with other fluids or with personnel, extra precautions must be taken in heat-exchanger design to eliminate the possibility of such contacts. Normal exchanger vents and drains must be provided at high and low points of fluid compartments to reduce the likelihood of pockets of liquid (or solidified) sodium at shutdown. Wherever possible, tubes should be sloped to provide positive drainage by gravity. Crevices in which liquid sodium can be retained by surface tension or physical entrapment should be kept to a minimum.

These considerations apply to hazards to personnel and equipment during start-up and shutdown periods. During operation, however, leakage to the atmosphere is of concern. The probability of leakage from the equipment is customarily minimized by integral construction of the vessel walls, i.e., by substituting welded joints for gasketed joints and by requiring more than normal evidence of leaktightness during and after fabrication. In general, the equipment discussed in this section should be designed according to the *ASME Boiler and Pressure Vessel Code*, Sections III and VIII, for primary or secondary coolant usage, respectively. Reference 22 presents considerations relating to total strain and stress rupture.

3-2.5 *Air-Cooler Arrangement*

On a typical arrangement the supporting structure, which carries the cooling elements, forms one unit with the plenum chambers. The cooling air is supplied by axial-flow fans and is forced through the elements. The fan rings are rigidly connected to the bottom wall of the plenum chamber. Of the numerous possible types of air coolers, the two types of construction preferred for use in refineries and the petrochemical industry

are (1) "horizontal" construction where the cooler elements are arranged horizontally and (2) "roof" construction where the elements are arranged in the form of a pitched roof. Both types are suitable for large-scale construction and therefore for the many cooling and condensing processes where large quantities of heat have to be dissipated within the most varied temperature ranges (Fig. 3.2).

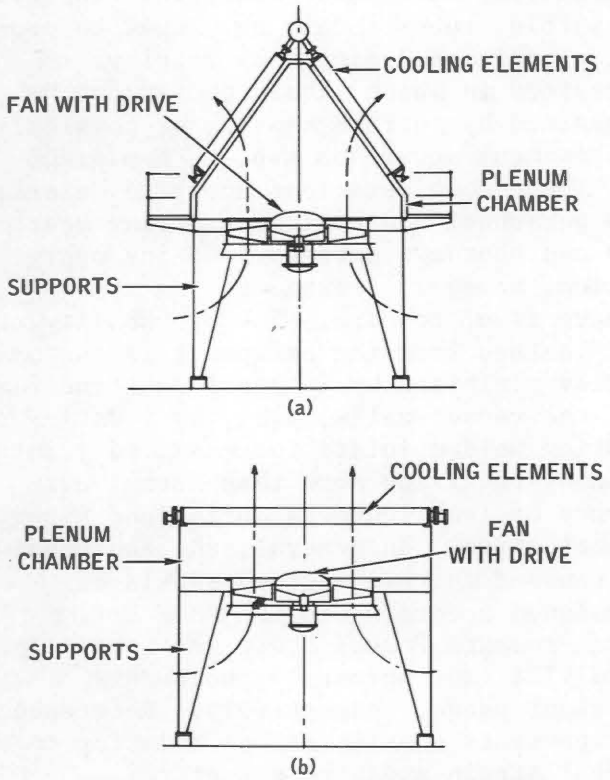

Fig. 3.2 Arrangement of cooling bundles for roof (a) and horizontal (b) construction of an air cooler. (From Ref. 19. Reproduced with permission of Industrieverlag v Hernhaussen K G.)

One of the advantages of roof construction is that less floor space is required. In horizontal construction the simple arrangement of the pipework appears to be advantageous, particularly if the combination of several cooling processes is involved.

3-2.6 *Fans and Fan Drives*

Design and construction techniques for the fans and fan drives discussed here [19] are applicable to liquid-metal systems if the higher fluid temperature (typically 1200°F) is considered.

Since air-cooled plants are installed out-of-doors, fans and fan drives must be durable and must be designed so that all parts requiring maintenance are easily accessible. All motor parts that are subject to wear (bearings, gears, etc.) should be designed for at least 50,000 operating hours. [19]

Axial-flow fans up to about 5¼ ft (1600 mm) in diameter are usually mounted on the driving-motor shaft. The limits for this kind of application are given by the fan noise, which increases with rising circumferential speed. Driving the fan directly by the motor is the best solution with respect to operating reliability; however, since this type of operation is limited to relatively small fan sizes, it will seldom be found in large air-cooler plants in refineries. Fans using vee-belt-drive speed reduction are frequently found in refineries. Such a drive is reasonable in price and is sufficiently durable if the mounting and bearings are carefully designed. This drive is suitable mainly for fans of 5¼ to 11½ ft (1600 to 3500 mm) in diameter. The range of application is restricted to a fan-shaft power of about 25 kw (Fig. 3.3).

For fan powers higher than 25 kw, reduction gears are used. [19] Typical arrangements include a bevel gear coupled to a horizontal driving motor located on the floor and a vertical fan drive shaft connected to the gearbox through a universal joint. This can be replaced by a more compact construction with a spur gear. The fan wheel is arranged on the drive shaft of the

gearbox in an overhung position, and its bearing lies in the gearbox itself. The driving motor is of the flanged type, directly coupled with the gearbox input shaft. Reduction gears for axial-flow fans up to capacities of about 100 kw have been used.

Since the operating reliability of the gears depends mainly on the perfect lubrication of the tooth surfaces and the bearings, oil-circulation pumps must be installed at the larger capacities. The reliability of the plant can be increased by controlling oil temperature and flow by thermometers with alarm indicators and flow-sensitive relays. [19]

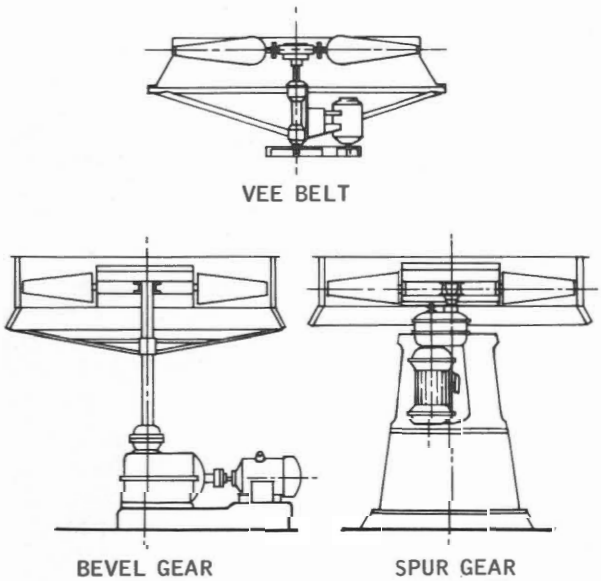

Fig. 3.3 Fan drives. (From Ref. 19. Reproduced with permission of Industrieverlag v Hernhaussen K G.)

Air-handling ability of fans needs further investigation. One exchanger manufacturer uses fans no larger than 12 ft to avoid maintenance problems on bearings. [23]

3-2.7 *Operation and Control*

Since air-cooled heat exchangers are usually designed for ambient air temperatures that are reached or even exceeded during relatively few hours of the year, they have a cooling margin during the rest of the year which rises with decreasing air temperatures.

The following equation may be used to approximate power consumption of an air-cooler fan: [19]

$$N = \frac{V\,\Delta p_T}{102\eta}\ \text{kw} \qquad (3.10)$$

where N = fan power consumption (kw)
V = airflow rate (m^3/sec)
Δp_T = total pressure difference (mm H_2O)
= $\Delta p_{stat} + \Delta p_{dyn}$
Δp_{stat} = static pressure difference in cooler system (mm H_2O)
Δp_{dyn} = velocity head to be produced in fan ring (mm H_2O)
η = efficiency of fan with respect to total pressure

Economic performance can sometimes be improved at low air temperatures by reducing cooling airflow, thereby reducing electrical power consumption. This volume reduction can be achieved simply by stopping some fans. Numerous small fans must be used to facilitate appreciable saving of power in this manner, and this in turn leads to a considerably higher installation cost, particularly in connection with electrical supplies. [19]

A more flexible performance is achieved by use of double-wound pole-changing motors for the fan drive. The air quantity decreases almost linearly with speed, but the static pressure in the fin-tube system falls as the 1.6th to 1.8th power of the air inlet velocity; thus a power saving of about 70% is gained by reducing the 6/4 pole motor to the lower speed and so reducing the fan speed to two-thirds. [19]

A combination of economic operation and product-side control can be obtained by using fans with blades that can be adjusted while running; the air quantity is thus continuously controlled by the blade adjustment. The product outlet temperature produces a signal to the control which can effect a blade adjustment either pneumatically, hydraulically, or electromechanically.

Figures 3.4 and 3.5 illustrate pneumatic and electromechanical control systems, respectively. Power savings through the use of various fan-control techniques are discussed in Ref. 19.

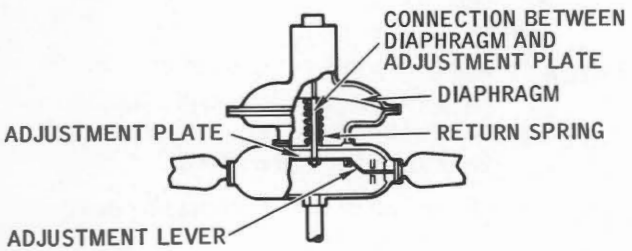

Fig. 3.4 Pneumatically adjustable fan. (From Ref. 19. Reproduced with permission of Industrieverlag v Hernhaussen K G.)

The liquid-metal temperature can also be controlled by variable airflow louvres. This kind of throttling by itself results in no fan power saving, however.

Another possibility for liquid-metal temperature control is the use of a bypass around the cooler, i.e., mixing of hot (uncooled) and cooled liquid-metal streams.

3-2.8 *Fan Noise*

Fan noise is caused by air separation at the fan blades at sections within the fan housing. Drive motors and reduction gears add to the fan noise. Fan noise may be estimated from [19]

$$L = A \sqrt[3]{U}$$

where L is noise level in phons [24, 25] and U is circumferential speed of blade types in milliseconds. The factor A depends on the fan diameter and the air quantity. The following table refers to normal supply:

Fan diameter, ft	2.56	3.28	6.55	9.83	13.1	16.4
Fan diameter, mm	800	1000	2000	3000	4000	5000
Noise level factor A	23	23	23	22.5	21	19

For further details and applications see Ref. 19.

3-2.9 *Installations*

This section summarizes the design and operating experience of specific units.

(a) *Aircraft Reactor Test (ART).* To investigate design and fabrication problems inherent in compact, high-performance heat exchangers for aircraft nuclear propulsion (ANP) applications, experimenters at the ANP Division of Oak Ridge National Laboratory (ORNL) tested liquid-metal (NaK-air) coolers (radiators). Twenty coolers were operated at 1200 to 1700°F. The coolers, nominally rated at $\frac{1}{2}$ and $1\frac{3}{4}$ Mw, employed cross-countercurrent airflow over small-diameter Inconel U-tubes. Brazed to these U-tubes were copper fins plated with stainless steel to form a compact matrix of extended heat-transfer surface. Figures 3.6 and 3.7 illustrate the two basic designs tested. [26, 27]

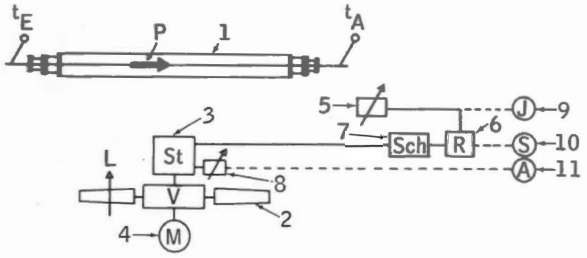

Fig. 3.5 Diagram for electromechanical fan control. (From Ref. 19. Reproduced with permission of Industrieverlag v Hernhaussen K G.)

1 Cooler element
2 Variable fan
3 Blade positioner
4 Motor
5 Response signal
6 Control
7 Switchgear
8 Blade-angle transmitter
9 Response indicator
10 Command indicator
11 Blade-angle indicator
P Product
L Cooling air
t_E Product inlet temperature
t_A Product outlet temperature

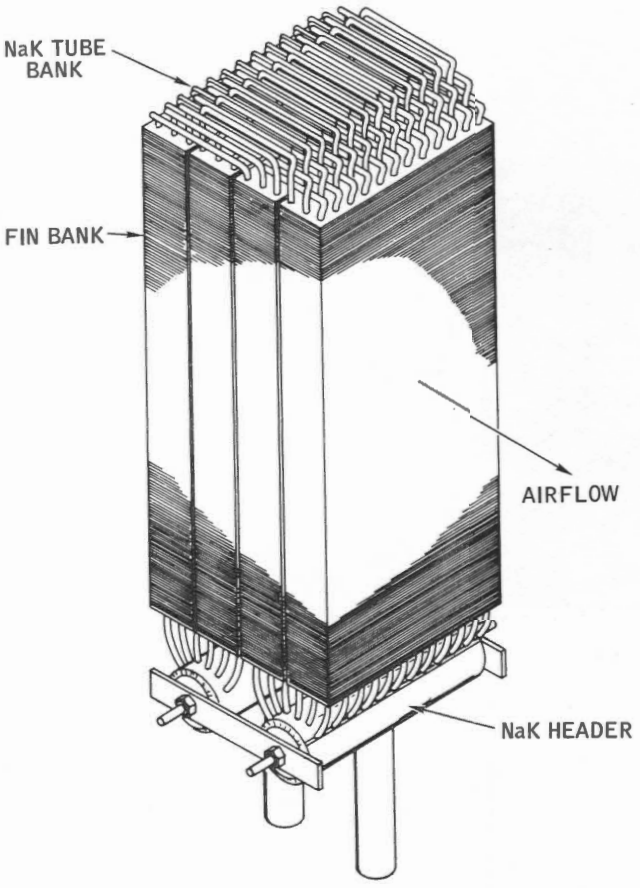

Fig. 3.6 Aircraft Reactor Test ½-Mw(t) radiator.

The high-conductivity stainless-steel-clad-copper fin material used in the radiators required edge treatment after shearing to prevent oxidation of the copper core. Slurried aluminum powder was applied to the edges of a stack of fins, and the fins were heated to alloy the copper and aluminum. This aluminum bronze effectively prevented fin deterioration and loss of heat-transfer effectiveness. The fins were punched and slipped over the Inconel tubes, the extruded periphery of the punched hole serving as a spacer between fins.

The first ORNL test unit was operated successfully in 1952, some six months after the radiator design and development program was initiated, with solid stainless-steel fins. The heat-transfer performance was somewhat inferior to that calculated, apparently because air streaming between the tubes left low-velocity regions in the tube wakes and thus rendered the fins in these regions less effective.

As the test program progressed, tube failures occurred which could not be accounted for by any of the thermal strains envisioned in the preliminary stress analyses. The temperature distribution in a cross-flow heat-transfer matrix leads to an odd three-dimensional distortion and a complex stress distribution. Figure 3.8 shows the temperature distribution

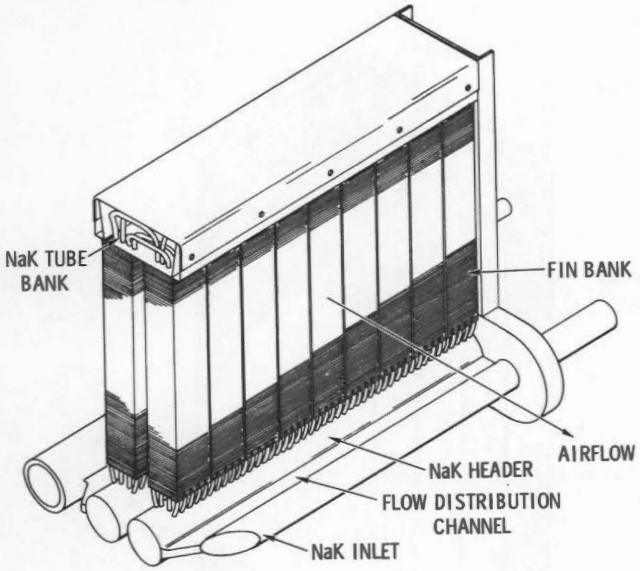

Fig. 3.7 Aircraft Reactor Test $1^3/_4$-Mw(t) radiator.

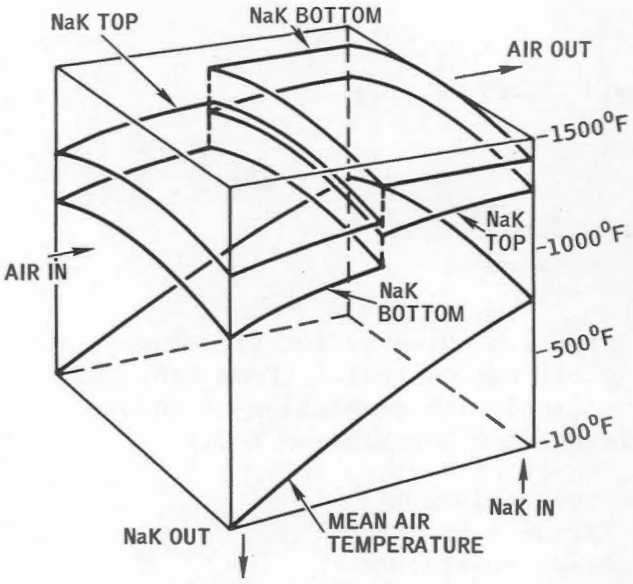

Fig. 3.8 Temperature distribution through the NaK-to-air cooler radiator.

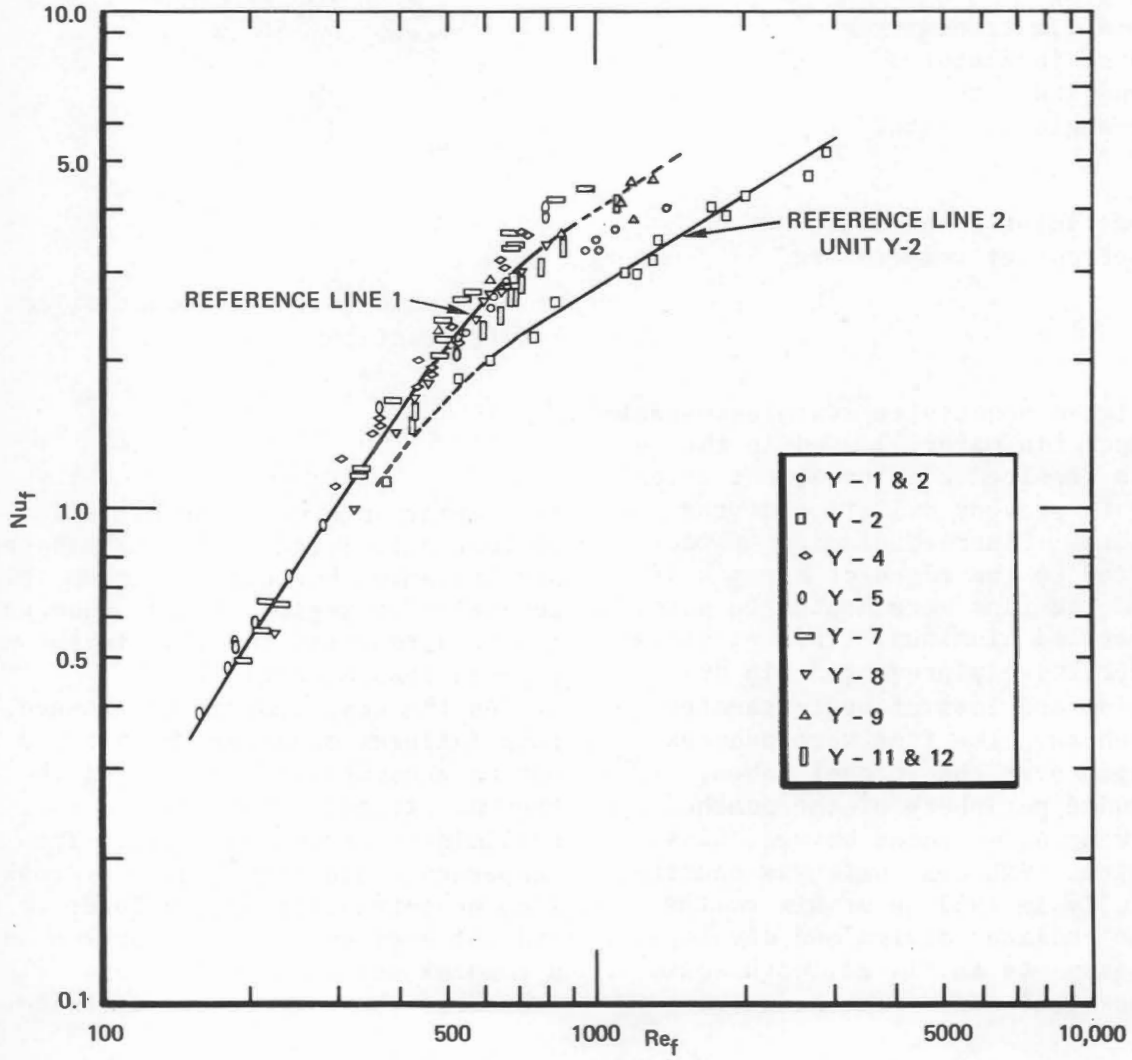

Fig. 3.9 Radiator performance for ten ½-Mw(t) *Y* units.

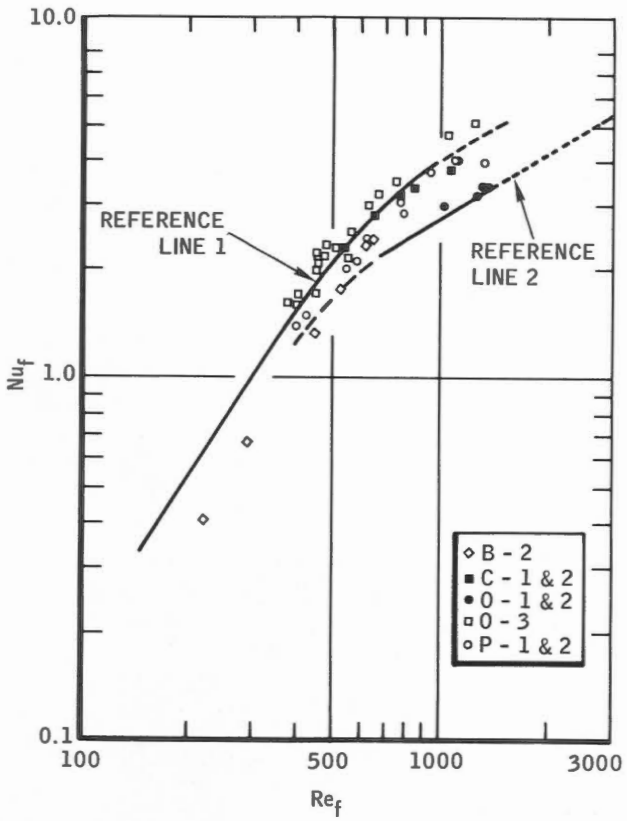

Fig. 3.10 Radiator performance for eight ½-Mw(t) units.

for a typical case. The radiator matrix is three-dimensional so that thermal expansion occurs not only in the airflow direction, but also transverse to the airflow, both along and across the tubes. Therefore it is necessary to allow for differential thermal expansion between strip or plate fins and the header sheet, between various tubes in the heat-transfer matrix, and between such tubes and any support structure or baffles desired. Provision must also be made for changes in temperature distribution associated with temperature transients in the liquid circuit [22].

Performance data were obtained on eighteen ½-Mw(t) units [26,28]. Because of test-equipment limitations, the heat load on the radiators was based on the measured NaK flow rate, and the airflow rates were then calculated from the air-temperature rise across the radiator. The test results from ten

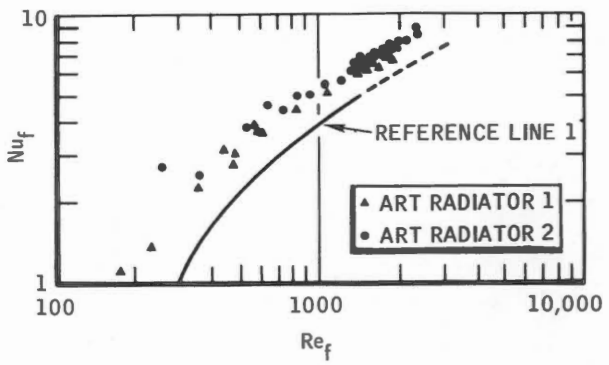

Fig. 3.11 Composite heat-transfer data for Aircraft Reactor Test numbers 1 and 2.

½-Mw(t) units manufactured by a single vendor are plotted in Fig. 3.9. Line 2 on the graph shows results from one of the very early ½-Mw(t) units whose performance was significantly below that of later units tested. Figure 3.10 shows lines 1 and 2 of Fig. 3.9 along with data on eight additional ½-Mw(t) radiator units manufactured by four other vendors. The bulk of the units had performance capabilities in good agreement with line 1, Fig. 3.9. A few of the units, however, gave reduced performance.

A performance test was carried out on two $1^3/_4$-Mw(t) ART prototype radiator units. The performance results from these tests are shown in Fig. 3.11 along with line 1, Fig. 3.9, previously established for the ½-Mw(t) radiator units. The data indicate an improved performance over that of the ½-Mw(t) units. This apparently stemmed from improvements in testing techniques. One of the difficulties encountered in testing the ½-Mw(t) units was the elimination of bypass air around the radiator units. The necessity for avoiding rigid structural restraints on the unit complicated the task of sealing the air duct. In addition, temperature traverses across the discharge air ducts indicated some degree of airflow and temperature asymmetry. In the design of the test stand for the $1^3/_4$-Mw(t) ART radiator units, careful attention

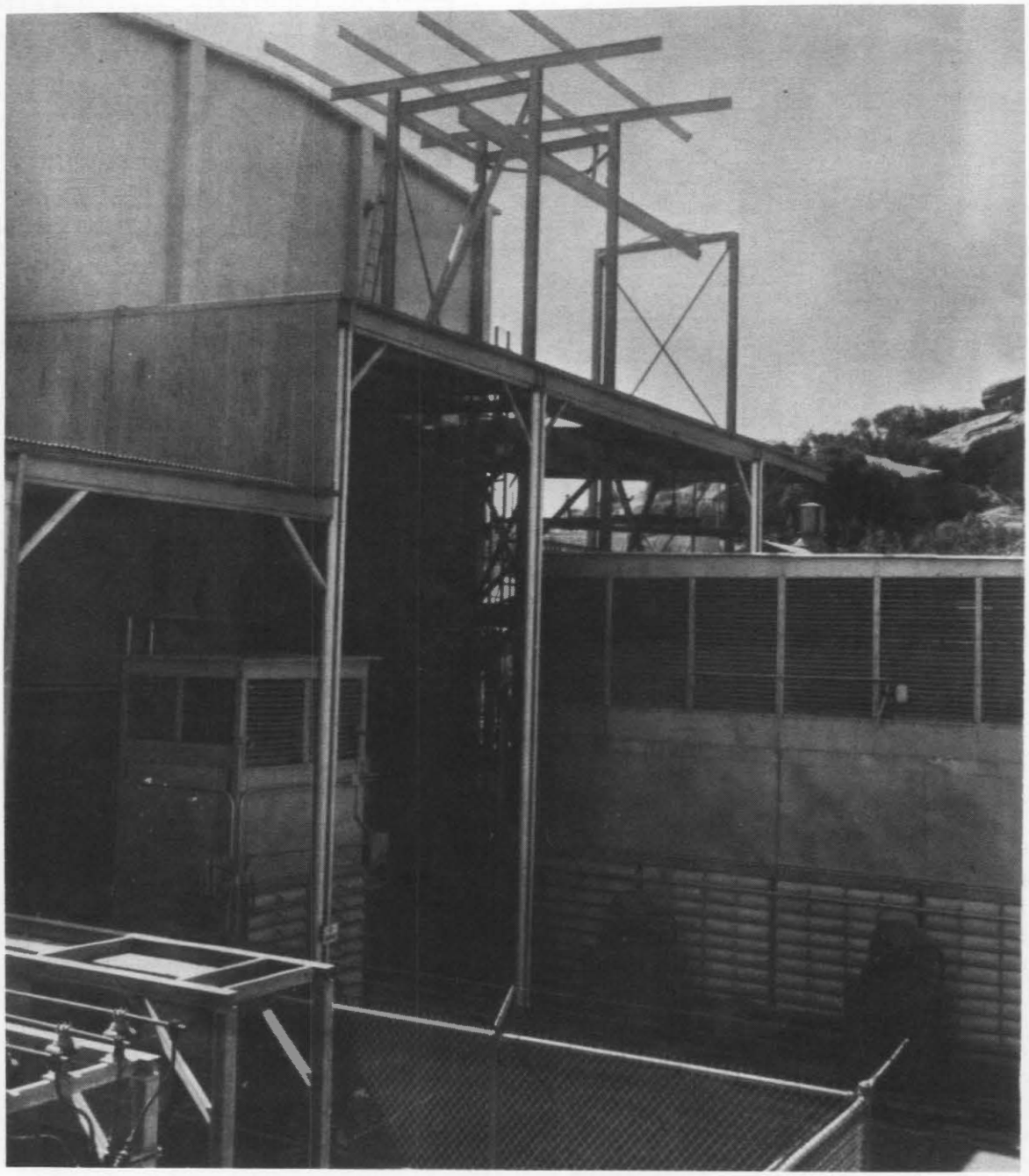

Fig. 3.12 Main and auxiliary air-blast heat exchangers for the Sodium Reactor Experiment.

was given to the radiator mounting and bypass air seals. Air-temperature measurements were made with thermocouple grids, and, in general, the radiator instrumentation was somewhat more extensive than for smaller radiator units on the heat-exchanger stands.

(b) *Sodium Reactor Experiment (SRE).* The SRE used the sodium-to-air coolers shown in Fig. 3.12 (also referred to as air-blast heat exchangers) to dissipate the reactor heat. (The main cooler was in parallel with a steam generator.) The main air-blast heat exchanger (see

detailed sketch in Fig. 3.13) consisted of four U-shaped tube bundles installed in a protective housing above d-c electric-motor-driven fans. The tubes are similar to those in the SRE *IHX* (1 in. OD by 16 BWG wall thickness) but have external 410 stainless steel fins 2 in. in diameter spaced eight per inch. All tubes are connected in parallel from headers at one side of the assembly. The direction of airflow is normal to the secondary sodium flow. Mechanically operated louvres are installed above the tube bundles to assist in controlling airflow. Tubular electric heaters are mounted below the tube bundles for preheating the system and for providing makeup heat during low-power operation. These heaters maintain a temperature of 350°F during shutdown. [29,30]

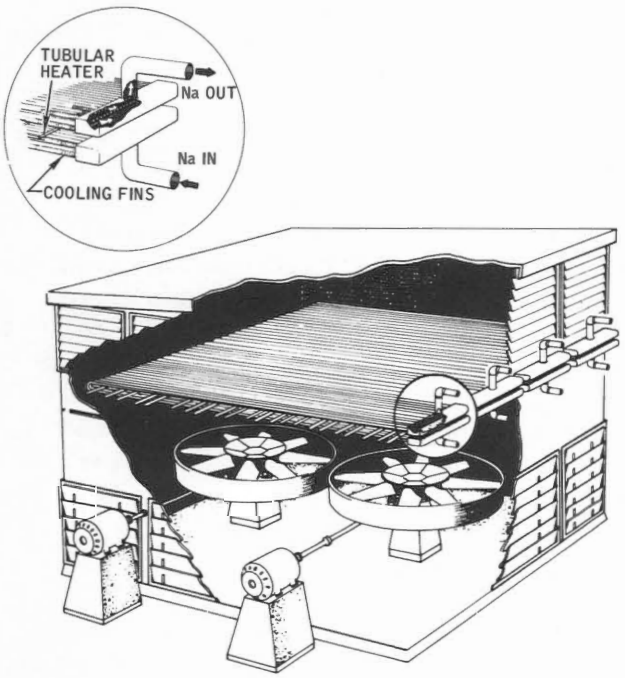

Fig. 3.13 Sketch of the Sodium Reactor Experiment main air-blast heat exchanger.

The main air-blast heat exchanger contains 204 U-tubes 26 1/2 ft long. They provide 23,600 sq ft of heat-removal surface for a heat removal of 20 Mw(t). At normal operating power the the estimated heat-transfer coefficient is 8.3 Btu/(hr)(sq ft)(°F), and the exit air temperature is 277°F with an inlet air temperature at 100°F. Below the tube bundles are two 11-ft-diameter five-bladed fans, each driven by a 50-hp variable-speed d-c motor. The auxiliary air-blast (foreground in Fig. 3.12) is similar in design but has only 30 U-tubes 8 ft long. It has a heat-removal rating of 1 Mw(t) with a design heat-transfer coefficient of 5.8 and utilizes a 5-ft-diameter fan driven by a 5-hp variable-speed d-c motor.

Operation with this unit resulted in high heat loss, which was resolved by using line and component heaters (required for preheating) during critical times, i.e., following a scram.

(c) *Southwest Experimental Fast Oxide Reactor (SEFOR).* The SEFOR air-blast coolers are forced-air finned-tube heat exchangers designed for the following conditions: [31]

	Main	Auxiliary
Power, Mw(t)	20	1
Sodium inlet temperature, °F	670	670
Sodium outlet temperature, °F	550	550
Air inlet temperature, °F	90	90
Air outlet temperature, °F	493	403
Heat-transfer coefficient design, Btu/(hr)(sq ft)(°F)	9.0	7.3

The main air-blast cooler consists of the heat-exchanger tube bundle, support structure, blower, blower drive, and blower speed control.

The cooler tube-bundle surface area, of 26,300 sq ft, consists of 270 finned stainless-steel U-tubes 1.0 in. in outside diameter by 0.072 in. in wall thickness. The fins are 0.030-in.-thick carbon steel helically wound at seven per lineal inch of tube in a plowed groove. The U-tubes are mounted

horizontally, 45 across and 6 deep, to produce a tube bundle of 12 layers of tubes. Inlet and outlet manifolds consist of 16-in.-diameter pipe sections to which tube sheets are welded. The sodium nozzles are located so that the hot secondary sodium enters the top of the bundle to prevent stratification and promote natural circulation. The overall size of the tube bundle is about 13 ft wide, 17 ft long, and 4 ft deep.

The main cooler tube bundle is supported about 16 ft above grade with the blower located at grade and to one side of the tube bundle. Air is ducted from the blower discharge upward through a transition duct, plenum chamber, and the tube bundle. Steel gratings are mounted above and below the heat-exchanger tube bundle for protection against flying objects. The tube bundle and support structure are designed for 300-mph wind loads. The bundle can be isolated to maintain sodium temperature during downtime with three sets of pneumatic, remote-operated, insulated doors located above and below the tube bundle. The tube bundle housing is insulated, and Calrod heaters are mounted between the bottom of the heat exchanger and lower grating to preheat the unit during start-up or to maintain temperatures during shutdowns.

Cooling air is supplied by a floor-mounted scroll-type double-inlet centrifugal blower rated to deliver 700,000 lb/hr of air at 6.5 in. H_2O pressure. The blower has manually operated, variable-inlet-guide vanes for control at very low load conditions. A 250-hp motor drives the blower. The sodium outlet temperature from the main air-blast cooler is controlled at a given set point by a temperature indicator controller that adjusts the blower speed through an ampli-speed magnetic drive. [31]

(d) *Cadarache*. The air-cooled exchangers at Cadarache (nests of finned tubes) have been shown to be satisfactory and have sufficient capacity to dissipate the rated power at the design temperatures for the secondary coolant. [32]

A leak in the 10-Mw(t) air exchanger was discovered because of the smoke produced. This leak was caused by porosity in a weld at a very inaccessible spot; this led to external corrosion of the faulty tube and of neighboring tubes. Two tubes out of a total of 262 had to be cut and sealed off.

Exchangers for Rapsodie will be manufactured in separate units to make the the welds more accessible to avoid incidents of this kind. [32]

(e) *Atomic Power Development Associates, Inc., (APDA)*. At the Fermi reactor an air cooler was used in conjunction with high-temperature precritical tests. [33] The cooler bundle was installed in the furnace and served a dual function, i.e., as a heating coil. This is discussed in more detail as a heater in Sec. 3-6.

(f) *BOR*. The Russian BOR will use air-cooled heat exchangers as backup in advanced sodium-cooled plants.

In each secondary circuit loop of BOR, apart from the heat exchanger and pump, there is a steam generator. In addition, there is an air-cooled heat exchanger designed for a thermal capacity of 30 Mw which can be connected to any secondary circuit loop instead of the corresponding steam generator. The flow of air through the heat exchanger is produced by fans. [34]

(g) *Sodium Components Test Installation (SCTI)*. The SCTI cooler, rated at 8.5 Mw(t), is used as a heat sink in reducing the temperature of the sodium to provide the required thermal transients for the test heat exchangers (Fig. 3.14). It is constructed of 6-in. 304-stainless-steel inlet and outlet sodium headers with 14 in.-long finned tubes making 14 passes across the air stream. The finned tubes are 1 1/2 in. long with a 3.4-in. outside diameter and 0.050-in.-thick fins spaced five per inch. [35,36,37]

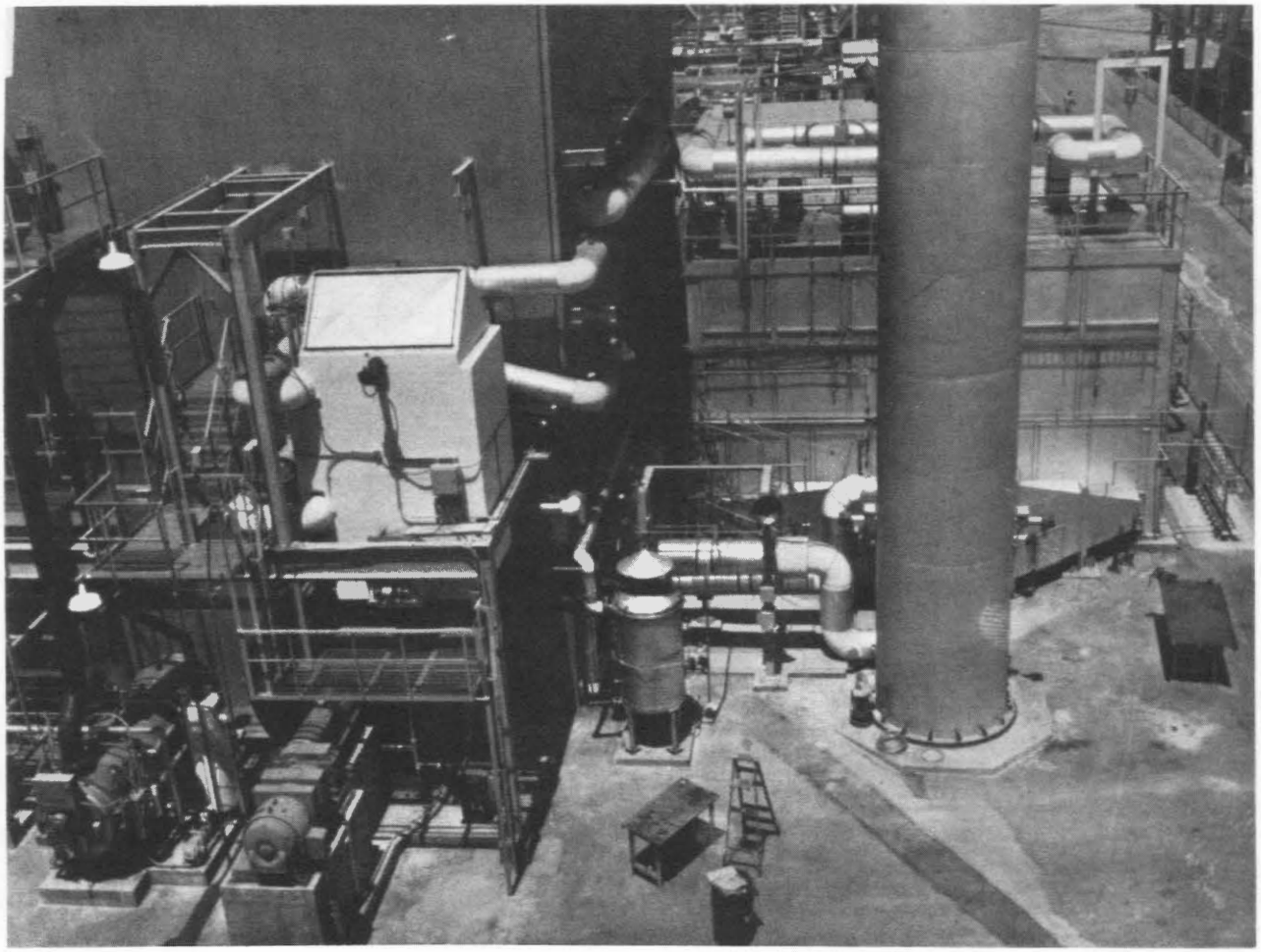

Fig. 3.14 Sodium cooler for the Sodium Components Test Installation.

(h) *Fast Flux Test Facility (FFTF).* At present a conceptual evaluation indicates that the FFTF will use extended-surface forced-air heat dumps to dissipate approximately 430 Mw(t) of heat generated in the reactor. [38] This could become the largest installation of air-cooled-sodium heat exchangers in one plant or facility.

(i) *Lithium-Cooled Reactor Experiment (LCRE).* The Connecticut Advanced Nuclear Engineering Laboratory (CANEL) nonnuclear LCRE system test used a 5-Mw(t) air-cooled heat exchanger. The liquid metal was NaK. By Sept. 1, 1964, it had operated for over 9000 hr at design conditions. [39]

(j) *Experimental Breeder Reactor No. 2 (EBR-II).* An air-cooled heat exchanger is used in EBR-II in the shutdown cooling system. NaK flows in a closed system through an immersion-type bayonet heat exchanger in the primary sodium system and the air-cooled heat exchanger.

NaK flow is upward into the finned-tube air-cooled heat exchanger, which is located in an air stack with the damper outside the reactor-containment building. The heat is transferred to the atmosphere by natural convection of air. The cooled NaK then flows down-

ward into the inlet of the bayonet cooler. [40]

The rate of heat release from the system is controlled by the position of the stack dampers. Normally the dampers are automatically controlled, but manual control is also possible in the event of failure of the automatic system. During reactor operation the dampers are closed and a minimum flow of NaK occurs in the shutdown cooling system. This method of operation prevents the freezing of NaK in cold weather, provides for positive starting when the dampers are opened, and reduces thermal shock on the system. When the stack dampers are opened, the thermal head on both the NaK and the air side is increased. This gives rise to increased flow of both fluids, which, in turn, causes increased heat removal from the bulk sodium.

(k) *Prototype Fast Reactor (PFR).* Air-cooled heat exchangers, similar to those in EBR-II will be used in the PFR for shutdown or decay cooling.

(l) *Sodium Pump Test Facility (SPTF).* The proposed SPTF [41,42] requires sodium coolers for temperature control of the sodium. The conceptual designs have considered air-cooled heat exchangers or cooling devices attached to the sodium piping. Either cooling arrangement has to dissipate approximately 5 Mw(t) at sodium temperatures of 400 to 1200°F to maintain temperature stability.

(m) *Mine Safety Appliances Co. (MSA).* The details of the MSA sodium cooler are shown in Fig. 3.15. Sodium was passed from a 3-in. double-extra-strong pipe manifold through 13 1-in.-OD by 16-BWG finned tubes into a discharge manifold. The sodium tubes made six passes through the air stream. The fin material was 4 to 6% Cr Mo steel 0.024 in. thick, and the fins were 2 in. in outside diameter. They were spirally wound on the tubes at a pitch of five per inch. The finned length on each pass was 2 ft 5 in. The tubes were formed in a serpentine manner with a bare section U bend between passes. The unfinned length was not in the air stream. [43]

Air passed upward through the shell side of the cooler at a maximum rate of 27,000 lb/hr. The airflow rate was controlled manually by a damper on the blower inlet.

The overall size of the cooler is 3 ft by 2 ft 8 in. by 2 ft 2 in. The unit was designed for the following conditions:

1. Heat load of 3,500,000 Btu/hr.
2. Heat-transfer surface of 426 sq ft.
3. Mean temperature difference of 900°F.
4. Sodium volume of 1.15 cu ft.

The performance of the cooler can be expressed by

$$U = 0.0391G^{0.59} \qquad (3.11)$$

where U is overall heat-transfer coefficient [Btu/(hr)(sq ft)(°F)] and G is air-mass flow rate (lb/hr/sq ft). Experimental data points (Fig. 3.16) lie within ±20 to 30% of the values computed from this equation, which was recommended by the manufacturer as his design equation. Comparison with Eq. 3.8 shows a Re or G dependence of 0.6; this is in fair agreement with Eq. 3.11.

In an attempt to get a better correlation, the effects of (1) the sodium entrance temperature, (2) the air entrance temperature, (3) the viscosity and thermal conductivity of the air evaluated at the wall mean temperature, at the air-bulk mean temperature, and at the air-film mean temperature, and (4) possible natural convection were investigated. Correlations using these factors did not reduce the deviation. Fifteen separate methods of correlation were tried, but most resulted in plots with clumps of data that could be correlated in almost any way without changing the deviation significantly.

This deviation in results is caused by the difficulty of measuring air temperatures in the discharge ducting. The discharge temperature was measured by nine thermocouples on a grid in the 2.5-ft-square duct. The velocity profile

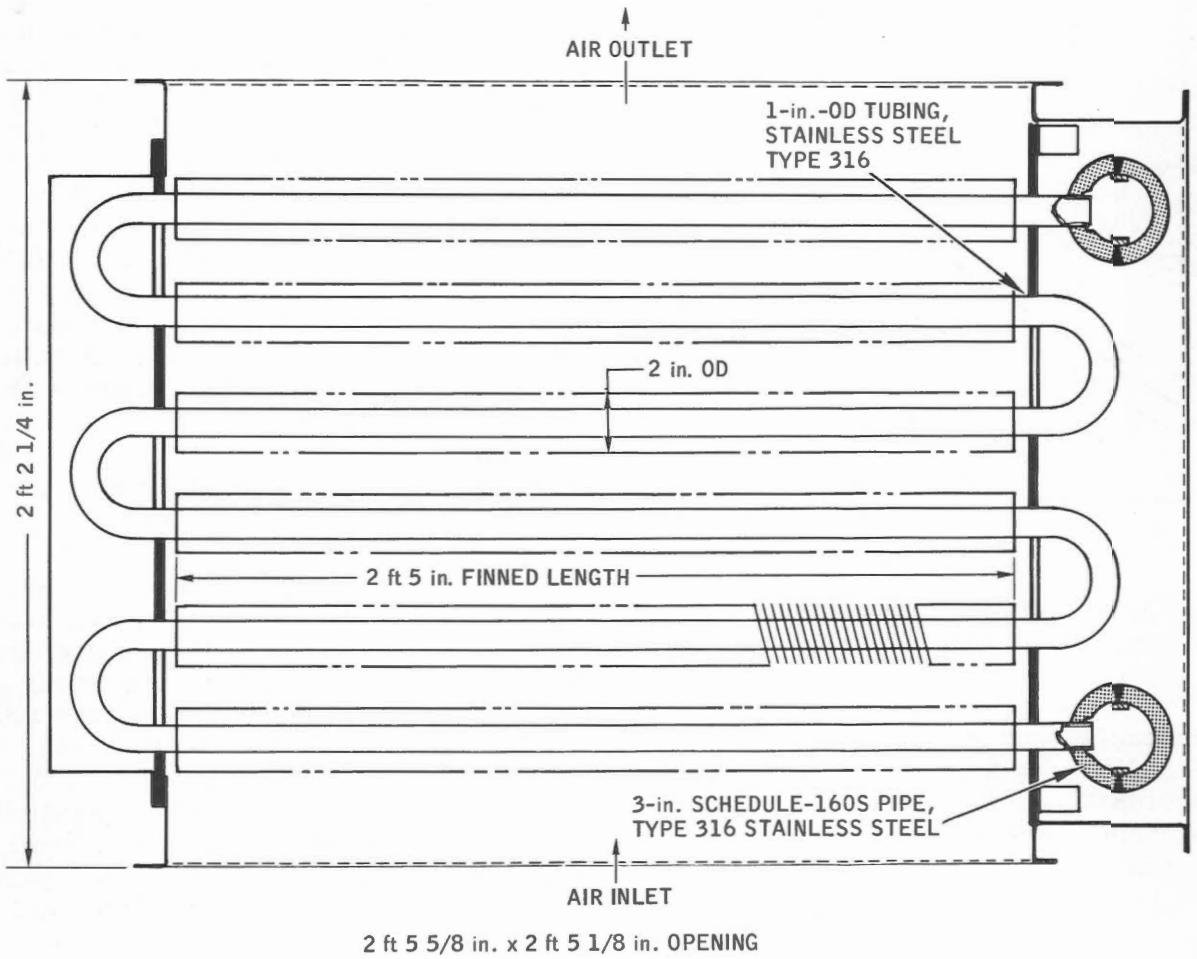

Fig. 3.15 Sodium cooler at Mine Safety Appliances.

in the duct was measured at various flow rates to minimize the errors in the temperature measurement. However, the scatter in the data is believed to be due to these measurements. [43]

(n) *Comitato Nazionale per l'Energia Nucleare, Italy (CNEN).* The cooler consists of an air-sodium heat exchanger with finned tubes mounted in a cold-air conduit. The inlet and outlet sodium collectors will be connected by a series of finned tubes mounted in parallel. [44]

At the exchanger approximately 50 kw must be transported by the sodium flow of about 4400 kg/hr at a temperature of 1100°F at the inlet and 1040°F at the outlet.

Cooling airflow is about 8.3 m^3/min. The blower has a capacity of 14 m^3/min and is installed with a bypass around the cooler and an air lock that permits regulation of the flow. Differential manometers will be installed across the cooler.

The air temperature will be measured on the inlet section and at several points on the discharge section. The thermocouples for measuring the temperature of the discharged air will be suitably shielded against thermal radiation from the nest of tubes so that the temperature measurement will not be affected.

Airflow will be measured by a pitot tube located in the discharge conduit

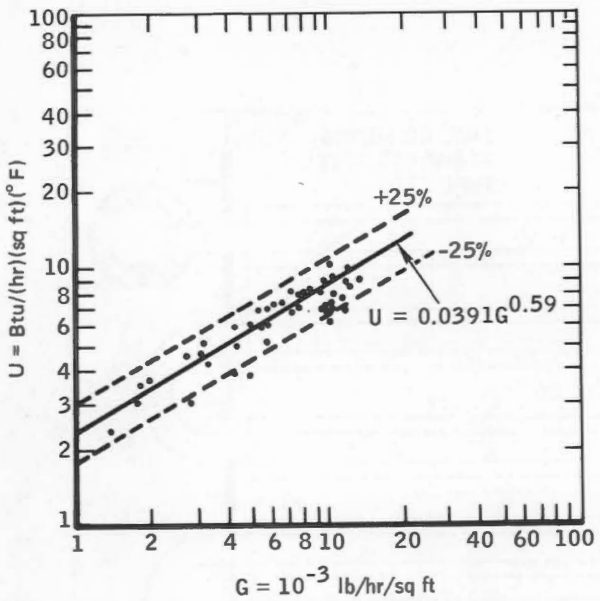

Fig. 3.16 Performance of the Mine Safety Appliances sodium cooler.

in a suitable manner.

(o) *SNAP*. The SNAP-8 Experimental Reactor (S8ER) employed the air-blast heat exchanger shown in Figure 3.17 as the system heat sink. Design conditions for the heat exchanger were as follows:

	NaK condition	
	1	2
Rate heat load, Btu/hr	2.05×10^6	2.05×10^6
Rated flow, lb/hr	4.89×10^4	4.9×10^4
Temperature in, °F	1250	950
Temperature out, °F	1050	750
Design temperature, °F	1400	1400
Design pressure, psia	100	100
Maximum pressure drop, psig	5	5

The S8ER heat exchanger operated for over 8700 hr (1 year) with an inlet temperature of 1250°F and for over 10,000 hr at greater than 1000°F before shutdown. The core was of tube-and-fin construction with six fins per inch. The tubes were fabricated from 1 1/2-in.-diameter Schedule 40 tubing with 3.4-in.-OD by 0.030-in.-thick stainless-steel fins helically wound into preplowed grooves in the tubing. The heat exchanger was oriented horizontally with the inlet and outlet manifolds on the same end. The tube-bundle arrangement consisted of four rows of four tubes each. NaK entered the inlet manifold at the bottom, split between the four tubes, made four passes through the air stream, and then exited through the outlet manifold at the top. Air was blown straight up through the heat exchanger by a squirrel-cage blower. Inlet and outlet louvers and fan speed were used to vary cooling as required. A metal shield was positioned over the air-blast heat exchanger to protect it from direct rainfall. The active portion of the tube bundle was 54 in. long, 20 in. wide, and 17 in. high.

Destructive postoperative examination of the heat exchanger did not reveal any impending failures and indicated that considerable life was still available at shutdown.

A similar tubular heat exchanger with the same design requirements is to be used as the primary heat sink for the SNAP-8 Developmental Reactor (S8DR). The heat exchanger is shown in Fig. 3.18. The tube bundle is 48 in. long, 24 in. wide, and 8 in. high and is fabricated from 192 4-ft-long by 3/4-in.-diameter tubes. NaK enters the inlet manifold on one side, makes one pass through the air stream, and exits through the outlet manifold on the other side.

3-3 LIQUID-METAL-TO-NONMETALLIC-LIQUID COOLERS

The use of nonmetallic liquids in liquid-metal coolers has occurred almost exclusively in steam generators (Vol. II, Chap. 4) where the water steam combination is the nonmetallic cooling liquid.

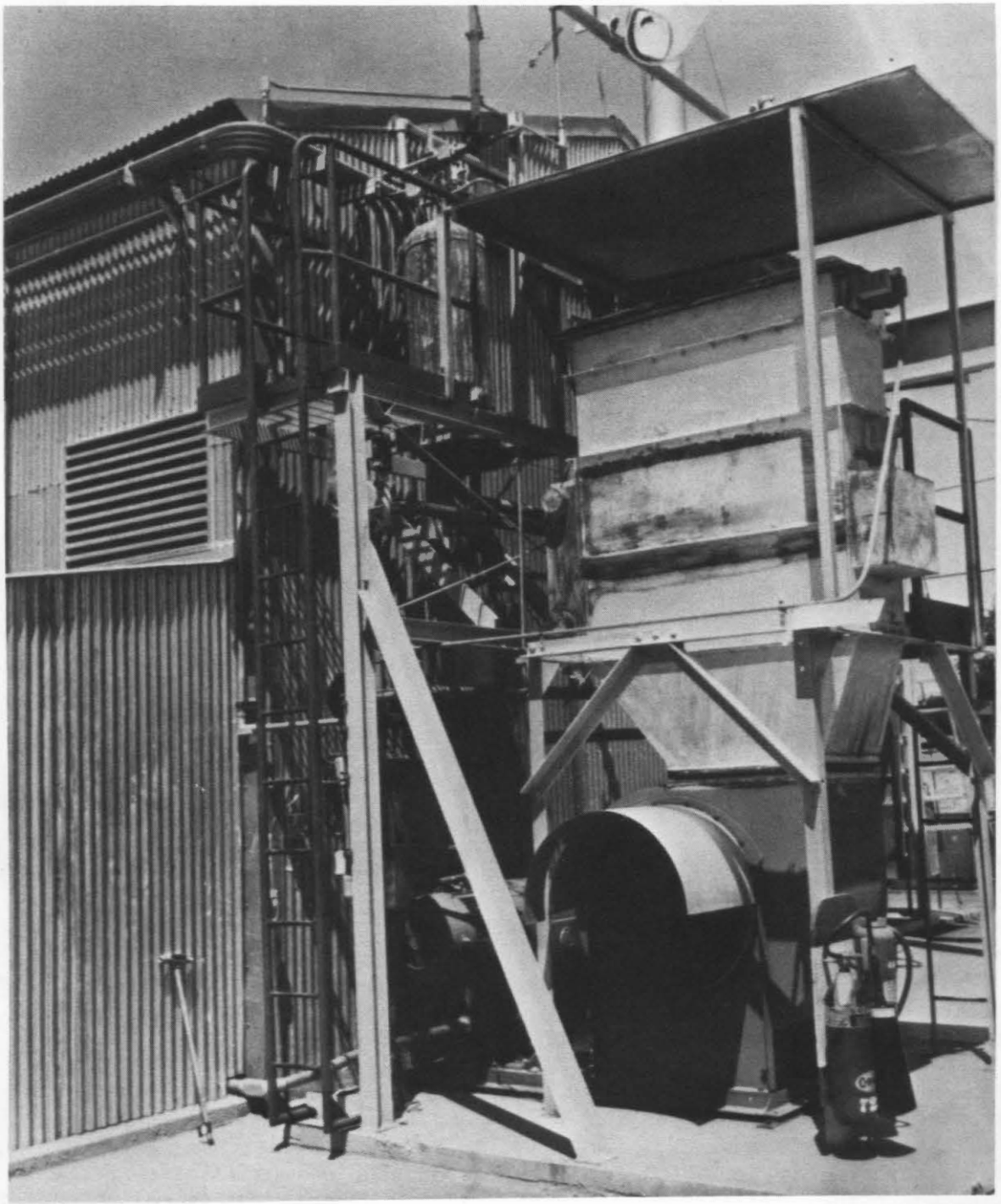

Fig. 3.17 NaK cooler (air-blast heat exchanger) for the SNAP-8 Experimental Reactor.

Steam generators will not be included in the subsequent discussion of non-metallic coolers.

The use of nonmetallic liquids (such as hydrocarbons) in preference to a gaseous coolant would be dictated by

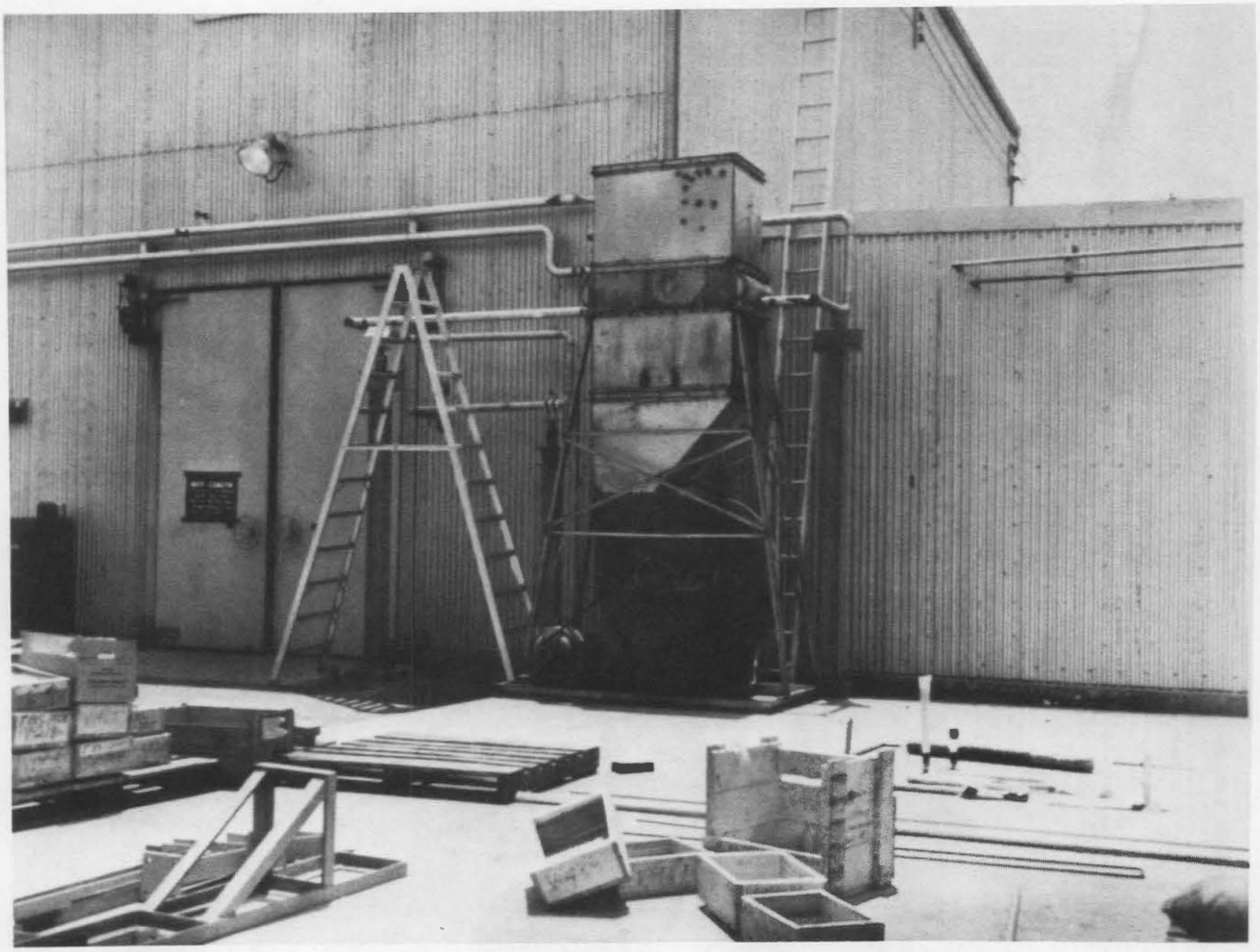

Fig. 3.18 NaK cooler (air-blast heat exchanger) for the SNAP-8 Developmental Reactor.

requirements such as heat flux, coolant flow area, and temperature driving force. [45]

Systems and components using various hydrocarbon fluids to cool the sodium are as follows:

1. Cold traps initially installed in the SRE where the cold trap is envisioned as a sodium-to-fluid cooler) used boiling toluene. This was subsequently changed to a Tetralin cooling jacket. Final modifications resulted in gas cooling of the cold trap. (For more detail, see Chap. 1.)

2. Freeze-seal pumps in the SRE initially used Tetralin as a heat sink. Difficulty with leakage and compatibility resulted in a change to NaK. [45] The cooling coils around the case and shaft freeze seals can be viewed as sodium coolers.

Liquid-metal coolers using nonmetallic liquids have not been in widespread use. Instead, fluids such as NaK and air have been used almost exclusively.

3-4 SODIUM-NaK HEATERS - MAIN CLASSIFICATIONS

Two main classifications for sodium-NaK heaters are:

1. Heaters for preheating system components and for maintaining liquid metal at flowing temperature.
2. Heaters for simulating the reactor core in heat-transfer and corrosion studies. The second classification includes (1) heaters for producing liquid-metal stream temperatures corresponding to normal reactor operation and (2) heaters of special design to produce high heat fluxes (about 1,500,000 Btu/hr/sq ft) corresponding to reactor fuel-burnout conditions.

Heaters for preheating liquid-metal piping systems are discussed in Vol. II, Chap. 2.

This section discusses heaters for preheating system components (other than piping), heaters for maintaining liquid metal at temperatures corresponding to normal reactor operation and special heaters for high-flux investigations.

3-5 SODIUM-NaK HEATERS FOR COMPONENT PREHEAT AND MAINTAINING FLOW TEMPERATURE

Heaters used to preheat components and maintain liquid metal at flow temperature have used (1) fossil fuels (gas and oil), (2) steam, (3) hot gas, and (4) electricity. Fossil-fuel-fired preheating systems are not used as extensively as other systems because it is difficult to maintain and ventilate combustion equipment in test installations or in reactor environments.

Steam and hot-gas preheating systems have been placed in operation. These systems consist of a centrally located heater which supplies heat to tracing lines. Tracing lines for sodium and NaK preheating generally consist of 1/4- to 1-in. carbon-steel pipe strapped or metallurgically bonded to the component to be preheated.

Electrical preheating systems are more extensively used than the other methods. The ease of control of electrical circuits, the readiness with which the heating elements may be installed, and the ease of maintenance have led to the adoption of electrical preheating for most sodium-NaK installations now in operation.

Several techniques have been developed for electrical preheating. Among these are cartridge resistance heaters, induction heating methods, and the heating of the component by making it a portion of a directly connected circuit.

Cartridge or rod heaters are fastened to the outer surface of the component to be preheated. Small staples (usually series 300 stainless steel in strip form) are tack welded to the outer surface in such a manner as to force the heater into good thermal contact. Commercially available heat-resistant putty containing a large percentage of graphite or lamp-black is supplied as filleting to improve heat transfer. The heater is provided with a backup reflector consisting of a strip of stainless steel. Care must be taken to avoid bending the heaters sharply within the heated length. The heater terminals must be brought out through the thermal insulation with which the component is usually provided. Typical installations are described in Refs. 26,35 to 37, and 46 to 49.

Induction preheating systems are not extensively used for component preheating in sodium and NaK systems since these systems are constructed of series 300 stainless steels, which are nonmagnetic. The component must be clad with a shell of mild (magnetic) steel to achieve a reasonable efficiency. This increases the cost of preheating with this system. An additional drawback is the fact that the transfer of heat to the component is retarded by lack of close fit between cladding and component.

Direct electrical heating systems in which the component itself or a portion thereof forms part of a directly connect-

ed circuit have been used to some extent. However, the nature of most components makes the use of this system unsuitable because of the variation in current density with wall thickness of the component. Uneven heating is produced where this occurs. Reference 26 describes an application of this method.

As mentioned previously, all electrical systems have the advantage of ease of control. The particular control system for a given application will be governed by the characteristics of the application. The simplest control system utilizes magnetic contactors in an on-off switching circuit controlled by a temperature-sensing device. A more accurate maintenance of temperature can be obtained by using variable autotransformers or saturable-core reactors.

Since solid-state devices capable of handling large currents are now available, the solid-state device known as the silicon-controlled rectifier, which has no moving parts, shows promise of filling the long-standing need for compact, infinitely variable, low-cost, reliable power control.

3-6 SODIUM-NaK HEATERS FOR REACTOR-CORE SIMULATION

As mentioned previously, sodium-NaK heaters for reactor-core simulation are in two categories: (1) heaters for simulating normal reactor operation and (2) heaters of special design for studies of simulated fuel-element burnout.

Fossil-fuel-fired heaters have been used extensively for this application. Tangential gas burners were used at MSA in heat-exchanger tests with sodium on a 3000-kw system. Gas-fired heaters have also been used at ORNL. [26] A 35-Mw gas-fired heater was installed at Atomics International [33-35] (Fig. 3.19).

If fossil fuel is competitive with electric power on a price basis, the fossil-fuel-fired systems are usually chosen over electrical systems for large-scale reactor-core-simulation studies because of the added complexity of installing electrical heaters.

In contrast to the application of electrical heaters to the outer surface of components for preheating, electrical heating systems for reactor-core simulation should be designed so that the heating elements are immersed in the liquid metal. Immersing the elements, however, presents two disadvantages:

1. A leaktight weld must be made between the heater sheath and the wall of the component. Crevices on the liquid-metal side must be avoided; the construction technique to be followed here is the same as that in the welding of tubes to tube sheets in sodium-heated steam generators. If crevices are permitted, sodium or NaK collecting in the crevice during operation will react with moisture-laden air that finds its way into the liquid-metal side of the component when it is shut down for maintenance purposes. Special machining of the component wall is necessary. [50]

2. Care must be taken to make certain that the liquid-metal level rises until the heaters are completely submerged before applying full-line voltage to the heater circuit. If the heaters are operated at full-line voltage for any length of time before being submerged, failure due to overheating will very likely result.

Heaters for this service must be designed to operate dependably while producing enough heat to boil liquid metal. Since these requirements are difficult to satisfy with rod-type heaters of ordinary construction, special heaters have been developed. [51-57] These heaters are designed for direct contact with liquid metal, as heat fluxes in liquid-metal-boiling studies must be accurately known. Indirect heating methods in which heat is applied to containment systems from external sources are not desirable for this application.

One problem that has been encountered

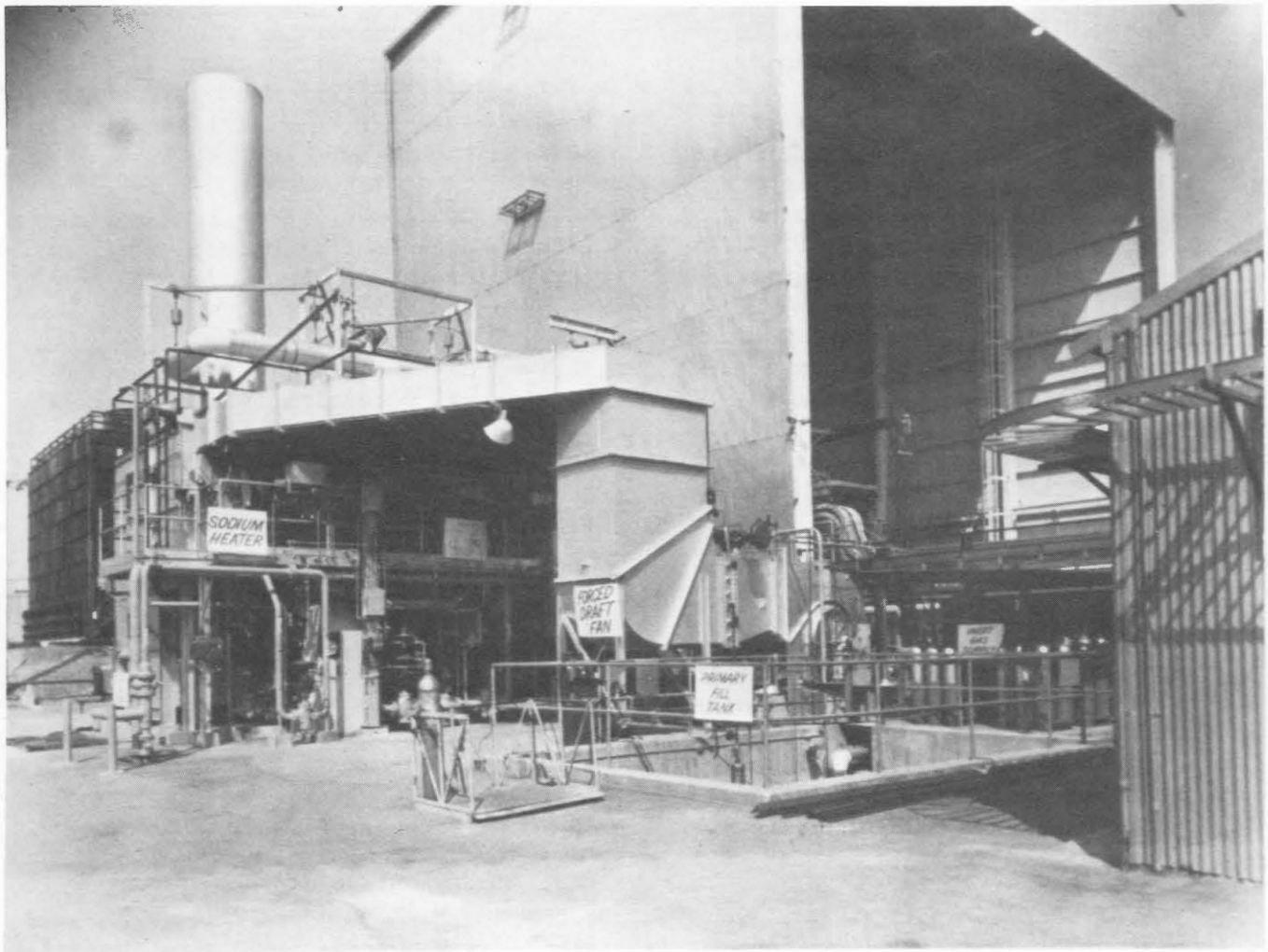

Fig. 3.19 Gas-fired 35-Mw heater for the Sodium Components Test Installation.

in the use of high-current electrical immersion heaters is the effect of the magnetic field surrounding the heater on the liquid metal; it causes an apparent increase in viscosity and a change in heat-transfer characteristics in the immediate neighborhood of the heater. The mechanism of this phenomenon is the subject of continuing investigation.

REFERENCES

1. D.Q. Kern, *Process Heat Transfer*, McGraw-Hill Book Company, Inc., New York, 1950.

2. *Proceedings of ASME Symposium on Air-Cooled Heat Exchangers*, 7th National Heat Transfer Conference, Cleveland, Ohio, Aug. 3, 1964, American Society of Mechanical Engineers.

3. W. Schoenman, Aircooler Optimization Aided by Computer, in *Proceedings of ASME Symposium on Air-Cooled Heat Exchangers*, 7th National Heat Transfer Conference, Cleveland, Ohio, Aug. 3, 1964, American Society of Mechanical Engineers.

4. F.J. Schulenberg, Finned Elliptical Tubes and Their Application in Air Cooled Heat Exchangers, *Trans. ASME (Amer. Soc. Mech. Eng.), Ser. B: J. Eng. Ind.*, pp. 179-190, May 1966.

5. F.W. Lohrisch, What Are Optimum Conditions for Air-Cooled Exchangers? *Hydrocarbon Process. Petrol. Refiner*, *45*(6): 131-136 (1966).

6. F.W. Lohrisch, How Many Tube Rows for Air-Cooled Exchangers? *Hydrocarbon Process. Petrol. Refiner*, *45*(6): 137-140 (1966).

7. G. Theoclitus and T.L. Eckrich, An Experimental Technique for Determining the Effectiveness of Extended Surfaces, in *Proceedings of ASME Symposium on Air-Cooled Heat Exchangers*, 7th National Heat Transfer Conference, Cleveland, Ohio, Aug. 3, 1964, American Society of Mechanical Engineers.

8. K.A. Gardner and T.C. Carnavous, Thermal Contact Resistance in Finned Tubing, *Trans. ASME (Amer. Soc. Mech. Eng.), Ser. C: J. Heat Transfer*, *82*(4): 279-293 (1960).

9. R.L. Chambers and E.V. Somers, Radiation Fin Efficiency for One-Dimensional Heat Flow in a Circular Fin, *Trans. ASME (Amer. Soc. Mech. Eng.), Ser. C: J. Heat Transfer*, *81*(4): 327-329 (1959).

10. H.M. Hung and F.C. Appl, Heat Transfer of Thin Fins with Temperature-Dependent Thermal Properties and Internal Heat Generation, *Trans. ASME (Amer. Soc. Mech. Eng.), Ser. C: J. Heat Transfer*, *89*(2): 155-162 (1967).

11. M.H. Cobble, Nonlinear Fin Heat Transfer, *J. Franklin Inst.*, *277*: 206-216 (1964).

12. B. Lubarsky and S.J. Kaufman, *Review of Experimental Investigations of Liquid-Metal Heat Transfer*, USAEC Report NACA-1270, Lewis Flight Propulsion Laboratory, Nov. 4, 1954.

13. O.E. Dwyer, Eddy Transport and Liquid Metal Heat Transfer, *A. I. Ch. E. (Amer. Inst. Chem. Eng.) J., 9:* No. 2, pp. 261-268 (1963).

14. E. Skupinski, J. Tortel, and L. Vautrey, Determination of the Coefficients of Convection of a Sodium-Potassium Mixture in a Circular Tube, *Int. J. Mass Transfer*, *8*(6): 937-951 (1965).

15. L.J. Cohan and W.J. Deane, Elimination of Destructive Self-Excited Vibrations in Large Gas- and Oil-Fired Utility Units, *Trans. ASME (Amer. Soc. Mech. Eng.), Ser. A: J. Eng. Power*, *87*(2): 223-228 (1965).

16. J.H. Chester, The Aerodynamic Approach to Furnace Design, *Trans. ASME (Amer. Soc. Mech. Eng.), Ser. A: J. Eng. Power: 81*(4): 361-370 (1959).

17. R.W. Cantes and L.E. Johnson, Use of Flow Models for Boiler Furnace Design, *Trans. ASME (Amer. Soc. Mech. Eng.), Ser. A: J. Eng. Power*, *81*(4): 371-379 (1959).

18. A.A. Putnam, Flow-Induced Noise in Heat Exchangers, *Trans. ASME (Amer. Soc. Mech. Eng.), Ser. A: J. Eng. Power*, *81*(4): 417-422 (1959).

19. H. Kassat, *Air-Cooled Heat Exchangers in Oil Refineries*, translated from *Erdöl u Kohle Erdgas Petrochemie, 16:* 388-394 (1963), GEA Airexchangers Inc.

20. K.A. Gardner, Rational Design

Temperature Limits for Interference-Fit Finned Tubing, in *Proceedings of ASME Symposium on Air-Cooled Heat Exchangers*, 7th National Heat Transfer Conference, Cleveland, Ohio, Aug. 3, 1964, American Society of Mechanical Engineers.

21. C.B. Jackson (Ed.), *Liquid Metals Handbook, Sodium-NaK Supplement*, USAEC Report TID-5277, Atomic Energy Commission and Bureau of Ships, July 1, 1955.

22. A.P. Fraas, Design Precepts for High-Temperature Heat Exchangers, *Nucl. Sci. Eng., 8:* 21-31 (1960).

23. Chemical Processing, *Air-Cooled Exchangers Mushroom in CPI*, August 1966.

24. T. Baumeister, *Marks Mechanical Engineers Handbook*, McGraw-Hill Book Company, Inc., New York, 1958.

25. *Encyclopedia of Science and Technology*, McGraw-Hill Book Company, Inc., New York, 1960.

26. R.E. MacPherson and M.M. Yarosh, *Development Testing and Performance Evaluation of Liquid-Metal and Molten-Salt Heat Exchangers*, USAEC Report CF-60-3-164, Oak Ridge National Laboratory, Mar. 17, 1960.

27. R.E. MacPherson et al., Design Testing of Liquid-Metal and Molten-Salt Heat Exchangers, *Nucl. Sci. Eng., 8:* 14-20 (1960).

28. M.M. Yarosh, Evaluation of the Performance of Liquid-Metal and Molten-Salt Heat Exchangers, *Nucl. Sci. Eng., 8:* 32-43 (1960).

29. C. Starr and R.W. Dickinson, *Sodium Graphite Reactors*, Addison-Wesley Publishing Company, Inc., Reading, Mass., 1958.

30. W.E. Parkins, SRE Engineering Description, in *Proceedings of the SRE-OMRE Forum, Los Angeles, Nov. 8-9, 1956*, USAEC Report TID-7525, pp. 7-40, Atomics International, Jan. 15, 1957.

31. G. Billuris et al., SEFOR Plant Design, paper presented at the National Topical Meeting on Fast Reactors, Operating, Under Construction, and Planned for Construction, San Francisco, April 10, 1967, American Nuclear Society.

32. L. Vautrey, Test Rigs for the Rapsodie Coolant Circuits, *Nucl. Eng., 8:* 321-323 (1963).

33. R.H. Costello et al., *APDA Reactor Components Test*, Report APDA-14, Atomic Power Development Associates, Inc., November 1962.

34. A.I. Leipunskii et al., The BN-350 and BOR Fast Reactors, in *Fast Breeder Reactors*, Conference Proceedings, London, May 17-19, 1966, pp. 243-274, Pergamon Press, Inc., New York, 1966.

35. Atomics International, *Technical Description of a Sodium-Component Test Installation*, USAEC Report NAA-SR-5993, Jan. 4, 1961.

36. R. Cygan, Sodium Components Test Installation, in *Proceedings of the Sodium Components Information Meeting, Palo Alto, Calif., Aug. 20-21, 1963*, USAEC Report SAN-8002, pp. 131-136, San Francisco Operations Office, AEC, and General Electric Company.

37. Atomics International, *Sodium Components Test Installation Description*, Report NAA-SR-Memo-11671, May 1, 1968.

38. E.R. Astley, The Conceptual Evaluation of a Fast Flux Test Facility, paper presented at the National Topical

Meeting on Fast Reactors, Operating, Under Construction, and Planned for Construction, San Francisco, April 10, 1967, American Nuclear Society.

39. E.M. Douthett, *SNAP-50/Spur Program - Space Power Systems Engineering*, p. 549, Academic Press, Inc., New York, 1966.

40. L.J. Koch et al., *Experimental Breeder Reactor II (EBR-II) Hazard Summary Report*, USAEC Report ANL-5719, Argonne National Laboratory, May 1957.

41. M.R. Mahone (Ed.), *Sodium Pump Test Facility (SPTF) Overall Conceptual System Design Description*, USAEC Report NAA-SR-Memo-12160, Atomics International, Feb. 23, 1967.

42. J.R. Blanchfield, Jr., *Conceptual Design and Cost Estimate for Sodium Pump Test Facility*, USAEC Report WCAP-2526, Westinghouse Electric Corp., November 1963.

43. R.A. Tidball, F.L. Mangold, S.N. Tower, and T.A. Ciarlariello, *Final Report on the 1000-kw Air-cooled, Liquid-Metal Heat Transfer Loop*, USAEC file No. NP-5751, Mine Safety Appliances Co., Aug. 16, 1955.

44. P. Colombo, Comitato Nazionale per l'Energia Nucleare, *Preliminary Design for a Test-Component Loop with Liquid Sodium at Elevated Temperature*, USAEC Report AEC-tr-5310, translated from Italian, Oak Ridge National Laboratory, 1962.

45. G.E. Deegan et al., *Design Modifications to the SRE During FY 1960*, USAEC Report NAA-SR-5348 (Rev.), Atomics International, Feb. 15, 1961.

46. R.E. Holtz, Heating Techniques for Liquid-Metal Loops, in *Proceedings of the Conference on Application of High-Temperature Instrumentation to Liquid-Metal Experiments, Argonne, Ill., Sept. 28-29, 1965*, USAEC Report ANL-7100, pp. 9-22, Argonne National Laboratory.

47. R.W. Atz, *The Large-Component Test Loop - Description and Operating Capabilities*, USAEC Report NAA-SR-Memo-8217, Atomics International, Feb. 18, 1968.

48. J.A. Leppard, Sodium Component Test Installation, in *Proceedings of Sodium-Components Development Program Information Meeting, Chicago, June 16-17, 1965*, USAEC Report CONF-650620, pp. 166-177, Chicago Operations Office, AEC.

49. R.W. Atz, *The Large-Component Test Loop - Description and Operating Capabilities*, Report NAA-SR-Memo-8217, Atomics International, Feb. 18, 1963.

50. Babcock and Wilcox Co., *Sodium-Heated Steam Generator Development. Progress Report No. 14*, USAEC Report BAW-1280-14, June 1964.

51. D. Logan et al., *Boiling Liquid Metals and Two-Phase Investigations*, Report NAA-SR-TDR-12485, Atomics International, June 1967.

52. B.R. Hayward, E.L. Babbe, and D.K. Darley, *High-Heat-Flux Heater Development, Preliminary Performance Tests*, USAEC Report NAA-SR-12242, Atomics International, Dec. 31, 1966.

53. R.C. Noyes, *Boiling Studies for Sodium Reactor Safety. Part I. Experimental Apparatus and Results of Initial Tests and Analysis*, USAEC Report NAA-SR-7909, Atomics International, Aug. 30, 1963.

54. J.B. Heineman, Forced-Convection Boiling Sodium Studies at Low Pressure, in *Proceedings of the Conference on Application of High-Temperature Instrumentation to Liquid-Metal Experiments, Argonne, Ill., Sept. 28-29, 1965*, USAEC Report ANL-7100, pp. 189-194, Argonne National Laboratory.

55. Oak Ridge National Laboratory, Forced-Circulation Boiling-Potassium Corrosion Loops, in *Annual Progress Report*, ORNL-3650, pp. 42-45, 1963.

56. R.E. Barry and R.E. Balzhiser, Condensation of Sodium at High Heat Fluxes, in *Proceedings of the Third International Heat Transfer Conference, Chicago, Ill., Aug. 7-12, 1966*, Report CONF-660801, Vol. II, pp. 318-328, American Institute of Chemical Engineers, New York, 1966.

57. C.J. Baroczy, *A Systematic Correlation for Two-Phase Pressure Drop*, USAEC Report NAA-SR-Memo-11858, Atomics International, Mar. 11, 1966.

Chapter 4

Radiators, Condensers, and Boilers

R. E. BEDFORD and J. M. HOWARD

4-1 INTRODUCTION

A relatively new area in the field of liquid-metal heat-exchanger design is the design of radiators, condensers, and boilers for space power plants that produce electricity for the propulsion, guidance, and communications equipment of space vehicles. This chapter presents the factors that must be considered in the design of these components for liquid-metal service in the space environment. Both the direct-condensing radiator, in which the working fluid changes from a vapor to a liquid within the radiator, and the sensible-heat radiator, in which the working fluid maintains its phase but loses sensible heat and temperature, are discussed. In addition, the heat-exchanger type of condenser, which uses liquid metal for both the coolant and condensing fluid, is considered. The boilers considered are of the indirectly heated type in which both the primary (heating) fluid and the secondary (boiling) fluid are liquid metals.

In this chapter attention is restricted to sodium and NaK alloy coolants. The general areas of fluid flow and of liquid-metal heat transfer are discussed in detail in Vol. II, Chaps. 1 and 2, respectively; therefore the only aspects of these subjects considered here are those unique to radiator, condenser, or boiler design.

4-2 RADIATOR-DESIGN CONSIDERATIONS

The design of radiators to be used with liquid-metal working fluids involves many special technical disciplines, including:

1. Radiative heat rejection.
2. Fluid mechanics and stability of zero-gravity environment for single- and two-phase flow.
3. Materials selection.
4. System and vehicle integration.
5. Mechanical design for withstanding launch loadings.
6. Meteoroid protection.

In addition, the space application requires that the radiator be light, compact, and highly reliable. The technical areas involved in the design of a space radiator are summarized here and are described in considerable detail in subsequent sections.

In some respects the heat-transfer analysis of a space radiator is less complex than many designs for ground use as only radiation, not convection, is involved. The importance of minimizing either weight or area, however, requires greater design accuracy than is normal for heat-transfer analysis since factors of ignorance add weight or area. The basic theories of radiative heat transfer are well-known. Recent work has been concerned with the application of basic theory to special cases of interest to the radiator designer. This chapter is concerned primarily with the design of a finned-tubed surface. Either a vapor is condensed or liquid is cooled in the tubes, and a large portion of the heat is radiated from the fins attached to the tubes. The heat-transfer analysis of this configuration involves the thermal resistance of the fins, the emissivity of the radiator surface, and interchange between the tubes and the fins. The resistance of the condensing film is of secondary importance for low-temperature direct-condensing radiators since the radiation heat transfer usually governs. In high-temperature radiators the condensing and convective heat-transfer coefficients may become important.

Another major problem area in the design of radiators relates to fluid mechanics and stability. A detailed knowledge of condenser fluid mechanics is important in the design of a direct-condensing radiator. A stable liquid-vapor interface, constant inventory, and constant pressure drop must be maintained in the radiator condenser to prevent transients in the remainder of the power system.

Meteoroid protection is accomplished by using an extended radiator surface where only tubes containing the heat-transfer fluid are susceptible to damage and require protection. This protection can be provided either by armor (thick tube walls) or bumpers (thin shields placed at some distance from the tube).

Erosion of heat-rejection surfaces by micrometeoroids and sublimation of materials in the vacuum of space are minimized by the proper selection and application of materials. A radiating surface should have a high emissivity in the infrared spectrum, a low absorptivity in the solar spectrum, be resistant to mechanical erosion, and should not evaporate in a vacuum. Fin and tube materials should be light, easy to fabricate, low cost, and should have a high thermal conductivity. In addition, tube material must be compatible with sodium and NaK.

The integration of the radiator with the launch vehicle and power plant is a major problem. The radiator must be contained along with the remainder of the power plant in a relatively small section of the vehicle. Therefore packaging and radiator deployment are important considerations in the design of any large space radiator. These integration problems, though important, depend on the specific application and for this reason are not considered in any detail in this chapter.

4-2.1 *Thermal Considerations*

This section outlines the techniques used in designing a radiator or radiative condenser that is thermally adequate for a specific application. Many combinations of materials, fin thicknesses, and numbers of tubes can be used in the design of a radiator of a required heat-rejection capability. The final choice is usually fixed either by a limit on the area available for the radiator, or by an optimization in terms of weight, area or cost effectiveness.

(a) *Radiator Concepts and Configurations*

From a thermal point of view, there are two basic radiator concepts that

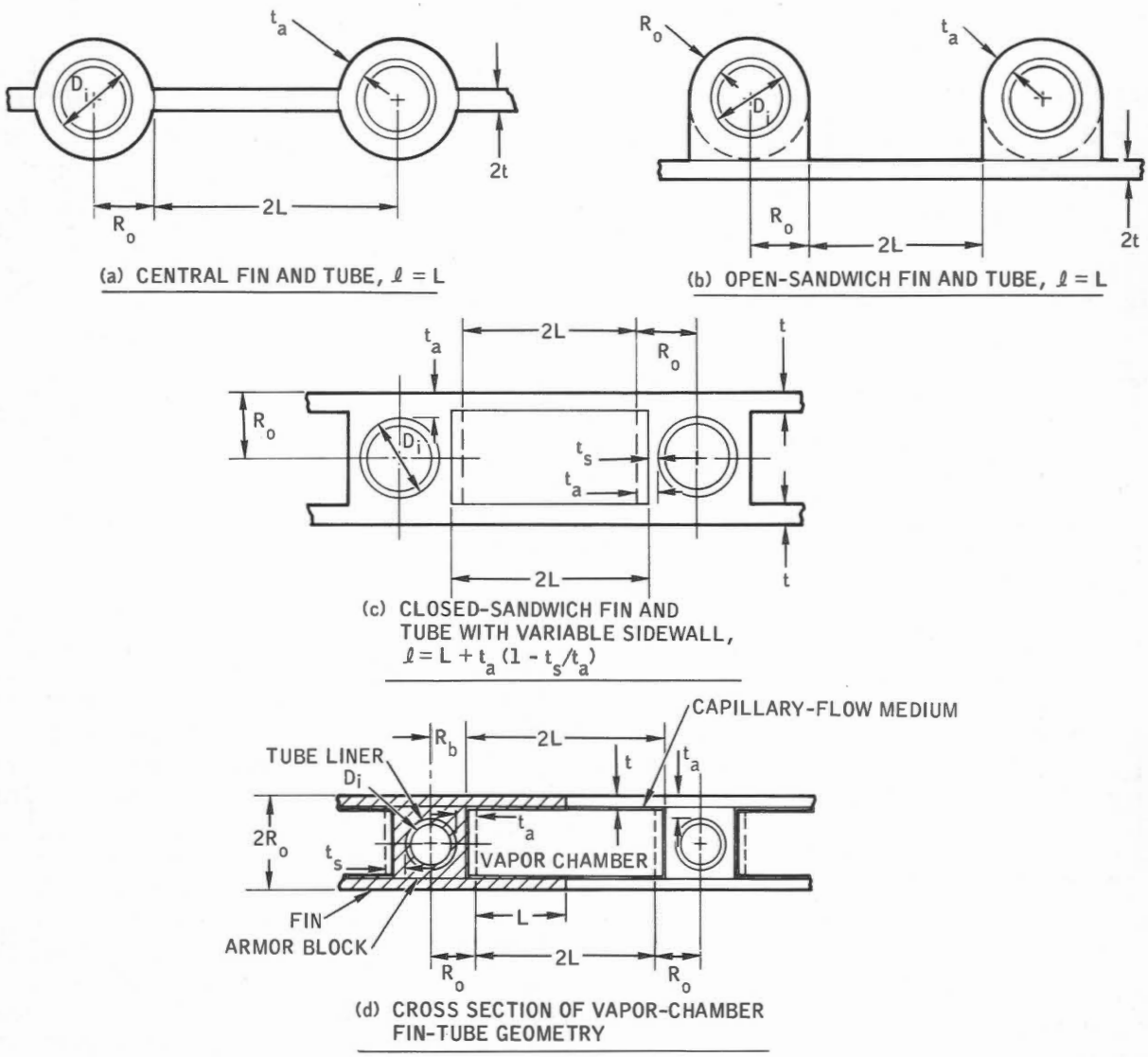

Fig. 4.1 - Radiator fin-tube configurations

deserve consideration. The first concepts, the tube-and-solid-fin arrangements shown in Fig. 4.1 (a, b, and c), are early approaches to radiator design. There are many possible variations of tube-and-fin geometry; however, the thermal problems are essentially the same for each. The sodium or NaK passes through the tubes. The armor on either the tube or the fin protects the tube from meteoroid penetration. Heat from the fluid is conducted through the tube walls and into the fins. Depending on the radiator geometry, either one or both of the fin-tube surfaces radiates this heat to space. If a meteoroid punctures a fin, a very small amount of surface area is lost, and heat-rejection capability of the radiator drops by a negligible amount. On the other hand, puncture of a tube causes the coolant to leak out, a generally catastrophic event. For this reason the tubes are heavily armored and spaced far apart. Tube spacing is limited by the temperature drop resulting from heat conduction through

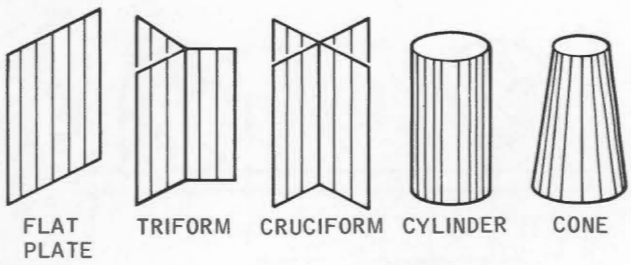

Fig. 4.2 - Radiator configurations.

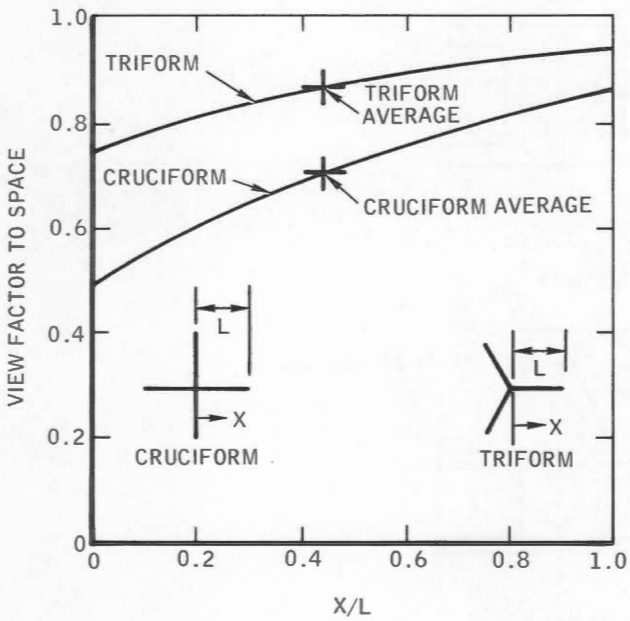

Fig. 4.3 - Local view factor to space for triform and cruciform configurations.

the fins.

The second concept, the vapor-chamber fin [Fig. 4.1 (d)], proposes to reduce radiator weight and area by providing for an essentially isothermal fin between tubes. This is accomplished by replacing the single solid fin, which transfers heat by conduction, with a double-wall fin that forms a hollow chamber, which contains a heat-transport fluid. The working fluid can then be boiled off the tube surfaces of the chamber and

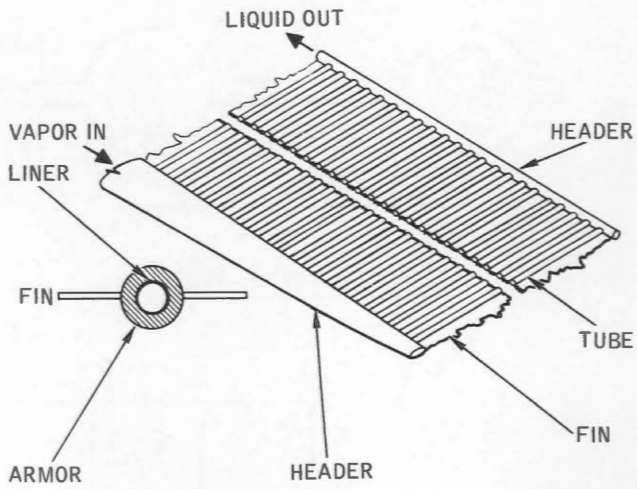

Fig. 4.4 - Plane finned-tube direct-condensing radiator.

condensed on the fin surfaces to produce a fin of constant temperature and high radiating effectiveness. Condensate is then returned to the boiling surface by some means of capillary pumping that is essentially insensitive to gravity forces [1]. In the radiator application the vapor-fin chamber, which is vulnerable to meteoroid penetration, can be compartmented into a large number of sealed segments to minimize the effect of puncture on the operative area. The principle of transporting heat by boiling and condensing a fluid in conjuction with the return of the condensate through a capillary medium has been established experimentally in heat pipes [2, 3]. The application of the vapor-chamber fin concept to space radiator design is analyzed in Ref. 4.

Of the fin-tube configurations shown in Fig. 4.1, the central fin construction (a) is the geometry considered in most analytical studies. However, it may be less practical to fabricate than some alternate geometries.

The open-sandwich construction (b) is the most easily fabricated; it lends itself to tube-to-fin furnace brazing, torch brazing, or welding,

depending on the tube and fin materials, strength requirements, and/or furnace capacity. Its use in a conical or cylindrical panel configuration with the tubes on the inside makes maximum use of the meteoroid protection effect of the fins.

The closed-sandwich concept (c) has the advantages of strength and the meteoroid protection afforded by the fin location for any panel configuration but is somewhat more difficult to fabricate than the open-sandwich concept.

Five typical radiator configurations are shown in Fig. 4.2. The panel choice, of course, is determined by the envelope available. In general, the flat plate is the lightest for a given heat rejection but requires greater envelope dimensions. Conversely, the cone and cylinder may be heavier but will fit into a smaller envelope. The triform and cruciform fall between the flat plate and cone or cylinder with regard to weight and envelope size. In brief, the optimum radiator configuration can be determined only in the specific case, including in particular the launch vehicle integration for each case.

For the triform and cruciform configurations, the view factor to space may be considerably less than unity. Figure 4.3 shows the local view factor from radiators of these configurations to space [5]. The integrated values of the view factors, 0.866 for the triform and 0.707 for the cruciform, can be used as constants over the entire surface without sizable overall error. Figure 4.4 shows a flat-plate solid-fin-and-tube direct-condensing radiator of the central-fin type.

(b) *Nomenclature for Secs. 4-2.1 to 4-2.4.*

A	Area of radiating surface
A_t	Total radiating area of radiator
A_v	Outside area of vulnerable surface (tubes, headers, etc.) in radiator
a	Albedo, the fraction of solar radiation incident on the earth which is reflected
a_t	Correction for a finite target; i.e., the target that will be penetrated by a projectile is a times the depth of penetration in an infinitely thick target (due to spalling)
B	Tube center-to-center spacing
C_p	Specific heat of liquid
C_{pv}	Specific heat of vapor
c	Sonic velocity in armor $(12\sqrt{E_t g_0 / P_a})$
D	Hydraulic diameter of tube = D_i for circular tube
D_{cr}	Critical tube diameter for interface stability
D_i	Inside diameter of tube
D_{H1}	Inside diameter of vapor header at inlet
D_{H2}	Inside diameter of vapor header at entrance to last tube supplied by header
D_{LH}	Diameter of liquid header
D_{VH}	Diameter of vapor header
D_o	Outside diameter of tube
D_1	Inside diameter of vapor header in Section 1 (Fig. 4.10)
D_2	Inside diameter of vapor header in Section 2 (Fig. 4.10)
d	Particle diameter (cm)
E_t	Modulus of elasticity of meteoroid armor
$F_{E(SR)}$	Radiator view factor for earth's reflected solar radiation (albedo)
$F_{E(T)}$	Radiator view factor for earth's thermal radiation
F_s	Radiator view factor for direct solar radiation
$F_>$	Cumulative flux (particles/m^2-day)
f	Friction factor
g	Local acceleration

g_0	32.2 ft/sec^2
g_c	Gravitational acceleration at earth's surface
G_x	Mass velocity at position x along header
H	Earth thermal radiation constant
H_L	Liquid-header length
h	Heat-transfer coefficient inside radiator tube
h_B	Boiling heat-transfer coefficient of heat-transfer fluid in vapor-chamber fin
h_c	Condensing heat-transfer coefficient of heat-transport fluid in vapor-chamber fin
h_{fg}	Heat of condensation of vapor
h_{in}	Heat content of fluid entering radiator
h_{out}	Heat content of fluid leaving radiator
K	Entrance loss coefficient
k	Thermal conductivity of fin material
k_t	Thermal conductivity of tube-wall material
L	Minimum fin half-length (Fig. 4.1); one-half the tube center-to-center distance less the outside tube radius
L_c	Condensing length; length from tube inlet to liquid-vapor interface
L_{cr}	Critical condensing length
L_{0c}	Reference condensing length
l	Actual fin half-length (Fig. 4.1)
M	Mass of vapor
m	Minimum particle mass (g)
$\dot{m}$	Mass flow rate
$\dot{m}_x$	Mass flow rate at position x along header
N	Number of radiator tubes
N_c	Conductance parameter, $N_c = \sigma l^2 T_0^3/kt$
n	Number of g's acceleration = $= g/g_0$
P	Pressure (absolute)
$P(0)$	Probability of no penetration of vulnerable area by meteoroids in a period of τ days
P_0	Total pressure at inlet of tube
P_i	Pressure at liquid-vapor interface in radiator tube
P_{i_0}	Liquid-vapor interface pressure at design point
P_m	Pressure of vapor in vapor manifold
P_{m0}	Pressure of vapor in vapor header at design point
$(\Delta P)_f$	Frictional pressure drop
$(\Delta P)_H$	Header pressure drop
Q	Net heat transferred from radiator to sink
Q_{space}	Heat load from space
R	Gas constant
R_b	Tube sidewall to tube centerline dimension, $R_O - L$
Re	Reynolds number
Re_0	Axial Reynolds number based on diameter
R_O	Outside tube radius
S	Solar-radiation constant
T	Radiating-surface temperature
T_0	Fin-base temperature
T_{00}	Fin-base temperature at design point
T_{01}	Fin-base temperature at radiator inlet
T_{02}	Fin-base temperature at radiator outlet
T_b	Bulk-fluid temperature
T_E	Effective fin-base temperature for evaluation of surface effectiveness, η_O
T_f	Fluid temperature
T_i	Temperature of vapor at liquid-vapor interface
T_{in}	Temperature of fluid at radiator inlet
T_m	Temperature of vapor in manifold
T_{out}	Temperature of fluid at radiator outlet
T_s	Effective radiant-sink temperature
T_{sat}	Saturation temperature of vapor at the radiator-inlet pressure
ΔT_w	Temperature drop between condensing fluid and base of fin

ΔT_{w0} Temperature drop between condensing fluid and base of fin at design point
t Half-thickness of the fin
t_a Tube armor thickness
t_s Tube sidewall thickness
U Overall heat-transfer coefficient
V Meteoroid velocity (cm/sec)
$V_{(Z)}$ Average axial velocity at position Z
V_0 Inlet axial velocity (vapor) at tube inlet
V_0^1 Inlet axial velocity to perturbed tube
V_1 Average vapor velocity in Section 1 of vapor header (Fig. 4.10)
V_2 Average vapor velocity in Section 2 of vapor header (Fig. 4.10)
X_0 Vapor quality at radiator inlet
x Distance along header length
y Momentum loss factor
Z Axial distance along tube
Z_R Distance from tube inlet to point of runback
α Flux-mass relation of meteoroids (5.71×10^{-10})
α_s Absorptivity of radiator surface to solar radiation
β Constant (1.34)
γ Cratering coefficient
ε Radiating surface emissivity
σ Stefan-Boltzmann radiation constant [0.1713×10^{-8} Btu/(hr)(sq ft)($^\circ R^4$)] surface tension
η_0 Surface effectiveness defined as the ratio of the heat rejected by the radiating surface to the heat that would be rejected if the surface were all at the fin-base temperature (radiation from tube surfaces included in this definition)
ϕ^2 Ratio of two-phase pressure gradient to single-phase vapor-pressure gradient
λ Heat-transfer parameter for vapor-chamber fin
ρ_a Density of meteoroid armor
ρ_f Density of fin material
ρ_L Density of liquid phase of working fluid
ρ_p Meteoroid density (g/cm^3)
ρ_t Armor density (g/cm^3)
ρ_v Density of vapor phase of working fluid
μ_L Viscosity of liquid phase of working fluid
μ_v Viscosity of vapor phase of working fluid
τ Exposure time in days

(c) *Radiation Heat Transfer*

The basic equation that governs the net radiant heat transfer from a surface is the familiar Stefan-Boltzmann law, given by

$$Q = \varepsilon \sigma A (T^4 - T_s^4) \tag{4.1}$$

where T_s is the sink temperature and T is the surface temperature.

The sink temperature can be defined as the temperature that a passive surface would reach if it were in thermal equilibrium with its environment. It is an effective temperature rather than a true temperature because of its dependence on the radiating surface properties. The environmental heat input to a radiator operating in space can be expressed as

$$Q_{\text{space}} = \alpha_s S F_s A + \alpha_s S F_{E(SR)} \alpha A + \varepsilon H F_{E(T)} A \tag{4.2}$$

and the net heat transfer can be written as

$$Q = \varepsilon \sigma A T^4 - Q_{\text{space}} \tag{4.3}$$

The equivalent sink temperature can be determined from Eqs. 4.1 to 4.3 as

$$T_s = \left(\frac{1}{\varepsilon \sigma}\right)^{1/4} \left[\alpha_s S F_s + \alpha_s S F_{E(SR)} \alpha + \varepsilon H F_{E(T)}\right]^{1/4} \tag{4.4}$$

Equation 4.1 describes the heat transfer from a surface at a constant temperature T, but radiators generally employ extended radiating surfaces that are not at a constant temperature. The performance of extended surfaces is conveniently described in terms of a variable called the surface effectiveness. The surface effectiveness is the ratio of the actual heat rejected by the extended surface to the heat that would be rejected if the surface were all at the temperature T_0 (where T_0 is the fin-root temperature), i.e.,

$$\eta_0 \equiv \frac{Q_{actual}}{\varepsilon\sigma A_t (T_0^4 - T_s^4)} \qquad (4.5)$$

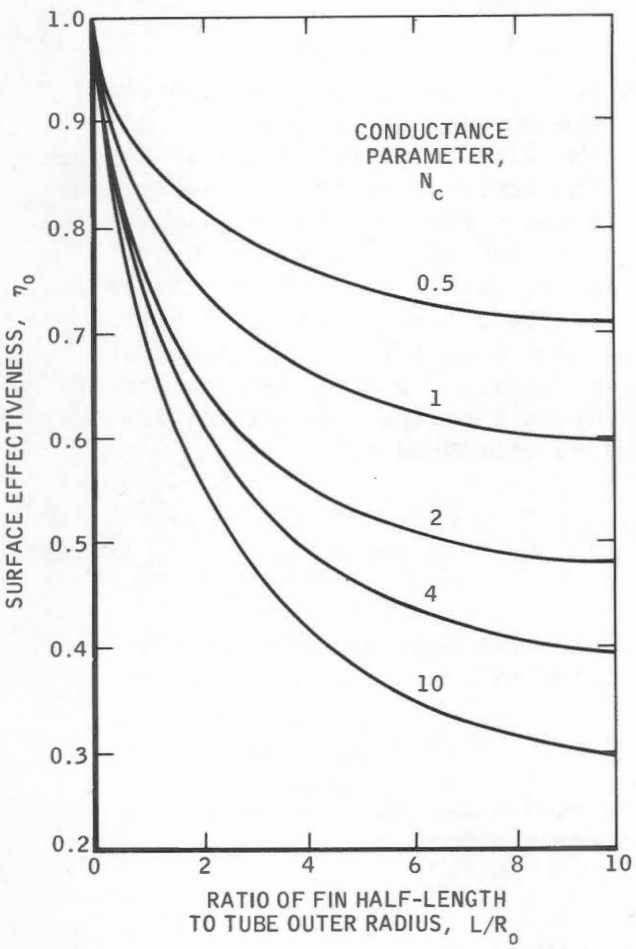

Fig. 4.5 - Surface effectiveness for central fin and tube configuration with radiation from both sides.

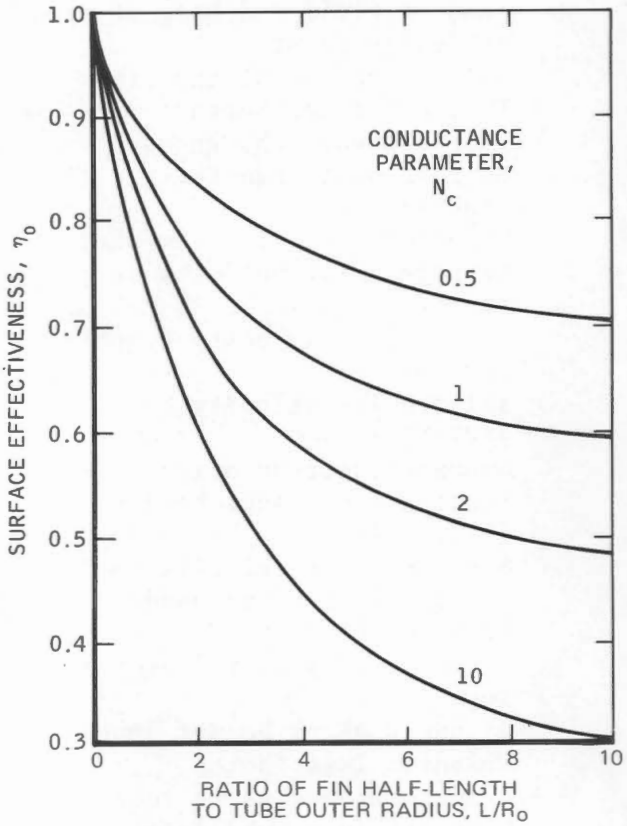

Fig. 4.6 - Surface effectiveness for open-sandwich fin-tube configuration with radiation from both sides.

The analytic solution of the radiant heat-transfer fin problem is quite complex. To determine the surface effectiveness, we must solve second-order differential equations expressing the relation between conductive and radiative heat transfer in the fin-tube element. Since methods of solution are described in the literature [6], they are not discussed here. The surface effectiveness has been determined for a variety of fin-tube geometries [7]. The surface effectiveness for Fig. 4.1 (a) and (b) expressed in terms of two dimensionless parameters is shown in Figs. 4.5 and 4.6, respectively. These parameters are the ratio of fin half-length to tube outer radius L/R_O, which describes the effective cavity of the fin and tube, and the conduc-

tance parameter N_c (sometimes called the radiation modulus), which describes the ratio of the radiating potential of the fin to its conducting potential. The conductance parameter is defined by the relation $N_c = \sigma l^2 T_o^3/kt$ for a black body. For Fig. 4.1 (a) and (b), $l = L$.

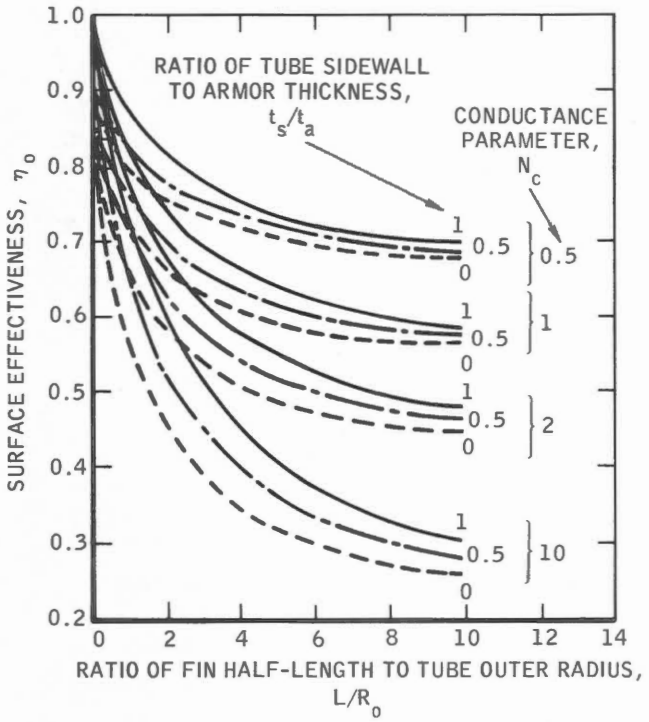

Fig. 4.7 - Surface effectiveness for closed-sandwich fin-tube configuration with radiation from both sides.

An additional parameter is required to describe the variable-tube sidewall thickness used in the closed-sandwich design in Fig. 4.1 (c). This parameter is the ratio of the actual sidewall thickness of the tube to the thickness specified by the meteoroid protection criteria t_s/t_a. The surface effectiveness for the closed-sandwich configuration is shown in Fig. 4.7.

Several specific assumptions were used to derive the fin-tube efficiencies [7] shown in Figs. 4.5 to 4.7:

1. Incident radiation from external sources is negligible.

2. The radiator surfaces act as black bodies with incident and emitted radiation governed by Lambert's cosine law.

3. Steady-state one-dimensional heat flow occurs in the fins with the fin-base temperature equal to the temperature of the tube outer surface.

4. Fin and tube material properties are constant and evaluated at the fin-base temperature.

5. The development of the fin and tube angle factors is based on an infinite longitudinal extent of fin and tube.

6. Fin thickness is neglected in the determination of the view factor from the base surface to the fin.

7. Temperature on the outer tube surface is constant circumferentially and longitudinally.

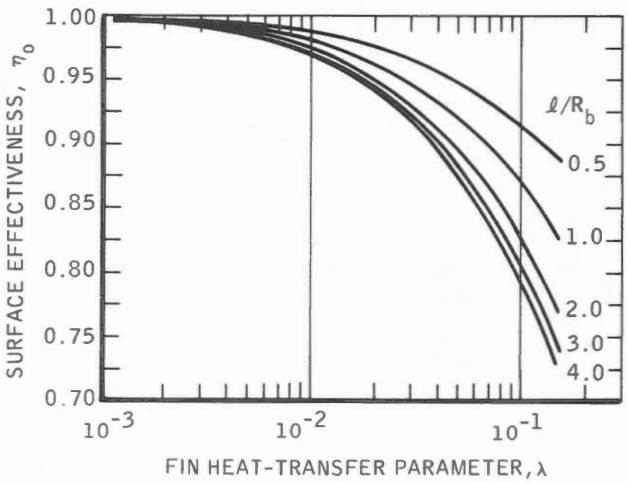

Fig. 4.8 - Surface effectiveness for vapor-chamber fin with radiation from both sides [4].

The total radiating effectiveness based on the base surface temperature for the vapor-chamber fin configuration [4] is shown in Fig. 4.8 as a function of the heat-transfer parameter and the ratio l/R_b [see Fig. 4.1 (d)]. The heat parameter, λ, is defined by

$$\lambda = \frac{\sigma \varepsilon T_0^3}{h_B} \left[\frac{l}{R_o - t} + \frac{h_B}{h_c} \right] \qquad (4.6)$$

where h_B and h_c are the boiling and condensing heat-transfer coefficients, respectively, of the heat-transport fluid in the vapor-chamber fin.

(d) *Effective Temperature for Evaluating* η_0

The equations so far developed assumed that the temperature of the base surface is a constant (T_0). In the condensing region of a radiative condenser this assumption is appropriate if the static pressure change is small. This is not true for the sensible-heat radiator, where T_0 varies between T_{in} and T_{out} of the fluid flowing in the tubes (neglecting for the present, the temperature drops associated with the fluid film and conduction through the tube wall). The preferable method of analysis for variable T_0 would be an integration over the radiating from T_{in} to T_{out} with the evaluation of η_0 at each point [8]. In many instances, however, it is sufficient to define an effective temperature to evaluate the surface effectiveness between T_{in} and T_{out}. The effective temperature is defined by [9]

$$T_E \equiv \left[\frac{3 T_{01}^3 T_{02}^3}{T_{01}^2 + T_{01} T_{02} + T_{02}^2} \right]^{1/4} \qquad (4.7)$$

where T_{01} and T_{02} are the inlet and exit base-surface temperatures.

(e) *Heat Rejected per Unit Area*

For the sensible-heat radiator the surface area required can be expressed as [9]

$$A_t = \frac{c_p \dot{m}}{3 \varepsilon \sigma \eta_0} \left[\frac{1}{T_{02}^3} - \frac{1}{T_{01}^3} \right] \qquad (4.8)$$

or, in terms of the heat rejected per unit area,

$$\frac{Q}{A} = \frac{3 \varepsilon \sigma \eta_0 (T_{01} - T_{02})}{\left[\frac{1}{T_{02}^3} - \frac{1}{T_{01}^3} \right]} \qquad (4.9)$$

The sink temperature, T_s, was neglected in Eqs. 4.8 and 4.9; this is a valid simplification for radiators operating above 1000°F.

Note that the equations presented in the previous discussion do not account for the effect of heat conduction in the fin in the direction of fluid flow; the differences in sink temperature around the radiator such as would occur in, for example, a cylindrical radiator; or the effect of maldistribution of flow, which would lead to an asymmetry of the temperature distribution between the tubes. More rigorous heat-transfer models have been developed in the literature to account for these effects [5, 8, 10].

(f) *Fluid-to-Fin Heat Transfer*

The preceding section showed the dependence of the radiated heat on the base-surface temperature, T_0. In general, the fluid temperature rather than the base-surface temperature is specified. The difference between these temperatures is composed of two parts: The temperature drop through the tube wall to the fin, and the drop through the fluid film. The general equation for the rate, Q, at which heat must be rejected by a radiator is

$$Q = \dot{m}(h_{in} - h_{out}) \qquad (4.10)$$

If constant specific heats can be assumed for the single-phase regions of heat rejection, Eq. 4.10 can be approximated by

$$Q = \dot{m}\left[C_{pv}(T_{in} - T_{sat}) + X_0 h_{fg} + C_p(T_{sat} - T_{out})\right] \quad (4.11)$$

The fluid flow rate, inlet temperature, pressure, quality, and the desired exit temperature are fixed by system requirements and can be considered as input available to the radiator designer. The cycle fluid is also selected during the system studies, so that fluid properties such as density, specific heat of liquid and vapor, and heat of condensation are available to the designer (see Vol. I, Chap. 1) and the fluid heat load can be calculated. For most applications sodium and NaK are used simply as a coolant rather than as the working fluid in a vapor cycle, in which case Eq. 4.11 reduces to

$$Q = \dot{m}\, C_p(T_{in} - T_{out}) \quad (4.12)$$

The heat from the fluid is transferred to the inside surface of the tube by convection and to the outside surface of the tube by conduction. The heat transferred to a length dx of the tube outer surface is given by

$$dQ = U(\pi D_o)(T_b - T_0)dx \quad (4.13)$$

where T_b is the bulk-fluid temperature. The overall heat-transfer coefficient U based on the outside tube area is obtained from

$$U = \frac{1}{[(D_o/D_i)/h] + [D_o \ln (D_o/D_i)2k_t]} \quad (4.14)$$

where h is the film coefficient of heat transfer, which can be calculated as prescribed in Vol. II, Chap. 2.

Equation 4.13 can be used to predict the bulk-fluid to fin-base-temperature difference in terms of the local heat flux per unit length. In radiative condensers the heat flux is nearly constant along the radiator. In sensible-heat radiators, however, the temperature, and thus the radiative heat flux, changes markedly along the radiator length. In Fig. 4.9 the bulk-fluid temperatures at the inlet and outlet (T_{in} and T_{out}) are specified, but T_{01} and T_{02} are not. A heat balance on the element of tube and fin length dx gives (neglecting axial conduction)

$$U\pi D_o\, dx(T_{in} - T_{01}) = \varepsilon\sigma\eta_0 A\, dx(T_{01}^4 - T_s^4) \quad (4.15)$$

where A is the surface area per unit length of the fin-tube element. Equation 4.15 can be solved directly for T_{01}, and T_{02} can be determined in the same manner. Once the entrance and exit fin-base temperatures are known, the radiator area can be determined [11].

(g) *Heat Pipes*

The heat pipe consists of an evacuated enclosure containing a capillary structure along its inside walls and a small quantity of fluid that wets the capillaries and has a significant vapor pressure at the required operating temperature. The fluid evaporates at the heat-input end, condenses on the peripheral surfaces, and returns to the boiling interface by capillary action along the walls. Operation is similar to that of the vapor-fin chamber described in Sec. 4-2.1(a).

The design characteristics, along

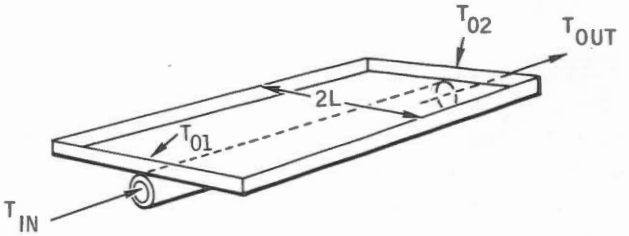

Fig. 4.9 - Tube-fin element.

with a summary of recent work pertinent to heat pipes, is covered in detail in Chap. 5 and is not discussed further here.

4-2.2 *Fluid Flow*

A detailed knowledge of single-phase and condensing fluid mechanics is important in the design of a radiator. The major factors related to fluid mechanics that must be considered in the design of radiators are:

1. Fluid pressure losses and flow regimes.
2. Inlet- and outlet-manifold design.
3. Stability.

(a) *Fluid Pressure Losses and Flow Regimes*

Techniques for the determination of pressure losses are treated extensively in Vol. II, Chap. 1, and are not repeated here. The total overall change in static pressure between the inlet and outlet of the radiator can be subdivided as follows:

1. Inlet header frictional pressure drop.
2. Header-to-tube turning and entrance loss.
3. Tube pressure changes: For direct-condensing radiators pressure change in tube includes the two-phase condensing pressure drop, pressure rise due to momentum recovery, and the frictional pressure loss in the liquid subcooling leg. For the sensible-heat radiator the tube pressure drop is the frictional loss in the liquid.
4. Tube-to-exit-header turning loss.
5. Exit-header frictional pressure loss.

To accurately compute the pressure drop in a radiative condenser requires a step-by-step procedure with the application of local pressure-drop data appropriate to the local flow pattern. Various flow patterns that may be encountered in a condenser are:

1. Stable-film annular flow.
2. Unstable-film annular flow with entrained liquid.
3. Slug flow and bubbly flow.
4. Single-phase liquid.

For the sensible-heat radiator, of course, only single-phase liquid flow is of concern.

The pressure also depends on the flow regime of each phase. For the radiative condenser four types of flow are possible:

1. Viscous (liquid phase)-viscous (vapor phase).
2. Viscous-turbulent.
3. Turbulent-viscous.
4. Turbulent-turbulent.

The type of flow is evaluated from the film and vapor Reynolds numbers. For Reynolds numbers greater than 2000 flow is turbulent. Most condenser designs of interest fall under viscous-turbulent or viscous-viscous flow regimes.

(b) *Manifold Design*

In the design of a radiator, consideration must be given to the sizing of the liquid and vapor manifolds. When more than one radiator tube is to be operated in parallel, it is desirable to produce equal loading and similar conditions in each tube. Distribution of flow to each tube is influenced by the manifold design. If vapor-flow distribution is unequal, condensing and subcooler lengths will vary from tube to tube. Variations in condenser-tube inlet pressure, tube diameter, condenser pressure drop, and tube heat-rejection rate all lead to variations from tube to tube which can cause unequal inventory distribution.

The inlet-vapor manifold should be designed for constant static pressure at the inlet of each tube. The design procedure utilizing this criterion, the static-regain method, attempts to control the static-pressure regain due to loss of fluid velocity when fluid is removed at the manifold outlets. This static-pressure regain should be equal

to the static-friction pressure drop in each section so that a constant static-pressure manifold is obtained.

The velocity is reduced at each condenser tube take-off so that the recovery in static pressure due to this reduction offsets the friction in the succeeding sections. Thus uniform static pressure is maintained at all branches. Under ideal conditions, from 0.7 to 0.8 of the velocity head is recovered, the balance being dissipated in dynamic losses, not considering the changes in section shapes or direction. In practical design, an average recovery of 0.5 is obtained.

A typical section of a vapor header [12] is shown in Fig. 4.10. By the static-regain method, the pressure drop due to friction, $(\Delta P)_f$, in Section 2 of the figure, is offset by recovery in static pressure in Section 1 due to reduced velocity $(\Delta P)_R$,

$$(\Delta P)_f\Big|_2 = (\Delta P)_R\Big|_1 \tag{4.16}$$

or

$$\frac{fB}{D_2}\left(\frac{\rho_v V_2^2}{2g_c}\right)_1 = \frac{0.5\rho_v}{2g_c}(V_1^2 - V_2^2) \tag{4.17}$$

Velocity V_2 is not known but can be expressed as a function of flow rate $\dot{m}_2$ and diameter D_2:

$$V_2 = \frac{4\dot{m}_2}{\pi\rho_v D_2^2} \tag{4.18}$$

and introducing constants α and β, where

$$\alpha = \frac{1.625}{\rho_v^2}\ \text{ft}^6/\text{lb}^2$$

and

$$\beta = \frac{3.25fB}{\rho_v^2}\ \text{ft}^7/\text{lb}^2$$

Equation 4.18 reduces to

$$D_2^5 - \alpha\left(\frac{\dot{m}_2}{V_1}\right)^2 D_2 - \beta\left(\frac{\dot{m}_2}{V_1}\right)^2 = 0 \tag{4.19}$$

The vapor-header friction factor, f, is determined from a Moody diagram.

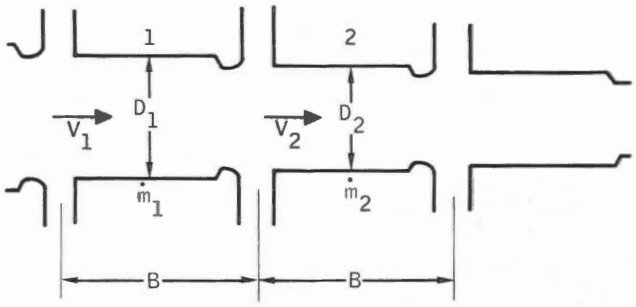

Fig. 4.10 - Typical vapor-header section [12].

The superiority of vapor headers designed by static-regain methods over constant-diameter headers was proved by numerous tests using mercury and nitrogen [10, 13]. The liquid levels in condenser tubes supplied by constant-diameter headers were grossly unbalanced and their locations were unpredictable, but, in headers designed by static-regain method, liquid-interface positions were maintained within 3%.

A header designed for constant static pressure at the inlet of each tube is usually very similar to one designed for a constant vapor velocity. Because of this similarity and the simplicity of the constant velocity header, the latter type of header is often used in radiator-condenser design. The constant-velocity criterion requires that the header(s) consist of symmetrical section(s) generated by a rotated parabola given by

$$y^2 = 4bx$$

where the constant b describes the distance from the vertex of the parabola to its focal point as shown in Fig. 4.11. Design equations for vapor headers designed on this basis are developed in Ref. 2. For preliminary designs the vapor header inlet and outlet diameters can be approximated by assuming that velocity in the header is constantly equal to the tube-inlet velocity. Under these assumptions for the configuration shown in Fig. 4.4,

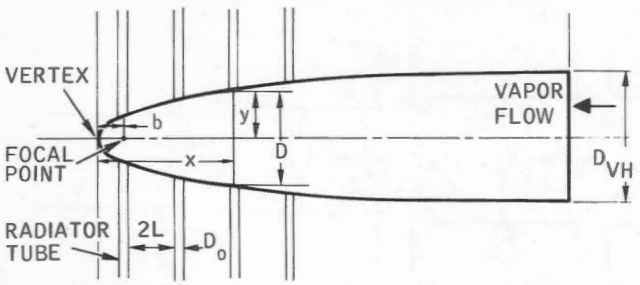

Fig. 4.11 - Detail of parabolic header geometry.

$$D_{H1} = D_i \sqrt{N}$$
$$D_{H2} = D_i \qquad (4.20)$$

where D_i is the tube inside diameter and N the number of tubes.

The design of liquid headers for the radiator can be simplified by assuming that the headers are tubular with uniform diameters. If we also assume that the working fluid enters the inlet header at the middle and leaves the outlet header at the same position (Fig. 4.12), such a design could provide some saving in header weight since in such an arrangement each half of the header handles only one-half of the total mass flow and header diameter can be reduced for constant pressure drop. Other arrangements, e.g., U- or Z-type headers, are described in the literature [12].

The following equation [8] should be satisfied for equal flow distribution among the tubes:

$$\dot{m}_x = \frac{\dot{m}}{2} - \frac{\dot{m}x}{H_L} \qquad (4.21)$$

The allowable pressure-drop relation is obtained by integrating

$$dp = (2fG_x^2 dx / g_0 D_{LH} \rho_L)$$

where the mass velocity is now evaluated from Eq. 4.21 and the continuity equation for constant diameter as

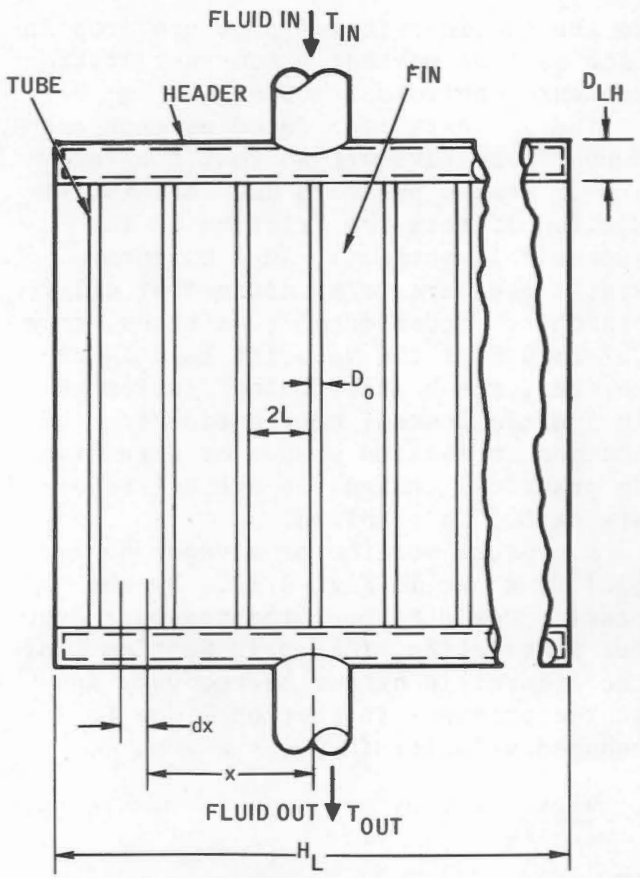

Fig. 4.12 - Radiator configuration for liquid-header design.

$$G_x = \rho_L V_x = \frac{4\dot{m}[0.5 - (x/H_L)]}{\pi D_{LH}^2} \qquad (4.22)$$

The friction factor with turbulent flow assumed in the headers is given by

$$f = \frac{0.046}{\mathrm{Re}^{0.2}} \qquad (4.23)$$

The pressure drop for an element of header length dx is then

$$-dp = 4.411 \times 10^{-3} \times \left(\frac{\dot{m}^{1.8}\mu_L^{0.2}}{D_{LH}^{4.8}\rho_L}\right)\left(0.5 - \frac{x}{H_L}\right)^{1.8} dx \qquad (4.24)$$

The integration of Eq. 4.24 yields the desired relations between length, diameter, mass flow rate, and pressure drop:

$$(\Delta P)_H = \frac{0.2263 \times 10^{-3} \dot{m}^{1.8} \mu_L^{0.2} H_L}{D_{LH}^{4.8} \rho_L} \quad (4.25)$$

When the header diameter is taken as the dependent variable, Eq. 4.25 becomes

$$D_{LH} = 0.174 \dot{m}^{0.375} \mu_L^{0.0417} \left[\frac{H_L}{(\Delta P)_H \rho_L}\right]^{0.208} \quad (4.26)$$

(c) *Flow Stability*

Radiator-condenser instability is very undesirable since in its worst forms it can have catastrophic effects on system performance. Primarily these instabilities cause large pressure fluctuations or even cause large slugs of vapor to enter the effluent liquid stream. Either of these effects could cause large fluctuations in system performance or premature system shutdown due to pump or bearing failure. The major forms of instability examined analytically and experimentally are discussed in this section.

(1) *Types of Instability.* Three types of instability that may occur in direct-condensing radiators in a negative zero gravitational or force field were examined in the literature: Interface instability, runback instability, and liquid-leg instability. The first two are single-tube phenomena; the last is peculiar to multiple parallel-tube operations.

Interface Instability. Interface instability, the inability to maintain a relatively stable meniscus, does not appear to be a critical parameter in itself in a condensing system that has restoring forces in the form of vapor drag and/or impinging droplets. The primary influence appears to be in promoting runback instability. The nature of the instability and the experimental determination of the critical Bond number are discussed in greater detail in Refs. 14 to 16.

Liquid-Leg-Instability (Single Tube). This instability, which may occur in a system of parallel condensing tubes, causes the liquid leg of a perturbed tube to spill into the vapor manifold. The resultant effect could be a significant pressure fluctuation, but no vapor should be entrained in the effluent liquid stream. This instability is primarily a function of the condensing length, the entrance pressure loss, and the degree of condensing vapor momentum recovery and can occur only if there is a negative pressure drop, i.e., if the pressure rise due to vapor momentum recovery exceeds the frictional losses.

Liquid-Leg Instability (Multiple Tube). This is the most severe form of instability since it may cause liquid to spill into the vapor manifold and vapor to spill into the liquid manifold. If the vapor in the liquid manifold does not condense before it reaches the pump, it may deprime the pump, shutting down the system. If it does condense, it may raise the temperature of the liquid enough to reduce the net positive suction head to the pump below the critical value to maintain adequate pump performance. Parallel-tube instability occurs when the acceleration forces opposing condensing exceed a critical value. The critical value is primarily a function of the condensing length, flow rate, and pressure drop.

Runback Instability. Runback instability has been noticed in wetting system condensing against gravitational forces. Runback occurs when the vapor drag can no longer support the weight of the liquid in the annular film; thus the liquid bridges the tube, trapping vapor behind it and shortening the condensing length. The net effect can be large pressure fluctuations detrimental to system performance.

(2) *Predicted Stability Limits and Experimental Observations.*

Interface Instability. The critical tube diameter above which the interface is unstable is approximated by [17]

$$D_{cr} \approx 1.84\left[\frac{\sigma}{g/g_c(\rho_L - \rho_V)}\right]^{1/2} \quad (4.27)$$

In this relation the constant actually varies slightly depending on tube material and surface finish.

In most applications considered to date, the interface in the condensing tubes is stable either because the acceleration level is essentially zero in space, and hence the tube diameter is below the critical diameter, or because the direction of any applied acceleration is from the vapor to the liquid and therefore is inherently stable. As an example of the negative-g design margin, consider a local acceleration of 0.05 g; the critical diameter would be about 4.5 times the value on earth.

Liquid-Leg Instability (Single Tube). To simplify the pressure-drop equation for the purpose of examining the factors influencing condensing stability at zero g, we assume incompressible flow and, to account for the fact that condensation occurs and the stream velocity varies along the condensing tube, we assume that the area is constant, not varying with distance, and that

$$V(Z) = V_0^1\ (1 - \frac{Z}{L_c}) \quad \text{(uniform condensing rate)}$$

$$V_0^1 = V_0\frac{L_c}{L_{0c}} \quad \text{(the flow into a given tube is proportional to the condensing rate)}$$

This represents a very special case, but the major conclusion can be shown to be essentially independent of these particular assumptions.

The resulting pressure-drop equation based on these assumptions is [10]

$$P_i = P_0 + (2 - \bar{y} - K)\frac{\rho_v V_0^2 L_c^2}{2g_c L_{0c}^2} - \frac{4\rho_v V_0^2 L_c^2}{2g_c D L_{0c}^2}\int_0^1 \phi^2 f L_c\left(1 - \frac{Z}{L_c}\right)^2\left(d\,\frac{Z}{L_c}\right) \quad (4.28)$$

which gives for the interface pressure, assuming an average $\phi^2(\bar{\phi}^2)$ and an average $f(\bar{f})$,

$$P_i = P_0 + \left[(2-y-K)\frac{L_c^2}{L_{0c}^2} - \frac{4L_c^3\bar{\phi}^2\bar{f}}{3DL_{0c}^2}\right]\frac{\rho_v V_0^2}{2g_c} \quad (4.29)$$

Equation 4.29 shows that the condenser will be completely stable as long as $(2 - y - K) < 0$ or the condensing length is greater than the critical condensing length when $(2 - y - K) > 0$. By differentiating Eq. 4.29 and setting it equal to zero, we find the critical length to be

$$L_{cr} = \frac{2 - y - K}{(2\bar{\phi}^2\bar{f}/D) - g_0\rho_L(n/\rho_v V_0^2)} \quad (4.30)$$

Figure 4.13 is a graph of Eq. 4.29, showing the interface pressure on the vapor side vs. condensing length for equilibrium conditions at each condensing length. From this figure the criterion for stability in zero g when one tube out of many is perturbed is seen to be

$$\frac{dP_i}{dL_c} < 0$$

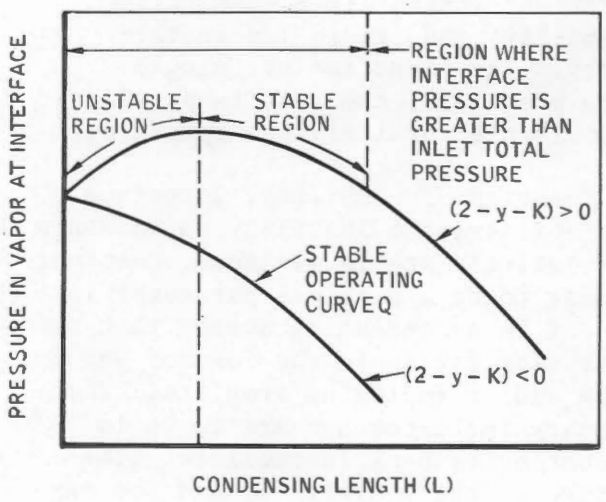

Fig. 4.13 - Typical radiator-condenser pressure variations.

The figure shows that it is possible, with small momentum losses during condensing, to have an interface static pressure greater than the incoming total pressure; hence the interface might move toward the inlet.

Liquid-Leg Instability (Multiple Tube). A disturbance that causes the liquid level to rise in all the tubes decreases the condensing area. A reduced condensing area must operate at higher temperature to reject the same amount of heat, and the higher temperature corresponds to a higher saturation pressure. Because of the frictional pressure loss of the vapor as the interface moves, the pressure drop along the tube increases, reinforcing the interface pressure variation due to heat-rejection requirements. This may be ameliorated by the increase in inlet-vapor pressure (due to increased temperature), tending to maintain liquid level.

When only one tube out of many is perturbed in the direction of a shorter condensing length, it is not required to reject the same amount of heat. The rising tube pressure causes part of the flow that would normally enter that tube to be diverted and distributed among the others. The increase in the heat load of the other tubes is small if there are many tubes and their performance is virtually unaffected; the main restoring force of the multitube assembly, the rise in condensing pressure, is no longer available to the single tube. The only restoring force remaining is the pressure gradient down the tube; if this is insufficient, the liquid leg in the perturbed tube will eventually spill into the vapor manifold.

The necessary condition for stable operation at the design interface is

$$-\left(\frac{\partial P_i}{\partial Z}\right)_{L_{0c}}, \text{ vapor side} \qquad (4.31)$$

$$-\left(\frac{\partial P_i}{\partial Z}\right)_{L_{0c}}, \text{ liquid side}$$

where Z is axial distance. The critica value of negative acceleration (opposite to vapor flow direction) at which the instability occurs can be found by the following analysis [18].

The following equations describe the operation of a simplified system.

1. Liquid-static head.

$$P_i = P_0 + \rho_L(L_{0c} - Z)n\frac{g_0}{g_c} \qquad (4.32)$$

where

$$\frac{g_0}{g_c} = 1 \text{ lb}_f/\text{lb}_m$$

2. Heat transfer (constant-width radiator).

$$\dot{m}h_{fg} = \sigma\varepsilon\eta A_t(T_0^4 - T_S^4) \qquad (4.33)$$

and, since flow rate is constant.

$$T_0^4 = T_S^4 + \frac{L_{0c}}{Z}(T_{00}^4 - T_S^4) \qquad (4.34)$$

where T_{00} represents the fin-base temperature at the design point.

3. Fluid temperature (saturated).

$$T_f \simeq \frac{T_m + T_i}{2} = T_0 + \Delta T_w \qquad (4.35)$$

where ΔT_w is the temperature drop between the condensing fluid and the base of the radiating fin:

$$\Delta T_w = T_{w_0}\frac{L_{0c}}{Z} \qquad (4.36)$$

4. Saturation equation (Clausius-Clapeyron). At both the interface and the vapor manifold of the radiator-condenser, the vapor is assumed saturated; thus

$$T_i = f(P_i) \qquad (4.37)$$

and

$$T_m = f(P_m) \qquad (4.38)$$

5. Pressure-drop approximation. An approximate pressure-drop equation for the radiator with constant flow is

$$P_m^2 - P_i^2 = (P_{m0}^2 - P_{i0}^2)\frac{Z}{L_{0c}} \qquad (4.38)$$

where $P_{m0} - P_{i0}$ is the pressure drop at the design point. Equation 4.32 can be differentiated directly to yield

$$-\left(\frac{dP_i}{dZ}\right)_{\text{liquid side}} = -n\rho_L \frac{g_0}{g_c} \qquad (4.39)$$

where $g_0/g_c = 1$ in magnitude and has the units lb_f/lb_m. Combining the heat-transfer equations and pressure-drop equation and solving for $-(dP_i/dZ)_Z$ yields

$$-\left.\frac{dP_i}{dZ}\right|_{L_{0c}} = \frac{\frac{P_m}{2}\left[1 - \left(\frac{P_i}{P_m}\right)^2\right]\frac{dP_i/dT_i}{dP_m/dT_m} + 2\left(\frac{dP_i}{dT_i}\right)\left[\frac{T_{00}}{4}\left(1 - \frac{T_S^4}{T_{00}^4}\right) + \Delta T_{w_0}\right]}{L_{0c}\left[1 + \frac{P_i}{P_m}\frac{dP_i/dT_i}{dP_m/dT_m}\right]} \qquad (4.40)$$

where dP/dT can be obtained from the Clausius-Clapeyron equation,

$$\frac{dP}{dT} = \frac{Mh_{fg}}{R}\frac{P}{T^2} \qquad (4.41)$$

Applying the stability criterion to the two equations for the pressure gradients results in the following limit for the number of negative g's, n:

$$n < \frac{\frac{P_m}{2}\left[1 - \left(\frac{P_i}{P_m}\right)^2\right]\frac{dP_i/dT_i}{dP_m/dT_m} + 2\left(\frac{dP_i}{dT_i}\right)\left[\frac{T_{00}}{4}\left(1 - \frac{T_S^4}{T_{00}^4}\right) + \Delta T_{w_0}\right]}{\rho_L L_{0c}\frac{g_0}{g_c}\left[1 + \frac{P_i}{P_m}\frac{dP_i/dT_i}{dP_m/dT_m}\right]} \qquad (4.42)$$

The critical value of n can be computed by setting n_{cr} equal to the right-hand side of Eq. 4.42 and inserting the design-point values.

Acceleration beyond this value results in large shifts in the interface location and/or vapor entering the liquid manifold when the pressure regulator and zero-g interface are essentially at the same station. Therefore this acceleration represents an upper limit for negative-g operation. Typically this form of instability is not a severe limitation, with the exception, perhaps, of very low interface pressures.

Runback Instability. Runback occurs in a tube below critical diameter in a wetting system condensing against gravitational forces when the vapor drag can no longer maintain upward flow of the annular liquid film. Consequently the condensate flows back against the vapor flow. As the falling film thickens, it eventually bridges the tube. The location of this bridge is called the runback point. The bridging by the liquid decreases the heat-transfer area available for condensing; this causes the vapor pressure to rise quickly. The pressure differential thus created across the runback slug is sufficient to slam the slug back into the liquid leg; this causes pressure oscillations that can be of significant magnitude. An analysis of runback under wetting conditions is reported in Ref. 12. Runback was assumed to occur at the point where the shear forces went to zero. It was found that the distance from the condenser inlet to the point of runback could be expressed by the relation

$$\frac{\left(\frac{Z_R}{L_c}\right)^{\frac{1}{3}}}{1 - \frac{Z_R}{L_c}} = \frac{8.75\rho_v V_i^2\left(\frac{1 + 2D\mathrm{Re}_0}{64L_c}\right)}{g_c^{\frac{2}{3}}\rho_L^{\frac{1}{3}}\mu^{\frac{2}{3}}\left(\frac{g}{g_c}\right)^{\frac{2}{3}}\mathrm{Re}_0^{\frac{4}{3}}} \qquad (4.43)$$

From experimental data Koestel *et al.* [12] determined that, to minimize the effects of runback slugging for tubes of less than 0.5 in. in diameter, the distance to the point of runback should be greater than 0.8 of the condensing length ($Z_R/L = 0.8$). This provides a relation between minimum allowable tube-inlet velocity, tube diameter, and level of negative acceleration forces which must be satisfied to avoid excessive pressure and flow accelerations. (Note that runback does not occur in zero-g environment.) Since Eq. 4.43 relates the minimum inlet velocity required to the tube diameter and acceleration level it also sets the minimum pressure drop required for a stable condensing flow under a given acceleration.

4-2.3 *Meteoroid Protection for Space Radiators* *

Meteoroids of varying size, density, and velocity are hazards encountered by space vehicles. If the integrity of a particular component were diminished or lost by a puncture resulting from a collision with one of these meteoroids, suitable precautions would have to be taken. This is precisely the case with radiator-condenser tubes.

Meteoroids, of cometary and asteroidal origin, travel in eccentric orbits within our solar system. About 20% of those near the earth are members of a meteoroid shower whose behavior can be predicted; consequently they can be avoided. The remaining 80%, however, are sporadic in nature and must be treated on a probability basis. Protection from meteoroids requires the determination of (1) the frequency of the meteoroids, (2) the mass, density, and velocity of the meteoroids, and (3) the penetrating power, assuming the mass, density, and velocity are known. Many earth observations and satellite experiments have been performed to determine items 1 and 2, but most have had significant limitations of time, area, or sensitivity; i.e., only meteoroids above a certain minimum size could be counted.

Many data have been obtained directly from satellite experiments employing various kinds of impact sensors such as photomultiplier cells, microphone detectors, pressurized cells, and capacitance wafer panels. The last two types, employed on the Explorer (16 and 23) and the Pegasus (1, 2, and 3) space vehicles, respectively, measure the rates of puncture of thin materials. Calibration relations and particle-impact equations provide estimates of the minimum meteoroid mass associated with the sensor punctures. Values of particle flux and mass were established for the satellite experiments.

Indirect measurements of meteoroid particle flux and mass were obtained from evaluating the zodiacal light and from radar and photographic observations of meteors. The particles observed by these indirect techniques are primarily cometary meteoroids in orbit around the sun. From the indirect and direct methods, particle-flux data are available over a range of particle mass from around 10^{-13} to 1 gram. Although there are unresolved discrepancies in the low-mass range, the flux-mass variation for space-radiator design is reasonably well defined.

The meteoroid minimum mass against which a radiator must be protected is related to the radiator meteoroid hazard parameter.

$$\frac{A_v \tau}{-\ln P(0)} \tag{4.44}$$

For system power output from several kilowatts to several megawatts, the radiator hazard parameter varies from around 10^4 to 10^7 m^2-days, corresponding

*Material in this section is from S. Lieblein and J.H. Diedrich, Material and Geometry Aspects of Space Radiators, *Nucl. Appl.*, *3*(2): 82-93 (1967).

to minimum meteoroid masses of from 10^{-4} to 10^{-2} gram. For this region of particle mass, a design flux-mass variation can be established from consideration of the data from the Pegasus flight experiments and the radar and photographic meteor observations (heliocentric cometary particles). The cumulative flux, $F_>$, in units of particles/(m^2-day) is essentially a power function of the minimum particle mass, m, in grams:

$$F_> = \alpha m^{-\beta} \tag{4.45}$$

Considerable work has been done on hypervelocity impact into various simulated radiator materials using a light-gas gun. Projectile velocities of 7.6 km/sec were achieved with the light-gas gun for routine firing of spherical projectiles with diameters of 1/16 to 1/8 in. (1.6 to 3.2 mm). Although the projectile velocities are lower than the meteoroid velocities (17 to 20 km/sec), comparable levels of particle kinetic energy can be obtained with these projectile sizes. Initial results of the hypervelocity impact tests indicated that radiator tubes can sustain several modes of critical damage (Fig. 4.14).

In addition to cratering and perforation, dimpling and spalling of the inner surface of the tube can occur at thicknesses larger than the thickness necessary to prevent perforation. Dimpling of the inner surface causes a restriction of the flow passage, and spalling releases metal fragments into the circulating fluid.

The tube armor required to prevent a given mode of damage is

$$t_a = a_t P_\infty \tag{4.46}$$

where a is the damage-thickness factor corresponding to the inner-surface damage mode of interest and P_∞ is the crater depth that would be incurred in a relatively thick target of the same material. The crater depth is related to the target and projectile properties

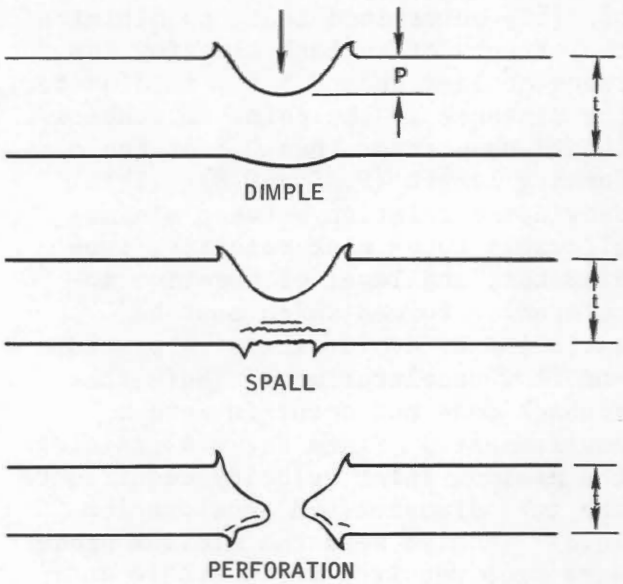

Fig. 4.14 - Definition of projectile damage modes. [From S. Lieblein and J.H. Diedrich, Material and Geometry Aspects of Space Radiators, *Nucl. Appl.*, *3*(2): 82-93 (1967).]

by the relation [19]

$$\frac{P_\infty}{d} = \gamma \left(\frac{\rho_p}{\rho_t}\right)^{\frac{1}{2}} \left(\frac{V^2 \rho_t}{E_t}\right)^{\frac{1}{3}} \tag{4.47}$$

The crater, perforation, dimple, and spall characteristics of a wide range of materials are listed in Table 4.1 in terms of cratering coefficient (Eq. 4.47) and damage-thickness factor (Eq. 4.46). The damage-thickness factors of Table 4.1 are incipient values defined as the ratio of the target thickness corresponding to the onset of the particular damage mode to the crater depth, P_∞. Thickness factors greater than these values would have to be used to prevent the damage. In general, armor weight is approximately proportional to the term $\rho_t^{\frac{5}{6}} E_t^{-\frac{1}{3}}$.

4-2.4 *Materials Selection*

Any practical radiator for a space environment must have a suitable con-

TABLE 4.1 - Results of Hypervelocity Impact Tests

Material	Cratering coefficient,* γ	Rear-surface damage factors†		
		Dimple, t/P_∞	Spall, t/P_∞	Perforation, t/P_∞
2024-T6 aluminum	1.97	2.5	2.3	1.7
316 stainless steel	1.67	2.4	1.9	1.4
Nb-1% Zr	1.39	4.5	4.0	1.7
Beryllium	2.05			
Graphite (ATJ)	1.18			
Inconel-718	1.55	3.0	2.5	
L-605	1.77	2.5	2.1	1.7
A-286	1.99	2.4	1.9	1.4
Vanadium	1.38			
Molybdenum	1.57			

*Room-temperature values. Additional data are given by Clough and Diedrich [20].

†Threshold or incipient values.

tainer and radiating materials that possess high emissivity characteristics, the strength required for a structurally sound design, and the ability to withstand the deleterious effects of the environment to which it is exposed. These materials must lend themselves to available fabrication methods and must withstand the rigors of high-temperature operation over extended periods of time in space without adversely affecting the thermal and mechanical functioning of the radiator.

An ideal material for a high-temperature radiator should have:

1. High emissivity to allow maximum utilization of the radiator surface.
2. High thermal conductivity for fin efficiency.
3. Low density to minimize weight.
4. Resistance to penetration by meteoroids.
5. Resistance to the space environment; notably sublimation or erosion.
6. Compatibility with sodium or NaK.
7. Ductility to facilitate packaging and deployment.

Obviously no one material has all these qualifications, and therefore combinations of materials are required for radiator construction.

High emissivity is best provided by coating the radiator surface with high-emissivity coatings as described later. The fin material is normally selected for its low density and high thermal conductivity. Pyrolytic graphite, beryllium, stainless-steel-clad copper, and niobium have been considered for high-temperature radiators. For lower temperatures aluminum and magnesium have been considered. The criteria for meteoroid protection are discussed in Sec. 4-2.3. Niobium, stainless steels, and cobalt alloys are of interest for tube material.

(a) *Radiator Heat-Transfer Materials* Spacecraft radiators or radiator-condensers achieve maximum effectiveness by use of thermal-control coatings that exhibit a high thermal emittance and a low solar absorptance. Generally, the radiator surface area and weight are proportional to the thermal emittance property of the surface coating; thus

judicious coating selection is of major importance to the radiator design.

As a result of recent extensive effort in the development of emittance coatings for use at elevated temperatures, a wide choice of stable coating systems is available for use on spacecraft radiators. Table 4.2 contains the results of a literature survey conducted to determine the most effective coatings, their applicable temperature range, the methods of application, the substrates applicable, and the testing duration.

Thermal-control coatings for spacecraft radiators are selected primarily for their optical properties, stability, and integrity in the space environment. Also of extreme importance is the design operating temperature of the radiator.

Because of the effect of solar input on a radiator coating surface, reference design coatings can be categorized by radiator design temperature. Two temperature regions of radiator operation are discussed here: (1) between 300 and 700°F and (2) above 700°F.

For radiators operating between 300 and 700°F, the thermal emittance property is the dominant factor. A low solar absorptance property contributes a measurable bonus to the net heat-rejection capability of a radiator operating in this temperature region. A successful coating for use in this temperature range, developed for the SNAP-2 and -10A systems, is designated the AI 93 system [18]. The AI 93 system utilizes a bilayer coating consisting of a subcoat containing a Cr-Co-Ni oxide mixture and a top coat containing stannic oxide. Both layers use aluminum phosphate as the binding agent. Between 300 to 700°F the total hemispherical emittance of the AI 93 is 0.90 minimum, and the solar absorptance is 0.35 maximum. AI 93 has undergone complete qualification in a simulated space environment and, in addition, has attained an excess of 1000 hr of successful operation in the space environment at temperatures exceeding 700°F.

A foremost consideration in the selection of a coating for use at 700°F and above is the ability to withstand the severe conditions of thermal shock and stress associated with start-up and operation at these temperatures. Also, it is desirable to select a coating that does not use filler agents, binding agents, or other additives that may contribute to emittance degradation after long-term operation at these elevated temperatures. In this temperature range the solar absorptance has little effect on the thermal effectiveness of the coating.

Plasma-arc spray coatings meet these requirements, and two very succesful high-emittance coatings developed for this application are calcium titanate and iron titanate. The emittance of these coatings is shown in Table 4.2.

Selection of the right fin material is as important as the emittance of fin coatings. Two properties are of foremost interest for heat-transfer and weight optimization: High thermal conductivity and low density.

For radiating fins the volume of fin material to reject unit heat, Q, is inversely proportional to fin thermal conductivity, k, and emissivity, ε, squared [21]:

$$\frac{\text{Volume}}{Q} \propto \frac{1}{k\varepsilon^2} \tag{4.48}$$

Therefore, if ρ_f is the density of the fin material, fin weight, W, per unit rejected heat is

$$\frac{W}{Q} \propto \frac{\rho_f}{k\varepsilon^2} \tag{4.49}$$

Minimum fin weight will be achieved when $k\varepsilon^2/\rho_f$ is a maximum. Since ε is a function of the surface coating, k/ρ_f is the governing parameter for fin material to achieve minimum weight.

Figure 4.15 and Table 4.3 [21] show the conduction parameter (k/ρ) values as a function of temperature for

TABLE 4.2 - Radiator Emittance Coatings

Coating	Substrate base	Application method	Thickness, mils	Effective temperature range, °F	Total hemispherical emittance		Solar absorptivity (α_s)	α_s/ε_H
					Duration tested in hard vac.,	ε_H		
			Single Oxides					
Chromic oxide (Cr_2O_3)	Nb-1% Zr	Plasma-arc sprayed	4	500 to 2100	8	0.82 to 0.70		
Stabilized titanium oxide	Nb-1% Zr	Plasma-arc sprayed	4	1700	400	0.87		
Titania (TiO_2)	Nb-1% Zr	Aluminum phosphate bonded	1	300 to 1000	3	0.80 to 0.83		
			5	300 to 1000	5	0.76 to 0.88		
	Aluminum 1100	Plasma-arc sprayed		700	15,000			
	Aluminum 6061	Plasma-arc sprayed		700	15,000			
	347 S.S.	Plasma-arc sprayed		650	13,000			
Titania (50%) alumina (50%)	Aluminum	Plasma-arc sprayed		300 to 900	35	0.70 to 0.80		
	310 S.S.	Plasma-arc sprayed	2.4	300 to 1340	150	0.84 to 0.89		
	Nb-1% Zr	Plasma-arc sprayed		1450	300	0.82		
Silica (SiO_2)	Nb-1%	Aluminum phosphate bonded	5	300 to 1000	4	0.86 to 0.70		
	Magnesium		5			0.83	0.210	0.25
Silicon monoxide (SiO)	Aluminum					0.70	0.51	0.73
Beryllium oxide (BeO)								0.421
Magnesium oxide (MgO)								0.168
Aluminum oxide (Al_2O_3)								0.16
Zirconium oxide (ZrO_2)								0.14
Nickel oxide (NiO)	Nb-1% Zr	Plasma-arc sprayed	3	1000 to 2100	2	0.74 to 0.86		
Cobalt oxide (CoO)	Nb-1% Zr	Plasma-arc sprayed	4	300 to 2200	5	0.79 to 0.87		
Stannic oxide	Copper	Aluminum phosphate bonded	3	500 to 700		0.87 to 0.84		
	Copper	Potassium silicate binder	3	500 to 700		0.88		
Zinc oxide (ZnO)	Copper	Potassium silicate binder	2	600 to 700		0.79 to 0.77		
			Multiple Oxides					
Iron titanate	310 S.S.	Plasma-arc sprayed	4	1350	5300	0.88		
	Nb-1% Zr	Plasma-arc sprayed	4	1700	6250	0.85		
Iron titanate, alum. titanate	Nb-1% Zr	Plasma-arc sprayed	5	1000 to 2200	4	0.82 to 0.89		
Alum. oxide-alum. titanate	Nb-1% Zr	Plasma-arc sprayed	4	1700	1000	0.83		
Barium titanate ($BaTiO_3$)	Nb-1% Zr	Plasma-arc sprayed	4	1700	100	0.71		
	Aluminum	Plasma-arc sprayed	1	440		0.75	0.65	0.86
	Aluminum	Plasma-arc sprayed	3	440		0.82	0.61	0.74
	Aluminum	Plasma-arc sprayed	5	440		0.87	0.74	0.85
Calcium titanate ($CaO \cdot TiO_2$)	Aluminum	Plasma-arc sprayed	2	440		0.75	0.72	0.96
	Aluminum	Plasma-arc sprayed	3.5	440		0.82	0.70	0.85
	Aluminum	Plasma-arc sprayed	4.5	440		0.88	0.70	0.795

TABLE 4.2 - Radiator Emittance Coatings (Continued)

Coating	Substrate base	Application method	Thickness, mils	Effective temperature range, °F	Total hemispherical emittance		Solar absorptivity (α_s)	α_s/ε_H
					Duration tested in hard vac.,	ε_H		
Calcium titanate ($CaO \cdot TiO_2$)	310 S.S.	Plasma-arc sprayed	4	1350	6300	0.90		
	Niobium	Plasma-arc sprayed	4	1450	300	0.92		
	Nb-1% Zr	Plasma-arc sprayed	4	1000 to 1800		0.89 to 0.85		
Strontium titanate ($SrO \cdot TiO_2$)	Nb-1% Zr	Plasma-arc sprayed	4	900 to 1400	21	0.76 to 0.88		
	Stainless steel	Plasma-arc sprayed		1450	17	0.89		
	Aluminum	Plasma-arc sprayed	1.4	440		0.81	0.73	0.90
	Aluminum	Plasma-arc sprayed	3.4	440		0.82	0.76	0.93
	Aluminum	Plasma-arc sprayed	5.0	440		0.83	0.64	0.77
Zirconium titanate	Nb-1% Zr	Plasma-arc sprayed	4	1700	312	0.82		
	Aluminum	Plasma-arc sprayed	2.4	440		0.83	0.46	0.55
	Aluminum	Plasma-arc sprayed	2.9	440		0.83	0.38	0.46
	Aluminum	Plasma-arc sprayed	5.0	440		0.86	0.37	0.43
Silicon carbide and silicon dioxide mixture	1100 Aluminum 6061 Aluminum	Aluminum phosphate bonded		700	12,800			
Ni-Cr spinel	Nb-1% Zr	Plasma-arc sprayed	4	1000 to 1800	30	0.7		
	Nb-1% Zr	Plasma-arc sprayed	2	1000 to 2100	5	0.87		
	310 S.S.	Aluminum phosphate bonded	3	1000 to 1450		0.88		
	310 S.S.	Aluminum phosphate bonded	2	1450	550	0.83		
	310 S.S.	Aluminum phosphate bonded	2	1000 to 1350		0.88		
	Aluminum 1100	Aluminum phosphate bonded		700	15,000			
	Aluminum 6061	Aluminum phosphate bonded		700	15,000			
Rokide-A	Aluminum	Rokide process			570 sun hr			0.59
	Stainless steel	Rokide process				0.80	0.21	0.26
Rokide-C	310 S.S.	Rokide process		1450	300	0.85		
			5			0.789	0.898	1.14
Rokide-MA	Aluminum	Rokide process	1	440		0.55	0.55	1.00
	Aluminum	Rokide process	2.5	440		0.71	0.58	0.82
	Aluminum	Rokide process	5.5	440		0.82	0.41	0.50
Rokide-ZS	Aluminum	Rokide process	2	440		0.79	0.54	0.68
	Aluminum	Rokide process	7.5	440		0.89	0.45	0.51
	310 S.S.	Rokide process	4	1000 to 2200	6	0.64 to 0.56		
	Nb-1% Zr	Rokide process	5	300 to 1450	300	0.78 to 0.83		
Cr-Co-Ni spinel	Copper	Aluminum phosphate bonded	2	500 to 700		0.86		

TABLE 4.2 - Radiator Emittance Coatings (Continued)

Coatings	Substrate base	Application method	Thickness, mils	Effective temperature range, °F	Total hemispherical emittance		Solar absorptivity (α_s)	α_s/ε_H
					Duration tested in hard vac.,	ε_H		
Non-Oxide								
Crystalline boron	Nb-1% Zr	Plasma-arc sprayed	1	1300 to 1700	6	0.70 to 0.76		
	Niobium	Plasma-arc sprayed	3	1000 to 1350		0.85		
	Molybdenum	Plasma-arc sprayed	3	1000 to 1500		0.88		
Zirconium diboride-molybdenum disilicide (BORIDE-Z)	Nb-1% Zr	Plasma-arc sprayed	4			0.85		
Acetylene black		Xylol bonded				0.72 to 0.92		
Silicon carbide (SiC)	310 S.S.	Aluminum phosphate bonded		1000 to 1300		0.88 to 0.85		
	1100, 6061 Al	Aluminum phosphate bonded		700	15,000			
	Nb-1% Zr	Aluminum phosphate bonded	4 to 8	300 to 1450	350	0.92 to 0.90		
	Nb-1% Zr	Aluminum phosphate bonded		1000 to 1400		0.87 to 0.88		
	374 S.S.	Aluminum phosphate bonded		700	1500			
Boron carbide (B_4C)	Nb-1% Zr	Aluminum phosphate bonded	6	900 to 1400	3	0.90 to 0.95		
ATJ graphite				1700 to 2900		0.87 to 0.82		
Acheson graphite				1600 to 3400		0.72 to 0.83		
Boron nitride	Tantalum	Synar bonded	3	300 to 1200	27	0.82 to 0.682		
Boron nitride (potassium silicate binder)	Copper		2	500		0.83		
				600		0.80		
				700		0.78		
Stably Oxided Metallic Surfaces								
Lithiated nickel oxide	310 S.S.	Slurry spray and sinter		300 to 1450	375	0.81 to 0.85		
Chromium black	310 S.S.	Electroplated		1450	300	0.89		
	Nickel	Electroplated		1450	800	0.90		
Oxided-KennamentalK-151-A	310 S.S.	Plasma-arc sprayed	4	700 to 1600	24	0.85 to 0.82		
Oxidized 310 S.S.	310 S.S.	Grit blast, Oxide at 1800°F		300 to 1450	330	0.83		
Dow-1	Magnesium					0.53	0.64	1.2
Dow-10	Magnesium					0.85	0.89	1.05
Dow-15	Magnesium					0.08	0.19	2.4
Dow-17	Magnesium					0.82	0.72	1.25
Coating Systems								
Al 93 (NA 0109-023) Subcoat (Cr-Co-Ni spinel) Topcoat (stannic oxide)	Copper	Aluminum phosphate bonded	3	600	2000	0.91	0.35	0.387
Al 93 (NA 0109-020/022)	Aluminum and alloys	Aluminum phosphate bonded	3	600	2000	0.91 to 0.92		
Al 93 (NA 0109-014)	Titanium	Aluminum phosphate bonded	3					

TABLE 4.3 - Material Properties*

Material	Density, lb/cu ft	Conduction parameter, $k/\rho f$ at 1400°F	Thermal stress parameter, $\sigma_b/E\alpha$, at 1200°F	Thermal shock parameter, $\sigma_b k/E\alpha$, at 1200°F
Commercial graphite	109	0.365	330	13.5×10^3
Beryllium	116	0.400	15	0.79
Pyrolytic graphite	130	0.590 1.100	220	17.5
Wrought aluminum	172			
Aluminum powder metallurgy	172			
Titanium	283	0.039	21†	1.8†
Vanadium	381	0.023	155	1.25
316 stainless steel	500	0.029	71	0.95
Niobium	530	0.072	165	5.7
Copper	530	0.375	121	24.2
Molybdenum	638	0.102	98	6.2
Tantalum	1036	0.034	148	6.6
Beryllium oxide	188	0.092	58	1.7

*From J.H. Diedrich and S. Lieblein, Materials Problems Associated with the Design of Radiators for Space Power Plants, in Power Systems for Space Flight, *Progr. Astronaut. Aeronaut.*, *11*: 647 (1963).

†Value at 800°F.

TABLE 4.3 - Continued

Material	Penetration resistance parameter, $\rho^{5/6}/E^{1/3}$, at 1400°F	Sublimation rate, in./year		Yield strength $(\sigma_y)_2$, lb/in. at 1400°F
		At 1400°F	At 1600°F	
Commercial graphite	4.7×10^{-2}	$< 10^{-10}$	$< 10^{-9}$	2.4×10^{3}
Beryllium	1.9	4.1×10^{-3}	0.15	2.1
Pyrolytic graphite	3.5	$< 10^{-10}$	$< 10^{-9}$	14.8
Wrought aluminum		8.0×10^{-3}	0.3	
Aluminum powder metallurgy		8.0×10^{-3}	0.3	
Titanium		$< 10^{-6}$	$< 10^{-5}$	
Vanadium	6.2	$< 10^{-7}$	$< 10^{-6}$	11.8
316 stainless steel	6.8	$< 10^{-5}$	1.4×10^{-4}	18.9
Niobium	7.8	$< 10^{-10}$	$< 10^{-9}$	10.9
Copper		4×10^{-4}	0.032	1.3
Molybdenum	6.9	$< 10^{-11}$	$< 10^{-10}$	18.6
Tantalum	11.4	$< 10^{-16}$	$< 10^{-15}$	18.9
Beryllium oxide	2.3	$< 10^{-9}$	$< 10^{-8}$	13.4

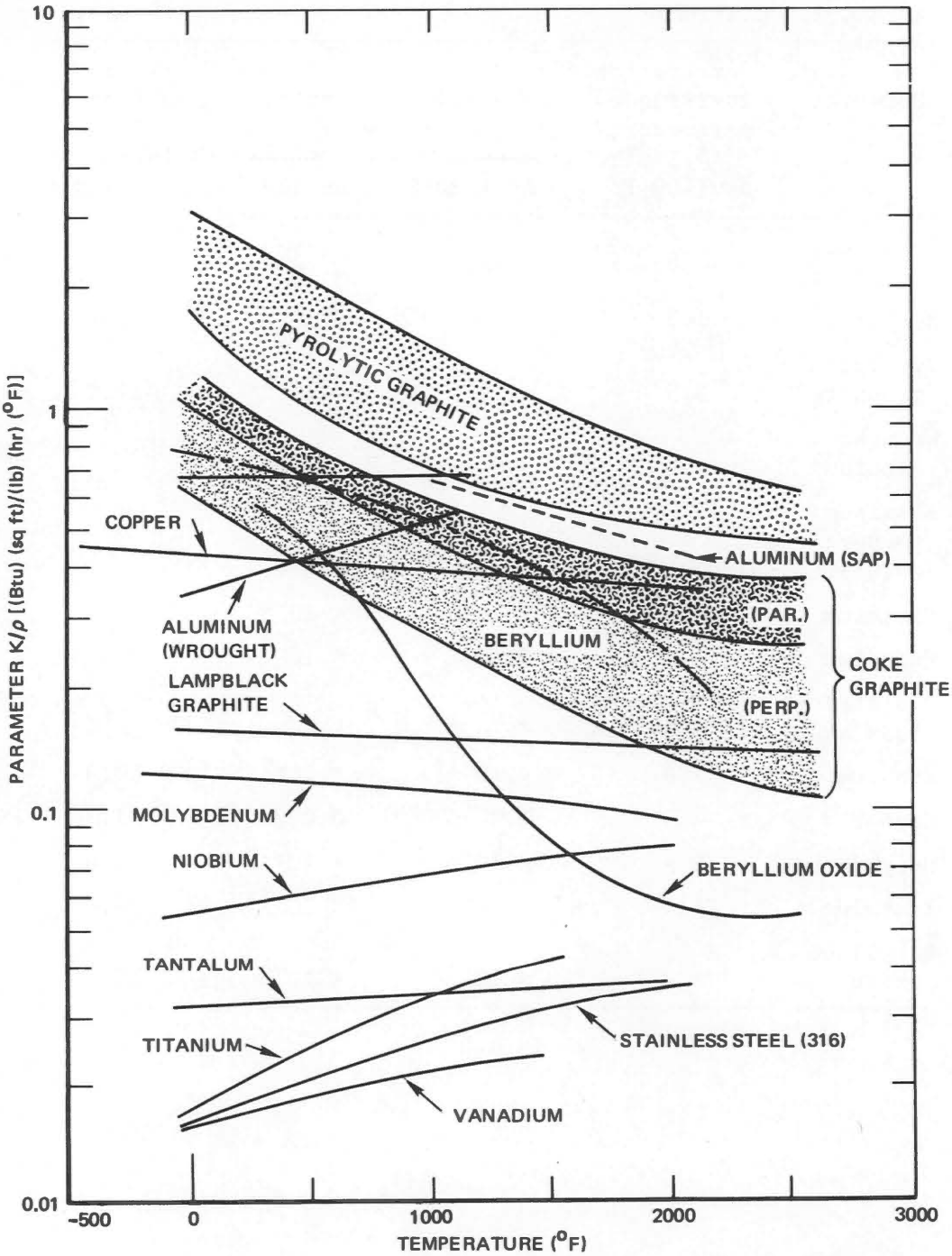

Fig. 4.15 - Conduction parameter vs. temperature. [From J.H. Diedrich and S. Lieblein, Materials Problems Associated with the Design of Radiators for Space Power Plants, in Power Systems for Space Flight, *Prog. Astronaut. Aeronaut.*, *11*: 627-653 (1963).]

representative materials.

If armor is bonded to fins or a tube, coefficients of expansion must not differ too markedly if joining problems are to be avoided. Local coefficient of thermal expansion as a

function of operating temperature is given for typical radiator materials in Fig. 4.16.

The maximum operational temperature, T_{max}, for a plate in a thermal-shock environment is given by the following relation [21] for a critical value of stress, σ_b; thermal conductivity, k; modulus of elasticity, E; coefficient of thermal expansion, α; and Poisson's ratio, μ:

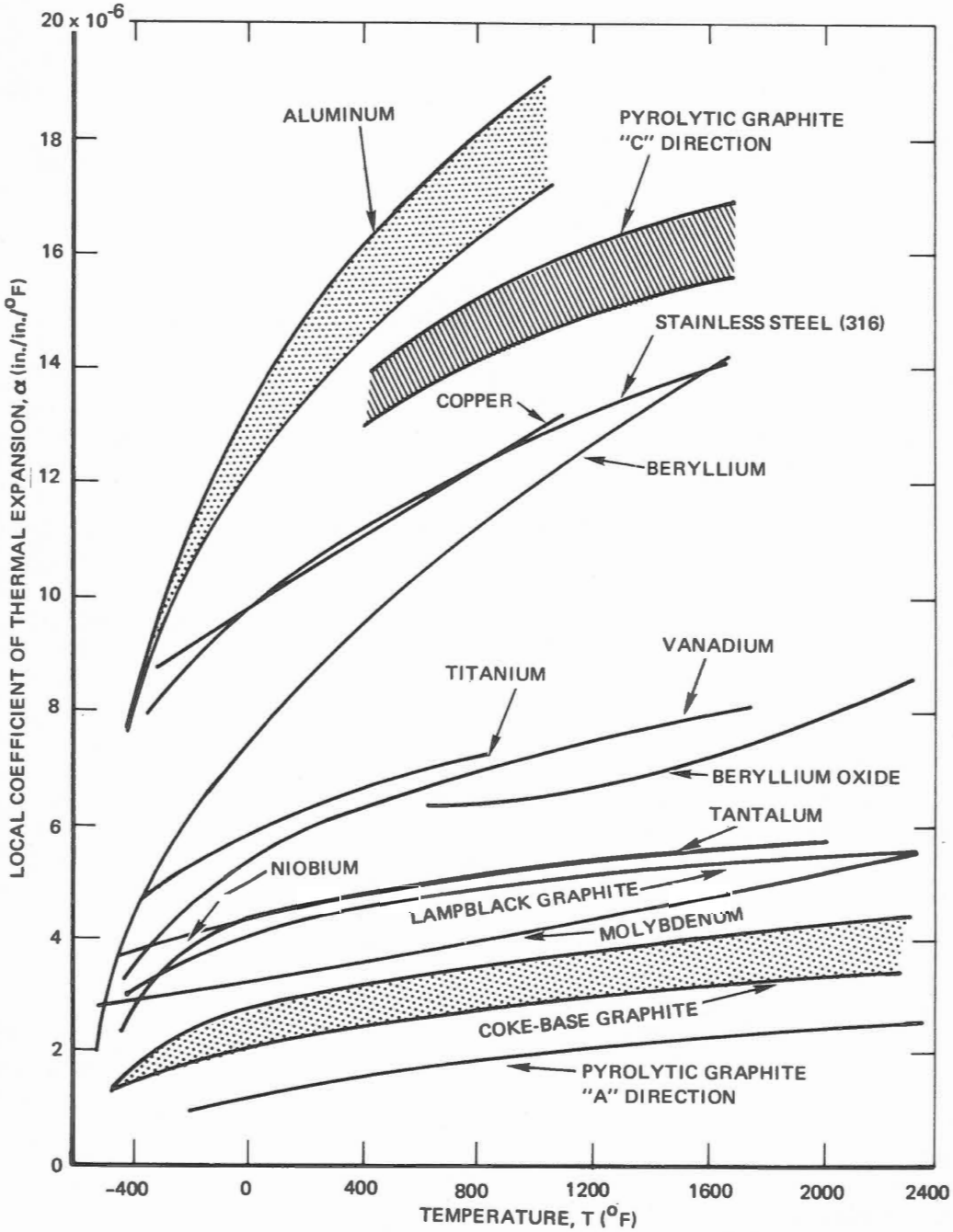

Fig. 4.16 - Local coefficient of expansion vs. time. [From J.H. Diedrich and S. Lieblein, Materials Problems Associated with the Design of Radiators for Space Power Plants, in Power Plants, in Power Systems for Space Flight, *Progr. Astronaut. Aeronaut.*, *11*: 627-653 (1963).]

$$T_{max} \propto \frac{\sigma_b k}{E\alpha} (1 - \mu) \qquad (4.50)$$

The parameter $\sigma_b k/E\alpha$ is used to compare the relative shock resistance of brittle materials. A similar parameter, $\sigma_b/E\alpha$, is used when heat-transfer conditions or part dimensions nullify the effect of thermal conductivity. Both parameters are shown in Table 4.3 for a range of materials and temperatures [21]. Other limiting parameters, such as sublimation rate or yield strength, are indicated for representative materials in Table 4.3.

The preceding discussion was concerned with tube puncture and the attendant loss of fluid or dimpling and spalling of the inner surfaces of tubes which can lead to flow restriction. However, other damage mechanisms may be of serious consequence for radiator operation. Effects of local stress concentration and microcrack formation in a nonpuncture impact can also cause difficulties in long-term operation. Erosion effects of micrometeoroid particles on high-emissivity coatings must also be considered.

Clearly some form of protection against damage from impacting meteoroids must be provided for radiator surfaces. For a given resistance to damage, the protection used should involve the least weight and complexity and the greatest reliability. Two general concepts of protection are usually considered. The first, the armor concept, uses a solid mass of material to physically stop an impacting particle before any serious damage can occur. In the second, the bumper concept, a relatively thin shield of material displaced from the vulnerable surface is used to fragment an impacting particle and spread its energy over a greater area.

Many geometric forms for finned-tube radiators are possible, as indicated in Fig. 4.17. The configurations on the left are based primarily on the armor concept; those on the right embody the bumper principle.

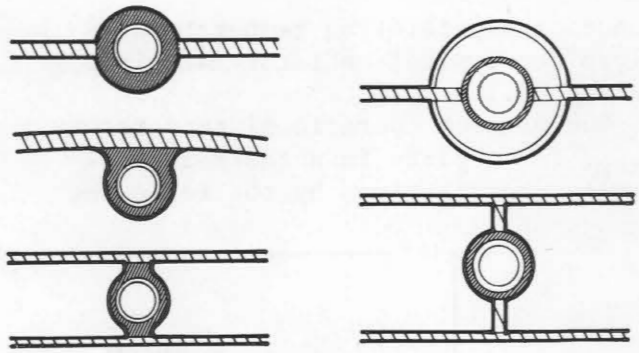

Fig. 4.17 - Armor and bumper configurations for fluid-filled tubular radiators.

Theoretically, repairing or sealing techniques using, for example, self-sealing materials, plugging solids, double-wall tubes, etc., could be used to correct any damage from impact. Sealing also could be achieved by cut-off or pinching mechanisms that isolate the damaged tube. However, these methods would require a leak detection or sensing device for activation. To date, a practical repairing or sealing device has not been demonstrated.

The use of redundant radiator segments was proposed as a means of reducing radiator vulnerability [22]. In this concept the radiator is divided into a large number of segments that can be isolated in the event of a puncture or other failure. Spare segments can be carried along to be activated when needed to maintain power, or a reduced power can be accepted as segments are lost.

(b) *Compatibility and Corrosion*

The compatibility of the various materials with sodium and NaK is treated in Chap. 2 and is not further considered here.

4-3 CONDENSERS

The design of liquid-metal condensers presents problems not usually encountered in ordinary condenser designs. Usually both the condensing

fluid and the coolant are liquid metals presenting unique materials-compatibility problems and having heat-transfer characteristics that differ markedly from those of common engineering fluids. The primary application for liquid-metal condensers considered here is in the heat-rejection systems for Rankine-cycle space power plants. Therefore the condensers must be able to operate in any orientation, in gravity fields ranging from zero to one or more and in a vacuum environment at elevated temperatures for 10,000 hr or more.

This section outlines the techniques used in designing a condenser that is thermally adequate for a specific application. Normally the application defines such parameters as terminal temperatures, heat load, flow rates, allowable pressure drops, condensing pressure, and geometric limitations. Many combinations of materials and geometries can be used in the design of a condenser of a required thermal capability. The final choice is usually determined by an optimization in terms of weight, volume, or cost effectiveness.

Condensers for use with sodium and NaK fall into one of three categories: Radiative, jet, or heat exchanger (convective). Condensation in a radiative condenser occurs by removal of the heat from the vapor by direct radiation to space. This type of condenser is considered in Sec. 4-2.

4-3.1 *Jet Condensers*

The jet condenser is very compact relative to a direct-condensing radiator or a heat-exchanger condenser. Jet condensing can provide significant pressure augmentation to circulate the liquid in the heat-rejection loop. Preliminary analyses have indicated that for space applications significant weight savings are possible using a jet-condensing system [23, 24]. A schematic of a jet-condensing heat-rejection system is shown in Fig. 4.18(a).

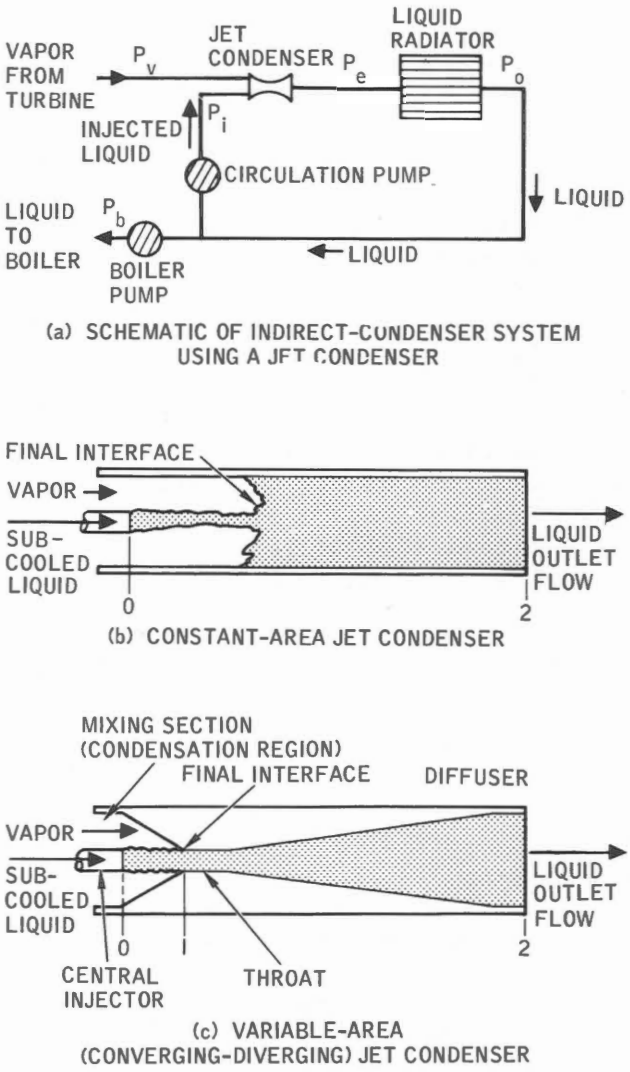

Fig. 4.18 - Jet-condenser system and types.

In the jet condenser subcooled-liquid working fluid is injected into the vapor stream. Physical mixing of the vapor and liquid and subsequent condensation of the vapor occur within a relatively short distance downstream of the region of injection. The resulting condensate-liquid flow circulates through a sensible-heat liquid radiator where the heat absorbed by condensation is rejected. Part of the resulting subcooled liquid is bypassed

and reinjected into the jet condenser, and the remainder is returned to the boiler loop.

(a) *Nomenclature* [25] *for Sec.* 4-3.1

A	Area (sq ft)
A_1	Area ratio of injector to tube inlet
A_2	Area ratio of injector to throat
C_p	Specific heat of liquid (Btu/lb/°F)
d	Diameter (ft)
g	Constant = $32.2(lb_m/lb_f)(ft/sec^2)$
h_{fg}	Heat of vaporization (Btu/lb)
K_d	Diffuser loss coefficient
L	Length (ft; in.)
$\dot{m}$	Mass flow rate (lb/hr)
$\dot{m}_R$	Ratio of injected liquid mass flow to vapor mass flow (saturated vapor flow for quality less than unity)
P	Pressure (psia)
ΔP_a	Pressure rise from jet-condenser inlet to outlet (psid)
ΔPi	Pressure drop across injector (psid)
$\Delta \mathring{P}_\ell$	Ratio of pressure rise, ΔP_a, to dynamic pressure of injected liquid
$\Delta \mathring{P}_v$	Ratio of pressure rise, ΔP_a, to dynamic pressure of inlet vapor flow
$\Delta \mathring{P}_{th_\ell}$	Ratio of pressure rise from inlet to throat to dynamic pressure of injected liquid
$\Delta \mathring{P}_{th_v}$	Ratio of pressure rise from inlet to throat to dynamic pressure of inlet vapor flow
Q_R	Heat rejected to liquid jet from condensing vapor (Btu/hr)
r	Radius (ft)
Re	Reynolds number
T	Temperature (°F); time (sec)
V	Velocity (ft/sec)
X	Distance (ft; in.)
α	Angle (°); thermal diffusivity (sq ft/sec)
α_t	Turbulent diffusivity for heat (sq ft/sec)
μ	μth characteristic root of Bessel's Function (J_0)
ρ	Density (lb/cu ft)
β	Ratio of liquid to vapor densities
τ_w	Wall shear stress (lb/sq ft)
χ	Jet utilization factor $(T_{\ell e} - T_{\ell 0})/(T_{ve} - T_{\ell 0})$

Subscripts

0	Inlet of jet condenser, station number
1	Throat of jet condenser, station number
2	Outlet of jet condenser, station number
b	Bulk; boundary
c	Condensation
(calc)	Calculated
d	Diffuser
e	Exit, outlet of jet condenser
i	Injector
j	Jet
ℓ	Liquid
m	Mixed
s	Saturated conditions
t	Tube
v	Vapor
w	Wall

(b) *Theoretical Flow and Analysis*

Schematic illustrations of two types of jet condensers [Fig. 4.18 (b) and (c)] show the two simple geometries, constant area and variable area.

Vapor flows from left to right and enters the condenser at Station 0, where subcooled liquid is also injected in the form of a central jet. Vapor and liquid flow concurrently through a mixing chamber with simultaneous mass transfer, heat transfer, and momentum exchange. With sufficient heat exchange between vapor and subcooled liquid, the vapor condenses.

(1) *Condensation Mechanisms.* Transport of vapor from the main flow stream to the subcooled-liquid jet is primarily a result of the pressure difference between the vapor and the subcooled-liquid boundary. For a free boundary with no net mass transfer, the vapor pressure at the boundary must be in equilibrium with the saturation

pressure of the liquid phase (neglecting surface-tension effects):

$$P_{vb} \approx P_{\ell b} \approx P_s(T_{\ell b}) \qquad (4.51)$$

Large pressure gradients will occur at Station 0, Fig. 4.18 (b or c). The liquid is at the lowest temperature and saturation pressure in the mixing chamber.

Rapid transfer of the vapor to the liquid can occur at liquid saturation pressures less than one-half the vapor pressure. Maximum vapor flow rate condensing on the jet at this point is proportional to the jet area and the sonic velocity of the vapor. As vapor is condensed on the jet, the heat released by condensation raises the jet temperature and liquid saturation pressure. The pressure difference between the vapor and the liquid jet is reduced, and the flux of vapor to the jet decreases. An increase in the temperature of the liquid jet surface (reducing condensing vapor flux) results, as the bulk temperature of the jet is raised due to heat addition from the condensing vapor. A radial temperature gradient in the jet is required to remove the heat of condensation released at the surface, and the surface temperature will be greater than the bulk temperature for heat transfer into the jet.

These effects are illustrated in Fig. 4.19, an idealized representation of the vapor and liquid temperature gradients at different axial locations in the mixing chamber. The initial temperature field (at 0) has a large local temperature (and pressure) gradient in both the vapor and the liquid near the interface. As condensing occurs, the bulk temperature, T_j, is raised, and the temperature gradient within the liquid phase decreases. The jet-surface temperature, $T_{\ell b}$, increases as the vapor temperature gradient decreases. As complete condensation of the vapor is approached, the bulk temperature of the fluid approaches its final value. The difference in free-stream vapor pressure, P_{v0}, and the saturation pressure for the bulk temperature, $P_s(T_j)$, may still be significant. However, the surface temperature of the jet, $T_{\ell b}$, must be greater than the bulk temperature, T_j, to transfer heat to the interior. Therefore the local vapor pressure difference, $P_{v0} - P_s(T_{\ell b})$, may be small, and low condensation rates will occur.

It has been postulated that condensation of vapor on the liquid jet can produce significant conversion of thermal energy to directed kinetic energy (velocity head) [26]. Empirical correlations with theory appear to verify the hypothesis [25]. Thus jet condensers can theoretically operate both as condensers and as vapor-driven circulation pumps.

(2) *Pressure Rise.* Several complex changes occur during condensation of the vapor on the liquid jet. If the liquid phase is a solid cylinder of a constant radius, r_ℓ, injected into the vapor at a constant velocity, $V_{\ell 0}$, and if vapor temperature, T_{v0}, remains constant throughout the mixing chamber, the rate of heat conduction and convection into the interior of the liquid is

$$\chi = \frac{T_{\ell e} - T_{\ell 0}}{T_{v0} - T_{\ell 0}} = \sum_{\mu=1}^{\mu=\infty} \frac{4}{\beta_\mu^2} \left\{ 1 - \frac{1}{\beta_\mu^2} \frac{V_{\ell 0} r_\ell^2}{L_c(\alpha+\alpha_t)} - \left[1 - \exp\left(\frac{\beta_\mu^2 L_c(\alpha+\alpha_t)}{V_{\ell 0} r_\ell^2} \right) \right] \right\} \qquad (4.52)$$

In this expression the temperature of the liquid at the exit, $T_{\ell e}$, is related to initial conditions of the jet and vapor (T_{ℓ_0}, T_{v_0}, V_{ℓ_0}, r_ℓ); to the properties at the flow (α and α_t); and to the distance traversed by the jet (L_c).

Analysis of the variable-area jet

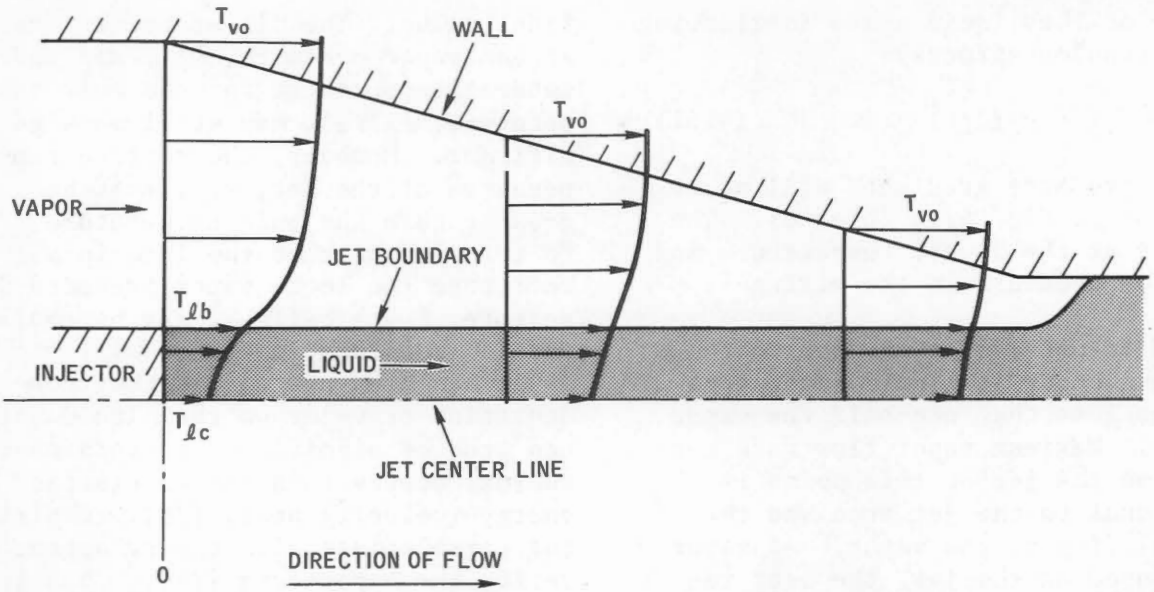

Fig. 4.19 - Idealized temperature profiles in a jet condenser with constant vapor temperature at wall [25].

condenser in Fig. 4.18 (c) resulted in the following expression for total pressure rise (recovery) across the condenser in terms of (1) geometry and inlet flow parameters and (2) the shear stress of the vapor on the wall and internal pressure distribution at the wall [25]:

pressure. Figure 4.22, which shows the effect of density ratio, indicates that the jet condenser becomes a more effective pressure-recovery device at lower vapor pressures.

The effect of the ratio of injector to tube area is illustrated in Fig. 4.23 for given density and injector-to-

$$P_2 - P_0 = P_0\left(\frac{A_{t_0}}{A_{t_1}} - 1\right) + \frac{\dot{m}_{v_0}^2}{g\rho_v A_{t_1}(A_{t_0} - A_{\ell_0})} + \frac{\dot{m}_{\ell_0}^2}{g\rho_\ell A_{t_1} A_{\ell_0}} - \frac{\dot{m}_T^2}{g\rho_\ell A_{t_1}^2} + \frac{\dot{m}_T^2}{2g\rho_\ell}\left(\frac{1 - K_d}{A_{t_1}^2} - \frac{1}{A_{t_0}^2}\right)$$

$$- \frac{\tau_w A_w \cos\alpha}{A_{t_1}} - \frac{1}{A_{t_1}}\int_0^{X_1} P_w \pi d_t \tan\alpha \, dx \qquad [4.53]$$

Figure 4.20, illustrating predicted performance of variable-area jet condensers, shows the calculated throat- and diffuser-pressure rise in reference to injected-liquid dynamic pressure vs. mass-flow ratio of liquid to vapor at given liquid-to-vapor-density and injector-to-tube-inlet-area ratios. Figure 4.21 shows the relations in reference to the inlet-vapor dynamic

throat-area ratios. Increasing values of $\mathring{A}_2$ result in increases in the nondimensional pressure rise referred to injected-liquid dynamic pressure or an increase in the effectiveness of the jet condenser as a pumping device. However, the absolute magnitude of pressure rise is increased as lower injector-to-tube-area ratios are used.

Figure 4.24 indicates the corre-

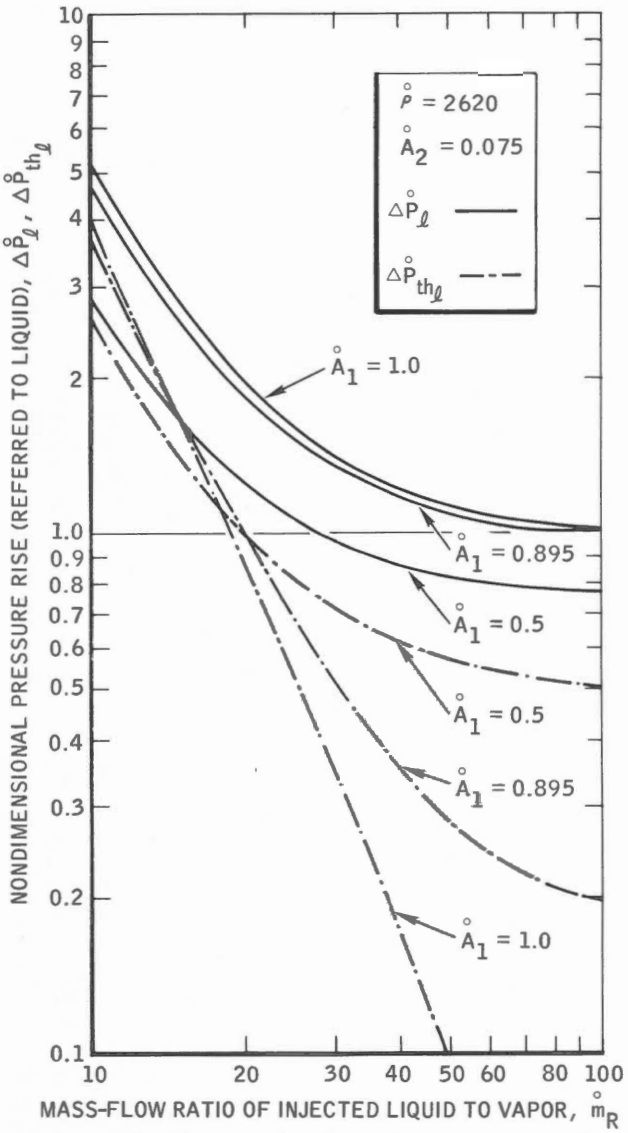

Fig. 4.20 - Calculated pressure rise (referred to liquid) for variable-area jet condenser, showing effect of injector-to-throat-area ratio [25].

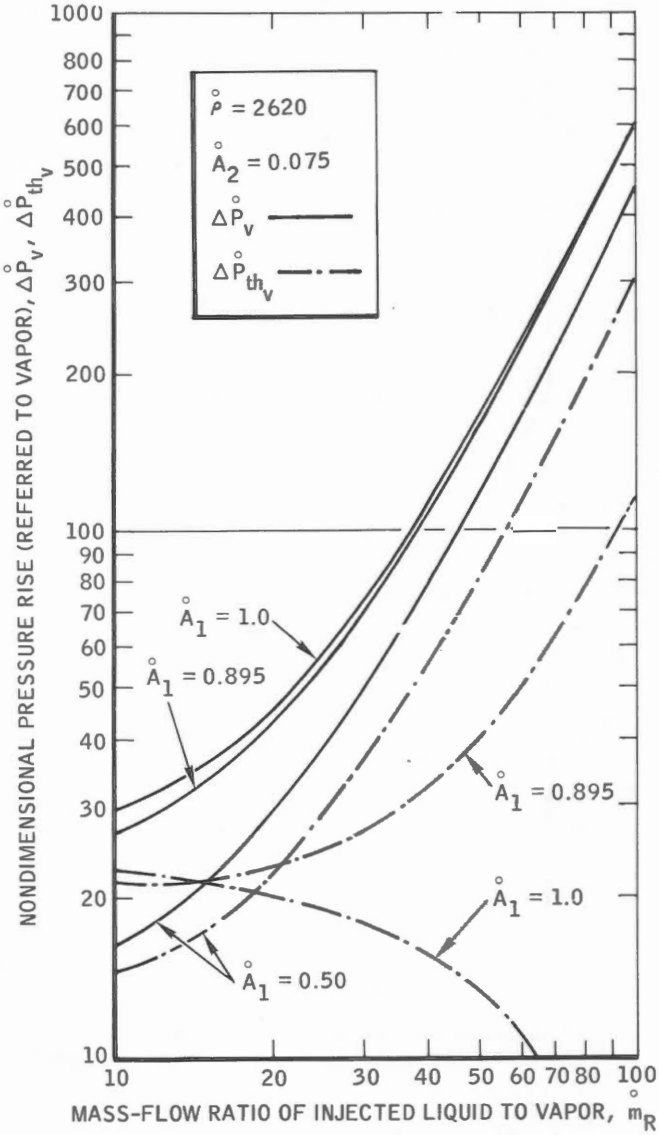

Fig. 4.21 - Calculated pressure rise (referred to vapor) for variable-area jet condenser, showing effect of injector-to-throat-area ratio [25].

lation of test data to predicted data achieved in an experimental program utilizing two-phase mercury flow. The experimental values of pressure rise for larger geometries agree to within about 30 and -25% with values predicted by the analysis. The recommended equation for predicted pressure rise is

$$\Delta\mathring{P}_\ell = 2\mathring{A}_1 \left[1 + \left(\frac{\mathring{\rho}}{\mathring{m}_R^2}\right) \frac{\mathring{A}_2}{1 - \mathring{A}_2}\right] - \left(\mathring{A}_1^2 + \mathring{A}_2^2\right) \left(1 + \frac{1}{\mathring{m}_R}\right)^2 \quad (4.54)$$

4-3.2 *Convective Condensers*

The heat-exchanger (convective) condenser causes condensation by transferring the heat to another working fluid. Since most condensers employing sodium and NaK as working fluids are of the heat-exchanger variety, the discussion in the following paragraphs is restricted to this type. A typical heat-exchanger condenser using NaK as the coolant is shown in Fig. 4.25. This condenser was designed for use in

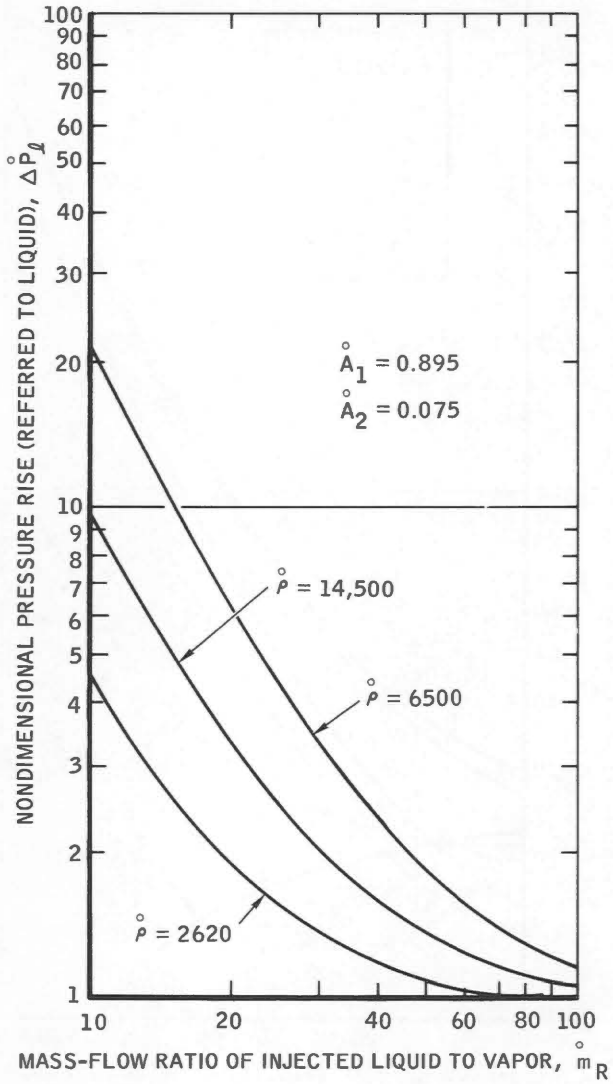

Fig. 4.22 - Calculated pressure rise (referred to liquid) for variable-area jet condenser showing effect of liquid-vapor-density ratio [25].

the SNAP-8 mercury Rankine space power plant.

(a) *Nomenclature for Sec.* 4-3.2

A	Surface area
A_{mw}	Mean wall surface area
C_{pc}	Specific heat of coolant
$C_{p\text{cond}}$	Specific heat of condensing fluid
D_i	Inside diameter of condenser tubes
D_O	Outside diameter of condenser tubes

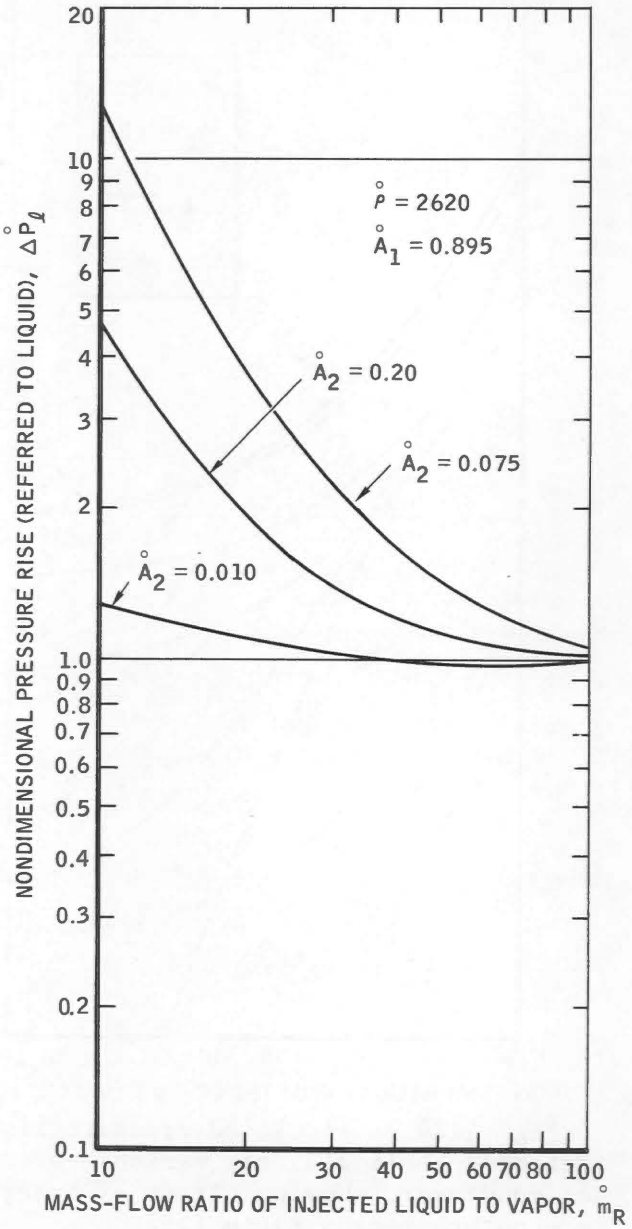

Fig. 4.23 - Calculated pressure rise (referred to liquid) for variable-area jet condenser showing effect of the ratio of the injector area to total inlet area [25].

h_c	Heat-transfer coefficient, coolant to tube wall
h_h	Heat-transfer coefficient, hot (condensing) fluid to tube wall
k	Thermal conductivity
k_{tw}	Thermal conductivity of tube-wall material
$\dot{m}_c$	Mass flow rate of coolant

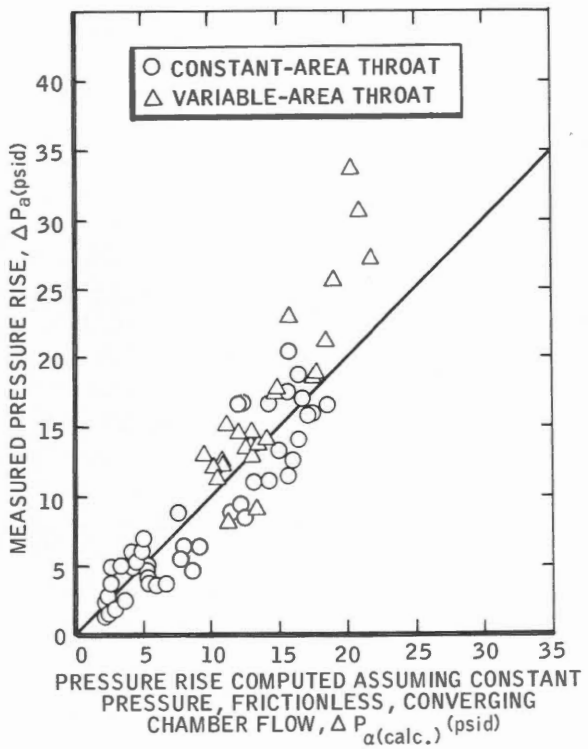

Fig. 4.24 - Comparison of calculated values with measured pressure rise in large-diameter jet condensers for all test runs with interface in throat and with steady-state conditions [25].

$\dot{m}_{cond}$	Mass flow rate of condensing fluid
Q	Overall heat transferred
T_c	Temperature of coolant
T_h	Temperature of hot (condensing) fluid
T_{ci}	Temperature of coolant at liquid-vapor interface
T_{cin}	Temperature of coolant at inlet to condenser
$T_{cond\ in}$	Temperature of condensing fluid at inlet to condenser
$T_{cond\ out}$	Temperature of condensing fluid at exit from condenser
t	Tube wall thickness
ΔT_{lm}	Log-mean-temperature difference
ΔT_1, ΔT_2	Temperature driving potentials at the terminals of heat exchanger
U	Overall heat-transfer coefficient

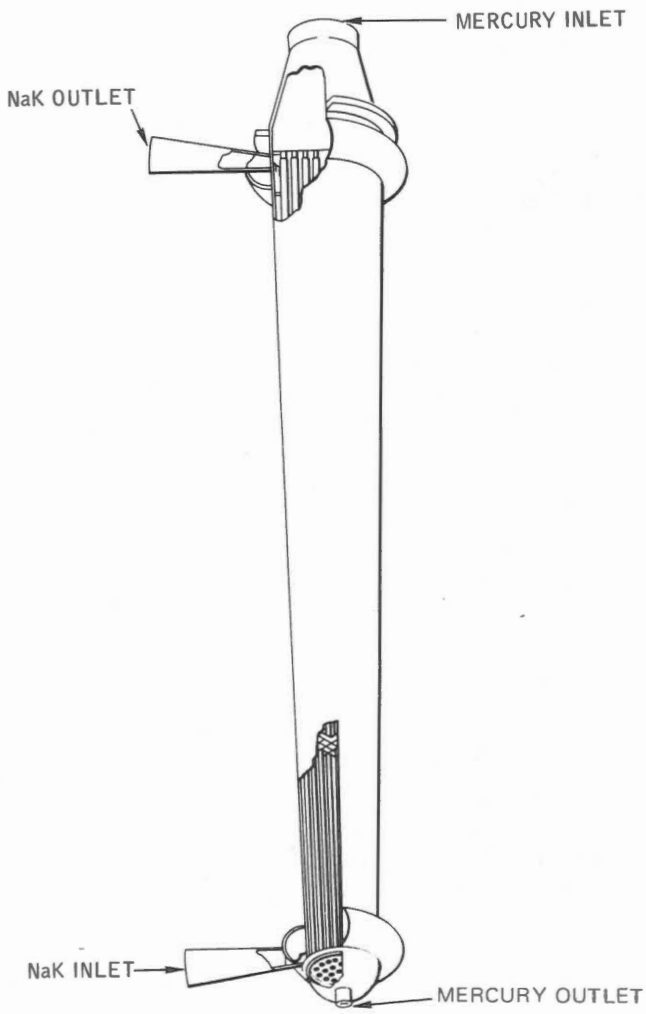

Fig. 4.25 - SNAP-8 condenser.

U_1, U_2	Overall heat-transfer coefficient at terminals of heat exchanger

(b) *Thermal Considerations*

Various techniques are available for the determination of the required tube length for any particular cross-sectional geometry for a given set of flow rates and terminal temperatures. Each of these is derived by considering the heat transfer across a differential element. These techniques differ because of the assumption made in the integration process.

The heat transferred per unit time across a differential element of a heat

exchanger at steady state is

$$dQ = U\,(T_h - T_c)\,dA \tag{4.55}$$

If the elemental heat-transfer surface area, dA, refers to the surface adjacent to the cold fluid, the local overall heat-transfer coefficient, U, is given by

$$U = \frac{1}{\frac{1}{h_h}\frac{dA_c}{dA_h} + \frac{t}{k}\frac{dA_c}{dA_{mw}} + \frac{1}{h_c}} \tag{4.56}$$

For a tube with circular cross section, U can be calculated from

$$U = \frac{1}{\frac{D_o}{D_i h_h} + \frac{D_o \ln(D_o/D_i)}{2k_{tw}} + \frac{1}{h_c}} \tag{4.57}$$

As is apparent from Eq. 4.57, the heat-transfer coefficients of both fluids must be known to determine U, especially if h_h and h_c are of the same order of magnitude, as in liquid-metal condensers.

When the specific heats of both fluids, U, and cross-sectional dimensions are assumed constant with length, Eq. 4.55 can be integrated to yield the following equation for parallel and counterflow heat exchangers:

$$A = \frac{Q}{U\,\Delta T_{lm}} \tag{4.58}$$

where

$$\Delta T_{lm} = \frac{\Delta T_2 - \Delta T_1}{\ln\,(\Delta T_2/\Delta T_1)} \tag{4.59}$$

Equation 4.55 can also be integrated for a variable U. When U is assumed to vary linearly with the temperature difference between the two fluids and other conditions are the same as those assumed for Eq. 4.58 the following equation [27] results:

$$A = \frac{Q\,\ln\left(\frac{U_1\,\Delta T_2}{U_2\,\Delta T_1}\right)}{U_1\,\Delta T_2 - U_2\,\Delta T_1} \tag{4.60}$$

Hess et al. [28] derived additional equations to account for variations of both U and cross-sectional dimensions with length.

If only approximate answers are needed in the design of a liquid-metal condenser, the equations given are useful despite the fact that the assumptions may not be completely satisfied. The usual procedure is to divide the condenser into two distinct sections, the condensing region and the subcooler region. The log-mean-temperature approach (Eq. 4.58) is then applied separately to each section of the condenser. In this procedure the coolant temperature at the vapor-liquid interface in the condenser, T_{ci}, must be calculated. If it can be assumed that the temperature of the condensing fluid is constant in the condensing region, the coolant interface temperature can be calculated by

$$T_{ci} = \frac{\dot{m}_{\text{cond}}\,C_{p\ \text{cond}}}{\dot{m}_c\,C_{pc}}\,(T_{\text{cond in}} - T_{\text{cond out}}) + T_{c\ \text{in}} \tag{4.61}$$

where $\dot{m}$ refers to flow rate and C_p to specific heat. This procedure is useful when the uncertainties in predicting local variations of the heat-transfer coefficient on the static pressure (and consequently the temperature of the condensing fluid) outweigh the error introduced by the assumptions. In general, however, greater accuracy is probably required in designing a liquid-metal condenser than that provided by the procedure described above. Methods accounting for the local variations of the condensing heat-transfer coefficient would be preferred since heat-transfer coefficients for condensing liquid-metal flows vary considerably with vapor quality and thus with length. Also, the temperature variation of the condensing fluid depends on the pressure drop along the condensing tube since local saturation

temperature depends on local static pressure.

A method of accounting for the effects of local variations of the heat-transfer coefficients and the static pressure of the condensing fluid is to divide the condenser into a number of smaller increments and employ a stepwise method of solution. In such a procedure changes across one increment are evaluated to determine the input values for the calculations on the next increment. The increments can be chosen so that they have the same heat load, the same coolant-temperature rise, or the same change in the quality of the condensing fluid. The calculation begins at the condensing-fluid-inlet end of the condenser where the temperatures and pressures of both fluids are known. The length of the first increment is calculated using the appropriate relations. The changes of the quality, static pressure, and temperature of the condensing fluid across this increment provide the additional information needed to solve for the length of the second increment. This procedure is then repeated until the desired condition of the condensing fluid at the end of the condenser is reached. Thus the condenser length is obtained by considering it to be composed of many smaller condensers operating in series.

The accuracy of this numerical-integration technique increases as the condenser is subdivided into smaller increments. For a given number of increments, using an integrated form of Eq. 4.55 inside each increment instead of using average values for U and the temperature difference may give an increase in accuracy.

The length of the individual increments can be calculated by the log-mean-temperature-difference approach: Assume that the temperature of the condensing fluid remains constant at its inlet value and evaluate the condensing heat-transfer coefficient by using the average quality of the condensing fluid in the increment. In reality, however, the overall heat-transfer coefficient, U, varies across an increment of the condenser, and methods that account for a variation of U are more desirable.

Equation 4.60 can be used to evaluate the increment lengths in counterflow condensers with cross-sectional dimensions that are constant with length. Hess et al. [28] derived equations to evaluate increment lengths in tapered condensers with cross-sectional dimensions that vary with length. These equations are complex and for this reason are not included here.

The stepwise design method described is particularly suited for solution by digital computers. A computer program using this procedure has been developed for shell and tube condensers [28].

As indicated previously, the heat-transfer coefficients of both fluids must be known to calculate the overall heat-transfer coefficient. The single-phase heat-transfer coefficients for sodium and NaK can be predicted from the correlations given in Vol. II, Chap. 2. The few existing experimental data on condensing heat-transfer coefficients for liquid metals indicate h_c to be substantially lower than predicted by theory although excellent correlations with theory were attained in experiments with condensing fluids other than liquid metals [29, 30]. Therefore one practical way to use the technique is to assume a constant condensing heat-transfer coefficient based on appropriate experimental data and to account for variations in liquid-coolant heat-transfer coefficient.

(c) *Condenser Configuration*

The selection of the configuration for a liquid-metal condenser for a particular application is influenced by several factors, including weight, volume, reliability, ease of manifolding, ease of fabrication, accommodation of thermal expansion, flow stability, and thermal performance. A number of different configurations

investigated for use with liquid metals are:

1. Shell-and-tube condensers:
   a. Constant diameter.
   b. Tapered diameter.
   c. Hockey stick.
2. Concentric tube with the condensing flow inside the annuli between the concentric tubes. A brief description of the design features for each of these condenser configurations follows.

(1) *Shell-and-Tube Condensers.* The shell-and-tube condenser is particularly attractive for use in space power plants with liquid-metal working fluids. The shell serves as a good pressure vessel, and the basic construction provides for a minimum number of metal-to-metal joints, thereby improving reliability. Shell-and-tube condensers for liquid-metal service generally use a counterflow arrangement, the condensing fluid flowing through the tubes and the coolant flowing axially through the shell. The counterflow arrangement is required to meet the temperature design conditions since the coolant exit temperature may be considerably higher than the condensate exit temperature. Condensation inside the tubes is normally used in preference to the more conventional method of condensing outside the tubes because the condenser must operate in a zero-g environment in space applications. With the condensing flow inside the tubes, fluid pressure and shear effects instead of gravity can be used to drive the condensate from the condenser.

A constant-diameter shell-and-tube condenser designed by Pratt and Whitney Aircraft [28] for a Rankine-cycle space power plant is illustrated in Fig. 4.26. The condenser consists of a bundle of circular tubes attached to tube sheets at either end. The tube bundle is arranged in a hexagonal pattern using an equilateral triangular pitch. The tube bundle is enclosed in a cylindrical shell that employs a hexagonal liner to direct flow through the tube bundle. The shell is joined to the tube sheets at both ends through toroidal-type manifolds. The manifolds are designed with sufficient flexibility to accommodate the differential thermal expansion between the shell and tube. Orifice plates at both ends of the shell maintain a uniform distribution of coolant across the shell. Orifices are also placed at the exit of each tube. To insure a uniform distribution of flow to all tubes, these orifices are sized so that the static pressure drop across them is greater than the static pressure rise of the condensing flow through the tubes.

A tapered, shell-and-tube-condenser configuration is illustrated in Fig. 4.27. The construction is similar to the constant-diameter configuration except that the cross-sectional dimensions decrease with length in the direction of the condensing fluid flow. The tapered configuration may offer some advantages over the constant-diameter configuration. Since the cross-sectional area of the tubes decreases with length, the tapered tubes maintain a higher average vapor velocity; this results in a higher average heat-transfer coefficient for the condensing flow. In addition, there is some evidence that condensing flow is more stable inside tapered tubes, as observed for mercury [31]. However, later experiments showed no apparent increase in stability for condensing flow inside tapered tubes [32]. There may be some advantages to tapered designs, but they are more difficult to manufacture.

Many shell-and-tube heat exchangers are designed so that each tube can flex independently to relieve the stresses that develop from differentials in the thermal expansion of individual tubes. This flexibility was accomplished in a number of ways. For example, some heat exchangers have long thin tubes that bow under the action of thermal stresses. Others have tubes bent into a U-shape which are free to grow in the

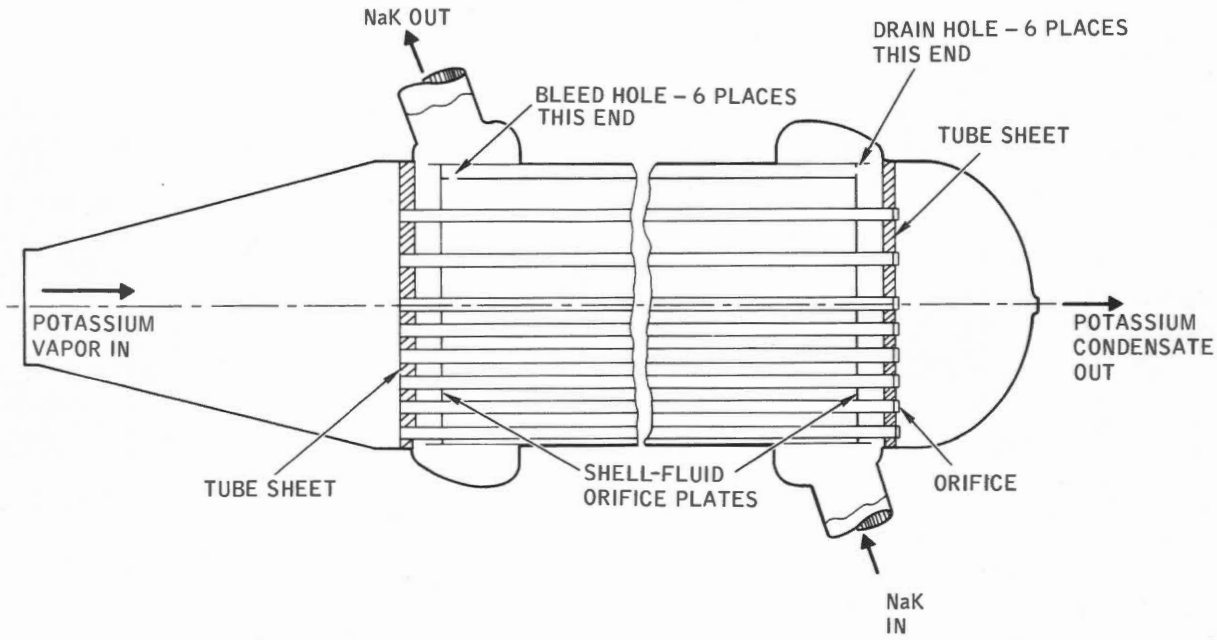

Fig. 4.26 - Constant-diameter NaK-cooled liquid-metal condenser for 1 Mw(e) nuclear space power plant.

axial direction. For liquid-metal heat exchangers, many designers have found it expedient to bend the tubes about 45° instead of into a complete U, a design illustrated by the hockey-stick condenser shown in Fig. 4.28.

(2) *Concentric-Tube Condenser.* A concentric-tube condenser (Fig. 4.29) consists of a bundle of concentric tubes with manifolding arrangements to direct the coolant fluid through the central tube and the condensing fluid

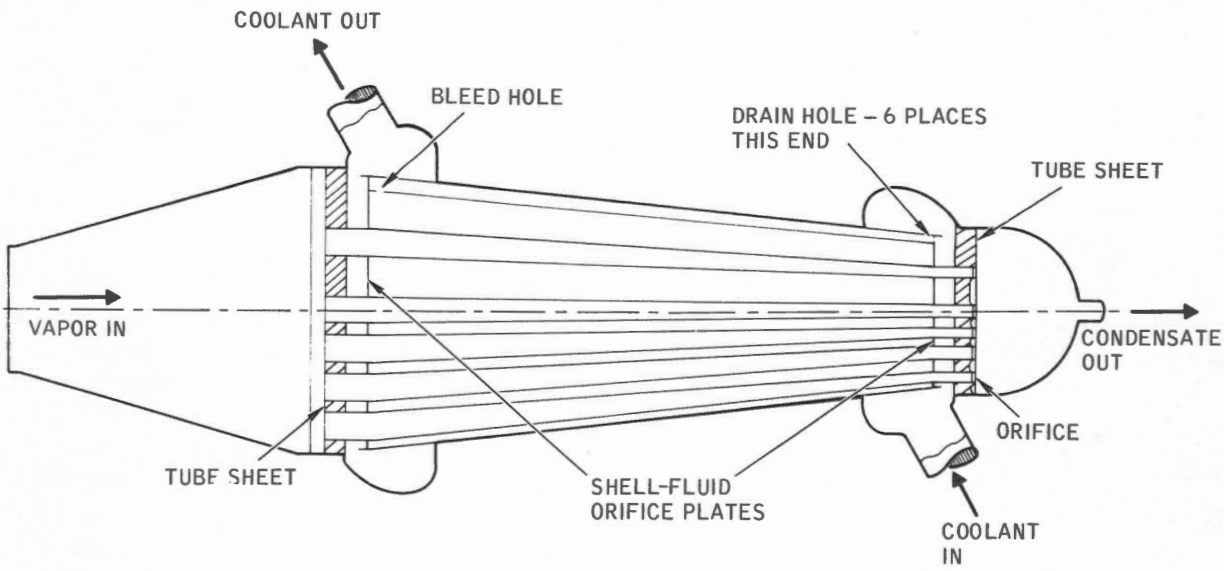

Fig. 4.27 - Tapered liquid-metal condenser for nuclear space power plant.

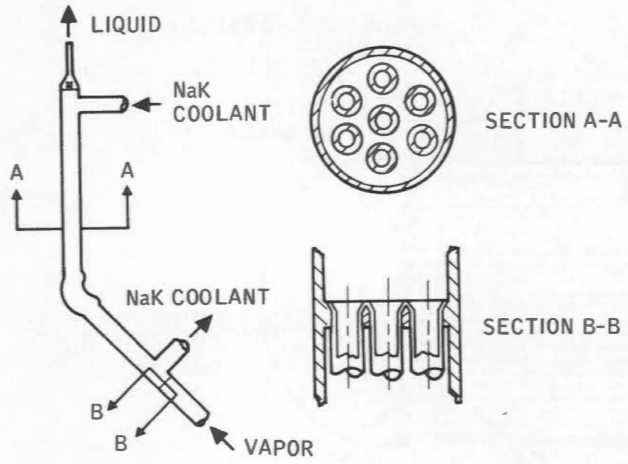

Fig. 4.28 - Hockey-stick condenser.

through the annular passages between the outer and the central tubes. Swirl devices in the annular passage remove condensate from the heat-transfer surface, thereby increasing the condensing heat-transfer coefficient. Separate tube sheets are required at each end for the outer tubes and the central tubes. The tube sheets at each end are separated to permit the condensing fluid to flow between them.

Compared with the shell-and-tube condenser, the concentric-tube condenser is heavier, less reliable, and more difficult to fabricate.

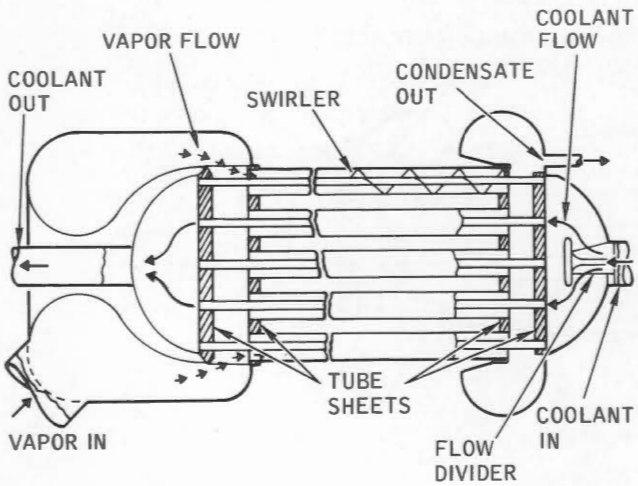

Fig. 4.29 - Concentric-tube condenser.

4-3.3 *Fluid Flow*

(a) *Pressure Drop*

Since the techniques for computing pressure drops for both single-phase and condensing flow are discussed in Vol. II, Chap. 1, only an enumeration of the various pressure losses to be considered in condenser design is given here. The overall change in static pressure across the condenser can be subdivided into the following components:

1. Coolant pressure losses.
   a. Entrance losses.
   b. Orifice losses (if orifices are used).
   c. Frictional loss through shell.
   d. Exit losses.
2. Condensing-fluid pressure losses.
   a. Inlet manifold drop.
   b. Tube entrance losses.
   c. Tube pressure changes, including two-phase condensing pressure drop, pressure rise due to momentum recovery, and frictional loss in subcooling region.
   d. Orifice losses.
   e. Exit losses.

(b) *Flow Stability*

Flow stability is discussed at length in Sec. 4-2.2(c) for radiative condensers. In general, the same stability considerations apply to heat-exchanger condensers.

(c) *Flow Distribution*

In a typical shell-and-tube condenser (Fig. 4.30), the coolant enters from the inlet pipe and is distributed circumferentially by the coolant inlet manifold. The coolant then flows radially inward through the circumferential gap between the shell and the tube sheet and enters the passage between the tube sheet and the adjacent orifice plate. The coolant flows radially inward through this passage

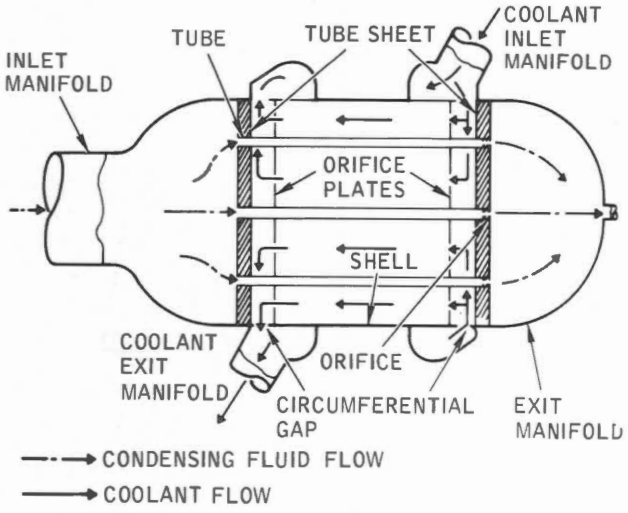

Fig. 4.30 - Typical flow pattern for constant-diameter shell-and-tube condenser.

and is dispersed through the holes in the inlet orifice plate into the main shell section. The coolant flows axially through the main shell section and then through the holes in the orifice plate at the exit end of the shell. The coolant is collected in the passage between this orifice plate and the adjacent tube sheet, where it flows radially outward. The flow continues radially outward through the circumferential gap between the tube sheet and the shell and is collected by the coolant exit manifold.

The coolant flow must be distributed uniformly in the radial direction as it flows through the main shell section of the condenser (Fig. 4.30) to obtain high thermal performance. The coolant distribution is strongly influenced by the relative pressure drop across various portions of the flow path. As the pressure drop across an orifice plate increases relative to the radial pressure loss for the flow between the orifice plate and the adjacent tube sheet, the coolant distribution becomes more uniform across the shell. The pressure drop across the orifice plate should be several times as large as the radial drop to obtain an acceptably uniform coolant distribution in the main shell.

A uniform distribution of the coolant flow in the main shell section of the condenser is also promoted by a uniform distribution of the flow through the circumferential gaps between the shell and the tube sheets (Fig. 4.30). As the pressure drop across each gap increases relative to the other pressure drops in the flow path, the flow through gaps becomes more uniform in the circumferential direction.

It is desirable to design shell-and-tube condensers to distribute the fluid to each tube as uniformly as possible. The use of an orifice on each tube to provide a static-pressure drop greater than the static-pressure rise of the condensing flow promotes a uniform flow to each tube. Since the flow rate in each tube depends strongly on the heat-transfer rate along the tube, it is desirable to keep the heat-transfer rates from each tube as uniform as possible at any axial position. Since the radial cross flow between the tube sheets and their adjacent orifice plates represents an area of nonuniform heat-transfer rates, the length of the tube exposed to this radial cross flow should be kept to a minimum.

4-3.4 *Mechanical Design*

The two primary areas of concern in the mechanical design of a liquid-metal condenser are materials compatibility with the working fluids, NaK and sodium, and the configuration of the tube-to-header joints. The capability for a long operational life requires materials that will not corrode or erode in either liquid-metal environment. The materials-compatibility problem with sodium and NaK is treated in Chap. 2.

Since numerous tube joints are required, the tube-header configuration is the main design problem. Two approaches that have been used with success are a welded and back-brazed

joint and a rolled-and-welded joint.

The welded and back-brazed joint, shown schematically in Fig. 4.31, is formed by using a trepanned header, automatic tungsten electrode, inert-gas (TIG) weld, and a subsequent back braze at 1800°F in a hydrogen atmosphere. Condensers fabricated by this method have accumulated over 2000 hr of service without failure [33]. The rolled-and-welded joint, shown schematically in Fig. 4.32, eliminates the costly and time-consuming back braze, replacing it with a grooved header into which the tube was rolled prior to welding. Both joints have passed nondestructive tests including helium leak checks and proof tests [26].

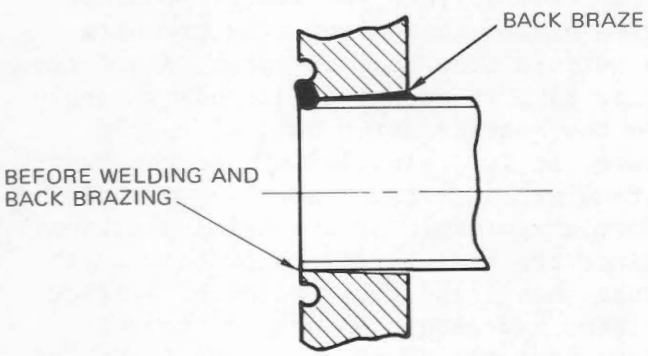

Fig. 4.31 - Welded and back-brazed joint schematic.

Once the materials are selected and the fabrication process for the tube headers developed, the remainder of the mechanical design of a liquid-metal condenser is considered straightforward heat-exchanger fabrication.

4-4 BOILERS

This section outlines the techniques used in designing a liquid-metal boiler for space power plant applications. Normally the application defines such parameters as terminal temperatures, exit quality, heat load, flow rates, allowable pressure drops, and any geometric limitations. The general design

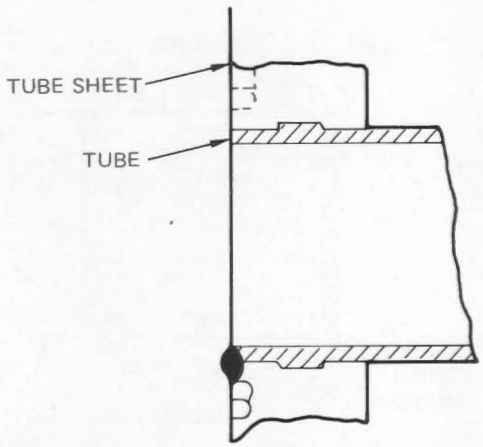

Fig. 4.32 - Rolled-and-welded joint schematic.

problem is to determine the combination of materials and geometry which provides the required thermal capability with minimum weight, volume, and, if possible, cost.

4-4.1 *Types of Boilers*

Like condensers, liquid-metal boilers for use in a space environment present design problems considerably different from their earthbound counterparts. For instance, since buoyancy forces are absent in a zero-g environment, a boiler that will operate satisfactorily in space must be of the forced-circulation variety. Two boiler concepts are usually considered, the recirculating type and the once-through type. Systems utilizing these two boiler concepts are shown schematically in Fig. 4.33. In the once-through boiler, the working fluid is heated from a subcooled liquid to superheated vapor. The vapor is then expanded in the turbine, condensed, and returned to the boiler by the condensate pump. The recirculating system requires the addition of separation equipment, a subcooler, and an additional pump to raise the pressure of the recirculated liquid to the boiler-inlet pressure. The recirculating boiler does not heat the thermodynamic working fluid to dry vapor. The moisture in the outlet fluid from

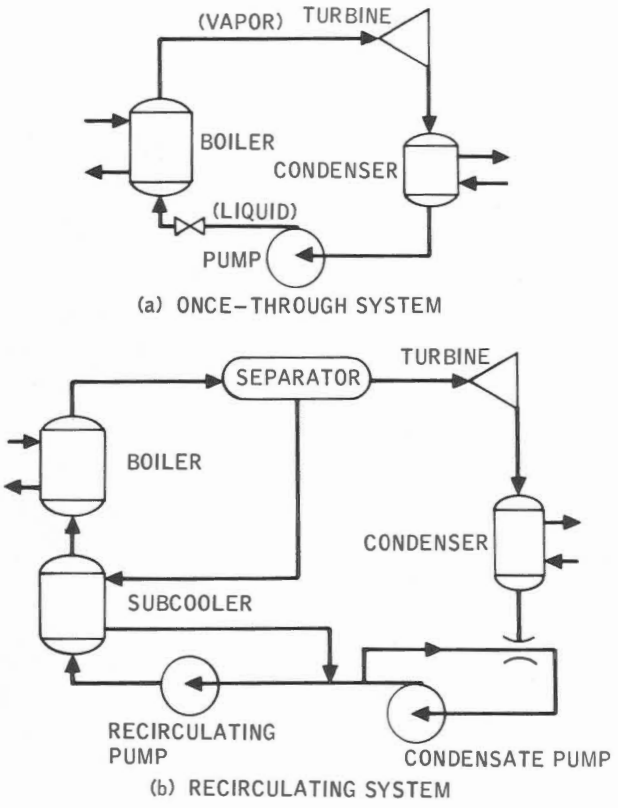

Fig. 4.33 - Boiler concepts.

the boiler is extracted by the separation equipment, and the dry vapor is supplied to the turbine. Following expansion in the turbine, the vapor is condensed and returned to the boiler by the condensate pump and boiler circulation. The liquid extracted in the separator is subcooled by the condensate in a subcooler and supplied to the suction of the boiler recirculating pump with sufficient subcooling to avoid cavitation.

The once-through boiler has been studied most intensively because the primary application of liquid-metal boilers has been in space power plants of relatively small power output, and the addition of liquid-vapor separators to such small systems increases their complexity and size an unwarranted amount. However, the once-through boiler has some inherent disadvantages that tend to counterbalance the advantages of simplicity and compactness.

The penalty frequently paid for using once-through boilers is low average heat-transfer coefficients. Superheaters characteristically have low heat-transfer coefficients, but since the percent of total heat added in the superheater is quite small, the low heat-transfer coefficient does not cause a significant increase in total boiler size. When the low heat-transfer coefficient occurs in the evaporation section, however, boiler size may be seriously affected.

Most of the heat added to a working fluid is used in the evaporation process. The effectiveness of the heat-transfer surface depends strongly on keeping the liquid phase in close proximity with the surface. In recirculation boilers this is not particularly difficult, because of the large ratio of liquid-to-vapor flow. In once-through boilers, however, the heat-transfer surface rapidly becomes blanketed with vapor, reducing heat transfer. Boilers that have been constructed include features to offset the blanketing effect of the vapor. The most effective device is a swirl promoter located within the boiler tube which produces an artificial gravity field that tends to separate the liquid to the wall and the vapor to the tube center. The effectiveness of the heat-transfer surface can be increased approximately threefold by this method. Pressure drop is also increased significantly when swirl devices are added.

4-4.2 *Nomenclature for Sec.* 4-4.3

A	Heat-transfer area
C	An empirical constant
C_{pN}	Specific heat of NaK
D	Tube diameter
G	Flow-mass velocity
G_0	Total flow-mass velocity
h	Heat-transfer coefficient
h_B	Heat-transfer coefficient of boiling fluid

h_h Heat-transfer coefficient of heating (primary) fluid
h_L Heat-transfer coefficient of boiling fluid in subcooled-liquid region
h_v Heat-transfer coefficient of superheated vapor
h_{fg} Latent heat of vaporization
h_G Heat-transfer coefficient in diffusion-limited heat-transfer region
K_G Dimensionless mass-transfer coefficient
k_l Thermal conductivity of liquid (boiling fluid)
k_v Thermal conductivity of vapor
L Length of boiler
L_c Boiler length of critical quality
$\dot{m}_{Hg}$ Mass flow rate of mercury
$\dot{m}_N$ Mass flow rate of NaK
N Number of tubes
Nu Nusselt number = hD/k_v
Nu_0 Drop Nusselt number
Q Heat-transfer rate
Re_0 Total flow-rate Reynolds number
S Slip; ratio of vapor-to-liquid velocity
T_B Local temperature of boiling fluid
T_h Local temperature of heating fluid
T_{Hg} Mercury temperature
T_N NaK temperature
T_{N_c} NaK temperature at point of critical quality
T_{N_i} NaK inlet temperature
T_{N_o} NaK outlet temperature
T_{sat} Saturation temperature
T_W Wall temperature
ΔT_m Mean NaK-to-boiling-mercury temperature difference
U Overall heat-transfer coefficient
U_{N-W} Heat-transfer coefficient of NaK and tube
x Vapor quality
x_c Critical vapor quality (dry-wall condition)
α Swirl-wire pitch angle
β An empirical constant
δ_o Swirl-wire diameter
ρ_l Liquid density
ρ_v Vapor density
μ_v Vapor viscosity

4-4.3 *Thermal Considerations*

The general heat-exchanger-design relations discussed in Sec. 4-3.2(b) for condensers can also be applied to the design of a liquid-metal boiler for a given set of flow rates, terminal temperatures, and geometry. As with condensers, however, the required surface area must be calculated in a stepwise manner to account for the variation in heat-transfer and fluid-flow regimes along the boiler length.

The heat transferred per unit time across a differential element of a boiler at steady state is

$$dQ = U\,(T_h - T_B)\,dA \tag{4.62}$$

If the elemental heat-transfer surface area, dA_h, refers to the surface adjacent to the heating fluid, then the local overall heat-transfer coefficient is given by

$$U = \frac{1}{\frac{1}{h_B}\frac{dA_h}{dA_B} + \frac{1}{h_{int}}\frac{dA_h}{dA_{int}} + \frac{1}{h_h}} \tag{4.63}$$

where the coefficient h_{int} represents conduction through the interface (commonly a tube wall) between the two fluids, A_h is area at heating surface, A_B is area at boiling surface, and A_{int} is the mean area of the tube wall.

When only approximate calculations are required, the log-mean-temperature approach (Eq. 4.58) can be applied by dividing the boiler into regions and using average heat-transfer coefficients for each region. The usual procedure is to divide the boiler into three parts: (1) the preheating section, (2) the wet-wall boiling section, and (3) the dry-wall boiling and superheating section. The heat-transfer rate for each section is then calculated on the basis of average heat-transfer coefficients and the log-mean-temperature difference. In the preheating section the inlet fluid is

heated to its saturation temperature. In the wet-wall boiling section, the quality is increased from 0 to approximately 80 to 90%, the range in which wet-wall boiling, and therefore a relatively high boiling heat-transfer coefficient, can be expected. In the dry-wall boiling and superheating section, the boiling fluid is heated from about 80% quality to the desired superheat. In this section the boiling-fluid heat-transfer coefficient can be expected to be low.

If greater accuracy is required in the boiler design, methods accounting for the local variation of the boiling heat-transfer coefficient are necessary since heat-transfer coefficients for boiling liquid-metal flows vary considerably with vapor quality. Also, the temperature variation of the boiling fluid depends on the pressure drop along the boiler tube since local saturation temperature depends on local static pressure.

The most practical method of accounting for the effects of local variations of the heat-transfer coefficients is to divide the boiler into a number of smaller increments and employ a stepwise method of solution. Using such a procedure, we evaluate changes across one increment to determine the input values for the calculations on the next increment.

Determination of the heat-transfer coefficients for liquid-metal boilers is complicated by the differences in flow patterns occurring as the volume fraction of the vapor increases along the boiler tube. A separate heat-transfer correlation is required for each flow pattern. For alkali-metal boilers the variations in flow regimes as the boiling fluid passes through the boiler [34] are shown in Figs. 4.34 and 4.35. The two-phase flow patterns shown are:

1. Bubbly flow: This pattern occurs at very low quality and consists of individual bubbles of vapor entrained in the liquid flow. The bubbles are formed at nucleation sites on the wall.

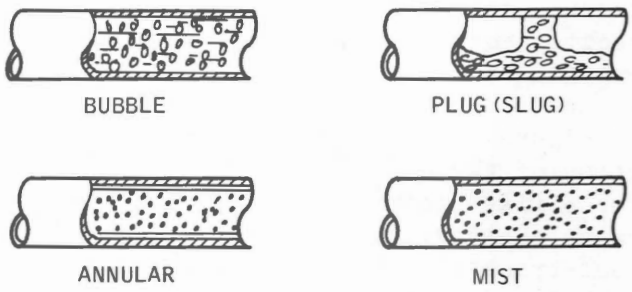

Fig. 4.34 - Two-phase flow patterns in boiler tubes [34].

2. Plug, or slug, flow: As the quality of length-to-diameter ratio increases, the individual bubbles agglomerate and grow to form plugs, or slugs, of vapor which periodically pass a given point on the wall.

3. Annular flow: At higher quality, the vapor flows in a high-velocity core in the center of the pipe, and a thin film of liquid covers the pipe wall. Liquid droplets are generally dispersed in the vapor core.

4. Mist flow: At high quality, the liquid film on the wall disappears and all the liquid is dispersed throughout the vapor as droplets.

In the subcooled (preheater) and the superheater regions single-phase flow

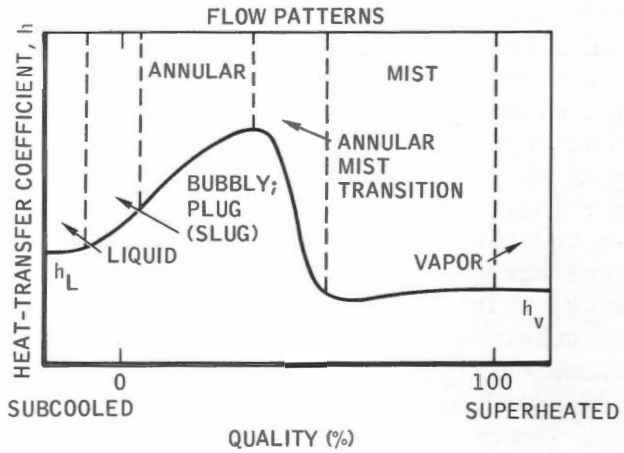

Fig. 4.35 - Characteristic forced-convection vaporization heat-transfer coefficient [34].

exists, and conventional forced-convection correlations can be used to predict the heat-transfer coefficients h_L and h_v.

Figure 4.35 illustrates the variation of the heat-transfer coefficient for a fixed geometry and flow rate with vapor quality. It can be seen that the heat-transfer coefficient increases with increasing quality. At a critical quality, x_c, which varies considerably with fluid, geometry, and heat flux, there is a rapid decrease in the heat-transfer coefficient toward the value characteristic of vapor flow. When the quality reaches 100%, the coefficient equals the vapor heat-transfer coefficient, h_v.

In the bubbly-flow regime, the volume fraction of the vapor is very small and thus has little effect on the liquid velocity. Bubbles grow and depart from nucleation sites on the wall much as they do in nucleate pool boiling. Depending on the wall temperature, fluid properties, and the nucleation characteristics of the wall, the nucleate-pool-boiling heat-transfer mechanism may or may not dominate the forced-convection heat transfer to the liquid occurring between the bubble nucleation sites. In the very narrow quality range over which bubbly flow exists, the heat-transfer rate can be predicted by superimposing liquid forced convection and nucleate pool boiling [35], if the superheat temperature difference ($T_W - T_{sat}$) is not great enough to produce film boiling.

As the vapor volume fraction and the tube length-to-diameter ratio increases, the individual bubbles grow and agglomerate to form plugs or slugs of vapor, which occur periodically along the tube. Even though the vapor volume fraction has increased, the corresponding quality is still very low. However, the presence of the larger volume fraction of vapor begins to cause a significant increase in the liquid velocity in the plug-flow regime. The heat-transfer mechanism is probably the same as in the bubbly-flow regime: A superposition of forced convection to a liquid and nucleate pool boiling; it can be conservatively estimated by ignoring the increase in velocity.

In a typical boiler the bubbly- and plug- (slug-) flow regimes exist over a very small fraction of the total boiler length. In addition, superimposing the nucleate-boiling heat flux and the forced-convection heat flux has a relatively small effect since the forced-convection heat-transfer coefficient is generally greater than 1000 Btu/(hr)-(sq ft)-(°F) with liquid metals. Consequently the increased heat transfer provided by boiling in these flow patterns can be ignored. This yields a slightly conservative result and eliminates the need to predict liquid-metal nucleate-pool-boiling heat-transfer characteristics. It must, of course, be demonstrated that film boiling cannot occur.

In annular flow the vapor is generated primarily by vaporization from the liquid-vapor core interface inside the tube, and not by the formation of bubbles at the wall. The heat-transfer mechanism is similar to that for film condensation inside a tube; heat is transferred through the liquid film to the interface with the vapor core. The heat-transfer coefficient for this process is much higher than that for nucleate boiling, especially with liquid metals. In the annular flow region, the boiling heat-transfer coefficient is substantially greater than the heating-fluid coefficient. Therefore the heating-fluid coefficient, combined with the wall resistance, is controlling with respect to the required heat-transfer area, and knowledge of the exact value of the annular-flow boiling coefficient is of minor importance for design purposes.

The quality corresponding to the abrupt decrease in heat-transfer coefficient shown in Fig. 4.35 marks the start of the wall-drying process, which eventually produces a completely

dry wall and mist flow. The heat-transfer coefficient undergoes a rapid decrease beyond this point since heat is transferred directly to the low-thermal-conductivity vapor in the dry spots. After the heat is transferred to the vapor, it is transferred to the liquid droplets; the mist-flow vaporization process actually takes place in the interior of the pipe rather than at the wall. For this reason, the temperature of the vapor in the mist-flow regime is always greater than the saturation temperature. When the wall is completely dry, the mechanism of heat transfer is forced convection to a gas, and the heat-transfer coefficient can be predicted from conventional forced-convection correlations for gases.

It is important to delay the onset of wall drying in the boiler because the low heat-transfer coefficients associated with mist flow would require a prohibitively heavy boiler to provide complete vaporization of the fluid.

The high-quality dry wall is caused simply by vaporization of the liquid film on the wall, as a result of conduction heat transfer through the liquid, while the vapor core still contains a dispersion of liquid droplets formed upstream at lower quality and carried along by the vapor [36]. The volume fraction of these liquid droplets is very small, but they account for a substantial mass fraction because of the high liquid-to-vapor density ratio; the quality at the point where dry wall is attained is due entirely to the mass of liquid in the droplets. Thus the dry wall condition can be overcome if a method can be found to reattach the liquid droplets to the wall.

The use of twisted-tape or swirl-wire inserts in the boiler tubes to centrifuge the liquid droplets to the wall appears to be a promising method of postponing the occurrence of dry spots to higher quality and maintaining a high-transfer coefficient to high quality since the wall will be maintained partially wet as long as liquid exists in the tube. Because of the complexity of the two-phase annular-flow process, analysis is extremely difficult and uncertain.

A number of rather complicated correlations have been suggested to predict heat-transfer coefficients for tubes with twisted-tape inserts, but they do not provide much more accuracy than is obtained by simply inserting the equivalent diameter and resultant velocity in conventional correlations.

The boiling and single-phase heat-transfer coefficients for sodium and NaK can be predicted from the correlations given in Vol. II, Chap. 2.

For NaK-to-mercury boilers a detailed boiling-research experimental program was conducted [37] to obtain local heat-transfer data that would allow stepwise design of boilers as a function of quality and temperature difference along the tube length. These data were successfully correlated through the definition of three boiling regimes. These were the contact region, where nonwetting-liquid drops are in constant contact with the tube wall and the heat is transferred by conduction to the drop; the intermittent-contact region, where the drops intermittently contact the wall; and the film region, where the drops never contact the wall. This correlation resulted in the following three design equations [37]:

1. Contact-boiling region (nonwetted):

$$\mathrm{Nu} = \frac{1}{32}\mathrm{Nu}_\delta^2\left(\frac{k_l}{k_v}\right)^2\left(\frac{D}{\delta_0}\right)^2\frac{(1-x)^{\frac{1}{3}}}{x}\frac{\rho_v}{\rho_l} \quad (4.64)$$

where

$$\mathrm{Nu}_\delta = 0.80 \text{ (for } 0 < x < 100\%).$$

2. Intermittent-contact boiling region:

$$\mathrm{Nu} = 234C^4 \left(\frac{k_v}{k_l}\right)^4 (1 - x)^{\frac{4}{3}} \frac{x\delta_0}{D} \times \left(\frac{DG}{\mu_v} \frac{\mu_v h_{fg}}{k_v \Delta T_m} \tan \alpha\right)^2 \quad (4.65)$$

where

$C = 2.3$ (for $0 < x < 40\%$) and

$C = 3.0$ (for $40\% < x < 100\%$).

3. Film-boiling region:

$$\mathrm{Nu} = \frac{6^{\frac{1}{3}}}{4} \beta^{\frac{4}{3}} \frac{(1 - x)^{\frac{2}{3}}}{x^{\frac{1}{3}}} \frac{D}{\delta_0} \left(\frac{DG}{\mu_v}\right)^{\frac{2}{3}} \times \left(\frac{\rho_v}{\rho_l} \tan \alpha\right)^{\frac{2}{3}} \left(\frac{\mu_v h_{fg}}{k_v \Delta T_m}\right)^{\frac{2}{3}} \alpha \quad (4.66)$$

where

$\beta = 0.43$ (for $0 < x < 40\%$) and

$\beta = 1.0$ (for $40\% < x < 100\%$)

The SNAP-2 model 5C (Fig. 4.36) boiler was designed by using these equations, and the predicted performance [38] is shown in Fig. 4.37, along with actual data. The design equations, based on dry-wall, conduction boiling, are very conservative with respect to conditioned (wet-wall, nucleate boiling) performance.

It was recently shown [39] that conditioned boiler performance data can be closely matched if the mercury-side (nucleate-boiling) film resistance is completely neglected over the wetted fluid-film region of the boiler and a drop mass-transfer model is used for the region where the drops are being carried along in the vapor stream (spray-annular flow pattern as illustrated in Fig. 4.38). In this latter region the drops strike the wall by the turbulent motion (eddy diffusion) of the vapor, and it is assumed that any drop reaching the wall is vaporized. The heat flux in this region is given by [40]

$$Q/A = K_G S (1 - x) G_0 h_{fg} \quad (4.67)$$

or in terms of heat-transfer coefficient,

$$h_G = \frac{K_G S(1 - x)G_0 h_{fg}}{T_W - T_{\mathrm{Hg}}} \quad (4.68)$$

The dimensionless mass-transfer coefficient, K_G, based on the analogy between mass and momentum transfer, is given by

$$K_G = \frac{0.023}{\mathrm{Re}_0^{0.2}} \text{ (for } S = 1) \quad (4.69)$$

The critical quality x_c at which the wetted-film heat-transfer rate exceeds the calculated diffusion-limited rate represents the point at which the fluid film disappears and the mass-transport mechanism takes over. The critical quality can be computed [32] by

$$U_{\mathrm{N-W}}(T_{\mathrm{N}_c} - T_{\mathrm{Hg}}) = K_G S(1 - x_c)Gh_{fg} \quad (4.70)$$

where $U_{\mathrm{N-W}}$ is the combined heat-transfer coefficient for the heating fluid (NaK) and the tube wall. The resistance of the evaporating liquid film has been neglected. T_{N_c} is a function of x_c and can be determined from a heat balance (Fig. 4.38):

$$T_{\mathrm{N}_c} = \frac{\dot{m}_{\mathrm{Hg}} h_{fg}}{\dot{m}_{\mathrm{N}} C_{p\mathrm{N}}} (x_c - 1) + T_{\mathrm{N}_i} \quad (4.71)$$

A combination of Eqs.4.70 and 4.71 yields

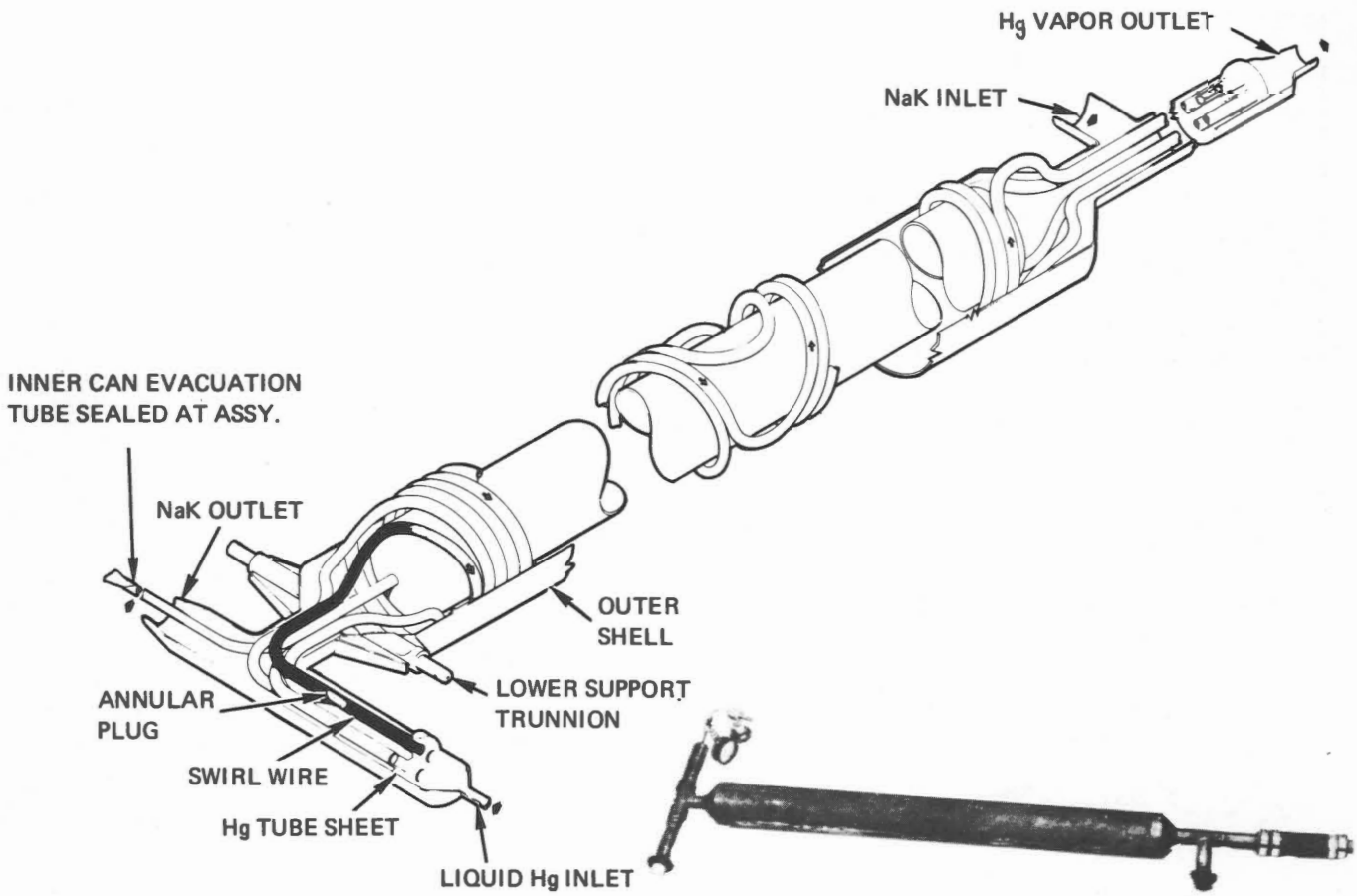

Fig. 4.36 - SNAP-2 model 5C boiler. Overall dimensions: 6.5 ft long × 4.0 in. OD. Hg tubes: 4 tubes, 29 ft long, 3/8 in. OD × 0.020 in. wall. Swirl wire: 0.040 in. diameter × 1.0 in. pitch. Insert tube: 54 in. long × 1/4 in. OD. Dry weight: 30 lb.

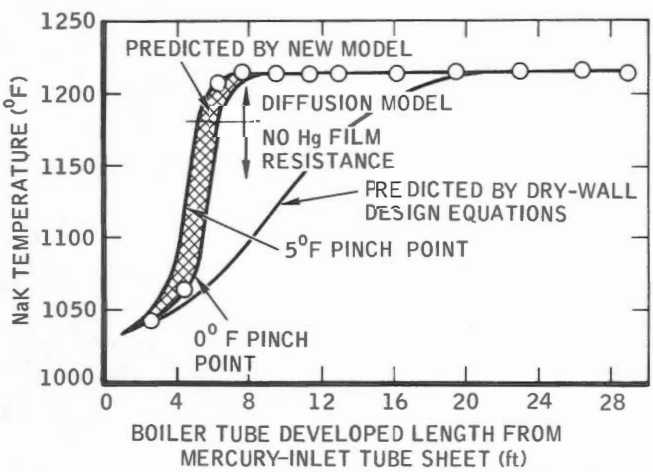

Fig. 4.37 - Predicted model 5C boiler profiles and comparison to data. o, model 5C boiler data.

$$U_{N-W}\left[\frac{\dot{m}_{Hg}}{\dot{m}_N C_{pN}}(x_c - 1) + (T_{N_i} - T_{Hg})\right] = K_G S\,(1 - x_c)\,G_0 h_{fg} \qquad (4.72)$$

from which x_c can be determined.

The heating length, L_c, up to the point where dry-wall boiling occurs, as defined by Eq. 4.70 in terms of x_c, can be computed as illustrated in the subsequent analysis [39]. The overall heat-transfer coefficient U over the length L_c is primarily determined by the tube-wall and NaK resistance. Therefore

$$U_{N-W} = \frac{\dot{m}_N C_{pN}\,dT_N}{\pi D N\,(T_N - T_{Hg})\,dL} \qquad (4.73)$$

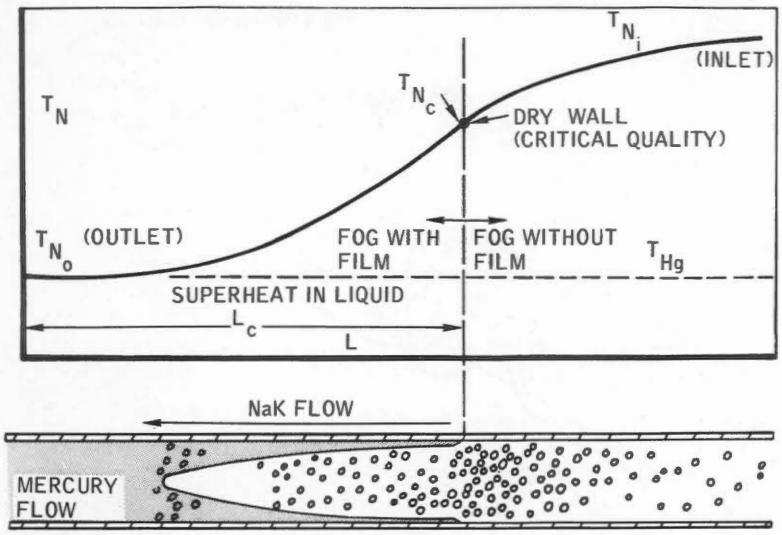

Fig. 4.38
Spray-annular boiling.

Rearranging Eq. 4.73 to solve for dL and integrating yields

$$L\Big|_0^{L_c} = \frac{\dot{m}_N C_{pN}}{\pi D N U_{N-W}} \ln (T_N - T_{Hg})\Big|_{T_{N_o}}^{T_{N_c}}$$

$$L_c = \frac{\dot{m}_N C_{pN}}{\pi D N U_{N-W}} \ln \frac{T_{N_c} - T_{Hg}}{T_{N_o} - T_{Hg}} \qquad (4.74)$$

or, if the temperature profile is to be computed,

$$L = \frac{\dot{m}_N C_{pN}}{\pi D N U_{N-W}} \ln \frac{T_N - T_{Hg}}{T_{N_o} - T_{Hg}} \qquad (4.75)$$

To compute the NaK temperature profile and boiling length for $L > L_c$, we proceed as follows:

$$\frac{1}{U} = \frac{1}{U_{N-W}} + \frac{1}{h_G} \qquad (4.76)$$

Thus,

$$\left(\frac{1}{U_{N-W}} + \frac{1}{h_G}\right)^{-1} = \frac{\dot{m}_N C_{pN}\, dT_N}{\pi D N\, (T_N - T_{Hg})\, dL} \qquad (4.77)$$

Substituting Eq. 4.68 yields

$$\left[\frac{1}{U_{N-W}} + \frac{T_W - T_{Hg}}{K_G S (1 - x) G_0 h_{fg}}\right]^{-1} = \frac{\dot{m}_N C_{pN}\, dT_N}{\pi D N\, (T_N - T_{Hg})\, dL}$$

$$dL = \frac{\dot{m}_N C_{pN}}{\pi D N U_{N-W}} \frac{dT_N}{T_N - T_{Hg}} + \frac{\dot{m}_N C_{pN}}{\pi D N K_G S (1 - x) G_0 h_{fg}} \frac{T_W - T_{Hg}}{T_N - T_{Hg}}\, dT_N$$

If we substitute the heat balance,

$$1 - x = \frac{\dot{m}_N C_{pN}}{\dot{m}_{Hg} h_{fg}} (T_{N_i} - T)$$

$$G_0 = \frac{4\dot{m}_{Hg}}{\pi D^2 N}$$

we obtain

$$dL = \frac{\dot{m}_N C_{pN}}{\pi D N U_{N-W}} \frac{dT_N}{T_N - T_{Hg}} + \frac{D}{K_G S 4} \frac{T_W - T_{Hg}}{T_N - T_{Hg}} \frac{dT_N}{T_{N_i} - T_N} \qquad (4.78)$$

To be conservative, let $T_W = T_N$; then Eq. 4.79 becomes

$$dL = \frac{\dot{m}_N C_{pN}}{\pi D N U_{N-W}} \frac{dT_N}{T_N - T_{Hg}} + \frac{D}{K_G S 4} \frac{dT_N}{T_{N_i} - T_N} \qquad (4.79)$$

Integrating, Eq. 4.79 yields

$$L\Big|_{L_c}^{L} = \frac{\dot{m}_N C_{pN}}{\pi D N U_{N-W}} \ln (T_N - T_{Hg})\Big|_{T_{N_c}}^{T_N} +$$

$$\frac{D(-1)}{K_G S4} \ln (T_{N_i} - T_N)\Big|_{T_{N_e}}^{T_N}$$

$$L - L_e = \frac{\dot{m}_N C_{pN}}{\pi D N U_{N-W}} \ln \frac{T_N - T_{Hg}}{T_{N_e} - T_{Hg}} +$$

$$\frac{D}{K_G S4} \ln \frac{T_{N_i} - T_{N_e}}{T_{N_i} - T_N} \qquad (4.80)$$

The boiler profile predicted by this analysis for the SNAP-2 model 5C boiler is also shown in Fig. 4.37. Because of the higher pressure drop resulting from the large excess superheat length in the model 5C boiler, the boiler operates with about a 5°F pinch point. This method of analysis represents the data quite well, and only a small portion of the boiling region exhibits the diffusion-limited heat-transfer characteristic (81% < x < 100%).

Operating experience [38] showed that the performance of NaK-to-mercury boilers is not always predictable; heat-transfer rates in a given boiler may vary as much as an order of magnitude at different times under the same parametric conditions. For example, a boiler operating favorably with high boiling heat-transfer coefficients and producing relatively high boiler-outlet quality and high vapor superheat is said to be conditioned. In deconditioned boiler operation low heat transfer occurs, and low mercury-outlet quality and low superheat result. Figures 4.39 and 4.40 represent typical conditioned and deconditioned performance of the SNAP-2 NaK-to-mercury boiler.

An evaluation of boiler-test experience, coupled with a review of related experimental data and applicable literature, led to the formulation of several possible mechanisms for the deconditioning process. The only two that seemed reasonable after detailed scrutiny were:

1. Deconditioning was strictly the result of loss of surface wetting and was caused by the presence of contaminants such as air, water, or oil.

2. Deconditioning resulted from the washing out of nucleation sites, which gave rise to superheated liquid. This liquid would intermittently flash, setting up a slug-flow pattern which then caused the poor heat-transfer characteristics.

Two basic experimental programs were proposed to evaluate these hypotheses [41]. One was a pool-boiling test to evaluate the effect of wetting on nucleate-boiling heat transfer and to evaluate the effects of air, water, and oil contamination on the wetting characteristics of the boiler surface. The other test was a single-tube forced-convection test to evaluate the use of artificial nucleation sites as a means of preventing slug flow and thus poor heat transfer. A third test program [38] to evaluate tube-to-tube conditioning and stability effects was also proposed. The conclusions drawn indicate that the primary cause of boiler deconditioning is loss of surface wetting. Although other phenomena such as slug flow may accompany deconditioned boiler operation, they are the results of, rather than the causes of, boiler deconditioning. The establishment of vortex flow does not produce conditioned boiler performance unless wetting also occurs. No attempt to obtain larger liquid superheats with mercury (lack of nucleation sites) has been successful to date.

The primary cause of prolonged boiler deconditioning problems has most probably been the presence of organics in the boiling loop. Air and water can temporarily decondition a boiler, but deconditioning as a result of oil contamination is much more permanent in nature.

The low heat-transfer coefficient of a deconditioned boiler requires a large tube wall-to-mercury temperature difference or a large heat-transfer area to transfer the required thermal energy. For space application, where the

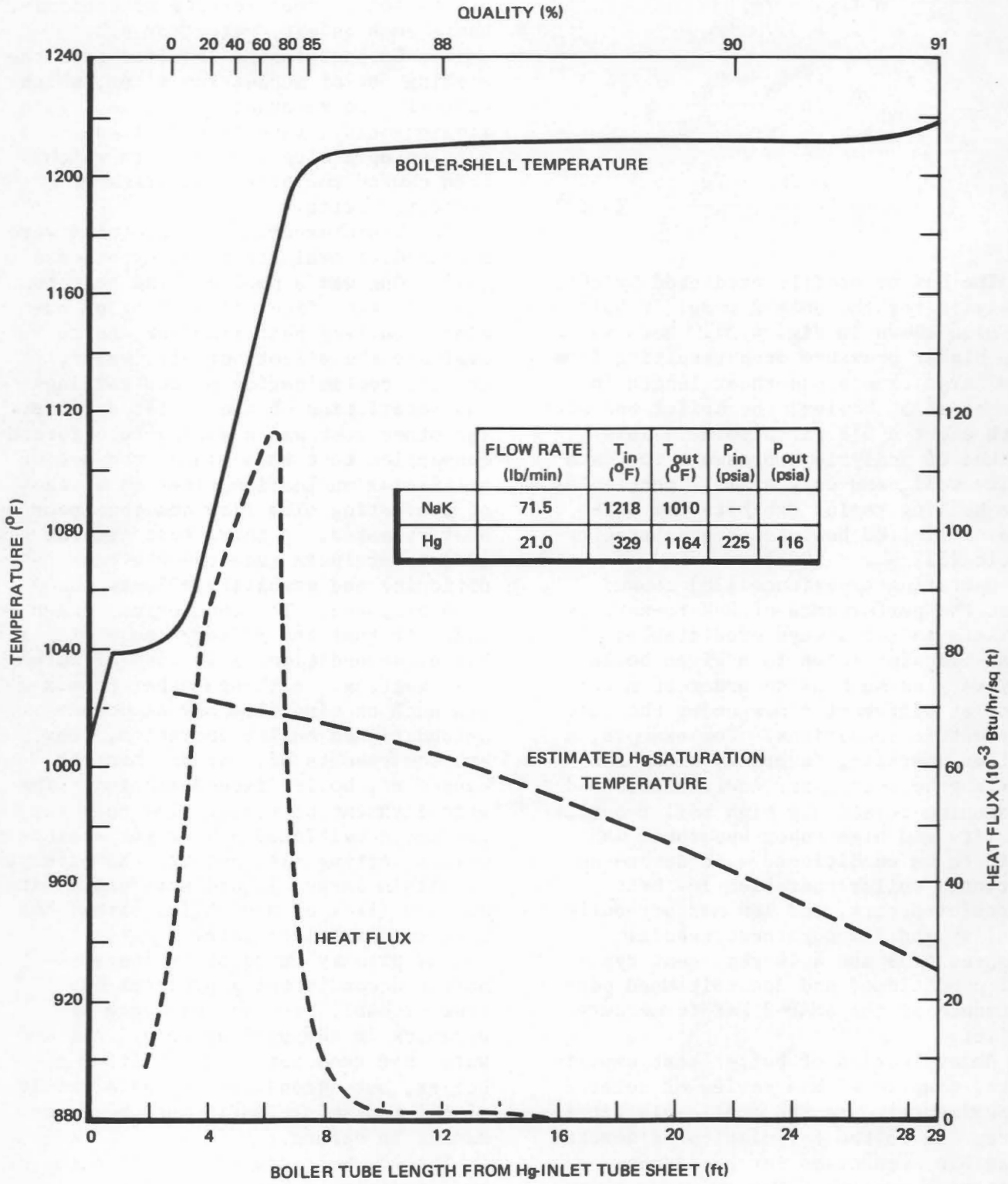

	FLOW RATE (lb/min)	T_{in} (°F)	T_{out} (°F)	P_{in} (psia)	P_{out} (psia)
NaK	71.5	1218	1010	–	–
Hg	21.0	329	1164	225	116

Fig. 4.39 - Temperature and heat-flux profiles for the conditioned model 5C-5 boiler.

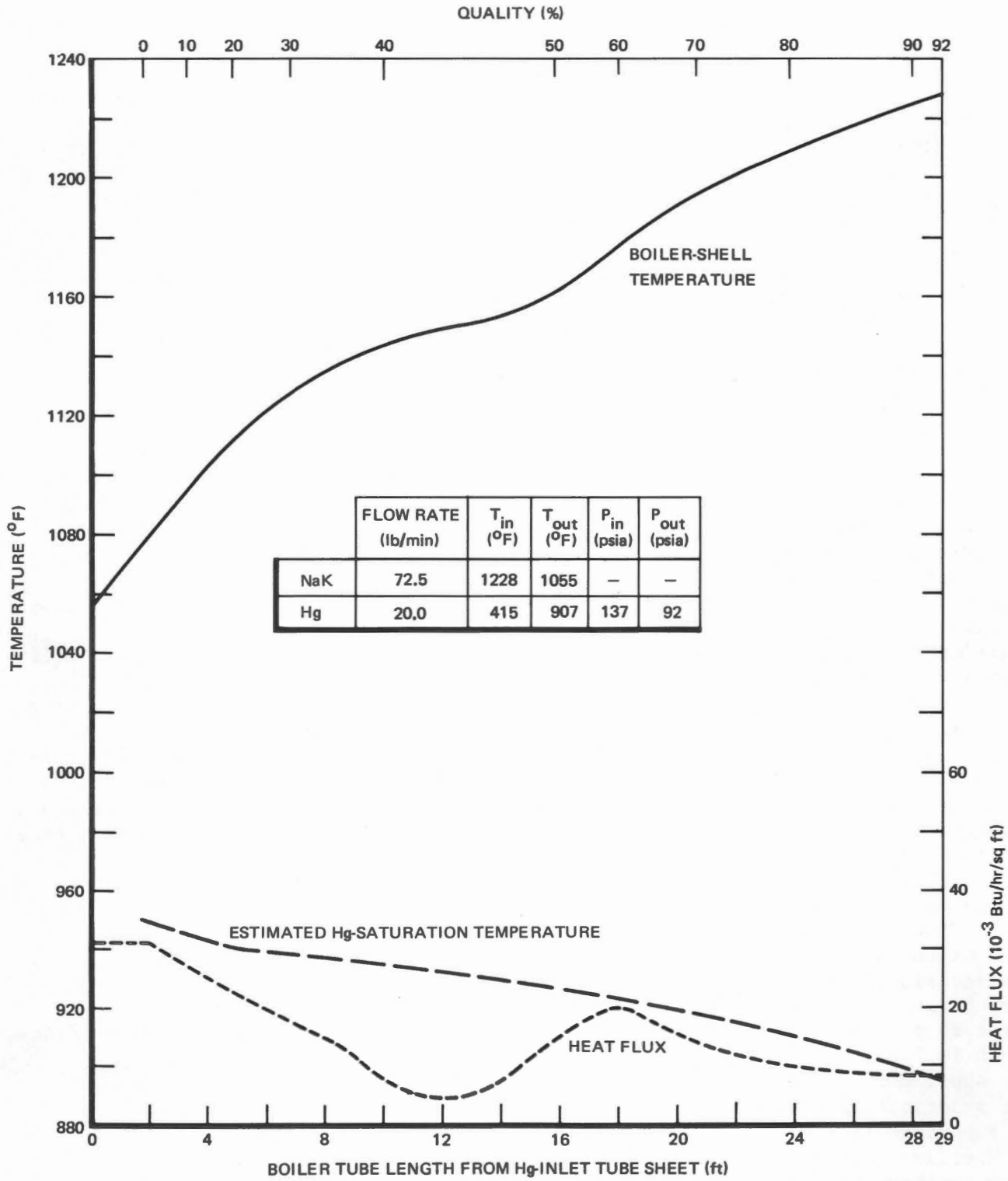

	FLOW RATE (lb/min)	T_{in} (°F)	T_{out} (°F)	P_{in} (psia)	P_{out} (psia)
NaK	72.5	1228	1055	–	–
Hg	20.0	415	907	137	92

Fig. 4.40 - Temperature and heat-flux profiles for the deconditioned model 5C-5 boiler.

minimization of size and weight are extremely important, boiling heat-transfer area and boiler size are very limited. A boiler designed to ensure adequate performance under deconditioned operation suffers severe weight and boiling-heat-transfer-area penalties relative to a design for conditioned operation. Also, a design for deconditioned operation requires that additional mercury inventory be available for the suppressed-boiling section that forms if the boiler conditions (a highly probable event). These considerations indicate that boiler design for deconditioned operation is not practical, and conditioned boiler operation should be ensured through proper process design control.

4-4.4 *Boiler Configuration*

The selection of a configuration for a liquid-metal boiler for a particular application is influenced by several factors including weight, volume, reliability, ease of fabrication, accommodation of thermal expansion, flow stability, and thermal performance. The preceding discussion of study results for NaK-mercury boilers is generally applicable to all once-through boilers.

Several flow schemes can be considered for a liquid-metal boiler design:

1. Counterflow (throughout).
2. Counter-counterflow.
3. Parallel-counterflow.

Each of these flow arrangements has been considered [42] for NaK-to-mercury boilers, and the NaK-mercury temperature profiles for these designs are shown in Fig. 4.41. Parallel flow in the superheat section of the boiler is not practical if a significant degree of superheat is required.

Most designs have used the counterflow arrangement (see Fig. 4.42). The boilers shown in the figure were developed for the SNAP-2 mercury Rankine system. However, higher exit-vapor qualities can be obtained by using the counter-counterflow or parallel-counterflow designs [42].

A comprehensive conceptual boiler-design study [42] was conducted to evaluate how best to meet the boiler requirements for advanced mercury Rankine applications. Its primary objectives were to improve the NaK-to-mercury interface reliability and to decrease the overall boiler size. Figure 4.43 shows some of the boiler concepts considered. Of those studied, concepts b, c, and d were considered the most promising approaches for advanced applications.

4-4.5 *Fluid Flow*

A knowledge of both single-phase and boiling fluid mechanics is important in the design of a liquid-metal boiler. The major factors related to fluid mechanics which must be considered are:

1. Fluid pressure losses and flow regimes.
2. Flow distribution and stability.

(a) *Fluid Pressure Losses and Flow Regimes*

The techniques for computing pressure drops for both single-phase and two-phase (boiling) flow are treated in Vol. II, Chap. 1. The discussion here is limited to an enumeration of the various pressure drops to be considered in boiler design. The overall change in static pressure across the boiler can be subdivided as follows:

1. Heating-fluid pressure losses.
   a. Entrance losses.
   b. Orifice losses (if orifices are used).
   c. Frictional loss through shell.
   d. Exit losses.
2. Boiling-fluid pressure losses.
   a. Inlet-manifold drop.
   b. Tube-entrance losses.
   c. Tube pressure changes including preheater frictional loss, two-

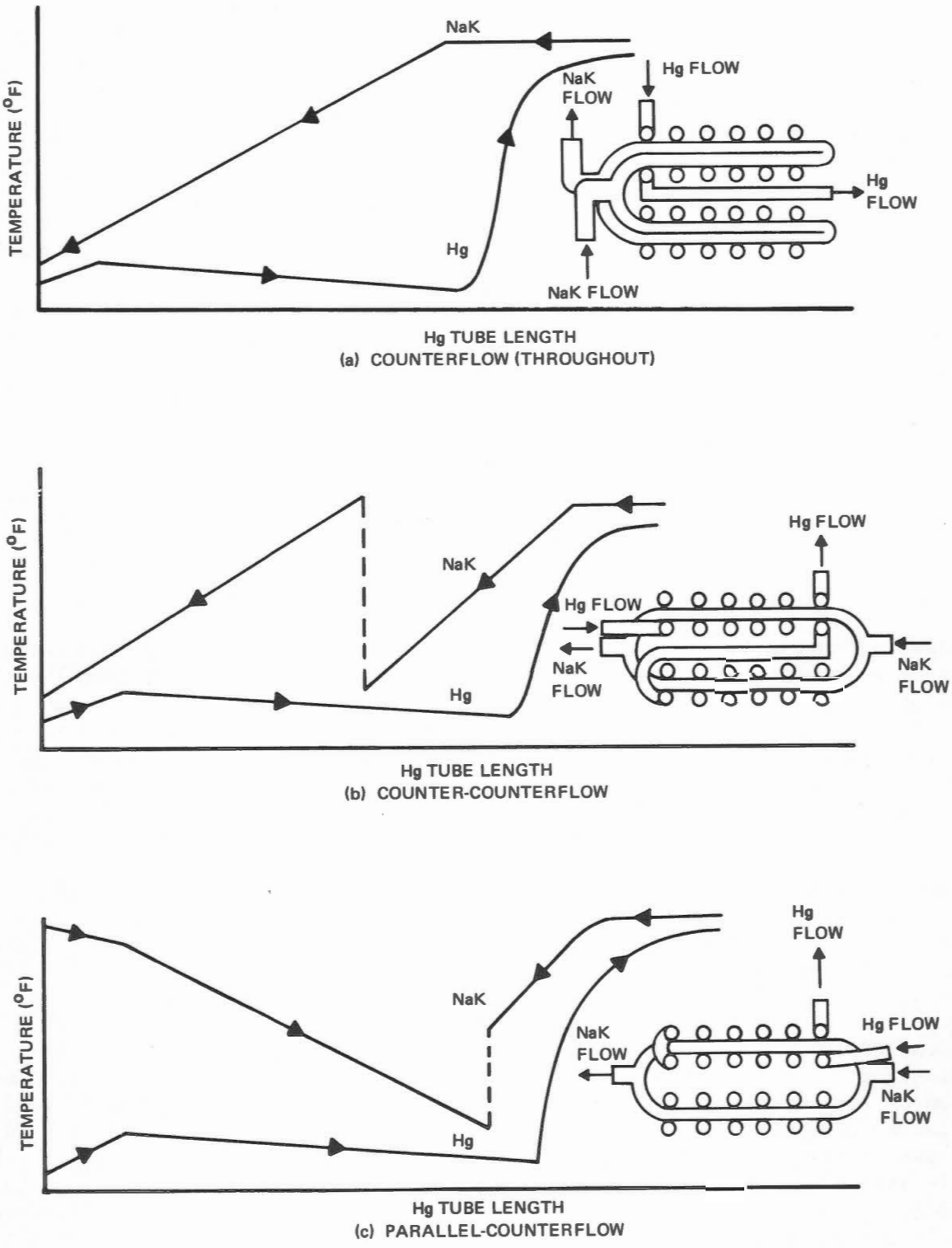

Fig. 4.41 - Boiler temperature profiles and flow designs.

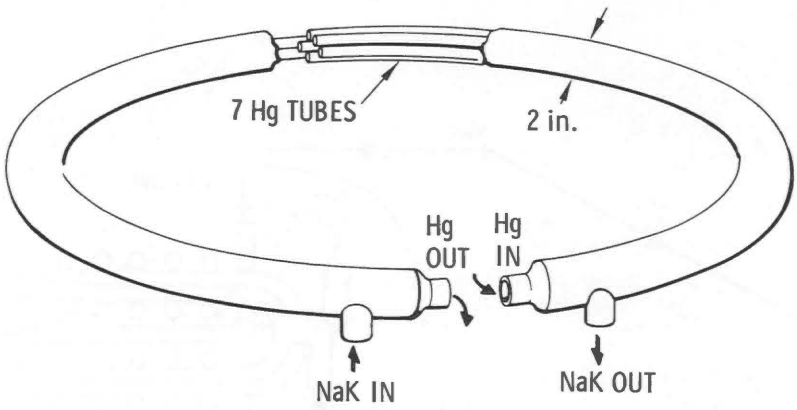

(a) 27-ft HELICAL BOILER

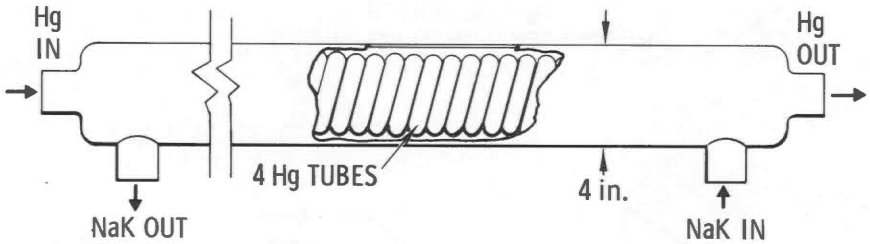

(b) 8-ft STRAIGHT-SHELL BOILER

Fig. 4.42 - Counterflow boiler configurations.

phase (boiling) pressure drop, and pressure drop in superheater region (effects of turbulators and inserts must be considered).

d. Orifice losses.

e. Exit losses.

To accurately compute the pressure drop in a boiler requires a step-by-step procedure with application of local pressure data appropriate to the local flow pattern. Various flow patterns that may be encountered in a liquid-metal boiler are described in Sec. 4-4.3.

(b) *Flow Distribution and Stability*

A primary area of concern is stable operation of a system including two-phase flow in some of the components and, in particular, in the boiler. A system is stable if, when it is distributed from its operating point, it inherently returns to the same point. The stability of the system depends not only on the stability of each of the components but also on the manner in which the components interact. Although two-phase components may be stable by themselves, component interactions can cause the system to become unstable. Stable operation of two-phase components is therefore as much a system problem as it is a component-design problem.

Boiler-stability problems are numerous and complex. Two primary areas are described: The flow patterns that may exist in a boiler tube and the negative-resistance characteristic of a boiler.

The complicated flow patterns that result from forced-convection boiling within a hollow-tube boiler are shown in Fig. 4.44. The boiling fluid flows within a tube and is heated by a second fluid that moves in a surrounding shell. At the beginning of the boiler tube, the fluid is all-liquid and at a temperature below the boiling point (the saturation temperature). The graph in the lower part of the figure illustrates

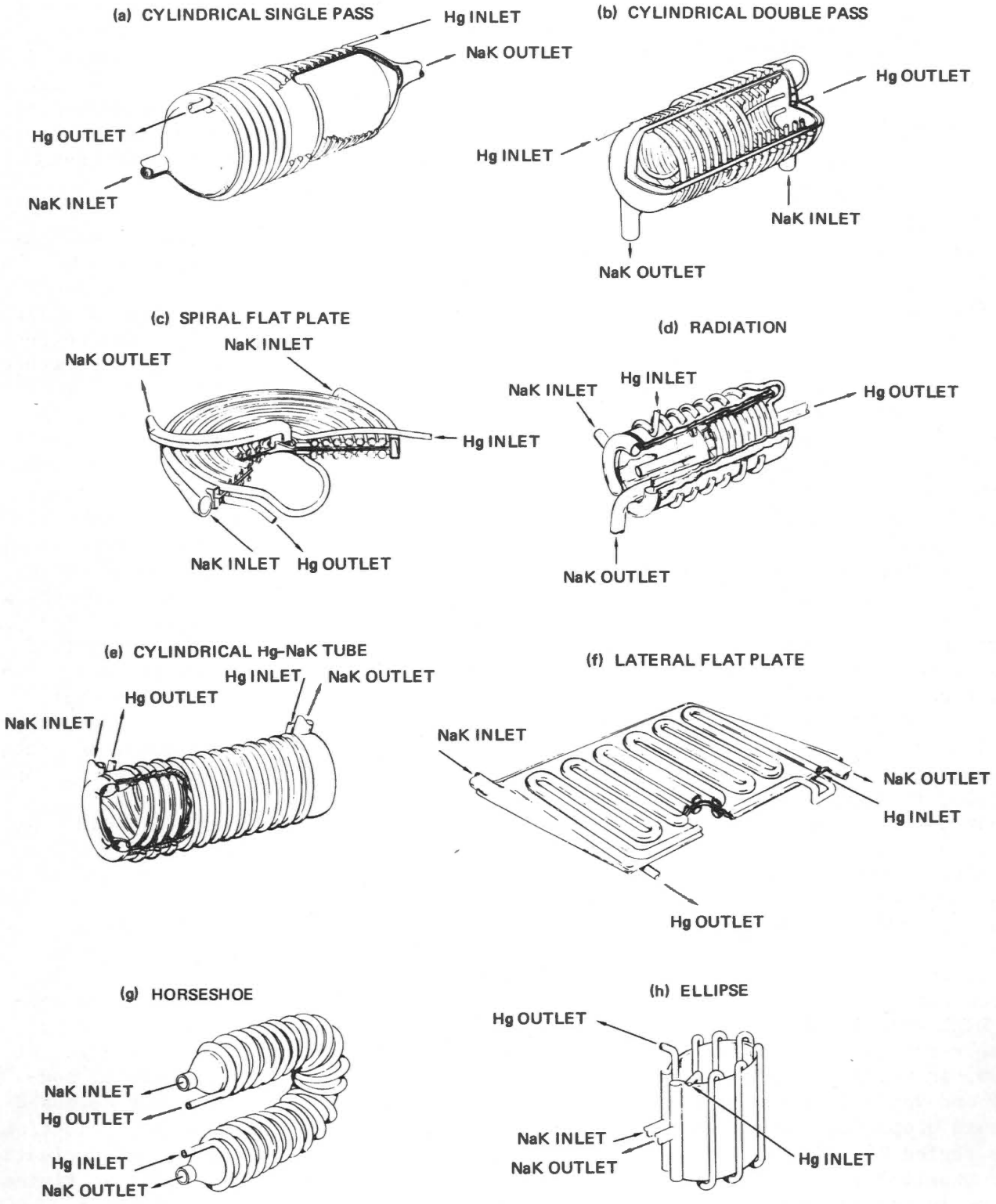

Fig. 4.43 - Advanced boiler concepts.

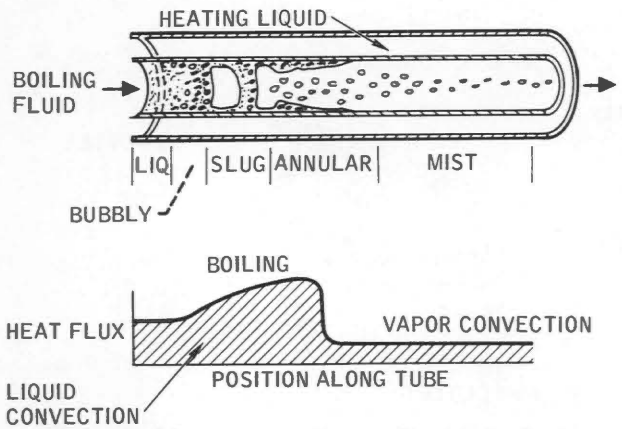

Fig. 4.44 - Two-phase (boiling) flow regimes.

the heat flux into the boiler tube. In the all-liquid region, the heat transfer is generally relatively low since it occurs by ordinary forced convection, although subcooled nucleate boiling can markedly increase the heat flux. As the liquid is heated, the portion near the wall reaches the boiling point. Bubbles are then formed near the wall; the core of the fluid remains liquid. Here the heat transfer begins to increase because of the boiling action. The bubbly-flow regime is reached when the core of the liquid approaches the boiling point and bubbles extend over the entire tube cross section. These bubbles then coalesce, forming large vapor masses. The result is the slug-flow regime, with the flow rapidly alternating between liquid and vapor. Liquid is still flowing along the wall, and the heat transfer is very high. The vapor slugs then merge and annular flow, in which an annulus of liquid flows along the wall and vapor flows at high velocity down the center of the tube,results. The last regime is mist flow, in which the wall is essentially dry and vapor is carrying entrained liquid droplets. Somewhere prior to the region of a dry wall, the heat transfer experiences a transition and very abruptly decreases to a low heat-flux rate. This transition point may fluctuate up and down the tube in a rapid, uncontrolled manner.

A number of inherent boiler-stability problems are tied to these flow regimes. The slug-flow regime is inherently very unstable and causes violent surges in pressure and flow. These surges are believed to be largely responsible for the fluctuations in the heat-transfer transition point occurring further downstream in the tube.

Another instability occurs at the very start of the boiling process. The initiation of boiling in liquid metals is erratic because of a bubble-nucleation problem. Most liquids begin to boil when heated only a few degrees above their normal boiling temperatures, but liquid metals can be heated to several hundred degrees above their normal boiling temperatures and still remain entirely liquid. Then at some point the liquid in the boiler suddenly breaks to form an interface and to flash into vapor. Flash vaporization results in a sudden release of energy that causes violent bumping, geysering, and water hammer in the fluid. The outrush of vapor may send a surge of flow and pressure around the power-conversion loop, thereby forcing cooler liquid back into the boiler tube, refilling the tube with liquid, and setting up another superheating and geysering cycle.

The highly superheated liquid state that can be obtained with alkali metals is caused by conditions unfavorable for bubble formation. Studies have shown that bubbles originate at gas- or vapor-filled cavities or nucleation sites such as pits and scratches in the boiler-tube surface. Under such conditions boiling can be initiated and maintained with only a few degrees of superheat. With alkali metals, however, the systems are highly degassed to help reduce corrosion and oxidation; thus the gas available at the nucleation sites is depleted. Also, these fluids wet the surface exceedingly well, thereby tending to fill many of the larger cavities and render them inactive. These combined effects are the

primary cause of the bubble-nucleation problem with liquid metals.

In addition to these flow-pattern instabilities, a forced-flow boiler has, in general, a negative-resistance characteristic in its operating range. Some data that illustrate this characteristic are shown in Fig. 4.38. Here the pressure drop for a hollow boiler tube is plotted as a function of the weight flow of the fluid. The data shown are for sodium, but similar data are obtained with other fluids. The solid lines show the pressure drops for all-vapor and all-liquid flows, and the broken parallel lines between these limits represent nominal exit-vapor quality values. A negative resistance is characterized by a decrease in pressure drop with increasing flow, i.e., a negative slope of the curve. The slope of the curve can become negative because an increase in total flow results in a decrease in exit quality and hence a decrease in vapor velocity and pressure drop.

On the negative-slope portion of the curve, any flow disturbance tending to increase the flow leads to a reduction in pressure drop, which, in turn, causes a further increase in flow rate. An increased flow rate creates an unstable region of boiler operation that leads in many cases to severe boiler and system instabilities. The magnitude and location of this negative slope are a function of many variables including liquid subcooling, heat input, fluid pressure level, boiler internal configuration, etc. Thus a whole family of such curves can be generated to cover the operating range of a particular boiler tube.

Note that the region of negative slope does not necessarily indicate that the boiler is unstable in this operating range, but it does indicate that, when the boiler is coupled with an unsuitable feed-system resistance, an energy source exists which could become a driving force for a system instability.

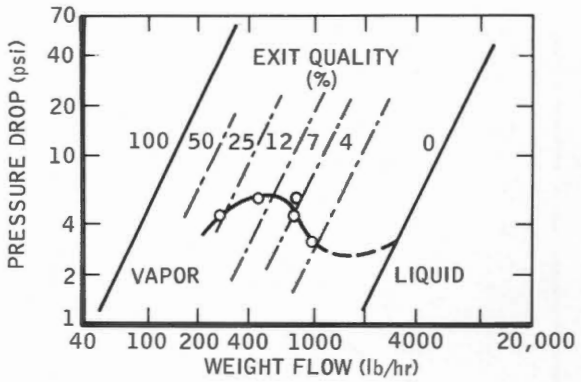

Fig. 4.45 - Boiling pressure drop for sodium.

The negative slope of the boiler operating curve (Fig. 4.45) can be eliminated by adding a high-resistance device at the inlet of each boiler tube. An orifice (Fig. 4.46) whose pressure drop increases with the square of the weight flow has frequently been used for this purpose. The overall boiler pressure drop is then made up of the sum of the boiler-tube and orifice pressure drops. This combined pressure drop of the sodium boiler tube and an orifice is shown in Fig. 4.47 as a function of weight flow. The combined pressure-drop curve obviously has only a positive slope; thus the negative-resistance characteristic of the boiler tube has been eliminated as an instability source. An orifice, being a high-resistance element, also tends to decouple the boiler from disturbances originating upstream in other components. By itself, however, an orifice at the boiler inlet does not solve the slug-flow and the bubble-initiation problems.

Of the various inlet devices presently being used for space boiler applications, the central plug and helical spring shown in Fig. 4.48 merit discussion. In this configuration the plug, by reducing the flow area, increases the liquid velocity and thus enhances the heat transfer, while the spiral-flow path moderates the slug flow by centrifuging the heavier liquid

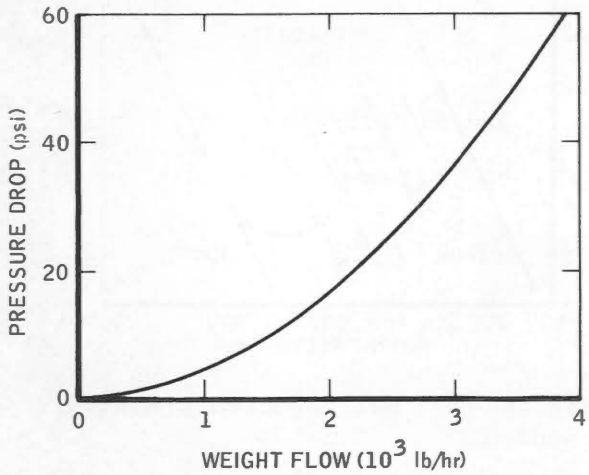

Fig. 4.46 - Orifice pressure drop square-law inlet resistance.

to the wall of the tube. With this device, however, the point of initiation of boiling is uncertain, and, depending on the operating conditions, slug flow may or may not occur. The device alone does not solve the bubble-initiation problem; however, artificial nucleation sites in the form of reentrant cavities could circumvent its shortcoming.

An advanced technique that attempts to solve all the previously discussed instability problems is shown in Fig. 4.49. A schematic drawing of the proposed boiler-tube inserts is shown. The inserts consist of a small center-

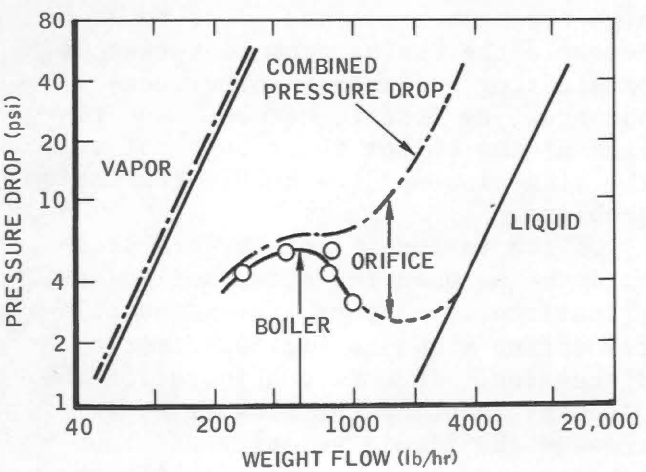

Fig. 4.47 - Boiling pressure drop for sodium showing effect of orifice.

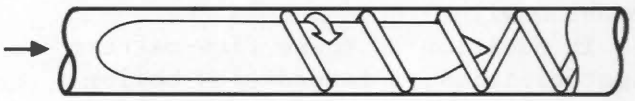

Fig. 4.48 - Center plug and spring boiler-inlet insert.

tube device at the boiler inlet followed by a helical spring. Upstream of the small center tube, the flow is all liquid. The center tube creates a significant pressure drop near the tube outlet where the incoming liquid approaches its saturation or boiling temperature and then provides a spray-type, flashing discharge. The vaporization of a small portion of the flow by flashing provides the vapor required to initiate boiling, and thereby eliminates the bubble-nucleation problem. Furthermore, since the flashing location is fixed by the center-tube outlet, initiation of boiling is fixed and known. Downstream of the spray, an annular flow pattern is quickly established, the liquid spiraling along the tube wall and the vapor flowing down the center of the tube. The liquid-vapor interface is wavy but apparently unbroken.

A center-tube insert should entirely eliminate the bubbly- and slug-flow regimes, decouple the upstream feed components, provide positive resistance, and forcibly initiate boiling at a fixed location with a prescribed flow regime. Cavitation damage to the inlet-restriction can, however, decrease the operating life of the boiler.

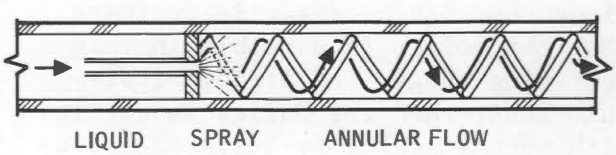

Fig. 4.49 - Center tube and spring boiler-tube-inlet insert.

REFERENCES

1. G.M. Grover, T.P. Cotter, and G.F. Erickson, Structures of Very High Thermal Conductance, *J. Appl. Phys.*, *35*(6): 1990-1991 (1964).

2. R.P. Krebs, H.C. Haller, and B.M. Auer, *Analysis and Design Procedures for a Flat, Direct-Condensing, Central Finned-Tube Radiator*, Report NASA-TN-D-2474, National Aeronautics and Space Administration, 1964.

3. H.C. Haller, *Analysis of a Double Fin-Tube Flat Condenser Radiator and Comparison with a Central Fin-Tube Radiator*, Report NASA-TN-D-2558, National Aeronautics and Space Administration, 1964.

4. H.C. Haller, S. Lieblein, and B.G. Lindow, *Analysis and Evaluation of a Vapor-Chamber Fin-Tube Radiator for High-Power Rankine Cycle*, Report NASA-TN-D-2836, National Aeronautics and Space Administration, 1965.

5. National Aeronautics and Space Administration, *User's Manual for Use with TRW Space Radiator-Condenser Design and Performance Analysis Computer Program*, Report NASA-CR-65362, April 1966.

6. S. Lieblein, *Analysis of Temperature Distribution and Radiant Heat Transfer Along a Rectangular Fin of Constant Thickness*, Report NASA-TN-D-196, National Aeronautics and Space Administration, 1959.

7. H.C. Haller, *Comparison of Heat-Rejection and Weight Characteristics of Several Radiator Fin-Tube Configurations*, Report NASA-TN-D-2385, National Aeronautics and Space Administration, 1964.

8. A.V. Saule, R.P. Krebs, and B.M. Aver, *Design Analysis and General Characteristics of Flat-Plate Central-Fin-Tube Sensible-Heat Space Radiators*, Report NASA-TN-D-2839, National Aeronautics and Space Administration, 1965.

9. R.A. Stone (Ed.), *Radiators for SNAP-50/SPUR*, Report AFAPL-TR-64-143, Garrett Corp., March 1965.

10. V.H. Heiskala, R.C. Smith, E.A. Elliot, and R.T. Lancet, Mercury Rankine (SNAP-2) Radiator Condenser Development Experience, in *AIAA Specialists Conference on Rankine Space Power Systems, NASA Lewis Research Center, Cleveland, Ohio, Oct. 26-28, 1965, Volume I*, USAEC Report CONF-651026, pp. 582-640, American Institute of Aeronautics and Astronautics.

11. M. Coombs and R. Stone, Space Heat Rejection, in *Space Power Systems Conference*, November 1963.

12. A. Koestel et al., *Space Radiator Study*, Report ASD-TDR-61-697, TRW, Inc., October 1963.

13. R.T. Lancet et al., Fluid Mechanics of Condensing Mercury in Low Gravity Environment, in *Proceedings of a Symposium on Fluid Mechanics and Heat Transfer Under Low Gravity, June 24-25, 1965, Palo Alto, Calif.*, USAF Office of Scientific Research and Lockheed Aircraft Corp.

14. N. Zuber and M. Tribus, *Further Remarks on the Stability of Boiling Heat Transfer*, USAEC Report AECU-3631, University of California, Department of Engineering, January 1958.

15. Thompson Ramo Wooldridge, Inc., *SNAP-II Power Conversion. Topical Report No. 13. Offbase Testing*, Report TRW-ER-4670.

16. R.J. Kiraly and A. Koestel, *SNAP-II Power Conversion System. Topical Report No. 8, Mercury Condensing Research Studies*, USAEC Report NAA-SR-6301, Atomics International,

May 31, 1961.

17. R. Bellman and R.H. Pennington, Effects of Surface Tension and Viscosity on Taylor Instability, *Quar. Appl. Math., 12*: 181 (1954).

18. R.C. Smith, J.R. Crosby, E.A. Elliot, and R.D. Galletly, *Radiator Condenser Design Manual*, USAEC Report NAA-SR-Memo-12139, Atomics International, Nov. 1, 1966.

19. S. Lieblein and J.H. Diedrich, Material and Geometry Aspects of Space Radiators, *Nucl. Appl., 3*(2): 82-93, (1967).

20. N. Clough and J. Diedrich, *Results of Hypervelocity Impact into Radiator Materials*, Report NASA-TM-X-52142, National Aeronautics and Space Administration, 1965.

21. J.H. Diedrich and S. Lieblein, Materials Problems Associated with the Design of Radiators for Space Power Plants, in Power Systems for Space Flight, *Progr. Astronaut. Aeronaut., 11*: 627-653 (1963).

22. R.E. English and D.C. Guentert, Segmenting of Radiators for Meteoroid Protection, *Amer. Rocket Soc. J., 31*: 1162-1164 (1961).

23. R. Denington, A. Koestel, A.V. Saule, L.I. Shure, G.T. Stevens, and R.B. Taylor, *Space Radiator Study*, Report ASD-TR-61-697, TRW, Inc., Apr. 30, 1962.

24. R. Platt, *Investigation of a Jet Condenser for Space Power*, Report NASA-TN-D-3045, National Aeronautics and Space Administration, October 1965.

25. L. Hays, Liquid-Metal Jet Condensers, in *Proceedings of 1963 High-Temperature Liquid-Metal Heat-Transfer Technology Meeting, Oak Ridge, Tenn., Sept. 4-6, 1963*, USAEC Report ORNL-3605 (Vol. 2), pp. 153-197, Oak Ridge National Laboratory, December 1964.

26. Aerojet-General Corp., *The Mixing of Vapor and Liquid Jets*, Report No. 1344, October 1957.

27. L. Hays, *Condenser Space Heat Rejection Systems*, EOS Report No. 500, ABMA CONT DA-04-495-506-ORD-2007, December 1960.

28. H.L. Hess, H.R. Kunz, and S.S. Wyde, *Analytical Study of Liquid-Metal Condensers, Volume I. Design Study*, Report PWA-2320 (Vol. 1), Pratt and Whitney Aircraft, July 15, 1964.

29. B. Misra and C. F. Bonilla, *Heat Transfer in the Condensation of Metal Vapors: Mercury and Sodium Up to Atmospheric Pressure*, Chemical Engineering Progress Symposium Series 52, No. 18, pp. 7-21, 1956.

30. General Electric Company, *Alkali Metals Boiling and Condensing Investigations*, Quarterly Report 1, 1962.

31. National Aeronautics and Space Administration, *Government-Industry Conference on Mercury Condensing, Pasadena, Calif., Apr. 18, 1961*, Report NASA-TN-D-1188, pp. 2-45, February 1962.

32. S.S. Wyde and H.R. Kunz, *Experimental Condensing-Flow Stability Studies*, Report PWA-2315, Pratt and Whitney Aircraft, Apr. 15, 1964.

33. A.H. Kreeger and J.N. Hodgson, Design and Development of the SNAP-8 Multitube Condenser, in *AIAA Specialists Conference on Rankine Space Power Systems, NASA Lewis Research Center, Cleveland, Ohio, Oct. 26-28, 1965*, Volume I, USAEC Report CONF-651026, pp. 641-668, American Institute of Aeronautics and Astronautics.

34. P.J. Berenson, *Forced-Convection Vaporization of Potassium in a*

Single Tube, USAEC Report TID-21331, Garrett Corp., November 1964.

35. W.H. Rohsenow and H.Y. Choi, *Heat Mass and Momentum Transfer*, Prentice-Hall, Inc., Englewood Cliffs, N.J., 1961.

36. P.J. Berenson and R.A. Stone, *A Photographic Study of the Mechanism of Forced Convection Vaporization*, Preprint No. 21, from 51st National Meeting, Heat Transfer and Space Technology, San Juan, P.R., Sept. 9, 1963, American Institute of Chemical Engineers, New York, 1963.

37. R.G. Gido and A. Koestel, *The SNAP-II Power Conversion System. Topical Report No. 17. Mercury Boiling Research*, USAEC Report NAA-SR-6309, Atomics International, October 1962.

38. E.G. Baumeister, *Mercury Rankine Program Boiler Development Summary*, USAEC Report NAA-SR-12233, Atomics International, Jan. 15, 1967.

39. A. Koestel, *Mercury Rankine Program (SNAP II) Boiler Conditioning: Phase I Results*, USAEC Report NAA-SR-6322, Atomics International, June 23, 1966.

40. K. Goldmann, H. Firstenberg, and C. Lombardi, Burnout in Turbulent Flow - A Droplet Diffusion Model, *Trans. ASME (Amer. Soc. Mech. Eng.), Ser. C, J. Heat Transfer* (1961).

41. A. Koestel and T.T. Shimazaki, *Mercury Rankine Program Deconditioning Problem and Planned Investigation*, Report NAA-SR-10860, Atomics International, June 1965.

42. R.F. Block et al., *A Study of Conceptual Mercury Boiler Designs for Advanced Multiple-System Applications*, Report NAA-SR-TDR-11769, Atomics International, February 1966.

Chapter 5

Applications

Principal Author: K. A. BONYHADY

Contributing Authors: B. P. BROOKS and J. M. HOWARD

5-1 INTRODUCTION

Liquid metals are used over a wide range of applications in modern industry and science because of their unique properties of

1. High heat capacity.
2. High thermal conductivity in a wide temperature range.
3. Relatively low melting point.
4. High boiling temperature and low vapor pressures at high temperatures.
5. Relatively low density.
6. Relatively low electrical resistivity.
7. Abundant availability in nature.
8. Relatively inexpensive process for mass production.
9. Rapid reactions with water.
10. Strong absorption of oxygen.

Preceding chapters described applications of sodium and NaK alloy primarily as heat-transport media. This chapter is concerned mainly with applications other than heat transport, although some duplication in this field may occur to present a more complete discussion. The general areas of discussion presented here are:

1. Temperature equalization.
2. Heat pipes.
3. Bearing lubricants.
4. Gas generation.
5. Controls.
6. Electrical applications.
7. Magnetohydrodynamics (MHD).
8. Optical applications.
9. Chemical applications.
10. Scientific applications.

5-2 APPLICATIONS FOR TEMPERATURE EQUALIZATION

This section discusses the use of alkali metals for temperature equalization in metal components. Figure 5.1 gives the melting and boiling points of the liquid metals for comparison of their applicability [1]. Typical applications are as follows:

1. Exhaust valves of large (200 hp and above) internal-combustion engines can be filled with NaK (60% of their

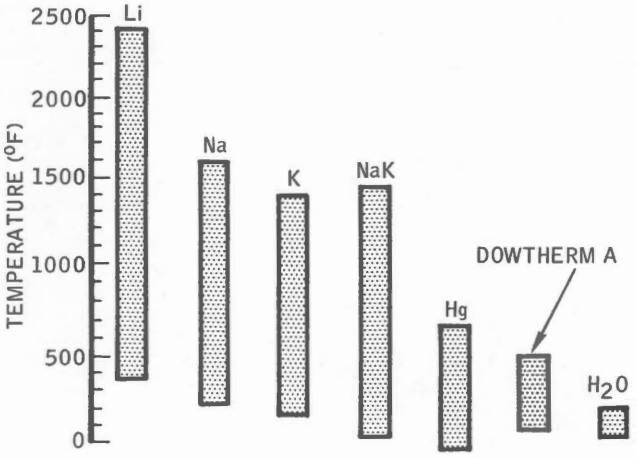

Fig. 5.1 - Liquid range of selected fluids [1].

void volume) to reduce the valve-seat temperatures as shown in Fig. 5.2. The valve material is an alloy of 14 Cr, 14 Ni, 0.55 Si, 0.5 Mo, 0.45 C and 2.5 W. During operation the splashing NaK transfers heat from the valve head to the stem and to other connected metal parts [1,2].

2. The cooling water in die-casting plants can be replaced with NaK. This was proposed during World War II based on the experience with exhaust valves. The Doehler-Jarvis Division, National Lead Co., in their Toledo, Ohio, plant, filled the magnesium cast cores with sodium in the vertical position and then turned them to the horizontal position. This cooling technique made the cast parts more uniform, prolonged the core life, and increased production. Since this World War II experience, many die-casting machines use liquid-metal-cooled casting heads and can operate faster [2].

Similarly, sodium or NaK cooling increases the productivity of glass-bottle casting machines due to improved temperature control.

3. Because they are easily close temperature controlled, the alkali metals can be used as heat-treating media. More-uniform products reduce both rejects and production costs [2]. Figures 5.3 and 5.4 depict basic heat-

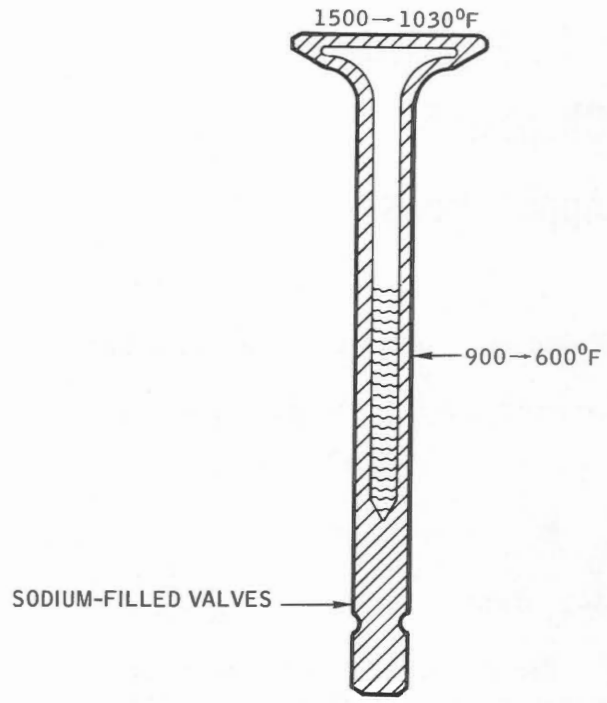

Fig. 5.2 - Cross section of automotive valve with 60% NaK filling.

treatment methods.

5-3 HEAT-PIPE APPLICATIONS

It is a well-known phenomenon that heat applied to a fluid near its boiling point evaporates the fluid. This process absorbs a large quantity of heat at almost no temperature change and at a very small pressure increment. If we use the arrangement shown in Fig. 5.5, the slight pressure increment in the evaporation section is enough to drive the vapor down to the condensation section through the vapor channel, which has a very low resistance at laminar flow conditions. Mechanical pumping is one method used to return the condensate to the evaporative section. Since laminar flow needs very little pumping power at this normally short distance, the capillary effect can produce sufficient power to accomplish this fluid transport, even against the small pressure head differences. This eliminates any moving

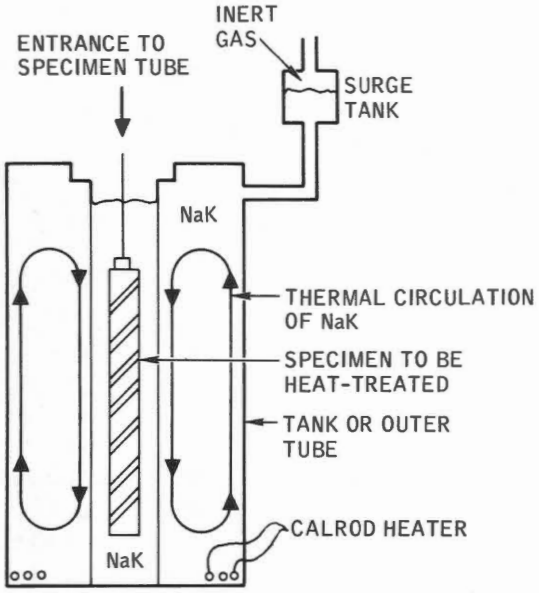

Fig. 5.3 - Heat-treating furnace.

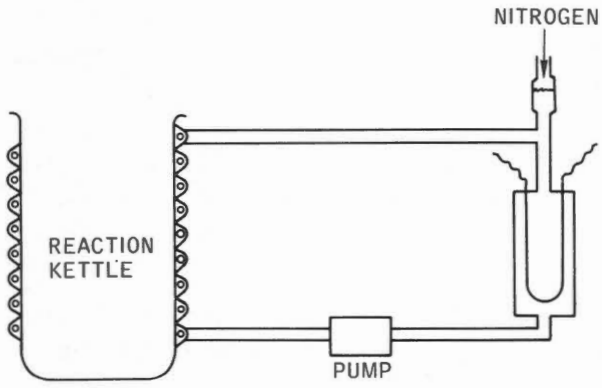

Fig. 5.4 - Electrically heated high-temperature reaction kettle.

mechanical component from the system and makes it operable and particularly attractive in zero-gravity-field applications. If we apply these principles to an actual loop, we have the so-called heat pipe, first proposed by Grover [3] in 1963.

Compared with conventional heat exchangers, the heat pipe has several advantages: (1) heat transfer at minimum temperature difference, (2) minimum

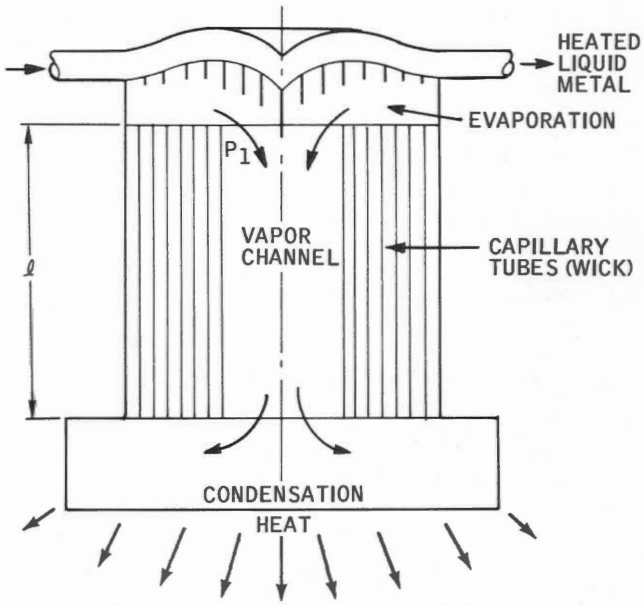

Fig. 5.5 - Operational schematic of a heat pipe.

weight of the heat exchanger, (3) no moving parts necessary for operation of the loop, and (4) large heat transfer at high efficiency.

However, there are three problems to solve: (1) to establish actual design criteria and data, (2) to find the best-fit heat-transfer media, and (3) to find the compatible materials to realize the design conditions.

5-3.1 *Heat-Pipe Design Criteria* [4]

Heat applied to a fluid at its boiling point changes the media from liquid to vapor phase; i.e., it changes the cohesive forces between the fluid molecules. Kelvin's equation expresses this phenomenon mathematically:

$$p_{gas} - p_{liq} = m\gamma \qquad (5.1)$$

where p_{gas} = vapor pressure
p_{liq} = liquid pressure
m = surface curvature
γ = surface tension

The value of γ can be interpreted as the energy necessary to increase the surface area of the unit fluid surface.

Capillary action is effective in fluid transport if the fluid wets the capillary tube material, in which case $m > 0$.

The highest value of m can be achieved if $m_{max} = 4/d$ where d is the hydraulic diameter of the capillary tube. Since both vapor and liquid are in thermal balance,

$$\ln \frac{p_{gas}}{p_0} = - \frac{\rho_{gas}}{\rho_{liq}} \frac{m\gamma}{p_0} \tag{5.2}$$

where p_0 is vapor pressure on the liquid surface, ρ_{gas} is vapor density, and ρ_{liq} is liquid density (the concave fluid surface reduces the surface pressure). If $p_1 = m_1\gamma$, the pressure at the vapor stage, and $p_2 = m_2\gamma$, the pressure at the liquid stage, then the pressure difference

$$p_1 - p_2 = \frac{32\nu_{gas}}{F_{gas}d_{gas}^2} Wl \tag{5.3}$$

where F_{gas} is the cross section of vapor flow area, W is mass flow, ν is kinematic viscosity, and

$$p_2 - m_2\gamma - (p_1 - m_1\gamma) = \frac{32\nu_{liq}}{F_{liq}d_{liq}^2} Wl \tag{5.4}$$

where F_{liq} is the cross section of liquid flow area. If we assume linear function,

$$p_1 - p_2 = p_0(T_1) - p_0(T_2) - \frac{\rho_{gas}}{\rho_{liq}}(m_1 - m_2)\gamma = \Delta p_0 - \frac{\rho_{gas}}{\rho_{liq}}(m_1 - m_2)\gamma \tag{5.5}$$

The heat load in unit time can be expressed as $Q = hW$, where h is the heat of evaporation. If we substitute the Clausius-Clapeyron equation,

$$\Delta p_0 = \frac{h\rho_{gas}}{T}\Delta T \tag{5.6}$$

and rearrange, the heat load is

$$Q = \frac{h^2\rho_{gas}}{32T\left(\frac{\nu_{gas}}{F_{gas}d_{gas}^2} + \frac{\rho_{gas}}{\rho_{liq}}\frac{\nu_{liq}}{F_{liq}d_{liq}^2}\right)} \frac{\Delta T}{l} \tag{5.7}$$

If we replace

$$\frac{\nu_{liq}}{\nu_{gas}} \frac{F_{gas}d_{gas}^2}{F_{liq}d_{liq}^2} = \alpha$$

then

$$\Delta p = \frac{m_1 - m_2}{1 + \alpha}\gamma \tag{5.8}$$

If the capillary column base is always covered with liquid, $m_2 = 0$, and the required maximum value of m_1 is calculable from the hydraulic and capillary data.

If the pressure drop in the vapor channel is $4\gamma/[(1 + \alpha)d_{liq}]$,

$$\Delta T = \frac{4T\gamma}{d_{liq}h\rho_{gas}}\left(\frac{1}{1 + \alpha} + \frac{\rho_{gas}}{\rho_{liq}}\right) \tag{5.9}$$

and the maximum heat flow is determined by

$$Q = \frac{h\gamma}{8ld_{liq}\left(\frac{\nu_{gas}}{F_{gas}d_{gas}^2} + \frac{\nu_{liq}}{F_{liq}d_{liq}^2}\right)} \tag{5.10}$$

where l is the length of the capillary duct section (see Fig. 5.5). For example, assume that $T = 900°K$, $F_{gas} = d_{gas}^2\,\pi/4$, and $d_{gas} = 2$ cm and that the fluid is sodium, the evaporation heat, h, is 4.331×10^6 watt sec/kg; the surface tension, γ, is 0.1395 watt sec/m^2; the dynamic viscosity of the fluid, ν_{liq}, is 2.025×10^{-4} kg/m sec; the fluid density, ρ_{liq}, is 0.794×10^3 kg/m^3; the kinematic viscosity of the saturated vapor, ν_{gas}, is 1.973×10^{-5} kg/m sec; and its density, ρ_{gas}, is 1.55×10^{-2} kg/m^3; then the optimal geometry is achieved if $\alpha = 1$ and

$$d_{liq} = d_{gas}^2 \frac{F_{gas}}{F_{liq}} \frac{\nu_{liq}}{\nu_{gas}} \tag{5.11}$$

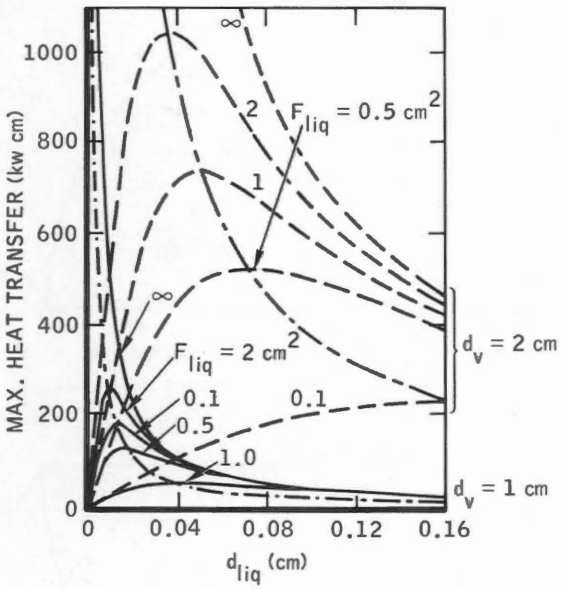

Fig. 5.6 - Maximum heat transfer vs. hydraulic diameter of a capillary.

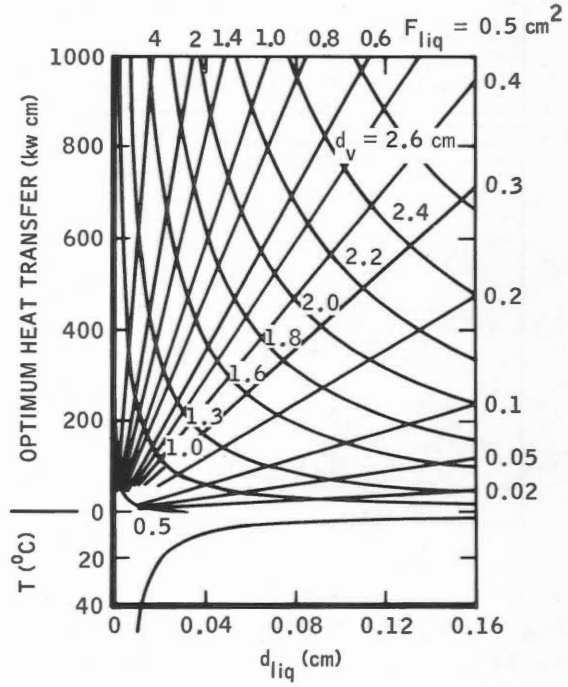

Fig. 5.7 - Diagram for determining optimum geometrical dimensions of a heat pipe at 900°K sodium.

If Δp in the vapor channel is only half of the available osmosis pressure, the maximum achievable heat load is

$$(Q\ell)_{max} = \frac{h\gamma F_{gas} d_{gas}^2}{16\nu_{gas} d_{liq}} \qquad (5.12)$$

and the necessary temperature difference is

$$\Delta T = \frac{2T\gamma}{h\rho_{gas} d_{liq}} \qquad (5.13)$$

The maximum heat-flow value is valid if the flow is laminar, i.e., $(Q)_{opt}(d_{gas}/F_{gas}) < \nu_{gas}\rho_{gas}h$ Re critical, which leads to the value

$$\frac{(Q)_{opt}}{d_{gas}} < 1.54 \text{ kw/cm}$$

for these data.

Figures 5.6 and 5.7 give some design support, showing the maximum heat-transfer values and heat-pipe geometrical dimensions as a function of the hydraulic diameters of the capillary tubes at 900°K sodium temperature.

References 3 and 4 report on actual tests. A 1.9-cm-OD 1.6-cm-ID 30-cm-long 347-stainless-steel tube contained a wick made of 5-layer 100-mesh 0.13-mm-diameter 304-stainless-steel screen. The filling was 15 g of solid sodium. After evacuation, outgassing, filling, and seal welding, this heat pipe was tested with another heat pipe 90 cm long and filled with 40 g of sodium. A 1-kw electrical heat input operated the tube. Results are shown in Fig. 5.8. Chromel-Alumel thermocouples measured the temperatures along the tube. In the evaporation zone the temperatures were constant but decreased suddenly at the cool end of the tube. This decrease was more rapid than that calculated. This heat pipe was built for a thermionic electrical energy converter for space applications where the heat-rejection end will serve as a space radiator. Maximum heat-transport capacity was measured as 30 watts/cm^2. Additional heat-pipe design information is given by Cotter [5] and Kemme [6].

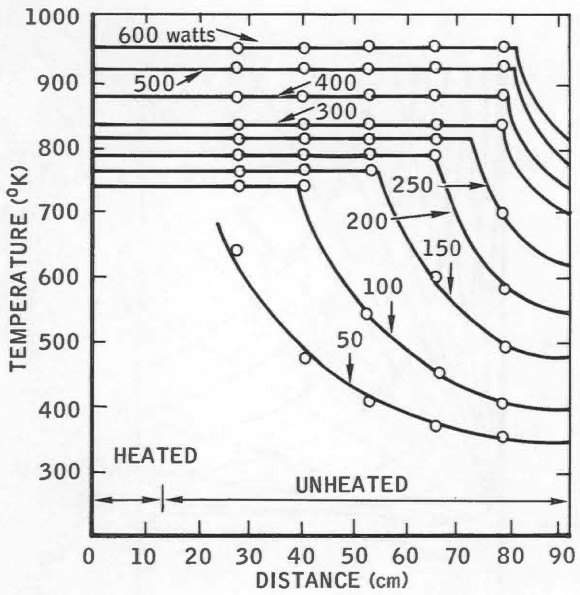

Fig. 5.8 - Heat-pipe-wall temperatures along the tubes at varying heat inputs.

5-3.2 *Heat-Pipe Construction and Experiments*

The most critical part of a heat pipe is the capillary. The operation of a capillary built as axial grooves on the inside of the cylindrical heat-pipe wall is predictable [7]. Less expensive wicks can be built from one to three layers of wire mesh (10 to 100/sq in.) tightly installed against the inside pipe wall, but their performance is hardly predictable unless preliminary tests conforming accurately to the geometry of the layers are conducted [5,8,9]. For the present a combination of these two capillaries produces the highest heat and weight efficiencies [6]. Many other types of capillaries have been tried (e.g., porous materials with fair heat conductivity, sintered metal powders, and even felts), but all exhibited undesirable features of one kind or another, e.g., low temperature limits and high manufacturing costs. In addition, performances could not be predicted with acceptable design accuracy [10].

A prerequisite of any wick is that it provide good heat conductivity to the outside pipe wall but poor heat conductivity to the vapor channel [11].

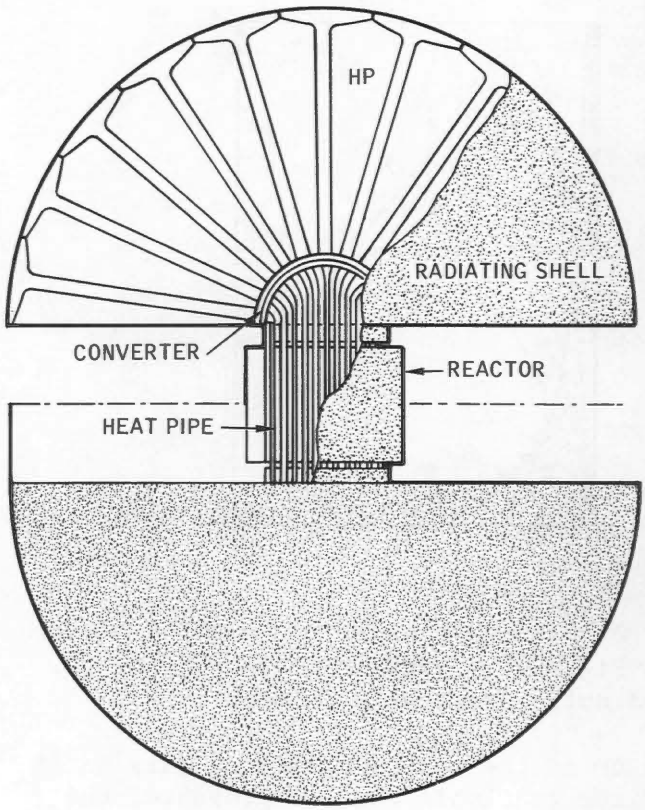

Fig. 5.9 - Fast cylindrical reactor cooled by heat pipes for out-core thermionic converters.

A description of a heat-pipe system (Fig. 5.9) for thermionic spacecraft reactors is given in Refs. 12 and 13. Sodium heat pipes conduct the reactor heat to the thermionic converters and then further to the radiator surfaces.

Sodium was successfully used for heat pipes in a temperature range of 500 to 1900°C (Ref. 14). Nickel pipe was usable between 500 and 900°C, and 347-stainless-steel pipe was usable, between 400 and 800°C, but tungsten pipe showed the lowest mass transfer at temperatures up to 1900°C. Entrapped gas released from the tungsten pipe considerably reduced the effectiveness of the heat pipe when a gas pocket developed in the condenser section after 420 hr of operation at the maximum temperature. Therefore the heat pipe above the maximum operating temperature must be

completely outgassed before the pipe is filled with fluid [14].

It is very important for start-up and for proper operation that the whole wick be completely wetted with the liquid at the highest expected heat load. A small excess of the liquid has an insignificant deteriorating effect on the heat transfer [10].

Besides material compatibility, the necessary start-up, wick-configuration, wick-installation, and pipe-length effects were compared with calculated design values in a test loop. Only in the low-temperature range was there considerable deviation from the previously reported good agreement between theory and test data. This condition resulted from a momentum interaction between vapor and returning liquid [6,15]. A good summary of the status of present heat-pipe developments is given in Ref. 10.

5-4 BEARING-LUBRICANT APPLICATIONS

In closed-cycle power-generating systems for space applications, liquid metals are used as working fluids and as heat-transfer media. Because of high-operating-temperature requirements and limitations as to weight and size of the components, these working fluids find additional application as bearing lubricants for rotating devices. Bearing temperatures of the order of 400 to 1500°F are anticipated [16]. These temperatures, plus the effects of high vacuum in space, prevent the use of conventional lubricants.

Although some properties of the liquid metals limit their use as lubricants, successful applications have been made by giving proper consideration to the limitations. The action of liquid metals in reducing most of the metal oxides, their low viscosity, and the tendency toward self-welding of containing parts in the presence of the liquid metal are properties limiting their use as lubricants.

Rolling-element bearings, self-pressurizing hydrodynamic bearings, and externally pressurized hydrostatic bearings are the major liquid-metal bearing applications evaluated to date [16]. Of these, the rolling-element bearings appear to be the least promising [17]. The hydrostatic-type bearing showed good results in specific applications [18].

5-5 APPLICATION FOR GAS GENERATION

A unique application of sodium in connection with hydraulics is a gas-generating system based on a properly controlled sodium-water reaction. It is proposed that the buoyancy of the hydrogen gas produced by this reaction could be used to recover objects (such as wrecked ships) submerged in deep waters. No divers are required if the steel containers within which the reaction takes place at salvage depth are provided with remotely controlled underwater Thermit welding units [19].

The following facts support this proposal: (1) generation of hydrogen from water and sodium is more economical under the circumstances considered here than any other mothod; (2) solubility of hydrogen in water is low; (3) NaOH, a byproduct of the reaction, is soluble in water; and (4) hydrogen closely follows the perfect gas law and provides maximum buoyant force.

According to the chemical reaction

$$2Na + 2H_2O \rightarrow 2NaOH + H_2 \qquad (5.14)$$

23 lb of sodium generates 1 lb of hydrogen gas, and the net heat absorbed is
469 kilojoules/gram mole NaOH -
286 kilojoules/gram mole H_2O =
183 kilojoules/gram mole heat, which is equivalent to

$$\frac{183 \times 0.948 \times 454}{23} = 3440 \text{ Btu/lb Na} \qquad (5.15)$$

Each of these values is valid at standard environmental conditions, and, using the perfect gas law, we can use the following three equations to cover

any other phase:

$$\text{Weight of gas} = \frac{pvm}{RT} \qquad (5.16)$$

$$\frac{T_1}{T_2} = \left(\frac{P_1}{P_2}\right)^{(k-1)/k} \qquad (5.17)$$

$$\frac{P_1 V_1}{T_1} = \frac{P_2 V_2}{T_2} \qquad (5.18)$$

where p = pressure (psia)
v = volume (cu ft)
m = molecular weight
T = absolute temperature
k = ratio of specific heat
R = gas constant = 10.72 for these units

A system should be provided to control the speed of ascent and to maintain the proper gas pressure in accordance with the hydrostatic depths and the structural strength of the containers. Preliminary heat-transfer calculations indicate a hydrogen temperature of approximately -100°F at the time of surfacing from a depth of 8500 ft. This temperature should cause significant icing.

The solubility of hydrogen gas with water is estimated by using Henry's law, $N = P/H$ (N is mole fraction of gas in solution; P is partial pressure of the gas in question, mm Hg; and H = Henry's constant, 45.5×10^6 for these units). At a pressure of 250 atm, nominally 0.42% of the gas would be absorbed by water.

Based on Eqs. 5.16 to 5.18 and on the selection of proper tank, attachment grid, and controls, equipment weighing 5400 lb would produce an 18.75-ton buoyant force. Figure 5.10 shows the buoyant force of the hydrogen generated from 1 lb of sodium as a function of seawater depth.

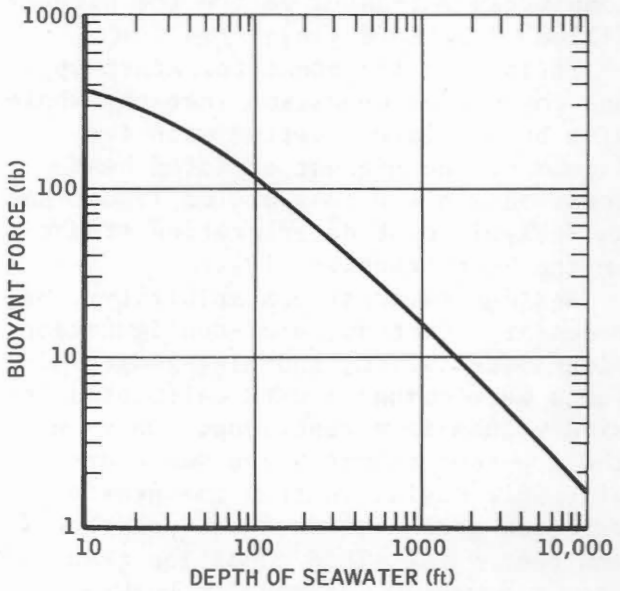

Fig. 5.10 - Net buoyant force provided by the hydrogen gas produced from reaction of 1.0 lb of sodium vs. depth of seawater (gas cooled to 40°F).

5-6 CONTROLS APPLICATIONS

At velocities below Mach 1 most aircraft utilize hydraulically actuated control systems using oils and oil-base silicon mixtures as the actuating medium. To achieve sustained flight at velocities in excess of Mach 1 the control systems may be subjected to temperatures beyond the capabilities of the conventional oils, and significant changes in system components and actuating media become necessary. At the higher Mach-number velocities associated with advanced aircraft, these changes become increasingly sophisticated.

Such hydraulic controls require (1) ability to operate at temperatures as high as 800 to 1000°F, since many parts of the airplane-control surfaces may reach these temperatures; (2) high pressures to 3000 psig or over to produce the large controlling forces at a minimum possible weight; (3) low viscosity, which may reduce the pipe sizes and pump dimensions; (4) good thermal conductivity for small cooling heat exchangers; (5) low electrical resistivity that allows the use of electromagnetic pumps having high reliability and no moving parts; (6) long-term operation

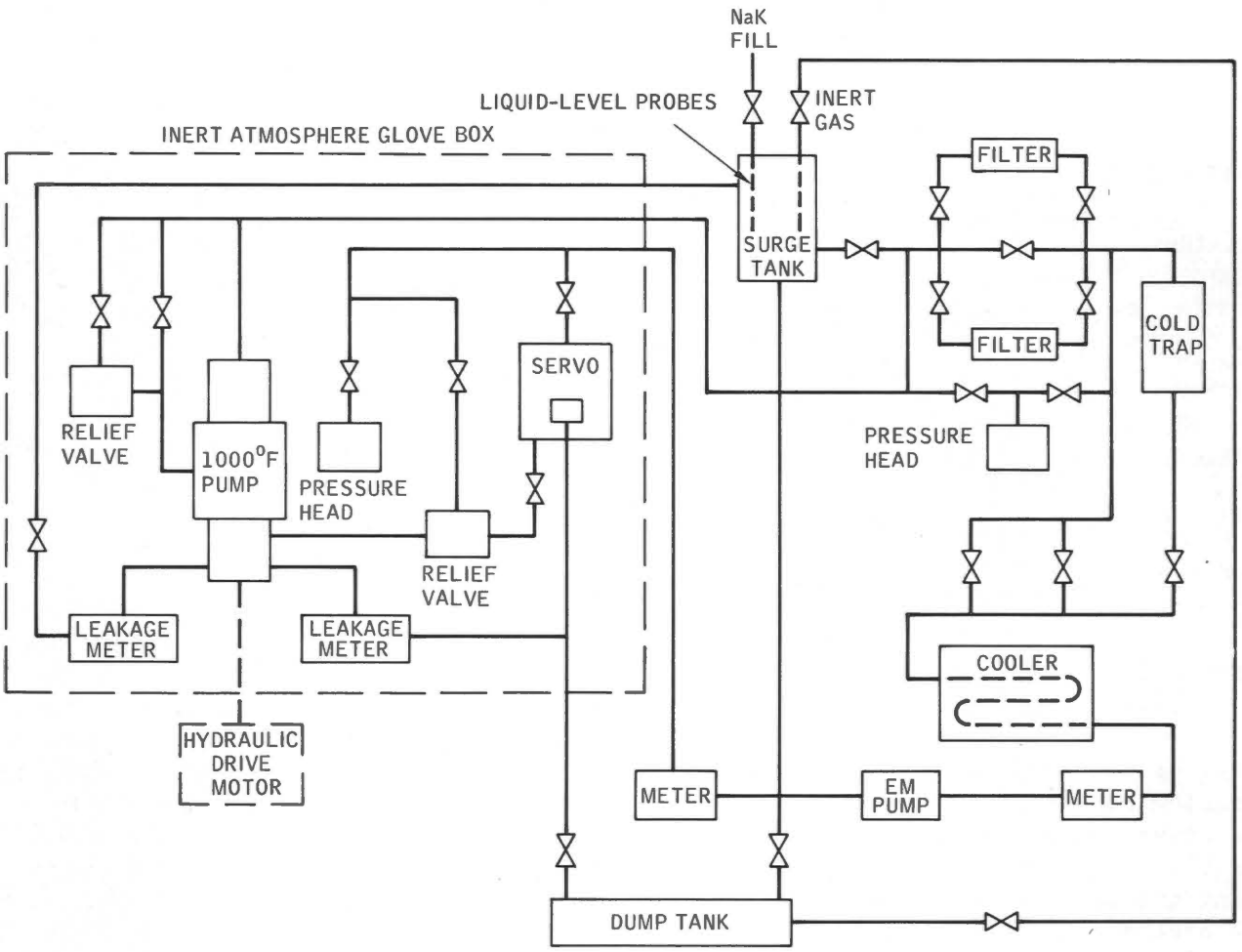

Fig. 5.11 - Hydraulic servotesting with liquid NaK.

without corrosion; (7) abundant availability of the hydraulic fluid at low costs; and (8) liquid-phase hydraulic fluid at ambient temperatures.

At the present time NaK comes closest to satisfying these requirements. A special test loop (Fig. 5.11) was built and operationally tested for this purpose [20-23]. Preliminary test reports show that components already in operational conditions in individual test loops [24,25] satisfy most requirements for control systems. A centrifugal-type pump generates 3000 psig at 1200°F NaK temperature with 7-gpm flow at 35,000 rpm (over 30 hr operation was logged). The control valve was made of molybdenum with carbides at its moving surfaces. The linear-actuator housing was 442 stainless steel with titanium carbide liner at its moving sections. Shafts are sealed with inert-gas bellows. A linear variable-inductance-type transducer is also a part of the test loop [23,25].

Figures 5.12 and 5.13 show how NaK is used for controlling the radiation surface of the heat sink. The hydraulic pressure, which is a function of the temperature of NaK and is balanced by springs, can open and close shutters that maintain the power output during the decay of the isotope. Lead telluride is the junction material [26].

5-7 ELECTRICAL APPLICATIONS

Although the low electrical resis-

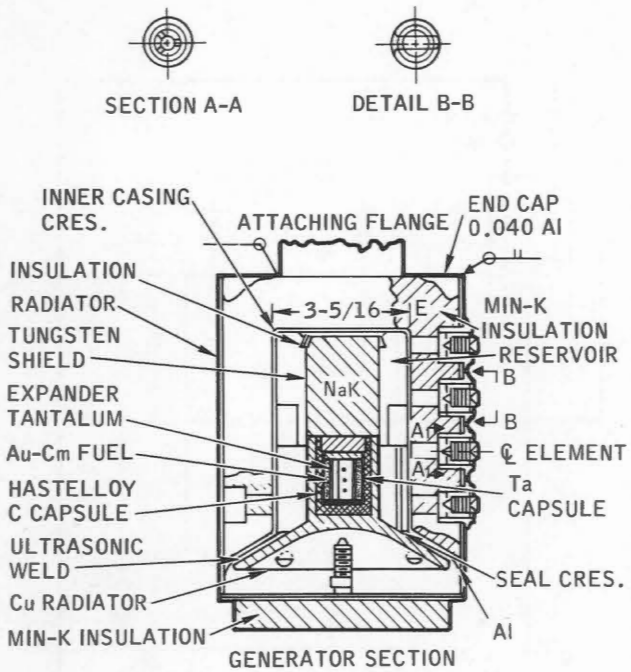

Fig. 5.12 - Thermoelectric generator (13 watts).

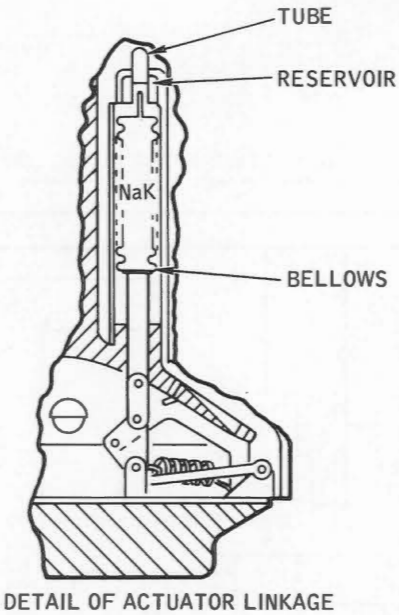

Fig. 5.13 - NaK control mechanism.

tivity of sodium is well known, its application as a conductor did not appear attractive until an inexpensive and flexible cover material capable of providing the required cover properties (polyurethane plastic) was developed. Limited applications of sodium conductor wires or busses existed as early as 1932. Advancements in spacecraft technology led to fundamental research on thermoelectric generators using the Seebeck effect and on thermionic generators using the Edison effect. Both applications can utilize liquid metals or vapors as the primary energy-transfer media from a thermal source.

5-7.1 *Electrical Conductors*

After silver (1.59), copper (1.67), gold (2.19), and aluminum (2.65), sodium is fifth in line of electrical resistivity (4.2 μohm cm), but sodium is almost three times lighter than aluminum. Where raw material and manufacturing costs are compared with costs of electrical power losses per identical cable lengths, sodium shows a highly competitive value, even if the effect of mass production on its price is disregarded.

Sittig [2] reported that in 1932 the Dow Chemical Company used a sodium-filled iron pipe as a cable for a 4000-amp dc load without any adverse effect. As soon as leakproof, long-lasting, low-priced, plastic (polyurethane) tubing could be manufactured in sufficient lengths, Union Carbide Corporation developed a sodium cable in its Bound Brook, N.J., plant [27-30]. Simplex Wire & Cable Co., Cambridge, Mass., produces these cables, and Burndy Corp., Norwalk, Conn., manufactures the fixtures necessary for their application. Commonwealth Edison Company is using experimental lines in their rural distribution network as underground cables for 600 volts. Boston Edison Company tested one cable at 15,000 volts and Ohio Power Company tested another cable at 2000 volts; neither of them reported any adverse experiences during service of almost a year.

Figure 5.14 shows a group of different types of sodium cables [28] and Fig. 5.15 presents a cable-connector concept used for these power cables.

Taylor and Post [29] described the

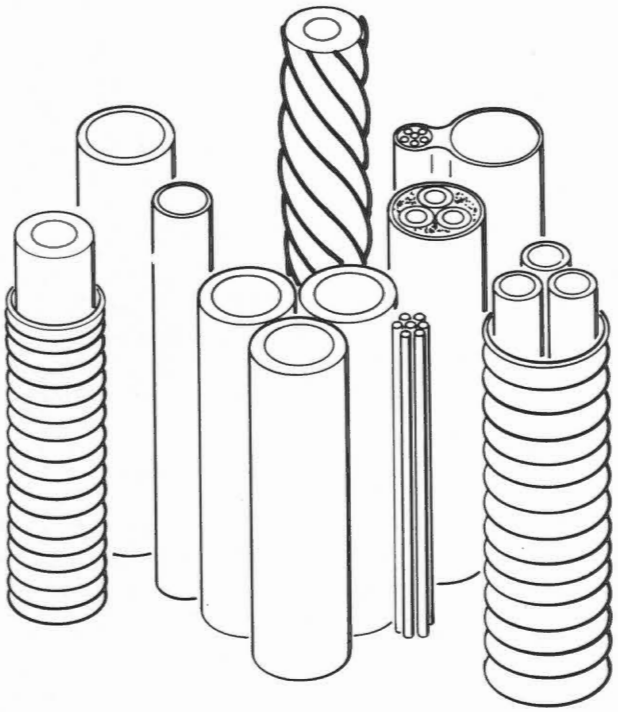

Fig. 5.14 - Group of plastic-insulated sodium power cables.

fabrication and heat-transfer calculations for sodium coils used in laboratory thermal and mechanical stability tests at cryogenic temperatures. Further developments for the cryogenic-type sodium coil are described in Ref. 31, which also gives additional data on the design and problems involved in a similar experiment.

5-7.2 *Thermoelectric Power Generation*

The high electrical conductivity of the alkali metals provides new approaches to the generation of electrical power. A general survey of the electrical-power-operating field gives an overall view of the present research in this area.

The three basic energy sources for space applications, solar, nuclear, and chemical, can produce electrical energy by thermal or mechanical means or by combination of the two. Figure 5.16 is a graphical perspective of the problem [32]. Usually the more direct the conversion is, the more efficient it is.

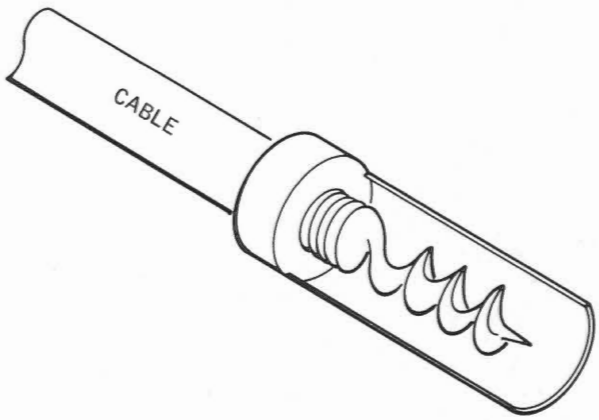

Fig. 5.15 - Cable connector for sodium power cable.

Conventional power-generating methods (discussed in Vol. II, Chap. 2) use alkali metals as the heat-transfer medium. Power-generating methods discussed in this section convert heat energy into electricity in a more direct way, e.g., by using the Seebeck effect in thermoelectric cells or by applying the Edison effect in thermionic generators.

One of the best-known methods of generating electricity is based on the Seebeck effect. This has been thoroughly investigated for the purpose of thermocouple temperature measurement. Two dissimilar metals are joined at one end and their opposite ends are kept at different temperatures. The generator voltage becomes greater as the temperature difference between the joint and the opposite ends increases. Increasing the contacting surface at the joint allows for higher current draw. Because the voltage of one junction is very low, many joints should be connected in series to increase the voltage output.

Advances in solid-state physics opened up new fields of investigation that extend the application of this phenomenon. On the hot end of a metal or semiconductor, more electrons become free than on its cold end. This starts an electron travel toward the cold end, giving it a greater negative charge. After a short duration this

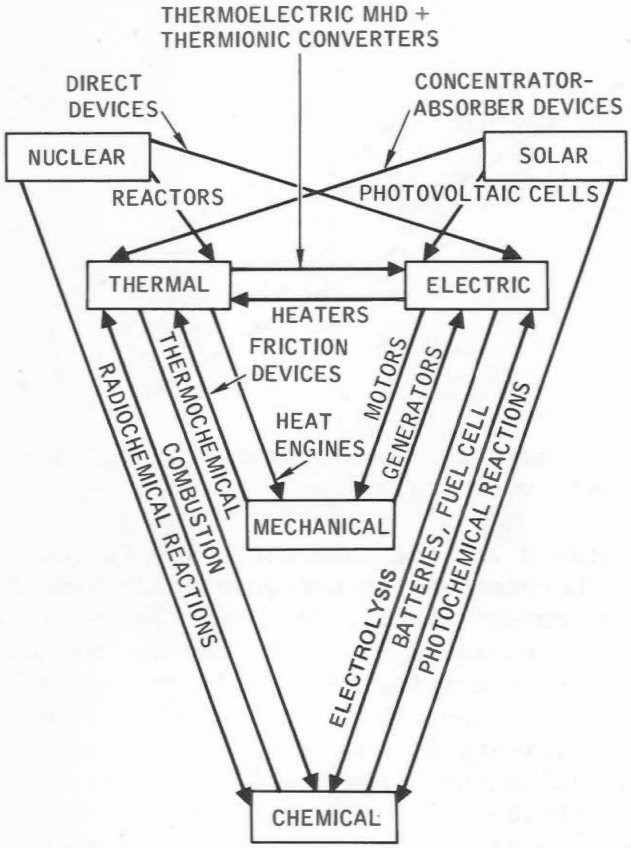

Fig. 5.16 - Energy conversion schemes.

electron travel is stopped because the cold end becomes saturated with electrons. Since more free electrons are available on the hot end of a semiconductor than on a metal, the heated semiconductor junctions can produce higher voltages than the metal thermocouples. Still the voltages of the individual junctions are low; for usable voltage ranges they must be cascaded.

Before an efficient thermoelectric power source could be built, optimized thermal and electrical conductivity had to be achieved. If the thermal conductivity of the joint materials is high, the materials allow a greater amount of heat to flow away from the junction. Since the temperature must be kept constant, low thermal conducting materials show higher thermal efficiencies.

If the electrical conductivities are low (i.e., high electrical resistivities), more electrical power is lost to

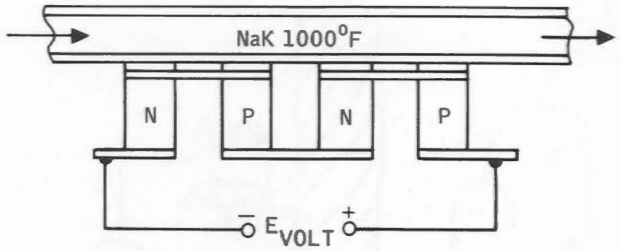

Fig. 5.17 - Simple thermoelectric element. (Data from J.E. Hove and W. C. Riley, *Ceramics for Advanced Technologies*, John Wiley & Sons, Inc., New York, 1965.)

ohmic resistance.

In general, the efficiency of the thermoelectric generator is proportional to the square of the Seebeck coefficient of the junction materials and to the reciprocal of their thermal and electrical conductivities.

The original SNAP-10 generator was designed for lead telluride junctions at temperatures below 900°F. Temperatures were supplied by reactor-heated NaK. The newer SNAP-10A generator uses germanium silicide junctions good up to 1000°F with average efficiencies above 6%. A schematic of a single thermoelectric generator element heated by NaK is shown in Fig. 5.17 [32], *N* means *n*-type and *P* means *p*-type semiconductor materials.

Bloom and Weddell [26] described a 13-watt generator powered by a ^{242}Cm isotope for a 6-month operational life. It weighs 16.6 lb and occupies 230 cu in. A variation of this generator was designed to operate on the moon's surface; it supplies 13 watts for 2 months and weighs 6.2 lb at 350-cu-in. volume.

5-7.3 *Thermionic Generators*

Edison first observed that electric current flows across the gap between separated hot and cold metals in a vacuum. The explanation of this Edison effect is that the high temperature drives free electrons from the basic material, building up an electron cloud

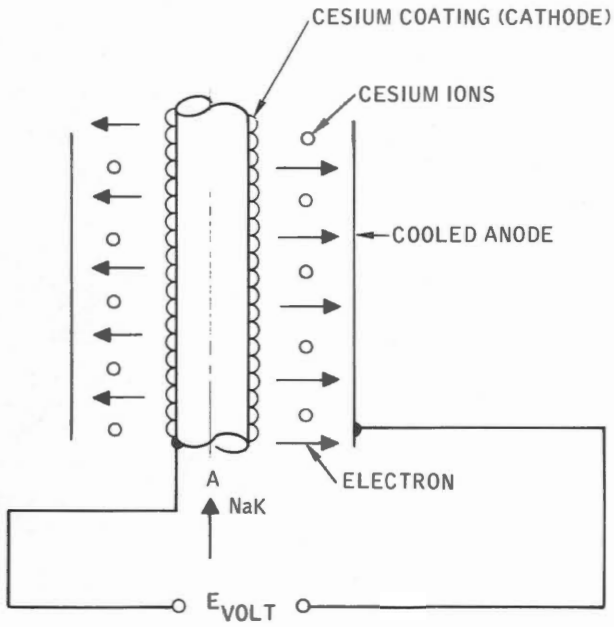

Fig. 5.18 - Edison effect.

around it. Some of these electrons hit the cold electrode, which absorbs them as a negative electric charge. The closer and cooler the second electrode is, the greater the electron absorption is. The charging current can be further increased by filling the vacuum with positive gas ions (cesium), applying an electrical or magnetic field to the gap, or using positively charged grids to accelerate the electrons toward the cold electrode. The electrical-power-generation efficiency increases with greater temperature differences. Figure 5.18 shows the principal scheme of the Edison effect.

References 32 and 33 describe one such system where a reactor-heated NaK stream supplies the heat for the cathode and a space radiator takes the heat from a coolant circulating around the anode.

Ulrich [34] described an example of a cesium-filled diode in which nuclear-reactor-generated thermal energy is used to heat the cathode and to keep the cesium in the gap near its boiling point. The anode is cesium-coated rubidium cooled by potassium or NaK flowing through a space radiator. The main problem of this generator is to maintain the narrow space between the two electrodes.

Hill and Gietzen [35] presented an analytical study for the feasibility of a 1-Mw(e), unmoderated, nuclear thermal source driving a thermionic electrical generator. The influences of the different materials (Be, Mo, Nb, and W) on the output power are discussed.

Another study [36] analyzed the technical problems of a lithium-heated cesium-vapor-driven and NaK-cooled system expected to be used as a spacecraft primary-propulsion power source. Estimated plant specific weight is 19.4 lb/kw(e), including 2.8 lb/kw(e) reactor shielding. Peak-load temperature is calculated for 2600°K; normal operation would require 2200 to 2300°K.

5-7.4 *Liquid-Metal Cells*

Electrical cells can generate electrical energy from chemical energy directly or indirectly. If the chemical process is not reversible, one or more cell parts must be intermittently removed and replaced. With a reversible chemical process the cell must be connected to a proper electrical power source to restore the original chemical status by recharging the cell.

In general, the current output of a cell can be calculated from Faraday's laws: (1) the amount of chemical change produced by an electric current is proportional to the quantity of electricity; and (2) the amounts of different substances liberated by a given quantity of electricity are proportional to their chemical equivalent weights, where the equivalent weight is the ratio of the atomic weight to the valence change. In mathematical form the process current is

$$I = \frac{96{,}500G}{et} \tag{5.19}$$

where 96,500 is the coulomb value of electricity necessary to separate 0.001118 g of silver from its compounds

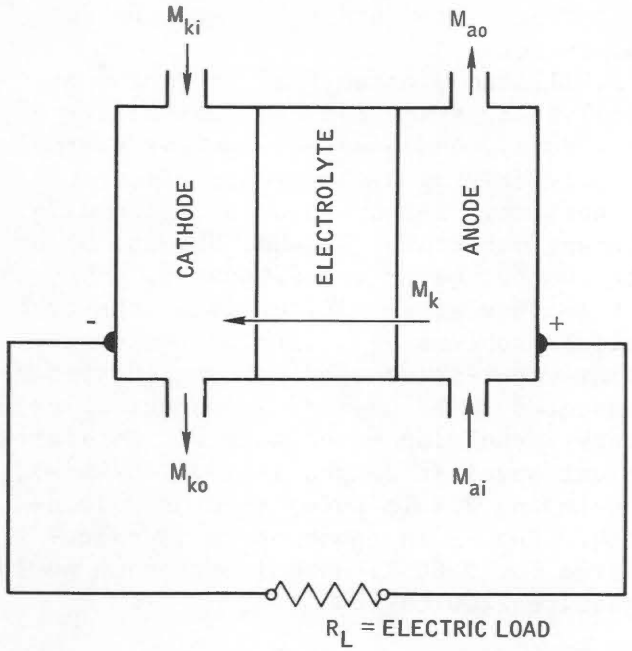

Fig. 5.19 - Schematic of a Hg-K(NaK) cell.

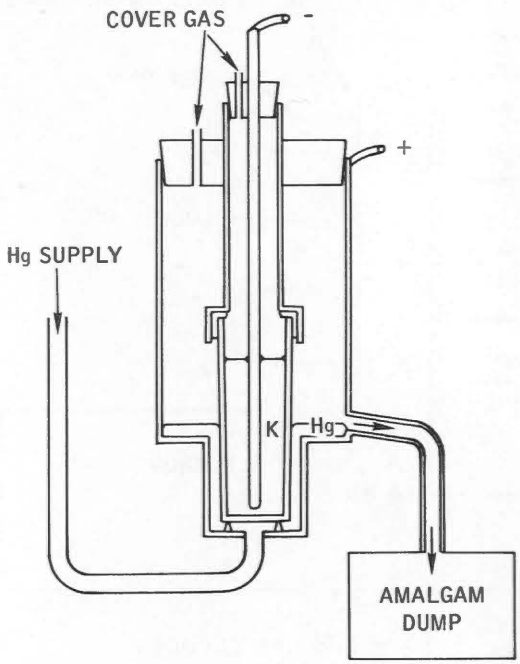

Fig. 5.20 - Arrangement of the Hg-K(NaK) cell.

by electrical currents, G is the weight of the substance participating in the reaction in grams, e is equivalent weight, and t is time in seconds.

The electrical contact potential between two different materials, E, is calculable from

$$E = E_0 + \frac{RT}{nF} \ln \frac{a_1}{a_2} \qquad (5.20)$$

where E_0 = constant (this can be taken from the electrode-potential series of the elements)
R = gas constant
T = absolute temperature
n = valence change
a_1 = metal ion activity of one electrode (anode) to the electrolyte
a_2 = ion activity of the electrolyte to the other electrode (cathode)
F = Faraday number = 96,500 coulombs

Alkali metals can be used for building electrical cells; one type is the Hg-K cell, and the other is the Na-S cell.

Henderson [37] described a research cell composed of mercury and potassium (or NaK) as shown in Figs. 5.19 and 5.20. Since NaK is liquid at normal ambient conditions, its application might save start-up problems in the Hg-K cell.

The open voltage characteristics and the current density as a function of the cell length can be calculated from the equations of the previous introductory section. For the closed loop of Fig. 5.19, the voltage distribution is

$$E = \frac{RT}{nF} \ln \frac{a_{ka}}{a_{kc}} - I_x R_x W \, dx \qquad (5.21)$$

where x = distance in direction of metal flow in the cell
R = vapor constant
T = absolute temperature
a_{ka} = activity of potassium at x distance in anode
a_{kc} = activity of potassium at x distance in cathode
I_x = current density
R_x = resistance at x
W = cell width

Application of Faraday's laws transforms Eq. 5.20 into

$$E = \frac{RT}{nF} \ln \frac{\left(\frac{M_{ki} - \int_0^x M_{kx}dx}{M_{ai} - \int_0^x M_{kx}dx}\right) a_a{}^x}{\left(\frac{M_{ki} + \int_0^x M_{kx}dx}{M_{ai} + \int_0^x M_{kx}dx}\right) a_c{}^x} - \frac{nFM_{kx}}{39} R \qquad (5.22)$$

where M_{ai} and M_{ki} are mass flow of potassium into anode and cathode, respectively, M_{kx} is its mass flow at point x, and $a_a{}^x$ and $a_c{}^x$ are ion activity coefficients in anode and cathode. If this equation is solved along the cell length, a typical group of curves (Fig. 5.21) can be obtained. Deviation between theoretical and measured values is attributed to the diffusion characteristics between potassium and mercury.

Figure 5.20 gives the arrangement of the cell, and Fig. 5.21 gives its operational results.

Another liquid-metal cell uses liquid sodium and liquid sulfur as the cathode and anode. They are separated by a crystalline, ceramic-type diaphragm serving as an electrolyte. Operation of the cell is based on an electrochemical process in which the liquid sodium gives up an electron to the external electric circuit and a sodium ion diffuses into the liquid sulfur through the diaphragm and forms sodium sulfide. During recharging this chemical process is reversed and thus builds up pure liquid sodium and liquid sulfur.

The diaphragm is a sintered solid ceramic of 90% theoretical-density beta alumina. Working temperature of the cell is between 250 and 300°C. Specific weight at slow (2 to 5 hr) discharge is 150 watt hr/lb. At 15 min rapid discharge, specific weight is 10 lb/kw compared with 31 lb/kw for the lead-acid battery. Since the cell is completely sealed, no chemical or vapor can escape and no maintenance is required other than recharging. Further research is now in progress to use the cell for powering automotive vehicles [38].

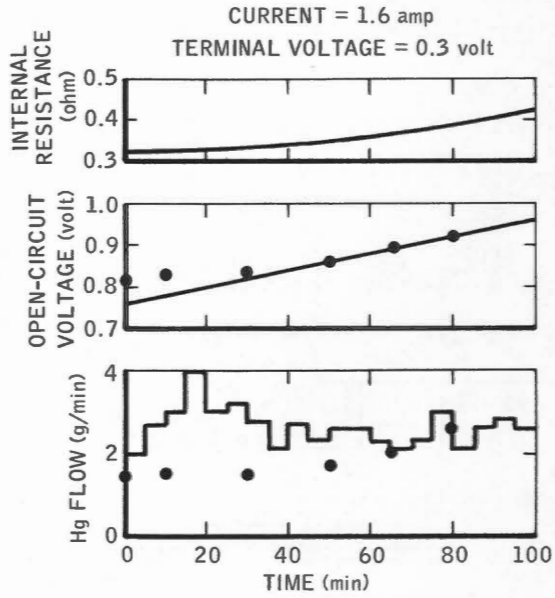

Fig. 5.21 - Results of operation of the Hg-NaK cell.

5-7.5 *Arc Tunnels*

An aerodynamic wind tunnel was designed, built, and operated [39] with sodium vapor for atomic and macroscopic research. Sodium heated to 300°C was pumped from the reservoir into a nozzle made from molybdenum and coated with aluminum oxide. The nozzle ejected the sodium vapor against the orifice of the arc constrictor. Flow velocities were controlled so that a doughnut shape was formed by sodium, and its temperature was closely controlled. The arc was generated between the nozzle as anode, and a cathode was placed behind the arc constrictor. Both the cathode and the arc constrictor were fabricated from molybdenum and coated with aluminum oxide.

Sapphire windows allowed observation of the electrodes and monitoring of the arc column by photoelectric or spectrophotometric instruments. Strip-chart recorders registered the temperature history of the electrodes. Maximum duration of the arcs was limited to 30 sec in each run. Molybdenum with aluminum

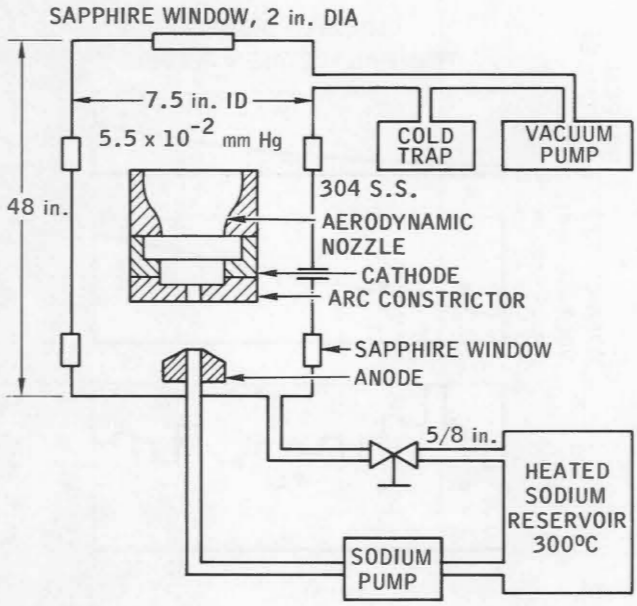

Fig. 5.22 - Sodium supply of an aerodynamic wind tunnel.

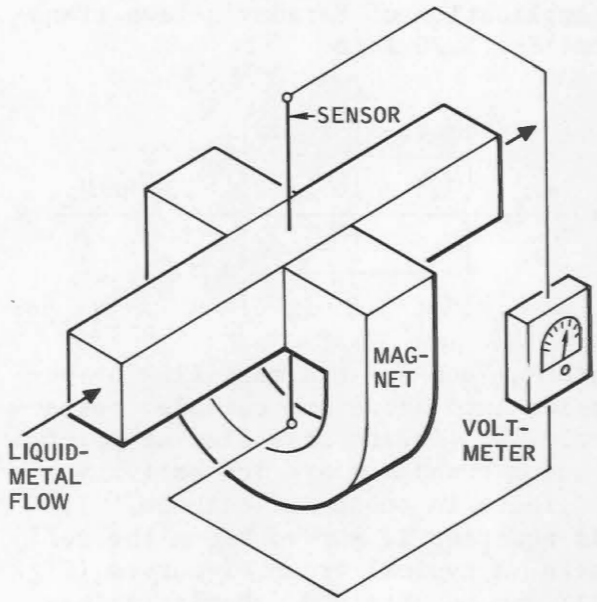

Fig. 5.23 - Schematic of magnetic flowmeter.

oxide coatings was selected as the electrode material because its melting point (2625°C) is high enough to preclude interference with the arc-spectrum analysis. The arc-tunnel schematic is shown in Fig. 5.22.

5-8 MAGNETOHYDRODYNAMIC APPLICATIONS

Faraday's basic electromagnetic induction law states that an electromotive force (measured in volts) is induced in electrical conductors when they cut magnetic lines. This law is illustrated in the magnetic flowmeter schematic of Fig. 5.23, which shows the conducting liquid-metal flow passing between the poles of a permanent magnet. The induced electrical voltage is displayed on a voltmeter.

If B is magnetic flux density (i.e., magnetic lines per square centimeter), l is the length of conductor in the magnetic field in centimeters, and v is the velocity of the conductor intersecting the magnetic lines in centimeters per second, then the generated electromotive force is

$$E = Blv10^{-8} \text{ volt} \qquad (5.23)$$

Each of the four parameters must be translated into a mutually perpendicular system, and any three of the parameters will determine the fourth.

Electrical power applied in place of the voltmeter in Fig. 5.23 drives the liquid metal with a velocity v. This is the basic principle of the simplest electromagnetic pump. Varying the application methods of the magnetic field and the electrical conductors and their relative speed makes possible the different types of magnetic liquid-metal pumps.

Reversed electromotive force applied to a flowing liquid-metal pump acts as an electromagnetic brake or as an electromagnetic flow-control valve. A multiphase electromagnetic field is used to stir liquid metals [40,41]. (For details see Vol. IV, Chap. 1.)

Besides the magnetic induction, there is the Hall effect [42], which can also be used to generate an electromotive force by placing an electrical conductor in a horizontal plane (x-y direction)

exposed to a magnetic field in the vertical (z) direction. The moment an electrical current is applied in the x direction (flow direction), an electromotive force measured in volts appears in the y direction.

If J is the current density carried by the conductor, B the magnetic field density, E_H the electrical field (Hall field), and R the so-called Hall coefficient, then

$$E_H = RJB \tag{5.24}$$

where $R = -1/ne = -\mu/\sigma$

n = number of the electrical current carriers (electrons or holes) per cubic meter

e = electrical charge of the current carrier = 1.60×10^{-19} coulomb for an electron or a hole

μ = mobility of the current carrier (m^2/volt/sec)

σ = electrical conductivity of the current conducting material [$(ohm\text{-}m)^{-1}$]

The Hall effect is applied for d-c electric-power generation in test loops where the magnetohydrodynamic fluid is a noble gas "seeded" either with liquid metals or with their compounds to increase the electrical conductivity of the fluid.

If the conduit is replaced with a semiconductor having higher Hall coefficients, the output voltage can be calibrated as a measure of the magnetic-field flux density.

Some other applications of both the Faraday induction and the Hall effect in connection with liquid metals can be found in the pump and instrumentation chapters of this handbook (Vol. IV, Chap. 1, and Vol. III, Chap. 4, respectively.)

5-8.1 *Magnetohydrodynamic and Magnetoplasmadynamic Power Generation*

If an electrically conducting fluid such as a liquid metal is driven through a magnetic field, the electromotive force generated (measured in volts) can be applied as useful electrical power. The properties of this electric power depend primarily on the fluid velocity, the magnetic flux density, the electrical resistance of the fluid within the effective magnetic field, and the electrical load resistance connected to the generator terminals. This type of generator , usually operating on Faraday's electrical induction principle, is called a magnetohydrodynamic (MHD) generator. If the fluid employed as conductor is a gas, the machine is called a magnetoplasmadynamic (MPD) generator.

Today's MHD generators employ liquid metals either in their liquid phase or as mixtures composed of their liquid and vapor phases. If the kinetic energy of the liquid is obtained by the expansion of gases or vapors using their thermal energy, the gases or vapors should be separated from the liquid to restore the necessary electrical conductivity of the MHD fluid before it enters the MHD generator. Although MPD generators can operate at supersonic velocities, their electrical power output is limited by the low electrical conductivity of the plasma. At the present time the value of the electrical conductivity, even for seeded plasmas, is about four orders of magnitude lower than that of an MHD liquid-metal fluid. Attempts are being made to improve the plasma conductivity with supplementary ionization. Further details are presented in subsequent sections of this chapter.

The MHD and MPD generators are proposed and investigated for spaceship applications primarily because (1) they can be built without any moving machine parts, which means higher reliability, and (2) they can operate in space in the the absence of gravity, depending only on the thermal energy of the heat source, which could be a nuclear reactor. The MHD generator seems to be a strong contender whenever a long-term electrical power supply is required for a spaceship. Naturally, closed-power generation cycles are preferred for the majority

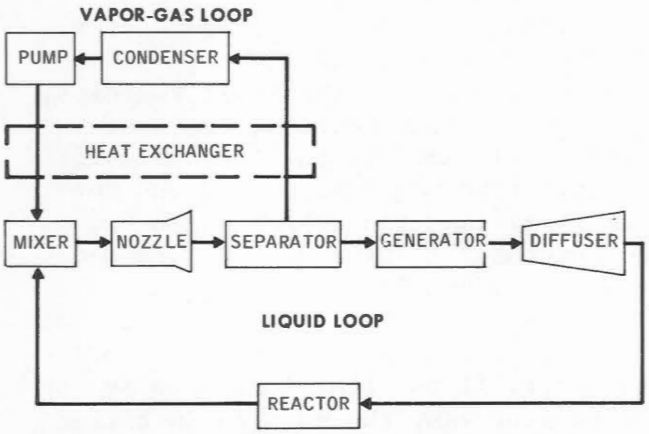

Fig. 5.24 - Block diagram of a two-phase two-component cycle.

of space applications.

Analytical and economic studies supported by experiments have shown that MHD liquid-metal generators can be used in commercial, large-scale, electrical power generation units as topping for the standard steam cycles and to improve plant efficiency. They may use either fossil fuel or nuclear energy sources. In both cases either an open or a closed cycle could be used.

The MHD and MPD cycles operate either with a single fluid or with two fluids. In the latter case one fluid is either a gas or a vapor and the other is a liquid metal. Even a single-fluid MHD generator usually has two loops; one circulates the fluid in the vapor phase, and the other circulates the fluid in the liquid phase. There are, however, proposals for single-phase single-cycle applications [43]. If a mixture of a gas and a liquid metal is the operating fluid, then it is usually called a liquid-metal-seeded gas [44,45].

Figure 5.24 is a simplified block diagram of a bifluid, two-phase, closed-cycle-type MHD generator in which a liquid metal is heated to high temperatures in a nuclear reactor. This liquid is combined in a mixer with a liquid-metal vapor returning from a parallel loop and is then accelerated in a nozzle. Thereafter the vapor is separated from the high-velocity mixture, increasing

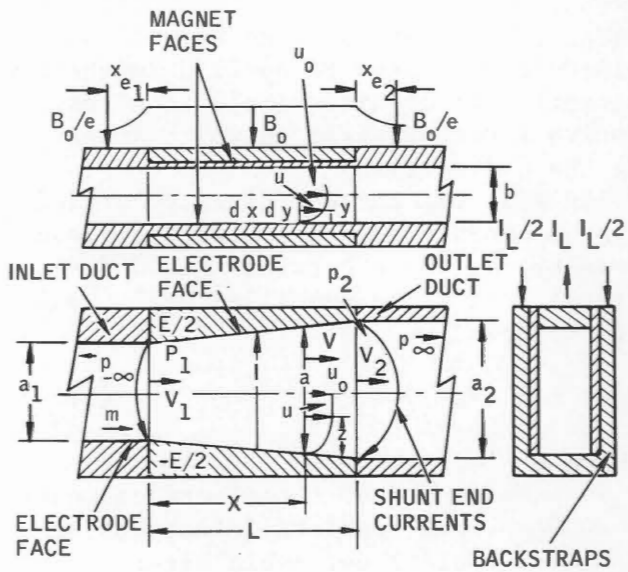

Fig. 5.25 - Idealized MHD generator.

the electrical conductivity of the fluid, which now enters the MHD generator where, while losing its velocity, it produces electrical power. A diffuser further reduces the velocity of the fluid leaving the MHD generator to lower the hydraulic friction losses in the return leg to the reactor. The previously separated gas-vapor mixture passes an economizer-type heat exchanger in a loop parallel to the liquid; then the vapor is reduced to its liquid phase in a condenser; and finally an EM pump returns the gas-vapor composition to the mixer where the cycle is repeated. Since there are no moving machine parts in this closed cycle, the MHD generator is useful for space-vehicle applications.

5-8.2 *MHD D-C Generators*

Elliott [46] reviewed the present status of the theoretical, physical, and material derivations for an MHD d-c generator, including the deviations between theory and actual performance of an experimental loop.

The calculations are based on an experimental generator with the geometric dimensions shown in Fig. 5.25, where a steady magnetic field B_0 is applied

along the L dimension and the exponential decrease on the two ends of the length (L) were provided to reduce the magnetic end-effect losses. End-effect losses are generated in the fluid since the liquid metal is not built from isolated, axial, liquid-metal streams. The electrical conduction between the streams can absorb large electrical energies if the magnetic field at the pole ends is not reduced rapidly. These lost energies must be taken also from the kinetic energy of the fluid.

Any MHD analysis is based on hydraulic and electrical requirements and assumptions of close approximations. The following approximations have been made: (1) the flow is turbulent with 1/7th-power velocity profile, (2) the shear forces are not affected by MHD, (3) the divergence angle of the generator is negligible if calculations are made with parallel velocity vectors, (4) the magnetic field is equal to the calculated field, and (5) the fluid properties are constant.

The basic equations state that the electrical resistance of $dx\ dy$ cross section in x distance from the duct entrance is $R = (a/\sigma)dx\ dy$, where a is the liquid column length and σ is electrical fluid conductivity.

The voltage induced in the element is

$$E_i(x,y) = B_0 \int_0^a u\ dz \tag{5.25}$$

where B_0 is the magnetic field density, u is fluid velocity at $dx\ dy$ cross section, and z is distance from the face of the electrode.

The ohmic heating loss is

$$dP_r(x,y) = \frac{(E_i - E)^2}{R} \tag{5.26}$$

If V is used as the bulk velocity,

$$Vab = V_1 a_1 b = \dot{v} = \int_0^b \int_0^a u\ dz\ dx \tag{5.27}$$

If μ is introduced as the loading ratio $\mu = E/B_0 V_1 a_1$ and the 1/7th-power profile assumption is used,

$$\frac{u}{u_0} = \left(\frac{y}{(b/2)}\right)^{1/7} \tag{5.28}$$

for $y \le (b/2)$. The hydraulic friction loss due to wall shear is

$$dP_f(x) = \left(\rho V^3 \frac{C_f}{2}\right)\left(2(a + b)dx\right) \tag{5.29}$$

where C_f is skin-friction coefficient.

The mean Reynolds number is $\mathrm{Re} = \dot{m}D_h/a_m b\mu_f$, where $\dot{m}$ is the mass flow rate, D_h is the hydraulic diameter, and μ_f is fluid viscosity. From the Prandtl number

$$(C_f)^{-1/2} = 4 \log\left[2\mathrm{Re}(C_f)^{1/2}\right] - 0.8 \tag{5.30}$$

For a linearly tapered channel, its mean width is

$$a_m = a_1 \frac{(a_2/a_1) - 1}{\ln(a_2/a_1)} \tag{5.31}$$

The total fluid input power, P_{m_0}, is equal to $P_{e_0} + P_r + P_f$, where P_{e_0} is output to the electrodes. The kinetic power to the electrodes is

$$P_k = \int_0^b \int_0^a \frac{\rho\mu^3}{2}\ dx\ dy \tag{5.32}$$

if ρ is liquid-metal density. For a slit channel approximation,

$$\int_0^a u^3 dz \approx u^3 a$$

$$P_k = 1.045\left(m\ \frac{V^2}{2}\right) \tag{5.33}$$

The magnetic field to be applied should be

$$B_0 = \left[\frac{\rho V_1 a_m}{\sigma b L\left[\frac{64}{63} - \mu\right]}\left\{\frac{128b}{245a_1}\left(1 - \frac{a_1}{a_2}\right) + \frac{b\ \Delta p}{\rho V_1^2 a_1} - \frac{C_f L}{a_2}\left(1 + \frac{b}{2}\left(\frac{1}{a_1} + \frac{1}{a_2}\right)\right)\right\}\right]^{1/2} \tag{5.34}$$

Based on studies by Sutton and coworkers [47-49], the end current power loss is

$$\Delta P_e = \frac{\sigma B_0^2 V_1^2 a_1^2 b\mu}{\pi[2\mu \ln 2 - (\alpha_1 + \alpha_2)]} \tag{5.35}$$

where

$$\alpha_1 = \frac{\pi x_{e1}}{a_1}\left\{1 - \frac{1}{\pi^{1/2}} \frac{\Gamma[\frac{1}{2}[(a_1/\pi x_{e1}) + 1]}{\Gamma[\frac{1}{2}[(a_1/\pi x_{e1}) + 2]}\right\} \tag{5.36}$$

and

$$\alpha_2 = \frac{\pi x_{e2}}{a_2}\left\{1 - \frac{1}{\pi^{1/2}} \frac{\Gamma[\frac{1}{2}[(a_2/\pi x_{e2}) + 1]}{\Gamma[\frac{1}{2}[(a_2/\pi x_{e2}) + 2]}\right\} \tag{5.37}$$

The net output power of the generator is $P_e = P_{e0} - \Delta P_e$. Combining all these equations gives

$$P_m = P_{m0} + \Delta P_m \tag{5.38}$$

or

$$P_m = \frac{\sigma B_0^2 V_1^2 a_1^2 b L(1 - \mu)}{a_m}\left[1 - \frac{1}{1 - \mu}\left\{\frac{1}{63} + \frac{a_m}{L}\left[\frac{\beta_1 + \beta_2}{2} - \frac{\mu(\alpha_1 + \alpha_2)}{\pi}\right] + \frac{[(64/63) - \mu]\{1 + (b/2)[(1/a_1) + (1/a_2)]\}}{\frac{128b}{245}\left(\frac{1}{a_1} + \frac{1}{a_2}\right)\left(\frac{a_2 - a_1}{LC_f} - \frac{245}{246}\right) + \frac{a_2 b\,\Delta p}{\rho V_1^2 a_1 L C_f}} - 1\right\}\right] \tag{5.39}$$

Based on these calculations, an experimental system was built and tested with the following results:

1. The maximum efficiency measured was 0.48 compared with 0.51 theoretical.
2. The actual field required 5 to 15% higher values than calculated.
3. The actual pressure in the duct rose 30% higher than calculated.
4. The output power was about 75 to 86% of the theoretical.

All the deviations could be caused by a small change of the skin-friction coefficient, which was very sensitive to the wetting behavior of the fluid. Small amounts of dissolved oxides had a strong influence on the wetting angle.

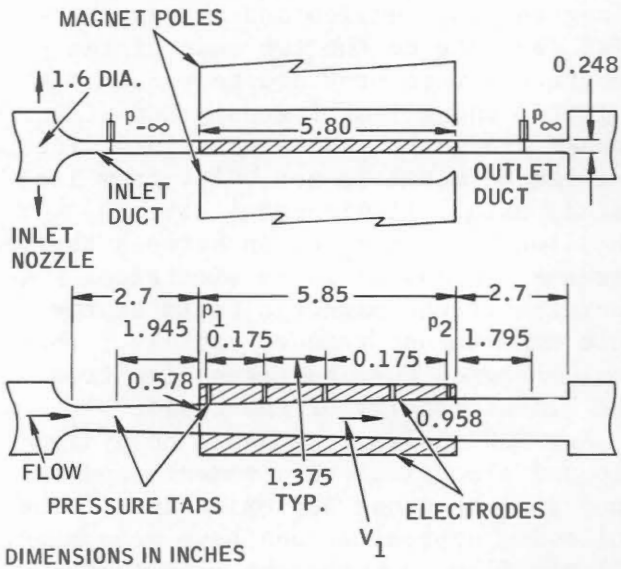

Fig. 5.26 - Geometry of an experimental generator.

Figure 5.26 gives the design dimensions of the test channels. Hays and Cerini [50] gave further test results for this generator.

Additional d-c generator designs and experiments are reported in Refs. 51 and 52. Deviations between theory and actual tests conform to the results reported in Refs. 46 and 53.

Sutton and Sherman [49] published a short report on a low-voltage, low-power, demonstration d-c generator, and Sense and Gelb [54] discussed selecting the proper fluid for MHD generator cycles where the MHD generator inlet void fraction is used as a parameter for cycle comparisons. The selected cycle is similar to that shown in Fig. 5.24. Either a Rb-Li or a Cs-Li bifluid

cycle seemed preferable over the Na-Li cycle, but no experiments were performed to prove this.

5-8.3 *MHD A-C Generators*

In the present state of MHD-generator development, direct current could be generated at a low voltage level (below 1 volt) only. Since alternating current is inherently easier to adapt to any kind of electrical power needs (it transforms to any voltage level and rectifies to produce direct current), the MHD a-c generators were developed. Single and multiphase experimental generators produced alternating current in a range from a few cycles up to a few hundred cycles.

One method used to generate alternating current indirectly is to translate the MHD d-c or MPD d-c generator output into alternating current by having no moving mechanical components [48].

Direct a-c generating methods are:

1. The simplest MHD a-c generator is similar to an induction-type commercial generator where the necessary slip velocity (V_s) for power production is provided between a traveling magnetic field (V_m) and the MHD fluid-flow velocity (V_f): $V_s = V_m - V_f$. (See Fig. 5.27 and Refs. 48 and 55 to 63.)

2. An experimental generator changes the electrical conductivity of the MHD fluid by periodic injection of liquid-metal slugs into the main flow of a liquid-metal vapor; this induces alternating current in the output windings. (See Refs. 43 and 64 to 70.)

3. One experiment used a solid-metal reciprocating piston combined with liquid metals to generate alternating current [69,71].

4. Seeding modulation in an MPD generator changes the electrical conductivity of the gas-vapor flow to generate a-c power [72,73].

5. Controlled flow-velocity pulsation can produce alternating current also [74].

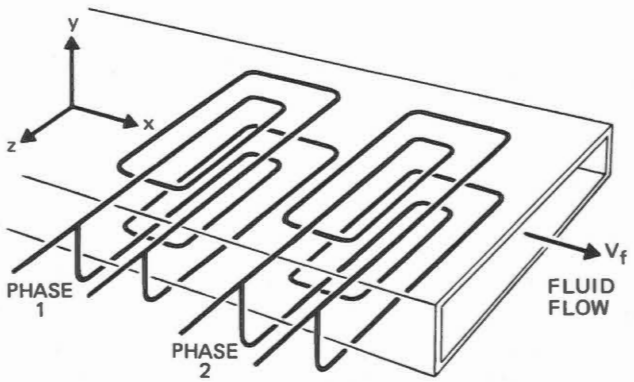

Fig. 5.27 - The flat, linear MHD a-c induction machine.

6. Three-phase a-c generators that apply vortex flow were proposed [75,76].

(a) *Induction-Type MHD A-C Generator*

Of all the a-c generating methods mentioned, the induction type is the most promising and the most extensively tested. Because of its operational similarity to induction-type commercial generators, it is usually called an MHD-induction generator. The electrical field potential vector ($\vec{E}'$) generated by induction is the product of the velocity ($\vec{V}$) relative to the fluid and magnetic fields and the magnetic induction vector ($\vec{B}$) (Faraday's law):

$$\vec{E}' = \vec{V} \times \vec{B} \qquad (5.40)$$

The generated current density ($\vec{J}$) is a function of the electrical conductivity (σ), $\vec{E}$, $\vec{V}$, and $\vec{B}$ (Ohm's law):

$$\vec{J} = \sigma(\vec{E} + \vec{V}_s \times \vec{B}) \qquad (5.41)$$

where $\vec{E}$ is electrical field strength relative to the moving fluid and $\vec{V}_s$ is synchronous velocity of the magnetic field. If V_f is the fluid velocity, then the slip is the percent deviation of the two velocities related to V_s:

$$\text{Slip} = \frac{V_s - V_f}{V_s} = S \qquad (5.42)$$

The gross efficiency (η) [i.e., the ratio of gross generator-output power (P_o) to the gross fluid-input power (P_i)] is

$$\eta = \frac{P_o}{P_i} = (1 - S)^{-1} \qquad (5.43)$$

Another term frequently used here is the wavelength, λ, which can be calculated from the a-c frequency, f, as $\lambda = V_s/f$ or $\lambda = Vf/f(1 - S)$. The engineering magnetic Reynolds number (Re_m^*) has a special meaning for induction generators, i.e.,

$$\frac{\text{Real power}}{\text{Reactive power}} = \sigma\, Re_m^* = \mu\sigma \frac{v_s}{K} \qquad (5.44)$$

where σ = electrical conductivity of the fluid (mho/m)
μ = permeability (henry/m)
v_s = synchronous velocity (m/sec)
K = wave number, calculable from

$$K = \frac{2\pi}{\lambda} \qquad (5.45)$$

Laminar MHD fluid flow is desirable for two reasons: (1) to avoid eddy currents in the fluids and (2) to reduce hydraulic friction losses. The second reason is not valid for constant-velocity generators, where the fluid velocity is determined by the frequency, f, of the a-c power and by the necessary slip.

As discussed in the fluid flow MHD section of Vol. II, Chap. 1, the magnetic Reynolds number and the Hartmann number are the characteristic data for an expected laminar flow. The frequently used form of the Hartmann number (M) is:

$$M = BL\sqrt{\sigma/\rho\nu} \qquad (5.46)$$

where B = magnetic induction (Weber/m^2)
L = characteristic length (m), a dimension normal to flow direction
σ = electrical conductivity (mho/m)
ρ = fluid density (kg/m^3)
ν = kinematic viscosity (m^2/sec)

When the friction factor depends upon both Re_m^* and M for a given geometry, a laminar regime prevails. Reasonably strong magnetic fields at $M > 100$ are capable of producing laminar flow up to $Re_m^* > 100{,}000$.

The engineering Hartmann number (M^*) is based on a fluid duct length-to-height ratio of 50, and, if L is the generator length,

$$M^* = BL\sqrt{\sigma/2\rho\nu} \qquad (5.47)$$

Induction-type MHD a-c generators release their electrical power through their stator windings; this eliminates the need for electrodes (with their leakproof-seal problems) required for MHD d-c generators.

(b) *MHD Cycle Comparisons*

Although the cycle shown in Fig. 5.24 was developed primarily for MHD d-c generators, it is applicable in principle to a-c generators also [77]. The basic characteristic of this cycle is the separation and removal of the low-electrical-conductivity component from the fluid flow before it enters the MHD generator. It can operate with one component in the liquid and vapor phases or with two components if the vapor or gaseous component is insoluble in the liquid fluid.

Figure 5.28 shows a condensing injector cycle developed for Cs, Hg, K, and Na as a one-fluid two-phase MHD generator [78]. The vapor generated in a heat source (reactor) passes into the so-called condensing injector where it is mixed with the returning liquid partially condensing the vapor. The thermal energy of the vapor increases the fluid kinetic energy, and condensation of the vapor increases the fluid electrical conductivity before it enters the MHD generator. The discharge of the generator is separated into vapor

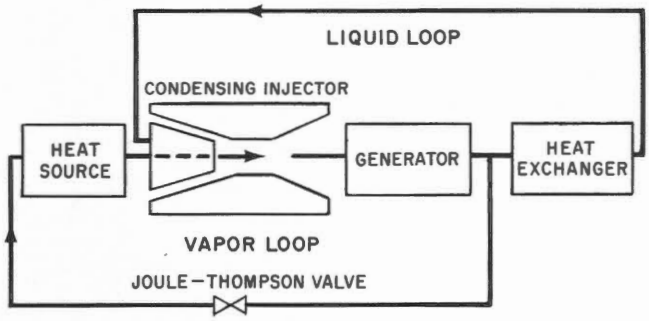

Fig. 5.28 - Schematic of a condensing-injector liquid-metal power cycle.

and liquid. The liquid flows back to the heat source at the same time the vapor passes through an economizer heat exchanger to the injector. A preliminary study showed a preference for cesium or potassium since sodium performance seems to be the lowest of the three liquid metals for this type of cycle.

A short study [75] suggested an MHD a-c generator (Fig. 5.29) in which the liquid phase of the fluid is accelerated by its own vapor in a duct built from two eccentric cylinders placed between the two poles of a magnet. The slowed-down fluid and vapor are then reheated in a reactor, and the partially evaporated liquid regains its necessary thermal energy. After returning to this vortex-type MHD generator the cycle repeats itself.

Alternating-current power can be produced in a slug-type MHD generator (Refs. 64, 67 to 70, 79, and 80) where liquid-metal slugs are injected into a liquid-metal vapor flow. Experiments proved that the slugs, as good electrical conductors, can produce sine-wave-shaped electrical voltage and current. Applied fluid is NaK vapor with NaK liquid slugs (Fig. 5.30).

A comparative study of a-c power generation [43] for topping steam plants showed that a 50% thermal-cycle efficiency is obtainable using liquid metal in the 2240 to 1100°F range and in steam below 1100°F.

A simplified cycle for topping power

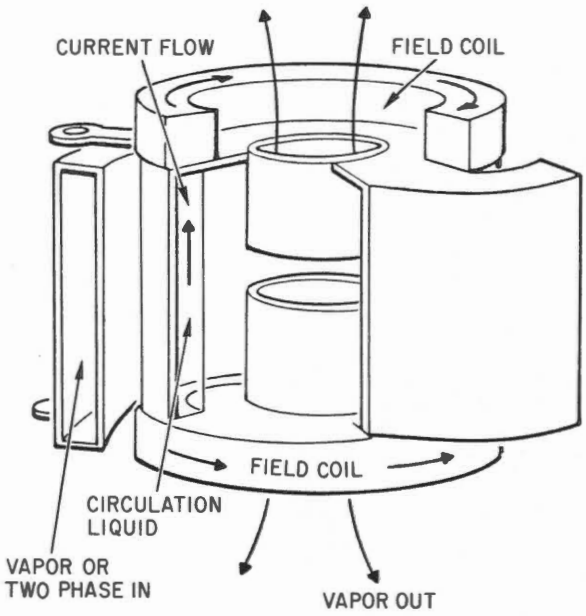

Fig. 5.29 - Vapor-driven liquid-vortex MHD generator. [From H.E. Weber and C.H. Marston, MHD with Liquid Metal, *Mech. Eng.*, *86*(8): 34-37 (1964.)]

plants [43,62] is shown in Fig. 5.31. In the actual cycle metal flows in a continuous stream through a closed two-cycle system. Liquid metal in the first loop is partially vaporized by the heat source. The resulting two-phase fluid expands by passing through a supersonic nozzle, and its thermal energy is transformed to kinetic energy. Downstream of the nozzle, atomized liquid (at considerably lower temperature) from the second loop is injected into the two-phase high-velocity stream. Because of momentum exchange, the injected stream is accelerated while at the same time, due to mass and heat transfer between the two streams, the vapor component of the two-phase fluid is condensed. The resulting fluid stream enters the generator predominantly as liquid phase traveling with high velocity and with a high electric conductivity. A major fraction of the kinetic energy is transformed into electrical energy within the generator. The effluent enters a diffuser where its

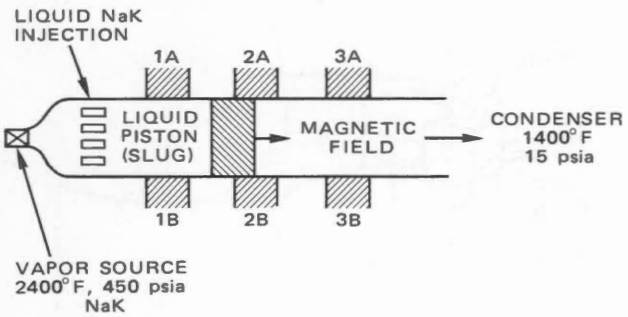

Fig. 5.30 - MHD a-c generator.

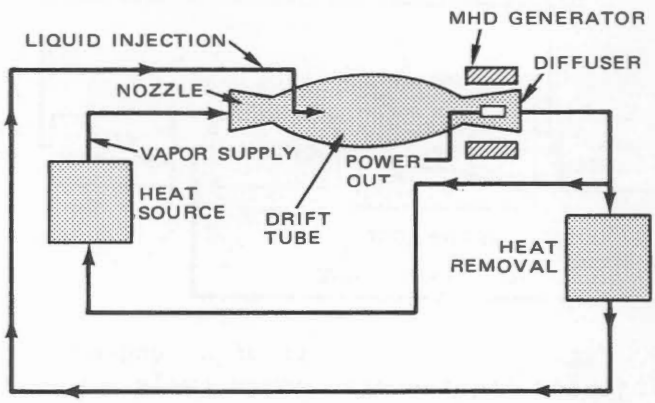

Fig. 5.31 - Liquid-metal liquid-injector MHD cycle. [43,62]

velocity is reduced by conversion of kinetic energy to pressure. The second loop then carries part of the metal through the heat-disposal unit which cools the liquid to the required injection temperature. This subcooled liquid is then returned to the injection point downstream of the expansion nozzle. Metal flowing in the first loop is returned to the heat source and the cycle is repeated. The fluid is two-phase NaK or potassium.

5-8.4 *MPD Generators*

The MHD generators use liquid-phase fluid for higher electrical conductivity, but the MPD generators try to compensate for the low electrical conductivity of the gaseous- (or vapor-) phase fluids with higher velocities (Mach number = 1.5) [44,45,81]. Seeding of the noble- or combustion-gas flow with liquid-metal vapors is a very effective way of increasing conductivity. Helium, argon, and neon are the best-suited noble gases, and cesium or potassium are preferred over sodium for seeding because sodium vapor contains a large percentage of dimer (hard-to-ionize) molecules [81]. In addition to the seeding, the high temperature of the plasma automatically provides thermal ionization for the fluid. Further ionization can be achieved by exposure of the plasma to a magnetic or electric field, or even to nuclear irradiation [44,45,69,76].

Since the electrical conductivity of the present MPD fluids is smaller by a magnitude of four than that of the MHD fluids, MPD fluids are not suitable for induction-type low-frequency (60 to 400 cps) a-c power generation, because of the adverse reactive-to-active-power ratio. In the very high flow-velocity range, the MPD fluids are more suitable for d-c generation, which requires that electrodes be insulated from the ducts at these very high temperatures (4000°F or higher) and also requires cooling of the magnet coils.

The most promising MPD generators use combustion gas for their operation. One such generator is being tested in the United States, and another serves as a utility power plant in the U.S.S.R.

An MHD "shock-tube" generator using a high-temperature noble gas and liquid-metal-vapor slugs is being tested in Germany [40,82,83]. This is a transition-type generator somewhat resembling the MPD types.

5-8.5 *MHD Cycle Components*

(a) *Heat Sources*

The nuclear reactor is planned as a heat source for space application in closed cycles. Its temperature is limited to approximately 2000°F. This is substantially less than the 4000°F that can be maintained in fossil-fuel heaters. Commercial power plants can use either nuclear or fossil-fuel chemical energy.

(b) *Mixers and Nozzles*

The two methods of achieving the necessary high fluid velocity with maximum efficiency are:

1. Provide a highly homogeneous gas (or vapor) and fluid mixture, and then use the thermal energy of the mixture to generate the fluid velocity in a nozzle. In this case the mixer serves as a two-component direct-contact heater where the thermal energy of a preheated liquid increases the thermal energy of another fluid in its vapor phase [46].
2. Produce the necessary homogeneous gas- (or vapor-) bubble-liquid mixture within the nozzle during flow acceleration, then the mixer, with its inherent losses can be eliminated to improve overall cycle efficiency [49,53,62,74, 76,84, and 85].

The breakup of liquid drops is an important phenomenon in the injection-type MHD cycles where liquid is injected into the high-velocity stream of gas, vapor, or a two-phase flow. No theory can predict these breakup-drop dimensions at this time, but the Weber number emerges as a possible criterion to estimate the best probability. The Weber number, We, is the ratio of the aerodynamic force on the droplet to the surface-tension force:

$$We = \frac{\rho_{gas} U^2 D}{2 g_c \sigma} \qquad (5.48)$$

where ρ_{gas} = gas (vapor) density (lb_m/cu ft)
D = droplet diameter (ft)
U = relative velocity between liquid-drop and gas-stream flow (ft/sec)
σ = surface tension of the liquid (lb_f/ft)
g_c = gravitational constant [(lb_m)(ft)/(lb_f)(sec^2)]

References 43, 49, 53, 58, 80, 84, 86, and 87 suggest that We = 6 be used as a starting value for design calculations.

Further improvement of the MHD fluid velocity and electrical conductivity can be achieved if a partial subcooled flow of liquid is injected into the two-phase high-velocity flow where the jet design utilizes momentum exchange phenomena [62,78,88].

(c) *MHD Generators*

The two principles applied to MHD or MPD generators to produce electrical power, Faraday's magnetic induction principle and the Hall effect, have similar components; these were briefly described earlier.

The variable-area MHD generators translate the kinetic (velocity) energy of the fluid into electrical energy at fairly low pressure [56].

In a constant-area generator, the pressure (potential) energy of the fluid is converted to electrical energy [63,66].

The main components of MHD generators are the duct and the magnetic field.

The duct, which carries the fluid conductor at high temperature and high velocity, should be nonmagnetic, with poor electrical conductivity, and should resist the internal-fluid pressure, corrosion, and erosion effects at high temperatures. Terminals are inserted in the duct wall only in d-c generators. They should have low electrical resistivity [50,51,55,61,89]. Fluid-friction losses in the duct can be reduced by replacing the liquid boundary layers with gas or vapor [90] or by using a thin liquid layer and filling the rest of the flow area with gas or vapor [63,87,89,90]. Fluid-friction losses are less critical in liquid-piston- (slug-) operated a-c generators. (For further detailed design information see Refs. 48, 53,57,59,63, and 89 to 96. Details on the Hall-type generator can be found in Refs. 60,61,87, and 97.)

Since, in the rotating electrical generators, the gap between the magnet poles and the electrical conductor is a small fraction of an inch, the magnetic-

field excitation is effective. In an MPD generator the fluid-carrying duct is relatively wide between the magnet poles. This means there is a heavy demand for excitation, which causes high electrical losses and lowers the generator efficiency. Cryogenic and superconducting magnets with liquid helium can reduce the excitation losses and magnet size and increase the magnetic flux density within reasonable physical dimensions [96,98]. Standard electromagnet design should provide circulating fluid cooling to remove the heat generated by the excitation losses and heat conducted to it from the MHD duct [82].

The MHD d-c generator efficiency depends to a great extent on the magnetic-field design at the inlet and outlet ends of the MHD fluid duct. These so-called "end losses" are caused by the electrical currents induced in the fluid streams by the stray magnetic fields at the ends of the magnet. These currents (eddy currents) generate heat losses between the MHD fluid streams before they can reach the generator terminals. The effects of the end losses are (1) unwanted heating and (2) velocity and pressure losses of the MHD fluid flow. Three methods used to reduce these end losses are:

1. Shape the stray magnetic field either by magnetic coil design (exponential field density reduction), or by compensating magnet coils that can suddenly reduce the magnetic fields to a minimum value.
2. Increase the electrical resistance between the MHD fluid streams by placing electrical isolating vanes in the duct at the inlet and outlet of the MHD generator sections next to the magnet pole ends.
3. Apply multipole pair magnetic fields.

Induction-type MHD a-c generators have the following major advantages:

1. They do not need extremely high fluid velocities.
2. Their electrical power output can be modified using electrical transformers or rectifiers.
3. There is no need for polarized electrodes; the load can be connected to stator winding terminals.
4. They are adaptable to lower fluid temperatures with reasonably good cycle efficiency.

(d) *Separators*

Before the fluid enters the MHD generator, the gas or vapor part of the fluid should be separated from the liquid. Two principles can be applied:

1. In a condenser the vapor phase is reduced to its liquid state by heat rejection, which automatically condenses all the vapors [69,76] in a two-component cycle. A two-phase one-component MHD generator that condenses the vapor at the inlet of the generator duct has been proposed [88]. Cool liquid is injected into the fluid-flow stream in the condensing ejector system, modifying the fluid flow and pressure simultaneously in accordance with cycle requirements [78]. A special economizer transfers its undesired heat energy to a steam cycle in a combination MHD and commercial steam-generator plant [62].
2. Density differences between gaseous and liquid phases can also be used for separation. Here the main flow direction is diverted against a knife-edge separator where the liquid inertia drives the fluid in the least-diverted direction under the knife edge, and the gaseous phase follows the duct above the knife edge. However, the high separation efficiency of 99% means high friction losses (up to 60%) in this type of a separator [46,52,55,84,89,99].

(e) *Diffusers*

Diffusers convert the fluid-flow velocities (after the fluid leaves the MHD generators) to pressure energy that can either eliminate or reduce pumping requirements.

5-8.6 *Experimental MHD and MPD Generators*

The largest units in the United States are built by Avco Corp. [61,87] to study MPD cycles and collect data for component designs. Faraday-mode operation produced 23,000 kw at 1000 volts. A smaller generator produced 1 Mw at 1000 volts in the Faraday mode and 930 kw at 2800 volts in the Hall mode for 10 to 15 sec duration. Jet Propulsion Laboratory built several test generators, one for direct current [46,52,84] with 10.8 kw, 0.59 volt, output and others for alternating current; their loads were 5 kw [77,92], 50 kw [58,92,95,100], and 1 kw [59,91]. These generators performed a total of 40 runs with 2 to 4 min duration. Presently a 300-kw unit is in the design stage. Argonne National Laboratory has built experimental test loops to gain theoretical and practical design information for d-c [43,53,89] and a-c [64, 66,89] generators. Atomics International built various MHD a-c-type generators; one unit produced 1840 kw at 215 volts [62,101], and another produced 7 kw at 200 volts [63]. Brookhaven National Laboratory reported on a-c test loops [67] studied to prove the feasibility of liquid-metal piston-type MHD generators [69,76]. The U.S.S.R. has a complete power plant in operation using a seeded MPD generator [102].

5-8.7 *MHD Bearings*

There is a strong trend toward increasing the operating temperatures of nuclear-reactor-powered generators up to the material limiting levels, approaching 2000°F, to achieve the best thermodynamic efficiency and to reduce the weight-to-power ratio for aircraft and spacecraft. Any rotating component in these systems requires bearings capable of operating at high temperatures. A 600°F lubricant temperature is the approximate limit for long-term bearing operations using silicon-oil-base lubricants, and 800°F is the maximum for short-term operation. Use of the MHD effect to develop liquid-sodium or NaK-lubricated bearings for very high temperature operation has been investigated recently.

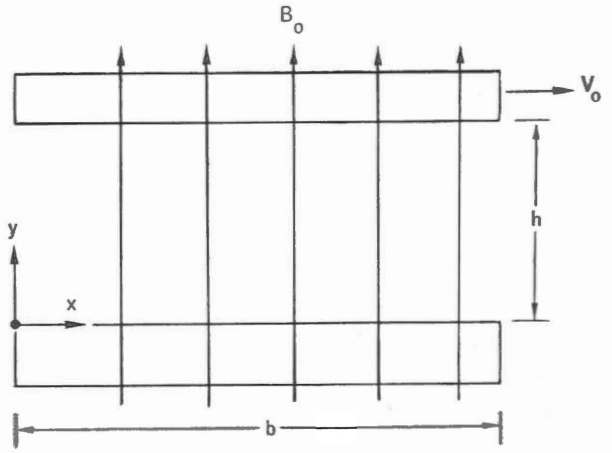

Fig. 5.32 - Basic MHD bearing configuration.

It is known from the MHD pump effect that the pressure of an electrical current conducting fluid can be increased if the fluid is exposed to a magnetic field. A local pressure gradient that increases the load-carrying capacity of the liquid-metal film can be developed.

Design considerations are based on the Navier-Stokes hydraulic equation [103,104]

$$\rho\frac{dv}{dt} = -\frac{dp}{dx} + \mu\left(\frac{\partial^2 v}{\partial x^2} + \frac{\partial^2 v}{\partial y^2}\right) \qquad (5.49)$$

where ρ = fluid density
v = fluid velocity
t = time
p = fluid pressure
x = position dimension in the direction of flow (Fig. 5.32)
y = position dimension in direction of fluid gap
μ = fluid viscosity

If we assume well-developed laminar flow, the velocity gradient is negligible in the x direction, and the equation reduces to:

$$\frac{dp}{dx} = -\mu\frac{d^2v}{dy^2} \qquad (5.50)$$

If this is combined with the x directional component of the Lorentz body force [105],

$$F_x = -\frac{1}{C} j_z B_0 \qquad (5.51)$$

and, with Ohm's law applied to the fluid stream,

$$j = \sigma(E + VB_0) \qquad (5.52)$$

where j = electrical current density in the fluid
E = electrical field potential
B_0 = magnetic flux applied across the fluid
σ = electrical conductivity of the fluid

Then the general MHD equation is

$$-\frac{dp}{dx} + \mu\frac{\partial^2 y}{\partial y^2} - j_z B_0 = 0 \qquad (5.53)$$

If we use the dimensionless quantities

$$M = B_0 h\sqrt{\sigma/\mu} = \text{Hartmann number} \qquad (5.54)$$

(considered as the MHD Reynolds number),

$$P = \frac{h^2 p}{\mu v_0 b} \qquad (5.55)$$

$$\eta = \frac{y}{h} \qquad (5.56)$$

$$\xi = \frac{x}{b} \qquad (5.57)$$

and

$$U = \frac{v}{v_0} \qquad (5.58)$$

and apply proper boundary conditions, we can derive the different MHD bearing design equations. The bearing load, the friction force acting on the moving part, and the necessary fluid flow rate can be calculated from the equations derived in Refs. 106 and 107. Reference 107 derives a group of equations stating that a nonuniform (gapped) magnetic field bearing has a higher load capacity and smaller friction force than the MHD bearing with constant magnetic flux.

Further improvement in bearing-load capacity and friction-loss reduction can be achieved with squeeze-film MHD bearings where two magnetic fields generate opposing pressures, increasing the lubricating film thickness. Design data are available in Refs. 108 and 109 for sodium at 1000°F.

The previous references treated the liquid-metal bearing theory based on infinite length in one direction. Kuzma [110,111] derived design equations based on commercial-type journal bearings by modifying geometrical and boundary conditions accordingly, including considerations of eccentricity. He referred to bearings for the cryogenic range where the high-coil current density provides very high magnetic-flux levels [110].

Transferring MHD bearing principles to thrust bearings, Kuzma and co-workers [112,113] described experiments showing close agreement with theoretical calculations of a one-step, self-acting, circular thrust bearing.

At the present time all the tests on MHD bearings have been performed at laboratory conditions. Field-type application tests are now in process. Results of bearing-material compatibility tests are detailed in Vol. IV, Chap. 2.

5-8.8 *Other MHD Applications*

Hydromagnets [114-116] utilize the low electrical resistivity and high thermal conductivity of silver, sodium, and NaK to generate magnetic fields above 10^5 gauss. Hydraulic pressure is used to force the liquid conductor radially inward through the space between two perforated coaxial cylinders placed in an axial magnetic field (Fig. 5.33).

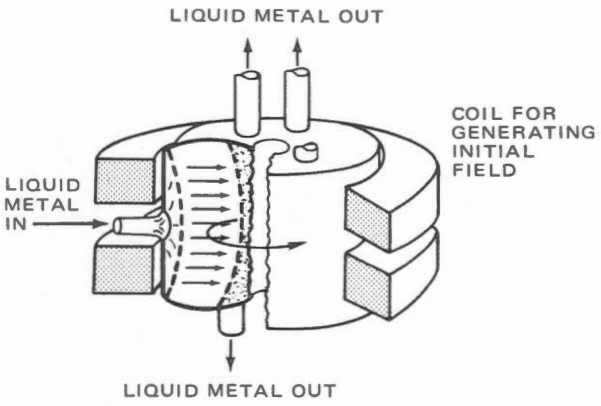

Fig. 5.33 - Compressing magnetic field.

The tangential current induced by the moving conductor generates a secondary magnetic field that strengthens the primary; thus the device acts as a self-exciting, internally short-circuited homopolar generator. This type of hydromagnet can be operated continuously or on a transient basis; in the latter case it acts like a chemical explosive. Theoretical calculations [116] showed that for continuous operation the magnetic Reynolds number (Re_m) and the ratio of the inner to the outer cylinder radius have considerably stronger effect than the hydraulic Re. If $Re_m \ll 1$, the amplification is a quadratic function of the radius ratio. The energy dissipation in the magnet depends on the square of the amplification and on the hydraulic Re.

5-9 OPTICAL APPLICATIONS

Some applications of liquid metals in connection with optical phenomena are:

1. Electrical lamps filled with low-pressure sodium vapor generate most of their light energy at the sodium *D* lines, to which the eye is very sensitive. This type of lamp can be used for highway lighting with good economy [21,117].
2. Some elements such as gold, copper, or calcium, alloyed with sodium or potassium can be used as photosensitive cell materials [2].
3. References 118 and 119 describe flame-photometric methods using alkali metals and analyzing alkali metals.
4. Sodium and potassium vapors released from rockets over 200 km above the earth at evening twilight conditions made it possible to measure wind velocities and directions. The sunshine reflected from the vapor clouds could be photographed with excellent results against the dark background of space. These photographs allowed the calculation of sodium and potassium vapor diffusion coefficients at high altitudes [120-122].

5-10 CHEMICAL APPLICATIONS

Since the first industrial production of sodium and NaK alloys, many patents and chemical procedures have been established based on their application. Some chemical applications of interest are discussed in the following text; sufficient references are given to permit further investigation by the reader.

5-10.1 *Inorganic Applications*

Sodium was used for the reduction of oxides in the production of industrial aluminum. This process was subsequently replaced by Hall's electrolytic aluminum-producing method [2]. Similarly, sodium is used in the production of industrial titanium [2].

In spacecraft sodium superoxide is utilized in the generation of oxygen for life support [123].

Sodium is used for gold production in small quantities [124].

Sodium is added to mercury to increase its wetting properties with most of the precious metals. Similar results are obtained when small quantities of sodium or potassium are added to plating materials.

Metal surfaces are prepared for plating and for chemical etching by the deoxidizing action of the liquid metals.

5-10.2 *Organic Applications*

The largest quantity of sodium in a single commercial application is used in manufacturing tetraethyl lead. This compound is used as an antiknock component in fuels used for internal-combustion engines.

Sodium can dehydrate certain tertiary (and higher grade) alcohols and ether compounds. In the presence of ammonia, sodium can produce hydrocarbons such as benzene, toluene, and xylene from alcohols. Alkoxides formed in the presence of sodium are reagents that produce electrodes for electrolysis from sodium amalgam and carbon. Alkoxides are reagents for producing sodium cyanate, which is used for case hardening of the surface of steel products [124].

Sodium-potassium alloy (NaK) mixed with carbon tetrachloride or with chloroform forms a strong explosive compound [2].

Alkoxides are the reagents used in the manufacturing of shortenings from lard and in the production of water-soluble fats and are the intermediate reagents in pharmaceutical processes such as for barbiturates, sulfa drugs, and antipyrene [124].

Sodium compounds are used as bleaching agents for textiles and for pulps [124]. Alkoxides represent an important part in the artificial indigo (blue dye) production.

Sodium is the polymerization-controlling reagent in rubber production and is used in the production of artificial rubber, called Buna ("bu" comes from butadiene and "na" is the chemical symbol for sodium).

A sodium-containing capsule included in a motor-lubrication loop extends the active life of the oil because of the deoxidizing effect of sodium [125].

Mixing sodium in glass can modify the optical properties of the glass [126,127].

A desalination process has been developed using sodium compounds [24].

5-11 SCIENTIFIC APPLICATIONS

During the preliminary phase of nucleic science, the alkali metals, mainly sodium, occupied an important position in the following areas: (1) its spectral lines are the basis for investigations for spectrum analysis and for chemical analyses; (2) its X-ray photography has given information regarding atomic, molecular, and crystalline structures; (3) sodium is an element that can be used in connection with investigations of quantum physics [128-136]; (4) sodium is among those elements studied to allow the prediction of heat and electrical coefficients of materials at high temperatures before actual measurements are made [137].

REFERENCES

1. L. Rosenblum, Liquid Metal Technology, in *Conference on New Technology, Cleveland, Ohio, June 4-5, 1964*, Report NASA-SP-5015, pp. 97-103, National Aeronautics and Space Administration, 1964.

2. M. Sittig, *Sodium, Its Manufacture, Properties and Uses*, Reinhold Publishing Corporation, New York, 1956.

3. G.M. Grover, T.P. Cotter, and C.F. Erickson, Structure of Very High Thermal Conductance, *J. Appl. Phys., 35*: 1990-1991 (1964).

4. M. Schindler and G. Woessner, Theoretical Considerations on Heat Transfer in Heat Pipes, *Atomkernenergie, 10*: 395-398 (Sept.-Oct. 1965).

5. T.P.Cotter, *Theory of Heat Pipes*, USAEC Report LA-3246, Los Alamos Scientific Laboratory, Feb. 23, 1965.

6. J.E. Kemme, *Heat-Pipe Capability Experiments*, USAEC Report LA-DC-7938, Los Alamos Scientific Laboratory, 1965.

7. S. Frank, J.T. Smith, and K.M.

Taylor, *Heat Pipe Design Manual*, Report MND-3288, Martin-Marietta Corp., February 1967.

8. J.E. Kemme, Heat-Pipe Capability Experiments, in *Proceedings of the Joint Atomic Energy Commission/Sandia Laboratories Heat-Pipe Conference, Albuquerque, N. Mex., June 1, 1966*, USAEC Report SC-M-66-623, Vol. I, pp. 11-26, Sandia Corp., October 1966.

9. L.S. Langston and H.R. Kunz, Liquid Transport and Heat-Transfer Properties of Heat-Pipe Wicking Materials, in *Proceedings of the Joint Atomic Energy Commission/Sandia Laboratories Heat-Pipe Conference, Albuquerque, N. Mex., June 1, 1966*, USAEC Report SC-M-66-623, Vol. I, pp. 45-46, Sandia Corp., October 1966.

10. Los Alamos Scientific Laboratory, Heat Pipe Systems, in *Space Electric Power R and D Program. Quarterly Status Report for the Period Ending Jan. 31, 1968*, USAEC Report LA-3881, pp. 3-7, Feb. 21, 1968.

11. W.A. Ranken and J.E. Kemme, *Survey of Los Alamos and Euratom Heat-Pipe Investigations*, USAEC Report LA-DC-7555, Los Alamos Scientific Laboratory, 1965.

12. R. Ruehle et al., Employment of Heat Pipes for Thermionic Reactors, *Atomkernenergie, 10*: 399-404 (Sept.-Oct. 1965).

13. J. Bohdansky, C.A. Busse, and G.M. Grover, *The Use of a New Heat Removal System in Space Thermionic Power Supplies*, Report EUR 2229.e., European Atomic Energy Community, 1965.

14. Los Alamos Scientific Laboratory, *Quarterly Status Report on Advanced Reactor Technology (ART) for Period Ending Jan. 31, 1966*, USAEC Report LA-3482, p. 64, February 1966.

15. Los Alamos Scientific Laboratory, *Quarterly Status Report on Advanced Reactor Technology (ART) for Period Ending Oct. 31, 1966*, USAEC Report LA-3625, p. 21, November 1966.

16. E.E. Bisson and W.J. Anderson, *Advanced Bearing Technology*, Report NASA-SP-38, National Aeronautics and Space Administration, 1964.

17. W. Markert, Jr. and K.M. Ferguson, Use of Rolling Contact Bearings in Low Viscosity Liquid Metal Lubricants, *Lubric. Eng. 13*(5): 285-290 (1957).

18. D.B. Vail, *The Performance of Tungsten Carbide Journal Bearings Operating in Liquid Metals*, USAEC Report KAPL-1079, Knolls Atomic Power Laboratory, Jan. 25, 1954.

19. C.W. Sprague, *Gas-Generation Technique for Recovering Submerged Objects*, USAEC Report SC-RR-65-380, Sandia Corp., September 1965.

20. R.C. Kumpitsch, *Research on Liquid Metals as Power Transmission Fluids. Progress Report No. 3, Mar. 1, 1959 to June 1, 1959*, USAEC file No. NP-8457, General Electric Company, Apr. 20, 1960.

21. R.C. Kumpitsch, Research on Liquid Metals as Power Transmission Fluids, in *Progress Report No. 4, June 1, 1959 to Feb. 1, 1960*, USAEC file No. NP-8458, General Electric Company, Apr. 20, 1960.

22. J.R. Granan and R.C. Kumpitsch, *Pumps for Liquid Metal Flight Controls*, Paper 66-FE-20, American Society of Mechanical Engineers, May 1966.

23. J.R. Granan and R.C. Kumpitsch, Liquid Metal Hydraulic System, *Design News, 20*: 122 (1965).

24. C.B. Jackson and J.W. Mausteller, Liquid Metals - Their Properties, Handling, and Applications, in *Modern*

Materials, Advances in Development and Applications, H.H. Hausner (Ed.), Vol. 2, pp. 401-452, Academic Press, Inc., New York, 1960.

25. J.R. Granan et al., Liquid Metal Systems for Flight Control Nearing Test Systems, *Space/Aeronautics, 46*: 87 (August 1966).

26. J.L. Bloom and J.B. Weddell, Thirteen-Watt Isotope Powered Thermoelectric Generators for Space and Lunar Impact Missions, in *Space Power Systems*, N.W. Sneider (Ed.), Vol. 4, p. 485, Academic Press, Inc., New York, 1961.

27. *Wall Street Journal*, Electrical Cable Using Sodium as Conductor, Feb. 2, 1966.

28. Nacon Corporation, *Plastic-Insulated Sodium Power Cables*, sales brochure, Boston, Mass.

29. C.E. Taylor and R.F. Post, *The Design of Large Cryogenic Magnet Coils, Paper No. 2*, USAEC Report UCRL-5631-T, Lawrence Radiation Laboratory, Oct. 30, 1959.

30. Sodium Conductors, *Prod. Eng.*, p. 32, Jan. 31, 1966.

31. C.E. Taylor and R.L. Nelson, *Test Results for a 7 1/8-Inch ID × 12-Inch-Long Sodium Cryogenic Coil*, USAEC Report UCRL-7401, Lawrence Radiation Laboratory, June 19, 1963.

32. J.E. Hove and W.C. Riley, *Ceramics for Advanced Technologies*, John Wiley & Sons, Inc., New York, 1965.

33. L. Rosenblum, Liquid Metals for Aerospace Electric-Power Systems, *J. Metals, 15*(9): 641 (1963).

34. A.J. Ulrich, Evaluation of a Thermionic Diode for Space Power Using a Liquid Metal Electron Collector, *Trans. Amer. Nucl. Soc., 7*: 377-378 (1964).

35. P.R. Hill and A.J. Gietzen, Analytical Study of Power Matching in Thermionic Reactor Cores, *Trans. Amer. Nucl. Soc., 7*: 378-379 (1964).

36. F.A. Ross and T.F. Plunkett, *Conceptual Design Analysis of a 5-Mwe Thermionic Reactor Space Propulsion Plant*, USAEC file No. NP-14985, Douglas Aircraft Co., February 1965.

37. R.E. Henderson, Liquid-Metal Cells, in *AMU-ANL Conference on Direct Energy Conversion, Argonne, Ill., Nov. 4-5, 1963*, USAEC Report ANL-6802, pp. 49-52, Argonne National Laboratory, December 1966.

38. N. Weber and J.T. Kummer, Sodium-Sulfur Battery, *Ford Science Front*, October 1966.

39. H.H. Hoehn, D. Levine, and A. Garcia, *Alkali Metal Arc Tunnel*, Report 129, U.S. Naval Ordnance Laboratory, White Oak, Md., NOLTR-64-82, August 1964.

40. A.E. Mikelson, Use of Stray-Field Pumps for Mixing of Liquid Metals, in *Problems of Magnetohydrodynamics and Plasma Dynamics. Proceedings of the Conference of Magnetohydrodynamics, Riga, July 2-10, 1958*, USAEC Report AEC-tr-4509, pp. 264-269, 1959.

41. M.G. Rezin, Construction of a Yoke Stator for Induction Mixing of Metals in Arc Furnaces, in *Problems of Magnetohydrodynamics and Plasma Dynamics. Proceedings of the Conference of Magnetohydrodynamics, Riga, July 2-10, 1958*, USAEC Report AEC-tr-4509, pp. 270-276, 1959.

42. *American Institute of Physics Handbook*, McGraw-Hill Book Company, Inc., New York, 1963.

43. M. Petrick, Liquid Metal MHD Topping Cycles, *Power Reactor Technol., 8*(4): 199-209 (Fall 1965).

44. A.W. Rowe and J.L. Kerrebrock,

Nonequilibrium Electric Conductivity of Two-Phase Metal Vapors, *AIAA (Amer. Inst. Aeronaut. Astronaut.) J.*, *3*: 361-363 (1965).

45. J.M. Smith, Nonequilibrium Ionization in Wet Alkali Metal Vapor, *AIAA (Amer. Inst. Aeronaut. Astronaut.) J.*, *3*(4): 648 (1964).

46. D.G. Elliott, DC Liquid-Metal MHD Power Generation, *AIAA (Amer. Inst. Aeronaut. Astronaut.) J.*, *4*(4): 627-634 (1966).

47. G.W. Sutton, H. Hurwitz, Jr., and H. Poritsky, Electrical and Pressure Losses in an MHD Channel Due to End Current Loops, *Amer. Inst. Elec. Eng. Trans.*, *80*(58): 685-695 (1962).

48. G.W. Sutton, *The Theory of Magnetohydrodynamic Power Generators*, General Electric Company, December 1962.

49. G.W. Sutton and A. Sherman, *Engineering Magnetohydrodynamics*, McGraw-Hill Book Company, Inc., New York, 1965.

50. L.G. Hays and D.J. Cerini, *Liquid Metal MHD Power Conversion*, Space Program Summary No. 37-40, Vol. 3, pp. 214-217, Jet Propulsion Laboratory, January 1968.

51. Argonne National Laboratory, *Reactor Development Program Progress Report, February 1964*, USAEC Report ANL-6860, Mar. 15, 1964.

52. D.G. Elliott, Liquid Metal MHD Power Conversion for Space, CONF-NEREM-TPM-1 (1965).

53. M. Petrick and K.Y. Lee, *Performance Characteristics of a Liquid-Metal MHD Generator*, USAEC Report ANL-6870, Argonne National Laboratory, July 1964.

54. K.A. Sense and G.H. Gelb, Cycle Analyses for Liquid Metal Power Conversion Systems Using a Bifluid MHD Generator, *AIAA (Amer. Inst. Aeronaut. Astronaut.) J.*, *5*(10): 1818 (1966).

55. M. Petrick and K.Y. Lee, *Liquid MHD Power-Cycle Studies*, USAEC Report ANL-6954, Argonne National Laboratory, June 1965.

56. E.S. Pierson and W.D. Jackson, *Channel-Wall Limitations in the MHD Induction Generator*, USAEC Report ANL-7148, Argonne National Laboratory, March 1966.

57. W.D. Jackson, E.S. Pierson, and R.P. Porter, Design Considerations for MHD Induction Generators, in *Magnetohydrodynamic Electrical Power Generation*, Proceedings of an International Symposium, Paris, July 6-11, 1964, European Nuclear Energy Agency, Paris, 1964.

58. D.G. Elliott and D. Cerini, *Liquid MHD Power Conversion*, Space Program Summary No. 37-39, Vol. 4, p. 117, Jet Propulsion Laboratory, May 1966.

59. D.G. Elliott, D. Cerini, and L. Hays, *Liquid MHD Power Conversion*, Space Program Summary No. 37-42, Vol. 4, p. 120, Jet Propulsion Laboratory, November 1966.

60. D. Jackson, Recent Developments in Closed-Cycle Plasma MHD Systems, *Power Reactor Technol. Reactor Fuel Process.*, *10*(2): 136 (1967).

61. J. Moszynski, Recent Developments in Open-Cycle MHD Power Systems, *Power Reactor Technol. Reactor Fuel Process.*, *10*(1): 20 (1966/67).

62. L.L. Prem, Analytical and Experimental Results of the Fluid Metal MHD Power Conversion Program, in *Electricity from MHD*, Symposium Proceedings, Salzburg, July 4-8, 1966, International Atomic Energy Agency, Vienna, 1966 (STI/PUB/128).

63. L.L. Prem, L.L. Wang, and S.J. Duszinsky, MHD Induction Generator and Its Projected Use in Central Stations, paper presented at the Winter Power Meeting, New York, Jan. 29-Feb. 3, 1967, Institute of Electric and Electronic Engineers.

64. Argonne National Laboratory, MHD AC Generator, Flashing Cycle, in *Reactor Development Program Progress Report, January 1964*, USAEC Report ANL-6840, pp. 85-87, Feb. 15, 1964.

65. Argonne National Laboratory, MHD Power Generation, Jet Pump Studies, in *Reactor Development Program Progress Report, June 1964*, USAEC Report ANL-6912, p. 88, July 21, 1964.

66. Argonne National Laboratory, *Reactor Development Program Progress Report, August 1965*, USAEC Report ANL-7090, Sept. 21, 1965.

67. J.R. Powell et al., A Liquid Metal Piston MHD Generator for Liquid Metal Rankine Cycles, *Trans. Amer. Nucl. Soc.*, *7*(2): 532 (1964).

68. J.R. Powell, J.P. Palmer, M.S. Zucker, W.W. Becker, and M. Maresca, *Summary of Direct Conversion Work*, USAEC Report BNL-8199, Brookhaven National Laboratory, March 1964.

69. J.R. Powell, M. Zucker, W. Becker, J. Palmer, and D. Findelstein, Liquid Metal Piston MHD Generator, in *Nuclear Engineering Department Annual Report, Dec. 31, 1964*, USAEC Report BNL-900, pp. 21-25, Brookhaven National Laboratory.

70. U.S. Atomic Energy Commission, *Fundamental Nuclear Energy Research*, 1964, Special Report, Division of Plans and Reports, Superintendent of Documents, U.S. Government Printing Office, Washington, 1965.

71. M. Zucker, J. Powell, J. Palmer, and A. Potter, The Solid Piston MHD Generator, in *Nuclear Engineering Department Annual Report, Dec. 31, 1964*, USAEC Report BNL-900, pp. 24-25, Brookhaven National Laboratory.

72. L.G. Bezusy, Electrical Parameters of a Synchronous MHD Generator with Pulsating Electrical Conductivity of the Medium, in *Electricity from MHD*, Symposium Proceedings, Salzburg, July 4-8, 1966, International Atomic Energy Agency, Vienna, 1966 (STI/PUB/128).

73. C. Pavlin and L. Pascual, Application of Fluid Switching to MHD Energy Conversion, in *Electricity from MHD*, Symposium Proceedings, Salzburg, July 4-8, 1966, International Atomic Energy Agency, Vienna, 1966 (STI/PUB/128).

74. E. Brocher and J.L. Chevalley, An AC MHD Generator with Pulsating Flow in a Preheated Gas, in *Electricity from MHD*, Symposium Proceedings, Salzburg, July 4-8, 1966, International Atomic Energy Agency, Vienna, 1966 (STI/PUB/128).

75. H.E. Weber and C.H. Marston, MHD with Liquid Metal, *Mech. Eng.*, *86* (8): 34-37 (1964).

76. V.J. Ibberson and D. Harris, Non-Steady Modulated MHD Systems, in *Electricity from MHD*, Symposium Proceedings, Salzburg, July 4-8, 1966, International Atomic Energy Agency, Vienna, 1966 (STI/PUB/128).

77. D. Elliott et al., *Liquid MHD Power Conversion*, Space Program Summary No. 37-37, Vol. 4, p. 118, Jet Propulsion Laboratory, 1966.

78. M. Petrick, Liquid Metal MHD, *IEEE (Inst. Elec. Electron. Eng.) Spectrum*, *2*(3): 137 (1965).

79. Argonne National Laboratory, MHD-AC-Generator Flashing Cycle, in *Reactor Development Program Progress*

Report, June 1964, USAEC Report ANL-6912, p. 88, July 21, 1964.

80. R.R. Barthelemy and B. Stephan, Experimental Evaluation of MHD Generators Operating at High Hall Coefficients, in *Electricity from MHD Generators*, Symposium Proceedings, Salzburg, July 4-8, 1966, International Atomic Energy Agency, Vienna, 1966 (STI/PUB/128).

81. F.H. Shair and F. Cristinzio, *Theoretical Performance for MHD Generators Utilizing Non-Equilibrium Ionization in Pure Alkali Metal Vapor System*, Report R62SD94, General Electric Company, January 1963.

82. R. Radebold, *Magnetohydrodynamic (MHD) Impact Flow Tube. Report No. 1. Introduction of the Project, Problem Proposal for the Investigation*, USAEC Report ANL-Trans-38, translated from German by E.K. Wilip, Argonne National Laboratory, May 13, 1963.

83. R. Radebold, H. Lang, and T. Schulz, Energy Conversion with Liquid Metal Working Fluids in MHD Staustrahlrohr, in *Electricity from MHD*, Symposium Proceedings, Salzburg, July 4-8, 1966, International Atomic Energy Agency, Vienna, 1966 (STI/PUB/128).

84. D.G. Elliott et al., *Liquid Metal MHD Power Conversion*, Paper 64-760, American Institute of Aeronautics and Astronautics, 1966.

85. Argonne National Laboratory, *Reactor Development Program Progress Report, September 1965*, USAEC Report ANL-7105, p. 67, Oct. 20, 1965.

86. G.A. Brown and E.K. Levy, *Liquid Metal MHD Power Generation with Condensing Ejector Cycles*, Paper SM-74/171, American Institute of Aeronautics and Astronautics, July 1966.

87. J. Teno, T.R. Brogan, and L.R. DiNanno, Hall Configuration MHD Generator Studies, in *Electricity from MHD*, Symposium Proceedings, Salzburg, July 4-8, 1966, International Atomic Energy Agency, Vienna, 1966 (STI/PUB/128).

88. L.L. Prem and W.E. Parkins, A New Method of MHD Power Conversion Employing a Fluid Metal, in *Magnetohydrodynamic Electrical Power Generation*, Proceedings of an International Symposium, Paris, July 6-11, 1964, European Nuclear Energy Agency, Paris, 1964.

89. M. Petrick, MHD Generators Operating with Two-Phase Liquid Metal Flows, in *Electricity from MHD*, Symposium Proceedings, Salzburg, July 4-8, 1966, International Atomic Energy Agency, Vienna, 1966 (STI/PUB/128).

90. E.S. Pierson, *A Hydromagnetic D-C Converter*, Report ASD-TR-61-102, Massachusetts Institute of Technology, January 1961.

91. D.J. Cerini and D.G. Elliott, Performance Characteristic of a Single-Wavelength Liquid Metal MHD Induction Generator with End-Loss Compensation, in *Eighth Symposium on Engineering Aspects of Magnetohydrodynamics, Stanford, Calif., Mar. 28-30, 1967*, pp. 503-510, Stanford University Press, Stanford, Calif., 1967.

92. D. Elliott et al., *Liquid MHD Power Conversion*, Space Program Summary No. 37-36, Vol. 4, p. 98, Jet Propulsion Laboratory, November 1965.

93. F. Engeln and W. Paschka, End Effects on the Linear Induction MHD Generator Calculated by Two-Sided LaPlace Transform, in *Electricity from MHD*, Symposium Proceedings, Salzburg, July 4-8, 1966, International Atomic Energy Agency, Vienna, 1966 (STI/PUB/128).

94. J.D. Welly, End Losses in MHD

Generators, in *Electricity from MHD*, Symposium Proceedings, Salzburg, July 4-8, 1966, International Atomic Energy Agency, Vienna, 1966 (STI/PUB/128).

95. D. Elliott et al., *Liquid MHD Power Conversion*, Space Program Summary No. 37-28, Vol. 4, p. 91, Jet Propulsion Laboratory, March 1966.

96. R. Barthelemy and C.E. Oberly, Optimum Magnets for MHD Generators, in *Electricity from MHD*, Symposium Proceedings, Salzburg, July 4-8, 1966, International Atomic Energy Agency, Vienna, 1966 (STI/PUB/128).

97. P.J. Novacki, *Recent Developments in the Direct Conversion of Heat into Electricity by Means of MHD Electrical Power Generation*, Paper SM-74/115, American Institute of Aeronautics and Astronautics, July 1966.

98. W. Peschka and C. Carpetis, On Some Aspects of the Use of a Cryogenically Cooled Primary-Windings System for an AC MHD Generator, in *Electricity from MHD*, Symposium Proceedings, Salzburg, July 4-8, 1966, International Atomic Energy Agency, Vienna, 1966 (STI/PUB/128).

99. A.G. Hammitt, Magnetohydrodynamic Liquid Metal Power Conversion Systems, in *Electricity from MHD*, Symposium Proceedings, Salzburg, July 4-8, 1966, International Atomic Energy Agency, Vienna, 1966 (STI/PUB/128).

100. D.G. Elliott, D.J. Cerini, and L.G. Hays, *Liquid MHD Power Conversion* Space Program Summary No. 37-40, Vol. 4, p. 63, Jet Propulsion Laboratory, July 1966.

101. L.L. Prem and T.C. Wang, Fluid Metal MHD-Steam Binary Cycle Power Generation, *Proc. Amer. Power Conf., 28*: 282-292 (1966).

102. L.L. Prem, C.J. Baroczy, J.A. Landoni, E.M. Mouradian, N.A. Marazzo, and M.J. D'Amico, *Technology of Magnetohydrodynamics, Final Technical Report*, Report AI-68-117, Atomics International, October 1968.

103. R.C. Binder, *Advanced Fluid Mechanics*, Vol. II, Prentice-Hall, Inc., Englewood Cliffs, N.J., 1958.

104. T.G. Cowling, *Magnetohydrodynamics*, Interscience Publishers, New York, 1957.

105. J.A. Shercliff, *A Textbook of Magnetohydrodynamics*, Pergamon Press, Inc., New York, 1965.

106. W.T. Snyder, The MHD Slider Bearing, *J. Basic Eng., 84*: 197 (1962).

107. D.C. Kuzma, The MHD Parallel Plate Slider Bearing, *J. Basic Eng., 87*: 778 (1965).

108. D.C. Kuzma, MHD Squeeze Films, *J. Basic Eng., 86*: 441 (1964).

109. F.T. Dodge, J.F. Osterle, and W.T. Rouleau, MHD Squeeze Film Bearings, *J. Basic Eng., 87*: 805 (1965).

110. D.C. Kuzma, The MHD Journal Bearings, *J. Basic Eng., 85*: 424 (1963).

111. D.C. Kuzma, The Finite MHD Journal Bearings, *J. Basic Eng., 86*: (1964).

112. D.C. Kuzma, E.R. Maki, and R.J. Donnelly, The MHD Squeeze Film, *J. Fluid Mech., 19*: 395-400 (1964).

113. E.R. Maki, D.C. Kuzma, and R.J. Donnelly, The MHD Thrust Bearing, *J. Fluid Mech., 30*: 83-95 (1967).

114. I.M. Kirko, *Magnetohydrodynamics of Liquid Metals*, special research report translated from Russian, Consultants Bureau Enterprises, Inc., New York, 1965.

115. H.H. Kolm, Hydromagnet, a Self Generating Liquid Conductor Electro Magnet, *Bull. Amer. Phys. Soc.*, *5*: 381 (1960).

116. O.K. Mawardi, On the Theory of Hydromagnet, *Bull. Amer. Phys. Soc.*, *5* 381 (1960).

117. Philips Research Laboratories, Semiconductors Cast New Light on an Old Problem, *Sci. Amer.*, *219*(1): 9 (1968).

118. J.A. Dean, Flame Photometric Methods in Metallurgical Analysis, *Analyst*, *85*: 621-629 (1960).

119. C.H. Ko and H.S. Cheng, Activation Analysis of Trace Impurities in Aluminum, *J. Chinese Chem. Soc.*, *12* (1-2): 39-50 (1965).

120. E. Manring, J. Bedinger, H. Knaflich, and R. Lynch, Upper Atmospheric Wind Profiles Determined from Three Rocket Experiments, in *IGY Rocket Report*, No. 7, pp. 49-60, National Academy of Science and National Research Council, 1963.

121. E. Manring and H. Knaflich, Some Measurements of the Coefficient of Diffusion in the Upper Atmosphere, in *IGY Rocket Report*, No. 7, pp. 61-71, National Academy of Science and National Research Council, 1963.

122. W. Nordberg and W. Smith, Grenade and Sodium Rocket Experiments at Wallops Island, Virginia, Book 1, pp. 119-63 (1963).

123. Soviets Get Oxygen from Superoxide, *Missiles and Rockets*, p. 33, Jan. 10, 1966

124. J.W. Mellor, *Comprehensive Treatise of Inorganic and Theoretical Chemistry*, Vol. II, Supplement II, Part I, John Wiley & Sons, Inc., New York, 1961.

125. Anonymous, *Chem. Trade J.*, *137*: 1192 (1955).

126. A. Lecreiner, *Chim. & Ind. (Paris)*, May Special No. 443-5.

127. H. Jebsen-Marwedel, *Glass Ind.*, *17*: 247-302 (1936).

128. A.V. Grosse, *Simple Relationship Between Electrical Conductivity of Liquid Metals and Temperature Over Their Entire Liquid Temperature Range*, USAEC Report TID-21647, Temple University, Nov. 22, 1964.

129. A.E. Powers, *Application of the Ewing Equation for Calculating Thermal Conductivity from Electrical Conductivity*, USAEC Report KAPL-2146, Knolls Atomic Power Laboratory, Apr. 7, 1961.

130. A.V. Grosse, *Thermal Conductivity of Liquid Metals Over Their Entire Range*, USAEC Report TID-21737, Temple University, Dec. 7, 1964.

131. R.D. Hudson, Measurement of the Molecular Absorption Cross Section and the Photoionization of Sodium Vapor Between 1600 and 3700 Å, *J. Chem. Phys.*, *43*(5): 1790-1793 (1965).

132. J.R. Christman and H.B. Huntington, Theory of Molten Alkali Alloys. I. NaK System, *Phys. Rev.*, *139*(1A): A83-A90.

133. D. Rozhdetvenskii, *Anomalous Dispersion of Sodium Vapor*, Report AD-453045, translated from German by S.W. Kellogg and Valip Zilius, Air Force Research Laboratories, September 1963.

134. C.C. Bradley, T.E. Faber, E.G. Wilson, and J.M. Ziman, A Theory of the Electrical Properties of Liquid Metals. II. Multivalent Metals, *Phil. Mag.*, *7*: 865-867 (1962).

135. J. M. Ziman, A Theory of the

Electrical Properties of Liquid Metals. I. The Uni-valent Metals, *Phil. Mag.*, *6*: 1013-1034 (1961).

136. R. Bowers, C. Legendy, and F. Rose, Oscillatory Galvanomagnetic Effect in Metallic Sodium, *Phys. Rev. Letters*, *7*: 339-341 (1961

7: 339-341 (1961).

139. P.L. Kirillov and N.S. Grachev, Determination of Sodium Vapor Pressure at Temperatures from 880 to 1300°C, *Inzh. - Fiz. Zh. Akad. Nauk Belorus. SSR.*, *2*(5): 3-7 (1959) (in Russian).

Index